

**Proceedings of the
International Symposium
on Advanced Radio Technologies/
ClimDiff 2008**

June 2-4, 2008

**Patricia J. Raush, General Chair
Kristen E. Davis, Publications**



**U.S. DEPARTMENT OF COMMERCE
Carlos M. Gutierrez, Secretary**

Meredith Attwell Baker, Acting Assistant Secretary
for Communications and Information

June 2008

DISCLAIMER

Certain commercial equipment, components, and software are identified to adequately present the underlying premises herein. In no case does such identification imply recommendation or endorsement by the National Telecommunications and Information Administration, nor does it imply that the equipment, components, or software identified is the best available for the particular applications or uses.

**INTERNATIONAL SYMPOSIUM
ON
ADVANCED RADIO TECHNOLOGIES/
ClimDiff 2008**

June 2-4, 2008 · Boulder, Colorado

Sponsored by:

National Telecommunications and Information Administration (NTIA)

Institute for Telecommunication Sciences (ITS)

NTIA Office of Spectrum Management (NTIA/OSM)

Union of Radio Science (URSI)

University of Colorado Department of Interdisciplinary Telecommunications

2008 ISART Technical Committee:

Patricia J. Raush, General Chair, NTIA/ITS

Timothy J. Riley, Technical Chair, NTIA/ITS

Timothy X. Brown, University of Colorado

Nicholas DeMinco, NTIA/ITS

Christopher Behm, NTIA/ITS

Paul McKenna, NTIA/ITS

Alakananda Paul, NTIA/OSM

Christopher Haslett, Ofcom

Carol Wilson, CSIRO

Merhala Thurai, Colorado State University

Bertram Arbesser-Rastburg, European Space Agency

Mike Willis, STFC Rutherford Appleton Laboratory

CONTENTS

ISART Technical Papers

<i>Frequency Use Status Investigation and Spectrum Utilization Metric</i> Sang Yun Lee, Seung Yeop Lee, Sung Hee An, Kyong Goo Park and Ok Suk Seo	1
<i>Spectrum Withdrawal and Relocation Algorithm in Korea</i> Min Ho Lee, Sang Yun Lee, Seung Yong Nam and Ghee Chil Son	7
<i>Radio Noise: Recent Considerations of Man-Made Noise</i> Les Barclay	17
<i>Dynamic channel model for static mobile terminals in indoor environments</i> Yoshichika Ohta and Teruya Fujii	22
<i>A Mobile-to-Mobile Propagation Measurement System</i> Robert T. Johnk, Paul McKenna, Peter Papazian, Nicholas DeMinco, Geoffrey Sanders, Heather Ottke, Brian Arment, Jason Shankel and David Strouse.	28
<i>A Methodology for Approximating BPSK Demodulator Performance in the Presence of Various Undesired Signals</i> Michael Cotton	36
<i>Using a split model improve the simulation of industrial environment propagation conditions</i> S. Benferhat and M. Misson	43
<i>Measurement data for improving ITU-R Recommendation P.1812</i> Mike Willis, Ken Craig and Nick Thomas	50
<i>Diffraction Model Comparisons Using the ITU-R 3K1 Correspondence Group Database</i> K.H. Craig, M.J. Willis, N.J. Thomas and S.A. Callaghan.....	58
<i>A Comparative Analysis of Multiple Knife-Edge Diffraction Methods</i> Nicholas DeMinco and Paul McKenna	65
<i>Estimating SRTM terrain height errors and their effect on profile interpretation</i> David Bacon.....	70
<i>Local Fading Characterization in Ground-Wave Propagation at MW Band</i> D. de la Vega, U. Gil, S. López, P. Angueira, I. Angulo, D. Guerra and J.L. Ordiales	75
<i>Digital Mobile Networks: Limitations and Possibilities</i> Christopher Haslett	83

<i>Deterministic Equations for Computer Approximation of ITU-R P.1546-2</i> Sid Shumate	86
<i>A Simplified Analytical Urban Propagation Model (UPM)</i> Chrysanthos Chrysanthou	96
<i>Radio Communications for Emergency Responders in High-Multipath Outdoor Environments</i> Kate A. Remley, Galen Koepke, Christopher L. Holloway, Chriss Grosvenor, Dennis G. Camell and Robert T. Johnk	106
<i>New Challenges in the Understanding Of Surface Wave Propagation</i> Les Barclay	112
<i>Polarization and Space Diversity Antenna Using 2 Inverted-F 1x2 Sub-Arrays for RFID Reader Applications</i> Jong-Sung Kim	118
<i>Modeling and Analysis of the Interference Potential of Cognitive Radio Devices to Wireless Microphones Operating in TV bands</i> Ramandeep S. Dhillon and Timothy X. Brown	123
<i>High-Resolution Propagation Measurements using Conventional EMC Test Antennas – A Numerical Study</i> Robert T. Johnk	133
<i>CW Vital Signs Detection with Ranging Capability</i> A. Wiesner	139
<i>Design and Implementation of a Portable Software Radio</i> Brian P. Dunn, Michael L. Dickens and J. Nicholas Laneman	145

ClimDiff Technical Papers

<i>Using Rain Microstructure Information from 2-D Video Disdrometer for Propagation Predictions at 20 GHz</i> M. Thurai, V. N. Bringi and G.J. Huang	152
<i>Four-Year Rain Attenuation Statistics of Ku-Band Up and Down Links Simultaneously Observed in Japan and Indonesia</i> Yasuyuki Maekawa, Yoshiaki Shibagaki, Toru Sato, Mamoru Yamamoto, Hiroyuki Hashiguchi and Shoichiro Fukao	161
<i>A Unified Method for the Prediction of Rain Attenuation in Slant Paths and Terrestrial Links Using the Full Rainfall Rate Distribution</i> L. A. R. da Silva Mello and M. S. Pontes	169

<i>Angular Dependence of Satellite Diversity Effects on the Attenuation Statistics Obtained from Ku and Ka Band Signals of the Geostationary Satellites in Japan</i> Yasuyuki Maekawa and Takeshi Hatsuda	177
<i>Implementing Adaptive Transmit Power Control in Fixed Terrestrial Links: Spectrum Management and Interference Issues</i> S. A. Callaghan, I. Inglis, P. Hansell	185
<i>Preliminary Analysis of Radiowave Propagation Data Using a Gigabit Radio Link Operating at 83.5 GHz Close to Oslo in Norway</i> Terje Tjelta and Tor Ove Breivik	195
<i>Micro Rain Radar Measurements of Rainfall in Madrid: First Results</i> Pilar García-Vila, Ana Benarroch, Pedro García, José M. Riera.....	201
<i>A Study on Formulating the Statistical Characteristics of the Rain Rate Duration</i> Akio Sato	208
<i>Statistics of Rainfall Rate Dynamics</i> Rubén Hernández, Ana Benarroch, Pedro García, José M. Riera	214
<i>Generating Year-Equivalent Databases of Fractally Synthesised Rain Rate Fields</i> S. A. Callaghan	220
<i>Preliminary Study of Rain Attenuation Time Series Synthesizers for Tropical and Equatorial Areas</i> Marcio Rodrigues, Guillaume Carrie, Laurent Castanet, Frédéric Lacoste and Luiz Silva Mello.....	230
<i>An Empirical Study of Location Variability for Mobile Systems</i> R.F. Rudd.....	238
<i>Wave Propagation over Irregular and Inhomogeneous Terrain</i> Mauro S. Assis and Jorge L. Cerqueira	246
<i>Anomalies in the Application of the Cascaded Knife-Edge Diffraction Model</i> Carol Wilson and Steve Salamon	252
<i>Reducing Discontinuity in Practical Prediction of Diffraction Loss in Irregular Terrain</i> Steve Salamon and Carol Wilson	259

Frequency Use Status Investigation and Spectrum Utilization Metric

Sang Yun Lee¹, Seung Yeop Lee¹, Sung Hee An¹, Kyong Goo Park², and Ok Suk Seo²

¹ Radio Spectrum Research Team, Korea Radio Promotion Agency (KORPA)
78 Garak-dong, Songpa-gu, Seoul, 138-803, Korea
Tel: +82-2-2142-2167, Fax: +82-2-2142-2155
e-mail: {sylee76, yeopcp, ash-iris}@korpa.or.kr

² Radio Environment Team, Central Radio Management Office (CRMO)
100, Garak-dong, Songpa-gu, Seoul 138-160, Korea
Tel: +82-2-3400-2333, Fax: +82-2-2142-2347
e-mail: {gyonggu, osseo}@kcc.go.kr

Abstract - In this paper, frequency use status investigation and spectrum utilization metric are considered as a basis of spectrum management for efficient use of spectrum resources. Frequency use status investigation through DB investigation and RF signal measurement is described and some results of Korea are presented. As spectrum utilization metric, M-SUE (Modified-Spectrum Use Efficiency) which unifies actual spectrum resource occupancy and spectrum efficiency in a single quantity is proposed, and spectrum efficiencies for simple cellular and relay radio system are also analyzed.

I. INTRODUCTION

As wireless communication technologies evolve and their applications become prevalent in almost areas, the demand for spectrum resources also grows rapidly. Nowadays it is widely acknowledged that frequency becomes scarce resource and which is demonstrated by several cases such as European 3G frequency auction, where 20MHz frequency band was priced up to multibillion-dollar.

There has been increasing concerns on solving frequency scarcity problem. As a technical measure, technologies with high spectral efficiency such as MIMO(Multiple Input Multiple Output) are being adopted in new standards and spectrum sharing technologies such as CR(Cognitive Radio) and UWB(Ultra Wideband) are being studied actively [1-3]. From the fact that nearly all demands are crowded under 3GHz band, technologies which enables to utilize higher frequency band are also being investigated [4].

Spectrum refarming (or redevelopment) is another measure to promote efficiency of spectrum resources. Spectrum refarming is defined as a combination of present and future administrative, financial and technical measures within the limits of frequency regulation in order to make a specified frequency band available for a different kind of usage or technology [5]. Though, there are many factors to be considered including technical advancement, public interests, law systems, industrial policy, etc., actual use status of

spectrum resources may be a fundamental basis in establishing spectrum refarming plan.

In this paper, frequency usage status investigation conducted by CRMO (Central Radio Management Office) and KORPA (Korea Radio Promotion Agency) under Korea Communications Commission (previously Ministry of Information and Communications) in 2007 is presented. As spectrum utilization metric, M-SUE (Modified-Spectrum Use Efficiency) which quantifies actual spectrum resource occupancy and spectrum efficiency in a single quantity is proposed and spectrum efficiencies for simple cellular and relay radio system model are analyzed.

The rest of paper is organized as follows. In section II, frequency use status investigations in Korea and part of their results are presented. Novel spectrum utilization metric, M-SUE and spectrum efficiencies for simple cellular and relay radio systems are considered in section III. Finally, conclusions are drawn in section IV.

II. FREQUENCY USE STATUS INVESTIGATION

Korean Radiowave Act states that frequency use status investigation can be conducted for the purpose of spectrum refarming and the frequency band can be refarmed when the use level of the frequency band is low. Though, in order to determine frequency band whose use level is low, there are many aspects to be

The publication of this paper does not indicate endorsement by the Korean Government or KCC (Korea Communications Commission).

investigated including not only technical but also social, economical aspects, in what follows, only technical aspect will be considered.

A. Radio Station Registration DB Investigation

As in many countries, radio station registration DB, which is called RBMIIS (Radio Broadcasting Management Integrated Information System), is operated in Korea. From this DB, we extracted statistics of radio stations and channel use status over all frequency range. For the convenience of analysis, the range of investigation frequency is divided into 25 sub bands mainly according to services and propagation characteristics in each sub band. Investigation items are listed in Table 1.

Table 1. RBMIIS investigation items

	Item	Description
Radio station usage status	Distribution by region	Number of radio stations registered in local communication office
	Distribution by operator	Number of radio stations by radio station operator
	Distribution by time	Temporal changes in the number of radio station
	Distribution by radio station type	Number of radio stations by the type of radio station
Channel usage status	Designation and actual usage status	Number of designated channels and actually used channel and their ratio
	Regional distribution	Number of channels by region
	Operator distribution	Number of channels by radio station operator
	Total bandwidth of each service	Total sum of bandwidth (reused frequency included)

According to the investigation results, the total number of radio station is 772,288 (cellular mobile stations are excluded.) and the number of designated frequency channel is 6,292 at June, 2007. The distribution of radio station by type and the distribution of channels by services are shown in Fig. 1 and Fig. 2, respectively. It is shown that the two-way radio station and land mobile station occupy over 60% of all radio stations and 89% of channels are used for terrestrial

service.

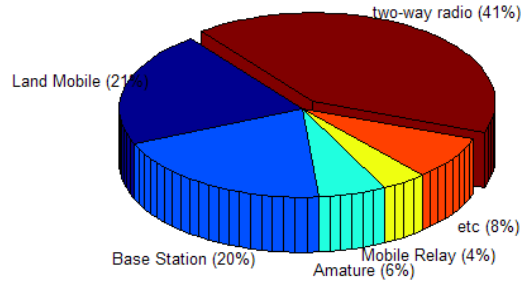


Fig. 1 Radio station usage status

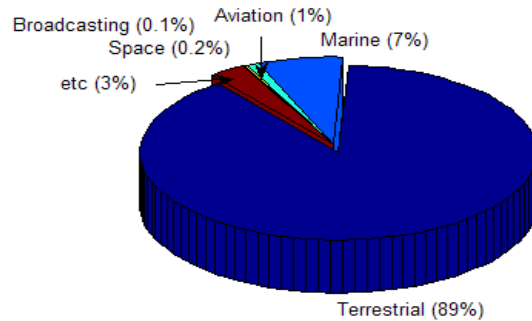


Fig. 2 Frequency channel usage status

Though the number of channels is counted in order to find out the proportion of actually used channels in all designated channels, it may seem inappropriate to consider the number of channels as a frequency usage metric because the number of frequency channel may vary with multiplexing technique even if the same amount of bandwidth is used. For example, in single carrier wideband systems such as DS-CDMA (Direct Sequence-Code Division Multiple Access) system, multiple communication channels are accommodated in the same frequency channel through multiplexing using orthogonal codes. Thus, another metric, e.g. bandwidth normalized by carrier frequency, may be considered as a good candidate for frequency usage status metric [6]. Detail results of frequency use status investigation in Korea can be seen in [7].

B. Spectrum Usage Measurement

In order to investigate actual spectrum usage status, spectrum usage measurement which investigates the temporal and spatial occupancy rate of frequency channels is also required. The measurement was carried out by using RMS (Radio Monitoring System) installed at 13 locations over the country. A vehicular monitoring system was also used at 10 locations in

order to cover regions where the coverage of the RMS does not reach and the density of radio stations are relatively high.

The occupancy of frequency channels is measured by sweeping all channels periodically. The shorter sweeping period (also called revisit time) is, the more measuring accuracy can be achieved due to the higher sampling rate for the measured frequency channel. From Nyquist theorem, in order to detect transmission length shorter than T_i , sweeping period should be shorter than $T_i/2$. Since the sweeping period of RMS system is limited approximately 1.2 seconds or 70,000 sweeps a day, RMS can detect signal whose transmission length is over 0.6 sec, which may be long enough to detect signals for conventional land mobile systems. This number of sweeps (or samples) is also sufficiently large enough to achieve 10% relative accuracy and a 95% confidence level [8].

A frequency channel is decided to be occupied when the received signal strength above a certain threshold level. Though determination of the threshold level is critical since it may affect measurement result significantly, a standardized threshold level model which fits well into measurement results has not been introduced yet. Thus, threshold levels were obtained by measuring noise level, i.e. field strength of unused frequency channels are measured at all measurement locations. Part of results is shown in Table 2.

Table 2. Average noise level (part) (unit: dB μ V/m)

Area	Band		
	300MHz	800MHz	900MHz
Seoul (Urban)	26.00	20.80	11.30
Seoul (Suburban)	4.63	4.75	6.23
Jeju (Urban)	16.79	15.47	14.52
Jeju (Suburban)	5.47	1.73	0.85
Daejon (Urban)	11.37	17.43	16.20
Daegu (Urban)	8.20	9.66	8.43

In Table 2, it is shown that noise levels are high at urban areas and low at suburban areas, which seems reasonable considering there are many noise sources around urban areas. However, dependency of frequency bands cannot be easily found because many factors such as the number of radio stations in the vicinity of the corresponding frequency band, their transmitting power, and service type etc, may contribute to noise level enhancement and these factors may not depend on frequency bands.

Table 3. Frequency occupancy rate

Service	Frequency Band (MHz)	Number of Channels	Occupancy Rate (%)
Pager	161-169	53	0.65
	318-321	384	0.25
	322-329	384	1.74
	923-925	72	2.16
TRS	371-400	146	11.13
	806-866	848	0.14
W-Data	898-900	160	0.01
	938-940	160	7.20
Total		2,207	

Table 3 shows measurement results of frequency occupancy rate. Since measured frequency bands were selected among bands considered as having low occupancy rate, all bands show low occupancy rate as expected. Furthermore, some bands shows significantly low occupancy approaching near 0% and these bands may be considered as candidates for spectrum refarming. Results in Table 3 also support the suggestion of using opportunistic communication techniques (e.g. cognitive radio) in order to solve spectrum resource scarcity problem [9].

III. SPECTRUM UTILIZATION METRIC

In order to identify the degree of efficient use of spectrum resources and to determine frequency bands where usage level is low based on frequency use status investigation of section II, spectrum utilization metric should be considered.

Spectrum resource (U) is generally defined as physical resources (frequency bandwidth (B), time (T), and geometric space (S)) which is used exclusively or denied to other users. Thus, the amount of spectrum resources is given by the product of these three quantities, i.e.,

$$U = B \times S \times T \quad (1)$$

which is called as spectrum usage factor or spectrum space, etc.

As a spectrum utilization metric, 'spectrum efficiency' was introduced [10]. In a sense that the term 'efficiency' is used to relate how much output can be produced based on a certain amount of input, spectrum efficiency can be defined as

$$\text{Spectrum Efficiency} = M / U \quad (2)$$

where M is useful effect and U is the amount of spectrum resources. Useful effect is commonly defined

as transferred information but this can be defined differently as the purpose of communication systems as shown below.

Since spectrum efficiency of (2) mainly depends on technologies systems adopted, spectrum efficiency of a frequency band becomes high if the system is designed in a spectrally efficient manner by means of mod/demod or multiplexing scheme, network configuration etc. If M is replaced by capacity, which can be obtained from Shannon theorem, spectrum efficiency may represent maximum system efficiency of a given network configuration [11].

Since the spectrum efficiency does not reflect the actual use of spectrum resources except M , however, it is difficult to be used by regulators as a metric for spectrum management which aims to promote efficient use of spectrum resources. Thus, modified spectrum utilization metric not only representing spectrum efficiency should be considered in order for regulator to use as a tool for spectrum management.

A. Modified Spectrum Use Efficiency (M-SUE)

Considering the role of government in spectrum use process, process of spectrum use can be decomposed into three steps. First, the government allocates spectrum resources to service providers, second, service providers deliver communication services to end users, finally, end-users use them. Fig. 3 shows the whole spectrum use process, where the amount of spectrum resources provided by government and used by service providers are denoted as U_g and U_a respectively.

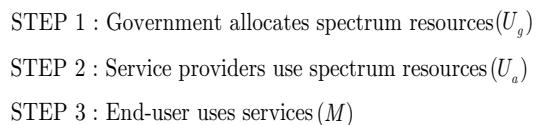


Fig. 3 Spectrum use process

Thus, metrics for efficiency measure of each step can be defined as follows. As a metric to measure the actual usage rate of spectrum resources, spectrum occupancy (η_{occ}) can be defined as

$$\eta_{occ} = U_a / U_g \quad (3)$$

where U_g is the amount of spectrum resources given by government and U_a is the amount of spectrum resources actually used by service provider. Spectrum efficiency (η_{eff}) also can be defined as the amount of

useful effect based on actually used spectrum resources, which is expressed as

$$\eta_{eff} = M / U_a \quad (4)$$

where M is useful effects resulted from the use of spectrum resources(U_a). As discussed above, η_{eff} mainly depends on the performance and network configurations of communication systems.

Thus, overall efficiency can be defined as

$$\eta = \eta_{occ} \eta_{eff} \quad (5)$$

We call this overall efficiency as modified spectrum use efficiency (M-SUE). It should be noted that any comparison of M-SUE should be performed only between radio systems providing identical radiocommunications services as is in spectrum efficiency [12]. This is because the purpose of systems for different services, e.g. land mobile radio system and radar system, are not commensurate with each other.

B. Spectrum Occupancy (η_{occ})

Using the definitions in (1) and (3), spectrum occupancy can be rewritten as

$$\eta_{occ} = (B_a / B_g)(S_a / S_g)(T_a / T_g) \quad (6)$$

where subscript a and g denotes ‘actually used’ and ‘provided by government’ respectively. Terms in (6) can be obtained from the result of spectrum use measurement. B_a can be simply calculated as

$$B_a = N_c \times B_c \quad (7)$$

where N_c is the number of occupied frequency channels and B_c is channel bandwidth. The value of S_a depends on transmission power, antenna pattern, propagation model, geographical feature, etc. T_a becomes frequency occupancy rate when setting T_a as 1.

C. Spectrum Efficiency (η_{eff})

Using the definitions in (1) and (4), spectrum efficiency can be rewritten as

$$\eta_{eff} = M / (B_a S_a T_a) \quad (8)$$

where M is useful effect, which can be defined differently as the purpose of systems in question. Since direct calculation of (8) is difficult in many cases, some manipulations according to network configurations can be considered.

1. Cellular Radio System

Spectrum efficiency of cellular system whose service area is S and bandwidth is B is given by

$$\eta_{\text{eff,cell}} = E_t / BS \quad (9)$$

where E_t (bps) is total average information rate originated in area S and can be expressed by

$$E_t = \rho SE \quad (10)$$

where ρ is average subscriber density (km^{-1}), A is cell area (km^2), and E is average information rate (bps) per subscriber. From eq. (9) and (10), spectrum efficiency of cellular system can be rewritten as

$$\eta_{\text{eff,cell}} = \rho E / B. \quad (11)$$

Since total traffic arose in a cell is limited by base station capacity, i.e.,

$$\rho AE \leq C_{\text{MAX}} \quad (12)$$

where C_{MAX} is capacity of base station, spectrum efficiency of cellular system is also limited as

$$\eta_{\text{eff,cell}} \leq C_{\text{MAX}} / BA. \quad (13)$$

From eq.(13), it can be seen that spectrum efficiency of cellular system can be increased by adopting technologies with high spectrum efficiency (C_{MAX} / B) or reducing cell area. This also means that there is tradeoff between spectrum and economical efficiency since reducing cell area may increase cost to install additional base stations.

In a similar manner of above, regional distribution of spectrum efficiency also can be calculated based on radio station distribution in a cell [13].

2. Point-to-Point (p-p) Relay Radio System

In case of p-p relay system, it is reasonable to consider useful effect as total distance over which the information is transferred because the purpose of relay system is to transfer information over long distance [12]. Thus, spectrum efficiency of p-p relay system can be defined as

$$\eta_{\text{eff,relay}} = E_r D / SB \quad (14)$$

where E_r is total transferred information rate, D is the distance over which the information is transferred. By using simple radio station installation model as in Fig. 4, sector area S where transmitted RF signal can cover can be obtained as

$$S = (1/2)R^2\theta_{\text{HP}} \quad (15)$$

where R is sector radius, θ_{HP} is half-power beamwidth. The sector radius can be computed by using propagation model as described in [12].

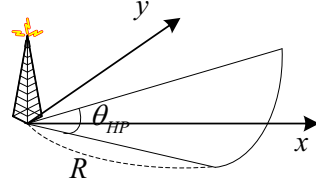


Fig. 4 Sector area of p-to-p relay radio system

Consider spectrum efficiency of a p-p relay radio system having $N(\geq 2)$ stations as in Fig. 5. For the simplicity of problem, we assume that $D = \sum_{i=1}^N R_i$, which is valid when $D \gg \{R_i\}_{i=1}^N$ and $\theta_1 = \dots = \theta_N = \theta$ without loss of generality.

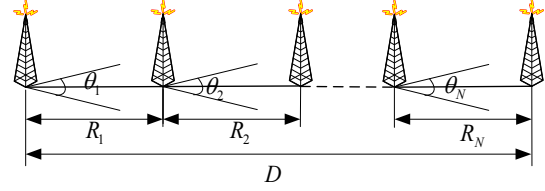


Fig. 5 Approximation of p-to-p relay radio system with $N(\geq 2)$ stations

Thus, spectrum efficiency of a p-p relay system with multiple stations is given by

$$\eta_{\text{eff,relay}} = \frac{E_r D}{SB} \cong \frac{2E_r (R_1 + R_2 + \dots + R_N)}{B\theta(R_1^2 + R_2^2 + \dots + R_N^2)}. \quad (16)$$

Using Cauchy-Schwarz inequality, $(\sum_{i=1}^N x_i y_i)^2 \leq (\sum_{i=1}^N x_i^2)(\sum_{i=1}^N y_i^2)$, and letting $x_i = 1$, $y_i = R_i$, eq. (16) yields

$$\eta_{\text{eff,relay}} \leq 2E_r / B\theta R_1 \quad (17)$$

where equality holds when $R_1 = \dots = R_N = D / N$. This means that maximum spectrum efficiency can be achieved when radio stations of given number N are installed at equi-distances. This also means that the spectrum efficiency of p-p relay system increases as the

distance between relay stations decreases, i.e. there is tradeoff between economical efficiency as in cellular systems.

IV. CONCLUSIONS AND FUTURE WORKS

In this paper, frequency use status investigation and spectrum utilization metric are considered as a basis of spectrum management for efficient use of spectrum resources. Frequency use status investigation through DB investigation and RF signal measurement is described and some results of Korea are presented. Measurement results of some bands show very low spectrum occupancy as reported other literatures [2, 9].

In order to incorporate investigation results (e.g. RF signal measurement results) into the traditional spectrum efficiency, M-SUE is proposed, which unifies actual spectrum resource occupancy and spectrum efficiency in a single quantity. Spectrum efficiencies for simple cellular and relay system model are analyzed, which shows that there is tradeoff between spectrum and economic efficiencies in network configuration aspect.

Considering that the aim of spectrum management is not only confined to maximize spectrum efficiency, M-SUE may be insufficient as spectrum utilization metric. Therefore, metric which quantifies economical or functional efficiencies should also be investigated [14, 15]. Though some metrics to evaluate economical and social benefit are considered in [7], e.g., spectrum resources' contribution in the revenue of industries or in decreasing price index, there are still much to be considered to evaluate the efficiency of spectrum resources and this may be why market based frequency management is introduced in many countries.

REFERENCES

- [1] D. Gesbert, M. Shafi, D. Shiu, P. Smith, and A. Naguib, "From theory to practice: an overview of MIMO space-time coded wireless systems," *IEEE J. Select. Areas Commun.*, pp.281-302, 2003.
- [2] Q. Zhao and B. M. Sadler, "A Survey of dynamic spectrum access," *IEEE Sig. Proc. Mag.* Vol. 24, pp.79-89, May 2007.
- [3] D. Porcino and W. Hirt, "Ultra-wideband radio technology: potential and challenges ahead," *IEEE Commun. Mag.*, vol 41, pp. 66-74, July, 2003.
- [4] B. Razavi, "Gadgets gab at 60 GHz," *IEEE Spectrum*, vol 45, pp. 46-58, Feb, 2008.
- [5] ECC Report 16, "Refarming and secondary trading in a changing radiocommunications world," Sept. 2002.
- [6] Ofcom, *Spectrum Framework Review*, 2004.
- [7] CRMO, KORPA, *Frequency Use Status Investigation* (in Korean), 2007.
- [8] Rec. ITU-R SM.1536, "Frequency channel occupancy measurements," 2001.
- [9] A. Ghasemi and E. Sousa, "Spectrum sensing in cognitive radio networks: requirements, challenges and design trade-offs," *IEEE Commun. Mag.*, vol 46, pp. 32-39, April, 2008.
- [10] L. Berry, "Spectrum metrics and spectrum efficiency : proposed definitions," *IEEE Trans. Electromagn. Compat.*, vol. EMC-19, no. 3, pp. 254-260, 1977.
- [11] M-S. Alouini and A. J. Goldsmith, "Area spectral efficiency of cellular mobile radio systems," *IEEE Trans. Veh. Tech.*, vol. 48, no. 4, pp 1047-1066, 1999.
- [12] Rec. ITU-R SM.1046-2, "Definition of spectrum use and efficiency of a radio system," 2006.
- [13] G. Chan and B. Brown, "A measure of spectrum utilization in land mobile bands," in *Proc. of Canadian Conference on Electrical and Computer Engineering*, 1996, May, pp. 52-55.
- [14] J. Robinson, "Spectrum allocation and economic factor in FCC spectrum management," *IEEE Trans. Electromagn. Compat.*, vol. EMC-19, no. 3, pp. 182-190, 1977.
- [15] J.W. Burns "Measuring spectrum efficiency - the art of spectrum utilization metrics", in *Proc. of IEE Conf. on getting the most out of radio spectrum*, 25 Oct. 2002, London, UK.

Spectrum Withdrawal and Relocation Algorithm in Korea

Min Ho Lee, Sang Yun Lee, Seung Yong Nam, and Ghee Chil Son
Radio Spectrum Resource Research Team, Korea Radio Promotion Agency
78, Garak-dong, Songpa-gu, Seoul, 138-803, Korea
Tel: +82-2-2142-2161, Fax: +82-2-2142-2155
e-mail: {ammi, sylee76, namsy, skc}@korpa.or.kr

***Abstract** - Due to the broadening of spectrum usage and development of new communication technologies, there are many on-going studies on how to secure radio spectrum resources. Spectrum withdrawal and relocation system went into effect in some advanced countries such as US, France and Japan. They have secured spectrum for the introduction of new radio-communication services(AWS, 4G etc). It was predicted at the ITU-R WP8F meeting(19th, France) that the future mobile communication spectrum needs of the 840MHz and 1,720 MHz bands will be used from the year 2010 and 2020. In Japan, it is foreseen in the Radio Vision Japan(2003, MIC) that the spectrum demands for the bands 340 MHz, 480 MHz, 1380 MHz will become necessary in 2008, 2010 and 2013. Spectrum planning is considered to be associated with the development of a national spectrum strategy and the spectrum strategy is normally expected to cover a period of 5 to 10 years (Rec. ITU-R SM.1603). However, the methods to secure radio spectrum for the timely introduction of newly developed radiocommunication services within 2 or 3 years after spectrum planning will be provided in this paper.*

I. Introduction

As a result of the rapid growth of wireless telecommunications, the radio spectrum came to play a big role in developing many new and technology-based telecommunications services. The demand for spectrum has been rapidly increasing with the growth in telecommunications services and radio technologies. However, as the radio spectrum is limited in amount though unlimited in value, every country is facing scarcity to become scarce of spectrum and eagers to maximize the efficiency of spectrum use. Recently, in order to resolve these problems, every country has moved towards market-based or market-oriented mechanism for spectrum management and spectrum management tools such as spectrum withdrawal and relocation.

At the last WRC-07, the band 450~470MHz (20 MHz) and 2.3~2.4GHz (100MHz) were allocated for 4G(IMT) on a global basis. Also, the band 790~862 MHz (72 MHz) was allocated for 4G(IMT) in Region 1 and the band 698~806MHz (108MHz) was allocated in both Region 2 and Region 3. The band 3.4~3.6GHz(200MHz), which is mainly used for communication and broadcasting relay, was also designated for 4G(IMT) in 8 countries in Asia, 80 countries in Europe, and 14 countries in American region. As the above bands has been allocated already for existing services, spectrum withdrawal and relocation may be performed and applied according to this paper.

Such international level studies and results related to spectrum withdrawal and relocation has been released by the ITU(Spectrum redeployment as a method of national spectrum management”, Rec. ITU-R SM.1603), ECC(Refarming and Secondary Trading in a Changing Radiocommunication World, ECC Report 16), etc.

The above reports recommend administrative, financial and technical measures for spectrum withdrawal and relocation.

License revocation is an administrative act of withdrawing rights of frequency use from a licensed user. However, it should be noted that such action in principle violates general principles of administrative law, forbidding withdrawal of privileges given to a legal or private person by a prior administrative act without good reason or compensation. Therefore, this is only acceptable when the early warning is given. With regard to financial measures, compensation for relocation is the underlying principle. As for technical tools, various methods are to be considered including sharing studies and retuning of new equipment. The most important factor in prompt relocation is to provide equivalent system(comparable capacity of systems) to existing services. It can be considered as a financial relocation tool.

The publication of this paper does not indicate endorsement by the Korean Government or KCC (Korea Communications Commission).

II. Concept of spectrum withdrawal and relocation

1. Definitions

- Spectrum withdrawal : Retrieve all or part of assigned spectrum band
- Spectrum relocation : Assigning spectrum in replacement for withdrawn spectrum



Fig. 1. Spectrum withdrawal and relocation

2. Spectrum withdrawal and relocation at ITU-R and ECC

B. Measures of withdrawal and relocation at ITU-R and ECC

Table 1. Measures of withdrawal and relocation

Measures		Details
Financial Measure	Compensation to incumbent spectrum user[F1]	<ul style="list-style-type: none"> • Process is accomplished by financial compensation to incumbent users • This measure is considered for short-time case
	Spectrum pricing [F2]	<ul style="list-style-type: none"> • In case of congestion due to inefficiency in use of technology and disordered band, higher spectrum usage fee may be imposed in order to introduce efficient technology and induce voluntary relocation of the band
	License fee waiver[F3]	<ul style="list-style-type: none"> • If licensee relocate within appropriate time or replace existing technology with effective one, license fee may be exempted
	Tax bonus[F4]	<ul style="list-style-type: none"> • Compensation could be implemented to existing users by tax reduction. • Tax reduction should be within the scope of national and international law
	Compensation to end users [F5]	<ul style="list-style-type: none"> • Not only for the operator but also for the end users, incentive such as subsidizing terminal devices for TV and Radio digital transition cost is needed
	Radio Equipment take-back Incentive [F6]	<ul style="list-style-type: none"> • In this case, payment for taking back consumers' radio equipment could accelerate or even enable the planned redeployment. Also, it could promote exchange of old equipment for new one for low price.
Administrative measure	License revocation[A1]	<ul style="list-style-type: none"> • License revocation is an administrative act of withdrawing rights of frequency use from a licensed user. The license may be revoked upon or before the expiration of license term(normally license may be extended after the end of its validity period) or license may be revoked before its end of expiry and some financial compensation is paid to the licensee (e.g. tools F1).
	Issuing overlay licenses (overlay auctions) [A2]	<ul style="list-style-type: none"> • Overlay licenses may be used to give overall rights of managing some blocks of spectrum, already encumbered with prior users, usually holding site-specific (apparatus) licenses or licenses for operating in an area lesser than that, authorized by the overlay license. The owner of overlay rights would negotiate with users of spectrum to determine when and how it should be vacated

A. Required condition for withdrawal and relocation

Most of relocation conditions focus on changes of service, application and development of technologies.

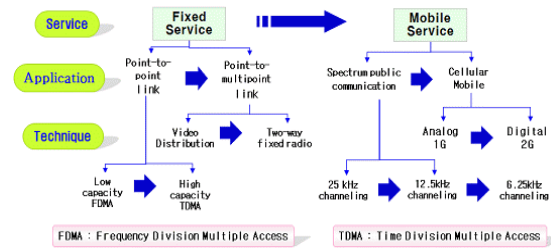


Fig. 2. Withdrawal and relocation condition

Table. 1 Measures of withdrawal and relocation(Continued)

Measures		Details
Administrative measure	Encouragement (authorization) of secondary spectrum trading [A3]	• Creation of a secondary market through the introduction of spectrum trading could provide a powerful mechanism to redistribute spectrum dynamically in response to changing conditions. It could also provide market information feedback to guide administrative pricing and help license fees to be set at the economically optimal level. However, establishing trading procedure and system will take certain amount of time.
	changing license conditions(removing barriers) [A4]	• By using this measure, administrations allow withdrawal and relocation by incumbent users themselves, when the intended change of radio use does not imply or require change of ownership for frequency use and does not pose interference problems.
	License expiry [A5]	• The qualification of "first choice" is due to the fact that waiting for the expiry of the radio licenses does (1) not incur costing any extra money to taxpayer and (2) not generate a breach of the confidence spectrum users put in the spectrum management authority.
Technical measure	Imposed sharing (time-limited, conditional) [T1]	• By this measure administrations may require that the incumbent user accept some kind of sharing with a new service. Such sharing may be time-limited or involving some compensatory provisions, if there is a burden involved on incumbent user.
	Extended tuning range of equipment [T2]	• This measure is very useful if the refarming need is identified well in advance, so that all new equipment for the incumbent networks may be required to have extended tuning ranges. Then, when the refarming is triggered, relocation of the incumbent user to an alternative frequency band may take place much more easily and with fewer resources involved.
	Re-programming of software-defined radio equipment[T3]	• Through the SDR(software defined radio) technology, spectrum withdrawal and relocation is possible. However, this is considered as a future withdrawal and relocation tool.
	Encouraging or imposing use of frequency agile equipment [T4]	• This is an indirect precautionary measure, similar to the one described as T-2 above. It may become much more important with the arrival of software-defined radio. Then the obligation or encouragement to use a software-defined radio may prepare the ground for later ultimate refarming at a short notice by means of the tool described as T-3.

Table 2. Initial condition and relocation methods for spectrum withdrawal and relocation

Required condition	Relocation methods	Duration
<ul style="list-style-type: none"> • Change to the allocation • Carrier license cancelation • Low usage level spectrum • Frequencies which need band maintenance (disordered bands or high density bands) 	1) Compensation	2~3 years
	2) Revocation of license (administrative)	5~10 years
	3) Termination of equipment life cycle	10~15 years

3. Spectrum withdrawal and relocation in Korea

In case of development of services, application, advanced technology, and frequency bands which are not efficiently used, more active spectrum withdrawal and relocation shall be performed, if any required conditions for withdrawal and relocation occurs. A withdrawal and relocation procedure described in this paper is a method in order to secure new spectrum bands timely taking any loss and relevant compensation into consideration.

III. Condition of Spectrum Withdrawal and Relocation

Conditions such as change to the frequency allocation, cancelation of carrier license or network business registration, low usage of frequency band, and disordered or high density bands shall induce spectrum withdrawal and relocation. (Korean Radio Waves Act Article 6-2)

1. Phases of spectrum withdrawal and relocation

The procedure for spectrum withdrawal or relocation is divided into 4 steps as mentioned previously.

Firstly, at the spectrum withdrawal and relocation creation stage, details such as national and international spectrum usage status, trend and judgment of spectrum usage level in some specific bands, requirement of private users need to be considered.

Secondly, at the policy establishment step of spectrum withdrawal and relocation, consideration on the legal procedure and detailed plan is necessary on the basis of withdrawal and relocation conditions. After the establishment of spectrum withdrawal and relocation policy, consultation and hearing must be performed in order to reflect the views of relevant experts and licensees.

Thirdly, at the decision and execution phase of spectrum withdrawal and relocation policy, public announcement procedure and relevant compensation cost and process shall be made.

Fourthly, at the final step, compensation is made through the government fund until the execution of withdrawal and relocation and once the new user is decided, the new comer will be made to pay the withdrawal and relocation cost to the government.

2. Judging compensation by the classified spectrum assignments and required conditions

Spectrum for carriers such as mobile communication, WiBro, LBS is assigned by price or beauty contest. Assigning spectrum by price is similar to auction system where competition and judgment is performed in parallel. This type of assignment will guarantee usage right for 20 years.

Spectrum which is assignment by beauty contest does not compete or pay price. In case of the carriers the spectrum is assigned by the price. In order to perform spectrum withdrawal and relocation, compensation should be made except when the business license have been canceled. But in reality, it is very difficult to withdraw and relocate the spectrum because the original price which is paid by the carrier has to be returned.

Spectrum for private radiocommunication services is designated and operates radio station based on authorization and declaration. In case of conditions such as change to the frequency allocation, low frequency band usage level, maintenance of the band due to disorder or high density uses, compensation is required by spectrum fund.

On the other hand, in regard with the public and military usage, it is not compensated but required to plan the government budget.

Table 3. Phases of spectrum withdrawal and relocation

Phase	Subject	Items to be considered
Preparation	Spectrum usage status investigation	Spectrum DB and radio propagation measure, social-economical index etc.
	National & international frequency allocation trend	WRC/ITU-R and global allocation trend
	Assessment and analysis of actual spectrum usage status investigation	Search low usage level frequency bands
	On request of the user	User returns the spectrum bands
Policy establishment	Initial condition for spectrum withdrawal and relocation occurred	<ul style="list-style-type: none"> • Examine legal, technical, and economical aspects • Estimate spectrum withdrawal and relocation cost • Secure government fund for the estimated compensation cost
	Policy establishment	Establish policy, announcement, principal procedure
	Collect opinion	Experts consultation and hearing
Decision and execution of policy	Announce spectrum withdrawal and relocation	Duration of spectrum withdrawal and relocation process
	Compensation for incumbent users	Compensation cost calculated and requested by incumbent user
	Finalize and announce compensation cost	Review and finalize compensation cost by government
Operation and completion	Pay compensation cost to incumbent user	
	Execute spectrum withdrawal and relocation	
	Collect compensation cost from new comer	New carrier pays compensation cost to the government

Table 4. Determination of compensation in accordance with required conditions and classified assignment services

Services	Conditions	Change to allocation ¹⁾	Cancellation of business license	Low usage level	Maintenance of frequency band
	Classified assignment				
Carrier services	Assignment by price	<ul style="list-style-type: none"> • Compensation not required • Should return the assignment price when withdrawing 	<ul style="list-style-type: none"> • compensation not required • Should return the assignment price in withdrawing 	<ul style="list-style-type: none"> • In principle, compensation should be made • Doesn't return the assignment price in withdrawing²⁾ 	<ul style="list-style-type: none"> • In principle, compensation should be made • Doesn't return The assignment price in withdrawing²⁾
	Assignment by beauty contest	<ul style="list-style-type: none"> • compensation required 	<ul style="list-style-type: none"> • compensation not required 	<ul style="list-style-type: none"> • Compensation required 	<ul style="list-style-type: none"> • Compensation required
Private Radiocommunication services	Assignment by designation	<ul style="list-style-type: none"> • compensation required (In case of public use, planning government budget³⁾) 	N/A	<ul style="list-style-type: none"> • Compensation required (In case of public use, planning government budget³⁾) 	<ul style="list-style-type: none"> • Compensation required (In case of public use, planning government budget³⁾)
Public services (military)	Assignment by designation	<ul style="list-style-type: none"> • Mainly used for public use, planning government budget 	N/A	<ul style="list-style-type: none"> • Mainly used for public use, planning government budget³⁾ 	<ul style="list-style-type: none"> • Mainly used for public use, planning government budget³⁾

notes : 1) Due to the change of international allocation, all administrations have accepted in common. Secondary allocations does not have to be compensated.
 2) Withdrawal and relocation may be difficult due to the existing duration of usage right which is effective.
 3) Withdrawal and relocation of public (including government use) is not a loss but can be considered as a government budget.

IV. Investigation on Spectrum Usage

Basic information on spectrum usage status includes spectrum allocation, assignment, allotment and use of radio station facilities. The main aim is to analyze development trends of radio technologies and industry status and examine annually number of radio stations, channels and possessed facilities, electronic data rate, frequency band/channel occupancy considering spectrum bands, frequency characteristics and classified services according to RR. Also it aims to examine social and economical impacts considering domestic use and geographic characteristics.

Spectrum usage status investigation is performed in order to make basis for spectrum withdrawal and relocation. It is important to investigate and analyze the usage status, collect statistical and relevant index information which can be utilized as a basic material and solve the problem of lacking spectrum resources. In this way low usage level band can be identified.

As for investigation methods, fundamental investigations are examination of DB and radio-based industrial statistics or frequency channel/band occupancy measurement. Questionnaire can be performed as a supplement survey.

Table 5. Spectrum Usage Status Investigation Items

Main trend	main items(i)		Detailed investigation(iii)
Status of Radio Stations	a) number of stations by classified service and frequency bands b) number of stations by users c) number of stations by year d) number of stations by region e) number of stations by services f) number of stations by users in the band and number of transmitters	Search low usage level spectrum(ii)	Low usage level spectrum band; a) detailed usage status and demand forecast b) development trend of spectrum usage technology c) international spectrum usage trend d) public interest such as national security or safety of life
Spectrum Status	a) spectrum allotment and frequency channel usage status b) number of used frequency channels by users c) number of used frequency channels by region d) number of used frequency channels by service		
Social and economical impacts	a) Frequency usage fee by year and users b) Status of spectrum based industry c) Investment and research expenses on radio spectrum for service providers d) Technical development trend of spectrum usage		

V. Judgement criteria for Actual Frequency Usage level

Through spectrum usage status investigation and analysis, it is possible to identify low usage level bands and consider spectrum withdrawal and relocation. To promote efficient distribution of spectrum resources and judge the actual spectrum usage level, procedures and details are shown below.

- a) Spectrum usage status and demand forecast on existing users and new comer services
- b) Trend of spectrum usage technology development
- c) International trend of spectrum usage
- d) Public interest such as national security and safety of life

It is necessary to seek a method of efficient use resolving scarcity of spectrum and to maximize the efficient spectrum use by establishing specific judgment criteria for spectrum usage level and additional procedure. In this section, a method of judging the actual frequency usage level is presented.

For assessing the frequency usage level, the above 4 criteria are decomposed into evaluation indexes as listed in Table 6. Each index is quantitative or unquantifiable according to characteristics of each

index though quantitative indexes are more preferable to ensure its objectivity.

The frequency usage level can be evaluated by summing up scores of each index. Since decision criteria for usage level of specific frequency bands may differ according to their application, scores of each index must be weighted differently according to their application (e.g. commercial, non-commercial, public) when summed up.

A simple analysis method to decide when the usage level is low is considered. It is simply applicable to assess the usage of frequency band for business purpose by using two judgment criteria 1 and 2 in Table 6. As a methodology to assess usage of business purpose frequency band, we adopt BCG(Boston Consulting Group) matrix analysis.

BCG matrix is growth-share model matrix used to analyze market status and to develop proper strategy for business units. The matrix comprises 4 quadrants which are named by Question Mark, Stars, Cash Cows, Dogs as shown in Fig. 3. A business unit may fall into one of the 4 quadrants and, according to the location where the business unit belongs to, one can develop appropriate strategy or assign funding.

If evaluation target frequency band is not for the mobile communication operator, another axe which represents different criteria such as public use, national

security, and safety of life can be added. Also, we can apply additional weight on important services.

In the graph, the result can be shown as x-axis for spectrum usage status and y-axis for future spectrum demand. In Fig. 3 we can see that even though the usage status is low, if revenue or subscription growth

rate is high, it can be considered as 'Question Mark'. If usage rate and demand are both high, it is 'Stars'. With high usage rate but congested revenue or subscription growth rate, it is considered as 'Cash Cows'. Lastly, 'Dogs' represents low usage rate and low demand services.

Table 6. Detailed Evaluation Index for the judgment criteria for actual frequency usage level

Basis of Evaluation	Evaluation Index	quantitative/ unquantifiable
1. Spectrum usage status on target bands	1.1 Result of spectrum usage status investigation and analysis	quantitative
	1.2 Radio equipment acquisition cost, residual value, and transfer cost on the target bands	quantitative
	1.3 Frequency allocation change of the current year	unquantifiable
	1.4 Investigate economic or technical burden of the users caused by the change to radio equipments such as transmitter, antenna etc	unquantifiable
2. Spectrum demand forecast on target bands	2.1 demand forecast of existing services	quantitative
	2.1.1 increase and decrease of invest amount	
	2.1.2 Future investment plan	unquantifiable
	2.1.2.1 Number of subscriber and trend	quantitative
	2.1.3 Sales for 5 recent years	quantitative
	2.1.4 Expected sales(Questionnaire)	quantitative
	2.1.5 Economic Efficiency(Questionnaire)	unquantifiable
	2.2 Demand forecast of new service	unquantifiable
	2.2.1 Competition status of new operators	
	2.2.2 Investment plan and retrieval period of invested amount	unquantifiable
	2.2.3 Expected number of subscribers(Questionnaire)	quantitative
2.2.4 expected sales(Questionnaire)	quantitative	
2.2.5 Economic Efficiency	unquantifiable	
3. Development trends of spectrum usage technology	3.1 Efforts to enhance the efficiency of spectrum use technology	unquantifiable
	3.2 Accomplishment of technical development for providing relevant services	unquantifiable
	3.3 Localization ratio of facilities	quantitative
	3.4 Contribution to the enhancement of IT technology level	unquantifiable
	3.5 Possibility of replacement by other IT technologies (e.g optical, cable etc)	unquantifiable
	3.6 Development of new technology and conformity with the deployment trend	unquantifiable
4. International trend of spectrum usage	4.1 Radio Regulations(RR) International allocation(Article 5)	unquantifiable
	4.2 Frequency usage plan of ITU-R Study Groups(SG)	
	4.3 Spectrum usage plan of international organizations such as ISO, IMO and ICAO.	
	4.4 Issue frequency bands at international forums	
	4.5 Frequency allocation status in other countries	
5. Public necessity in regard with national security and safety of life	5.1 National safety and public order	unquantifiable
	5.2 Protection of people's life and property	
	5.3 Development of people's life and economy	
	5.4 Contribution to the development of science and technology	

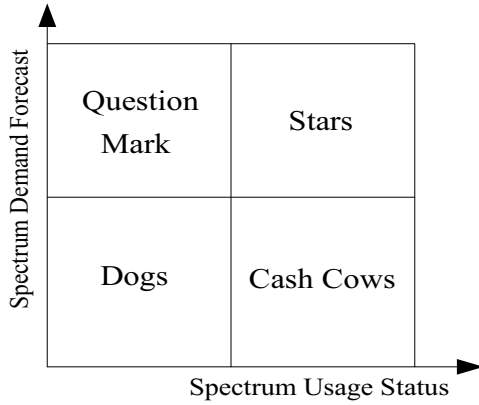


Fig. 3. Spectrum usage status vs. spectrum demand forecast graph interpreted as BCG matrix

Especially when it comes to 'Dogs', the relevant frequency band has low usage and this can be considered as target band for withdrawal and relocation.

Accordingly, to evaluate the actual spectrum usage result, 2 conditions must meet at the same time. The usage status can be considered as 'low' if the score sum is below total score threshold (noted as 'C').

Second condition is that the result of evaluation shall be located in the 'Dogs' area in the matrix. Field which satisfies both conditions is shown in the 'usage status-demand outlook' in Fig. 4.

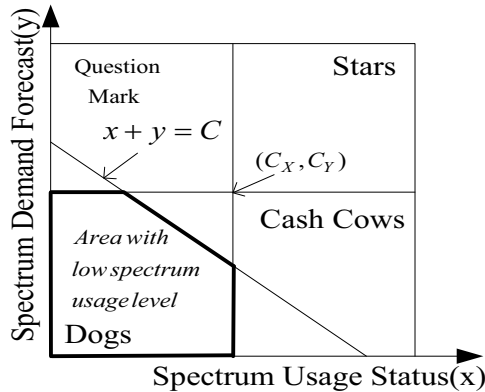


Fig. 4. Area with low spectrum usage level

Above area can be expressed mathematically as below

$$\{x, y \mid x + y \leq C\} \cap \{x, y \mid x \leq C_x, y \leq C_y\}. \quad (1)$$

Since reference point (C_x, C_y) is an important factor determining 'Dogs' area, it is necessary to create consensus from related experts in order to find

(C_x, C_y) through Delphi technique or analytic hierarchy process. Also, total score threshold(C) should be satisfied because low frequency usage areas shall not include 'Star' area.

Although the modified BCG matrix is confined to the 2-dimension, it is straightforward to extend to N dimensional matrix. Actually, this can be achieved by adding new criteria such as 'Publicity such as national security and safety of life' and this makes the 3-dimensional matrix. However, to construct and apply the matrix over 2 dimension would not be easy because the characteristics of new areas created by adding new criterion (or axis) to matrix may vary according to the new added criteria(or axis). Also there are problems on determine criteria score and total score threshold properly.

VI. Compensation

1. The calculation criteria of compensation

Compensation, which occurs as a result of spectrum withdrawal or relocation, is done on the basis of residual value of existing facilities of the user. It is divided into 2 types. First one is a spectrum withdrawal which existing users cannot use the frequency any more. Second one is spectrum relocation which allows users to use other frequency bands.

Compensation of spectrum withdrawal is carried out based on residual value of the existing facilities of radio stations while spectrum relocation has to consider additional financial cost when making compensation.

Table 7. Compensation calculation formula for spectrum withdrawal and relocation

	Formula for estimating compensation cost
withdrawal	Residual value of existing facilities + Removal cost + incidental expenses
relocation	Residual value of existing facilities + Financial cost of acquired new facilities + Removal cost + Moving cost + Incidental expenses

1.1 Calculation of Residual Value of Existing Facilities

It implies the calculation by the estimation method criteria of the number of usage years other than depreciation with regard to existing facilities which are to be removed after spectrum withdrawal and relocation. Residual value will be estimated by the present price taking the initial price into account.

Estimation of existing facilities is conducted by the most appropriate method according to characteristics of

object, assessment purpose or condition of estimation. The principle is that the rationality should be judged by comparing the cost derived from this process with the prices derived from the different process. The reason why depreciation is not used is that generally in case of radio facilities of high price, durable year for radio equipments is 5~10 years but actual duration is 15~20 years and this is considered when estimating the durable years.

1.2 Calculation of Removal Cost

Removal cost means the cost required for removing existing facilities in the spectrum withdrawal and relocation. This is not applied if existing users dispose a part of facilities or remove it with intention of re-usage.

1.3 Calculation of Financial Cost in accordance with Acquisition of new Facilities

This cost includes replacement of existing facilities or additional purchase of facilities to provide the service equivalent to existing one(comparable capacity of systems).

In case of replacement, financial cost implies interest cost that occurs by purchasing alternate facilities for the existing facilities remaining durable years which is estimated according to the cost method.

In case of additional installation, the financial cost concerning new radio stations installation implies interest cost that occurs by early purchase of additional facilities according to usage year remaining estimate based on the cost accounting method with regard to the existing facilities requiring additional installation to provide the service equivalent to existing one(comparable capacity of systems).

a) In case of facility replacement, financial cost(C_F) is given by

$$C_F = (C_A - V_{RE}) \times \left(1 - \frac{1}{(1+R)^N} \right). \quad (2)$$

b) In case of facility supplement, financial cost(C_F) is also given by

$$C_F = C_A \times \left(1 - \frac{1}{(1+R)^N} \right) \quad (3)$$

where C_A is acquisition cost of new facilities, V_{EF} is residual value of existing facilities, R is interest rate, and N is residual durable years.

1.4 Calculation of Moving Cost

Moving cost occurs when the existing facilities have to moved or the radio equipments need to be

changed(e.g. component replacement). This cost cannot exceed 50% of the cost in acquiring new facilities by which the existing ones are replaced or added.

Imposing moving cost may induce users to maintain existing facilities, but if durable year of the facility is short, residual value is low and moving cost may exceed purchasing cost. Accordingly, moving costs have not to exceed compensation cost.

Methods such as not allowing the moving cost caused by spectrum relocation to exceed the acquisition cost of new facilities. When replacing existing facilities with new ones, allowing 50% of acquisition cost of new facilities is considered appropriate.

1.5 Calculation of Incidental Expenses

Incidental expenses means the expenses occurred incidentally in the spectrum withdrawal and relocation such as radio station license fee, compensation calculation fee. The actual cost occurred is estimated as compensation.

2. Example of M/W equipment radio station compensation

Consider a compensation situation where

- Acquisition cost of existing equipments : \$114,000/M/W per link
- New equipments acquisition cost(C_A) : \$135,000
- 10% interest rate(R) is applied.
(refer to loan interest rates of monetary institutions).

Calculation procedure is as in followed.

- Compensation cost for existing facilities
1 year depreciation amount =
acquisition cost / total durable years =
\$114,000 / 15years = \$7,600 / year.

Residual value(V_{EF}) assuming 10 years remaining durable years out of total 15 years durable years:
Residual value =

$$\text{Remaining durable years} \times \text{1 year depreciation} = \\ 10 \text{ years} \times \$7,600 = \$76,000$$

- Using equation (3), financial cost can be calculated as follows

$$C_F = (135,000 - 75,000) \times \left(1 - \frac{1}{(1+0.1)^{10}} \right) \\ = \$36,252.$$

- M/W total compensation cost per 1 link
= \$76,000(residual) + \$36,252(finance)
= \$112,252.

According to this method, if the book value decreases, the financial cost will increase and the compensation cost will gradually decrease as durable year passes by. This may induce the existing users to make early negotiation on the compensation.

Table 8. Calculation of compensation cost by the year

Compensation (year)	Book value(\$)(I)	Financial cost(\$)(II)	PV financial cost(\$)(III)	Compensation cost(\$)(I+III)
0	114,000	0	0	0
1	106,400	40,040	21,068	127,468
2	98,800	47,060	25,714	124,514
3	91,200	52,560	29,843	121,043
4	83,600	56,540	33,384	116,984
5	76,000	59,000	36,252	112,252
6	68,400	59,940	38,355	106,755
7	60,800	59,360	39,585	100,385
8	53,200	57,260	39,823	93,023
9	45,600	53,640	38,936	84,536
10	38,000	48,500	36,770	74,770
11	30,400	41,840	33,156	63,556
12	22,800	33,660	27,902	50,702
13	15,200	23,960	20,791	35,991
14	7,600	12,740	11,581	19,181
15	0	0	0	0

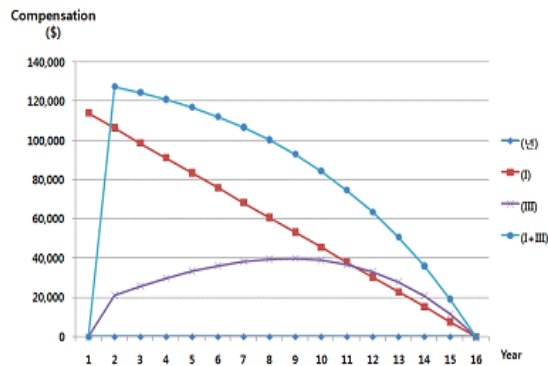


Fig 6. Compensation cost by the year

VII. Conclusions

This paper provides transparent guidelines by establishing the legal basis for the spectrum withdrawal and relocation so that the limited spectrum resources can be used fairly and efficiently.

To maintain consistency in law enforcement, the algorithm for spectrum withdrawal and relocation has been analyzed with objective and detailed preparation.

Step-by-step process has been clarified for future consideration by arranging the conditions of withdrawal and relocation process.

To promote efficiency of spectrum usage, the current status has been analyzed accurately and the results have been used to provide criteria for predicting future demands. Withdrawal and relocation methods for the bands of low usage level have been proposed for the introduction of new services.

In Korea, the approximate value of 1MHz spectrum resource amounts to \$0.25M annually in the subscriber-based mobile communication service industry. The annual revenue from this service is about \$1.9Billion. Thus, securing frequency for new mobile communication service is expected to contribute to the national economy in a vast amount.

This paper will be applied in order to establish the flexible spectrum resource management system based on the market mechanism. Spectrum usage status investigation and confirmation/analysis of statistical data will provide the objective calculation index and basis for judgment related. Also, it will be applied for estimating compensation cost that occurs from spectrum withdrawal and relocation.

At the ITU-R RA-07 meeting in 2007, WiBro(or mobile WiMax) technology has been decided as one of six standards for IMT and at the WRC-07 meeting, the band of 450~470MHz, 470~806/864MHz, 2.3~2.4GHz and 3.2~3.4GHz have been allocated for 4G. This study is expected to be utilized for the timely introduction of new radiocommunication service and securing spectrum resources.

References

- [1] ECC "Refarming and Secondary Trading in a Changing Radiocommunication World" ECC Report 16, 2002
- [2] ITU "Spectrum Redeployment as a Method of National Spectrum Management" ITU-R Rec SM.1603
- [3] MIC Japan "Radio Vision" 2003
- [4] NTIA "Commercial Spectrum Enhancement Act" 2004
- [5] FCC CFR Part 23 "International Fixed Public Radiocommunication Services" Oct. 2007.
- [6] FCC CFR Part 101 "Fixed Microwave Services" Oct. 2007.
- [7] FCC NOTICE OF PROPOSED RULEMAKING WT Docket No.02-353 "Service Rules for Advanced Wireless Services in the 1.7GHz and 2.1GHz Bands November 22, 2002

Radio Noise: Recent Considerations of Man-Made Noise

Les Barclay
Barclay Associates Ltd
Lancaster University

Abstract

Radio noise sets a limit to the performance of radio systems and networks. Internal noise is controllable through receiver design but external noise often sets the limit. The natural sources of noise are not subject to significant change. However man-made noise, due to the use of electrical and electronic machinery and equipment, varies with the environment and circumstances, and may change as the use of electricity and telecommunications develop. The definition of man-made noise needs further consideration with the aim of defining useful categories and of distinguishing between the integrated background noise and emissions from specific pieces of equipment. Recent measurements have been made at VHF in Europe and a databank for the measurements has been established within the ITU-R

1. Introduction

All radio communication circuits have a limitation to their performance, apart from that due to propagation distortion in the channel, which is set by the background of noise or interference against which signals are received. Simplistically, a background of interference from other radio transmissions may be controlled by procedures for spectrum management and regulation. Unwanted emissions associated with radio equipments may be controlled by setting standards for the relative levels of such emissions, although there are probably no effective ways of taking the effect of such emissions on the performance of a specific circuit into account. But broadband noise from natural sources, together with emissions from non-radio equipment and other man-made sources, set an unavoidable background for radio reception.

Some radio networks are designed to operate against a background of interference from other transmitters in the same network, to provide a high density of service provision. If this is the case then increasing the power of each transmitter in the network will not improve the overall service, but reducing the power will eventually reach the condition where performance is limited not only by the mutual interference but also by the underlying noise.

It is thus important for predictions of radio system performance to understand and to have good data for the expected levels of noise.

2. Radio noise

2.1 Internal noise

The basic noise reference is taken as kTb , where k is Boltzmann's constant, T is the temperature (Kelvin) and b is the bandwidth. This represents the thermal noise power available in the input resistance of the receiver. The receiver noise factor (or the noise figure when expressed as a ratio in decibels), quantifies the degradation in the receiver due to additional noise in the receiver and noise resulting from attenuation in antenna feeders, etc. This internal noise is controllable to some extent through the design and implementation of the receiving equipment. However the overall noise background also includes external noise entering the system through the antenna, and, although it may be modified by antenna directivity, this cannot be avoided.

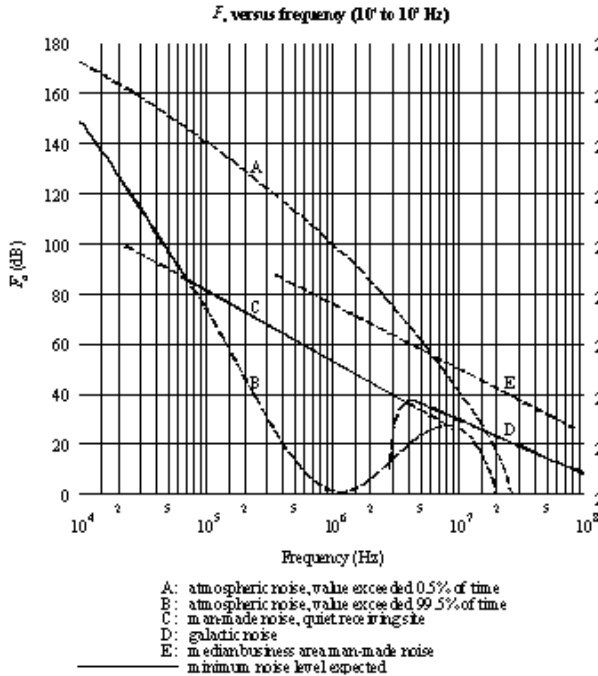
2.2. External noise

External noise may be from five types of source, each important in different parts of the radio spectrum:

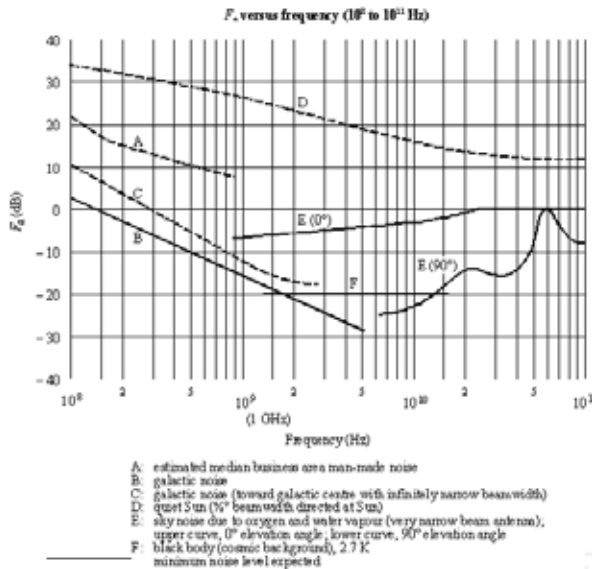
- noise due to attenuation in the atmosphere is significant at millimetric wavelengths
- noise from the Earth's surface, when the antenna directivity includes the surface, may be important at the higher frequencies where noise from other sources is low.
- noise from the galaxy may be observed at frequencies greater than the critical frequency of the F region of the ionosphere but is significant at UHF and SHF.
- noise due to lightning discharges is propagated worldwide by the ionosphere from the main thunderstorm regions in tropical areas, and

so is important at frequencies up to the maximum usable frequency for ionospheric propagation.

- noise from man made sources is important at frequencies up to the UHF band.



External Noise Figures, F_n , 100 kHz to 100 MHz
Figure 1



External Noise Figures, F_n , 100 MHz to 100 GHz
Figure 2

Figures 1 and 2, taken from ITU-R Recommendation P.372, summarise the range of external noise figures from these various types of source.

3. Noise characteristics

3.1 Gaseous and Galactic Noise

At higher frequencies noise from atmospheric gases, from the galaxy (although some astronomical sources have non-gaussian characteristics), and from the Earth's surface is gaussian in character. As received this has a Rayleigh distribution in amplitude with random phase. This kind of noise variation is the kind that is included in many system simulations, and this aspect of the performance of both analogue and digital may be predicted with confidence. The other sources of noise, while having a gaussian component, also include "impulsive" noise, making system simulation more difficult. Moreover other noise parameters may need to be used for a complete assessment of system performance, but these are scarcely ever defined.

3.2 Atmospheric noise due to lightning

This form of atmospheric noise arises from the emissions from lightning discharges, primarily from the return strokes from ground to cloud, with the ionised column itself acting as a large radiator. There may be a closely spaced succession of strokes associated with one event, but each is of short duration creating an impulse with energy extending into the HF band. Propagation effects tend to spread the energy in time, and the received signal at long distances has a more impulsive character at lower frequencies.

Recommendation P.372 contains seasonal maps of the hourly median noise figure for four-hour seasonal time blocks. These maps stem from the early CCIR Report 65, where noise grades were given for different parts of the world; the information being largely derived from the statistics of thunderstorm incidence. During the late 1950s a campaign of noise measurement was undertaken, notably deploying a number of ARN-2 measurement receivers (developed here in Boulder). Results from these equipments along with similar measurements made by other organisations are referenced in CCIR Report 322-3¹.

* The noise may not be truly impulsive but will often be observed with a time resolution determined by the receiver bandwidth, so that impulses or short pulses cannot be distinguished.

It should be noted that making a satisfactory rms detector for these equipments was not a trivial task at that time with the then current vacuum tube technology. These results were essentially used to calibrate the worldwide distribution derived from thunderstorm occurrence, along with a simple model of ionospheric propagation, to give noise figures. Later, these results were supplemented by additional information from other parts of the world, and the maps are now contained in Recommendation P.372.

This Report also gives statistics of the noise figures for other percentiles, as well as error estimates for the data.

In addition a method is given for determining the departure of the amplitude probability distribution of the noise from Rayleigh. Using the data measurable at the time, this method is based on a factor V_d , the ratio in decibels of the rms to the average values of the noise envelope voltage². However, although the APD may have been used to some extent in predicting the performance of LF systems, it does not seem to have been used to any great extent for HF predictions which use the noise figure only.

3.3. Man-made noise

The natural sources of noise, as outlined above, are understood and are not likely to change significantly with time. No doubt atmospheric noise due to lightning could be better modelled following a major measurement effort and with better modelling of the integrated propagation from the thunder storm sources, but the information available may be adequate for most practical purposes.

Man-made noise is very different. There is current interest in having good models for man-made noise at HF, but particularly at VHF and UHF, to enable assessments to be made of performance or coverage of radio systems and wireless networks, and also to establish a base line for watching for trends in changing future levels of the noise background.

When measurements were first made of man-made noise, in about the 1960's, a main source of noise was probably from the ignition systems of internal combustion engines, along with sparking, for example from the commutators of electric motors, and from power lines.

Specific pieces of nearby machinery or equipment may be an identifiable source of unwanted emission, and there is no clear definition as to what should be included within the general category of man-made

noise, and what should be excluded as being emissions from such specific pieces of equipment. Perhaps it was easier in those earlier days. The statistics of atmospheric noise due to lightning exclude the effects of local thunderstorms, so that in that case the noise is intended to be the integrated result of noise from many distant storms which could not easily be individually identified. Man-made noise could be treated in a similar way, and exclude emissions from specific identifiable sources. The uses of radio technology and the locations of potential sources of man-made noise made this a satisfactory approach 30 or more years ago. The data on man-made noise given in CCIR Report 258³, and now in ITU-R Recommendation P.372, could be interpreted in this way. They are largely based on measurements by Spaulding and Disney⁴ and show increased levels of noise in urban areas, perhaps roughly related to population density and the use of electricity in those areas.

In the modern situation this approach is less satisfactory. Ignition systems have improved with better suppression techniques in the engines. There is likely to have been an increase in the use of electricity per head, but differences in the way in which power is distributed in different parts of the world may be very significant. There are now emissions from a wide variety of commercial and domestic equipments. Some of these may be broadband resulting from contact sparking, etc., but now non-radio telecommunication systems (e.g. DSL and PLT/BPL) as well as IT equipments and other processor-based controllers may have emissions at specific bands of frequency.

Moreover the uses of radio have changed, with many uses of low power wireless systems and networks close to the user. As an extreme example, there is a need to determine noise levels within busy offices containing much electronic equipment and networking, where many noise sources will be close to the user.

It might be supposed that all non-radio equipments would be built to meet standards to give satisfactory levels of emission. In Europe manufacturers have to design and construct to meet standards, and they can then self-certify that these standards are met by placing a "CE" mark on the equipment. Unfortunately the procedures for confirming that standards are met are wholly inadequate, and there is evidence that some manufacturers are omitting the emission control components within a CE marked product. Moreover there is some uncertainty as to what constitutes a piece of equipment and what is a

sub-assembly to be included by another manufacturer into a complete product; for example switched-mode power supplies are components within computers, but may also be sold as separate products. Further, radiation may come not from a piece of equipment itself, but from the interconnecting wiring in large installations, or from non-radio telecommunications.

Thus there is a need for a debate on what is man-made noise. For what purpose are predictions needed? How can typical environments be defined? How can malfunctioning equipment be identified and excluded from measurements?

4. Man-made noise categories

The practical approach is to define a set of environmental categories which may be described and which are typical of the different environments in which radio systems may be deployed. This in itself is not easy. In the UK, communities of dwellings range from the smallest group of houses in hamlets, through villages, towns and cities. These names are in common use based on historical and administrative circumstances and there is no clear distinction to define the boundaries between them. Moreover the names give an indication of the size of the community but do not indicate the density of habitation. Beyond that, even if a satisfactory set of definitions could be made, it is unlikely that they would be understood in the same way in all parts of the world. ITU-R Recommendations are intended to give worldwide guidance.

Eventually it was decided to identify a relatively large number of categories so that data to be included in the ITU-R SG3 noise databank could be allocated, see Table 1. However the new data available so far are insufficient for these categories to be carried into the Recommendation, and no change has been made to the categories adopted by Spaulding and Disney, except to change the name from “business” to “city”, see Table 2.

5. Measurements of man-made noise.

As part of a spectrum monitoring project, measurements were made of man-made noise at 33 locations in the UK in 2006. Measurements were made at 209 and 425 MHz with a bandwidth of 1 MHz. Vertically polarised antennas were used and particular care was taken to eliminate pick-up in the feeder cables.

Rural	Quiet rural Rural Village
Commerce	Small office Large office Light industry/public buildings Heavy industry Shopping mall
Transport	Railway Road Airport terminal
Urban	Suburban Urban City centre

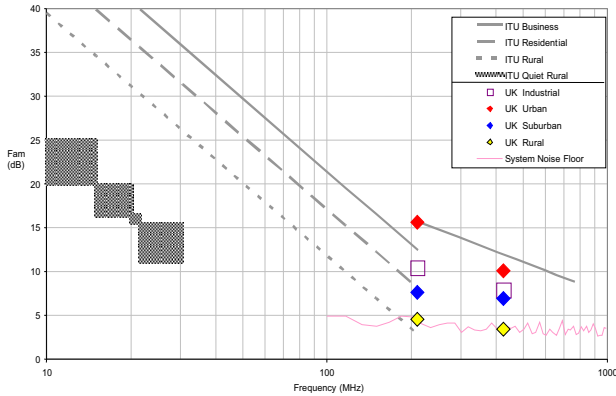
Environmental categories for the ITU-R SG3 man-made noise databank. Distinction is also made between noise measured outdoors and indoors
Table 1

City
Residential
Rural
Quiet rural

Environmental categories used for man-made noise in ITU-R Recommendation P.372
Table 2

The results were analysed using the method described in ITU-R Report P.2089⁶, enabling values of the noise figure due to the gaussian component to be determined, as well as parameters for the impulsive noise. In addition the impulsive noise was examined to establish the noise amplitude distribution, as well as the distributions of pulse duration, pulse interval and pulse repetition frequency. The data are stored in the ITU-R SG3 databank for future use as more results become available.

The noise figures established in the UK in 2006 are compared with the earlier results by Spaulding and Disney in Figure 3 and this indicates comparable results despite the passage of time.



Man-made median noise figures from ITU-R Recommendation P.372, with the addition of recent UK results
Figure 3

Also in 2006 rather similar studies were undertaken in Germany⁷. Opportunity was taken to bring the two sets of measuring equipment together. At several locations the two independent sets of equipment were used side by side and independent analyses of results were made. These yielded very similar results, giving great confidence in the measurement procedures being used.

The German and UK results were combined and additional tables added to ITU-R Recommendation P.372, see Tables 3 and 4.

Freq MHz	City			Residential			Rural		
	Fam	Δu	Δl	Fam	Δu	Δl	Fam	Δu	Δl
35	23	7	1.5	17	5	1	16	2	2
140	12	4	3	8	2	2	6	3.5	2
210	16	1	2	8	2	1	5	1	2
270	6	2	2	4	2	1	4	1	1
425	6	1	1	4	2	1	3	1	1

Outdoor man-made noise in Europe (dB rel kT_{0b})
Median noise figures Fam, and the upper and lower decile deviations, Δu , and Δl
Table 3

It is to be hoped that additional results will be provided to the ITU-R databank in the future to provide greater confidence in the statistics and to extend the information over a greater frequency range. At a future meeting of ITU-R Working Party 3J we should look forward to a study to amalgamate old and new work into a single set of presentations of man-made noise figures to aid future system design and planning.

Freq MHz	City			Residential		
	Fam	Δu	Δl	Fam	Δu	Δl
210	14	3	3	5	3	1
425	16	4	1	3	1	1

Indoor man-made noise in Europe (dB rel kT_{0b})
Median noise figures Fam, and the upper and lower decile deviations, Δu , and Δl
Table 4

6. Conclusion

Radio noise represents the limit to the background against which radio systems and networks may be designed and planned. While other sources of external noise are not expected to change significantly with time, man-made noise sources are changing with an increased use of electrical and electronic equipment and systems. New studies of man-made noise have been made and more are needed to add to the available data and to re-assess the way in which the data are presented.

7. References

1. CCIR Report 322-3 “Characteristics and application of radio noise data”, ITU Geneva 1986
2. W Q Crichlow, A D Spaulding, C J Roubique & R T Disney “Amplitude probability distributions for atmospheric radio noise” NBS Monograph 23, 1960.
3. CCIR Report 258-5 “Man-made radio noise”, ITU Geneva, 1990
4. A D Spaulding & R T Disney “Man-made noise” Part 1 OT Report 74-38, 1974; Part 2, OT Report 75-63, 1975, US Govt Printing Office, Washington DC
5. A J Wagstaff & N P Merrick “Autonomous Interference Monitoring System, Phase 2 Final Report” Vol 1, 2007
www.ofcom.org.uk/research/technology/research/statuse/aims2/aims2_1.pdf
6. ITU-R Report P.2089 “The analysis of radio noise data” ITU Geneva, 2006
7. Germany, “Man made noise in the VHF frequency range” ITU-R document 3J/184, 2007

Dynamic channel model for static mobile terminals in indoor environments

Yoshichika OHTA and Teruya FUJII
Laboratory, SoftBank Telecom Corp.
Tel. +81-3-5500-1852, Fax +81-3-5500-1853
yoshichika.ota@tm.softbank.co.jp

Abstract— More customers are now communicating via cellular phones in indoor environments. In such a situation, the terminals frequently remain static while being used. In order to evaluate the QoS of such terminals, a channel model that takes account of stationary usage is required. This paper proposes a channel model for static terminals in indoor NLOS and LOS environments by extending our proposed indoor NLOS channel model.

1. Introduction

Many more customers are now enjoying various wireless communication services such as cellular phone and WLAN, etc. in indoor environments. In this case, the mobile terminals (MTs) frequently remain stationary while in use. As a result, the communication characteristics are wildly different from those seen in outdoor mobile use for example.

In static usage, the MT itself doesn't move, but the environment around it changes due to moving obstacles such as people. In order to accurately evaluate the resulting propagation environment, a propagation model (channel model) that can simulate this environment is necessary. Regarding to the matter, the Question ITU-R 211-4/3 has a description of "What effect dose the movement of persons and objects within the room have on the propagation characteristics?" as an assigned question [1]. Many recent studies have tackled static terminals, but all base their modeling approaches on empirical formulae [2]-[4]. We took a different approach, a physical channel model for static terminals used in the indoor Non Line of Sight (NLOS) condition [5]. The proposed model can consider physical parameters such as moving area, number of moving obstacles (people), moving speed and direction in order to evaluate various situations preciously and furthermore easily. This model also was proposed to Recommendation ITU-R P.1238-5 [6] as a proposed revision at the last ITU-R WP3K meeting in Geneva (April 2007) [7].

The access points (APs) of indoor wireless services such as WLAN are generally set indoors and the radio path between AP and MT frequently is Line of Sight (LOS). Therefore, in order to evaluate the QoS of these services, a channel model that can evaluate not only NLOS environments but also LOS environments is strongly required.

This paper proposes a physical channel model for static terminals used in both the indoor LOS and NLOS conditions by extending our proposed indoor NLOS channel model. This model can evaluate various situations by changing the physical parameters [8]. We first theoretically analyze the received level and autocorrelation characteristics of the proposed model. Next we compare the results of the proposed model with

measured results and show that the proposed model well predicts the measured results.

2. Proposed model

Fig. 1 shows the basic concept of the proposed model [5]. It consists of two environments as shown in Fig. 1. One is the surrounding static environment (Fig. 1(a)); it contains no moving obstacle. The radio waves arrive at the terminal without being blocked by moving obstacles. The other is the surrounding moving environment (Fig. 1(b)); it contains only moving obstacles and only radio waves scattered by the moving obstacles arrive at the terminal. The proposed model combines the two environments in a direct manner (Fig. 1(c)).

Fig. 2 shows how we model the surrounding moving environment. A moving obstacle is assumed to block the radio waves and to absorb a part of their power as shown in Fig.2. As the obstacle moves, it blocks other radio waves, so the received level at the terminal changes dynamically.

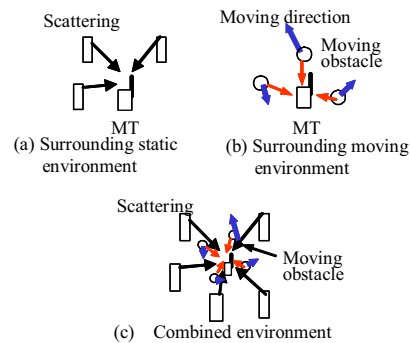


Fig. 1 Concept of modeling

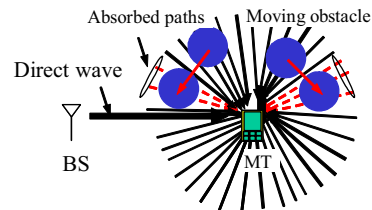


Fig. 2 Modeling of surrounding moving environment.

3. Analysis

3.1. Analysis model

Fig.3 shows the analysis model, which is two-dimensional. The only moving obstacles considered are people; the k th person is represented as a disk with diameter of Δw [m] separated from the terminal by r_k [m]. Each moving person walks in an arbitrary direction between 0 and 2π [rad] at a constant speed of v [m/s]. Each moving person moves within an arbitrary area $S(x,y)$ around the terminal. The number of moving people is N_{person} and a moving person absorbs a part of the power of the paths across his width of Δw .

We assume multipaths with the same power uniformly arriving from all horizontal directions as is typical of indoor NLOS propagation models and a direct path as shown in Fig. 2.

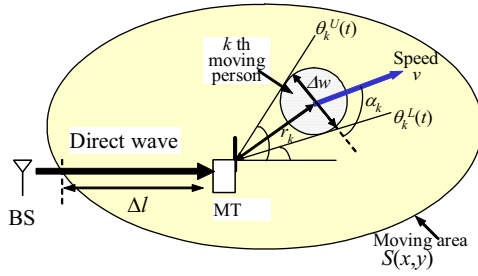


Fig. 3 Analysis model

3.2. Received level analysis

Let the position of a terminal be $(x, 0)$ and the direct path's level and the i th path's level at the terminal with position of x be $e_0(x)$ and $e_i(x)$, respectively. We assume that the number of paths is N_{path} and the path level absorbed by the k th moving person is $\eta_k(t)$. When the absorbed factor of paths by the moving person is taken to be ζ_{loss} , the received level at the terminal, $E(t, x)$, can be written as follows [9],[10].

$$E(t, x) = \begin{cases} \left(e_0(x) + \sum_{i=1}^{N_{path}} e_i(x) \right) - \sum_{k=1}^{N_{person}} \eta_k(t) \\ = (e_0(x) + e(x)) - e_G(t) & \text{(LOS)} \\ \left(e_0(x) + \sum_{i=1}^{N_{path}} e_i(x) \right) - \left(\zeta e_0(x) + \sum_{k=1}^{N_{person}} \eta_k(t) \right) \\ = ((1 - \zeta)e_0(x) + e(x)) - e_G(t) & \text{(NLOS)} \end{cases} \quad (1)$$

where

$$e(x) = \sum_{i=1}^{N_{path}} e_i(x) \quad (2)$$

$$e_G(t) = \sum_{k=1}^{N_{person}} \eta_k(t) \quad (3)$$

$$\zeta = 1 - \zeta_{loss} = 1 - |\zeta_{loss}| e^{j\theta_{loss}} \quad (4)$$

The absorbed factor ζ_{loss} is a complex number, so the absolute value of ζ is assumed to be constant with a

value between 0 and 1. In the proposed model, note that when the power of a path is perfectly absorbed, i.e. $|\zeta_{loss}| \rightarrow 0$, ζ is set to 1 from Eqn. (4).

From the assumption that multipaths arrive with the same power uniformly from all horizontal directions, each path $e_i(x)$ is given by

$$e_0(x) = A_0 \exp \left[j \left(\frac{2\pi x}{\lambda} \cos(\theta_0) + \phi_0 \right) \right] \quad (5)$$

$$e_i(x) = A \exp \left[j \left(\frac{2\pi x}{\lambda} \cos \theta_i + \phi_i \right) \right] \quad (i = 1, \dots, N_{path}) \quad (6)$$

where A_0 , θ_0 and ϕ_0 represent the amplitude, arriving angle, and phase of the direct path, respectively and A , θ_i and ϕ_i represent the amplitude, arriving angle and phase of the i th path, respectively. λ [m] is the wavelength. When wide sense stationary uncorrelated scattering (WSSUS) is assumed for each path, the following relation is satisfied.

$$\langle e_i(x) e_{i'}^*(x) \rangle = \begin{cases} |A|^2 & (i = i') \\ 0 & (i \neq i') \end{cases} \quad (7)$$

where $\langle \rangle$ represents the ensemble average and $*$ represents the complex conjugate.

$\eta_k(t)$ in Eqn. (1) can be determined from the lowest angle $\theta_k^L(t)$ and the highest angle $\theta_k^U(t)$ of paths absorbed by the k th moving person as follows.

$$\eta_k(t) = \sum_{i=\theta_k^L(t)}^{\theta_k^U(t)} \zeta e_i(x) = \zeta \sum_{i=\theta_k^L(t)}^{\theta_k^U(t)} e_i(x) \quad (8)$$

The first item of the right side of Eqn. (1), $(e_0(x) + e(x))$ and $((1 - \zeta)e_0(x) + e(x))$ represent the level blocked or not the direct path, respectively, and their values don't depend on time t . The second item of the right side of Eqn. (1), $e_G(t)$, represents the level due to the surrounding moving environment, which does depend on time t . When the number of absorbed paths is relatively large, the complex amplitude of absorbed paths, $e_G(t)$, follows a complex Gaussian distribution due to the central limit theorem; this is a noteworthy characteristic. From this characteristic, we find that the amplitude of LOS and NLOS cases in Eqn. (1) can be represented as a Nakagami-Rice distribution with K factor [11]. Here K is defined as the ratio of an arbitrary path's power to the summed power of the other paths. Let the received power be r_p , Nakagami-Rice distribution is given by [12].

$$p(r_p, K) = \frac{1}{s^2} \exp \left[- \left(\frac{r_p}{s^2} + K \right) \right] I_0 \left(\sqrt{4K \frac{r_p}{s^2}} \right) \quad (9)$$

where s^2 represents the multipaths' power; it corresponds to $|e_G(t)|^2$. $I_0(\cdot)$ is the first kind 0th-order modified Bessel function.

Thus the received level characteristics, $|E(t, x)|$, can be expressed as a combination of two Nakagami-Rice distributions with different K factors.

We can obtain the received power distribution by calculating the K factors and the ratio of the direct wave cut off.

3.2.1. K factors

First, we calculate the K factors. The K factors of LOS and NLOS, $K_{LOS}(x)$ and $K_{NLOS}(x)$, respectively, are given by.

$$K_{LOS}(x) = |e_0(x) + e(x)|^2 / |e_G(t)|^2 \quad (\text{LOS}) \quad (10)$$

$$K_{NLOS}(x) = |(1-\zeta)e_0(x) + e(x)|^2 / |e_G(t)|^2 \quad (\text{NLOS}) \quad (11)$$

When a moving person is at distance r_i , he absorbs the power of paths arriving at the static terminal within the angle width of $\Delta w/r_k$. Assuming that the total path

power is $P_m (= \sum_{i=1}^{N_{\text{path}}} |A|^2)$, each path has the same power

of $P_m / 2\pi$ and each path can be absorbed by only one moving person at one time; so $|e_G(t)|^2$ can be approximated as follows.

$$|e_G(t)|^2 \approx \sum_{k=1}^{N_{\text{person}}} |n_k|^2 = \sum_{k=1}^{N_{\text{person}}} P_m |\zeta|^2 \Delta w / 2\pi r_k \quad (12)$$

Moreover, assuming that the moving people are distributed uniformly in the moving area, $|e_G(t)|^2$ can be expressed as follows.

$$|e_G(t)|^2 = \frac{N_{\text{person}}}{S_a} \iint_{S(x,y)} \frac{P_m |\zeta|^2 \Delta w}{2\pi r} dx dy \quad (13)$$

where S_a represents the following moving area.

$$S_a = \iint_{S(x,y)} dx dy \quad (14)$$

N_{person} / S_a in Eqn. (13) can be identified as the average number of people per square meter.

3.2.2. Ratio of the direct wave cut off

Let the probability of a moving person cutting off the direct wave be q_{NLOS} . q_{NLOS} can be expressed as the probability that the center of the moving person falls within a rectangle with width Δw and length Δl between MT and BS in the moving area as shown in Fig.3.

$$q_{NLOS} = \frac{\Delta w \Delta l}{S_a} \quad (15)$$

The probability that the direct wave is not cut off or not by N_{person} people, α_{LOS} and α_{NLOS} , can be expressed as follows.

$$\alpha_{LOS} = (1 - q_{NLOS})^{N_{\text{person}}} \quad (16)$$

$$\alpha_{NLOS} = 1 - (1 - q_{NLOS})^{N_{\text{person}}} = 1 - \alpha_{LOS}$$

By using 3.2.1 and 3.2.2, the probability of the received level $E(t,x)$ can be expressed as follows.

$$P_{LOS}(r_p) = \alpha_{LOS} p(r_p, K_{LOS}) + \alpha_{NLOS} p(r_p, K_{NLOS}) \quad (17)$$

This formula can well explain an empirical formula in Reference [13].

3.3. Autocorrelation function of received level

In order to evaluate the time variant characteristics of the received level, we calculate the autocorrelation function.

First, we rewrite Eqn.(1) to the following equation.

$$\begin{aligned} E(t,x) &= e_0(x) + e(x) - \sum_{k=1}^{N_{\text{person}}} \sum_{i=\theta_k^L(t)}^{\theta_k^U(t)} (\zeta e_0(x) \delta(i) + \zeta e_i(x)) \\ &= \left(e_0(x) - \sum_{k=1}^{N_{\text{person}}} \sum_{i=\theta_k^L(t)}^{\theta_k^U(t)} \zeta e_0(x) \delta(i) \right) + \left(e(x) - \sum_{k=1}^{N_{\text{person}}} \sum_{i=\theta_k^L(t)}^{\theta_k^U(t)} \zeta e_i(x) \right) \\ &= E_d(t) + E_m(t) \end{aligned} \quad (18)$$

where

$$E_d(t) = e_0(x) - \sum_{k=1}^{N_{\text{person}}} \sum_{i=\theta_k^L(t)}^{\theta_k^U(t)} \zeta e_0(x) \delta(i) \quad (19)$$

$$E_m(t) = e(x) - \sum_{k=1}^{N_{\text{person}}} \sum_{i=\theta_k^L(t)}^{\theta_k^U(t)} \zeta e_i(x) \quad (20)$$

The autocorrelation function of $E(t,x)$ can be expressed as follows.

$$\begin{aligned} R(\Delta t) &= \langle E(t,x) E(t+\Delta t,x)^* \rangle \\ &= \langle (E_d(t,x) + E_m(t,x)) (E_d(t+\Delta t,x) + E_m(t+\Delta t,x))^* \rangle \\ &= \langle E_d(t,x) E_d(t+\Delta t,x)^* \rangle + \langle E_d(t,x) E_m(t+\Delta t,x)^* \rangle \\ &\quad + \langle E_m(t,x) E_d(t+\Delta t,x)^* \rangle + \langle E_m(t,x) E_m(t+\Delta t,x)^* \rangle \\ &= R_{dd}(\Delta t) + R_{dm}(\Delta t) + R_{md}(\Delta t) + R_{mm}(\Delta t) \end{aligned} \quad (21)$$

Here we show the final results of $R_{dd}(\Delta t)$, $R_{mm}(\Delta t)$, $R_{dm}(\Delta t)$ and $R_{md}(\Delta t)$ to reduce the page space. For the calculation, the following approximations are set with the help of Fig. 4.

$$\begin{aligned} \theta_k^U(t) &\approx \theta_k^L(t) + \Delta w / r_k \\ \theta_k^L(t+\Delta t) &\approx \theta_k^L(t) + v \Delta t \cos \alpha_k / r_k \\ \theta_k^U(t+\Delta t) &\approx \theta_k^L(t) + \Delta w / r_k + v \Delta t \cos \alpha_k / r_k \end{aligned} \quad (22)$$

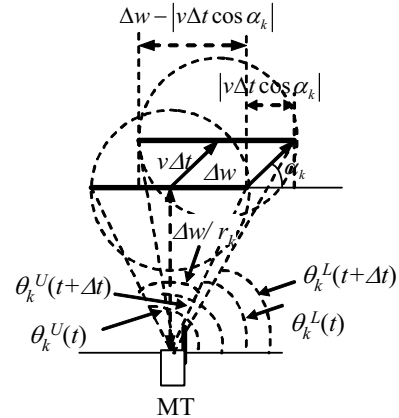


Fig.4 Positions of moving person

3.3.1. $R_{dd}(\Delta t)$

$$R_{dd}(\Delta t) = |e_0(x)|^2 - 2\text{Re}[\zeta] \sum_{k=1}^{N_{person}} \frac{|e_0(x)|^2 \Delta w}{2\pi r_k}$$

$$+ \begin{cases} \sum_{k=1}^{N_{person}} \frac{|\zeta|^2 |e_0(x)|^2 \Delta w}{2\pi r_k} \left(1 - \frac{2f_T |\Delta t|}{\pi}\right) & (v|\Delta t| \leq \Delta w) \\ \sum_{k=1}^{N_{person}} \frac{|\zeta|^2 |e_0(x)|^2 \Delta w}{2\pi r_k} \left\{ 1 - \frac{2f_T |\Delta t|}{\pi} - \frac{2}{\pi} \cos^{-1}\left(\frac{1}{f_T |\Delta t|}\right) \right\} \\ + \frac{2f_T |\Delta t|}{\pi} \sin\left(\cos^{-1}\left(\frac{1}{f_T |\Delta t|}\right)\right) \right\} & (v|\Delta t| > \Delta w) \end{cases} \quad (23)$$

where

$$f_T = v / \Delta w \quad (24)$$

Here f_T can be considered as the maximum frequency shift for the static mobile terminal.

3.3.2. $R_{mm}(\Delta t)$

$$R_{mm}(\Delta t) = \begin{cases} |e(x)|^2 + \sum_{k=1}^{N_{person}} \frac{P_m |\zeta|^2 \Delta w}{2\pi r_k} \left(1 - \frac{2f_T |\Delta t|}{\pi}\right) & (v|\Delta t| \leq \Delta w) \\ |e(x)|^2 + \sum_{k=1}^{N_{person}} \frac{P_m |\zeta|^2 \Delta w}{2\pi r_k} \left\{ 1 - \frac{2f_T |\Delta t|}{\pi} - \frac{2}{\pi} \cos^{-1}\left(\frac{1}{f_T |\Delta t|}\right) \right\} \\ + \frac{2f_T |\Delta t|}{\pi} \sin\left(\cos^{-1}\left(\frac{1}{f_T |\Delta t|}\right)\right) \right\} & (v|\Delta t| > \Delta w) \end{cases} \quad (25)$$

3.3.3. $R_{dm}(\Delta t)$ and $R_{md}(\Delta t)$

$$R_{dm}(\Delta t) = \left(e_0(x) - \zeta e_0(x) \sum_{k=1}^{N_{person}} \frac{\Delta w}{2\pi r_k} \right) e^*(x) \quad (26)$$

$$R_{md}(\Delta t) = \left(e_0^*(x) - \zeta^* e_0^*(x) \sum_{k=1}^{N_{person}} \frac{\Delta w}{2\pi r_k} \right) e(x) \quad (27)$$

Furthermore, assuming that the moving people are distributed uniformly in the moving area, $R(\Delta t)$ can be expressed as follows.

$$R(\Delta t) = \frac{N_{person}}{S_a} \iint_{S(x,y)} R(\Delta t) dx dy \quad (28)$$

3.4. Layout of moving area

In order to calculate the probability density function (PDF) and the autocorrelation function of received level, we need the actual layout of the moving area. Here we

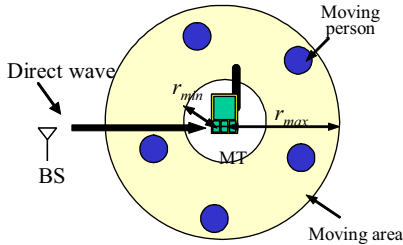


Fig.5 Layout of moving area

assume an annular area described by circles, centered on the terminal, with radii of r_{min} and r_{max} and that the moving people are located uniformly within the annular area as shown in Fig. 5. Then, $|e_G(t)|^2$ can be derived as follows.

$$|e_G(t)|^2 = \frac{N_{person}}{\pi(r_{max}^2 - r_{min}^2)} \int_{r_{min}}^{r_{max}} \frac{P_m |\zeta|^2 \Delta w}{2\pi r} 2\pi r dr \quad (29)$$

$$= \frac{N_{person} P_m |\zeta|^2 \Delta w}{\pi(r_{max} + r_{min})}$$

The K factors $K_{LOS}(x)$, $K_{NLOS}(x)$ and the autocorrelation function $R(\Delta t)$, the autocorrelation coefficient $R_N(\Delta t)$ and the autocovariance coefficient $\rho(\Delta t)$ can be obtained as follows.

$$K_{LOS}(x) = \frac{|e_0(x) + e(x)|^2}{P_m} \frac{\pi(r_{max} + r_{min})}{N_{person} |\zeta|^2 \Delta w} \quad (\text{LOS}) \quad (30)$$

$$K_{NLOS}(x) = \frac{|(1 - \zeta)e_0(x) + e(x)|^2}{P_m} \frac{\pi(r_{max} + r_{min})}{N_{person} |\zeta|^2 \Delta w} \quad (\text{NLOS}) \quad (31)$$

$$R(\Delta t) = \frac{N_{person}}{\pi(r_{max}^2 - r_{min}^2)} \int_{r_{min}}^{r_{max}} R(\Delta t) 2\pi r dr$$

$$= \begin{cases} |e_0(x)|^2 \left\{ 1 - \frac{2\text{Re}[\zeta] N_{person} \Delta w}{\pi(r_{max} + r_{min})} + \frac{N_{person} |\zeta|^2 \Delta w}{\pi(r_{max} + r_{min})} \left(1 - \frac{2f_T |\Delta t|}{\pi}\right) \right\} & (v|\Delta t| \leq \Delta w) \\ \left\{ 1 - \frac{2\text{Re}[\zeta] N_{person} \Delta w}{\pi(r_{max} + r_{min})} \right. \\ \left. + \frac{N_{person} |\zeta|^2 \Delta w}{\pi(r_{max} + r_{min})} \left(1 - \frac{2f_T |\Delta t|}{\pi} - \frac{2}{\pi} \cos^{-1}\left(\frac{1}{f_T |\Delta t|}\right) \right) \right. \\ \left. + \frac{2f_T |\Delta t|}{\pi} \sin\left(\cos^{-1}\left(\frac{1}{f_T |\Delta t|}\right)\right) \right\} & (v|\Delta t| > \Delta w) \end{cases}$$

$$+ \begin{cases} |e(x)|^2 + \frac{P_m N_{person} |\zeta|^2 \Delta w}{\pi(r_{max} + r_{min})} \left(1 - \frac{2f_T |\Delta t|}{\pi}\right) & (v|\Delta t| \leq \Delta w) \\ |e(x)|^2 + \frac{P_m N_{person} |\zeta|^2 \Delta w}{\pi(r_{max} + r_{min})} \left\{ 1 - \frac{2f_T |\Delta t|}{\pi} - \frac{2}{\pi} \cos^{-1}\left(\frac{1}{f_T |\Delta t|}\right) \right\} \\ + \frac{2f_T |\Delta t|}{\pi} \sin\left(\cos^{-1}\left(\frac{1}{f_T |\Delta t|}\right)\right) \right\} & (v|\Delta t| > \Delta w) \end{cases}$$

$$+ 2\text{Re}[e_0(x)e^*(x)] - 2\text{Re}[\zeta e_0(x)e^*(x)] \frac{N_{person} \Delta w}{\pi(r_{max} + r_{min})} \quad (32)$$

$$R_N(\Delta t) = R(\Delta t) / R(0) \quad (33)$$

$$\rho(\Delta t) = \frac{R(\Delta t) - |m|^2}{R(0) - |m|^2} \quad (34)$$

where

$$m = e_0(x) \left(1 - \frac{\zeta N_{person} \Delta w}{\pi(r_{max} + r_{min})} \right) + e(x) \quad (35)$$

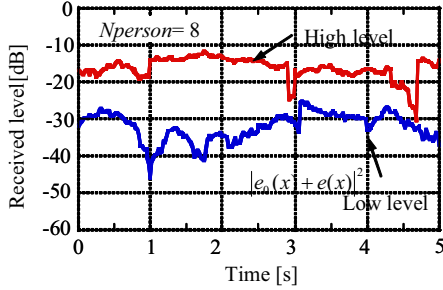


Fig. 6 Received level with direct wave by computer simulation

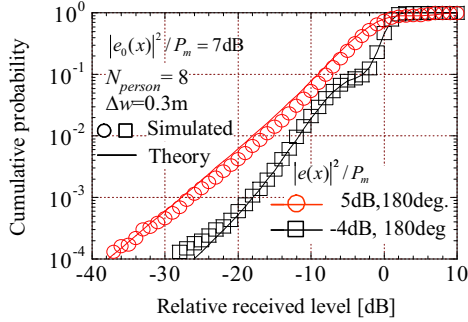


Fig. 7 Cumulative probability of received level

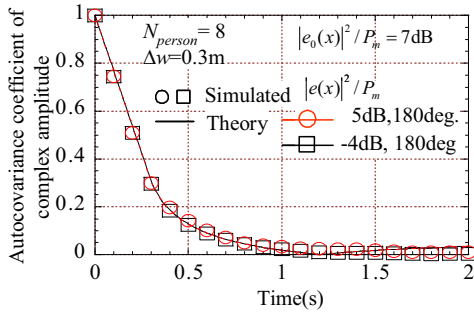


Fig. 8 Autocovariance coefficients of calculated and simulated complex amplitudes

From Eqns. (29) to (33), we find that the K factor $K(x)$, $R(\Delta t)$ and $R_N(\Delta t)$ strongly depend on $|e(x)|^2 / P_m$. While the autocovariance coefficient $\rho(\Delta t)$ depends on f_T , it hardly depend on parameters such as r_{min} , r_{max} and $|e(x)|^2 / P_m$.

3.5. Calculation results

In the calculations, we set Δw , v and N_{person} to 0.3m, 1m/s and 8, respectively, as a practical example. r_{min} and r_{max} were set to 2m and 6m, respectively. The attenuation power due to a person, $|\zeta_{loss}|^2$, is known, through experiments, to be 10-20dB, so attenuation factor $|\zeta|^2$ lies about between 0.97 and 0.99. For simplicity, we assume here perfect absorption, i.e. ζ is 1.

Fig.6 shows an example of the received level, $E(t, x)$, as determined by computer simulation as a parameter of

$|e(x)|^2 / P_m$. Here we set the power of direct wave to $|e_0(x)|^2 / P_m = 7\text{dB}$. From this figure, we find that $|e(x)|^2 / P_m$ is one of the most important parameters.

Fig.7 plots the cumulative probability of received power, r_p , calculated from Eqn. (17) with $|e(x)|^2 / P_m$ as a parameter. Here we set $|e(x)|^2 / P_m$ to 5dB and -4dB and these phases to 180 degree, respectively. For example, the corresponding K factors $K_{LOS}(x)$ and $K_{NLOS}(x)$ are about 14dB and 6dB respectively for $|e(x)|^2 / P_m$ of -4dB.

Fig.8 plots the autocorrelation coefficient, $R_N(\Delta t)$, and the autocovariance coefficient, $\rho(\Delta t)$, calculated from Eqns. (33) and (34) with $|e(x)|^2 / P_m$ as a parameter. In this condition, f_T is 3.3 ($v/\Delta w=1\text{m}/0.3\text{m}$). From this figure, we find that the autocovariance coefficient doesn't depend on the value of $|e(x)|^2 / P_m$.

4. Computer simulation and measurements

In order to confirm the proposed model, we carried out the computer simulation and measurements in a room of our laboratory.

The conditions of the computer simulation were exactly the same as those of the analytical calculation. In Fig. 7 and Fig. 8, we also show the computer simulation results at the same time. Since they show that the computer simulation is valid, we compare the measurement results to the computer simulation results hereafter.

The measurement room was 23m by 15m with a ceiling height of 3m; two of the walls were windows. It held common office equipment such as desks, tables, and shelves. The carrier frequency was 5.7GHz. The Rx antenna was omni directional in the horizontal plane. We made people walk around the received antenna at the constant speed of about 1m/s and measured the received level variation. The other parameters mirrored those of the calculations.

Fig.9 shows an example of the measured received levels with parameter $|e(x)|^2 / P_m$. We find that the simulation results shown in Fig. 6 are very similar to the measurement results.

Fig. 10 shows the cumulative probability of received power, r_p , with parameter $|e(x)|^2 / P_m$ as determined by computer simulation and the measurements.

Fig. 11 shows the autocorrelation coefficient and the autocovariance coefficient of received power, r_p , with parameter $|e(x)|^2 / P_m$ as determined by computer simulation and the measurements.

From these figures, we find that the proposed model is in extremely good agreement with the measured results. This confirms that proposed model is

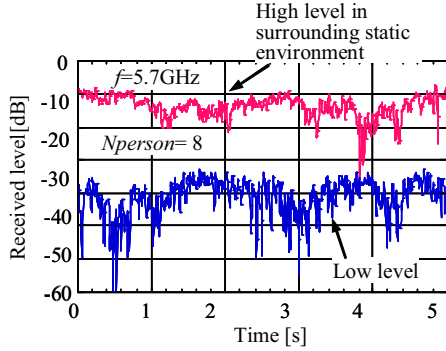


Fig. 9 Measured received level with direct wave

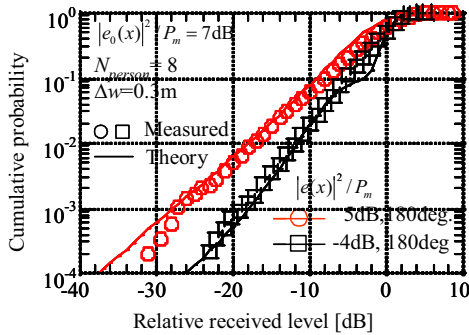


Fig.10 Cumulative probabilities of simulated and measured received power

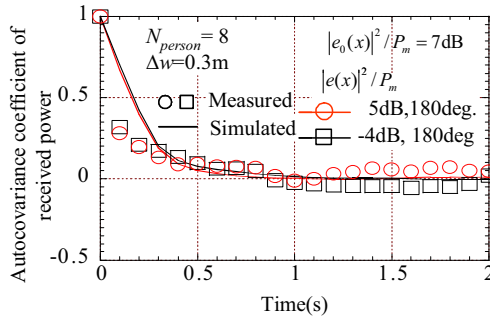


Fig. 11 Autocovariance coefficients of simulated and measured received power

sufficiently valid for mobile terminals in static indoor conditions.

5. Conclusions

We proposed a physical channel model for static terminals used in the indoor Line of Sight (LOS) condition by extending our proposed indoor NLOS channel model.

We started by theoretically analyzing the received level probability density function (PDF) and the autocorrelation function of the proposed model. Next, we compared the analysis results of the proposed model against measurement results and showed that the proposed model is valid as a channel model for static terminals used in the indoor LOS condition.

With respect to received level characteristics, we clarified that the received level can be described as a combination of two Nakagami-Rice distributions with different K factors.

The proposed model can evaluate various situations by changing the physical parameters and furthermore is simple, so it is very useful as a channel model for computer simulations.

References

- [1] Question ITU-R 211-4/3, "Propagation Data and Propagation Models for the Design of Short-range Wireless Communication and Access Systems and Wireless Local Area Networks (WLAN) in the Frequency Range 300 MHz to 100 GHz," ITU-R Questions, ITU, Geneva, 2007.
- [2] R. J.C. Bultitude, "Measurement, characterization and modeling of indoor 800/900 MHz radio channels for digital communications," IEEE Communications Magazine, Vol.25, No. 6, 1987.
- [3] H. Hashemi, et al., "Measurement and modeling of temporal variations of the indoor radio propagation channel," IEEE Trans. Veh. Vol. 43, No. 3, Aug. 1994.
- [4] V. Erceg, et al., "TGN Channel Models", Doc.:IEEE 802.11-03/940r4, May 2004.
- [5] T. Fujii and Y. Ohta, "Dynamic Channel Modeling for Static Mobile Terminals in Indoor NLOS Environments," Proceeding of IEEE 2007 VTC fall, 2007.
- [6] Rec. ITU-R P.1238-5, "Propagation data and prediction methods for the planning of indoor radiocommunication systems and radio local area networks in the frequency range 900 MHz to 100 GHz," Volume 2005 P series, ITU, Geneva, Aug. 2005.
- [7] ITU-R Doc. 3K162-E, "Proposed Revision to Recommendation ITU-R P. 1238-5 - Statistical Channel Model for Static Indoor Conditions -," ITU-R WP3K meeting, Geneva, April 2007.
- [8] Y. Ohta and T. Fujii, "Dynamic Channel Model for Static Mobile Terminals in Indoor LOS and NLOS Environments," Proceeding of IEEE 2008 VTC Spring, 2008 (To be published).
- [9] T. Fujii and Y. Ohta, "Channel Modeling for Mobile Terminals in Static Indoor Conditions," Proc. ISAP2007, Niigata 2007.
- [10] Y. Ohta and T. Fujii, "Empirical Received Level Modeling of Mobile Propagation in Static Indoor Conditions," Proc. ISAP2007, Niigata 2007.
- [11] W. C. Jakes, et al., Microwave Mobile Communications, John Wiley & Sons Inc. (1974).
- [12] Y. Karasawa and H. Iwai, "Modeling of signal envelop correlation of line-of-sight fading with application to frequency correlation analysis", IEEE Trans. Commun. , COM-42, 6, pp. 2201-2203. 1994.
- [13] J.A.Roberts and J.R. Abeyinghe, "A two-state Rician model for predicting indoor wireless communication performance", Proceeding of IEEE 1995 ICC Seattle, Gateway to Globalization, 1995.

*A Mobile-to-Mobile Propagation Measurement System

Robert T. Johnk, Paul McKenna, Peter Papazian, Nicholas DeMinco,
Geoffrey Sanders, Heather Ottke, Brian Arment, Jason Shankel, David Strouse
Institute for Telecommunication Sciences
325 Broadway
Boulder, Colorado USA
Contact: bjohnk@its.bldrdoc.gov

Abstract: *This paper describes a mobile-to-mobile propagation measurement system that is currently being developed at the Institute for Telecommunication Sciences under the sponsorship of the Office of Spectrum Measurement. This system uses a fixed transmitter truck and a moving receiver van to characterize radio-frequency channels of selected urban and rural environments. The transmitter and receiver architectures are described, and selected time- and frequency-domain measurement results are presented. The results obtained so far are very promising and demonstrate the versatility and effectiveness of this measurement system.*



Transmitter Truck



Receiver Van

Figure 1. The mobile-to-mobile measurement system with a stationary transmitter truck (with transmitting antennas deployed) and a moving receiver van.

1. Introduction

A mobile-to-mobile propagation measurement system is currently being developed at the Institute for Telecommunication Sciences (NTIA/ITS) under the sponsorship of the Office of Spectrum Management (NTIA/OSM). The system is a channel sounder and it is used to obtain propagation data at selected frequencies. The technologically advanced system is the culmination of many years of research by ITS engineers and scientists [1]–[8]. The transmitter and receiver are deployed on two vehicles, and can be used in a wide variety of environments. The transmitter truck is parked in a fixed location. Its antennas are deployed on tripods, and it transmits signals simultaneously on four separate channels. The receiver van

is driven over a prescribed route while it obtains data while the vehicle is in motion. The system transmits and receives a binary phase-shift keyed (BPSK) signal that is modulated with a maximum-length, pseudorandom noise (PN) sequence. The transmitted and received sequences are cross-correlated to produce high-resolution time-domain waveforms that are used to analyze the channel propagation characteristics between the transmitter and receiver. These waveforms are post-processed to yield useful parameters such as path loss and delay spread. In addition, the time-domain waveforms yield insight into multipath propagation effects, range, and location of reflectors. Both narrowband and broadband propagation parameters can be extracted. This system has the unique ability to measure propagation effects in both the time- and frequency-domains. In addition, it has the ability to acquire large amounts of data at frequent intervals, providing dense sets of propagation data.

* Certain electronic components are identified in this paper to specify adequately the technical aspects of reported results. In no case does such identification imply recommendation or endorsement by the National Telecommunications and Information Administration, nor does it imply that the material or equipment identified is necessarily the best available for the purpose.

The objective of this paper is to provide an overview of the mobile-to-mobile propagation measurement system deployment, operation, components, and data post-

processing. The purpose here is to give a conceptual and intuitive understanding of the system’s measurement and data acquisition processes.

2. System Features

The mobile-to-mobile propagation measurement system is deployed in the truck and van combination shown in Figure 1.

As shown in Figure 2, the transmitting equipment is mounted on racks in the control room in the back of an ITS-designed truck. The mobile-to-mobile propagation measurement system is operated from a fixed location with the transmit antennas mounted on tripods at a nominal height of 1.5 m. Electrical power is supplied by either external shore power or with an internal 5-kW generator. A well-designed climate control system provides both heat and air conditioning to ensure all-season, all-weather operation.

The receiving equipment is rack-mounted in a modified cargo van. The van has a custom-built, on-board generator that supplies 5 kW of power to ensure full mobile operation. The van is driven in prescribed patterns, and data are acquired at user-selected intervals and rates. Data can be acquired while the van is either stationary or in motion. An on-board, sophisticated GPS tracking system is used to generate precise location and range information while driving the routes.

The mobile-to-mobile propagation measurement system operates at selected channels in the frequency range of 183 to 5750 MHz. Bandwidths vary from 4 to 20 MHz—the narrower bandwidths are used to avoid potential interference with nearby services. Seven channels are available: 183 MHz (BW=4 MHz), 430 MHz (BW=20 MHz), 915 MHz (BW=20 MHz), 1350 MHz (BW=20 MHz), 1602.5 MHz (BW=10 MHz), 2260 MHz (BW=20 MHz), and 5750 MHz (BW=20 MHz).

The BPSK signals are transmitted with 511-bit maximum-length PN sequences that have chip rates of 2 Mbps, 5 Mbps, and 10 Mbps, with bandwidths of 4 MHz, 10 MHz, and 20 MHz, respectively. The resulting signal spectrum is spread over the channel with reduced peak power with noise-like spectral characteristics. The total transmitted power levels vary from 1 to 8 W, and the signal power is spread across the entire channel.

The transmitters and receivers are phase-synchronized using high-precision 10 MHz rubidium clocks that are calibrated to the National Institute of Standards and Technology (NIST) atomic clock. The received BSPK signals are downconverted using analog hardware, and then digitized at a 10-MHz intermediate frequency (IF) frequency using a high-speed data acquisition system.



Figure 2. Interior view of the transmitter equipment rack.

The transmitted and received sequences are cross-correlated (post-processing) to generate time-domain channel impulse responses with range resolutions that vary from 30 to 150 m, depending on the channel bandwidth.

The ability to generate high-fidelity waveforms is unique. Indeed, it provides a powerful tool that greatly facilitates the study of propagation effects. We can now assess such parameters as range (time-delay), and get a direct view of the multi-path scattering. In some cases, we can identify the source of the scattering (e.g. buildings, hills, power lines). The waveforms can be used to compute useful channel parameters such as the root mean squared (RMS) delay spread at any of the receiver locations. We can also investigate frequency-domain effects or parameters such as path loss (basic and excess), and both narrowband and broadband fading effects.

3. Transmitter Architecture

The transmit side of the system is implemented using a combination of commercial off-the-shelf (COTS) components, as well as components designed and fabricated by ITS. The transmitter is designed to operate on seven

Table 1. System channel grouping, frequencies, chip rates, and bandwidths.

Group	Channel Number	Frequency (MHz)	Chip Rate Mbps	Bandwidth (MHz)
1	1	430	10	20
	2	1350	10	20
	3	2260	10	20
	4	5750	10	20
2	1	183	2	4
	2	915	10	20
	3	1602.5	5	10
	4	5750	10	20

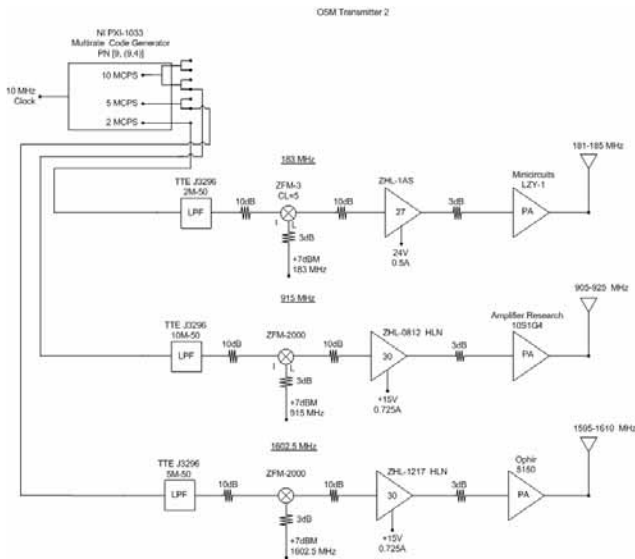


Figure 3. Group 2 transmit architecture with a variable chip rate.

different channels, but only four can be used at once. Thus we divide the channels into the two groups shown in Table 1. Group 1 contains the frequencies: 430 MHz, 1350 MHz, 2260 MHz, and 5750 MHz, and group 2 contains the frequencies: 183 MHz, 915 MHz, 1602.5 MHz, and 5750 MHz. The 5750-MHz channel is used with each configuration as a check on measurement repeatability. Each of the group 1 channels is modulated at a 10-Mbps chip rate, resulting in a channel bandwidth of 20 MHz. Group 2 on the other hand, is transmitted at different chip rates: 183 MHz (2 Mbps), 915 MHz (10 Mbps), 1602.5 MHz (5 Mbps). The signals are generated using a combination of a variable chip rate generator, signal generators, and an assortment of analog radio frequency (RF) hardware. Figure 3 shows how this is done for three of the Group 2 channels.

The heart of the transmitter system is a commercially-available programmable waveform generator. The generator is programmed to produce three separate 511-bit baseband PN sequences at chip rates of 10 Mbps, 5 Mbps, and 2 Mbps. The resulting sequences have peak voltages of ± 0.5 V. The generator has a stored 511-bit PN sequence and plays it back at the different chip rates. The 10 Mbps PN sequence repeats at an interval of 51.2 μ s, the 5 Mbps at 102.4 μ s, and the 2 Mbps at 255.8 μ s. The sequences are then low-pass filtered at bandwidths corresponding to the chip rates (e.g., $f_{lp} = 2$ MHz for 2 Mbps). Next, the sequences are input to a mixer, and up-converted to the desired RF frequency.

A synthesized generator, which is synchronized to a rubidium clock, provides the local oscillator drive. The mixer output power levels then are boosted with two stages of amplification, using a power amplifier as the output



Figure 4. Group 2 transmitting antennas deployed at a rural site.

stage. Attenuators are distributed throughout the system to ensure good impedance matching, and to provide a gain balance that minimizes nonlinear distortion and interference potential. The power amplifier outputs are directly connected to the antenna inputs for signal transmission into the environment.

The transmit antennas are deployed at a nominal height of 1.5 m to simulate a mobile-to-mobile wireless scenario. (see Figure 4.) Collinear dipole arrays are used on six of the channels, and a discone antenna is used on the remaining 183-MHz channel. A discone was used due to the lack of availability of collinear dipoles in this frequency range. The antennas are placed 3 to 4 m away from the truck, and are positioned to minimize blockage effects.

The antennas can be conveniently switched from the group 1 to the group 2 configuration. Switching from transmit configuration 1 to 2 involves changing out three antennas, changing the transmit cables, adjusting amplifier settings, performing transmitted power measurements, spectrum analyzer checks of the transmitted signal, and changing out filters and attenuators. All in all, this process takes about 20 minutes.

4. Receiver Architecture

The receiver, shown in Figure 5, consists of two main parts, an analog front-end and a high-speed digitizer.



Figure 5. Receiver system architecture

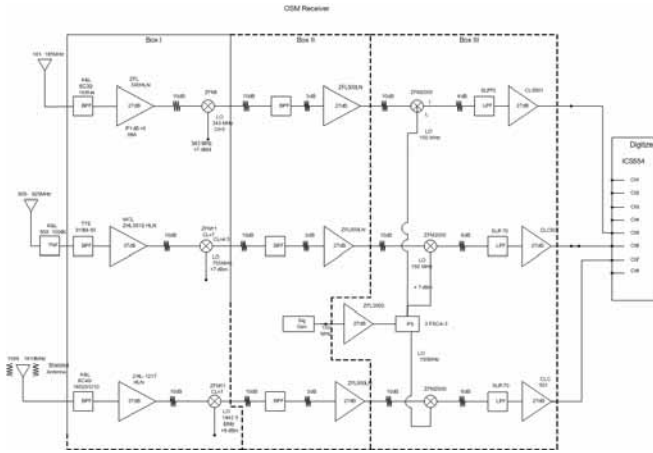


Figure 6. Group 2 receiver diagram (183 MHz, 915 MHz, and 1602.5 MHz).

The receiver is configured from both COTS and ITS-engineered systems. The purpose of the analog front-end is to downconvert the RF signal to a 10-MHz IF signal, which is fed into a high-speed digitizer. The digitized data is then post-processed to extract the propagation parameters of interest.

Figure 6 shows the details of the analog receiver front-end. It is configured in three separate components designed and fabricated by ITS.

The receiver employs a dual-conversion architecture. The signals from the antennas are bandpass filtered, amplified, and fed to the first mixer. The signals are then downconverted to the first IF frequency of 150 MHz, where additional amplification and filtering are applied. The signals are then downconverted to a 10-MHz IF signal. The second IF is filtered and amplified and fed to the inputs of a high-speed digitizer. Attenuators are used throughout the receiver chain to provide impedance matching at the mixer inputs, and to balance the gain characteristics of each channel—this maximizes dynamic range and ensures linearity.

This receiver has a fixed gain and it does not have an automatic gain control (AGC), which could filter out signal variations and bias the data. As a result, the system is deployed in a high-power mode for a distance of 100 m or greater, and a low-power mode (with power amplifiers removed) for transmit and receive antenna separations of 100 m or less. This approach is used to avoid saturating the receiver, which frequently occurs at closer distances.

Commercially-available synthesizers are used as local oscillator sources. Separate sets of measurements are conducted in the high- and low-power modes to provide data that is linear. The synthesizers are phase-locked to a master rubidium clock to ensure synchronization between



Figure 7. Interior view of the receiver mounted in the van.

transmitter and receiver. The equipment is securely and safely mounted on racks inside the van as shown in Figure 7.

The 10-MHz IF signal is fed into a high-speed digitizer card which samples the signal at a rate of 40 Mbps. The card is commercially available, and it contains four high-speed 14-bit analog-to-digital (ADC) converters, which digitize four 10-MHz IF channels simultaneously. Timing control is provided by an ITS-designed field programmable gate array (FPGA) and the ADC timing controller on the card. The card produces a 4-channel bit stream which is stored on a computer-controlled 300 GB redundant array of inexpensive disks (RAID). The computer and RAID are located in the back of the receiver van. A dedicated operator is required to operate and configure the system. Control software for the digitizer was written to ITS specification, and it provides a high level of control over the data acquisition modes and intervals. The system is configured to acquire large amounts of data while the van is moving, and 5 to 10 GB of data are typically acquired during a given measurement sequence.

5. Post-Processing

The ITS mobile-to-mobile propagation measurement system transmits a 511-bit PN sequence in the form of a BPSK RF signal. This signal propagates into the environment where it undergoes multiple reflections, diffractions, penetrates through structures, and ultimately reaches the receiver. The received signal is a combination of direct coupling between the transmitting and receiving antennas and multipath components. Thus, the received signal is a superposition of PN sequences that have traveled over the various propagation paths. Figure 8 shows a segment of the transmitted input PN sequence along with a segment of the digitized 10-MHz IF in which the distortion caused by propagation effects is visible.

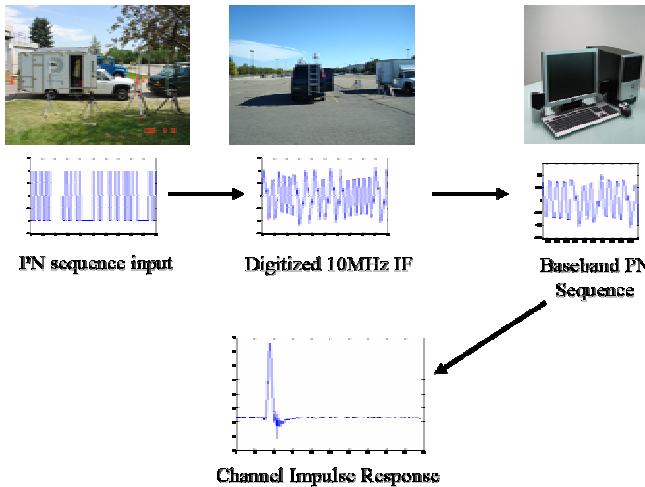


Figure 8. Impulse response extraction process.

To extract useful information, the digitized data are loaded into a computer and post-processed using an ITS-developed software program. The program converts the binary output of the digitizer into decimal format, and it separates the data from the four channels. Next, the program converts the digitized IF down to a baseband sequence with in-phase (I) and quadrature (Q) outputs. This is implemented by multiplying the IF sequence with a 10-MHz complex exponential. Figure 8 shows a segment of the I-component at various stages of transmission and reception.

An interesting and well-known property of a PN sequence is that it has an auto-correlation function that is an impulse function. We can exploit this property to convert a PN sequence into a time-domain waveform that corresponds to the channel impulse response. The channel impulse response is generated by cross-correlating the received PN sequence with the input PN sequence. The result is a complex time series with both I- and Q-components. Figure 9 shows the magnitude of the channel impulse response for selected 183-MHz measurements.

The channel impulse response is a high-resolution, time-domain waveform, which is used to extract useful propagation parameters. Much insight can be gained about the propagation from these waveforms.

Figure 9 shows 183-MHz impulse response magnitudes for a head-to-head through-calibration with the transmitter connected directly to the receiver through a cable and attenuator combination. In this case, there is total coupling between transmitter and receiver, and there is no scattering. Figure 9 also shows a channel impulse response measurement obtained in a rural environment. The impulse response is extended somewhat due to scattering from nearby hills and power lines. It can be seen in Figure 9 that

a

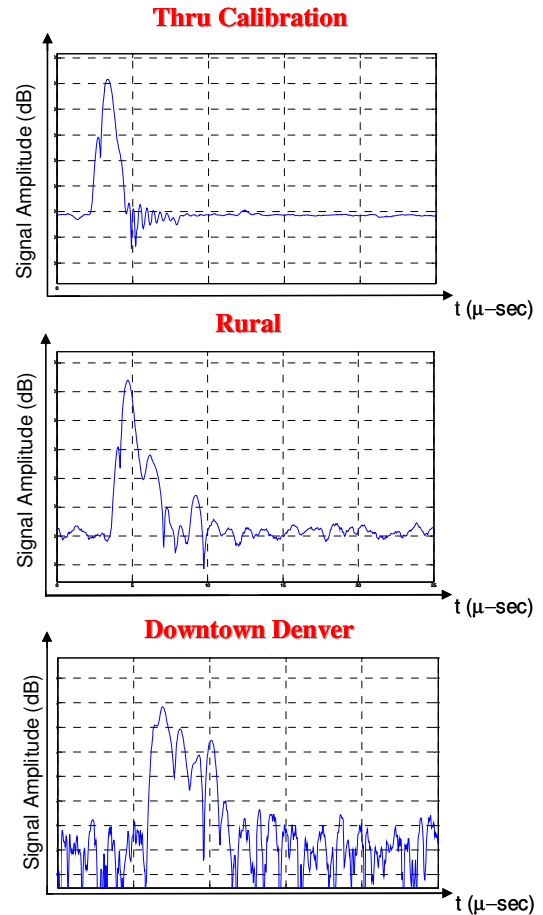


Figure 9. 183-MHz channel impulse response magnitudes obtained under different conditions.

much more complex and extended waveform is obtained when a measurement is performed in the urban canyon of downtown Denver, Colorado due to scattering from a multitude of nearby office buildings and other structures.

6. Broadband Time-Domain Results

One useful way to present measured propagation data is to combine channel impulse responses from multiple locations on one graph. In this case we plot time as the abscissa and the impulse number as the ordinate. The strength (magnitude) of the impulse can be represented on a color scale on the graph. The result is a two-dimensional graph that provides a lot of information about channel propagation effects along a given measurement route.

A series of system tests were performed in Boulder, Colorado during August, 2007. The transmit location and

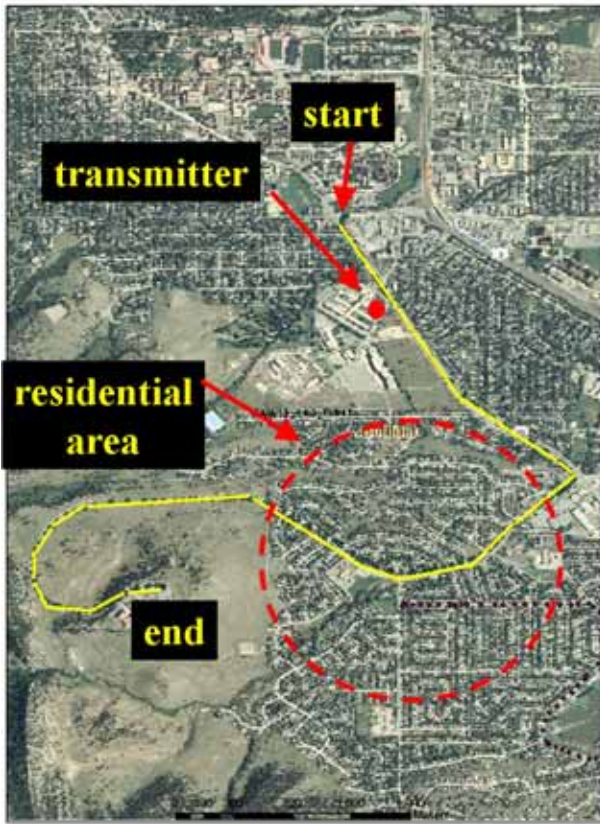


Figure 10. Transmitter location and receiver van route used for the August, 2007 tests in Boulder, Colorado.

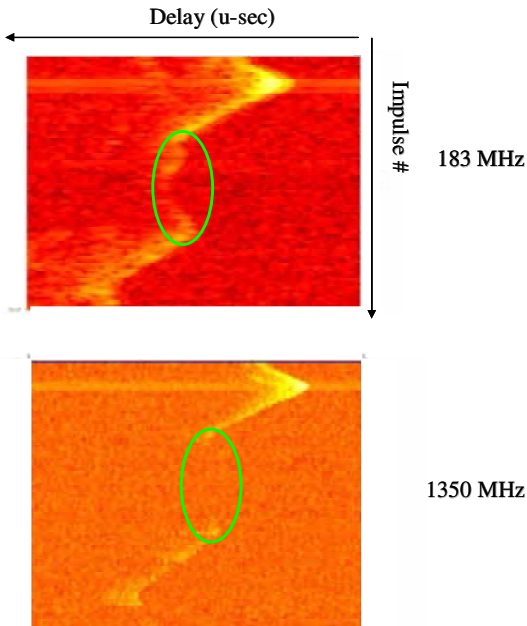


Figure 11. 183- and 1350-MHz channel impulse response data obtained for the route of Figure 10.

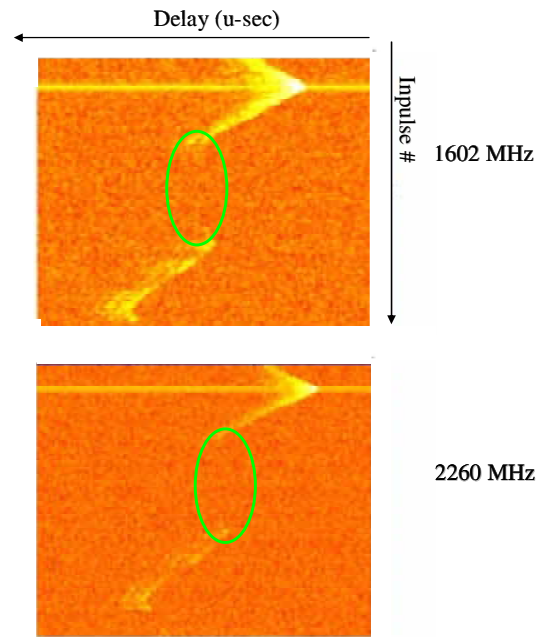


Figure 12. 1602- and 2260-MHz channel impulse response data obtained for the route of Figure 11.

drive route are shown in Figure 10. The transmitter truck was parked at the ITS Boulder Laboratories, and the receiver van was driven south on Broadway to Table Mesa Drive. The van then traveled in a westerly direction until it reached the summit of Table Mesa. Figures 11 through 13 depict combined impulse response results obtained from these tests.

Plots are provided for the 183-, 1350-, 1602-, 2260-, and 5750-MHz channels. The horizontal axis contains the time delay axis with a maximum value of 251 μsec for the 183-MHz band, 102 μsec for the 1602-MHz band and 51 μsec for the 1350-, 2260-, and 5750-MHz bands. The vertical axis corresponds to an impulse response obtained at even 5-second intervals along the entire length of the drive. The resulting graph contains 100 channel impulse responses.

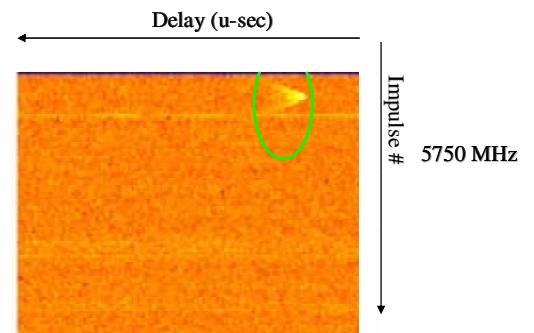


Figure 13. 5750-MHz channel impulse response data obtained for the route of Figure 10.

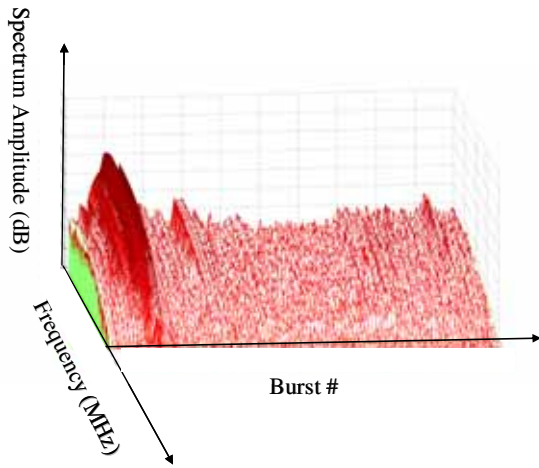


Figure 14. Frequency-domain amplitude spectra obtained from the 183-MHz channel impulse responses.

The graphs show impulse response strengths as a function of position along the drive. With the transmitter truck configured in the high-power mode, the van begins receiving data at the intersection of Baseline Road and Broadway, and heads southeast. As the van approaches the transmitter, the impulse response grows larger, and the time delay decreases as well.

As the van passes close to the transmitter location, the peak impulse response levels are quite strong, resulting in receiver saturation. This can be seen as a horizontal flash in all of the graphs. After the van passes the transmitter, the time delay of the impulse increases and the signal level drops as the distance increases.

The van then turns onto Table Mesa Drive and heads southwest. Due to blockage effects from a combination of private homes and low-rise apartment buildings in a large residential area, the signal levels drop noticeably during this portion of the drive (annotated with a green ellipse in Figures 11 and 12). The blockage effects become more pronounced at the higher frequencies. For instance, some signal is still visible at 183 MHz, while it disappears at 1350 MHz, 1602.5 MHz, and 2260 MHz.

After the van passes through the residential area and heads on a more westerly course, the signals on these four channels reappear for the duration of the drive. Conditions either approach line-of-sight or diffract over a nearby ridge. The 5750-MHz signal disappears completely after entering the residential area and does not reappear for the duration of the drive. The results indicate that, for these conditions, the lower frequencies propagate more effectively.

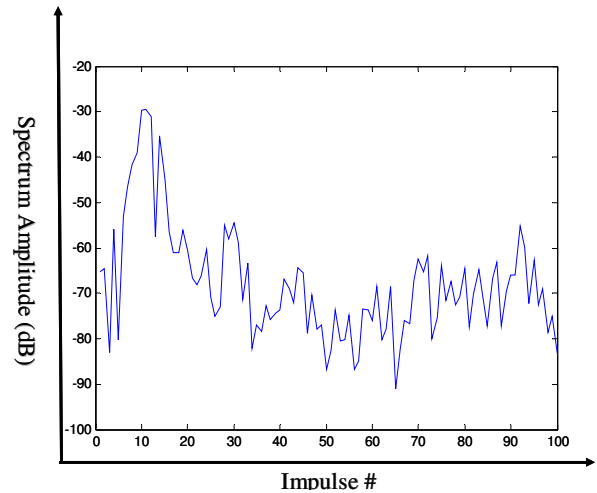


Figure 15. Frequency-domain amplitude spectra as a function of impulse number for a selected FFT bin. The data are sampled at 5-sec intervals.

7. Narrowband Frequency-Domain Results

The channel impulse responses can be processed to yield narrowband frequency-domain magnitude and phase information. The process consists of applying a fast Fourier Transform (FFT) to the channel impulse responses.

The frequency resolution is the inverse of the duration of the channel impulse response. A 51- μ sec impulse response duration yields a resolution of 19.6 kHz; a 102- μ sec duration corresponds to a resolution of 9.8 kHz, and a 255- μ sec duration yields a resolution of 3.9 kHz. These results can be used to examine narrowband fading effects.

Figure 14 shows the frequency domain results for the 183-MHz channel. Amplitude spectrum results are plotted over the 2-MHz channel as a function of bandwidth and the impulse number. The resulting three-dimensional plot is a composite of 100 FFTs (one FFT per impulse). Once again, peak signal levels are observed at the point of closest approach as the van passes the ITS lab parking lot. The plot exhibits complex behavior with rapid variations with respect to both frequency and impulse number. If we now select one frequency bin (3.9-kHz wide) and plot spectrum amplitude, we obtain the graph of Figure 15. The samples are obtained at 5-second intervals, and the signal level profile is clearly visible. Complex multipath effects account for the rapid variation in signal levels.

8. Conclusions

The ITS mobile-to-mobile propagation measurement system has been deployed in a variety of urban and rural environments. The system has the ability to acquire large amounts of data while the ITS receiver van is moving, and a

lot of propagation data has been obtained in both the time- and the frequency-domain. The results look promising and demonstrate the versatility and flexibility of this propagation measurement system.

9. Acknowledgements

We appreciate the generous support of our colleagues in the Office of Spectrum Management. In particular, we are indebted to Alaka Paul, Ed Drocella, Dave Anderson, and Karl Nebbia of OSM for excellent support, guidance and a high level of interest in our work. We also appreciate the generous level of support and guidance from Frank Sanders, Patti Raush, Randy Hoffmann, and Eric Nelson of the ITS management team.

10. References

[1] R.W. Hubbard, "Characteristics and applications of the PN channel probe," OT Technical Memorandum 76-218, 1976.

[2] K.C. Allen and W.A. Lindsey-Stewart, Method and apparatus for measuring the impulse response of a radio channel," United States Patent 5,371,760, Dec. 6, 1994.

[3] R.W. Hubbard, L.E. Pratt, and W.J. Hartman, "The measurement of microwave multipath in an airport environment," Department of Transportation Report FAA-RD-76-163, Jan. 1977. (NTIA sponsor report)

[4] R.W. Hubbard, R.F. Linfield, and W.J. Hartman, "Measuring characteristics of microwave mobile channels," NTIA Report 78-5, Jun. 1978.

[5] G.A. Hufford, R.W. Hubbard, L.E. Pratt, J.E. Adams, and S.J. Paulson, "Wideband propagation measurements in the presence of forests," U.S. Army Communications Electronics and Command Research and Development Technical Report CECOM 82-CS029-F, 1982. (NTIA sponsor report)

[6] J.A. Wepman, J.R. Hofmann, and L.H. Loew, "Impulse Response Measurements in the 1850-1990 MHz Band in Large Outdoor Cells," NTIA Report 94-309, Jun. 1994.

[7] P. Papazian and M. Cotton, "Relative propagation measurements between 430 MHz and 5750 MHz for mobile communication systems in urban environments," NTIA Report TR-04-407, Dec. 2003.

[8] P. Papazian and P. McKenna, "Short-range propagation measurements for interference model development," Proceedings of the International Symposium on Advanced Radio Technologies, pp. 94-99, NTIA Special Publication SP-07-445, February 26-28, 2007.

A Methodology for Approximating BPSK Demodulator Performance in the Presence of Various Undesired Signals

Michael Cotton

Institute for Telecommunications Sciences

Boulder, Colorado 80305

Email: mcotton@its.bldrdoc.gov

This paper describes a methodology for analyzing binary phase-shift keyed demodulator performance in the presence of various types of undesired signals. It utilizes models of the underlying random processes to determine the probability of a bit error. The basic calculation involves integrating the probability distribution function of the internal receiver noise (assumed to be Gaussian) plus the undesired signal. When this integral cannot be solved analytically, a sample-function analysis is utilized. Results are given that compare the effects of various undesired signals (i.e., continuous-wave, MPSK, impulsive noise, and gated noise) to those of Gaussian noise.

1. INTRODUCTION

This paper describes a methodology for the statistical analyses of various undesired signals plus receiver noise to determine how the signals affect demodulator performance. The work is funded jointly by the Office of Spectrum Management (NTIA/OSM) as part of *The President's Spectrum Policy Initiative* [1] and the Institute for Telecommunication Sciences (NTIA/ITS). NTIA/OSM will use the methodology to evaluate the interference effects of new spectrum sharing technologies. NTIA/ITS will use it to validate interference susceptibility measurements and support generalized receiver research.

2. METHODOLOGY

This analysis focuses on the detector subsystem of a binary phase-shift keyed (BPSK) digital receiver, which is responsible for transforming the complex baseband (CBB) received signal into information bits. Ideal BPSK receiver operation is assumed, so that the uncorrupted received source signal produces $\pm A$ when sampled, and all deleterious effects are caused by the undesired signal plus receiver noise. Amplification and down-conversion prior to demodulation are assumed to cause negligible effects beyond their intended functions. Within the demodulator, the receiver filter is a matched root-raised cosine (RRC) filter and the sampler is optimally synchronized. The RRC filter is specified by its roll-off factor (a) and cutoff frequency (f_0). For our purposes, RRC parameters are chosen as $a = 0.35$ and $f_0 = 0.5$ MHz. An important trait of the RRC filter is that the noise equivalent bandwidth $b = 2f_0 = T^{-1}$, where T is the bit period. Lastly, a typical operational scenario is specified by setting the signal-to-noise ratio (P_s/P_n) to approximately 8.4 dB; this corresponds to a probability of a bit error (\mathcal{P}_e) due to receiver noise of 10^{-4} .

\mathcal{P}_e is calculated from first-order statistics of the undesired signal plus receiver noise. For simple undesired signals, analytic solutions are available. Beyond the simple cases, a combination of analytic and simulation methods are used to approximate \mathcal{P}_e . In this quasi-analytic approach, a sample function of the undesired signal plus receiver noise is simulated and bandlimited by the receiver filter. \mathcal{P}_e is approximated as the number of samples that cause an error divided by the total number of samples in the sample function.

The undesired CBB signals considered here are:

- Complex Gaussian noise (CGN)
- Constant signal
- M-ary phase-shift keyed (MPSK) signal
- Impulsive noise
- Gated noise

CGN is a baseline to which the other undesired signals are compared. It also emulates the noisy nature of many modern ultrawideband (UWB) devices. A constant signal emulates an interfering spectral line due to a continuous-wave (CW) signal or a signal that is periodic in nature. MPSK is representative of co-channel interference-limited scenarios, while impulsive noise is representative of man-made noise limited scenarios. Gated noise emulates UWB signals that periodically turn on and off or hop in and out of the operational frequency band of the victim receiver.

Recent research [2] has explored the relationship between \mathcal{P}_e and the amplitude probability distribution (APD), which characterizes first-order amplitude statistics. At this point, this topic has not been fully evaluated for the undesired signals considered in this work. However, in support of this research, APDs have been provided along with the corresponding \mathcal{P}_e plots.

3. THEORETICAL ANALYSES

Analytic solutions for \mathcal{P}_e are available for undesired signals plus receiver noise (at the output of the victim receiver filter) that can be described accurately with a statistical model. This is the case for three BPSK operational environments: (1) receiver CGN in the absence of undesired signals, (2) undesired CGN + receiver CGN, and (3) undesired constant + receiver CGN.

Figure 1 illustrates signals and relevant reference points within the victim receiver. At the output of the receiver filter, $\hat{r}(t) = \hat{s}(t) + \hat{v}(t)$ is the received signal and $\hat{s}(t)$ is the received source signal uncorrupted by receiver noise and undesired signals. The composite undesired-plus-noise signal is given by

$$\hat{v}(t) = [\hat{u}(t) + \hat{\xi}(t)] * \hat{h}_R(t) = \hat{u}(t) * \hat{h}_R(t) + \hat{n}(t) \quad , \quad (1)$$

where $\hat{u}(t) + \hat{\xi}(t)$ is the undesired-plus-noise signal before the receiver filter, $\hat{h}_R(t)$ is the impulse response of the receiver filter, $\hat{n}(t)$ is the receiver CGN after the receiver filter, $\hat{\cdot}$ denotes CBB, and $*$ is the convolution operator.

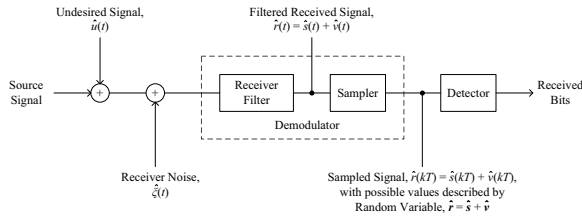


Fig. 1: Block diagram of the demodulator and detector subsystems inside a BPSK receiver with relevant signal nomenclature.

It is assumed that $\hat{r}(t)$ is optimally sampled at time kT within the k^{th} bit period, so that the sampled source signal, $\hat{s}(kT)$, is either $\mp A$ depending on whether a binary 0 or 1 was sent, respectively. Performance results are based on the detector decision process of the victim receiver. BPSK bit error probability is based on the real part of the sampled signal, i.e.,

$$r_x(kT) = \text{Re}[\hat{s}(kT) + \hat{v}(kT)] \quad , \quad (2)$$

where subscript x denotes the real part. The detector is a threshold device that decides a binary 0 was sent if $r_x(kT) \leq 0$ and a binary 1 was sent if $r_x(kT) > 0$. As illustrated in Figure 2(a), errors occur in two ways: (1) if $r_x(kT) > 0$ when a binary 0 was sent, and (2) if $r_x(kT) \leq 0$ when a binary 1 was sent.

In this study we are only interested in first-order statistics, hence, the discrete random processes $r_x(kT)$, $\hat{s}(kT)$, and $\hat{v}(kT)$ can be represented with random variables (RVs) \mathbf{r}_x , $\hat{\mathbf{s}}$, and $\hat{\mathbf{v}}$, respectively. Note that bold

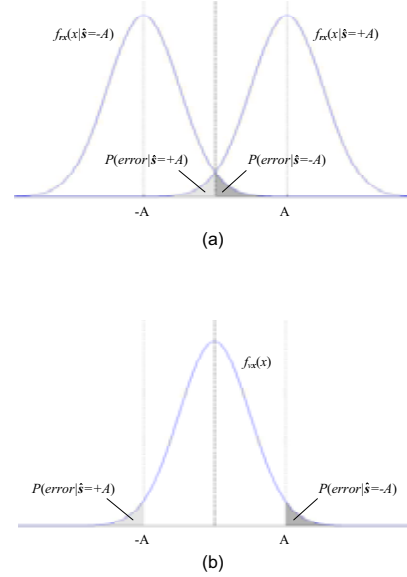


Fig. 2: Error probability for binary signaling.

font denotes a RV. \mathcal{P}_e is computed from the theorem of total probability

$$\mathcal{P}_e = \mathcal{P}\{\mathbf{r}_x > 0 | \hat{\mathbf{s}} = -A\} \mathcal{P}\{\hat{\mathbf{s}} = -A\} + \mathcal{P}\{\mathbf{r}_x \leq 0 | \hat{\mathbf{s}} = A\} \mathcal{P}\{\hat{\mathbf{s}} = A\} \quad , \quad (3)$$

where Equation (3) is simplified in two ways. First, it is assumed that binary 0 and 1 are equally probable, i.e., $\mathcal{P}\{\hat{\mathbf{s}} = \pm A\} = \frac{1}{2}$. Second, understanding that \mathbf{r}_x , given that $\hat{\mathbf{s}} = \pm A$, are just shifted versions of \mathbf{v}_x (as illustrated in Figure 2) allows for the conditional probabilities to be written as

$$\mathcal{P}\{\mathbf{r}_x > 0 | \hat{\mathbf{s}} = -A\} = \mathcal{P}\{\mathbf{v}_x > A\} \quad (4)$$

$$\mathcal{P}\{\mathbf{r}_x \leq 0 | \hat{\mathbf{s}} = A\} = \mathcal{P}\{\mathbf{v}_x \leq -A\} \quad . \quad (5)$$

Substitution and expressing the probabilities in integral form gives

$$\mathcal{P}_e = \frac{1}{2} \mathcal{P}\{\mathbf{v}_x > A\} + \frac{1}{2} \mathcal{P}\{\mathbf{v}_x \leq -A\} \quad (6)$$

$$= \frac{1}{2} \int_A^{\infty} f_{\mathbf{v}_x}(x) dx + \frac{1}{2} \int_{-\infty}^{-A} f_{\mathbf{v}_x}(x) dx \quad , \quad (7)$$

where $f_{\mathbf{v}_x}(x)$ is the probability distribution function (PDF) of \mathbf{v}_x .

Probability of a bit error is determined by evaluating the integrals in equation (7), as illustrated in Figure 2(b). Theoretical results are derived from analytic solutions, and quasi-analytic results are approximated by generating sample functions of the appropriate random processes. In the following subsections, theoretical results are presented for receiver CGN (i.e., no undesired signal), undesired CGN + receiver CGN, and undesired constant + receiver CGN.

3.1. Receiver CGN

Without the influence of an undesired signal, $\hat{\mathbf{v}}$ is zero-mean CGN. The real part is Gaussian distributed with zero mean and variance σ_n^2 , which is commonly abbreviated as $\mathbf{v}_x = \mathbf{N}[0, \sigma_n^2]$. The PDF of \mathbf{v}_x is

$$f_{\mathbf{v}_x}(x) = \frac{1}{\sqrt{2\pi}\sigma_n} \exp\left[-\frac{x^2}{2\sigma_n^2}\right]. \quad (8)$$

Substitution into equation (7) and change of variables allows for the integrals to be combined to give

$$\mathcal{P}_e = \int_{A/\sigma_n}^{\infty} \frac{1}{\sqrt{2\pi}} e^{-\lambda^2/2} d\lambda = Q\left(\frac{A}{\sigma_n}\right), \quad (9)$$

where $Q(\xi) = \int_{\xi}^{\infty} e^{-\lambda^2/2} d\lambda = \frac{1}{2} \operatorname{erfc}\left(\frac{\xi}{\sqrt{2}}\right)$ is the cumulative distribution function of the standard normal deviate.

It is useful to express error probability in terms of mean signal powers, i.e.,

$$\mathcal{P}_e = Q\left(\sqrt{2\frac{P_s}{P_n}}\right), \quad (10)$$

where $P_s = \mathcal{E}\{|\hat{\mathbf{s}}|^2\} = A^2$, and $P_n = 2\sigma_n^2$ is determined by b and the power density of the receiver noise.

Figure 3 illustrates \mathcal{P}_e versus P_s/P_n . Notice that $\mathcal{P}_e(P_s/P_n = 8.4 \text{ dB}) \approx 10^{-4}$. As stated previously, this defines the operational scenario of the BPSK receiver onto which the undesired signals are imposed.

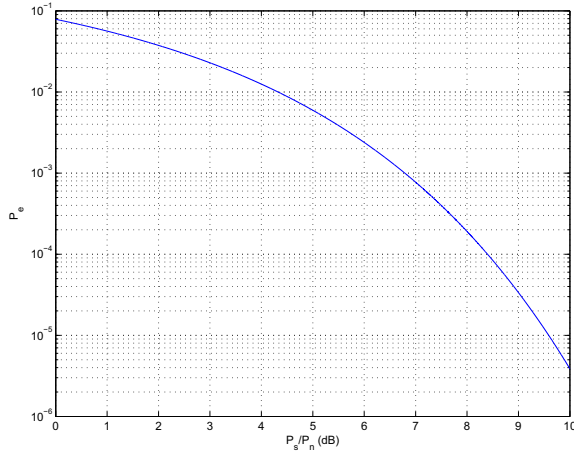


Fig. 3: Theoretical error probability vs. signal-to-noise ratio for a BPSK receiver operating in CGN.

3.2. Undesired CGN + Receiver CGN

Undesired CGN is the reference to which other undesired signals are compared in this study. Undesired Gaussian noise at the radio frequency is CGN at CBB

with a zero-mean Gaussian real part. As stated previously, receiver noise is also CGN. The sum of two independent Gaussian RVs is a Gaussian RV with a mean and variance equal to the sum of the means and variances. Hence, the PDF of $\hat{\mathbf{v}}_x = \mathbf{N}[0, \sigma_u^2 + \sigma_n^2]$ is

$$f_{\hat{\mathbf{v}}_x}(x) = \frac{1}{\sqrt{2\pi(\sigma_u^2 + \sigma_n^2)}} \exp\left[-\frac{x^2}{2(\sigma_u^2 + \sigma_n^2)}\right]. \quad (11)$$

Substitution into equation (7) gives error probability as

$$\mathcal{P}_e = Q\left(\frac{A}{\sqrt{\sigma_n^2 + \sigma_u^2}}\right) = Q\left(\sqrt{\frac{2\frac{P_s}{P_n}}{1 + \frac{P_u}{P_n}}}\right). \quad (12)$$

In this expression, average power of the undesired signal, $P_u = 2\sigma_u^2$, is determined by b and power density of the undesired CGN. Average power of the receiver noise, P_n is established by the specified signal-to-noise ratio. Equation (12) is a reference curve plotted in \mathcal{P}_e versus P_u/P_n graphs to compare other undesired signals to undesired CGN.

3.3. Undesired Constant + Receiver CGN

Undesired CW (assumed to be centered within the bandwidth of the victim receiver) at CBB is a constant with a real part equal to $v_c \cos \theta_c$, where v_c is the constant voltage and θ_c is the offset angle. Adding this constant only alters the mean of the resulting undesired-plus-noise signal, i.e., $\mathbf{v}_x = \mathbf{N}[v_c \cos \theta_c, \sigma_n^2]$, and the PDF is given by

$$f_{\mathbf{v}_x}(x) = \frac{1}{\sqrt{2\pi}\sigma_n} \exp\left[-\frac{(x - v_c \cos \theta_c)^2}{2\sigma_n^2}\right]. \quad (13)$$

Substitution into equation (7) and change of variable gives error probability as

$$\begin{aligned} \mathcal{P}_e &= \frac{1}{2} \sum_{k=0}^1 Q\left(\frac{A - (-1)^k v_c \cos \theta_c}{\sigma_n}\right) \\ &= \frac{1}{2} \sum_{k=0}^1 Q\left(\sqrt{2\frac{P_s}{P_n}} - (-1)^k \sqrt{2\frac{P_u}{P_n} \cos^2 \theta_c}\right), \end{aligned} \quad (14)$$

where $P_u/P_n = \frac{v_c^2}{2\sigma_n^2}$.

Figure 4 illustrates \mathcal{P}_e versus P_u/P_n for a BPSK receiver exposed to undesired constant with different phase offset angles, $\theta_c = \{0^\circ, 30^\circ, 45^\circ, 60^\circ, 90^\circ\}$. Notice that \mathcal{P}_e is dependent on θ_c , and more importantly that $\theta_c = 0$ degrees causes the highest error probability.

Figure 5 illustrates APDs for a variety of Nakagami-Rice distributions corresponding to different constant levels. Amplitudes of a constant plus CGN are independent of phase and described with the Nakagami-Rice PDF

$$f_{\mathbf{w}}(w) = \frac{1}{w_s} e^{-(w+w_c)/w_s} I_0\left(\frac{2\sqrt{w_c w}}{w_s}\right), \quad (16)$$

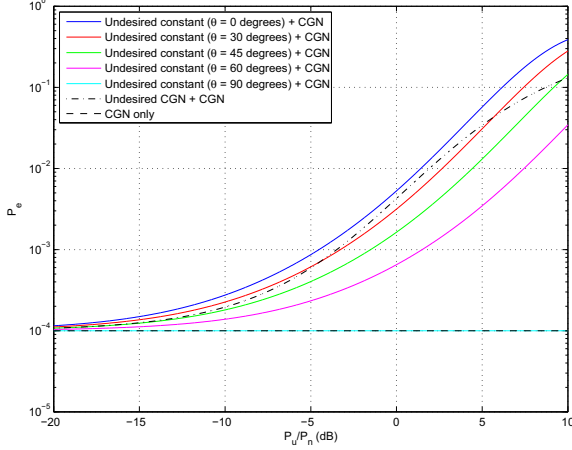


Fig. 4: Theoretical error probability versus P_u/P_n for a BPSK receiver operating at $P_s/P_n \approx 8.4$ dB and exposed to an undesired constant signal.

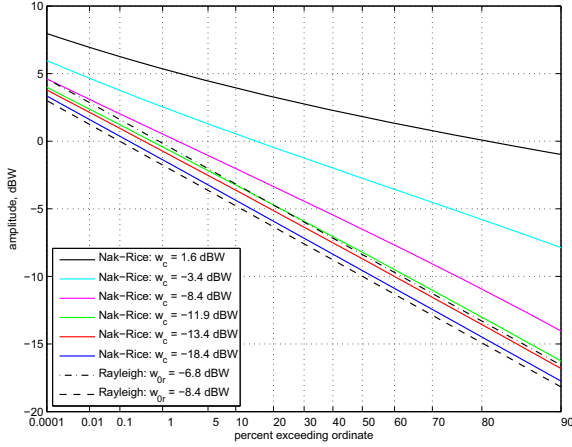


Fig. 5: Nakagami-Rice APDs of constant plus CGN ($w_s = -8.4$ dBW).

where $w_s = 2\sigma_n^2$ is the scattered power, $w_c = v_c^2$ is the constant power, and I_0 is a zero-order modified Bessel function. Equation (16) was integrated numerically with the Quadrature-Romberg algorithm to obtain the APD at a desired accuracy. Also illustrated are Rayleigh-distributed amplitudes of CGN with an APD defined as

$$\mathcal{P}\{\mathbf{w} > w\} = e^{-w/w_{0r}} \quad , \quad (17)$$

where $w_{0r} = \mathcal{E}\{\mathbf{w}\}$ is mean power and $\mathbf{w} = |\mathbf{v}|^2$ is normalized instantaneous power dissipated in a $1 - \Omega$ resistor. The APD of CGN is a straight-line on Rayleigh graph paper with w_{0r} corresponding to the 37th percentile. The two Rayleigh APDs in this figure describe noise amplitudes that produce $\mathcal{P}_e = 10^{-3}$ and $\mathcal{P}_e = 10^{-4}$ for a received BPSK signal with $\hat{s} = \pm 1$.

4. SAMPLE FUNCTION ANALYSES

Unfortunately, $f_{\mathbf{v}_x}$ is often too complicated to integrate analytically, especially when considering the effects of band-limiting by the victim receiver. When analytic solutions of equation (7) are unavailable, a quasi-analytic approximation is used. In this approach, a sample function of the undesired signal plus receiver noise, i.e.,

$$\hat{v}_k = \hat{u}_k * \hat{h}_{R,k} + \hat{n}_k \quad , \quad (18)$$

is used to represent realizations of the corresponding random process.

A CGN sample function can be generated with

$$\hat{n}_k = z_k e^{j\theta_k} \quad , \quad (19)$$

where z_k is a Rayleigh-distributed sample function, and θ_k is a uniformly-distributed sample function with values between 0 and 2π . The inverse method [3] is employed to generate less-common deviates from well-known distributions. From equation (17), for example, Rayleigh amplitudes can be generated by

$$z_k = \sqrt{w_{0r}} [-\ln(\psi_k)]^{1/2} \quad , \quad (20)$$

where ψ_k is uniformly-distributed between 0 and 1.

Probabilities in equation (6) are approximated with

$$\mathcal{P}\{\mathbf{v}_x > A\} \approx \frac{\ell_+}{L} \quad \text{and} \quad \mathcal{P}\{\mathbf{v}_x \leq -A\} \approx \frac{\ell_-}{L} \quad , \quad (21)$$

where ℓ_+ is the number of samples in $\text{Re}[\hat{v}_k]$ that exceed $+A$, ℓ_- is the number of samples in $\text{Re}[\hat{v}_k]$ less than or equal to $-A$, and L is the total number of samples in \hat{v}_k . Note that \mathcal{P}_e results given in this section were approximated with sample functions of $L = 10^7$, and APDs were calculated with 10^6 samples.

In the following subsections, expressions for generating \hat{u}_k are given for substitution into equation (18). Subsequent quasi-analytic approximations to \mathcal{P}_e versus P_u/P_n for a BPSK receiver exposed to MPSK + CGN, impulsive noise + CGN, and gated CGN + CGN are also provided. Note that it is necessary to calculate P_u explicitly from the sample function generated by $\hat{h}_{R,k} * \hat{u}_k$ because it depends on the power spectral density of the undesired signal in addition to the bandwidth of the BPSK victim receiver.

4.1. Undesired MPSK + Receiver CGN

MPSK signals are phase-modulated pulses passed through a transmit filter. Modulation is specified by the number of symbols (M), e.g., $M = 2$ for BPSK, and offset angle (θ_u), which orients the constellation in the complex plane. An MPSK sample function can be generated with

$$\hat{u}_k = \hat{h}_{T,k} * A_u \exp \left[j \left(\frac{2\pi m_k}{M} + \theta_u \right) \right] \quad , \quad (22)$$

where m_k are uniformly-distributed integers ranging from 0 to $M - 1$, and $\hat{h}_{T,k}$ is the impulse response of the RRC transmit filter.

Figure 6 gives performance curves for a BPSK receiver exposed to a BPSK interfering signal with $b_u = 1$ MHz, $a_u = 0.35$, and $\theta_u = \{0^\circ, 45^\circ\}$. Figure 7 illustrates APDs of sample functions for BPSK signals ($\theta_u = 0^\circ$) at a variety of mean powers.

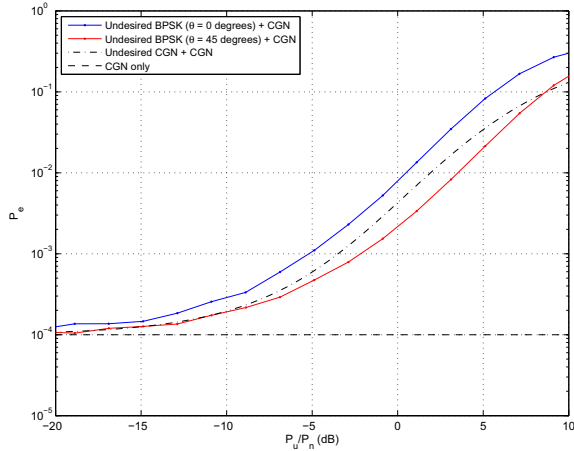


Fig. 6: Error probability versus P_u/P_n for a BPSK receiver ($b = 1$ MHz, $a = 0.35$) operating at $P_s/P_n \approx 8.4$ dB and exposed to undesired BPSK ($b_u = 1$ MHz, $a_u = 0.35$).

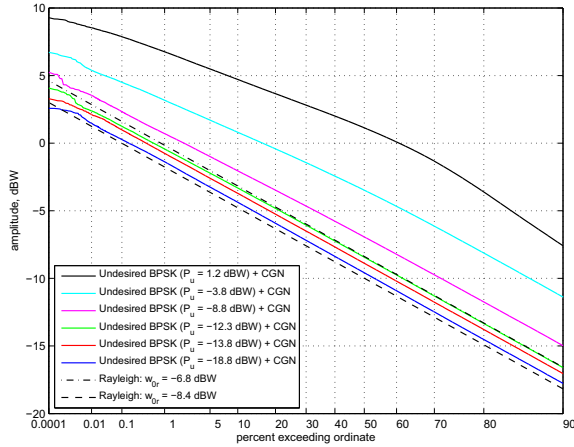


Fig. 7: APDs of undesired BPSK ($b_u = 1$ MHz, $a_u = 0.35$) plus CGN ($P_n = -8.4$ dBW) after the receiver filter ($b = 1$ MHz, $a = 0.35$).

4.2. Undesired Impulsive Noise + Receiver CGN

Impulsive noise can be due to unintentional man-made radiation, such as power lines and automotive ignition systems, or natural sources, such as lightning. The impulsive noise model described in this subsection was

developed and utilized in [4] to reduce measured man-made noise data to a meaningful set of noise parameters and consequently provide a straight-forward means for evaluating receiver performance.

Assuming uniform phase, a sample function of impulsive noise can be written as

$$\hat{u}_k = z_k^{(\alpha)} \chi_k e^{j\theta_k} , \quad (23)$$

where $z_k^{(\alpha)}$ is a Weibull-distributed sample function, and χ_k is a binary sample function that determines the presence of a pulse.

Weibull amplitudes are described by the APD

$$\mathcal{P}\{\mathbf{w} > w\} = \exp\left[-\frac{w}{w_{0w}}\right]^{1/\alpha} , \quad (24)$$

where w_{0w} and α are Weibull parameters. The inverse method permits generation of a Weibull-distributed sample function via

$$z_k^{(\alpha)} = \sqrt{w_{0r}} [-\ln(\psi_k)]^{\alpha/2} . \quad (25)$$

Mean power of a RV with Weibull amplitudes is $\mathcal{E}\{\mathbf{w}\} = w_{0w}\Gamma(\alpha + 1)$. Note that the Weibull APD reduces to equation (17) when $\alpha = 1$.

Pulse time of arrival is assumed to be Poisson distributed with pulse arrival rate γ . The probability that one pulse will arrive in Δt seconds is $\gamma\Delta t$; therefore, the presence of a pulse is determined by

$$\chi_k = \begin{cases} 1 & \text{if } \psi_k \leq \gamma\Delta t \\ 0 & \text{otherwise} \end{cases} . \quad (26)$$

Figure 8 gives performance curves for a BPSK receiver exposed to impulsive noise with $\alpha = 4$ and $\gamma = \{10^2, 10^3, 10^4, 10^5\}$ pulses per second. Figure 9 illustrates APDs of sample functions for impulsive noise ($\gamma = 10^3$ pulses/s, $\alpha = 4$) at various mean powers. Notice the high variability in mean undesired power when pulse events are rare.

4.3. Undesired Gated Noise + Receiver CGN

Undesired gated noise is a cyclo-stationary process used to emulate certain types of UWB signals that periodically turn on and off or hop in and out of the operational band of a victim receiver. To describe the amplitude and time statistics of undesired gated noise, a statistical model developed in [5] is employed. The model is written as

$$\hat{u}_k = z_k^{(\alpha)} g_k(T_g, \tau_{on}) e^{j\theta_k} , \quad (27)$$

where $z_k^{(\alpha)}$ is a Weibull-distributed sample function that can be generated with equation (25). The gating function is defined as

$$g_k(T_g, \tau_{on}) = \sum_{q=-\infty}^{\infty} R(k\Delta t - qT_g; T_g, \tau_{on}) , \quad (28)$$

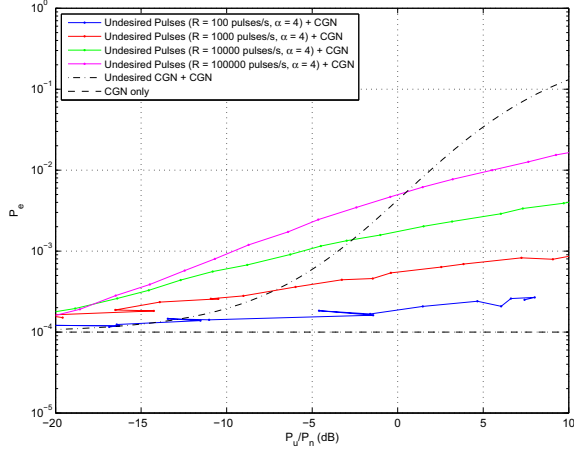


Fig. 8: Error probability versus P_u/P_n for a BPSK receiver ($b = 1$ MHz, $a = 0.35$) operating at $P_s/P_n \approx 8.4$ dB and exposed to undesired impulsive noise.

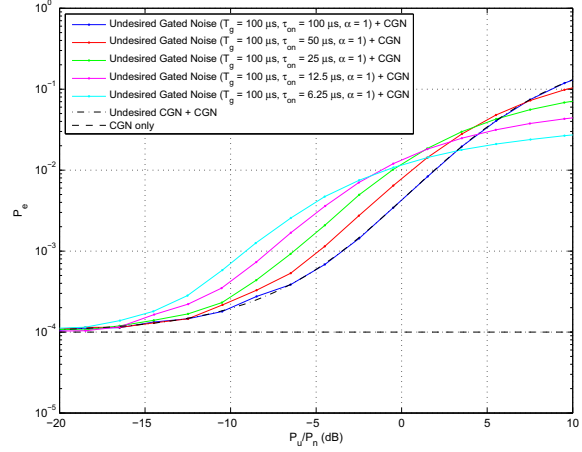


Fig. 10: Error probability versus P_u/P_n for a BPSK receiver ($b = 1$ MHz, $a = 0.35$) operating at $P_s/P_n \approx 8.4$ dB and exposed to undesired gated noise.

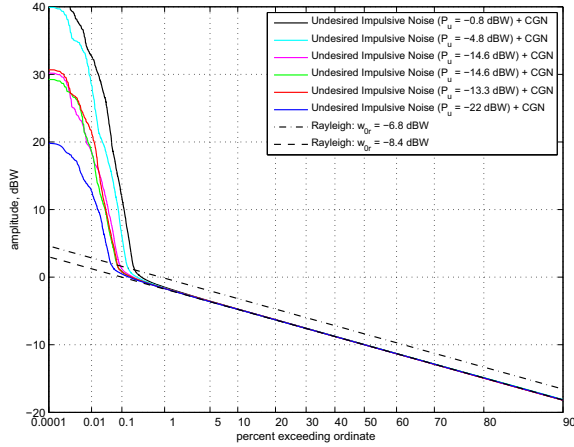


Fig. 9: APDs of undesired impulsive noise ($\gamma = 10^3$ pulses/s, $\alpha = 4$) plus CGN ($P_n = -8.4$ dBW) after the receiver filter ($b = 1$ MHz, $a = 0.35$).

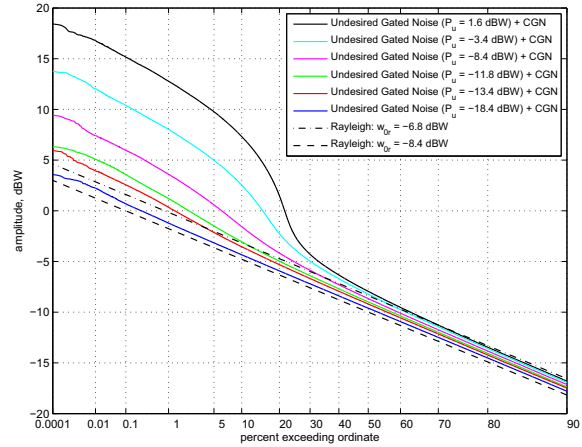


Fig. 11: APDs of undesired gated noise ($T_g = 100$ μ S, $\tau_{on} = 25$ μ S, $\alpha = 1$) plus CGN ($P_n = -8.4$ dBW) after the receiver filter ($b = 1$ MHz, $a = 0.35$).

where

$$R(t; T_g, \tau_{on}) = \begin{cases} 1 & \text{if } 0 \leq t < \tau_{on} \\ 0 & \text{if } \tau_{on} \leq t < T_g \end{cases}, \quad (29)$$

τ_{on} is the gate on-time, T_g is the gate period, and q is an integer.

Figure 10 gives performance curves for a BPSK receiver exposed to undesired gated-noise with $T_g = 100$ μ S, $\tau_{on} = \{100, 50, 25, 12.5, 6.25\}$ μ S, and $\alpha = 1$. Figure 11 illustrates APDs of sample functions for gated-noise ($T_g = 100$ μ S, $\tau_{on} = 25$ μ S, $\alpha = 1$) at various mean powers.

5. DISCUSSION

This paper describes a methodology for assessing demodulator performance in the presence of various types of undesired signals. The goal is to help spectrum engineers understand how different undesired signals affect a victim digital receiver in order to develop fair spectrum policy.

One application is to assess the interference effects of new spectrum sharing technologies. This is done by comparing P_e of an undesired signal to equal power of CGN. For the cases illustrated in this paper, undesired constant signals were generally less detrimental to BPSK demodulator performance than CGN. Undesired BPSK

appeared more-or-less “noise-like.” Impulsive noise with relatively low pulse rate was less detrimental than CGN, but its impact increased with higher pulse rates. Finally, both impulsive noise and gated noise were less detrimental than undesired CGN at relatively high P_u/P_n .

A second application is to validate receiver susceptibility measurements. Figure 12 compares \mathcal{P}_e predictions to susceptibility measurements of a digital television (DTV) receiver exposed to undesired gated Gaussian noise [5]. The tested DTV system utilized quadrature phase-shift keying (QPSK) with a RRC matched filter ($a = 0.35$) and a symbol rate of 19.51 Mbaud. The DTV receiver, operating at $P_s/P_n \approx 11$ dB, was exposed to gated Gaussian noise with on-time $\tau_{on} = 100 \mu\text{s}$ and gating periods $T_g = \{100, 200, 400, 800, 1600\} \mu\text{s}$. QPSK modulation is the superposition of two orthogonal BPSK modulations. Hence, QPSK \mathcal{P}_e predictions are identical to BPSK \mathcal{P}_e except for a 3-dB horizontal shift. Good agreement is demonstrated between quasi-analytic predictions and measurements.

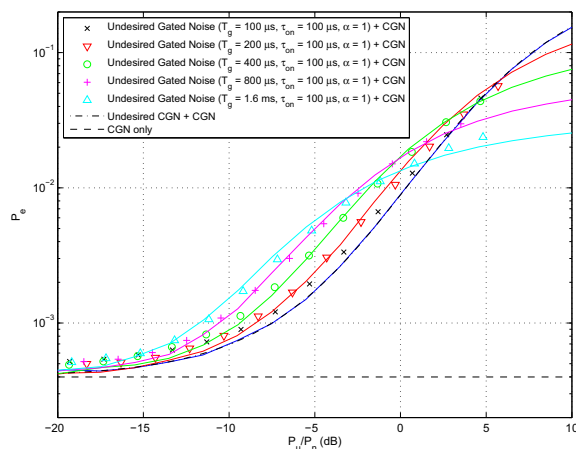


Fig. 12: Comparison between sample-function predictions (lines) and measured DTV susceptibility measurements (data points). QPSK receiver operated at $P_s/P_n \approx 11$ dB and was exposed to undesired gated-noise ($\tau_{on} = 100 \mu\text{s}$).

There are a number of areas where we intend to extend this work. An uncertainty analysis will be performed to achieve confidence intervals for the quasi-analytic results. This uncertainty is a function of L and can be observed in quasi-analytic \mathcal{P}_e results at low undesired power levels and sample-function APDs at low percentiles. The methodology will also be extended to other interferers, e.g., bursty noise, aggregate sources, radar pulses, orthogonal frequency-division multiplexing signals, and other types of noise. Finally, correlations between \mathcal{P}_e and statistical characteristics of \hat{v} (e.g., APD [2], level crossing statistics) will be further analyzed.

ACKNOWLEDGMENT

The author would like to thank Robert Achatz, Dr. Roger Dalke, and Dr. George Hufford for sharing knowledge and enthusiasm on the subject. A special thanks is extended to Dr. Hufford for sharing his insight in statistical distributions, which has been central to my understanding on the subject.

REFERENCES

- [1] Department of Commerce, “Spectrum management for the 21st century: Plan to implement recommendations of the President’s Spectrum Policy Initiative,” Mar. 2006.
- [2] K. Wiklundh, “Relation between the amplitude probability distribution of an interfering signal and its impact on digital radio receivers,” *IEEE Transactions on Electromagnetic Compatibility*, Vol. 48, No. 3, pp. 537–544, Aug. 2006.
- [3] M. Abramowitz and I.A. Stegun, *Handbook of mathematical functions*, NBS Applied Math Series 55, New York, NY: Dover Publishing, 1964.
- [4] R.J. Achatz, Y. Lo, P.B. Papazian, R.A. Dalke, and G.A. Hufford, “Man-made noise in the 136 to 138-MHz VHF meteorological satellite band,” NTIA Report 98-355, Sep. 1998.
- [5] M. Cotton, R. Achatz, J. Wepman, and P. Runkle, “Interference potential of ultrawideband signals: Part 2 - Measurement of gated-noise interference to C-band satellite digital television receivers,” NTIA Report TR-05-429, Aug. 2005.

Using a split model improve the simulation of industrial environment propagation conditions

S.Benferhat, M.Misson
LIMOS-CNRS, Network and Protocols Team, Blaise Pascal University
B.P. 86, 63172 Aubiere Cedex, France
{Sabri, Misson}@sancy.univ-bpclermont.fr

One of the main reasons to choose WLAN for applications in industrial environments is the mobility of the communicating entities they allowed. In that particular domain, the conditions of propagation of the radio signal are often much more complex than those in office buildings for example. In this paper, we point out the difference between the real propagation conditions in an industrial environment and the performances measured and given by a simulation process using default parameters. Measurement results are used to compute and to choose a propagation model for an 802.11b cell overlapping a production line. In such environment, a unique model must have a high random component to take into account the disparity of the links between the Access Point and the stations, and between multiple stations. In order to have more realistic results by simulation, a new path loss representation is used, a "split model" is proposed and introduced in an OPNET simulation process. The impact of this choice is shown by the evaluation of the frame loss rate causing by the hidden terminal effect. Parameters of the standard models hide this phenomenon, which leads to simulation results that are not accurate.

1. Introduction

CSMA/CA was chosen as the access method to the medium for the DCF option of the 802.11 WLAN standards. Carrier sensing is the basic operation in the CSMA scheme; it allows the communicating entities in range to schedule their transmissions and to reduce the interferences due to concurrent transmission [1] [2]. The possible traffic in cell of type 802.11 located in an industrial environment, depends mainly on the access method and the conditions of propagation.

The conditions of propagation have a very significant role on the carrier sense and on the size of the cell in which communicating entity can move. In an industrial environment this can reduce the range and mask the state of medium which cause problems to CSMA/CA mechanism. Numerous studies and measurements have been carried out to determine the characteristics of radio waves propagation in various environments [3] [4]. Many generic propagation models result from these studies [5]. To have meaningful results on the WLAN performances given by a modeling and simulation process, it is necessary to choose a correct propagation model fitting the environment of this WLAN. However, we face a great diversity of industrial environments that is why there is no appropriate propagation model. Because of the lack of a clear and precise definition of "industrial environment", this study is done for a generic application representative of an activity of a small production line.

In this paper, we show that the use of usual default models to evaluate the transmission activity in a radio cell overlapping a production chain is not appropriate. The results obtained by simulation can be very different from those obtained by measurements.

2. Definitions and Assumptions

2.1. Concept of cell

Wireless LAN deployment in an industrial environment must be evaluated in terms of performance and flexibility relatively to environmental threats. So far, to insure reliable system operation in a variety of indoor locations, there is really no substitute for a site survey to identify shaded areas and to determine the resulting range. This data should be used for simulation parameter setting and to plan the RF equipment deployment such as the choice of devices location for example.

We chose to work with 802.11b in infrastructure mode which allows a broader covering. In this mode the stations are associated to a particular station which plays the role of relay for the packet between the source and the destination. This entity called Access Point (AP) takes part in the infrastructure and each affiliated station must be in range of its AP. AP and Stations can manage different data rates according to the expected range.

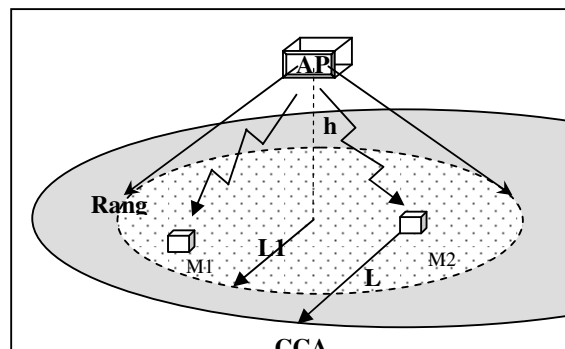


Figure. 1. Cell overlapping.

In this study, the zones of evolution of the mobiles are those defined by the (AP-Station) range allowing us the highest data rate provided by 802.11b standard solutions. A cell attached to an Access Point can be seen as the set of points of the zone of evolution of the communicating entities for which the received energy is higher than the threshold of decoding transmitted information. This threshold depends on the modulation and the bandwidth used. It is approximately -82 dBm for 802.11b with a data rate of 11 Mbps for example [6]. These points are usually represented as the surface of a disc whose radius is indicated by "Range" in (Figure. 1).

The CSMA/CA access method, like all the options of the CSMA type, probes the channel to know its state, a transmission being considered only if this state is "Idle". The occupation of the channel is also detected by the comparison of the received energy with a threshold. Thus, to emit it is necessary that the CCA (Clear Channel Assessment) of the 802.11 physical layer returns "Idle" as the value of the CCA Indicator. The threshold used to define this state is typically -95 dBm in the case of a WLAN such as WiFi (802.11b version) [2].

In Figure. 1, any transmission activity of a mobile M2 will be detected by any mobile in the grayed zone (as mobile M1). Because we are dealing here with wireless transmissions that conform to the 802.11b standard with a fixed data rate of 11 Mbps, the -82 dBm and -95 dBm are the two received powers (in dBm) which define respectively the distances L1 and L2, which will be used thereafter to study the conditions of traffic within a cell in an industrial environment.

2.2. Concept of industrial environment

The propagation of 2.4 GHz radio waves is relatively easy to define and model when the transmission is supposed to be in a free space area. It is not the same to describe the phenomenon of propagation which relates to a factory, or an assembly chain [7]. The deployment of such solutions is generally done by cartography the received powers by positioning before the Access Points in high points chosen more or less empirically. Such solutions work well, but if the performance (throughput, transit delay...) of such networks are compared with those resulting from a simulation step by using tools like OPNET [8] or NS2 [9], very significant differences are observed. That obliges us to reconsider the way of modeling the conditions of propagation in such an environment [10] [11] [12]. The goal of the study is to propose a way to simulate traffic conditions within an 802.11 cell overlapping an industrial area. In the absence of a reference model of such industrial environment, we chose a zone of deployment which is representative of an activity of production or an

assembly chain as shown in Figure. 2. It is an area composed with pieces of equipment arranged in many straight lines and separated by tracks in which circulate workmen and/or robots which represent the mobile entities requiring wireless communications.

A soap bar production line, used for the student training on automatic control systems, will be considered as a relevant and representative factory in which measurements given in the following were carried out. These measurements will be used to adjust the modeling process of the conditions of propagation and to explain certain malfunctions.

The cell we are dealing with covers a part of the factory which consists of 2 production lines: a central line (Figure. 2) and a lateral line (Figure. 3). The machinery of these lines produces cakes of soap and labels them.

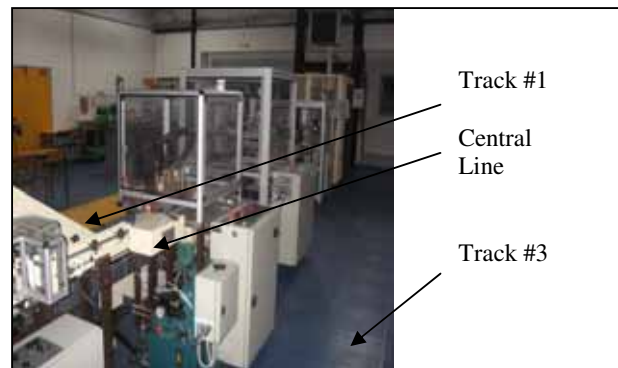


Figure. 2. Factory environment.

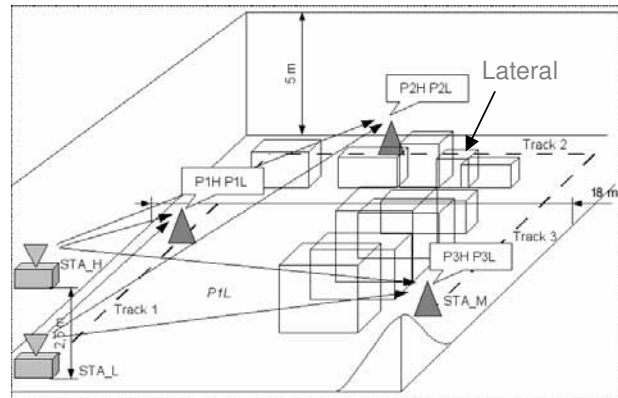


Figure. 3. Fitting of the machines.

3. Protocol of Measurements and Modeling of the Conditions of Propagation

3.1. Measurements

To study the conditions of propagation, we chose to measure the path loss effects between two fixed points (STA_L, STA_H) and a mobile station (STA_M) as shown in Figure. 4. The two fixed points are on the same vertical axis, the High Point is located at 2.5m above the ground. This location was chosen in order to represent the Access Point position. The low point and the mobile station are at about 50cm above ground level.

Measurements of the received power are carried out as the mobile station moves within a horizontal plan located 50cm above the ground surface, in the three tracks of the production unit (Figure. 3). These trajectories of the mobile station represent the possible footpaths of workman or a robot.

The measuring instrument used was developed from the extensions "wireless tools" of Linux [13]. They are APS allowing the users to have access to the information of the driver, to the configuration and the specific parameters of the wireless interfaces. Every 100ms we sent 100 packets from a mobile station to the AP and to the fixed station. The samples obtained are presented in Figure. 5.

Measurements show the power loss according to the distance between the transmitter and the receiver. Our goal consists in determining the appropriate parameters to the path loss which characterizes our environment.

A series of measurements was made for each of the zones: track#1, track#2 and track#3. The measurement results obtained for each track are a cloud of points as given in Figure. 5. All these points will be used for the linear regression computation and the $X(\sigma)$ approximation that will be presented in the following. To compare these results with those from the usual default models, we chose to plot points representing an average attenuation versus distance. These measurements are shown in Figure. 6.

Our measurements are framed by two curves obtained by simulation based on the two main models suggested by the simulation tools: Free Space Model ($1/D^2$) and a model with distance power loss coefficient equal to 4 ($1/D^4$) [7].

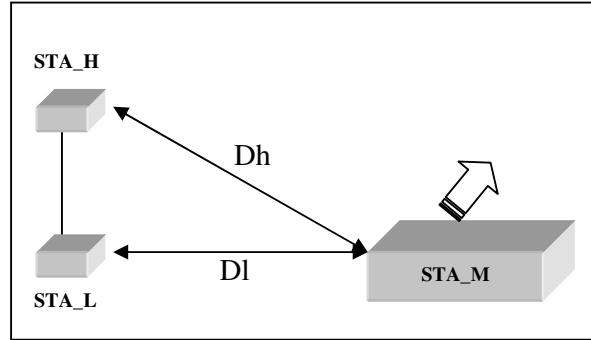


Figure. 4. Measurement process.

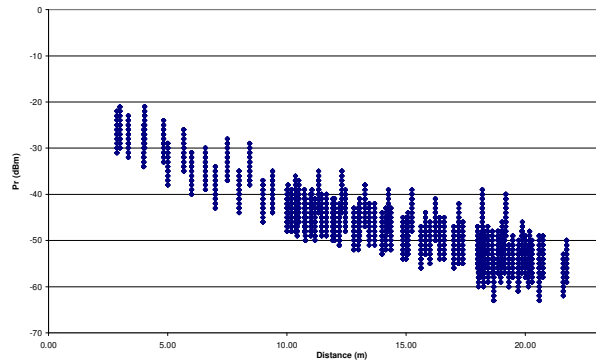
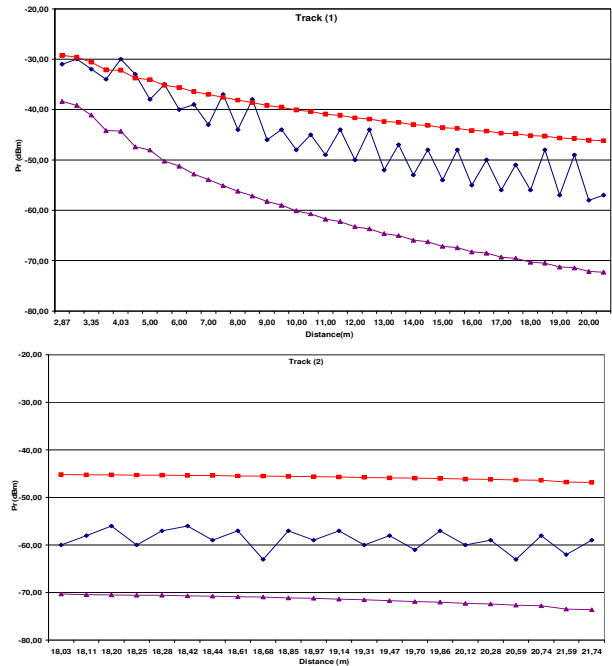


Figure. 5. Cloud of points obtained for track#1



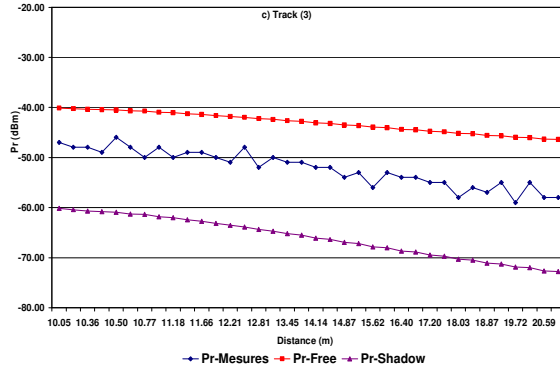


Figure. 6. Results per track

These curves do not give a good approximation of our measurements. In fact, Free Space is a model always too favorable even in the case of the track #1 for which there is no obstacle between the points of measurement. The curves for track#2 and track#3 correspond to a propagation which is done through a line of machine. The average slope of these curves does not correspond any more to a $1/D^2$ law. In these two cases, we can see that we approach the model in $1/D^4$ which remains most of the time too severe [12].

3.2. Modeling Process

We have just pointed out that in our case one of the models is too optimistic and the other is too pessimistic. To obtain results closer to reality from a simulation process, we decided to act on the propagation model by adjusting the parameters of the generic formula:

$$Pr = Pt + Gt + Gr - (Ctv + 10 * N * \log_{10}(D) + X(\delta)) \quad (1)$$

Equation (1) is given in its logarithmic form where:

Pr is the received power expressed in dBm.

Pt is the transmitted power expressed in dBm (in our case 20 dBm).

Gt and Gr are the transmitted and received antenna Gain, measured in dbi.

Ctv is a tuning variable which takes into account the frequency used, antenna cable losses ...

D is the distance between the transmitter and the receiver.

$X(\delta)$ introduces a random component with δ standard deviation to take into consideration the fact that the space is not homogenous.

D and Pr are measured.

Ctv and N are given by a linear regression of measurements as recommended in [7] and the acceptable law for $X(\delta)$ approached by the test of Kolmogorov [14].

For the different tracks, we obtained the following models for the received power shown in table 1.

Table 1. Pr Vs D Model per Track

Area	Model	Average $X(\delta)$ Normal law
Track #1	$Pr = 20 - (49.54 + 24.65 \log_{10}(D) + X(9.07))$	-3.89^{E-12}
Track #2	$Pr = 20 - (28.66 + 46.05 \log_{10}(D) + X(8.00))$	-0.01
Track #3	$Pr = 20 - (43.51 + 32.92 \log_{10}(D) + X(8.98))$	3.48^{E-13}
Track 1&2&3	$Pr = 20 - (43.52 + 32.57 \log_{10}(D) + X(9.04))$	1.87^{E-12}

3.3. Comments of the results

The obtained results for the estimation of the received power are given in Tab.1. They show that the path loss coefficient N follows $2 < N < 4$ except for track#2 which is a very short line with a lot of devices on the path of the signal.

The role of the random component $\chi(\delta)$ in the Pr estimation is very predominant because the standard deviation of the normal law is 8 dBm or more.

4. Modeling contributions

4.1 Comparison with ITU R-1238 Recommendations Model

To fit the average behavior of the signal propagation conditions in our environment, we propose an intermediate model which we call ITUR-1238 in the following. The choice of the parameters of formula (2) is driven by recommendations suggested by ITU for such application domain [15].

$$Pr = Pt - (20 \log_{10} f + N \log_{10}(D) + L_f(n) - 28) \quad (2)$$

Where:

- N: distance power loss coefficient

- f: frequency (MHz)

- D: separation distance (m) and $D > 1m$

- L_f : floor penetration loss factor (dB), not relevant in our case

- n: number of floors between the base station and portable

This model gives the intermediate curve, which fits well with our global measurements (Figure.7). In the previous graph, the random component is not taken into account. With the results obtained given in Table 1, it is possible to fix the parameters of equation (2) and we obtain:

$$Pr = 20 - (39.60 + 30 \log_{10}(D)) \quad (3)$$

4.2. Split model contribution

The dominant role of the random component let us consider the fact that horizontal signal propagation conditions can be far from those for vertical one.

Let us now consider the path loss effects according to whether it is a link with the high fixed point (Dh) or with the low point (Dl). We can note that

for track #1, the path loss of the high link is closest to a free space attenuation model; this latter is behaving more or less like an asymptote for our measurements. In the case of the low point the most severe path loss effects were noted in the case of the track #2 as shown on part (b) of Figure. 8. Let us compare the path loss effects according to Dh and DI link, the results are given in the three parts of Figure. 8. For each track, we can then clearly identify that the curve of the power received by the high fixed point differs from the one corresponding to the low fixed point.

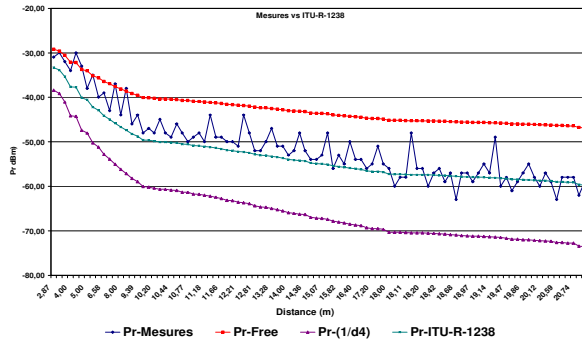


Figure. 7. ITU R-1238 model.

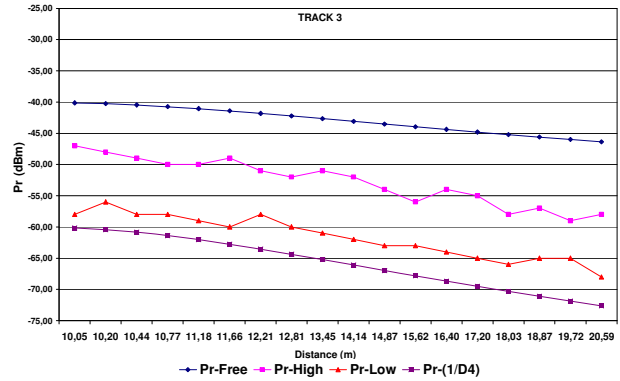
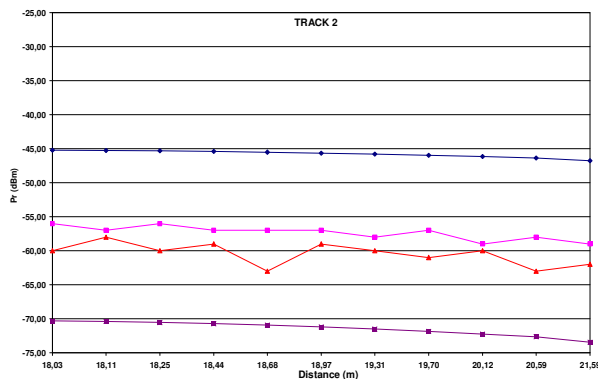
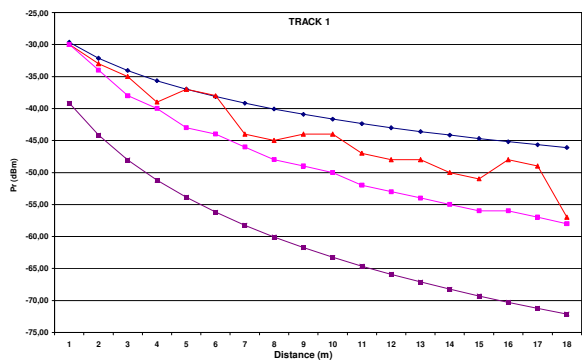


Figure. 8. Results per link type.

The fact of considering only one model of attenuation (usually following a $1/D$ law) for any of the link types is one of the reasons which explain the differences between the experimental results and those resulting from a simulation process.

By considering all these measurements it seems interesting to consider a model for the link (AP–Station) and another for the link (Mobile–Mobile). By using the same computation technique as the one just presented previously, we obtain a model depending on the type of link as given in Table 2. This model with two components is called “Split model” in the following.

Table 2. Pr Vs D Model per Track

Area	Model	$X(\delta)$ Average Normal law
AP-Mobile	$Pr = 20 - (47.80 + 28.91 \text{Log}_{10}(D) + X(3.36))$	2.61^{E-13}
Mobile-Mobile	$Pr = 20 - (44.85 + 37.54 \text{Log}_{10}(D) + X(3.87))$	-1.76^{E-12}

5. Simulation and Results

5.1 Identification of Hidden Areas

Our measurements and the just presented split model make it possible to illustrate the problems of the “hidden terminal” in such environment [16]. This is due to the fact that the conditions of propagation between access point and mobile on one hand, and between mobile on the other hand are significantly different.

Let us consider two mobiles (M1 and M2) located in the same cell with a distance D between them. As shown in Figure. 9, we suppose that these two mobiles are in range of the Access Point, i.e. the power received by M1 and M2 is higher than 82dBm. To manage the access to the medium, it is necessary that these two mobiles are able to detect a reciprocal activity, i.e. if M2 transmits, this activity must be seen

by M1 with a power higher than -95 dBm. Based on our split model, we will show that this condition is not always true.

By considering the same model of the path loss for the whole of the link as it is the case for various simulation tools, we assume that as long as the coefficient of the path loss N is between 2 and 4 L_2 is always higher than the double of L_1 . In this case, any activity in the zone covered by the Access Point will be detected by other mobiles regardless of their position in the cell.

In our case, the model is split according to the links AP/Mobiles and Mobiles/Mobiles, which is due to the conditions of propagation that are completely different. In the same cell some mobiles can be out of the CCA range of a transmitting mobile. In Figure. 10, by eliminating the effect of the random components from the formulas (4) and (5), we observe that the threshold of CCA detection (-95 dBm) appears well before the sensitivity threshold (-82 dBm) on the graph of equation 4. In this case in certain location, a mobile can be in the range of the Access Point, but its activity is not detected by some mobiles in the cell.

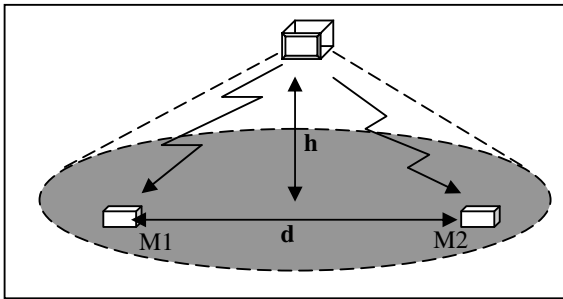


Figure. 9. Reference configuration.

In Figure. 10, distances L_1 and L_2 are introduced, the first one indicates the range of the mobile AP and the other L_2 indicates the radius of the disc in which an activity of M_2 can be detected. Our measurements showed that these two distances are determined by different conditions of propagation. To estimate them, it is necessary to use different models of propagation. Thus for L_1 a model with an attenuation following a $1/D^{2.8}$ law seems to be appropriate whereas for L_2 we need a more severe model, our measurements indicate a $1/D^{3.7}$ model as shown in Table. 2. We consider for the oblique link (M_2 to AP) model of type:

$$Pr = Pt - (47.80 + 28.91 \log_{10}(D) + X) \quad (4)$$

For the horizontal links, we consider:

$$Pr = Pt - (44.85 + 37.54 \log_{10}(D) + X) \quad (5)$$

If we retain -82 dBm as the power threshold of good reception and -95 dBm for the detection of

activity on the radio channel we find then respectively for L_1 and L_2 67m and 54m.

This is explained in Figure. 10 by the following description: If $D > L_2$ these two mobiles are exposed to the problem of the "hidden terminal" i.e. they are not able to detect if the other mobile has taken the initiative to transmit.

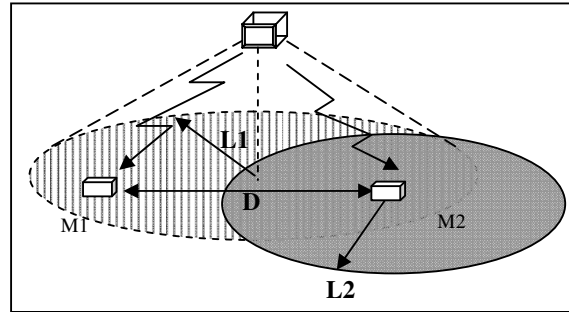


Figure. 10. Hidden zone.

5.2 Modifications of OPNET pipeline

In order to approximate the effects of the physical layer for wireless networks, OPNET employs a 14-stage computational pipeline to process transmitted packets [8]. The receiver power is calculated by the "power model" stage attribute of the radio receiver. The purpose of this stage is to compute the received power of the arriving packet's signal (in watts). In general, the calculation of received power is based on factors such as the power of the transmitter, the distance separating the transmitter and the receiver, the transmission frequency, and transmitter and receiver antenna gains. We have made major modifications to the default received power stage.

The most important modification at the stage is in the calculation of the received power based on our split model. Any packets received by station from AP or by AP from station, are calculated using model described by equation 4. And in the other hand all transmission detected by station and coming from another one, we use model described in equation 5.

Before deciding to access the medium a mobile has to check the state of the channel to know its state, a transmission being possible only if this state is "Idle". The area in which the channel is occupied ("Busy") is given by the range of the CCA. So when a mobile has to transmit, OPNET has to compute the received signal from all the mobiles within the cell with the propagation model (2) and the received signal from the AP with the propagation model (1).

- If one of these received power computations is higher than -95 dBm the channel is considered as "Busy" and the transmission is deferred.

- If the channel is “Idle” the frame is sent to the AP, before being relayed to the target mobile. The propagation model (1) is used to check if the received power is higher than -82 dBm. The random component $\chi(\delta)$ introduces some cases of failure.

5.3 Results Discussion

Figure. 11 give the number of received packets obtained by simulation. If the same model of path loss is used for all the stations we have few packets lost, because all the stations are in range of the CCA of all the others stations. Whereas in the case where the split model is used the number of packets in collisions due to the problem of the hidden terminal is considerable compared to the number of emitted packets. Any mobile such M1, outside the CCA of M2 is in a hidden area for M2. Hidden area is the hatched croissant in Figure. 10.

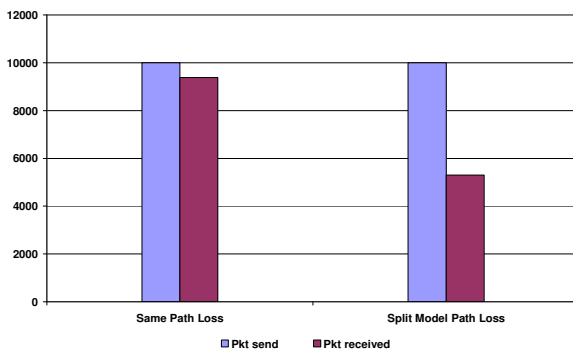


Figure. 11. Packets loss

Ces résultats n’auraient pas pu être constaté dans le cas où l’on utilise un model de propagation unique.

6. Conclusion

A simulation process done to evaluate the performance of a WLAN in an environment other than a free space requires the choice or the development of a model of propagation adapted to the local conditions of propagation. The default choice of the model suggested by simulation tools (mainly the Free Space model) cannot be satisfactory, because it is too optimistic in a great number of cases. A solution consists in fixing the parameters of a model of propagation adapted to the environment as that was done here with the ITU R-1238 model.

In an environment such as a workshop or factory, the difference between the conditions in horizontal propagation and those with an Access Point located in a high place, can be very significant. This generates medium access conflicts known as the “hidden terminal effect” in areas we called “hidden areas”. The

evaluation of such a consequence can be carried out by using a split model for the path loss attenuation.

References

- [1] K. Pahlavan, P. Krishnamurthy, "Principles of Wireless networks: A unified approach", Ed. Prentice Hall, Dec. 2001.
- [2] [IEEE 802.11 protocol] IEEE 802.11, Part 11: Wireless LAN Medium Access Control (MAC) and Physical Layer (PHY) Specifications, Standard, IEEE, August 1999.
- [3] P. Mariage, M. Liénard, P. Degauque, "Theoretical and experimental approach of the propagation of high frequency waves in road Tunnels," IEEE Trans. Antennas Propagation, vol. 42, No 1, pp. 75-81, Janvier 1994.
- [4] M. Moutairou, H. Aniss, G. Y. Delisle, "Underground mines application of wireless Mesh Networks," IEEE 13th International Conference on Telecommunications, ICT2006, Portugal, pp. 587-590.
- [5] T. K. Sarka, Z. Ji, K. Kim, A Medouri, and M. Salazar-Palma, "A survey of various propagation models for mobile communications," IEEE Antennas and propagation Magazine, vol. 45, No. 3, June 2003.
- [6] Intersil, "Measurement of WLAN Receiver Sensitivity", technical brief, February 2000.
- [7] T.S. Rappaport, "Wireless communications: principles and practice", Ed: Prentice Hall, 2002.
- [8] OPNET Modeler V 11.5.PL3 <http://www.opnet.com/>.
- [9] The network simulator - ns-2, www.isi.edu/nsnam/ns/
- [10] Takai M.; Bagrodia R.; Tang K.; Gerla M. "Efficient Wireless Network Simulations with Detailed Propagation Models" Wireless Networks, Volume 7, Number 3, May 2001, pp. 297-305(9)
- [11] Hashemi H., "The indoor radio propagation channel", Proc. of the IEEE, Vol. 81, n° 7, Jul.1993.
- [12] Neskovic A., Paunovic G., "Modern Approaches in Modelling of Mobile Radio Systems Propagation Environment", IEEE Communications Surveys, Third Quarter 2000, <http://www.comsoc.org/pubs/surveys>.
- [13] http://www.hpl.hp.com/personal/Jean_Tourrilhes/
- [14] Numerical Recipes in C: The art of scientific computation. Cambridge University Press, 1988-1992.
- [15] International Telecommunication Union, ITU-R Recommendation, P.1238: "Propagation data and prediction models for the planning of indoor radio-communication systems and radio local area networks in the frequency range 900 MHz to 100 GHz", Geneva, 1997.
- [16] C. Fullmer and J. Garcia-Luna-Aceves. " Solutions to Hidden Terminal Problems in Wireless Networks." In Proceedings of Sigcomm 1997, Cannes, France, 1997.

Measurement data for improving ITU-R Recommendation P.1812

Mike Willis, Ken Craig, Nick Thomas

Radio Communications Research Unit, STFC Rutherford Appleton Laboratory, UK

Tel: +44 1235 445492 Fax: +44 1235 446140 Email: m.j.willis@rl.ac.uk

Abstract

This paper describes the testing process for improvements to ITU-R Recommendation P.1812 including the development of a clean database of propagation measurements suitable for testing modifications to the recommendation. This database is based on an extension to the ITU-R Study Group 3 database of terrestrial propagation measurements to now include the additional data sets. Measurement records have been flagged with information regarding our confidence in the record accuracy and with other data to assist in grouping measurement sets for analysis. The updated database is presented along with the rationale behind the set of rules used in the categorisation of each measurement point. A web based data and model result extraction tool has been written to assist in quantitatively evaluating the performance of each proposed improvement to P.1812. Some sample results from this tool are provided to demonstrate the utility of the flagged database.

1. Introduction

ITU-R Recommendation P.1812 [1] is a new recommendation first published in 2007 that contains a path-specific propagation prediction method for point-to-area terrestrial services operating up to 3GHz. It is a simplified version of Recommendation ITU-R P.452 [2] that has been extended down in frequency range to 30 MHz. The new recommendation covers the time percentage range from 50% to 1% and predicts location variability from 1% to 99%. Where detailed terrain and clutter data is available, recommendation ITU-R P.1812 aims to give improved accuracy over the non path-specific model contained in Recommendation ITU-R P.1546 [3].

Improvements to a propagation prediction model can only be quantitatively evaluated through comparison with measured data. A database of terrestrial point to point propagation measurements has recently been assembled by ITU-R Study Group 3 [4] based on a concatenation of several existing measurement sets. While a great improvement over previously the available database, longer paths were still not well represented in this database. This database has now been extended by incorporating data from COST210 [5] and the Ron Sandell dataset [6].

During initial testing of diffraction models with the aim of improving ITU-R P.1812, an irreducibly high standard deviation of error was found for all candidate models. Further, these error distributions were not as expected and while some of this behaviour was undoubtedly due to weaknesses in the models, it was also clear that many of the larger prediction errors were being caused by erroneous measurement records. In any large set of measurement data some errors will inevitably occur, either at the time of the measurement or in subsequent processing. It was suspected that some serious problems with only few of the measurement results were causing some very large errors which were then masking the more subtle differences between prediction models.

To address this, an “improved” database [7] has been created through adding a quality classification to each measurement. This categorises each record as good, reasonably good, or not good. Through only testing against measurements classified as good or reasonably good, models can be checked against data considered to be accurate. Therefore prediction errors can only arise through deficiencies in the models. While categorising the measurement records the opportunity was taken to improve the tagging of each record to facilitate detailed statistical analysis of model performance against specified measurement parameters, for example antenna height above ground or climatic region. Useful model input data has also been added where appropriate, for example land/sea/coastal data, surface level refractivity and refractivity gradient. Including this data in the records reduces model run time and also allows standardised values to be used in verifying agreement between alternative software implementations of each model.

2. The contents of the measurement database

The extended database consists of 35,800 measurements covering 5832 paths. Each record is stored in XML format and contains the path data including a path profile, transmitter and receiver data and one or more field

strength measurements. Around 9% of the measurements are long term taken over periods of several months or years with the remaining 91% being spot measurements or measurements of unknown duration.

The geographical distribution of the overall dataset is shown in Figure 1. It includes 14 sets of data from the European Broadcasting Union (EBU), data from the Asian Broadcasting Union (ABU), data from two campaigns in the USA and data from a recent campaign in Switzerland. To increase the scope of the database, in particular to increase the number of long term measurements, the COST210 and Sandell datasets have been added.

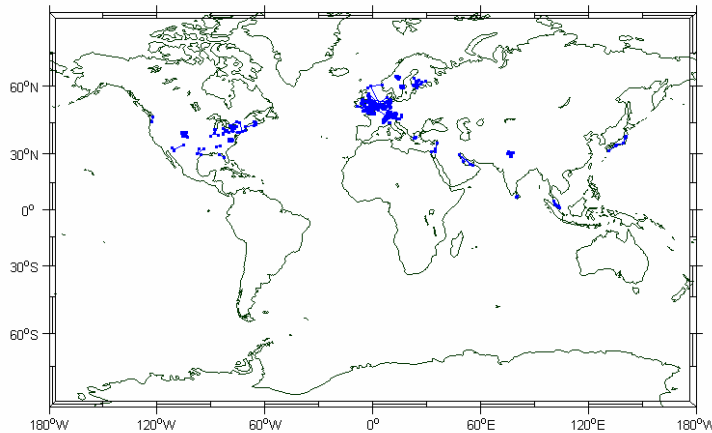


Figure 1 : Geographical distribution of data sets

Figure 1 shows that there is a strong bias towards Northern European and North American climates. The bulk of the data consists of measurements made in the continental USA with the majority of the remaining measurements made in Europe. The vast majority of the measurements lie within the scope of ITU-R P.1812 and are useful for developing the recommendation. A few measurements fall outside either the frequency range or the time percentage range of ITU-R P.1812 but all measurements, even if out of scope are retained in the database.

3. Measurement issues

Using the entire data set to test models produced some unusual results. The error statistic examined was the difference in dB between the predicted path loss and the measured path loss for each measurement. It is proposed that, in a good model, the distribution of this error metric should be approximately Gaussian in shape. Well known statistical metrics including mean and standard deviation, skewness can then be used in the comparison of prediction models.

The resulting error distributions for the complete database compared to ITU-R P.1812 were far from Gaussian. They were in many cases multimodal and with large mean offsets between data sets and standard deviations of the order of 10 dB or more. It was suspected that some of this discrepancy was being caused by a few of the measurements and a closer examination of the data revealed some problems.

In some cases the location of the terminals was not given to sufficient resolution. This puts a question over the accuracy of the supplied path profile. It also means the profile can not be re-generated using a terrain database. In other cases there were problems with the path profile, which was occasionally not monotonic, or of too low resolution to be useful.

Closer analysis of measurements with the model also showed some issues, for example apparently line of sight paths with high losses. In these cases it is possible that a ground reflection had caused a null in the antenna pattern which had not been correctly taken out through a height gain measurement. Another possibility is local terminal clutter, especially at lower antenna heights.

In some cases many height gain functions were provided, but without any information regarding clutter. This particularly affected the US data sets where the measurements were taken many years ago and the information about the local clutter has become lost. Using these results, which are essentially all the same path except for the terminal height, will clearly lead to errors and will also bias the statistics. There are frequently 10 or more height sample steps in each height gain set and without further information about local clutter, only the top height measurement should be taken for testing ITU-R P.1812 as it is the least likely to be affected by clutter. Separating height gain functions without clutter from those with clutter was considered to be too labour intensive.

Finally, it was discovered that with the addition of the COST210 and Sandell data sets some links were new duplicated within the database. Duplicate records have been were flagged to prevent their use in the analysis as this would cause a statistical bias.

4. Flagged data

To overcome some of the data issues a data flagging exercise was carried out. Each record was associated with a set of flags contained within the SQL database. These flags covered two major cases, validity and whether the measurement could be considered as long term. Further flags were then created to indicate if the measurement was part of a height gain set and whether it was the highest point in a set. The breakdown of the data into these categories is shown in Table 1.

Table 1 Flagging of measurement records

Field and Value		# Links (measurements)
Total		5832 (35840)
IsValid=0 (test links)		8 (24)
IsValid=-1 (TX, RX location concerns)		38 (130)
IsValid=-2 (profile concerns)		32 (104)
IsValid=-3 (clutter concerns)		341 (3226)
IsValid=-4 (duplicate link)		19 (27)
IsValid=-5 (LOS path loss concerns)		21 (823)
IsValid=1	InputsValid=1 IsTopRXHeightInGroup=1	5316 (11049)
IsValid=1 IsLongTerm=0	Total	4922 (29061)
	InputsValid=1	4914 (25309)
	InputsValid=1 IsTopRXHeightInGroup=1	4914 (9639)
IsValid=1 IsLongTerm=1	Total	428 (2307)
	InputsValid=1	402 (1410)
	InputsValid=1 IsTopRXHeightInGroup=1	402 (1410)

The most valuable data for testing the model are the long term measurements, however there are only 402 of these and they are not evenly distributed over the database. Figure 2(a) shows that the bulk of the point measurements are in the range up to 150km whereas Figure 2(b) shows that most of the long term measurements are in the 50-1000km range. It is also clear from Figure 2 that there are many more point measurements than long term measurements. Figure 3 repeats Figure 2 but this time for frequency. There is a strong bias in the data towards the VHF end of the spectrum, with the UHF region proportionately better represented in the long term data.

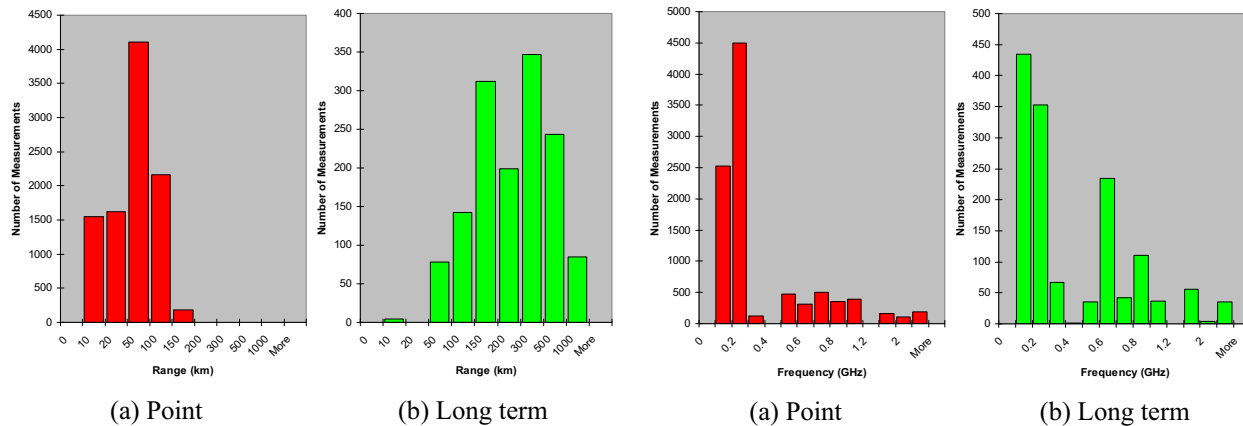


Figure 2 : Distribution of data sets with path length

Figure 3 : Distribution of data sets with frequency

The joint distribution of frequency and path length for all data are shown in Figure 4, there are some gaps in the parameter space for model testing but overall the coverage is reasonable.

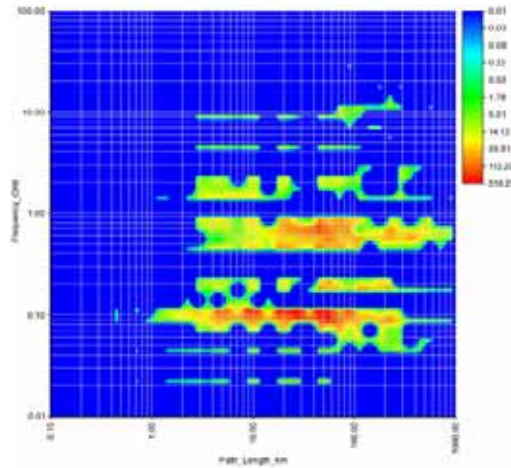


Figure 4 : Joint distribution of path length and frequency

5. Accessing the data

The measurement results have been stored in an SQL database which is available via the internet from [7]. A utility is included to output data in XML and also in the original ITU-R CSV format for backwards compatibility. It should be noted that added fields discussed in the previous section are not supported in the original CSV format.

The basic structure of the SQL database is shown in Figure 5. Each box represents a separate table in the database. The sizes loosely represent the actual dimensions of each table. The colour parts to each box represent that table’s unique key which should be used for cross-linking tables. Through the use of concatenated SQL queries data subsets can be extracted – for example a query might return all measurements with a path length of between 20 and 30km, made at frequencies above 300MHz. Alternatively, model derived parameters may be used, so a suitable query could return all cases where according to ITU-R P.1812 the troposcatter mechanism is dominant. Such queries soon become a very powerful tool for analysis.

Associated with the database is a web application which interfaces with GoogleMaps™. This allows details analysis of each link and the extraction of measurement records, model results and derived parameters. Results of database queries can be plotted as graphs or downloaded for further analysis. Figure 6 shows an example of the output, in this case a path profile. It also illustrates that the land/sea/coast data which is often needed by ducting models is now part of the dataset.

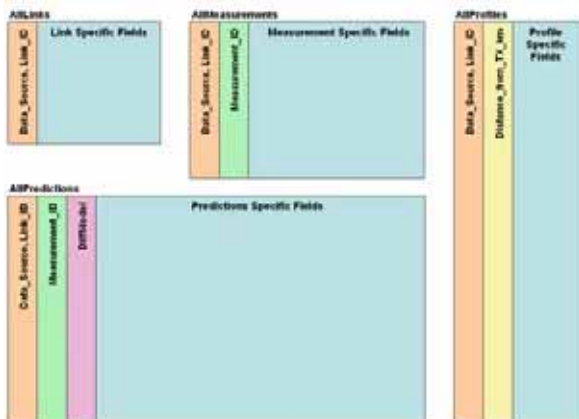


Figure 5 : Database organisation

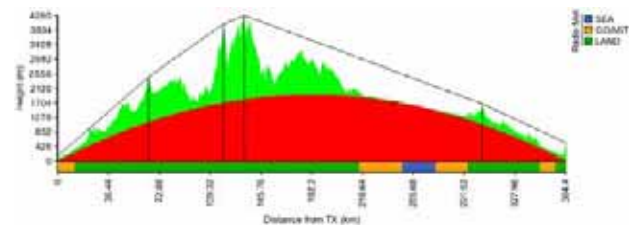


Figure 6 : Sample database output

6. Using the data

The cleaned data may be more useful for evaluating the differences between models. Studies are based on extracting test parameters based on SQL database queries so that sets of measurement parameters and model results may be compared. In Figure 7 the prediction error (model – measurement) is plotted for ITU-R P.1812 using all valid data. The plot looks odd with horizontal concentrations of data at certain path lengths which are features of the US data. It is hard to tell how well the model is performing; there is a very large spread of error.

Figure 8 shows the same result but with all but the top receiver heights excluded. The model can not be expected to allow for height gain when there is no terminal clutter data. Extreme values and banding at certain distances are still present in the dataset even once height gain groups are removed.

It was found that certain US data may be contaminated by clutter. Figure 9 shows the result with the US data removed. While this looks cleaner, the US data forms a large part of the database and it would be better to clean it up than to discard it. Figure 10 shows the same result as Figure 8 but with the US data from plains removed. The remaining data is now much easier to analyse and Figure 9 shows how we can now compare models.

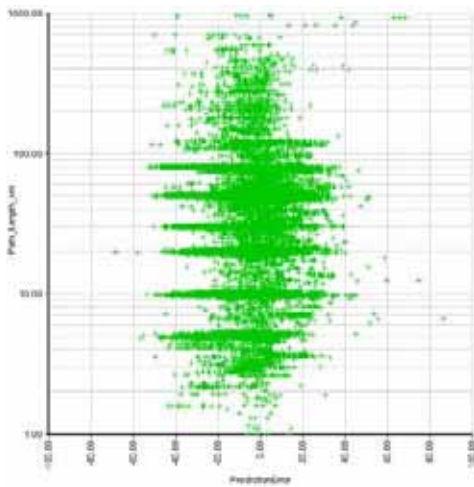


Figure 7: Sample analysis – unfiltered data

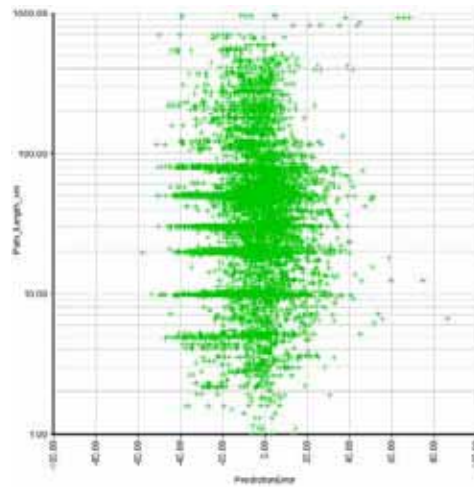


Figure 8: Sample analysis – height gains removed

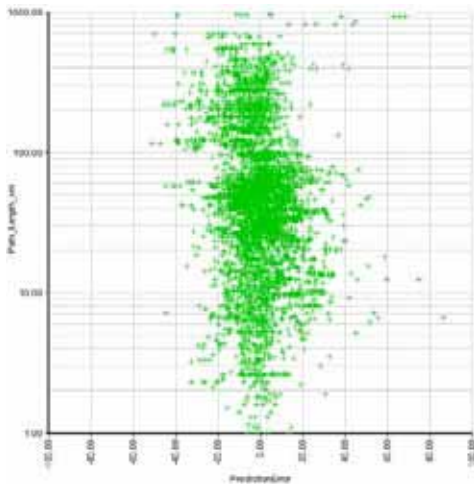


Figure 9: Sample analysis – top height data excluding US data

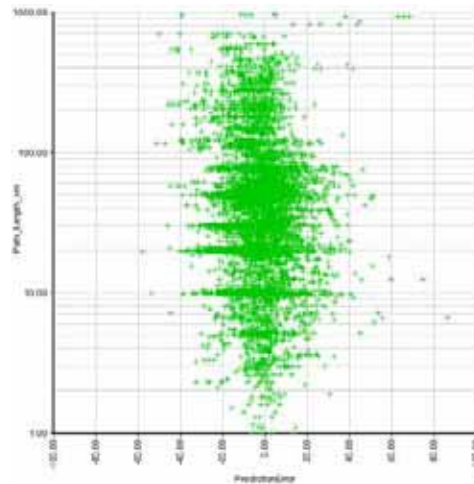


Figure 10: Sample analysis – filtered to exclude US plains data

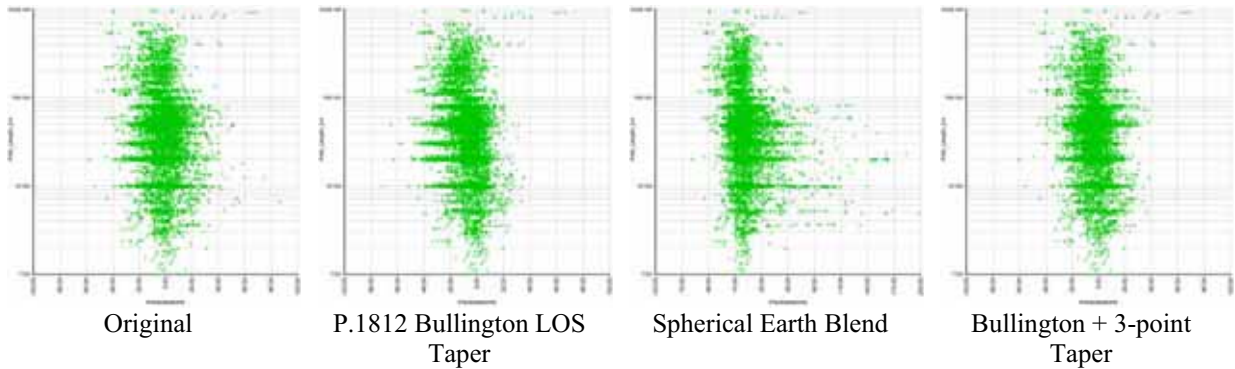


Figure 11: Comparison of some potential updated to ITU-R P.1812

7. Outliers

Once the data was filtered it became possible to investigate prediction outliers in more detail with the aim of improving the models. Figure 12 shows the error distribution for the current version of ITU-R P.1812 against the unfiltered and filtered data.

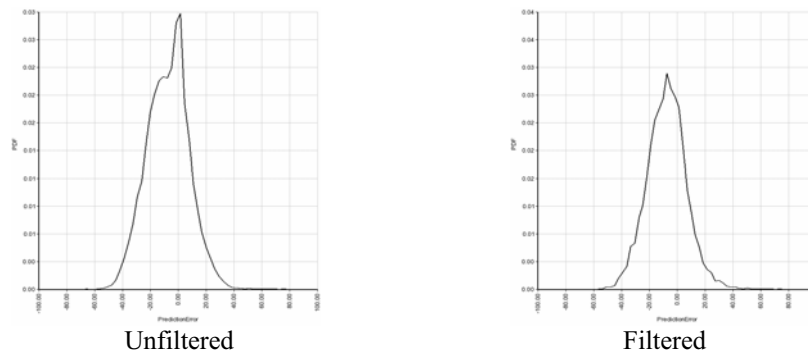


Figure 12: Error distribution for ITU-R P.1812

The filtered distribution is now much better than the unfiltered distribution; it is smooth and tending toward Gaussian. There is a small offset in the overall mean which is believed to be partially caused by unrecorded clutter. There is also a slight skewness, particularly in the long term results which is the result of a larger negative tail. There are still a few large outliers even in the filtered data and an exercise was carried out to investigate their cause through a detailed manual examination.

To make this process manageable, the prediction errors were converted to absolute values and ranked according to the magnitude of the prediction error. Around 100 points was considered manageable which corresponded to those measurements with an absolute prediction error of 40 dB or more.

As a first step the terminal locations were studied using aerial photography. In several cases there were discrepancies casting some doubt over the absolute accuracy of the path profiles. The positioning errors may also have been due to co-ordinate conversion errors or truncation, it is impossible to tell. Knowledge of measurement techniques does however demonstrate that some profiles were unlikely to be accurate. A measurement team investigating diffraction loss over a distant hill in a well planned campaign would be unlikely to position their receiver just over the brow of a local hill. Coincidentally this would place the team in the middle of a forest which is especially unlikely as they used an antenna height of only 1.5m. Small errors in terrain profile are able to produce large prediction errors. This indicates that the diffraction model in ITU-R P.1812 requires fairly accurate profile data; this accuracy requirement should be stated in the recommendation.

The particular path shown in Figure 13 showed an excess loss of 45 dB. Artificially modifying the profile to put the receiver at the top of the final hill reduced this error to 6 dB. Several of the outliers were located in similar terrain where small errors in transmitter or receiver location will lead to large errors in the prediction. It is to be expected that the location variability will be high in mountainous regions; a fault in the current model is that the required terrain accuracy is not specified.

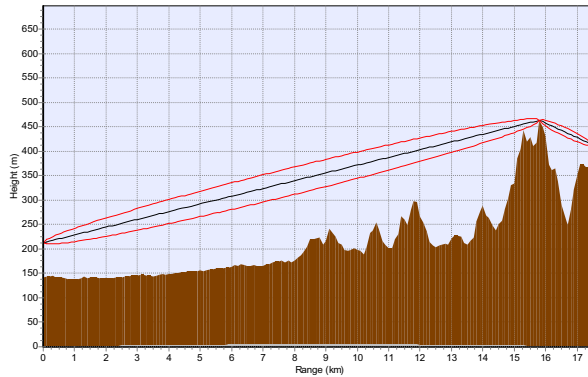


Figure 13: Suspect terrain profile – note final diffraction edge at far right.

Examination of the aerial photography showed that several outliers appeared to be due to clutter. In all cases the measured signal is much lower than that predicted. These outliers tended to be along long flat paths in the USA dataset. We are already aware several data sets contain height gain measurements around local clutter. The filtering process only selects the highest transmitter and receiver points for each measurement path, in the belief that these points are the least likely to be affected by local clutter. Also, shorter line of sight links showing excessive losses are automatically classified as invalid. There still remain paths with unknown clutter. This can be demonstrated by the USA data which is conveniently categorised into data taken in the plains and data taken in the mountains. Paths in mountainous regions are less likely to suffer from along path clutter as much of the path tends to be elevated.

One particular set of data illustrates this well where a single broadcast transmitter in Boulder, Colorado was measured with mountains to the west and plains to the east. Figure 14 demonstrates that the mean prediction error to the west is around 0 dB whereas to the east it is around -20 dB. This is believed to be the effect of clutter along the path. Clutter effects do not in general generate large outliers; however they will cause a shift in the mean prediction error. Clutter is taken account of in the models, but it is only possible where clutter data is provided. Accurate clutter databases tend to be expensive.

Some of the most significant outliers are clearly caused by problems with the models. The database is lacking in paths in areas prone to ducting and more work is needed in this area. An example is shown in Figure 15. This is a 900km path over warm sea in the Gulf region between Kuwait and the United Arab Emirates. This region is prone to ducting enhancement for more than 50% of the time. Several assumptions within the ITU-R P.1812 recommendation break down under this condition and the error is over 60 dB.

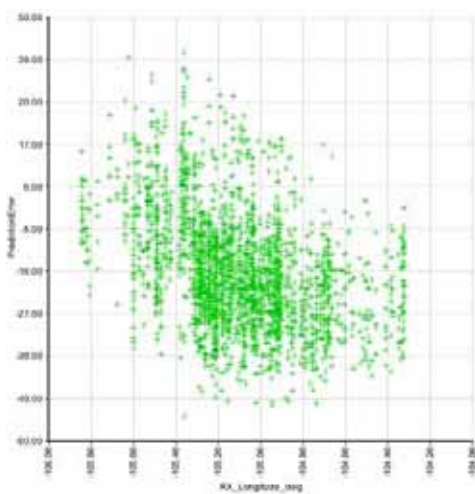


Figure 14: Evidence for clutter

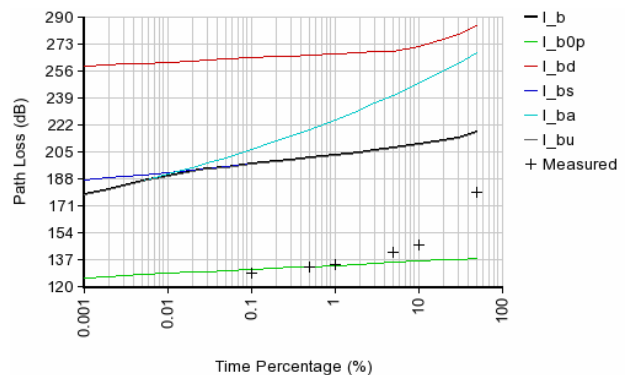


Figure 15: Example of a prediction failure

ITU-R P.1812 algorithm has incorrectly identified this path loss (l_b) as being dominated by troposcatter (l_{bs}) at 50% to 1% time. In practice the path is clearly dominated by ducting (l_{b0p} & l_{ba}) with the ducting time percentage greater than 50%.

All of the measurements with a disparity of more than 40 dB against the ITU-R P.1812 prediction were examined. The majority were found to be caused by clutter – which should be considered a weakness in the measurement data. Several others were suspected to be due to inaccuracies in terminal locations – which will require either less sensitivity in the model or some attention to more clearly defining the model requirements. There is a difficulty here as the sensitivity to terrain depends very much on the type of terrain, with mountainous regions being particularly sensitive to small changes in terminal location. The remaining outliers were where ducting was poorly modelled, particularly on longer sea paths or in the Gulf region – the ducting model needs to be improved.

8. Conclusions

An extended database of propagation measurements suitable for testing terrestrial propagation prediction models has been produced. This consists of XML records accessible using SQL. A web interface has been created to assist in extracting the data. A flagging exercise has been performed on this database to allow the measurements to be filtered according to a defined set of rules. This has greatly improved the usefulness of the data in comparing rival models.

A further web application has been written to allow the detailed analysis of the database and model results. An examination of the remaining prediction outliers using this application has identified areas where the propagation models need to be improved and also that some care is still needed in using measurement data appropriately. This improvement work is ongoing within ITU-R Study Group 3.

9. References

- [1] ITU-R Recommendation P.1812, “A path-specific propagation prediction method for point-to-area terrestrial services in the VHF and UHF bands”, Available from ITU <http://www.itu.int>
- [2] ITU-R Recommendation P.452-12, “Prediction procedure for the evaluation of microwave interference between stations on the surface of the Earth at frequencies above about 0.7 GHz”, Available from ITU <http://www.itu.int>
- [3] ITU-R Recommendation P.1546-3, “Method for point-to-area predictions for terrestrial services in the frequency range 30 MHz to 3 000 MHz”, Available from ITU <http://www.itu.int>
- [4] ITU-R Study Group 3 Propagation database. Available from the 3K1 correspondence group. <http://www.its.bldrdoc.gov/meetings/3k1/>
- [5] COST210 “Influence of the atmosphere on interference between radio communications systems at frequencies above 1 GHz”, Final Report edited by E. Ballabio, Published by the Commission of the European Communities, EUR 13407, 1991. ISBN 92-826-2400-5
- [6] Sandell, R.S. “Field strength prediction”, Communications Engineer, Volume 5, Issue 4, August-September 2007, pp35-39, ISSN: 1479-8352
- [7] Link database currently available from RAL at: <http://www.rcru.rl.ac.uk/njt/linkdatabase/linkdatabase.php>

Diffraction Model Comparisons Using the ITU-R 3K1 Correspondence Group Database

K.H. Craig, M.J. Willis¹, N.J. Thomas, S.A. Callaghan

Radio Communications Research Unit, STFC Rutherford Appleton Laboratory, UK

¹Tel: +44 1235 445492; Fax: +44 1235 446140; Email: m.j.willis@rl.ac.uk

Abstract

Various candidate diffraction models are being developed in ITU-R Working Party 3K for incorporation within the new path-specific propagation method for point-to-area terrestrial services, P.1812. Here we present statistical results of testing a number of these against a recently extended and quality-checked ITU-R Study Group 3 database of terrestrial propagation measurements [3]. Various statistical metrics for comparing the models are discussed.

1. Introduction

At the ITU-R Study Group 3 meeting in 2007, a draft new recommendation for a path-specific propagation method for point-to-area services was agreed and this was subsequently approved by correspondence as P.1812 [1].

In the drafting of this new recommendation, there had been considerable discussion concerning the diffraction model used within it. P.1812 uses the cascaded knife edge diffraction model given in ITU-R P.526-10 [2], based on a 3-edge Deygout construction. However a number of alternative models, including one based on a Bullington construction, had been discussed within ITU-R SG3 3K1 Correspondence Group (CG). As part of ongoing work, the CG has established a database of measurements [3].

This paper summarises the statistical results from testing P.1812, incorporating various modified diffraction models, against the 3K1 Correspondence Group measurement dataset.

2. Models

Apart from an implementation of P.1546-3, the models are all based on P.1812. The different versions of P.1812 are all obtained by substituting various diffraction models for the current 3-edge diffraction model. The list of models is:

- P.1546-3 [4]. This is the main ITU-R “path-general” method for point-to-area services. It has a long legacy going back to P.370 and is considered a reference for a non-path-specific model.
- P.1812 as published (3-edge diffraction model) [1].
- P.1812, but using the Bullington diffraction model in a form that includes an empirical, path length

dependent, correction term and a line-of-sight taper, as described in [5]).

- P.1812, but using three variations of the US FCC PTP diffraction model [6] that incorporates corrections for rounded obstacles. Further details are given below.
- P.1812, but using a long path distance correction to the Bullington method [7].

2.1. The PTP Model

The Point-to-Point (PTP) radio propagation model was given in a 1998 FCC Notice of Proposed Rulemaking for FM service. Although this model has not been officially adopted by the FCC, the model is often used by consulting engineers and by Commission staff to estimate the coverage provided by FM radio stations. The model and test results can be found on the FCC website [6].

A feature of the PTP model is that it blends knife-edge and smooth-Earth diffraction losses in a way that takes account of the terrain roughness. In our implementation, the PTP model has been applied to the three knife-edges of the P.1812 3-edge model. Three different assumptions have been made about which edges the knife-edge/smooth-Earth blend should apply to.

In the basic PTP method P.1812 is run as normal. In the diffraction calculation, a roughness factor is used. Roughness factors R_p , R_r and R_t are found for each of the principal, receiver and transmitter edges. To calculate a roughness factor, a straight line least squares fit is made to all available points within 10km of the edge, but not including the transmitter or receiver points. The standard deviation of the terrain heights about this line is calculated and ΔH is set to 90% of this value. The interpolation factors R_p , R_r or R_t are found

using the equation $R = 75/(\Delta H + 75)$. The loss for the edge is then calculated from:

$$\text{PTP Edge Loss} = J(v) + R \times (S(v) - J(v))$$

where $S(v)$ is the smooth earth loss calculated using the approximation:

$$S(v) = \max(21.66 + 27.35v, 0)$$

and where v and $J(v)$ are as defined in P.1812.

The basic PTP method can be applied to all edges or just the principal edge, and the losses can be combined in various ways. The basic PTP method was applied using 3 variations of these. In the following L_d is the overall diffraction loss, and L_m , L_t and L_r are the losses due to the principal, transmitter and receiver edges:

1. PTP method applied at the principal edge only; the edge losses were combined as:

$$L_d = L_m + (1 - \exp(-L_m/6))(L_t + L_r)$$
2. PTP method applied at all 3 edges with the combination of losses based on the value of the R factor at the principal edge:

$$L_d = L_m + (1 - \exp(-L_m/6))(L_t + L_r)(1 - R_p)$$
3. PTP method applied at the principal edge only with the combination of losses based on the value of the R factor on the principal edge:

$$L_d = L_m + (1 - \exp(-L_m/6))(L_t + L_r)(1 - R_p)$$

For reference, P1812 combines the (knife-edge) losses of the three edges using:

$$L_d = L_m + (1 - \exp(-L_m/6))(L_t + L_r + 10 + 0.04d)$$

For time percentages other than 50, these calculations are done at both 50% and $\beta_0\%$ time, and the diffraction loss at the required time percentage found by interpolation in the same way as in P.1812.

There are obviously many other variations for combining smooth-Earth corrections with a 3-knife-edge model.

3. Data

The dataset used for testing was the “cleaned” 3K1 Correspondence Group measurement database [3]. As well as the original 19 datasets (15 EBU, 2 US, ABU, Swiss) used for the 3-edge/Bullington comparisons presented in [5], this database contains 7 additional datasets (COST-210 and the Sandell measurements sorted into 6 frequency bands).

The subset of data used in this model testing used 5316 links/data files as defined by the data flags:

IsValid = 1
 IsWorstMonth = 0
 IsTopHeightInGroup = 1
 InputsValid = 1
 IsLongTerm = 0 or 1

4. Metrics

In this paper, we present results in the standard form of statistical means and standard deviations of the difference between the model predicted path loss and the measured path loss.

These simple statistical quantities are only valid as metrics if the distribution of errors is Gaussian. The model-minus-measured errors in the original “raw” datasets were often non-Gaussian. In particular several distributions were bimodal. However, the model errors for the datasets in the “cleaned” database are generally consistent with a Gaussian distribution (based on chi-square and Kolmogorov-Smirnov tests) and so we limit our metrics to the mean and standard deviation.

In the results we present the mean and standard deviation for each dataset within the database. We also provide means and standard deviations of all the data treated as one single, large dataset (>10,000 measured points). Three ways of combining the different datasets were used:

1. Results labelled “ALL” are obtained by simply considering all data points with equal weight, irrespective of data source. This would be appropriate if all data are equally good and unbiased (for example, correctly calibrated, and with clutter correctly identified). The results are representative of the conformance of the model to measurements made in a variety of conditions, geographical locations, and by different methods and operators, but include contributions from measurement, as well as model, errors.
2. Results labelled “Mean of datasets” give an “average” mean and standard deviation of the 26 individual datasets, obtained by simply taking the mean of the individual means and standard deviations. This approach gives equal weight to each dataset, rather than to each measurement, and so gives undue emphasis to the results from the smaller datasets. There is a very large variation in the sizes of the datasets used here (Figure 1). For example one dataset (USPhase1) contains 45% of the measurements in the entire database.

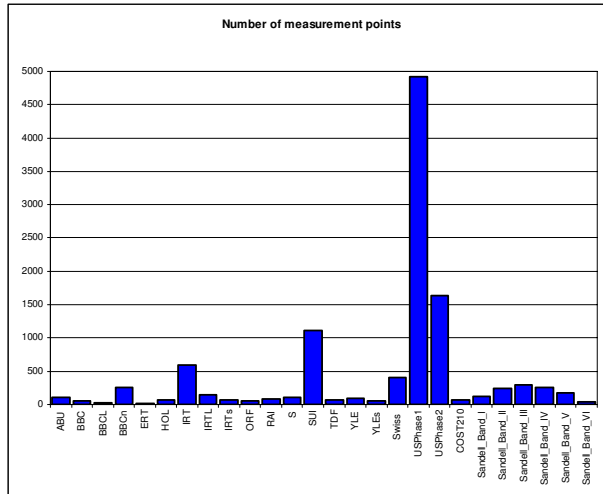


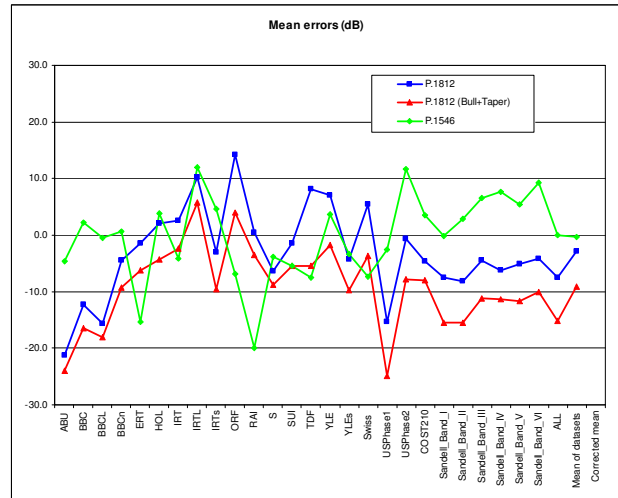
Figure 1: Number of measurements in each dataset

- Results labelled “Corrected mean” are only given for the standard deviation. These are obtained by (a) “correcting” the individual measurement values by subtracting the mean measurement value of the dataset to which the individual measurement belongs; (b) considering all the “corrected” measurement values to belong to the same statistical distribution, and (c) calculating the standard deviation of this aggregated dataset.

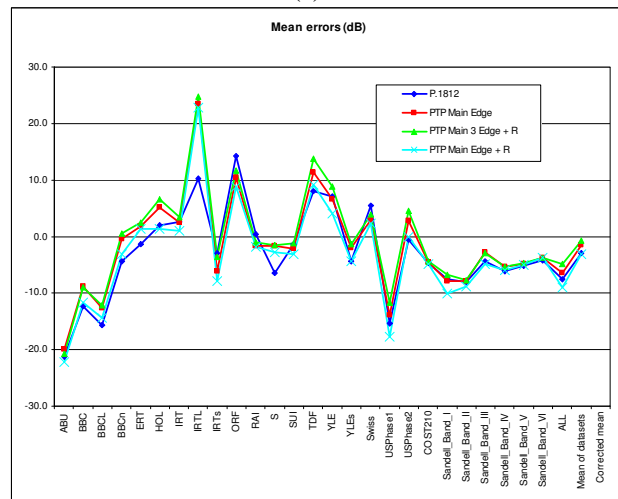
The rationale for this is the belief that several of the individual datasets include significant measurement biases (discussed later). The standard deviation calculated using the simple method of 1 above will therefore give an unduly pessimistic estimate, as it will include a contribution from the measurement error offsets between the means of the individual datasets. The “corrected mean” approach attempts to remove the measurement errors to first order.

5. Results

The testing results are presented graphically. Figure 2 shows the mean errors and Figure 3 the standard deviations of the errors, broken down by model and measurement dataset. The dataset name is given along the abscissa, and the graph lines are only shown to guide the eye.



(a)

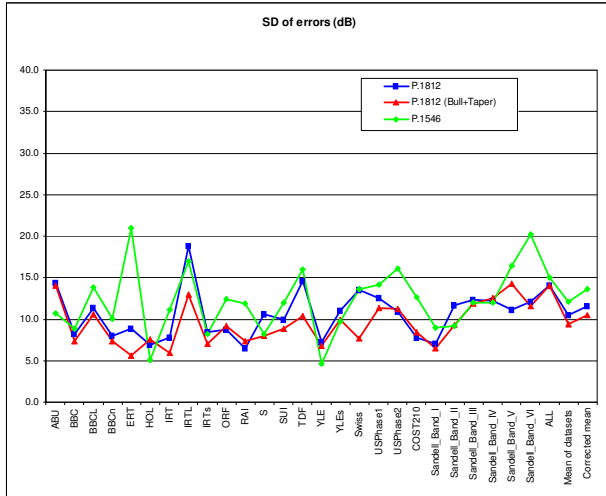


(b)

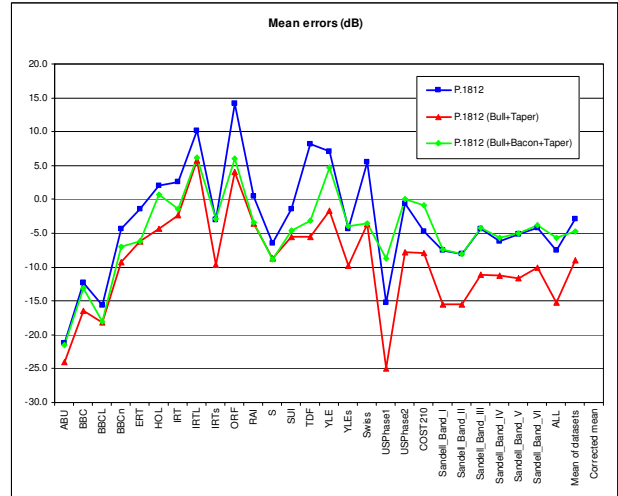
Figure 2: Mean errors (model-measurement)

Figure 4 shows, in expanded detail, the prediction error statistics of P.1812 using (a) the 3-edge diffraction method, (b) the Bullington diffraction method, and (c) the long path distance correction to the Bullington method given in Document CGD-16.

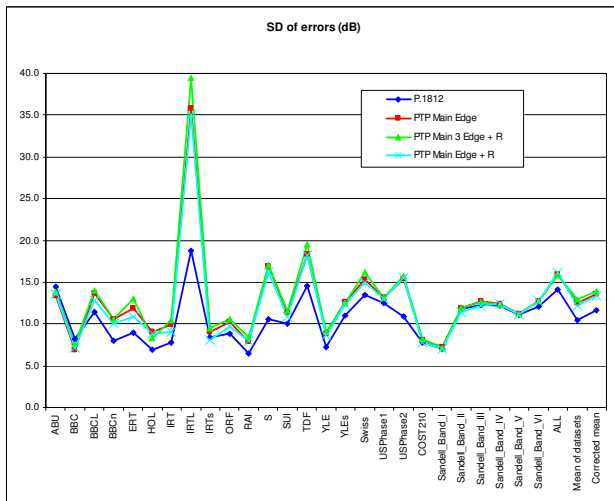
Figure 5 shows the effect of including, or ignoring, the clutter information given in the database. Only a few of the datasets include clutter information.



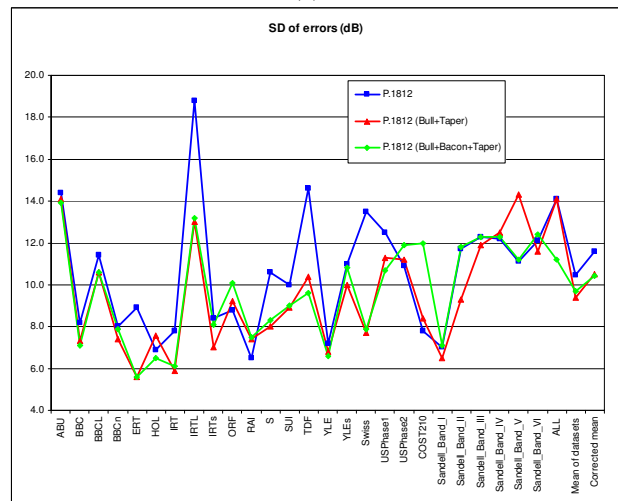
(a)



(a)



(b)



(b)

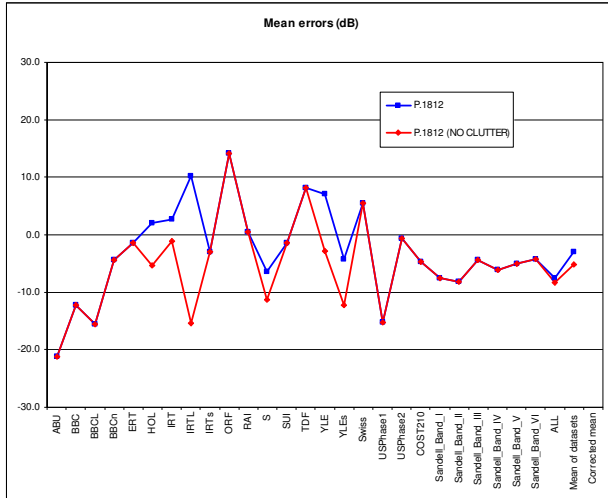
Figure 3: SD of errors (model-measurement)

Figure 4: 3-edge, Bullington and “adjusted” Bullington model

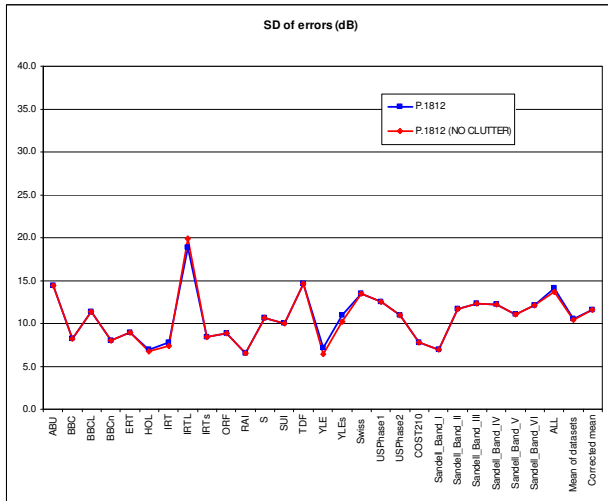
6. Discussion

Figure 2 shows that the mean errors vary greatly from dataset to dataset. This agrees with the more limited diffraction results on the unfiltered data obtained earlier [5]. Indeed the dataset-to-dataset variation in the mean error is generally larger than the variation between models. What is more, the terrain-based diffraction models (3-edge, Bullington and PTP) all show the same trends/biases in the means on different datasets (P.1546 is rather different because its “diffraction model” is not based on a full terrain profile analysis).

The obvious conclusion of these trends is that they are more due to biases in the measurements than to differences in the models themselves. This has already been discussed in Section 6.3 of [5], and further in [3]. So for example, the “over-prediction” of path loss by all models on the IRTL dataset may be due to calibration or dynamic range problems in the measurement data. In contrast, the “under-prediction” of path loss by all models on the USPhase1 data is probably due path clutter that is not identified in the CG database. These conclusions are supported by:



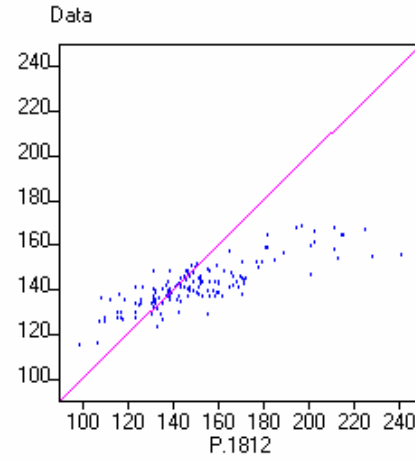
(a)



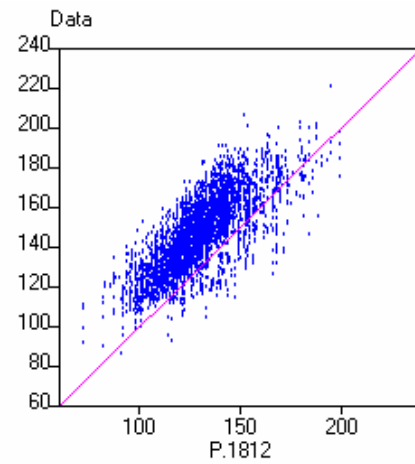
(b)

Figure 5: Effect of clutter on mean and SD of errors (model-measurement)

- the standard deviations of Figure 3: the USPhase1 data shows a standard deviation that is similar to the other datasets, compatible with a clutter “offset”, while the standard deviation of the IRTL dataset is exceptionally high;
- the scatter plots of the P.1812 predicted path loss against measurements shown in Figure 6: the scatter plot “slope” suggests a calibration issue or dynamic range problem, although unusual characteristics of the measurement environment cannot be ruled out;
- the histogram of the prediction errors shown in Figure 7 and Figure 8: the IRTL histogram is broader than that of the IRT dataset, while the USPhase1 and USPhase2 histograms are similar in shape, although with a mean offset for USPhase1.



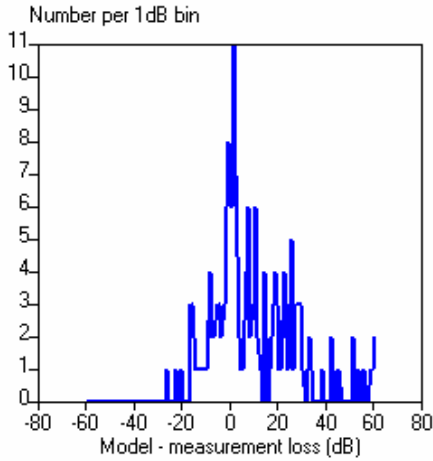
(a)



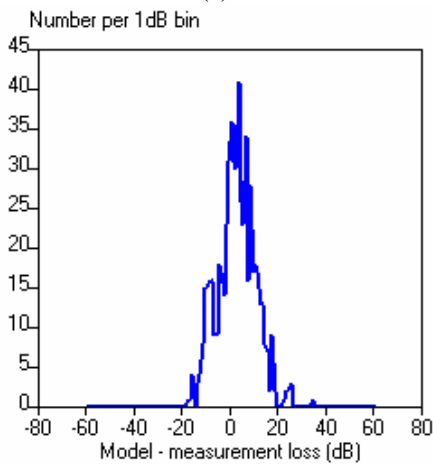
(b)

Figure 6: P.1812 (3-edge) model against measurements for (a) IRTL and (b) USPhase1

It is not therefore possible to make firm conclusions on the efficacy of a model based on the values of the mean prediction errors. This is of course well known, and most “practical” diffraction models (including the 3-edge and Bullington models in P.1812) incorporate empirical correction factors to take some account of environmental “unknowns” (such as clutter). However it is clear from Figure 2 that the Bullington version of P.1812 underpredicts loss compared with the 3-edge version on all datasets. In general, both models are underpredicting path loss compared with P.1546-3. As it happens, the mean prediction error for P.1546-3 on the whole aggregated dataset (the ALL result) is 0.0dB!



(a)

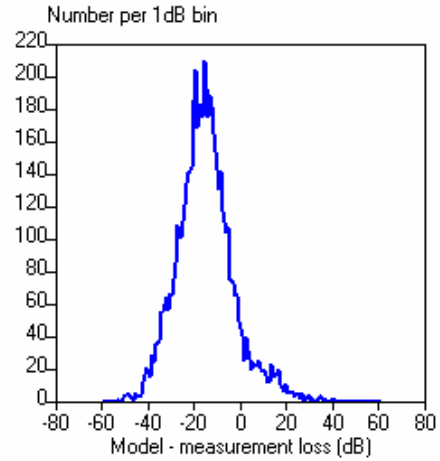


(b)

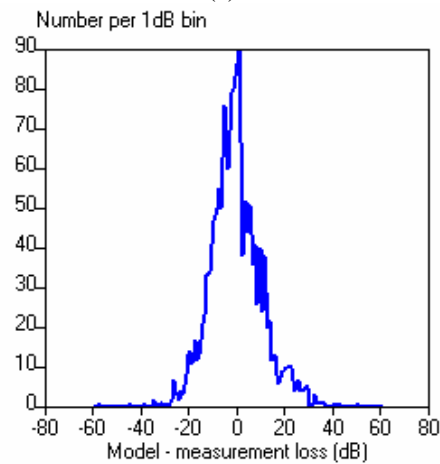
Figure 7: Histograms of (a) IRTL and (b) IRT

The various PTP models all give results that are close to the basic P.1812 results, so the inclusion of smooth-Earth obstacles does not make a significant difference.

Considering the standard deviations of Figure 3, there is much less variation between datasets (apart from IRTL) confirming that standard deviation is a better metric than the mean. The standard deviation of the Bullington version of P.1812 is generally (but not always) lower than that of the 3-edge version and of P.1546-3. For the aggregated datasets (ALL), the standard deviations of 3-edge and Bullington P.1812 are identical (14.1dB) and not much less than P.1546 (15.0dB), but the “Corrected mean” standard deviation is best for Bullington (10.5dB) followed by 3-edge (11.6dB) with P.1546 a poor third (13.6dB). The PTP models all give standard deviations that are worse than the basic P.1812 model.



(a)



(b)

Figure 8: Histograms of (a) USPhase 1 and (b) USPhase2

Figure 4 shows, in expanded detail, the prediction error statistics of P.1812 using (a) the 3-edge diffraction method, (b) the Bullington diffraction method, and (c) the long path distance correction to the Bullington method given in Document CGD-16. It shows that the CGD-16 model has overall mean errors similar to the 3-edge model and smaller than the Bullington model, and on individual datasets, generally lies between the two. The standard deviation of the CGD-16 model generally reproduces the lower standard deviation of the Bullington method, and overall is actually better than either the 3-edge or Bullington versions of P.1812, at 11.2dB (ALL) and 10.4dB (“Corrected mean”).

Figure 5 compares the statistics of (3-edge) P.1812 when the clutter information provided in the CG database files is either included or excluded. Clutter information is only available for 6 of the datasets. In all cases, using clutter increases the predicted loss as expected, although in two cases, the magnitude of the

mean prediction error also increases. Surprisingly, ignoring the clutter generally *decreased* the standard deviation of the error, and gave a smaller standard deviation overall. However, it is difficult to make any conclusions about the efficacy of the P.1812 clutter model based on these small differences.

7. Conclusions

On the basis of the models tested here, the “Long path distance correction to the Bullington method” given in [7] gives the best overall performance.

However it should be noted that a number of groups are active in investigating alternative models, and these must also be included before a final conclusion can be reached.

An additional important consideration is that P.1812 is designed for use on paths that are up to 3,000 km long. The testing done in this paper is dominated by paths which are less than 200 km long (see Figure 2 of [3]). In the context of P.1812 therefore, serious consideration has to be given to the performance of the models on longer paths, where a knife-edge diffraction approach may not be the best. Of course P.1812 includes propagation mechanisms other than diffraction, and troposcatter or ducting are likely to take over from diffraction as the dominant propagation mode on the longer paths. A reasonably pragmatic approach is needed to provide P.1812 with a diffraction model that gives statistically acceptable results for those ranges of parameters where diffraction dominates.

8. Acknowledgements

This work was funded by Ofcom and the authors wish to thank Ofcom for their support and interest.

9. References

- [1] ITU-R Recommendation P.1812, “A path-specific propagation method for point-to-area terrestrial services in the VHF and UHF bands”, 2007
- [2] ITU-R Recommendation P.526-10, “Propagation by diffraction”, 2007
- [3] Willis M., Craig K. and Thomas N., “Measurement data for improving ITU-R Recommendation P.1812”, 10th Int. Symposium on Advanced Radio Technologies, Boulder, Colorado, 2008
- [4] ITU-R Recommendation P.1546-3, “Method for point-to-area predictions for terrestrial services in the frequency range 30 MHz to 3000 MHz”, 2007
- [5] UK, “Bullington and 3-edge diffraction methods compared with measured results”, 3K1 Correspondence Group Document CGD-05, 2007.
- [6] H.K.Wong “Field Strength Prediction in Irregular Terrain—the PTP Model”, November 1, 2002, see <http://www.fcc.gov/oet/fm/ptp/>.
- [7] Bacon D.F. “Investigations of long path distance correction to the Bullington method”, 3K1 Correspondence Group Document CGD-16, 2008.

A Comparative Analysis of Multiple Knife-Edge Diffraction Methods

Nicholas DeMinco and Paul McKenna
Institute for Telecommunication Sciences
National Telecommunications and Information Administration
Phone numbers: 303-497-3660 and 303-497-3474
Fax #: 303-497-3680
ndeminco@its.bldrdoc.gov
pmckenna@its.bldrdoc.gov

Abstract: *This report describes the comparative analysis of four alternative methods to a rigorous method for computing multiple knife-edge diffractions in non-line-of-sight scenarios. These alternative methods are candidates for use with the short-range mobile-to-mobile radio-wave propagation model under development at the Institute for Telecommunication Sciences. The results of this analysis show where alternative methods that reduce computation time can be used for analyzing knife-edge diffractions while maintaining suitable accuracy.*

1. Introduction

A comparative analysis of different multiple knife-edge diffraction methods was performed to support the short-range mobile-to-mobile radio-wave propagation model under development at the Institute for Telecommunication Sciences (NTIA/ITS). The goal of this analysis was to investigate faster methods for computing multiple knife-edge diffractions.

When this comparative analysis is completed, the results of the ongoing analysis and measurement efforts will be used to develop algorithms for radio-wave propagation predictions in urban canyon, suburban residential, parking lot, rural, and indoor environments. These environments include both line-of-sight (LOS) and non-LOS scenarios. This paper addresses non-LOS scenarios. These algorithms will be implemented in ITS' short-range mobile-to-mobile propagation model.

While a rigorous method exists for computing multiple knife-edge diffractions, faster methods are needed for area coverage predictions in situations where many computations are required in different radial directions over many diffraction edges. Faster alternative methods for computing multiple knife-edge diffractions are approximations to the rigorous method, in that they obtain solutions by compositions of single knife-edge diffraction results. In contrast, non-approximated solutions for multiple knife-edge diffraction loss are computationally intensive, which can be a problem for complex environments.

The alternative methods that were investigated for computing multiple knife-edge diffractions are typically described as graphical techniques, where the

analyst must identify the most important edges through educated guesswork. It was therefore necessary to develop mathematical algorithms for these graphical methods. The mathematical algorithms enabled the comparison of the alternative diffraction methods with the rigorous diffraction method to determine a suitable method for the non-LOS propagation scenarios.

2. Diffraction Methods

An investigation was initiated to find an alternative multiple knife-edge diffraction prediction method by comparing the accuracies of four faster diffraction methods to the rigorous solution, first given by Vogler [1, 2]. [1, 2] contain computations for many diffraction loss scenarios involving multiple edges. The four alternative diffraction methods investigated were those by Bullington [3], Epstein/Peterson [4], Deygout [5] and Giovaneli [6]. Detailed graphical procedures for each of the methods can be obtained from the references cited above.

The Bullington method is the simplest to implement, but it is also the least accurate of the four alternative diffraction methods investigated. The Bullington method was found unsuitable for use due to inaccurate results of the diffraction computation even with only two edges.

The three remaining methods investigated claim to have improved accuracy when compared to Bullington's method, with only slight increases in complexity. The Epstein/Peterson method is straightforward to implement, and maintains reasonable diffraction loss prediction accuracy. The Deygout method is an improvement over the

Epstein/Peterson method. Giovaneli's method corrects the error in diffraction angle that Deygout's method uses, because it uses a diffraction angle that more closely coincides with that used for the Geometrical Theory of Diffraction.

The four alternative methods investigated were compared to the rigorous Vogler method [2]. This investigation is still in progress. A determination will be made of the most suitable alternative method to use for a wide variety of scenarios that would be encountered by ITS' short-range mobile-to-mobile radio-wave propagation model after this investigation is completed.

The original Vogler report [1] takes work by Furutsu [7] as its starting point. That work pertains to the problem of propagation over irregular terrain which is approximated as a series of rounded diffracting obstacles. Furutsu obtained a solution that utilizes a generalized residue series, which, unfortunately, is slowly convergent as the obstacles' radii tend to zero. By utilizing transformations of the residue series' solution to integrals, Vogler derived a multiple knife-edge diffraction solution involving multiple integrals over successive knife-edges, and introduced a series representation for these functions that is amenable to numerical solution. He made comparisons of the computed numerical values to certain analytic results.

Vogler derived the multiple knife-edge diffraction solution in [2] using the Fresnel-Kirchhoff theory [8], and showed that it is equivalent to the solution obtained in [1]. Whittaker [9], also obtained a similar result. Vogler then compared the results to the Geometrical Theory of Diffraction, the Epstein/Peterson method, and the Deygout method, for five equally spaced knife-edges having the same value of the diffraction angle at each edge. To compare Vogler's knife-edge diffraction method to the four alternative knife-edge diffraction methods discussed above, it was necessary to recode (and, therefore, revalidate) Vogler's computational method, since the original computer programs were unpublished and the actual code was not available. The validation exercise was limited, in that it was confined to reproducing the multiple knife-edge diffraction attenuation results quoted in [1, 2] (the FAMKE and PAMKE methods). The practical basis for both methods is the numerical evaluation of the repeated integrals of the complementary error function with a complex argument. The current implementation makes use of a somewhat more robust method of numerical evaluation for these functions developed by Gautschi [10], of which, Vogler was evidently unaware.

3. Diffraction Model Investigation

Even with modern computers, Vogler's rigorous diffraction loss computation method [1, 2] is computationally intensive when compared to any of the four alternative multiple knife-edge diffraction methods investigated. ITS' short-range mobile-to-mobile radio-wave propagation model needs a diffraction loss method for many diffraction edges that is faster than Vogler's rigorous method, because it will be used for analyses containing many diffraction paths. The rigorous diffraction method of Vogler has been verified to be extremely accurate when compared to measured data but, not surprisingly, the computational method run times for many edges can be excessive when compared to simpler, approximate computational methods.

All four of the alternative multiple knife-edge diffraction methods investigated are graphical techniques, and they are often computed manually. Mathematical algorithms for each of the four alternative diffraction methods were developed, so that they could be programmed and incorporated into ITS' short-range mobile-to-mobile radio-wave propagation model. The alternative diffraction method that is selected must apply to all of the possible diffraction edge geometries that could occur. The test scenarios included many variations of distances between edges, variations of edge heights, and variations of edge height-to-edge spacing ratios.

Preliminary comparisons of Vogler's method [2] with the methods of Epstein/Peterson and Deygout were performed for an assortment of scenarios. However, the results presented in [2] showed poor agreement between the Deygout results and Vogler's results, and fair to good agreement between the Epstein/Peterson results and Vogler's results. No comparisons of the Bullington or Giovaneli results were contained in [2].

Comparisons of all four alternative multiple knife-edge diffraction methods showed good agreement between the Vogler results and both the Epstein/Peterson and Giovaneli results for a variety of cases. This preliminary study showed better agreement between the Vogler results and the Epstein/Peterson results than the comparisons in [2], because the ITS version of the Epstein/Peterson method includes the sub-path obstacles that have negative heights with respect to the propagation path. Vogler's version of the Epstein/Peterson method does not include these sub-path obstacles with negative heights.

Tables 1 and 2 compare the four alternative methods investigated to the Vogler method for a variety of edge heights, distances between edges, and height-to-distance ratios. The losses in these tables are only the diffraction losses and do not include free space loss. Table 1 contains scenarios with six, five, four, three, and two diffraction edges. Table 2 contains a variety of cases, all with six diffraction edges.

The fifty cases in Tables 1 and 2 were chosen to represent a wide variety of scenarios representing real diffraction configurations that could occur in reality, and that would challenge the capability and computation limits of all of the alternative diffraction methods. A detailed description of each of the fifty cases would be beyond the scope of this paper. This paper represents ongoing work, and a more complete report will be written, which will describe all of the work in much greater detail.

Table 1. Diffraction loss in decibels for assorted diffraction scenarios with six, five, four, three, and two diffraction edges.

		Computational Methods with Diffraction Loss in Decibels				
Number of Diffraction Edges	Case Number	Bullington	Epstein & Peterson	Giovanelli	Deygout	Vogler
6	Case1a	11.209	38.803	39.202	39.202	20.769
	Case1b	16.156	42.002	42.842	42.842	27.861
	Case1c	45.694	112.849	114.929	114.929	114.433
	Case1d	25.628	51.690	54.019	54.019	49.239
	Case1e	16.995	42.667	43.590	43.590	29.298
	Case2a	11.002	33.146	33.298	33.298	21.516
5	Case2b	15.832	36.819	37.123	37.123	28.239
	Case2c	45.308	120.097	119.920	119.920	120.471
	Case2d	25.245	49.653	49.973	49.973	47.757
	Case2e	16.659	37.593	37.917	37.917	29.587
4	Case3a	11.472	27.768	27.927	27.927	20.446
	Case3b	16.558	32.068	32.412	32.412	26.631
	Case3c	46.164	95.708	96.709	96.709	97.205
	Case3d	26.096	44.628	45.408	45.408	43.636
	Case3e	17.409	32.932	33.310	33.310	27.857
3	Case4a	10.989	21.581	21.750	21.750	17.543
	Case4b	15.810	25.819	26.195	26.195	23.227
	Case4c	45.282	94.252	96.577	96.577	96.896
	Case4d	25.220	39.919	41.023	41.023	40.549
	Case4e	16.636	26.702	27.125	27.125	24.379
2	Case5a	9.949	15.369	15.550	15.550	13.991
	Case5b	14.084	19.348	19.722	19.722	18.626
	Case5c	43.107	70.511	71.272	71.272	71.448
	Case5d	23.072	31.751	32.434	32.434	32.244
	Case5e	14.832	20.165	20.573	20.573	19.558

The first 20 scenario comparisons of Table 2 demonstrate reciprocity of the methods. Here, the term reciprocity means that the predicted path loss is invariant when the transmitter and receiver terminals are interchanged. Cases 6a through 6e are reciprocal to Cases 7a through 7e, respectively, and Cases 8a through 8e are reciprocal to Cases 9a through 9e, respectively.

Table 2 shows cases that agree with each other because their height-to-distance ratios for each edge are the same, and hence yield the same diffraction parameter and diffraction loss, even though the heights and distances are different. Case Xc agrees with Case Xd, where X equals 6 through 10. However, the total losses will be different when free space loss is added to the diffraction loss.

The cases that demonstrate poor agreement in Tables 1 and 2 are those where Vogler shows in [2] that there should be a large deviation between his algorithm and the four alternatives investigated. Detailed analyses of the case scenarios were performed to determine the cause of these differences in diffraction loss computations.

Table 2. Diffraction loss in decibels for assorted diffraction scenarios with six diffraction edges. Cases 6 and 7 show respective reciprocity to each other, as do cases 8 and 9.

		Computational Methods with Diffraction Loss in Decibels				
Number of Diffraction Edges	Case Number	Bullington	Epstein & Peterson	Giovanelli	Deygout	Vogler
6	Case6a	13.384	41.076	42.192	43.307	25.412
	Case6b	19.252	46.356	48.244	50.408	34.207
	Case6c	29.085	59.485	62.113	66.638	54.283
	Case6d	29.083	59.485	62.113	66.638	54.283
	Case6e	20.167	47.353	49.333	51.667	35.797
	6	Case7a	13.384	41.076	42.192	43.307
Case7b		19.252	46.356	48.244	50.408	34.207
Case7c		29.085	59.485	62.113	66.638	54.283
Case7d		29.083	59.485	62.113	66.638	54.283
Case7e		20.167	47.353	49.333	51.667	35.797
6	Case8a	14.000	41.353	41.136	42.030	24.867
	Case8b	20.049	47.043	45.969	47.597	33.253
	Case8c	29.931	61.352	55.611	58.763	51.721
	Case8d	29.931	61.352	55.611	58.763	51.721
	Case8e	20.976	48.122	46.802	48.549	34.749
6	Case9a	14.001	41.353	41.136	42.030	24.867
	Case9b	20.049	47.043	45.969	47.597	33.253
	Case9c	29.931	61.352	55.611	58.763	51.721
	Case9d	29.931	61.352	55.611	58.763	51.721
	Case9e	20.976	48.122	46.802	48.549	34.749
6	Case10a	11.450	39.230	40.213	43.003	23.809
	Case10b	16.525	42.983	45.143	50.765	31.856
	Case10c	26.057	57.189	62.683	73.669	56.239
	Case10d	26.057	57.189	62.683	73.669	56.239
	Case10e	17.374	43.783	53.181	59.337	33.476

Respective reciprocity
between cases 6 & 7

Respective reciprocity
between cases 8 & 9

One reason for the differences between the Vogler method and the four alternative methods is that the ray path from one edge to the next consecutive edge is in the transition region, and near the incident or reflection shadow boundary. Computations of these ray-path angles and shadow boundaries confirm this.

Some differences depend on whether the sub-path edges (obstacles) are included in the diffraction loss

computation for the different methods. It was found by comparative computations that removing the sub-path obstacles improves the agreement between the Deygout method and the Vogler method, but degrades the Epstein/Peterson method's agreement with the Vogler method. Comparative computations show that the Deygout method achieves better agreement with the Vogler method when only the major three edges are included in the computation of diffraction loss.

Further investigations of geometric configurations representing additional scenarios are necessary. The mathematical models for the four alternative methods investigated will be coded for automated computation. Many additional diffraction scenarios representing real-life situations will be run comparing the four alternative methods with the Vogler method.

4.0 Conclusions

The work described here is still in progress. This paper has described the preliminary results of a comparative analysis of four alternative multiple knife-edge diffraction methods in place of a rigorous multiple knife-edge diffraction method to support the short-range mobile-to-mobile radio-wave propagation model under development at ITS. The goal of this analysis was to investigate faster methods for computing knife-edge diffractions.

Preliminary results of this analysis show where the alternative multiple knife-edge methods investigated can be used in place of the rigorous Vogler diffraction method to reduce computation time while maintaining suitable accuracy. The Bullington method was found unsuitable for use due to inaccurate results of the diffraction computation even with only two edges. In addition, the analysis showed that any one of the three other alternative methods investigated may be more suitable than the others for a particular knife-edge scenario. Which alternative diffraction method works best in a given scenario depends on how a method treats sub-path obstacles and the alignment of the deflection angles with the shadow boundaries at the edges.

When a ray path from one edge to the next consecutive edge is in the transition region and near the incident or reflection shadow boundary, the alternative methods fail to compute the diffraction loss correctly. The procedure and order of computing edge diffraction loss is different for each of the alternative methods investigated. As a result, for the same diffraction scenario, one method may avoid alignment of the ray path with the incident shadow

boundary, and another may align the ray path with the incident shadow boundary. The method that avoids this alignment will predict the diffraction loss with better accuracy, if the deviation of the ray path and incident shadow boundary is large enough.

An approach under study for selecting a diffraction method that achieves better accuracy is to use the one method that has the largest deviation between the ray path and the incident shadow boundary. Another approach under study is to determine the magnitude of the error using a Fresnel transition function that provides a correction to the alternative method predictions.

5.0 References

- [1] L.E. Vogler, "The Attenuation of Electromagnetic Waves by Multiple Knife-Edge Diffraction," NTIA Report, pp. 81–86, October 1981.
- [2] L.E. Vogler, "Further Investigations of the Multiple Knife-Edge Diffraction," NTIA Report, pp. 83–124, May 1983.
- [3] K. Bullington, "Radio Propagation at Frequencies Above 30 Megacycles," Proc. of the IRE, pp.1122–1136, October 1947.
- [4] J. Epstein and D. Peterson, "An Experimental Study of Wave Propagation at 850 MHz," Proc. of the IRE, pp. 595–611, May 1953.
- [5] J. Deygout, "Multiple Knife-Edge Diffraction of Microwaves," IEEE Trans. Ant. Prop., Vol. AP-14, No. 4, pp. 480–489, July, 1966.
- [6] C.L. Giovaneli, "An Analysis of Simplified Solutions for Multiple Knife-Edge Diffraction," IEEE Trans. Ant. Prop., Vol. AP-32, No. 3, pp. 297–301, March 1984.
- [7] K. Furutsu, "On the Theory of Radio-Wave Propagation Over Inhomogeneous Earth," Journal of Research NBS (Rad. Prop.), pp. 39–62, 1963.
- [8] G. Millington et al., "Double Knife-Edge Diffraction in Field Strength Predictions," Proc.Of IEEE, Monograph No. 507E, pp. 419–429, 1962.
- [9] J. H. Whittaker, "Fresnel-Kirchhoff theory applied to terrain diffraction problems," Radio Sci., 25, 5, pp. 837–851, 1990.

[10] W. Gautschi, "Evaluation of the repeated integrals of the coerror function," *ACM Trans. Math. Software* 3, 3, pp. 240–252, 1977.

Estimating SRTM terrain height errors and their effect on profile interpretation

David Bacon

dB Spectrum Services: dfbacon@btinternet.com tel:+441273 771128

SRTM height data shows discrepancies with Ordnance Survey height data in the UK with standard deviations less than 7m for 73% of mainland UK. The distribution of the discrepancies tends to be closer to Laplace (double-exponential) than normal, and is amenable to modelling. The auto-correlation of discrepancies decreases with separation such that errors can be assumed independent beyond about 300 m. A method is described for using an estimate of height errors to assess the risk factor in predicting a horizon elevation angle. For diffraction modelling no simple analytic method appears to be available for quantifying the effect of height errors, but a direct comparison for UK paths indicates that height accuracy is a significant issue.

1 Introduction

Terrain-height data from the Shuttle Radar Tomography Mission (SRTM) covers most of the world and is a valuable resource for predicting terrestrial radio-wave propagation. Since there is no practicable means to compare SRTM data with an absolute standard of accuracy, a comparison has been made with height data produced by the UK National mapping agency Ordnance Survey (OS).

2 General accuracy

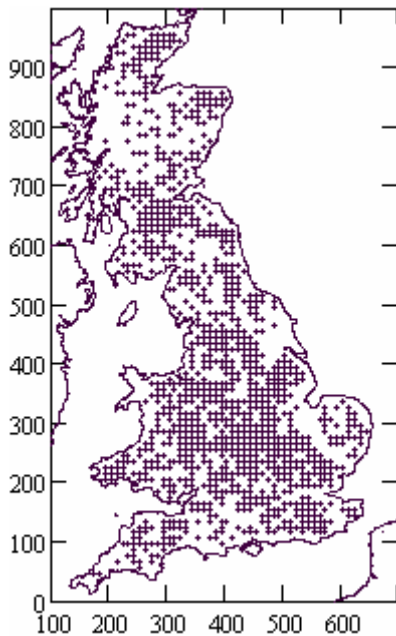


Fig 1. Tiles with $+1 \leq \text{mean}(\Delta h) < +3$

The height difference $\Delta h = H_{SRTM} - H_{OS}$ was sampled on a 100-m grid and analysed in 10-km square tiles. Only all-land squares were used, resulting in 1,899 tiles in the UK mainland.

Of these, 79 tiles contained one or more points where the SRTM height is missing. Most of these are in hilly regions, with a few in the high-rise urban areas. These errors are attributed to shadowing due to oblique radar view angles.

The mean of Δh tends to be positive. 97.5% of tiles have $-1 \leq \text{mean}(\Delta h) < +5$ m. Figure 1 shows the 60% having $+1 \leq \text{mean}(\Delta h) < +3$ m.

Figure 2 shows the 52% of tiles with standard deviation (SD) of Δh less than 5 m (bold symbols) and the additional 21.5% in the range 5 to 7 m (feint symbols).

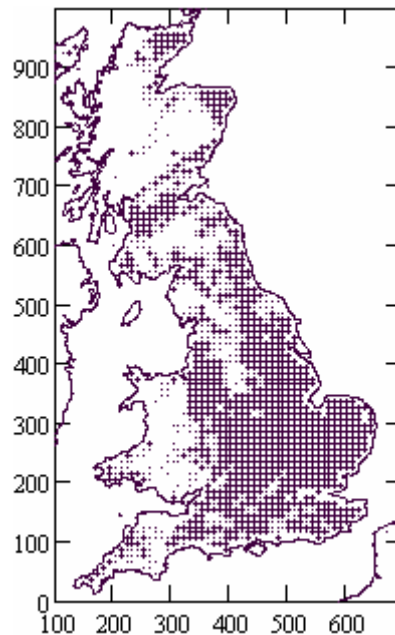


Fig 2. Tiles with $SD(\Delta h) < 5$, $SD(\Delta h) < 7$ m.

3 Distribution of Δh

The distribution of Δh within each tile tends to have a strong central tendency, with relatively few outliers. The histogram in Figure 3 is typical.

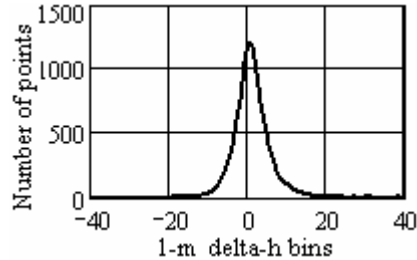


Fig.3. Typical distribution of (Δh)

Figures 4 to 6 shows the probability distributions of means, skewness and kurtosis for the Δh distribution for all tiles for which the SD is less than 20 m. The measure of kurtosis used is so-called “excess kurtosis”, for which the normal distribution gives zero and a double-exponential distribution gives 3.

There is considerable variation in these coefficients, but fairly clear trends. The mean of Δh tends towards about +1.8 m, and the distributions of Δh tend to have a small positive skewness and a kurtosis which suggests an exponential distribution.

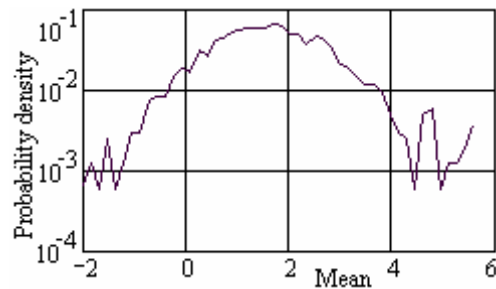


Fig.4. Distribution of means of (Δh)

4 Estimate of SRTM errors

The statistics reported above apply to the difference between SRTM and OS terrain heights. It can be assumed that the absolute errors in the two datasets are independent. Thus if their errors are of similar amplitudes, it is reasonable to estimate the SD of each as $1/\sqrt{2}$ of the SD of Δh . However, the distribution of errors appears to be “peakier” than the normal distribution, and thus estimates based on SD should be considered tentative.

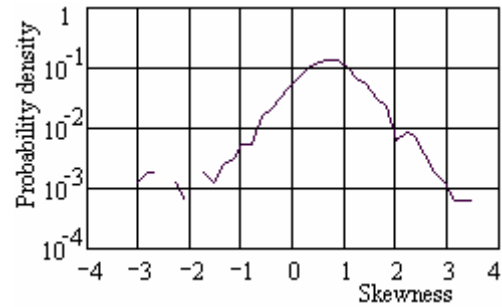


Fig.5. Distribution of skewness of (Δh)

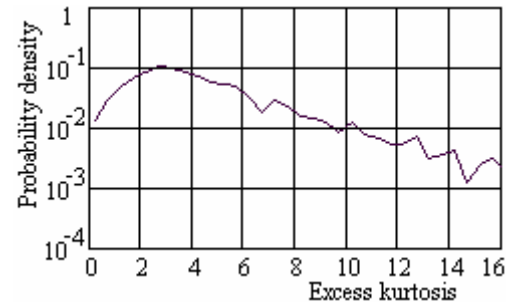


Fig.6. Distribution of excess kurtosis of (Δh)

For propagation prediction relative path shape is much more important than absolute height. On this basis further consideration of actual errors will be given after discussing how Δh affects profile interpretation.

5 Correlation distance

An important metric controlling how Δh affects profile interpretation is the correlation distance. A useful approximation is to assume that for two points separated by less than given distance height errors will be the same, and that errors will be statistically independent beyond that distance.

This concept was tested by calculating the Pearson’s R correlation coefficient of Δh as a function of point separation at 100-m increments within each 10-km tile for which no missing SRTM data is reported.

This was done separately for tiles in which the SD of Δh are in the ranges 0-5, 5-7, 7-10 and 10-20 m. The results, with all plots from each set of tiles in grey, and the median over-plotted in black, are shown in Figure 7 a) to d).

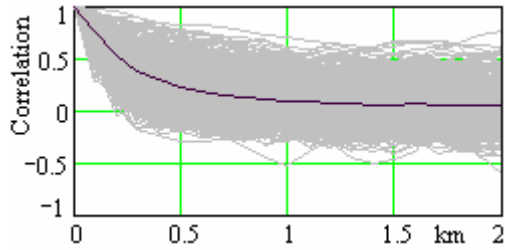


Fig 7 a). Correlation vs distance: $SD(\Delta h) < 5$ m (998 traces plus median)

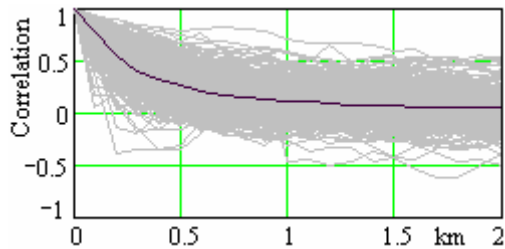


Fig 7 b). Corr vs distance: $5 \leq SD(\Delta h) < 7$ m (407 traces plus median)

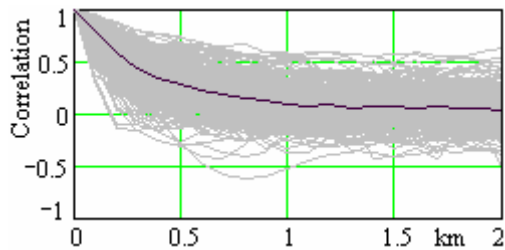


Fig 7 c). Corr vs distance: $7 \leq SD(\Delta h) < 10$ m (287 traces plus median)

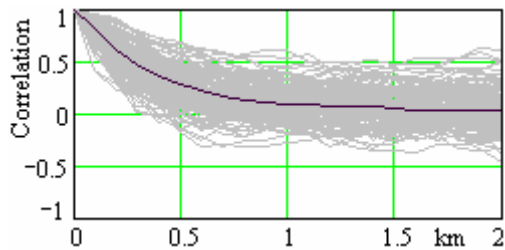


Fig 7 d). Corr vs distance: $10 \leq SD(\Delta h) < 20$ m (138 traces plus median)

Although there is considerable tile-to-tile variation, the median correlation coefficients all fall to 0.5 at about 250 m and are less than ± 0.1 for distances greater than 1.0 km.

The results shown in Fig 7 a)-d) show that to a good approximation height errors can be assumed to be correlated for points less than about 200 m apart, and decorrelated for points more than about 1 km apart. It would be ideal to take account of partial correlation in the intermediate range of distances, but since profile interpretation tends to be a computationally-expensive part of propagation modelling, assuming either full or zero correlation was adopted to limit the additional complexity. On the basis of the above analysis the demarcation distance was taken as 300 m. This is referred to as the decorrelation distance.

6 Required statistics

Profile interpretation can take terrain height errors into account provided two statistics are available:

- A cumulative distribution $P(\Delta h)$ giving the probability that the error does not exceed Δh .
- A decorrelation distance, d_c , within which height errors are assumed to be fully correlated, and beyond which they are assumed to be statistically independent.

Since the probability distributions of Δh for a selection of 10-km tiles were all found to be similar to Figure 3, it was decided to have one $P(\Delta h)$ to cover the UK without taking location within the country into account. Figure 8 shows the measured probability density function of Δh for all non-sea points at 100-m intervals, a total of the order of 7.10^7 points. It is noticeably more peaked than a simple dual-exponential distribution, and is consistent with the positive skew in Figure 5. An approximate model was thus fitted based on independent dual-slope exponentials for each half of the distribution.

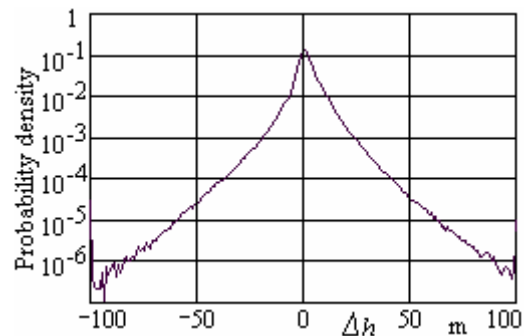


Fig.8. Measured distribution of Δh

However, the fitting exercise was conducted directly on a CDF generated from the data, since this is the form in which a model distribution is required.

The solid trace in Figure 9 shows the CDF generated from all measured Δh values. The dotted trace is the model used for $P(\Delta h)$ given by:

$$P(\Delta h) = \max\left[0.5 \cdot e^{0.33 \cdot \Delta h}, 0.015 \cdot e^{0.15 \cdot \Delta h}\right] \quad \text{for } \Delta h < 0 \quad (1a)$$

$$P(\Delta h) = 1 - \max\left[0.5 \cdot e^{-0.25 \cdot \Delta h}, 0.015 \cdot e^{-0.15 \cdot \Delta h}\right] \quad \text{for } \Delta h \geq 0 \quad (1b)$$

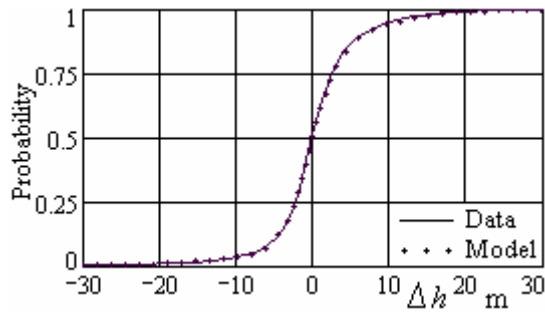


Fig.9. Cumulative distribution, data and model

As noted above, the decorrelation distance d_c was taken as 300 m.

7 Profile interpretation

The basic method for using the above statistics is described by an example. In propagation modelling it is often necessary to determine a horizon elevation angle. Figure 10 illustrates how height-error statistics can be taken into account during this operation. A graph of terrain height against distance, known as the profile, is represented by samples at intervals along its length.



Fig 10. Profile interpretation

First the profile point with the highest elevation angle at the transmitter 'T' is found. Let this be 'A', and assume that 'A' is more than d_c from 'T'.

All profile points within d_c of 'A' are now eliminated from further examination, as indicated by the profile underlining. From the remaining points, the point with the next-highest elevation angle is found. Let this be 'B'.

Points within d_c of 'B' are now eliminated, and the point with the next-highest elevation angle can be found. This continues until no further significant points exist.

Figure 11 shows the range of elevation angles possible for points 'A' and 'B'. Although the range

of height errors are the same for both points, their differing distances from 'T' result in different ranges of elevation angle due to each point.

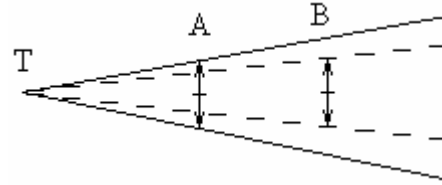


Fig. 11. Elevation angles for 'A' and 'B'

Since elevation angles are determined only by relative heights, the height at 'T' is considered error-free. This is consistent with using $P(\Delta h)$ from eq(1) since it applies to the discrepancies between two independent data sets.

Thus for a given horizon point the probability, Q , of the elevation angle error not exceeding $\Delta \epsilon$ is:

$$Q(\Delta \epsilon) = P(\Delta \epsilon \cdot d) \quad (2)$$

where ϵ is the elevation angle in mrad, and d is the distance of the point from 'T' in km.

If a significant horizon point is found within d_c of 'T', it is assumed that there are no relative height errors between the point and the height of 'T'. In this case, $Q(\Delta \epsilon)$ is a positive step from zero to 1 at $\Delta \epsilon = 0$.

Since the individual probabilities are statistically independent, for N horizon points the cumulative distribution of all errors $Q'(\Delta \epsilon)$ is given by the product of the individual distributions, that is:

$$Q'(\Delta \epsilon) = \prod_{n=1}^N [P(\Delta \epsilon_n \cdot d_n)] \quad (3)$$

Figure 12 shows Q plotted for points A and B in Figure 10, plus their combined distribution Q' . For clarity in this diagram point A has been moved closer to T to produce a wider distribution of Q_A .

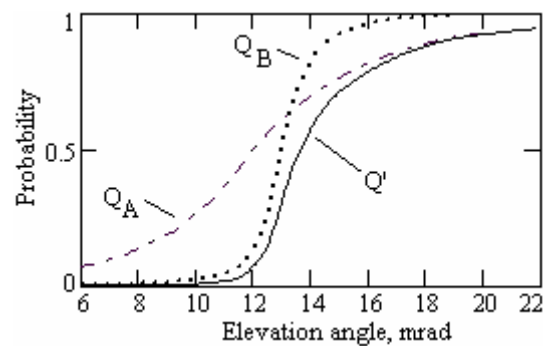


Fig.12. Separate and combined distributions

Thus eq(3) gives a good approximation of the risk factor for a horizon elevation angle not exceeding a

given value. This has been applied to predictions of wind-turbine visibility to radars.

8 Effect of height errors on propagation models

Section 7 shows that the effect of height errors on horizon elevation angles can be predicted on an analytic basis. However, because different profile points can form the horizon, depending on actual errors, there is a consequent uncertainty as to horizon distance.

This is significant for predicting the effect of height errors on propagation calculations. In particular, many diffraction models require more detailed profile information than just horizon elevation angles.

Two diffraction models currently of particular interest to ITU studies are:

- a) 3-edge diffraction model. This is a modified form of the Deygout method. It requires the distance and height of between 1 and 3 profile points (ITU 2005).
- b) A modified form of the Bullington model. For a transhorizon path this requires the horizon elevation angles, but not the their distances, for the two terminals. For a line-of-sight path it requires the distance and height of one point (ITU 2007).

Thus the method of Section 7 could be used for the Bullington method if it is known that a path will be transhorizon for all height errors within the probability range of interest. Otherwise, and in all cases for the 3-edge model, both heights and distances are required.

This suggests that the Bullington method, requiring less terrain information than the 3-edge method, should be less affected by height errors. This was tested by using both diffraction models to predict diffraction loss for profiles extracted from both SRTM and OS data. The statistics of two quantities were then calculated:

$$\Delta L_{d3} = L_{d3s} - L_{d3t} \quad (4a)$$

$$\Delta L_{db} = L_{dbs} - L_{dbt} \quad (4b)$$

where:

L_{d3s} = loss by 3-edge method for SRTM profile;

L_{d3t} = loss by 3-edge method for OS profile;

L_{dbs} = loss by Bullington method for SRTM profile;

L_{dbt} = loss by Bullington method for OS profile.

Table 1 shows the means and SDs of ΔL_{d3} and ΔL_{db} for 1,000 randomly-selected all-land paths within mainland UK with lengths from 1 to 100 km, for 300 MHz and 3 GHz. The antennas heights were 20 and 10 m above ground level.

Table 1: Sensitivity to height errors

GHz	3-edge: ΔL_{d3}		Bullington: ΔL_{db}	
	Mean	Std Dev	Mean	Std Dev
300	+0.55	5.01	+0.65	2.85
3,000	+0.39	8.29	+0.65	4.47

The SDs show that the Bullington method, with its smaller requirement for terrain information, is less affected by height errors.

9 Conclusions

A comparison with conventionally-surveyed data has shown that SRTM data has an SD of error of about 7 m for gently-rolling terrain and a de-correlation distance of about 300 m. An analytic method has been described to use these statistics to predict the error in calculating horizon elevation angle. This can be used, for example, to provide a risk factor for a given path being line-of-sight.

The calculation of diffraction loss normally requires more detailed terrain information, and a simple analytic method to assess the effect of height errors has not been found. A direct comparison between two diffraction models of current interest show that it is an advantage to require less terrain information.

As would be expected, the effect of height errors increases with frequency; about 5 dB SD of discrepancy was found between diffraction results using two terrain databases at 3 GHz.

At present, practical terrestrial-path models rarely achieve an SD against independent measurements of less than 8 dB. If the measurements and modelling contribute equally to such discrepancies, the corresponding modelling error SD is about 5 dB. Thus terrain height errors are a significant limitation on propagation modelling accuracy with currently-available terrain data.

References

ITU 2005: Recommendation ITU-R P.526-9 §4.4.2

ITU 2007: Document 3K/181 Annex 5, §2

Local Fading Characterization in Ground-Wave Propagation at MW Band

**D. de la Vega (david.delavega@ehu.es), U. Gil, S. López, P. Angueira, I. Angulo,
D. Guerra, J.L. Ordiales**

Department of Electronics & Telecommunications. University of the Basque Country.
Alda Urkijo s/n. 48013 Bilbao
Telephone: (+34) 946014127 Fax: (+34) 946014259

ABSTRACT

An exhaustive analysis about local fading in ground-wave propagation is presented in this paper. At Medium Wave band, big structures in the vicinity of the receiver, as bridges, overpasses or sign bridges, obstruct signal propagation causing local field strength fading occurrences of significant amplitude. These field strength fadings can cause audio dropouts or loss of service in the new digital radio services.

The study is based on field data obtained from a DRM (Digital Radio Mondiale) signal measurement campaign at Medium Wave band in Spain. The structures causing local fading are identified, and their most influent features determined. The relations between the local variations of the field strength and these structures features are obtained. As a result, the proper characterization of the field strength local fading when the receiver is located near these structures is obtained. The results of this study are useful for coverage planning purposes.

I. Introduction

Ground-wave propagation at MW band has traditionally been considered to be essentially constant, without significant changes with time or with atmospheric variability [1]. Thereby, the ground-wave propagated field strength at the receiver location would only depend on the electrical characteristics of the ground and on the distance between the transmitter and the receiver [2]. However, recent studies based on experimental field trials have empirically demonstrated that the location variability is significant at MF band [3]-[8], and it should be taken into account in the coverage estimations [9]-[10]. The main factors that cause this variation are terrain irregularities [11]-[12] and reception in urban environment [6], [9]. The results of these studies led the ITU-R to update in 2007 their recommendations about propagation at MW band, assuming that the signal amplitude does not remain constant for small changes in location, so that its probability distribution follows a log-normal law [13]-[14].

Some of the above-mentioned studies ([4]-[5], [8]-[9]) conclude that there is a significant influence of local fading occurrences when the receiver is near toll booths or power lines that must be characterized and included in the network planning tools. These fading occurrences could cause audio dropouts when the signal to noise ratio is near the threshold for good quality, and therefore, they should be considered when evaluating the percentage of any given area of a digital service. In fact, the ITU-R document [10] specifies that the fading margin and the man-made noise level have

to be determined for the system performance, especially in urban areas, in order to obtain reliable estimations at MW band.

New digital radio services at MW band (Digital Radio Mondiale, HD-Radio/IBOC) have more restrictive coverage requirements than the analogue systems, because a lower field strength level than the threshold for good reception will cause poor quality in an analogue system, but an audio dropout in a digital service [15]-[16]. For this reason, an accurate characterization of the ground-wave spatial variation is needed for these systems [9], [10].

Two different groups of structures placed near the receiver can cause local fading occurrences in ground-wave propagated signals:

- Big-sized structures, like bridges, pedestrian overpasses or sign bridges over the road, which obstruct the signal when considering mobile reception [4], [17].
- Electromagnetic noise sources, mainly power lines and electrical substations, which degrade considerably the SNR, as several studies have demonstrated [4], [7]-[9], [18].

The influence of these structures and noise sources has been evidenced in the above-mentioned studies, but a proper characterization is required to be included in the new propagation models. This study characterizes field strength variation in the nearness of different kind of structures located near the receiver, and analyzes the relation between the signal local variation and the features of such structures.

First, the paper presents a brief description of the

field trials. Next, the characterization of the considered structures and the methodology of the analysis are described. Finally, the evaluation and conclusions derived from the results are included.

II. Field Trials

DRM field strength measurements were carried out in 2004 using an experimental network set up in Spain. The digital signal was transmitted in the 1359 kHz frequency with a 9 kHz channel bandwidth [18]-[19]. Following subsections describe the main characteristics of the transmission infrastructure and the reception system.

A. Transmission Infrastructure

The DRM signal was transmitted from the station that the broadcaster RNE (Radio Nacional de España) has in Arganda del Rey, Madrid (Spain). This site is currently being used to broadcast regular MW and SW analogue emissions. The main features of this transmitting site are shown in Table 1.

TABLE 1
Transmitting Centre Characteristics

Transmission Centre	Arganda del Rey (Madrid)
Broadcaster	Radio Nacional de España (RNE)
Site location	3° 30' W ; 40° 19' N
Frequency	1359 kHz
Bandwidth	9 kHz
Radiating System	1.1 dBi vertical monopole Height: 30 m
Transmitted digital power (EIRP)	4 kW RMS
Transmission scheduling	8:30-14:00

B. Reception System

An extensive measurement campaign was carried out using a measurement vehicle equipped as shown in Figure 1. The measurement equipment is composed of three subsystems: the acquisition and distribution system, the measurement system and the control system.

Power measurements were performed by integrating the power spectral density over the 9 kHz signal bandwidth every DRM frame (400 ms). The quality of the digital signal was measured using a professional DRM receiver, and a GPS and a wheel tachometer provided accurate information of position and distance [18]-[19].

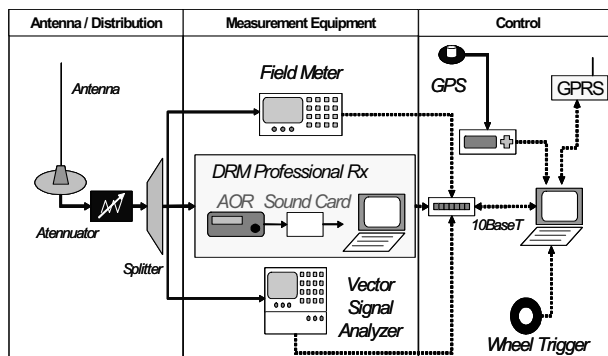


Fig. 1. Receiving system modules and equipment set

III. Analysis and Methodology

A. Identification of the Causes of the Local Fading Occurrences

The first step of the analysis tries to find out if it is possible to identify the causes of the fading occurrences, and therefore, to obtain relations between the signal variations and the most influent characteristics of the structures.

Two representative examples are shown in Figure 2 and Figure 3 to illustrate this analysis.

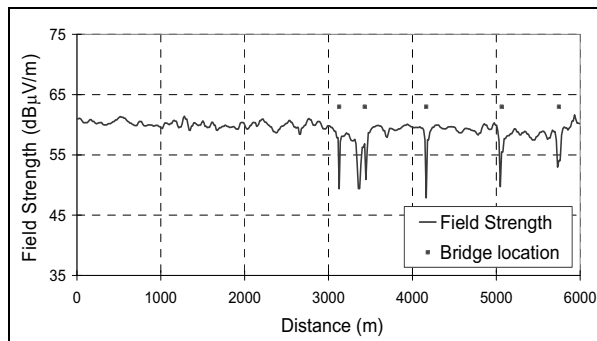


Fig. 2. Field strength level variations due to big-sized structures located near the receiver, in rural environment

Figure 2 shows the field strength recorded along a measurement route in rural environment. Reception conditions along the whole route are rural environment in open area, without significant variations in conductivity values, similar vegetation and no built-up areas. However, a remarkable increase of the location variability of the field strength is noticeable in the second part of the route (from 3 km to 6 km), presenting several local fading occurrences, down to 12 dB deep, as shown in Figure 2. These fading occurrences in the field strength are caused by several structures placed near the receiver. Five out of six drops in the field strength occur when the measurement vehicle went under a bridge. In these cases, a great

decrease in the received signal level is recorded. The remaining drop is due to the presence of a power line that crosses over the road.

It is clearly shown that, except for these fading occurrences mentioned above, the local mean of the field strength maintains similar values in both parts of the route.

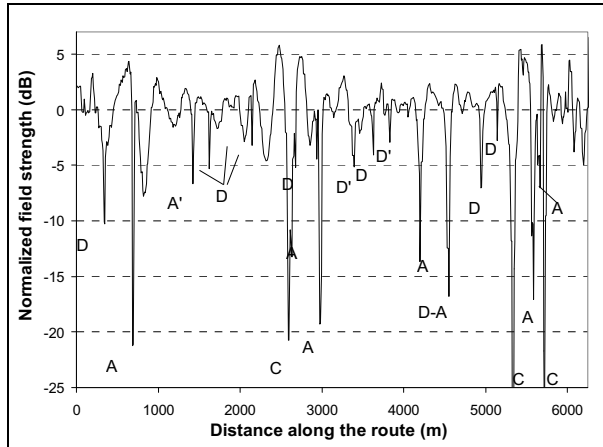


Fig. 3. Field strength level variations due to big-sized structures located near the receiver, in suburban environment

Figure 3 shows the normalized field strength registered in the relief road of a big city, in suburban environment. The positioning data provided by the GPS receiver have been used to identify the cause of each fading occurrence. Bridges and pedestrian overpasses have been labeled as 'A', railway overpasses have been termed as 'C' and the information panels over the road as 'D'.

As illustrated, there is a complete correlation between the relevant fading occurrences of the received signal and the presence of great structures in the nearness of the receiver location. The compilation of a significant number of items will allow the statistical characterization of the influence of these great structures on the field strength level.

B. Classification of the Structures Involved in the Analysis

The first step of the analysis consists in the classification of the structures that can cause significant variability of the instantaneous field strength level. First, a basic differentiation based on the nature of the field strength variation has been made: the structures that can cause obstruction in the signal reception and the electromagnetic noise sources have been analyzed in different groups.

The structures that can be found along the

measurement routes and cause reception obstruction have been categorized as follows:

- Bridges over the road where the mobile unit performed the field trials (highway and pedestrian overpasses).
- Sign bridges (information panels placed over the road, supported in both verges of the road) and cantilever signs (information panels placed over the road, supported in only one verge of the road), as shown in Figure 4.
- Railway overpasses.



Fig. 4. Examples of sign bridge (on the left) and cantilever sign (on the right)

On the other hand, the electromagnetic noise sources that have been included in the analysis are exclusively power lines, which are noise sources but they could also obstruct the reception when placed above the road.

Information about the features of each structure has been gathered, such as its geographic coordinates, width, material...

In order to avoid that the local variability could be influenced by the reception environment and to correctly characterize the influence of a single structure, only those samples placed in rural areas have been considered. Moreover, situations where two or more nearby structures could influence the received signal have not been taken into account.

A total of 164 occurrences that comply with the above-mentioned conditions have been included in the analysis:

- 75 bridges and highway overpasses and 6 pedestrian overpasses.
- 43 sign bridges and cantilever signs.
- 5 railway overpasses.
- 35 power lines.

Positioning data provided by the GPS receiver allow accurately associating the coordinates registered for the field strength fading occurrences with the structures location.

C. Parameters for Evaluating the Received Signal Quality

The parameters used to evaluate the quality of the

received signal are the following:

- Field strength level
- MER (Modulation Error Ratio): provides information about the IQ signal quality. The modulation error ratio is equal to the ratio of the RMS power of the ideal IQ constellation to the power of the error vector of the received signal. It is closely related to the signal to noise ratio (SNR) at these frequencies.
- AudioQ (Objective Audio Quality): indicates the objective quality of the decoded audio service as a percentage. It is measured as the quotient of the number of correctly decoded audio frames over the total number of transmitted audio frames. The criterion used to consider a specific audio service as good quality is that at least 98% of the transmitted audio frames must be correctly decoded [19].

D. Fading Characterization

The characterization of the local variation has been carried out using the normalized field strength values, in order to remove the large scale variations. For this purpose, the local mean values of the received signal have been estimated and removed from the instantaneous received signal to obtain the normalized field strength level [20]-[23].

Field strength fading occurrences have been characterized by evaluating the fade depth (in relation to their corresponding local mean) and the fade length (distance assessed in meters, considering the coordinates where the field strength is 3 dB lower than the local mean value). The decreases in MER and AudioQ have been calculated too.

As a result, representative figures of the fading characterization and the signal quality have been obtained. Furthermore, the most influential characteristics of the structures on the local signal variation have been determined, and related to the amplitude and length of the field strength fading occurrences.

IV. Results and Discussion

A. Analysis of the Fading caused by Reception Obstruction

Highway and pedestrian overpasses and, to a lesser extent, sign bridges and cantilever signs, cause variations in the parameters of the signal due to reception obstruction. Figure 5 illustrates an example of this situation.

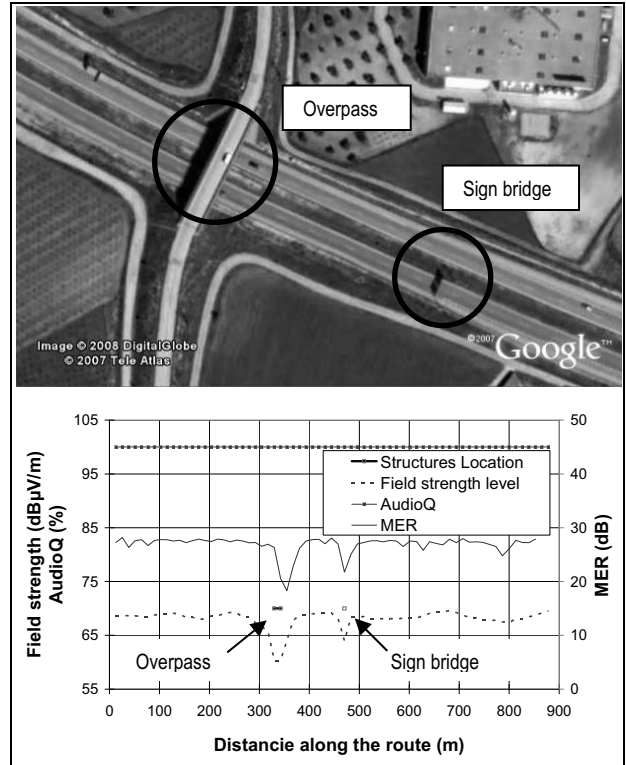


Fig. 5. Fading occurrences caused by an overpass and a sign bridge. Above, structures location, and below, field strength level, MER and AudioQ variations.

The most important aspects are the following:

- Field strength level presents a rapid decrease located in the vicinity of a bridge. This drop has its maximum amplitude under the structure (See Figure 5). These fading occurrences show a wide range of fade depths, being even greater than 15 dB in some occasions.
- MER shows a fading occurrence located around the bridge location, with similar characteristics of fade depth and fade length. This significant drop in the MER value means that the reception quality in terms of IQ constellation is degraded too.
- In most cases, AudioQ parameter maintains a value of 100%, featuring perfect audio quality and demonstrating the robustness of the DRM system. In the few cases where the field strength and MER decrease heavily, AudioQ may drop below the necessary threshold for good quality, causing audio dropouts and loss of service.

B. Fading Evaluation according to Structures Main Features

The width and orientation of the bridge with respect to the propagation direction have demonstrated to have a great influence on the local fading. Both aspects are considered to characterize MER and field strength

fading occurrences.

Table 2 shows the fade depth values classified according to the width of the structures. The obtained results indicate that the fade depth depends on the bridge width. In addition to this, the minimum values of the fading amplitudes caused by structures obstructing the reception have been determined. For highway or road overpasses this depth is 6 dB, 5 dB for the pedestrian overpasses, and 4 dB for sign bridges.

Furthermore, there is a progressive increase in the fade length with respect to the bridge width, as it can be observed in the median values as well as in the 10th and 90th percentiles depicted in Table 2. In general, the fade length takes values between 20 m and 40 m greater than the bridge width (this is, a fade length between 10 m and 20 m longer than the bridge width at each side of the overpass). Moreover, it can be stated that the minimum length for a fading occurrence due to an overpass is 20 m.

It can be shown that both cases present little deviation around the median value, so there is a clear correlation between bridge width and both fade depth and fade length.

On the other hand, the influence of the bridge orientation in the signal variations is also analyzed. The orientation of the bridge is determined with respect to the propagation direction (line connecting transmitter and receiver). For this purpose, bridges of the same width have been classified according to their orientation as “perpendicular”, “oblique” or “parallel”.

Figure 6 shows the fade depths caused by the bridges of 10-11 m width, classified as its orientation with respect to the propagation direction.

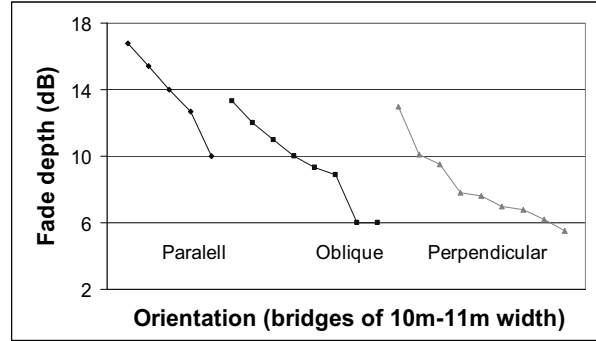


Fig. 6. Fade depth as a function of the bridge orientation with respect to the propagation direction.

There is a clear tendency of the fade depth with the bridge orientation. Overpasses that are aligned in the propagation direction obstruct the reception of the signal to a great extent, because all the bridge length blocks the reception. On the contrary, when the bridges are placed perpendicularly to the propagation direction, the fade depth is slightly lower (See Figure 6).

C. Relation between Field Strength and MER Fading

As shown in Figure 5, there is an almost linear relation between the field strength fade depths and the MER fade depths, with similar values for both parameters. This relation is depicted in Figure 7. Fade depth values are grouped around an imaginary diagonal line, indicating that the relation between field strength and MER fade values is almost 1:1, except when signal suffers a great drop. In those cases, MER fade depth values present greater amplitude than the field strength fade depth values.

TABLE 2
Fade depth and fade length of the field strength variations, as a function of the structure width

Structure	Width (m)	Depth (dB)			Length (m)		
		10 th percentile	< Median >	90 th percentile	10 th percentile	< Median >	90 th percentile
Highway or road overpass	18 - 24	21.9	< 23.1 >	28.3	40.2	< 51.5 >	66.4
	14 - 16	11.3	< 12.6 >	15.0			
	10 - 12	6.1	< 9.8 >	15.0	24.6	< 41.0 >	50.8
	6 - 9	6.0	< 8.3 >	10.1	23.6	< 30.5 >	44.1
	All	6.1	< 9.1 >	15.6	Between 10 m and 20 m longer than the bridge width at each side of the overpass		
Pedestrian overpass	2 - 3	5.3	< 6.5 >	8.6	12.0	< 17.5 >	29.0
Sign bridge	-	4.0	< 5.1 >	6.8	10.0	< 11.5 >	27.3
Cantilever sign	-		≈ 3			-	

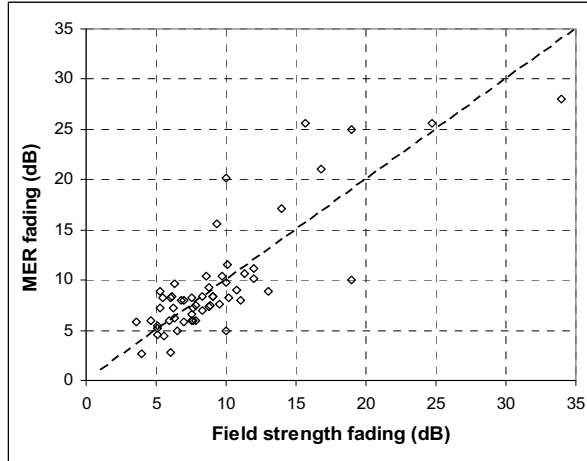


Fig. 7. Relation between MER and field strength fade depth values.

D. Critical Reception Situations

In this section, two particular situations in which the registered fade depth is significantly higher are described. The first one is the presence of two or more bridges very close to each other. The second one is the presence of railway overpasses.

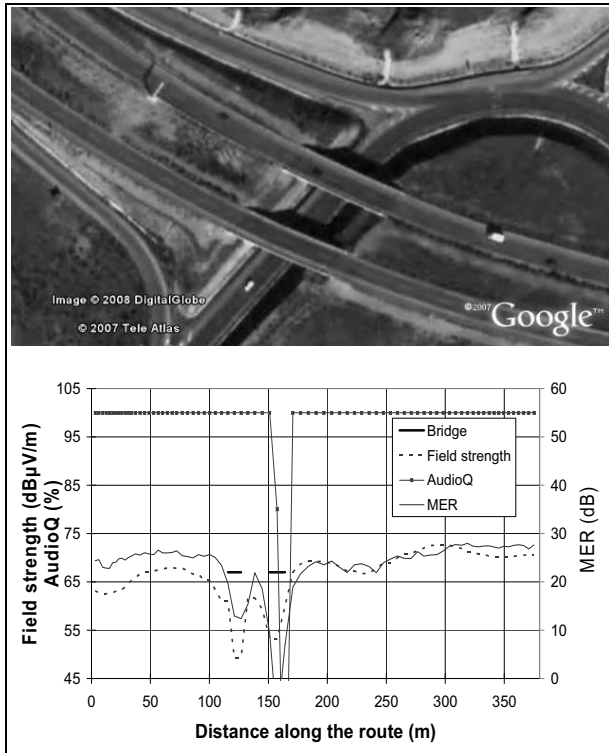


Fig. 8. Two bridges located very close to each other. Above, structures location, and below, field strength level, MER and AudioQ variations.

When two or more overpasses are located very close to each other, the field strength fade depth is higher than 20 dB. In these cases, the fade depth and the fade length depend both on the width and on the separation between the overpasses. Figure 8 shows an example of this situation.

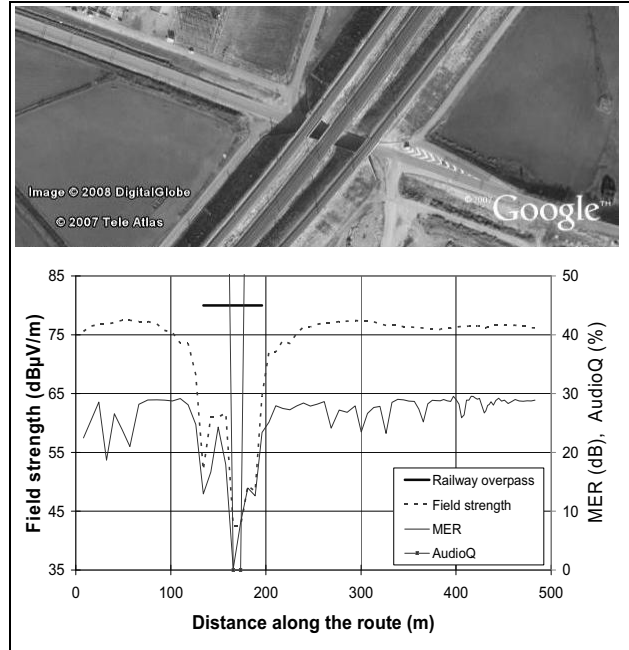


Fig. 9. AVE (high-speed train) railway overpass. Above, structures location, and below, field strength level, MER and AudioQ variations.

The railway overpasses present a greater influence, being the field strength decrease considerably deeper in the nearness of the structure (see Figure 9). Analyzed situations from the field data show that the fade depth value caused by a railway overpass is greater than the fade depth value due to a bridge of the same width. Fade depth occurrences between 22 and 37 dB were recorded in these situations.

Furthermore, these severe field strength fading occurrences often generate a drop in the AudioQ parameter, causing audio dropouts and loss of service.

E. Influence of Electromagnetic Noise Sources

Previous studies have stated that power lines generate a considerable electrical noise level at MW band [24]. This noise level depends both on the distance between the receiver and the power line and on the power line voltage.

When analyzing the variations of the received signal in the nearness of the power lines, it is clearly observed that this influence is not homogenous (Figure 10 shows two representative examples). This aspect is confirmed

in measurement campaigns carried out in Moscow [9], Macedonia [4] and Vietnam [8].

In general, the degradation in the received signal is a combination of two effects. First, the power lines generate high level of electrical noise at MW band, and consequently, the SNR decreases. Secondly, the wires obstruct the propagation of the signal, causing field strength fading. Depending on the reception conditions (situation and voltage of the power line, and distance to the receiver), one of the two above-mentioned causes could be more significant, and thereby have a greater influence on the signal.

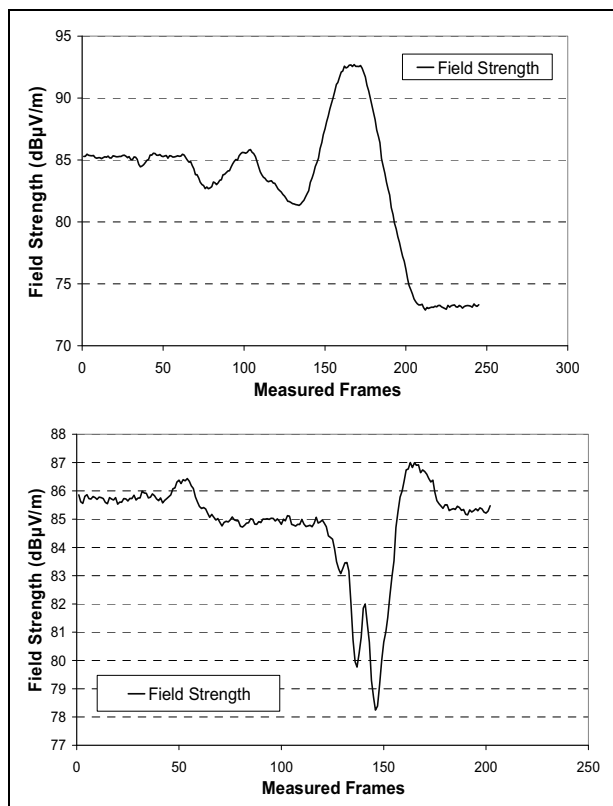


Fig. 10. Examples the field strength variation registered when the measurement mobile passes under a power line in two different situations.

This study has focused on the analysis of the mobile reception along the route where the power lines cross over the road. In most of the cases, fading occurrences in field strength and MER levels are registered when the measurement unit is in the vicinity of the power line. Figure 11 shows an example of this situation.

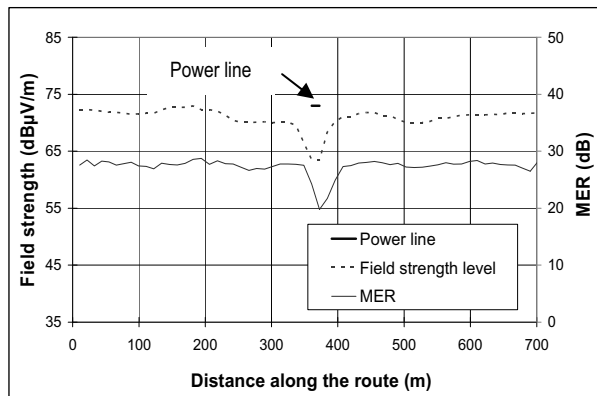


Fig. 11. Influence of a power line over the road. Figure shows field strength level and MER.

Table 3 summarizes the results obtained in the characterization of the field strength and MER variations generated by power lines. As it can be observed, there are many cases where fading depth is similar to the generated by a small bridge.

TABLE 3

Field strength and MER variations generated by power lines

	Field strength		MER
	Fade depth (dB)	Fade length (m)	Fade depth (dB)
90 th percentile	14.5	89.2	12.3
Median	8.5	40.0	8.0
10 th percentile	3.6	2.0	3.4

Although the statistical values are similar, the relation at each occurrence between the field strength fade depths and the MER fade depths is not clearly linear, as it is in the case of the obstruction caused by nearby structures. The reason is that, in the case of the power lines, the MER level is being affected also by the electrical noise from the power line.

V. Conclusion

In this paper, the local drops observed in the ground-wave propagation at MW band have been characterized, using the results of a DRM field trial carried out in Spain.

The study demonstrates that the significant field strength variations are mainly due to the presence of great structures in the nearness of the receiver location. Two types of structures have been differentiated. First,

great structures (such as bridges, overpasses or information panels), which obstruct the signal reception, causing field strength fading occurrences of significant amplitude. Secondly, the power lines, which cause a SNR reduction by the combination of two effects: the electrical noise generated by the power lines, and the obstruction of the wires on the propagation of the signal.

The field strength level, MER and AudioQ variations have been evaluated for every structure, and relations between the signal variations and the most influent characteristics of the structures have been found.

The compilation of a significant number of items allows the statistical characterization of the influence of these big-sized structures on the field strength level. As a result, relations between the structures features and the degradation of the received signal have also been found.

These results provide both a better characterization of the local field strength variation and useful values for network planning.

Acknowledgment

The authors would like to thank RNE and Telefonen-VIMESA for the transmission infrastructure they have provided for this measurement campaign, the colleagues within the DRM consortium for their help, and the Spanish Ministry of Science and Technology and the University of the Basque Country (UPV/EHU) for their financial support.

References

- [1] International Telecommunication Union, "Rec. ITU-R P.1321. Propagation factors affecting systems using digital modulation techniques at LF and MF", August 1997.
- [2] International Telecommunication Union, "Rec. ITU-R P.368-8. Ground-wave propagation curves for frequencies between 10 kHz and 30 MHz", March 2005.
- [3] D. de la Vega, S. López, D. Guerra, G. Prieto, M. Vélez, P. Angueira, "Analysis of the Attenuation Caused by the Influence of Orography in the Medium Wave Band", IEEE Vehicular Technology Conference VTC2007-Spring, April 2007.
- [4] F. Held and A. Giefer, "Macedonian DRM tests on Medium-Wave," DRM Document TC SE300, Consortium DRM, private communication, November 2004.
- [5] International Telecommunication Union, "Document 6E/175-E. Digital Radio Mondiale DRM daytime MW tests", March 2005.
- [6] International Telecommunication Union, "Document 3J/169-E. Statistical changes of a signal level in a city and its vicinities in ranges LF-MF", March 2007.
- [7] International Telecommunication Union, "Document 6E/403-E Digital Radio Mondiale (DRM): MW simulcast tests in México D.F.," October 2005.
- [8] International Telecommunication Union, "Document 6E/390-E. DRM Medium Wave Reception Tests in Vietnam", Agosto 2006
- [9] International Telecommunication Union, "Document 3J/123-E. Distribution of Signal Levels of a MF Ground-Wave in Zone of Service", September 2006.
- [10] International Telecommunication Union, "Document 6E/54-E. Digital broadcasting at frequencies below 30 MHz. MF and HF field-tests report summary. Final system performance report for IST-RADIATE 1999-20113 for ITU" February 2004.
- [11] N. DeMinco, "Propagation Prediction Techniques and Antenna Modelling (150 to 1705 kHz) for intelligent Transportation Systems (ITS) Broadcast Applications", IEEE Antennas and Propagation Magazine, vol. 42, pp. 9-34, August 2000.
- [12] N. DeMinco, "Medium Frequency Propagation Prediction Techniques and Antenna Modeling for Intelligent Transportation Systems (ITS) Broadcast Applications", NTIA Report 99-368, August 1999.
- [13] International Telecommunication Union, "Rec. UIT-R P.1321-2. Propagation factors affecting systems using digital modulation techniques at LF and MF", February 2007.
- [14] International Telecommunication Union, "Rec. UIT-R P.368-9. Ground-wave propagation curves for frequencies between 10 kHz and 30 MHz", February 2007.
- [15] M.C.D. Maddocks, I.R. Pullen "BBC RD 1993/11. Digital Audio Broadcasting: comparison of coverage at different frequencies and with different bandwidths", BBC Research Reports, 1993.
- [16] P.G. Brown, "Digital Radio: Coverage Prediction and Measurements of Location Variability", 11th International Conference on Antennas and Propagation, Conf. Publ. N° 480, April 2001.
- [17] D. de la Vega, U. Gil, P. Angueira, "Field strength variation in the proximity of big structures at MF band and ground-wave propagation," DRM Document TC MN019, Consortium DRM, private communication, September 2007.
- [18] G. Prieto, M. Velez, A. Arrinda, U. Gil, D. Guerra, D. de la Vega, "External Noise Measurements in the Medium Wave Band," IEEE Transactions on Broadcasting, Vol. 53, No 2, pp. 553 – 559, June 2007.
- [19] D. Guerra, G. Prieto, I. Fernández, J. M. Matías, P. Angueira, and J.L. Ordiales, "Medium Wave DRM Field Test Results in Urban and Rural Environments," IEEE Transactions on Broadcasting, Vol. 51, No. 4, pp. 431–438, Dec. 2005.
- [20] W. C. Y. Lee, "Estimate of local average power of a mobile radio signal", IEEE Transactions on Vehicular Technology, Vol. VT-34, N° 1, 1985.
- [21] J. D. Parsons, "The Mobile Radio Propagation Channel", 2nd. Edition, Ed. John Wiley & Sons LTD, 2000
- [22] D. de la Vega, S. López, U. Gil, J. M. Matías, D. Guerra P. Angueira and J. L. Ordiales, "Evaluation of the Lee Method for the Analysis of Long-term and Short-term Variations in the Digital Broadcasting Services at the MW Ban," 2008 IEEE International Symposium on Broadband Multimedia Systems and Broadcasting BMSB08, March 2008, accepted for oral presentation.
- [23] D. de la Vega, S. López, U. Gil, J. M. Matías, P. Angueira, M. M. Vélez and J. L. Ordiales, "Empirical Analysis of the Sample Correlation for the Planning of Field Trials in the Digital Broadcasting Services at MF Band," International Instrumentation and Measurement Technology Conference, I2MTC 2008, May 2008, accepted for oral presentation
- [24] A. D. Spaulding and R. T. Disney, "Man-made Radio Noise. Part I: Estimates for Business, Residential, and Rural Areas", DT Report 74-38, Office of Telecommunications, U. S. Department of Commerce.

Digital Mobile Networks: Limitations and Possibilities

Christopher Haslett
Ofcom, United Kingdom
Telephone: +44 207 981 3000
Fax: +44 20 7981 3730
Email: chris.haslett@ofcom.org.uk

Abstract

Mobile speech has been with us for some time now. Mobile television and “Mobile broadband” are now being talked about and piloted. The drive for ever-increasing capacity on mobile networks whilst working within the constraints imposed by bandwidth limits, thermal noise and interference poses very significant challenges. This paper examines the fundamental limitations of networks that aim to provide continuous coverage over a particular area. The likely effectiveness of modern technologies is assessed in the context of overall network performance. The final suggestion is that, whilst sophisticated technologies can deliver improvements, there is a strong argument for adopting a simple approach wherever possible. The United Kingdom has five operators offering 3G mobile services. A snapshot of the current situation there is presented as an indicator of the way operators are striving to determine an optimum solution.

Introduction

The purpose of any digital communications network is to provide the user with a channel of acceptably high bit rate and acceptably low BER. The BER requirement can be translated into a required E_b/N_0 . But the relationship between BER and E_b/N_0 is not fixed, it depends upon the modulation scheme. Generally, the simpler the modulation scheme (such as BPSK and QPSK) the lower the E_b/N_0 requirement for a given BER. This means that the more sophisticated schemes within UMTS such as HSDPA will need a higher energy per bit and thus more transmit power and thus produce more interference.

Experience Gained From Fixed Services

At Ofcom we are involved in the interference management of civilian microwave systems. It is these systems that first experimented with higher order modulation schemes: firstly 16QAM and then increasing up to 256 QAM.

The higher order modulation schemes are said to be more spectrally efficient. But that assertion is open to question. They can send a higher bit rate through a channel of a particular bandwidth but they also require a higher signal to noise-plus-interference ratio. Going from 16 QAM to 64 QAM will increase the throughput in a given bandwidth by a factor of approximately 1.5 but the amount of energy needed per symbol in a gaussian environment will increase by a factor of approximately 4 in order to maintain the same BER. By considering this fact, the simpler modulation schemes can be regarded as more spectrally efficient. A typical microwave link using QPSK (2 bits per symbol) will need a SNR of 12 dB whereas a 64 QAM (6 bits per symbol) link will need 26 dB. As any network becomes interference limited, this difference of 14 dB translates to a distance ratio of approximately 5 (if a propagation exponent of 2 is assumed) or a ratio of possible site densities of 25:1. This for a gain of a factor of 3 in throughput per unit bandwidth. Although the exponent in mobile systems is going to be closer to 3.5, the ratio of site densities for similar BERs is still in excess of 6:1.

Additionally, in any course on the fundamentals of UMTS, we talk about spread spectrum. This is the concept of transmitting low (e.g. 64 kbit/s) bit rates over a wide bandwidth (e.g. 5 MHz). This then allows us to operate in negative signal-to-noise ratio environments (a vital pre-requisite for single frequency networks). Once we are talking of bit rates in the Mbit/s, there is not much spreading going on and providing continuous coverage in a single frequency network is not going to be possible. The problem of deploying High-speed Downlink Packet Access (HSDPA) is further exacerbated by the challenge of sharing HSDPA and “normal” services on the same carrier. HSDPA needs its own spreading code thus denying it the reduction in mutual interference provided by downlink orthogonality. This makes simultaneous co-carrier downlink transmission of HSDPA and non-HSDPA services next to impossible. But all five United

Kingdom UMTS operators offer some HSDPA coverage (but all five UK UMTS operators have at least two carriers). But the fundamental laws dictate that, until the effectiveness of interference rejection and cancellation improves significantly, HSDPA will only cover isolated pockets, probably in low-interference (e.g. indoor) environments if deployed on a single carrier.

Capacity-increasing Techniques

Certain technologies can improve network capacity by directly addressing fundamental limitations. Signal to noise ratio, in combination with available bandwidth, imposes a direct limitation on throughput. It is common to talk about “signal to noise” ratio as though it were the same as “signal to noise-plus-interference”. The general story is that it is possible to overcome noise-imposed limitations by turning up the power but this is self-defeating, especially in a single frequency network, as it increases interference levels. But interference can be cancelled (without theoretical limit) and therefore any reduction in interference through interference cancellation will lead to an increase in capacity. However, there is no doubt that an extremely effective way of reducing interference is to not transmit the energy in the first place. In this respect, fast power control (that allows the transmitter to emit just enough power and no more) is a very significant feature in UMTS FDD systems. It permits the transmit power at any instant to be just sufficient to achieve the necessary BER over the channel. This technique minimises the power transmitted. Power control is not going to be anything like as effective in TDD networks due to the non-continuous nature of transmission in each direction. In UMTS FDD the fast power control is capable of changing the transmitted power 1500 times each second.

Lowering E_b/N_0 requirements will also improve network capacity. Unfortunately this means increasing BER. However, it should be noted that packet-based channels are more tolerant of high BER and increased use of IP should lead to an increase in network throughput. Also, any method of delivering more energy to the receiver for a given transmit power (e.g. by using directional antennas) or improving the E_b/N_0 at the receiver by some sort of diversity system is going to reduce interference and improve capacity. This suggests that so-called MIMO (Multiple Input, Multiple Output) systems

should have a significant impact both on coverage range and network capacity. To maximise any diversity gain, physical separation of the antennas is desirable. Hand held mobile terminals limit this and laptop computers are much more attractive from the viewpoint of supporting diversity transmission and reception at the mobile terminal. However, a relatively simple multi-beam antenna (e.g. using a Butler matrix array) at the base station only with a separate spreading sub pilot allocated to each beam represents a dramatic improvement over non-diversity systems.

Beyond 3G

Where does this leave 4G? Bit rates higher than bandwidths require positive signal to noise ratios and that makes providing continuous coverage very challenging without having many carriers available. High bandwidths are necessary. But does 4G necessitate continuous coverage at “4G bit rates”? If not, it can be delivered here and now. But whatever bit rates and network capacity proves to be possible with a 5 MHz bandwidth, you can get double that with a 10 MHz bandwidth. Interestingly, the debate regarding continuous coverage affects landline-based broadband systems. It is common in the UK to see “up to 8 Mbit/s” advertised as a bit rate. But, in practice, these are usually delivered via a telephone subscriber line and the bit rate achievable depends on the distance of the subscriber from the nearest distribution point. This leads to a picture of a map whereby the possible bit rate achievable decreases with distance from distribution points and the end result is not that different from what can be produced by a cellular radio network. The vision of “fibre to the home” is some way off from reality in the UK.

So where does this leave WiMax? WiFi has been a success: it delivers very high bit rates to laptop computers. But only over short distances and only in low-interference environments. Evidence suggests that users in apartment blocks are finding it to be a very ineffective solution as user penetration increases. The name WiMax carries with it the suggestion that it can provide WiFi-type performance in a mobile network that provides continuous coverage. Going for 10 MHz of spectrum per carrier is a good start in increasing capacity. It is acknowledged that it is not going to be able to provide high speed using a single carrier and a network will require typically a 50 MHz block of spectrum to be made available. The adoption of TDD as the most likely standard prevents fast power control. But OFDMA is a sophisticated multiple access method (note that each sub-carrier uses a simple modulation scheme to minimise E_b/N_0

requirements) offering multi-path diversity and good interference cancellation. But WiMax is not a magic solution and engineers will have to grapple with the same problems and issues as they have with UMTS.

3G in the United Kingdom

But UMTS is not likely to disappear in the near future. I will finish with a short summary of the situation in the United Kingdom.

The UK has awarded UMTS licences to five operators who share 12 FDD “slots” and four TDD “slots”. Only FDD is significantly deployed (the latest talk is of using the TDD carriers to roll out a mobile television service). It is notable that the incumbent fixed line operator does not have a mobile licence. Additionally there are Virtual Network Operators (e.g. Virgin mobile uses T-mobile’s network and has about 5 million subscribers). [1]

Mobile penetration (including GSM) is at 115%. 84% of adults are regular users. Using the mobile for internet browsing is becoming more common (driven by competitive pricing such as \$12 per month for unlimited use). 3G use is becoming more widespread with penetration at around 15%. [1]

All five operators have launched HSDPA-based services, mostly with users having a card plugged into a laptop PC.

Most interestingly, the UK government has proposed to take back some 900 MHz spectrum from GSM operators and re-auction it, barring the current holders from bidding in that auction (note that all GSM operators in the UK are also UMTS operators). This is seen as a spur to transfer traffic to the more efficient UMTS network. [2]

Summary

The general desire for delivery of high speed bearers to mobile users conflicts with bandwidth constraints and the need to serve multiple users. The simpler modulation schemes are more robust in a hostile radio environment and are additionally more tolerant of mutual interference. Limiting and cancelling interference are crucial to maximising capacity of shared spectrum. Advanced technologies using MIMO devices can increase network capacity but older techniques such as fast power control are also of significant value in FDD networks.

References

[1] Communications Market Report, Ofcom, UK, 2007.

http://www.ofcom.org.uk/research/cm/cmr07/cm07_print/

[2] Opening up Mobile Spectrum to Support Innovation and Competition, Ofcom, UK, 2007.

http://www.ofcom.org.uk/media/news/2007/09/nr_20070920

Deterministic Equations for Computer Approximation of ITU-R P.1546-2

Sid Shumate

Givens & Bell, Inc.

Email:tsunami@tidalwave.net Voice: (703) 754-2478 Fax:(703) 818 2425

Abstract:

This paper introduces a complete set of deterministic and deterministic-based equations and methodology for computer implementation of an approximation of the results obtained from the use of Figures 1, 9 and 17 in ITU Recommendation P.1546-2. This set of approximation equations and methodology are for use in computer software implementations estimating radio signal field strength over land, in the 10 MHz to 3GHz range, for a radio path length between 1 and 1000 km., with a reliability of 50% of locations, 50% of the time, and a receiver height at or below 25.3 m. The accompanying computer spreadsheet provides a full demonstration of the use of these equations. The only non-preset input data required consists of the transmitter and receiver heights, the frequency, and the path length. These approximation equations are based on Beer's Law, Snell's Law, Free Space Dispersion, Radiative Transfer Engine Theory, ITU Recommendations P.453-7, P.530-7, P.833-2 and P.1546-2, and the Generic Model of 1-60 GHz Radio Propagation through Vegetation.

Free Space Dispersion: The classic term “free space loss” is a misnomer; a more accurate term is “dispersion”. The classic textbook form of this equation, $FSPL = 20\log(d) + 20\log(f) + 32.44$ dB, does not function correctly below $d = 1$ km, nor does it include vertical path dispersion. Therefore, we prefer use of a version of the Free Space Dispersion (FSD) equation:

$$FSD = 10\log_{10}((h_1 - h_2)^2 + d^2) + 20\log_{10}(f) - 147 \text{ dB} \quad (1)$$

Where f is in Hz, and the horizontal earth surface path length, d , the transmitter height, h_1 , and the receive height, h_2 , are all in meters.

P.1546-2 uses maximum field strength value curves. Free Space Loss (FSL) is utilized on the figures as maximum (free space) lines. They are calculated using:

$$E_{\text{fs}} = 106.9 - 20\log(d) \text{ dB}(\mu\text{V}/\text{m}), d \text{ in km.} \quad (2)$$

Alternately, for more accuracy, using FSD:

$$E_{\text{fs}} = 106.9 - 10\log((h_1 - h_2)/1000)^2 + d^2) \text{ dB}\mu\text{V}/\text{m} \quad (3)$$

with d in km.

Two-ray multipath: A Bouguer Line analysis of the data indicates that no significant two-ray multipath contribution exists in the P.1645-2 data.

Developing Clutter Absorption Loss equations: Clutter absorption attenuation occurs along the path of the direct signal from the transmitter to the receiver. On a typical broadcast path, a signal from

a high transmitting site transmits into clear air. The receive site is at a relatively low height, 2 to 10 meters above ground level, and the “clutter layer”, consisting of a layer of foliage and other absorptive materials atop a smooth or irregular terrain, is taller than the receive antenna height. At a point along the direct signal path, the direct signal path enters the clutter layer. While the composition of the clutter varies tremendously from site to site, if the empirical database is extensive, and the clutter, on the average, can be considered to be relatively homogeneous in absorption per meter and in the height of the clutter layer, then it is possible to derive not only an average value of clutter attenuation per meter, but an estimate of the average clutter canopy height. We define C_{HR} as the average clutter layer height above the receiver; C_{HR} is equal to C_H , the average clutter height, less the effective receive height, h_2 . The clutter loss, at its simplest, can be a straight-line function of the form: $A = d * AB$, where AB is the Clutter Absorption coefficient, and d the absorption path distance. Such an equation exists: Beer's Law. Beer's Law is an extension of the Bouguer Law, which was rediscovered as the Lambert law of absorption. Beer's Law, defined for radio propagation is:

$$A_{CL} = AB * \text{clp} * c, \quad (4)$$

Where: A_{CL} is the attenuation of the signal in dB/meter; $A_{CL} = \log_{10}(\text{power in}/\text{power out})$ (5)

clp is the length of the path (in meters) that the signal follows through the absorbing medium

(ground clutter), and AB is the absorption factor function, defined in attenuation per meter, (dB/meter), the absorptivity of a theoretical, homogeneous, one-meter depth of statistically average clutter as derived from the figures in ITU-R P.1546-2. The coefficient c represents the density of the clutter, and is preset to $c = 1.0$.

Next, we determine an equation for the length of the direct propagation path that passes through the clutter, d_{cp} . To calculate the angle from the receive site back toward the transmit site, take the difference in height between the transmitting and receive antennas, divided by the total path distance, to obtain the tangent of the receive site take-off angle, θ_r . For a line-of-sight path, the trigonometric functions associated with θ_r are:

$$\tan \theta_r = (h_1 - h_2)/d = (C_H - h_2)/d_{cp} \quad (6)$$

$$\theta_r = \text{atan}((h_1 - h_2)/d) \quad (7)$$

$$\sin \theta_r = (h_1 - h_2)/r_0 = (C_H - h_2)/clp = C_{HR} / clp \quad (8)$$

$$r_0 = ((h_1 - h_2)^2 + d^2)^{1/2} \quad (9)$$

where C_{HR} , clutter height above receive height is:

$$C_{HR} = (C_H - h_2) \quad (10)$$

C_H = average of the clutter canopy height

d = flat earth surface distance between the transmit and receive antennas

h_1 = effective height of the transmit antenna

h_2 = effective height of the receive antenna

clp = cluttered path length, through clutter layer from entry point to receive antenna

d_{cp} = the portion of d under the clp .

r_0 = total length of direct signal path ray from transmit to receive antenna.

we then derive:

$$r_0 = (h_1 - h_2) / \sin \theta_r \quad (11)$$

$$clp * (h_1 - h_2) = r_0 * (C_H - h_2) = ((h_1 - h_2)^2 + d^2)^{1/2} * (C_H - h_2)$$

$$clp = (((h_1 - h_2)^2 + d^2)^{1/2} * (C_H - h_2)) / (h_1 - h_2)$$

$$clp = C_{HR} / \sin \theta_r = (C_H - h_2) / \sin \theta_r \quad (12a,b,c)$$

$$\text{where } \sin \theta_r = (h_1 - h_2) / ((h_1 - h_2)^2 + d^2)^{1/2} \quad (13)$$

From Beer's Law, the clutter attenuation A_{CL} , is equal to the average clutter absorption per meter function, AB, times the clutter path length, clp :

$$A_{CL} = AB * clp = AB * (C_H - h_2) / (\sin \theta_r) \quad (14)$$

Based on an assumption that the average clutter height effectively remains the same at all distances in the ITU Figures, we interpret from Figure 1 of P.1546-2, where we find: $f=100$ MHz, $h_1 = 10$ (or, $37.5/4=9.375$) meters transmitter height, and $h_2 = 10$ meters (rural) receive height. The statistical reliability is 50% of locations, for 50% of the time. We reference the non-free-space clutter attenuation

as being the vertical distance between the h_1 line and the maximum line.

Solving for the Clutter Factor coefficients: The next step is to quantify our constants and factors, and include a form of Radiative Transfer consideration to the Beer's Law equation. The value of AB is orders of magnitude smaller at 40 km than at 1 km. Since AB for a homogenous medium must be a constant, there is a second set of phenomenon at work here; Radiative Transfer. Our hypothetical simplified framework model for radio signal propagation consists of up to three significant considerations:

For a transmitting antenna at or below the clutter layer, the considerations in addition to FSL are:

1. Absorptive loss of the signal, as it travels vertically (and to some extent, horizontally) up from the antenna to the top of the clutter layer, and back down through the clutter layer to reach the receive antenna.

2. Radiative Transfer scatter and scatter function (surface wave) across the top of the clutter layer.

3. Absorptive loss of the signal that occurs near the start of the cluttered path as the Radiative Transfer scatter and scatter functions build up to swamp out the absorptive loss.

For a transmitting antenna above the clutter layer, the primary considerations in addition to FSL are:

1. Absorptive loss of the signal that occurs near the start of the cluttered path as the radiative transfer function builds up to swamp out the absorptive loss.

2. Radiative transfer across, through, and under the clutter layer from where the signal path enters the clutter layer, to the receive antenna.

Beer's Law Analysis: To separate out the Beer's Law absorption factor, AB, from the ITU data, we go to the $h_1 = 10$ line, where the entire radio signal path is below the clutter canopy line, and clp , the cluttered path distance = d , the flat earth radio path distance. By definition, d_1 , the portion of d , the path distance, above which the clp is found, is here also equal to clp , and at $h_1 = 10$, below the clutter canopy,

$$clp = d = d_1. \quad (15)$$

$$d_1 = C_{HR} / (\tan \theta_r) \quad (16)$$

On the $h_1 = 10$ curve, at $d=0$, $h_1 - h_2 = 0$; $clp = 0$, and $A_{CR} = AB(clp) = 0$.

On the $h_1 = 10$ curve, at $d=1000$ meters, $clp = 1000$ meters, and $A_{CR} / (clp) \leq AB$

At $h_1 = 10$ (9.375) m., and $d= 1$ km (1000 meters), $A_{CR} = 106.9 - 90 = 16.9$ dB, and

$AB \geq 16.9/1000 = 0.0169$ dB/meter: this value has already been reduced by the effect of Radiative Transfer over the first 1000 meters, so we can only say that the constant $AB > 0.0169$ dB/meter. The loss at 2 km is: $100.88 - 80.25 = 20.63$ dB; less the loss in the first km, the average loss in the second km is only 3.7 dB vs 16.9 dB in the first km; at 4 km, doubling the distance, the loss is $94.86 - 69.5 = 25.36$ dB, a 4.7 dB additional loss in 2 km; and an average of 2.4 dB loss in the 3rd and 4th km; so the Radiative Transfer function, RTE, quickly takes over from direct path propagation as the primary delivery medium of radio frequency field strength at the receive location, even in the first km.

The losses are therefore:

$$A_{CR} = AB(\text{clp}) - RTE \quad (17)$$

And this general equation includes the considerations for the condition of “at or under the clutter path” mentioned above, as the $AB(\text{clp})$ term includes the entry and exit losses from the transmitter to the top of the clutter layer, and from the top of the clutter layer to the receive antenna.

Even at $h_1 = h_2$, there can be some initial clutter absorption loss. Referring to ITU-R P.833-2, Attenuation in Vegetation^[5], Figure 1; note that in this example, the transmitting antenna is the same height as the receive antenna, and $h_1 = h_2$. From the chart, we notice that the moderation of absorptive loss in Radiative Transfer starts at zero at $d = 0$, where the initial clutter absorptive loss is represented by the straight line on the Excess loss vs. d graph. The loss reduction effect of Radiative Transfer increases with distance, causing the absorptive loss line to bend in a logarithmic manner, reducing to a horizontal line as d increases.

For all cases where the transmitting antenna height, h_1 is not equal to the receive antenna height, h_2 , the Radiative Transfer function, RTE, would vary with the distance d_1 , not clp . The distances clp and d_1 are nearly the same at far distance, but near the transmitter, as d , clp and d_1 approach zero, clp approaches the value of C_{HR} as $(\sin \theta_r)$ approaches 1.0; the RTE function approaches 0 as it varies with d_1 , which approaches $d_1 = (C_{HR} / \text{Infinity})$ as the $(\tan \theta_r)$ approaches $\tan (\pi/2)$ radians, or $\tan (90^\circ)$.

Therefore, at $h_1 = 10$:

At 0 km, $A_{CR[1]} = 0$, $\text{clp} = 0$, $d = 0$, and $RTE = 0$

At 1 km, $A_{CR[1]} = 16.9$, $AB > 0.0169$ dB/meter

At 2 km, $A_{CR[1]} = 20.63$

At 4 km, $A_{CR[1]} = 25.36$

At 2 km, without the RTE scatter and scatter function, i.e. where the clutter layer is so deep that the RTE scatter components are minimalized, the attenuation would be at least:

$$A_{CR[2]} = AB(\text{clp}) - RTE > .0169(2,000) - 0 > 33.8 \text{ dB.}$$

So in the second km, surface wave radiative transfer is reducing the attenuation by at least:

$$(33.8 - 20.63) \text{ dB} / 1 \text{ km} > 13.17 \text{ dB/km, and over the next doubling of distance, reducing the attenuation by at least: } A_{CR[4]} = AB(\text{clp}) - RTE > .0169(4,000) - 0 > 67.6 \text{ dB. } (67.6 - 25.36) \text{ dB}/2 \text{ km} > 42.24 \text{ dB}/2 \text{ km} > 21.12 \text{ dB/km.}$$

The rate of reduction of the scatter components, including the surface wave of the radiative transfer function, where both the transmitting antenna and receive antenna are below the clutter layer, triples between 1 to 2 km, and 2 to 4 km, a factor of $42.24/13.17 = 3.21$. Therefore, we can estimate that the rate of reduction of attenuation for the distance between 0 and 1 km is $13.17/3.21 = 4.1 \text{ dB}$, and therefore the attenuation for the Beer’s Law direct ray cluttered path should be at least $16.9 + 16.9/4.1 \text{ dB}$, or $> 22.02 \text{ dB per kilometer}$, giving us a new estimate of: $AB > 22.02/1000$, or $> 0.02202 \text{ dB/meter.}$

Repeating the above process with $AB > .02202 \text{ dB/meter}$, the iteration stabilizes with an $AB = .019526 \text{ dB/meter}$, and at $\text{clp} = 1 \text{ m.}$

$$A_{CR[\text{DeepClutter}]} = 0.01952(\text{clp}) = 0.0195 \text{ dB/m.} \quad (18)$$

Radiative Transfer The Radiative Transfer function, or Engine, (RTE) as defined in the Generic Model^[3], consists of a coherent component, I_{ri} , and an incoherent (diffuse) component I_d . I_d has two subcomponents, I_1 and I_2 . These are:

1. Absorption. This is Beer’s Law clutter absorption. Johnson, Schwering,^[2] refers to this as the “first term”; The Generic Model refers to this as the coherent component I_{ri} .
2. Scattering. The Generic Model refers to the two equations that comprise this component, combined, as the component I_1 . Johnson, Schwering, refers to this as the “second term.” In practice, its effect moderates the absorption loss I_{ri} for a very short distance, mid-path, as graphically displayed in Figure 3-18 of the Generic Model. The approximation combines consideration with I_2 .

3. The Scattering Function. The Generic Model refers to this as the non-coherent component I_2 ; Johnson, Schwering, refers to this as the “third term”. In practice, it quickly takes over from I_1 . The Generic Model uses an exponential term added to a straight-line function to model this component.

Each RTE component controls the loss value during a separate portion of the total path length. To derive the RTE coefficients from the P.1546-2 data, at 2 km, where the clutter layer is so deep that I_d (I_1 and I_2) is insignificant, the attenuation would be at least:

$A_{CR[2]} = AB(\text{clp}) - RTE >.0195 (2,000) - 0 > 39$ dB, and in the second km, I_d is reducing the attenuation by at least: 18.4 dB/km. Over the next doubling of distance, the attenuation is reduced by at least: 78.1 dB. From an analysis of these results a function of form:

$A_{SWRT} = C_{AB} + b*20\log(d_1 + 1)$ dB, d in km, (18) will serve as the form for an initial, interim, combined and simplified RET attenuation (first term) and scatter (second and third term) development equation valid for $d_1 = d \geq 1$ kilometer. At $h_1 = h_2$, C_{AB} should be a constant value, as the RET startup, entry and exit losses should be the same for all $d_1 = \text{clp} = d$. So we should be able to solve for a constant b that will stay approximately the same for all values of h_1 and h_2 when both are below the clutter canopy top, varying only with statistical variation in data, until we reach a point that is level with the top of the clutter layer.

C_{AB} is a function representing the initial absorption attenuation losses, the initial exit loss from the transmitting antenna to the top of the clutter layer, and any final entry loss to the receive antenna. The $b*20\log(d_1 + 1)$ term will represent the I_d loss moderation function for the RET with both terminals below the clutter line, C_H . The 1 is added so that the logarithmic function used, a common logarithm, or base 10 function, will properly solve to zero ($20\log_{10}$ of 1/1 is zero dB) when $d = 0$.

As we increase h_1 to approach the top of the clutter layer, C_{AB} will approach a minimum. This can be used to determine the approximate depth of the average clutter layer in P.1546-2. Solving for the data on each h_1 line starting with 10 meters, and fitting to match the P.1546-2 Figure 1. $h_1 = 10$ line data, and using d in lieu of d_1 , we obtain:

$$A_{SWRT} = C_{AB} + b*20\log(d_1 + 1) \text{ dB} \quad (19)$$

Solving at $h_1 = 10$ meters, $C_{AB} = 6.47$;

At $h_1 = 20$ meters, $C_{AB} = 1.638$, and
At $h_1 = 37.5$ meters, $C_{AB} = -1.966$

The negative value of C_{AB} at 37.5 meters, a nonsensical value, indicates that our calculation failed at 37.5 meters because d_1 no longer equals d; we have reached and exceeded the top of the average combined terrain roughness and absorptive clutter layer in the P.1546-2 data. By iteration, an average clutter canopy top value of $C_H = 25.30$ meters is obtained.

C_{HR} , the portion of C_H above the receive antenna height, h_2 , is then: $C_{HR} = C_H - h_2 = 15.3$ meters.

Determining an equation for C_{AB} : This at first appears to be a Beer’s Law formula, useable only for $h_1 \leq C_H$. The solution must equal zero at $h_1 = C_H$. This attenuation, C_{AB} , now identified as due to Radiative Transfer launch losses, and a part of I_{ri} , will follow the Beer’s Law equation:

$$C_{AB} = AB * \text{clp}_{[RTL]} \quad (20)$$

The distance that the signal must traverse through the clutter from the transmit terminal to the top of the clutter layer, clp , must be determined as;

$$\text{clp}_{[RTL]} = ((C_H - h_1)^2 + (d_{[RTL]})^2)^{1/2} \quad (21)$$

where $d_{[RTL]}$ is the ground level distance traversed by the radiative transfer primary ray rising from the transmitter antenna to the clutter layer canopy.

On attempting an iteration using:

$$C_{AB} = AB * \text{clp}_{[RTL]} \quad (23)$$

$$\text{clp}_{[RTL]} = (C_H - h_1) / \sin \theta_e \quad (24)$$

$$(\sin \theta_{e[h_1=20]}) = 1.91(\sin \theta_{e[h_1=10]})$$

$$AB_{[h_1=10]} = .44(\sin \theta_e)$$

$$AB_{[h_1=20]} = .23(\sin \theta_e)$$

It is found that an exponential parabolic solution should exist for RTE component I_i . Since we are solving for a value of field strength loss, the curves would match the inverse of the exponential *Sum of Contributions* curves in the Generic Model, Figure 3-18, and be a logarithmic function. It has already been found and shown that a single term of this logarithmic function is adequate to approximate the RTE I_d functions at or below the clutter canopy top, where $\text{clp} = d = d_1$. The form it would follow is:

$$A_{RTE} = \text{MIN}(I_{ri}, I_d) = \text{MIN}(I_{ri}, \text{MIN}(I_1, I_2)) \quad (25)$$

$$A_{RTE} = \text{MIN}((AB*(\text{clp})), \text{MIN}((20\log(a_1 d_1 + c_1)), (20\log(a_2 d_1 + c_2)))) \text{ dB} \quad (26)$$

Our model splits the RTE into three competing terms. The first, I_{ri} term is the straight-line function of the absorptive loss line function(s)

following Beer's Law. For the at-or-below canopy computations, it will be split into rising signal clutter absorption loss C_{AB} and Radiative Transfer absorptive launch loss, C_{AB2} . It is reduced by terms two and three, as the amount of the absorptive loss is undermined by the RTE function. It is determined that we can continue to use the single logarithmic equation to adequately approximate the RTE I_d function.

Solving for the RTE terms at or below the clutter canopy line: Using 2 points to solve for the RTE field strength attenuation losses at or below the clutter canopy line ($A_{RTE-ABC}$), in order to obtain the I_{ri} , or first term, absorptive functions, C_{AB} and C_{AB2} , at or below (ABC) the clutter line, using $A_{RTE-ABC} = C_{AB} + 1.34795 * 20 \log(d_1 + 1)$ dB, where $d_1 = d = \text{clp}$, results in:

$$C_{AB} = (C_H - h_1)(2 - 1.56 \exp(C_H - h_1))^{-1} \text{dB/m.} \quad (27)$$

Absorption Loss in the Radiative Transfer Launch Range; the second part of I_{ri} . In addition to the rise function above, a trans-clutter path absorptive loss function does briefly appear at the beginning of the radio path. The equation includes a decay exponent, to reflect the swamping, or bypass increasing with distance, of its effect by the radiative transfer function.

$$C_{AB2} = c e^{bd_1} = (x - a(C_H - h_1)) e^{bd_1} \quad (28)$$

A best fit to the data is then achieved with:

$$A_{RTE-ABC} = C_{AB} + C_{AB2} + 1.348 * 20 \log(d_1 + 1) \text{dB,} \quad (29)$$

where:

$$C_{AB} = (C_H - h_1)(2.06943 - 1.56184 \exp(C_H - h_1))^{-1} \text{dB/m} \quad (30)$$

and:

$$C_{AB2} = (17.98 - .84224(C_H - h_1)) e^{-0.00061(d_1)} \quad (31)$$

where d_1 , C_H and h_1 are in meters.

Which should be used with an "if" statement, as the above equations are valid only for $h_1 \leq C_H$. If $h_1 > C_H$, The equation for C_{AB} disappears, and the equation for C_{AB2} takes a significantly different form.

RTE Above the Clutter Line Several changes occur in the set of propagation phenomena when the transmitter height rises above the clutter layer while the receiver remains below the clutter layer. The logarithmic form of the term I_d of $A_{RET-ABC}$, changes, and would theoretically follow the form of:

$$A_{RETA} = \text{MIN}(AB * \text{crp} / TC, \text{MIN}((c_{11} * AB * \text{crp} + c_1 * \exp(1/d_1)), (c_{11} * AB * \text{crp} + c_1 * \exp(1/d_1)))) \quad (32)$$

In order to match the functional description of the three terms, I_{ri} , I_1 and I_2 , given in the Generic Model, section 3.6.4.

Above the clutter canopy, the radio signal will follow a two-ray path: from the transmitter to the clutter canopy, and through the clutter canopy to the receiver. Due to the effect of Snell's law, these two rays will not form a straight line. AB above the canopy will be multiplied by a function relating to T , the transmission coefficient, varying with the angle of incidence of the direct ray into the clutter canopy, according to the Fresnel equations. The angle of incidence, θ_i , the angle of the actual radio path with respect to the vertical (y) axis, will have to be calculated from Snell's Law, using the refractive indices of the atmosphere and the clutter canopy. The C_{AB} rise absorption function disappears above the canopy. The C_{AB2} function equation changes; as it now represents the radiation transfer effect launch losses from a signal arriving above the clutter canopy.

Absorption above the Clutter Canopy We look primarily to the 1 km data on each h_1 meter curve above the canopy, to determine and verify the equation for C_{ABA} (C_{AB2} above the clutter canopy), as the initial values of these curves represent only Beer's Law absorptive losses. On the $h_1 = 1,200$ m. curve, due to the effect of Snell's Law, it is determined below that the actual radio path traversed will not be long enough for the RTE I_d terms to have effect. In the primarily line-of-sight range, all losses will be Beer's Law absorption losses, i.e. RTE I_{ri} or first term losses. The absorption loss alone follows the function:

$$C_{ABA} = AB * \text{crp} / TC \quad (33)$$

Where T is the relative transmission coefficient of the incoming ray as per Snell's Law; a ratio representing the amount of incoming radio signal that will be transmitted through the clutter layer to the receive point. C will represent any other residual transmissive coefficient, including consideration of clutter orientation and reduction in T due to terrain roughness. The term crp represents the actual cluttered radio path length through the clutter as reduced by the effect of Snell's Law.

There are three considerations associated with this coefficient, related to the ratios of the refractive indices and dielectric coefficients of the two mediums, air and clutter layer.

1. The variation in the actual path of the radio signal, from the direct path between the transmitter and the receiver, caused by the difference between the incident angle of the refracted signal vs. a theoretical direct ray between the transmitter and the receiver. This difference causes the actual path refraction point on the clutter canopy to be farther from the transmitter than the theoretical direct ray, and requires a reduction adjustment in the length of clp (the new value is identified as crp) and d₁. This adjustment reduces the absorptive and radiative transfer losses.
2. The (actual) transmission coefficient, T, is a ratio of the signal arriving at the clutter layer top that is transmitted downward by refraction through the clutter layer to the receive point, relative to the signal arriving from the transmitter. The effect of the application of this coefficient would be to increase the loss.
3. The approach of the reflection coefficient toward 1.0 (and the associated approach of the transmission coefficient to zero) at low grazing angles over rough surfaces, as revealed by Barrick^[1]. At great distances from the transmitter site, or for very low transmit height, this would significantly reduce the reception by direct transmission through the canopy, and theoretically minimizes the direct signal absorptive loss components from the calculation at a significant distance from the transmitter, leaving primarily the surface wave I₂ component of the RTE to transfer energy to the receive site.

To solve for T requires the values of the cosine of the incident (cos θ_i) and transmissive (cos θ_t) angles. To obtain these in a spreadsheet or in computer code, it is first necessary to iteratively solve, using Snell's law, for the values associated with the actual radio signal path.

The Actual Radio Signal Path The center of the path of the radio signal does not follow the theoretical straight-line direct path ray from the transmitter, through the clutter canopy, to the receiver. Instead, by Snell's law, the angle of the refracted ray from the clutter canopy to the receiver, with respect to a vertical line, (which we will refer to as the transmissive angle, θ_t), is related to the incident angle, θ_i, of the actual path line between the transmitter and the clutter canopy with respect to a vertical line, by the Snell's law formula:

$$\sin \theta_i / \sin \theta_t = \eta_{cc} / \eta_s \quad (34)$$

where:

η_{cc} is the refractive index of the clutter at and below the canopy top.

η_s is the refractive index of the atmosphere at the surface of the clutter canopy layer.

The differences this makes in the transmitter take off angle, the receive take off angle, the uncluttered radio path length (urcp) and the cluttered radio path (crp), for what is now a two-ray calculation (here used for refraction, not reflection), can be most efficiently solved on a spreadsheet in a three cycle iteration (or, in code, an iteration repeating until the level of accuracy required is achieved). First, it is necessary to determine the values of θ_i and θ_t; this requires the refractive indices of air and the clutter canopy.

The refractive indices of air, vegetative clutter, and water: The refractive index of air is about 1.000301; of water is about 1.33. Our target area is over land, temperate climate; for P.1546-2, we need to consider foliage and other clutter in the continental Europe and the U.S. For these areas, a range of ε_r used by Tamir^[7] produces a starting value of η_g = 1.015, resulting in:

$$\sin(\theta_i) / \sin(\theta_t) = \eta_{cc} / \eta_s = 1.015 / 1.000301 = 1.0147$$

Later, data-matching iteration shows that the optimal value of η_{cc} for the average clutter canopy in P.1546-2 is:

$$\eta_{cc} = 1.0010 \quad (35)$$

then:

$$\sin(\theta_{ic}) / \sin(\theta_{tc}) = \eta_{cc} / \eta_s = 1.0007.$$

The incident angles are measured with respect to the vertical, or y-axis. It is not necessary to include the additional path length due to refraction. But the effect of the change in ratio of uncluttered path length to cluttered path length is significant.

Geometric calculation of the actual radio signal path parameters:

Step 1: calculate the earth curvature correction angle for the earth radius, θ_{Δc}: θ_{Δc} = d/r (36)

where: d is the total flat-earth radio path length from transmitter to receiver

r is the actual earth radius: 6,378,137 meters.

Step 2: calculate the earth curvature height; hc:

$$hc = (CH + r)(1 - \cos(\theta_{\Delta c})) \quad (37)$$

Step 3: calculate the equivalent curvature flat distance, dx: dx = (CH + r)sin(θ_{Δc}) (38)

Step 4: calculate the un-cluttered radio path w/earth curvature correction; ucrpc:

$$ucrpc = [(h_1 - CH + hc)^2 + (dx)^2]^{1/2} \quad (39)$$

Step 5: calculate the cosine of the flat earth incident angle; $\cos(\theta_i')$:

$$\cos(\theta_i') = (h_1 - CH + hc)/ucrpc \quad (40)$$

Step 6: calculate θ_i' :

$$\theta_i' = \arccos[(h_1 - CH + hc)/ucrpc] \quad (41)$$

Step 7: calculate the total incident angle; θ_{ic} :

$$\theta_{ic} = \theta_i' + \theta_{\Delta\epsilon} \quad (42)$$

Step 8: calculate the sin of the total incident angle;

$$\sin(\theta_{ic}) = \sin(\theta_i' + \theta_{\Delta\epsilon}) \quad (43)$$

Step 9: calculate the sin of the transmission angle,

$$\theta_{tc}: \sin \theta_{tc} = (\eta_a / \eta_g) \sin(\theta_{ic}) \quad (44)$$

Step 10: calculate θ_{tc} : $\theta_{tc} = \arcsin [(\eta_a / \eta_g) \sin(\theta_{ic})]$

Step 11: calculate $\cos \theta_{tc}$:

$$\cos(\theta_{tc}) = [1 - \sin^2(\theta_{tc})]^{1/2} \quad (45)$$

Step 12: calculate the cluttered radio path with earth correction; crpc:

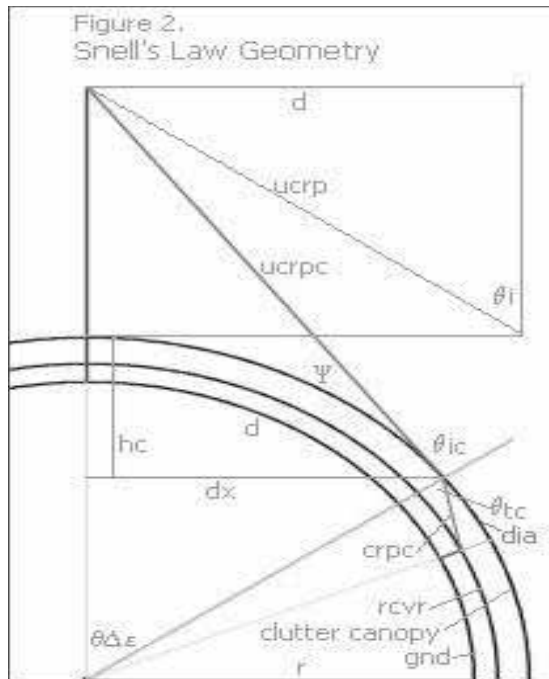
$$crpc = (CH - h_2) / \cos(\theta_{tc}) \quad (46)$$

Step 13: calculate the sin of the grazing angle Ψ ;

$$\sin \Psi = (\pi/2 - \theta_{tc}) \quad (47)$$

Step 14: calculate the clutter canopy surface distance; d_{1a} : $d_{1a} = crpc(\sin(\theta_{tc})) / (1 - 1/r)$ (49)

Step 15: repeat steps 1 to 13 using a new $d' = d$ (actual value) - d_{1a} until the required accuracy is obtained. For spreadsheet calculation, three iterations are adequate.



The Transmission Coefficient The transmission coefficient, T, is defined as: $T = 1 - R$, where R is the Reflection Coefficient. The reflection coefficient, R, calculation is different for horizontal and vertical polarization:

$$R_H = [(\eta_s \cos(\theta_i) - \eta_{cc} \cos(\theta_{tc})) / (\eta_s \cos(\theta_i) + \eta_{cc} \cos(\theta_{tc}))]^2$$

$$R_V = [(\eta_s \cos(\theta_i) - \eta_{cc} \cos(\theta_{tc})) / (\eta_s \cos(\theta_i) + \eta_{cc} \cos(\theta_{tc}))]^2 \quad (50,51)$$

The P.1546-2 curves are not separated by polarity, so are treated as circularly polarized, by averaging the horizontal polarity and vertical polarity results:

$$R = 0.5R_H - 0.5R_V; \quad T = 1 - R \quad (52 a,b)$$

For an air to clutter canopy interface, for most practical purposes, $R = .001$, $T = .999$ at the transmitter site, gradually reversing to $R=.999$, $T=.001$ at the horizon. Snell's law therefore contributes to the effects documented by Barrick at low grazing angles.^[2] The consideration of T, and the significant change in the length of the cluttered radio path, crp, versus the temporarily considered direct path, clp, is accommodated by modifying our Beer's Law equation for the RTE I_{ri} term:

$$C_{ABA} = AB * crpc / TC \quad (53)$$

The direct "cluttered path", clp versus the actual "cluttered radio path", crpc: The length of the cluttered radio path, due to the Snell's angle change at the clutter canopy, is significantly less than the direct ray path from the transmitter to the receiver. As θ_{ic} approaches 1.57 radians, i.e. the transmitter to clutter entry point ray approaches the horizontal, θ_{tc} stabilizes near 1.4004 radians for an air to clutter interface. At $d = 80$ km, with $h_1 = 1,200$ m., the portion of the direct ray that would pass through the clutter layer, clp, would be 1,029 meters; but due to angle of the refracted transmission ray, the actual radio path, crpc, has stabilized near 89.9 meters, and will not exceed 90.25 meters at $d = 1,000$ km.

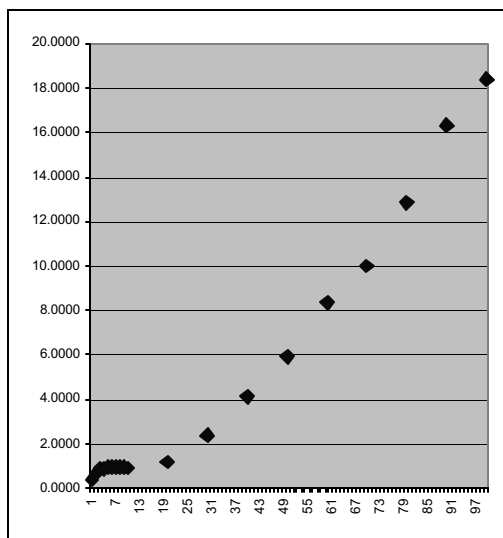
Absorption Losses above the Clutter Line We have previously derived an estimate from the P.1546-2 data, for AB in clutter deep enough that radiative transfer does not function, of 0.0195 dB/meter. Using this above the clutter line and adding consideration of the Snell's Law transmissivity, T, to accommodate the "clutter canopy signal splitter" represented by the reflected energy versus the transmitted (into the clutter) energy at the air to canopy top interface. T will vary with the incidence angle of the radio signal.

As a result of the significant shortening of the cluttered radio path by the effect of Snell's Law, the losses on the $h_1 = 1,200$ m. line of P.1546-2 out to 3 km are all Beer's Law absorption losses, a.k.a. RTE I_{ri} term losses; as the actual length of the canopy top traversed, (d_{1a}), due to the action of Snell's Law, is only 15 to 50 meters; not long

enough for the RTE I_d term phenomena to overtake the I_{ri} losses. Study of the curves resulting from plotting the non-FSL losses vs. distance indicate that the Beer's Law absorption losses apply for up to the first 50 meters of clutter canopy path length; from 50 meters to 225 meters, a second set of I_d effects provide the lowest losses; and from 225 meters onward, a third set of loss phenomenon are the controlling function. This can clearly be seen on the following $h_1 = 1200$ chart, Figure 1, where the initial, climbing I_{ri} loss line gives way to a relatively flat I_d line, which then transitions to a climbing flat curve.

The three distinct sections to the curve suggests the I_{ri} , I_1 , and I_2 Radiative Transfer functions; but the Generic Model indicates that the length of path distance that the I_1 function controls is short compared to the I_{ri} function, less than 15 meters in canopy top (d_{1a}) distance. The relatively flat area in the above chart from $d = 3$ km to $d = 20$ km is the I_d functions, and the rising curve past 300 meters of d_{1a} distance (20 km in the $h_1 = 1200$ m. chart) represents a third set of Snell's Law-related RTE phenomenon, here referred to as I_3 where at a distance, absorption of the scatter and cancellation with Snell's path main signal becomes a factor to the point that up to $\Psi \leq 0$, a Beer's Law absorption calculation using $AB = 0.0195 \text{ dB/m} * d_{1a}$ provides only slightly higher results. The I_3 mode continues past the horizon, functioning on side scatter up to $\Psi = -0.01$ rad, (0.5 deg.), where the propagation transitions to a post-horizon diffraction mode.

Figure 1; Non-FSL losses in dB vs. d in km., for $h_1 = 1200$ meters:



Approximation equations for the RTE I_{ri} functions:

The attenuation for the initial path distance above the canopy, out to 50 meters, are from RTE I_{ri} function, and take the form of the cluttered radio path corrected for earth curvature, crpc, multiplied by AB, the Beer's Law absorptive loss constant for average clutter, 0.0195 dB/meter, added to the transmissive loss, $A_T = -20\log(T)$.

$$I_{ri} = crpc * AB - A_T = 0.0195 * crpc - 20\log(T) \quad (54)$$

Approximation equations for the RTE I_d (I_1 and I_2) functions:

Two equations were derived to match the I_d data in P.1546-2; both apply to situations where the transmitter is above the canopy top, and the canopy top distance (d_{1a}) exceeds 250 meters. The first derives only from the $h_1 = 1,200$ meter line, and are arbitrarily assumed to apply only to $h_1 > 1,000$ m:

The entire function relates to the canopy top distance, d_{1a} ; and is a Beer's Law distance times loss/distance formula, with the absorption and dispersion loss term containing a total path distance-related term. The I_d , or combined I_1 & I_2 function approximation for $f = 100$ MHz, with h_1 at or above 1,000 m. is:

$$I_{1,2[h_1 > 1000m]} = d_{1a} [0.03 \exp^{-1.4d}] \quad (55)$$

The $h_1 = 1,200$ line is missing the vertical path length extension loss at locations near the transmitter site. The fact that the approximation equations for the RTE I_d function at the $h_1 = 1,200$ line do not match those for all other lines above the clutter line, is additional evidence that the data source and computation of the $h_1 = 1,200$ line may be eligible for review. For $f = 100$ MHz, and h_1 between 1,000 meters and the canopy top, the I_d equation changes to:

$$I_{1,2[h_1 > 1000m]} = d_{1a} [0.07 \exp^{-1.7d}] \quad (56)$$

The RTE I_3 function: The I_3 function applies for d_{1a} distances greater than 225 meters up to the past-horizon point where diffraction loss is less, or up to a major path obstruction. The entire function relates to the canopy top distance, d_{1a} ; which forms the primary distance component of a Beer's Law construct, with the absorption and dispersion loss terms containing two path distance-driven terms, and an effective transmitter height term. The last term provides consideration of an R-related reduction in RF level exciting the RTE canopy-top scatter wave for the first few km. from the

transmitter site, when low transmitter heights combine with high incident angles atop the canopy.

The I_3 approximation for $f = 100$ MHz, with h_1 above the clutter canopy and h_2 below the canopy, has been discerned by staged subtraction and regression to be:

$$I_3 = d_{1a} [0.00055d + \log(d)(0.041 - 0.0017(h_1)^{1/2} + 0.019) - 9(20\log(R)/\exp(h_1/37.5)) \quad (57)$$

where d is in km, and d_{1a} is in meters.

At and beyond the horizon: diffraction: Analysis of P.1546-2 Figure 1, produces the following approximation for diffraction losses beyond the horizon transition point, consisting of the combination of a distance term, $0.0665d + 48.35$, and a relative transmitter height term:

$$A_{\text{DIFF}[100\text{MHz}]} = 0.0665d + 48.35 - 356(h_1 - h_2)^{1/2} \quad (58)$$

The results of this equation apply where the value produced is less than the RTE I_3 term, or in all cases beyond the horizon, defined as where the combination incident angle above the clutter canopy, θ_{ic} , is greater than 1.59 radians.

Frequency Compensation Up to this point, we have derived only from Figure 1, with a frequency = 100 MHz. We now turn to an analysis of the change in the functions with frequency, derived from the $f = 600$ MHz and $f = 2,000$ MHz over-land figures.

Frequency Compensation beyond the horizon: From basic knife-edge diffraction theory, we expect: $A_{\text{freq}} = 20\log[(1/\lambda)^{1/2}]$, where λ the wavelength of the frequency, is equal to c/f , c is the speed of light in km/sec and f is the frequency in MHz. Carrying the square root across the logarithmic function, and substituting a constant, a , for the equivalent of $10\log(c)$, we obtain:

$$A_{\text{DIFF Frequency Comp.}} = 10\log(f_{\text{MHz}}) + a \quad (59)$$

Incorporating this frequency compensation into the earlier 100 MHz diffraction equation results in a complete diffraction approximation:

$$A_{\text{DIFF}} = 0.072d - 0.45(h_1)^{1/2} + 10\log(f_{\text{MHz}}) + 27 \quad (60)$$

Frequency Compensation for RTE I_3 Function:

For I_3 , the frequency compensation required swings from slightly negative to positive with distance, with an intercept point controlled by the transmitter height above clutter canopy top. Two equations describe the compensation: a negative compensation term applies prior to the zero

intercept point, and a positive compensation term applies after the zero intercept. The frequency compensation equations to be added to the result of the RTE I_3 computation each consists of a frequency and transmitter-height-controlled gain term multiplied by a distance term based on the distance from the zero intercept:

$$\text{Zero intercept} = 1.5(h_1 - \text{CH})^{1/2} \text{ meters} \quad (61)$$

If $d > 1.5(h_1 - \text{CH})^{1/2}$, FCI_{3B} applies; if not, FCI_{3A} applies. (62a)

$$\text{FCI}_{3A} = [-20((\log(f_{\text{MHz}}) - 2)/(h_1)^{1/2})] * [(1.5(h_1 - \text{CH})^{1/2} - d_{[\text{km}]})/1.5(h_1 - \text{CH})^{1/2}] \quad (62b)$$

$$\text{FCI}_{3B} = [10.2((\log(f_{\text{MHz}}) - 2)/(100 - 1.5(h_1 - \text{CH})^{1/2}))] * [d_{[\text{km}]} - 1.5(h_1 - \text{CH})^{1/2}] \quad (62c)$$

Frequency Compensation for RTE I_d (I_1 and I_2):

For the RTE I_d function (I_1 and I_2), the height and frequency compensation approximation equation term to add to the result of the RTE computations solves to be:

$$A_{\text{RTEfc}} = -((\log(f_{\text{MHz}}) - 2) * (h_2/h_1)) \quad (63)$$

Frequency Compensation for the Beer's Law – RTE I_{ri} component No frequency compensation is included for the direct absorption I_{ri} losses.

Sum Approximation Equation for Attenuation Above Clutter Canopy: The full form of the sum equation for Attenuation above clutter is:

$$A_{\text{RET-AC}} = A_{\text{RTE}(I_{ri}, I_d \text{ or } I_3)} + \text{FC}_{\text{RTE}(I_{ri}, I_d \text{ or } I_3)} \quad (64)$$

Transition points above the clutter canopy:

If the under-canopy top ground distance d_{1a} is less than or equal to 50 meters, then the I_{ri} mode results are used. The I_d mode results apply from 50 to 225 meters. If the under-canopy top ground distance d_{1a} is greater than 225 meters, and if the combined incident angle θ_{ic} is equal to or less than 1.5775 radians, then the I_3 mode results are used. If the under-canopy top ground distance d_a is greater than 275 meters, and if the combined incident angle θ_{ic} is greater than 1.5775 radians, but less than 1.59 radians, then the signal is in a transition at the horizon between I_3 and diffraction mode, and the lesser of these two attenuations is used. If the combined incident angle θ_{ic} is greater than 1.59 radians, diffraction results apply.

Transition points below the canopy top level:

When the transmitter is at or below the canopy top

level, the cluttered radio path distance is equal to the path distance d . The results of the equations given for the I_r and I_d functions are to be added together. If the path distance d is less than or equal to 6 km., the combined RTE I_r and I_d function results control the resultant attenuation. If the path distance d is greater than 6 km., and if the combined incident angle θ_{ic} is equal to or less than 1.595 radians, then the lesser of the RTE combined or diffraction mode results apply, and reveal the horizon transition point. If the path distance d is past 6 km., and if θ_{ic} is greater than 1.595 radians, then the path is beyond the horizon; diffraction mode results apply.

Combining the Results for the Deterministic Approximations Solution: The last step is to add any optional Two-Ray multipath attenuation, A_{2R} , and the Free Space Loss (or Dispersion), to the non-free-space attenuation computed above, with frequency compensation included, to obtain the total predicted attenuation:

$$A_{TOT} = A_{RTE-AC \text{ OR } RTE-BC \text{ OR } A_{DIFF}} + A_{2R} + FS \quad (65)$$

For a P.1456-2 land path, A_{2R} , the multipath attenuation, = 0. The equation then becomes:

$$A_{TOT} = A_{(RTE \text{ or } DIFF)[+FC]} + FSL. \quad (66)$$

The additional considerations given in P.1546-2 for special cases may then be applied to the attenuation results, and to determine field strength for a transmitted power of 1 kilowatt ERP:

$$E = 106.9 - A_{TOT} \quad (67)$$

Summary: The above deterministic and deterministic-based approximation equations, when implemented using the described methodology as a computational engine on a computer spreadsheet or in a computer program, adequately duplicate for general use, the results obtained from ITU-P.1546-2 for over-land paths, requiring only the input of four variables: the frequency, the transmitter height, the total path distance, and the receiver height. Besides providing a useful, practical tool; it is a proof of concept for the unified Beer's Law-based foundation and Snell's Law geometrical framework embodied within. The deterministic nature of the work allows extension to circumstances beyond the parameters of P.1546-2. This unified framework, as used here to assemble and analyze the various puzzle pieces of radio propagation theory, can also provide a foundation and framework for further study.

References:

1. "Grazing Behavior of Scatter and Propagation Above Any Rough Surface" by Donald Barrick. IEEE Transactions On Antennas and Propagation, Jan.1998.
2. "A Transport Theory of Millimeter Wave Propagation in Woods and Forests", by R. A. Johnson and F. Schwing, Center for Communications Systems. Research and Development Technical Report CECOM-TR-85-1, U. S. Army Communications-Electronics Command, February 1985.
3. "A Generic Model of 1-60 GHz Radio Propagation through Vegetation – Final Report" by N.C. Rogers, A Seville, J Richter, D Ndzi, N. Savage, RFS Caldeirinha, A.K. Shukla, M.O. Al-Nuaimi, K. Craig, E. Vilar and J. Austin. Prepared by Dr. Neil Rogers, Principal Investigator, QinetiQ, for a consortium comprised of QinetiQ, the Rutherford Appleton Laboratory, and the Universities of Portsmouth and Glamorgan, for the U. K. Radiocommunications Agency. First Issue, May 2002.
4. "Transmission Loss Predictions for Tropospheric Communications Circuits", Volume I, National Bureau of Standards Technical Note 101, Revised January, 1967, by P.L. Rice, A. G. Longley, K.A. Norton, and A.P. Barsis, Institute for Telecommunications Sciences and Astronomy, U. S. Dept. of Commerce National Telecommunications and Information Administration.
5. ITU Recommendations P.453-07, 1999; P.530-7, 1997; P.833-2, 1999; and P.1546-2, 2005.
6. "Prediction of Tropospheric Radio Transmission Loss Over Irregular Terrain, A Computer Method – 1968" ESSA Technical Report ERL 79 – ITS 67, by A. G. Longley and P.L. Rice, Institute for Telecommunications Sciences, U. S. Dept. of Commerce National Telecommunications and Information Administration.
7. "Radiowave Propagation along Mixed Path in Forest Environment", IEEE Transactions on Antennas and Propagation, T. Tamir, Vol.25, No.4, Nov. 1977.

Revised January 25, 2008.

Copyright © January 2008 by Sid Shumate and Givens and Bell, Inc. All rights reserved except that permission is granted for open publication with full content unmodified, by the National Institute of Standards and Technology, Dept. of Commerce, USA, as per the terms and conditions for presentation before the 10th International Symposium on Advanced Radio Technologies, 2-4 June 2008, in Boulder, Colorado.

A Simplified Analytical Urban Propagation Model (UPM)

Chrysanthos Chrysanthou
Space and Terrestrial Communications Directorate
Communications-Electronics Research Development and Engineering Center, Fort Monmouth, NJ 07703
Phone: (732) 427-6156
Fax: (732) 427-2150
E-mail: c.chrysanthou@us.army.mil

Dr. James K. Breakall
Department of Electrical Engineering
Pennsylvania State University, University Park, PA 16802
Phone: (814) 865-2228
E-mail: jimb@psu.edu

Kyle L. Labowski
Department of Electrical Engineering
Pennsylvania State University, University Park, PA 16802
E-mail: kll173@psu.edu

Abstract: RF propagation models such as TIREM and Hata used in spectrum management tools do not consider the impact of urban environments such as buildings and roads for the prediction of the propagation loss. Under the development of the Coalition Joint Spectrum Management Planning Tool (CJSMPT), US Army Communications Electronics Research Development and Engineering Center (CERDEC) took the initiative for quantifying the existing urban propagation models, both empirical and analytical, and developing a simplified urban propagation model for use in CJSMPT. The emphasis on this model was to have a minimal time and computational complexity and use data that represents the actual urban environment. The traditional empirical models developed from a set of measurements conducted in metropolitan cities between the base and mobile stations do not provide the expected accuracy since they do not consider the characteristics of the areas of interest. In addition, these empirical models do not address the propagation scenario from mobile to mobile stations. The analytical models determine the path loss as result of field reduction due to free space, multiple diffraction over passed building rows, and diffraction of the rooftop to a mobile station. However, these analytical models involve substantial amount of complexity due to the calculations of diffraction associated with multiple rows of buildings. To meet the needs for fast assessment of interference and de-confliction analysis in CJSMPT, a simplified analytical model was developed for addressing different propagation scenarios when the base station antenna is above, below and near the average rooftop level. This simplified analytical model uses as input parameters, data which is extracted from the Urban Technical Planner (UTP) developed by the US Army Topographic Engineering Center (TEC). The UTP data provides data of key aspects of the urban environment, including buildings, roads, water bodies, and vertical obstructions. The model uses the average input parameters calculated along a propagation path. This model may not be suitable for use in urban areas where only a few blocks of buildings are between both ends of the link. In this micro-cell scenario, other propagation processes such as reflections and diffractions on the side of the buildings need to be considered.

1 Introduction

The CJSMPT is a spectrum planning tool that will utilize RF propagation models for

performing automated interference and de-confliction analysis for on-the-move (OTM) military communications networks. Currently, RF propagation models such as Irregular Terrain Model (ITM) [1] and Terrain Integrated Rough

Earth Model (TIREM) [2] are utilized by most spectrum management tools. Although ITM and TIREM both account for the effects of the irregular terrain, these propagation models are not optimal for all the anticipated environments such as the urban and suburban areas in which the OTM wireless networks are expected to operate. Empirical and analytical models currently exist in public that address RF propagation in urban and suburban environments [3-6]. These models are primarily developed for predicting path loss for cellular mobile radio services. The Okumura, Okumura-Hata, and COST231-Hata are empirical models developed based on measurements in and around Tokyo, Japan. Bertoni and Walfisch-Ikegami models are analytical models that predict the path loss as result of field reduction due to free space, multiple diffraction over passed building rows, and diffraction of the last rooftop to a mobile station. The analytical models require as input parameters characteristics of the urban and suburban environments. The main parameters of interest for the urban and suburban environments are the height, size and shape of the buildings, the number of the buildings along the path, and the open space between buildings.

A simplified urban propagation model (UPM) was needed to meet the needs for fast assessment of interference and de-confliction analysis in CJSMP that would both minimize the computational time and complexity and use data that represents the actual urban environment including suburbs. In addition, this propagation model needed to address the mobile-to-mobile scenario, a use case for the OTM wireless networks. To develop the UPM model, an evaluation of the existing propagation models was performed to quantify and identify the strengths and deficiencies of each model as described in Section 2. From this evaluation, the UPM was derived as described in Section 3. In addition, the input parameters for the UPM that characterize the urban and suburban environments were extracted from the US Army TEC UTP as described in Section 4.

2 Comparison of Urban Propagation Models

There are two fundamental kinds of urban propagation models: empirical and analytical. Empirical models use actual measurements taken in a city of interest. The model then takes best fit lines to the data and produces an empirical formula. Analytical models, on the other hand, are based on electromagnetic principles tailored to the characteristics of a given propagation environment, i.e., urban environment. For urban environments, the main parameters of interest are generally the size and shape of the buildings, including the roofs, the number of buildings in the path, and the amount of open space along the path of interest.

The Okumura-Hata model is one of the most widely used urban propagation models [6]. It is based upon the data taken by Okumura in the city of Tokyo, Japan. Since it is empirically based, in order to use the model in a new city that is not like Tokyo, measurements are needed so that correction factors can be introduced into the model. The inputs are: height of transmitter and receiver antennas, frequency, distance between antennas, and the size of the city. The size of the city term is not well defined. It can either be a large city or a small/medium city, but what constitutes a large or a small/medium city is not rigorously defined.

The Walfisch-Ikegami (WI) and Bertoni models are both analytical models [3, 4]. The general form of these models is based on three propagation processes: free space path loss, reduction due to multiple diffractions of passed rows of buildings, and diffraction from the rooftop fields to ground level. The inputs to the WI model are: height of the transmitter and receiver antennas, average height of the buildings, average building separation, average street width, frequency, distance between antennas, and the angle of the propagation path with respect to the street [4]. The Bertoni model has inputs similar to the WI model, as described in Section 3 [3].

The main advantage of the analytical models is that the input can be customized so that the loss

prediction is relevant to the city of interest. In addition, the analytical models are more easily adaptable to new environments and scenarios than the empirical models. Therefore, our further analysis concentrates on a comparison of the WI and Bertoni analytical models.

The Bertoni and WI models provide similar results for the losses related to free space and diffraction of the rooftop fields to the ground level. The treatment of losses due to the field diffraction over the passed rows of buildings is the biggest difference between the two models. Bertoni's model is primarily constructed considering the position of the transmitter antenna relative to the average rooftop level: above, below and near the rooftop level as described in Section 3 [3]. In addition to the position of the transmitter antenna relative to the rooftop, above or below, the WI model also considers the type of the environment, city center or suburban [4].

The WI model has a lot of constraints for its application while Bertoni model does not have any such constraints. Important constraints for WI model are the frequency range, only from 800 to 2000 MHz, and the transmitter antenna height, only from 4 to 50 m. The limitation of the frequency range will prohibit the use of this model for military communications systems that operate in lower frequency ranges. Also, the limitation of the transmitter antenna height indicates that this model can not be used for mobile-to-mobile application, and that is one of the primary purposes for the development of the UPM model.

To better understand the differences between the two models regarding losses due to field diffraction over the passed rows of buildings, the comparison is split into three groups; for transmitter antennas located above, below and near the average rooftop level. When the transmitter antenna height is above the average rooftop level, Bertoni and WI models yield similar results as shown in Figure 1.

When the transmitter antenna height is below the average rooftop level, the results from the two models differ and are not easily comparable as

shown in Figure 2. However, WI model as discussed above has a limitation on the minimum transmitter antenna height (i.e., above 4 m).

When the transmitter antenna height is near the average rooftop level, the results from the two models are similar as shown in Figure 3.

Figure 9 also provides a comparison between the results generated by the Bertoni and WI models when contrasting the position of the transmitter antenna height relative to the rooftop level.

The three separate calculations for transmission loss based upon the height of the transmitter antenna relative to the average rooftop level allow a more precise prediction of the losses in the Bertoni model over the Walfisch-Ikegami model. This is especially valuable for the mobile-to-mobile scenario which is a scenario of special interest for the UPM model.

The Bertoni model is validated in [3, 7, and 8] for base stations elevated above the average rooftop level (see model in Section 3.2.1). However, the analytical models in Sections III-B-2 and III-B-3 used to predict the path loss for transmitter antennas below the average rooftop level are not well validated against actual measurements.

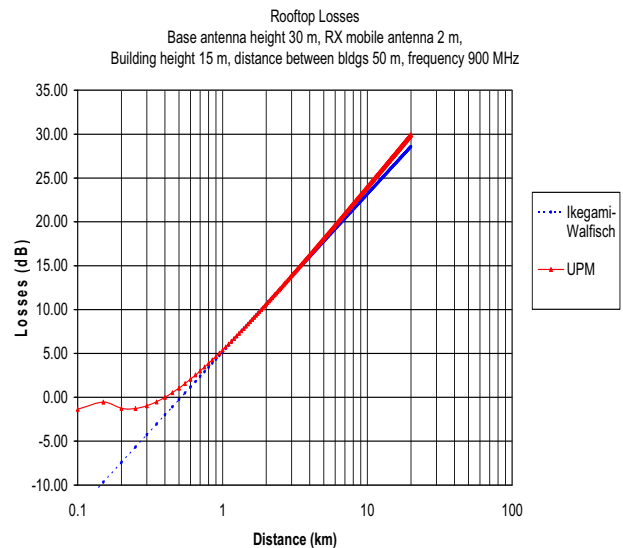


Figure 1. Rooftop losses for antennas above the average rooftop level

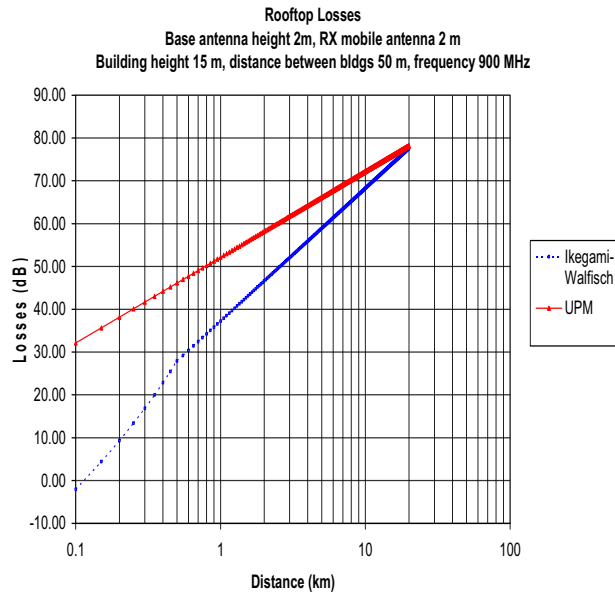


Figure 2. Rooftop losses for antennas below the average rooftop level

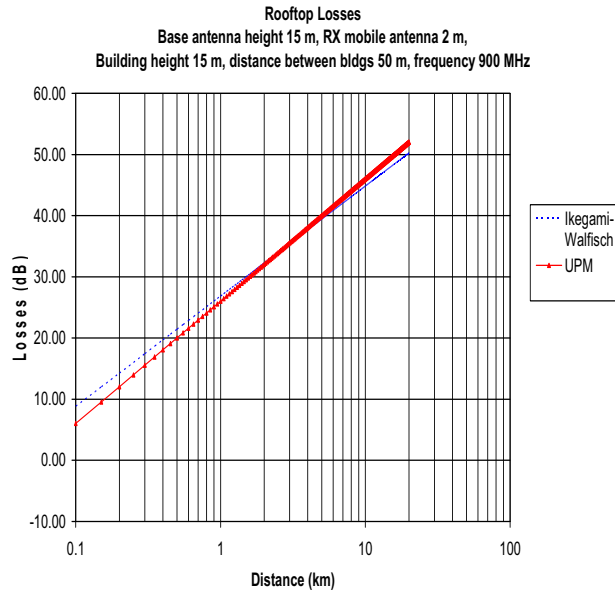


Figure 3. Rooftop losses for antennas near the average rooftop level

3 Description of UPM

Characteristics of urban and suburban environments such as buildings and roads significantly impact the RF propagation. An analytical model was developed at Polytechnic University that identifies the three most important components of the propagation

process in urban and suburban environments: (1) free space, (2) multiple diffraction due to passed rows of buildings, and (3) diffraction from the rooftop fields down to ground level [3, 7].

The free space process can be represented by a simple formula. The mechanism for representing the third propagation process relies on a calculation based on the geometrical theory of diffraction (GTD), since the OTM wireless networks will be generally in the shadow region of diffraction, where cylindrical waves are radiated from the rooftop edges of buildings adjacent to the OTM wireless network. The multiple diffraction process, the second propagation process, is computed using a physical optics approach [3]. However, this process, in its original format, is very complicated, computationally intensive, and does not meet the requirements for a fast assessment of interference and de-confliction analysis in CJSMP. Therefore, a simplified multiple diffraction process has been developed that considers three different regions with the transmitting (base) antenna above, below, and near the average rooftop level (i.e., building height) [8].

The total path loss L in dB can be expressed as the summation of the three propagation process as discussed above.

$$L = L_{fs} + L_{msd} + L_{rts} \quad (1)$$

Where L_{fs} is the free-space loss, L_{msd} is the reduction due to multiple diffractions of past rows of buildings, and L_{rts} is the reduction due to the diffraction from the rooftop fields to the ground level.

Figure 4 shows some of the input parameters required for the UPM model. Such parameters as building height (h_B), building separation (b), and road width (w) are characteristics of the urban and suburban environments. The average values of these parameters will be used as input for the UPM as described in the next section. Δh_B is the height difference between the transmitter antenna and the average building height. The frequency (f), transmitter (h_{bs}) and receiver

antenna heights (h_m), and distance between antennas (d) are network specific parameters.

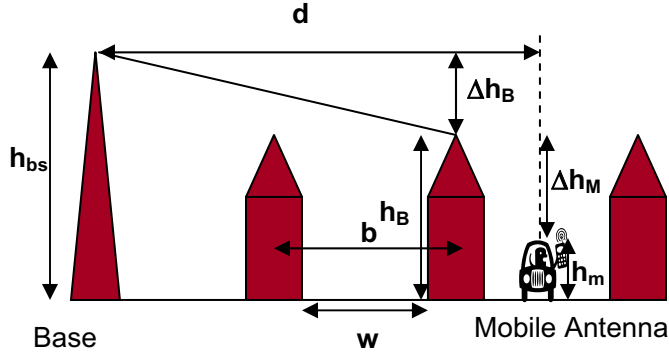


Figure 4. Input Parameters for UPM model

3.1 Free Space loss

The free space path loss is given by:

$$L_{fs} = 3243 + 20\log(d/km) + 20\log(f/MHz) \quad (2)$$

3.2 Reduction due to Multiple Diffractions of Passed Rows of Buildings

The losses from the multiple diffractions of passed rows of buildings is segmented into three different propagation scenarios considering the first Fresnel zone about the ray from the transmitter antenna to the last rooftop before the mobile antenna. These three propagation scenarios are

- Antennas located above the average rooftop level and the first rooftop level is lying outside the Fresnel zone.
- Antennas located near the average rooftop level and the first rooftop level is lying within the Fresnel zone.
- Antennas located below the average rooftop level and the Fresnel zone is completely blocked by the first building.

The dimensionless factor g_c given by $\frac{\Delta h_B}{\sqrt{b\lambda}}$ is

used to determine whether the first rooftop level lies, within or outside, or blocks the first Fresnel zone about the ray from the transmitter antenna to the edge of the last rooftop; Δh_B is approximately the vertical distance from the first rooftop to the ray, and $\sqrt{b\lambda}$ is the width of the first Fresnel zone at the first building.

3.2.1 Transmitter Antennas above the Average Rooftop Level

When g_c is greater than 1 ($g_c > 1$), the transmitter antenna is above the average rooftop level [3]. The first rooftop level lies outside the first Fresnel zone and plane waves are used for calculating the losses due to multiple diffractions of passed rows of buildings. Since the first rooftop lies outside the Fresnel zone, its associated effect on losses is negligible as shown in Figure 1. The losses are given by [3]

$$L_{msd} = -20\log(Q(g_p)) \quad (3)$$

where the field reduction factor is given by

$$Q(g_p) = 3.502g_p - 3.327g_p^2 + 0.962g_p^3$$

and

$$g_p \approx \frac{\Delta h_B}{d} \sqrt{\frac{b}{\lambda}}$$

3.2.2 Transmitter Antennas near the Average Rooftop Level

When $|g_c| \leq 1$, the transmitter antenna is near the average rooftop level. The first rooftop level lies within the first Fresnel zone and cylindrical waves are used for calculating the losses due to multiple diffractions of passed rows of buildings. Since the first rooftop lies within the Fresnel zone, its associated effect on losses is significant as shown in Figure 3. The losses are given by [3]

$$L_{msd} = -20\log(Q_M(g_c)) \quad (4)$$

The field reduction factor is expressed in terms of Borsma's functions and is given by

$$Q_M(g_c) = \sqrt{M} \left| \sum_{q=0}^{\infty} \frac{1}{q!} (2\sqrt{j\pi} g_c)^q I_{M-1,q}(2) \right|$$

where M is the number of the buildings. Borsma's function, $I_{M-1,q}(2)$, satisfies the recursive equation

$$I_{M-1,q}(2) = \frac{(M-1)(q-1)}{2M} I_{M-1,q-2}(2) + \frac{1}{2\sqrt{\pi M}} \sum_{n=1}^{M-2} \frac{I_{n,q-1}(2)}{\sqrt{(M-1-n)}}$$

With initial terms

$$I_{M-1,0}(2) = \frac{1}{M^{3/2}}$$

$$I_{M-1,1}(2) = \frac{1}{4\pi} \sum_{n=1}^{M-1} \frac{1}{n^{3/2}(M-n)^{3/2}}$$

When the transmitter antenna is located at the rooftop, the g_c is zero and the field reduction factor, Q_M , is reduced to a simple formula given by

$$Q_M = \frac{b}{d} \quad (5)$$

3.2.3 Transmitter Antennas below the Average Rooftop Level

When $|g_c| > 1$, the transmitter antenna is well below the average rooftop level. The first building completely blocks rooftop the first Fresnel zone, and cylindrical diffraction processes are used for calculating the losses. Since the first building blocks the Fresnel zone, its associated effect on losses is substantial as shown in Figure 2.

Figure 5 shows the mobile-to-mobile scenario that is very important for the analysis of OTM networks in CJSMP.

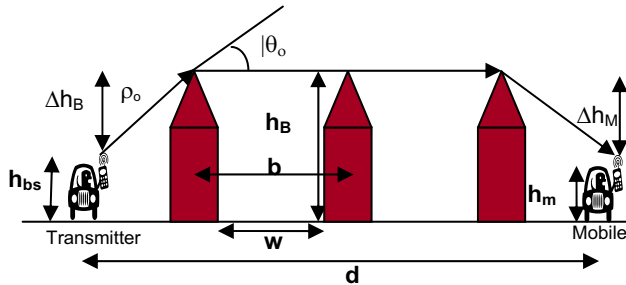


Figure 5. Parameters for mobile-to-mobile scenario

The cylindrical diffraction processes for computing the effective value of field reduction factor (Q_e) can be represented by an incident

cylindrical wave that is the same as that of a line source at the level of the rooftop and the GTD from the rooftop to ground level. The incident cylindrical wave is given in equation (5) and the GTD is given in equation (8). Thus, the effective value of the field reduction factor at the rooftop is given by

$$Q_e^2 = \frac{1}{\rho_o} |D(\theta_o)|^2 \left(\frac{b}{d-b} \right)^2$$

The losses are given by [3]

$$L_{msdr} = -10 \log(Q_e^2) \quad (6)$$

3.2.4 Modeling of Field Reduction Factors in UPM

The relationships between the different expressions of the field reduction factors are demonstrated in Figure 6 for 900 MHz, building height 15 m, distance between buildings 50 m, and distance 5 km. The dashed lines in the figure indicate the boundaries of the first Fresnel zone ($2\sqrt{\lambda b}$ distance between boundaries) at the rooftop level. The Q_e factor for low transmitter antenna is close to the $Q_M(g_c)$ factor for antennas below the rooftop level. However, as the antenna is raised to the rooftop level, $|g_c|$ decreases and the Q_e diverges from $Q_M(g_c)$. Similarly, the $Q_M(g_c)$ diverges from $Q(g_p)$ for antennas above the rooftop when g_c is less than 1 and $Q_M(g_c)$ merges into $Q(g_p)$ when g_c is greater than 1. Using g_c as the factor for selecting the appropriate field reduction factor leads to a smooth transition between the predicted losses as indicated in the UPM model in Figure 9. Therefore, the boundaries of the first Fresnel zone provides a good approximation to transition from the complex formula of $Q_M(g_c)$ to the simplified formulas of Q_e and $Q(g_p)$. The use of the second Fresnel zone for transition, at approximately -8 m and 8m in Figure 6, will provide more accurate results but the difference is not significant enough, when compared to Q_e and $Q(g_p)$, to merit the calculation of $Q_M(g_c)$ for a wider zone near the average rooftop level.

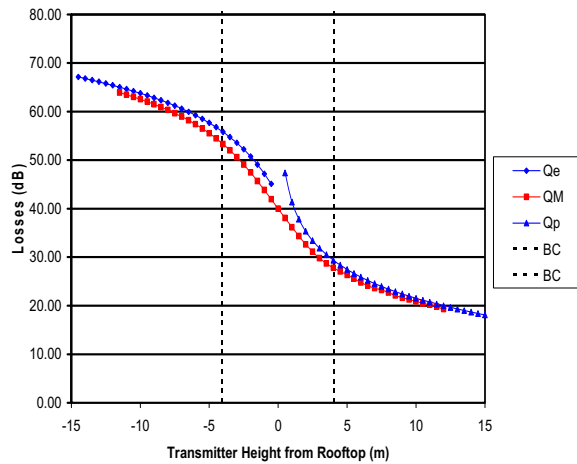


Figure 6. Modeling of Field Reduction Factors in UPM

3.2.5 Analysis of Field Reduction Factors

Figure 7 compares the expected multiple diffraction losses at different antenna heights versus distance for 900 MHz, building height 15 m, and distance between buildings 50 m. The corresponding values of g_c are -3.18, 0, and 3.67 for antenna heights of 2, 15, and 30m (i.e., below, near, and above the rooftop level respectively). The figure indicates that the effect on the losses due to the first building is negligible when the antenna is above the rooftop and is outside the Fresnel zone. However, the losses due to the first building become more substantial when the antenna comes near or below the rooftop, which is now lying inside the Fresnel zone. The losses for distances greater than 1km are about 18dB/decade for the antenna above the rooftop. The losses for the antennas near and below the rooftop are 20dB/decade.

Figure 8 compares the expected multiple diffraction losses at different antenna heights (i.e., above, near and below the rooftop) versus frequency for building height 15 m, distance between buildings 50 m, and distance 5 km. Again, the figure indicates that the losses due to the first building become substantial when the antenna comes near or below the rooftop. The variation in losses is reduced as the frequency increases.

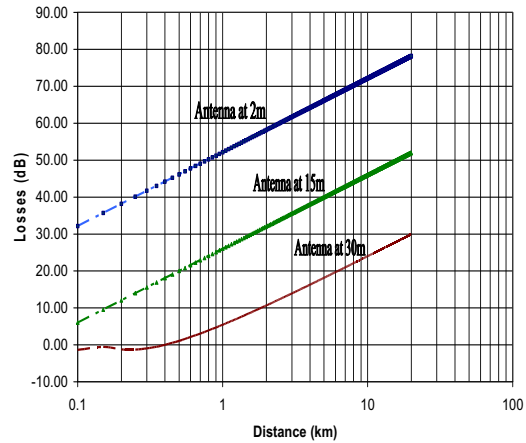


Figure 7. Comparison of multiple diffraction losses versus distance

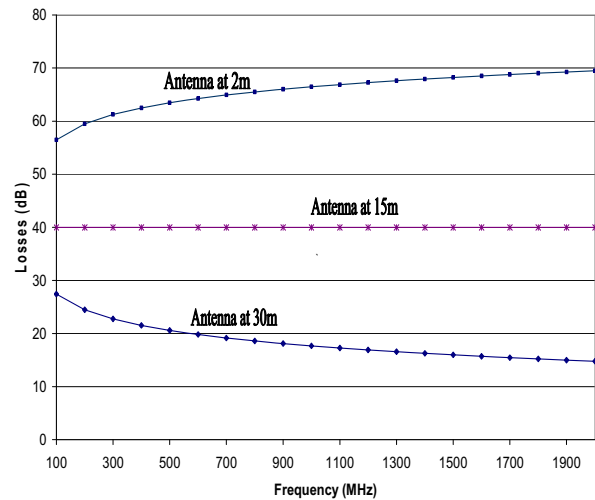


Figure 8. Comparison of multiple diffraction losses versus frequency

Figure 9 compares the multiple diffraction losses between the UPM model and the Ikegami-Walfisch model and indicates the differences. The most notable differences are for the scenarios when the transmitter antennas are below the rooftop level as discussed in Section 2.

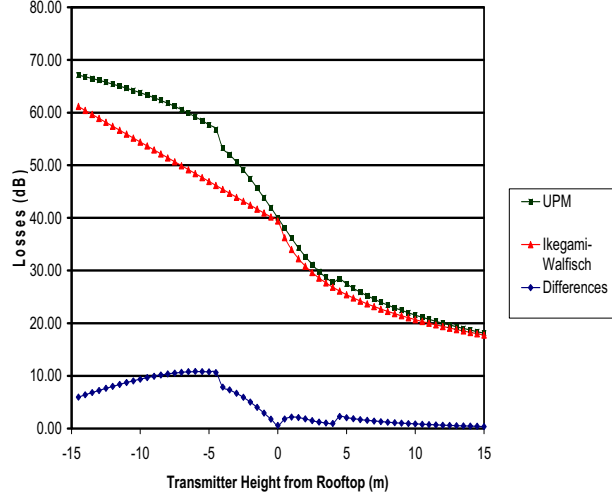


Figure 9. Comparison of multiple diffraction losses of UPM and Ikegami-Walfisch models

3.3 Diffraction Loss from Rooftop Fields to Ground Level

Figure 10 shows the four most important contributions as identified in [3] for the diffraction loss process from rooftop edges of buildings adjacent to the mobile antenna. The most significant contribution comes from the rooftop edge immediately before the mobile antenna.

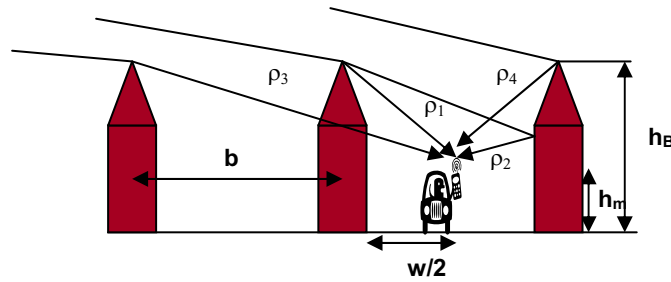


Figure 10. Parameters for the L_{rts} loss

Using GTD, L_{rts} is given by

$$L_{rts} = -10 \log \left[\frac{1}{\rho_1} |D(\theta_1)|^2 + \frac{|\Gamma|^2}{\rho_2} |D(\theta_2)|^2 + \frac{|T|^2}{\rho_3} |D(\theta_3)|^2 + \frac{1}{\rho_4} |D(\theta_4)|^2 \right] \quad (7)$$

where the diffraction coefficient for the absorbing screen is used

$$\|D(\theta_i)\|^2 = \frac{\lambda}{(2\pi)^2} \left[\frac{1}{\theta_i} + \frac{1}{2\pi - \theta_i} \right]^2 \quad (8)$$

for buildings with edge roofs

$$\begin{aligned} \rho_1 &= \rho_4 = \sqrt{\Delta h_M^2 + (0.5b)^2} \\ \rho_2 &= \sqrt{\Delta h_M^2 + (0.5b + w)^2} \\ \rho_3 &= \sqrt{\Delta h_M^2 + (1.5b)^2} \end{aligned}$$

and

$$\begin{aligned} \theta_i &= -\sin^{-1} \left(\frac{\Delta h_M}{\rho_i} \right) \text{ for } i=1,2,3, \text{ and} \\ \theta_4 &= \pi + |\theta_1| \end{aligned}$$

where Δh_M is the height difference between the receiver antenna and the average building height. The Γ gives the reflection coefficient of the building, and T gives the transmission loss through the building.

Equation (3) uses a GTD that is valid when the mobile antenna height is well below the rooftop within the shadow region. When the receiver antenna is closer to the rooftop within the transition region, the transition function, $F(S)$, as computed in [3], should be considered. The contribution of the transition function is $|D(\theta_i)F(S_i)|^2$ where i corresponds to each diffraction coefficient.

3.4 Total Path Loss

The models in Sections III-A thru III-C calculate the losses due to free space, multiple diffractions of passed rows of buildings, and diffractions from rooftop to ground level, and their summation provides the total path loss, L , as described in equation (1).

Figure 11 compares the total path losses between the UPM model and the Ikegami-Walfisch model and indicates the differences. The analysis is performed for 300 MHz, a frequency that is within the 225-400 MHz military band, building height 15 m, distance between

buildings 50 m, and distance 5 km. The difference between the models is within ± 5 dB.

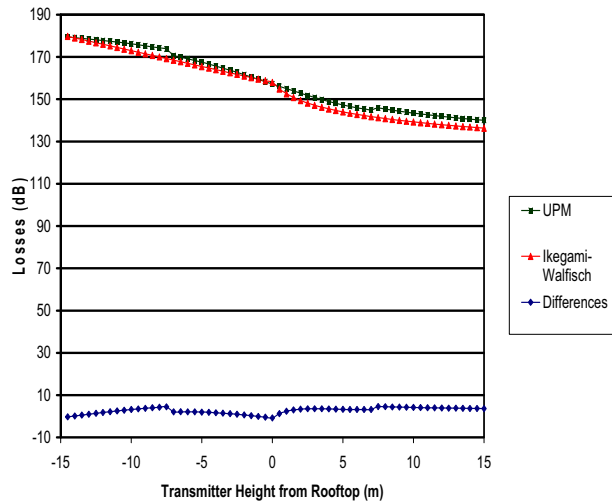


Figure 11. Comparison of total path losses of UPM and Ikegami-Walfisch models

4 Urban Environmental Data

The UTP developed by the US Army TEC provides data for key aspects of the urban environment, including buildings, roads, forests, water bodies, and vertical obstructions. The UTP data is divided into several layers that contain different types of features (e.g., roads, buildings). A list of attribute fields is associated with each feature (e.g., road width, building height). The data is stored in personal geodatabases that are in an ESRI data management structure.

The UPM model assumes that buildings and roads are uniformly distributed within an urban or suburban environment as shown in Figure 4. Therefore, the primary input parameters required for the UPM model are the average building height (h_B), average building separation (b), and average road width (w).

Attributes contained in the UTP data are used for determining the average values for the input parameters of the UPM model. Such attributes are the road width, building height, the number of building floors, building length and area. Other attributes such as building surface and roof shape can also provide information for

deriving the reflection coefficient and determining the predominant roof shape, edge or flat, for use in the UPM model.

A Windows Dynamic Link Library (DLL) is developed to extract the required data from the US Army TEC UTP database. For a given propagation path, described as two WGS-1984 geodetic points, the DLL library extracts the required data from the UTP database and computes and returns the average values of the primary input parameters for the UPM model.

5 Conclusions

The UPM was developed for providing the capability for predicting the path loss in cities by utilizing data that represents the actual characteristics of the urban and suburban environments. The UPM is a simplified propagation model for fast assessment of interference and de-confliction for use in conjunction with spectrum management tools, and exhibits reasonable accuracy but minimizes computational time and complexity. In addition, this propagation model considers all the suitable scenarios for wireless networks with transmitter antenna above, near, and below the average rooftop level.

6 References

1. G. A. Hufford, A. G. Longley, W.A. Kissick, A Guide to the Use of the ITS Irregular Terrain Model in the Area Prediction Mode, NTIA Report 82-100, US Department of Commerce, April 1982.
2. TIREM/SEM Handbook, ECAC-HDBK-93-076, Department of Defense, March 1994.
3. H. L. Bertoni, *Radio Propagation for Modern Wireless Systems*. Upper Saddle River: Prentice Hall, 2000.
4. COST231, Digital Mobile Radio Towards Future Generations Systems.
5. Y. Okumura, E. Ohmori, T. Kawano, and K. Fukuda, "Field strength and its variability in VHF and UHF land-mobile radio service," *Rec. Elec. Comm. Lab.*, vol. 16, pp. 825–873, 1968.
6. M. Hata, "Empirical Formula for Propagation Loss in Land Mobile Radio

- Services,” IEEE Trans. Veh. Tech., vol. VT-29, pp. 317–325, Aug. 1980.
7. J. Walfisch and H. L. Bertoni, “A theoretical model of UHF propagation in urban environments,” IEEE Trans. Ant. Prop., vol. 36, pp.1788–1796, Dec. 1988.
 8. H. H. Xia, “A Simplified Analytical Model for Predicting Path Loss in Urban and Suburban Environments,” IEEE Trans. Veh. Tech., Vol 46, NO. 4, November 1997.

Radio Communications for Emergency Responders in High-Multipath Outdoor Environments*

Kate A. Remley¹, Galen Koepke, Christopher L. Holloway, Chriss Grosvenor, Dennis G. Camell, and Robert T. Johnk²
National Institute of Standards and Technology, Boulder, CO 80305 USA
1. Corresponding author: ph. (303) 497 3652, email: remley@boulder.nist.gov
2. Institute for Telecommunication Sciences, Boulder, CO 80305 USA

We present measurement data to support development of technology and standards for broadband, digitally modulated radio communications used by emergency responders. Measurements were conducted at an oil refinery having extensive outdoor piping and other metal components. This structure represents a class of high-multipath, outdoor propagation environments that includes electrical generation facilities, chemical plants, and other outdoor, heavy industrial environments where reliable emergency responder communications is critical. The measurement results presented here quantify the extent of the multipath, loss, and other propagation effects in such high-multipath outdoor environments.

Keywords: emergency responder; excess path loss; multipath; propagation; radio wireless system.

1. Introduction

We report on measurements of parameters relevant to broadband, modulated-signal radio communication for the public-safety sector. Our tests were carried out at an oil refinery near Denver, Colorado in March, 2007. We performed three types of tests in these experiments: (1) received power at key public-safety frequencies; (2) excess path loss; and (3) waveform measurements of complex digitally modulated, broadband signals. Studying the issues related to radiowave propagation from these three perspectives gives us insight into the sources and significance of impairments for outdoor, high-multipath environments such as oil refineries, utility plants, chemical plants, and other heavy industrial environments.

Wireless communication using wideband, digitally modulated signals transmitted into and out of large structures is complicated by several factors. These include the strong attenuation of radio signals caused by losses in the building materials, scattering from structural features (multipath), and the waveguide effects of corridors and tunnels. Understanding the losses and their variability, decay times for reflected signals, the frequency-selective behavior of the channel, and the combined effect that these factors have on broadband digitally modulated signals can help system designers assess various technologies. This information also can help in designing and verifying network simulations, and ultimately will help with standards development.

The collection of data presented here shows a number of propagation effects relevant to transmission of broadband modulated signals in a high-multipath environment that may be encountered by public-safety and emergency-responder practitioners. We will show that transmitted signals

experience intense frequency-selective distortion and multipath across the signal's modulation bandwidth in the oil refinery. This can be a challenge when deploying robust wireless communications. We anticipate that this collection of data allow for development of methods to improve performance in this difficult propagation environment.

2. Current Research in Emergency Responder Communications

To aid in the development of standards that support reliable wireless communications for emergency responders, the Department of Justice, through the Community-Oriented Policing Services (COPS) program is supporting the National Institute of Standards and Technology (NIST) in the acquisition of data describing radiowave propagation in key emergency responder and public-safety environments. In past work by NIST [1-3], measurements were collected in buildings scheduled for implosion to simulate collapsed-building environments. The focus of current work is to study radiowave penetration into large buildings and structures where inadequate radio reception is often encountered. Four large structures were studied: a 12-story apartment building, an office corridor, a subterranean tunnel, and an oil refinery [4, 5]. Here we focus on the results from the oil refinery, representing the most difficult propagation environment for digitally modulated signals.

Many publications have described measurement characterization of the propagation environment with respect to loss, delay spread, bit error rate, and/or other wireless system figures of merit. Most of these publications (e.g., [6] and references cited therein) describe measurements intended to simulate communications via cellular telephone or other wireless systems. These systems consist of a fixed base station whose antenna is positioned high above the ground and a mobile user located at ground height. Few publications describe measurements that simulate point-to-point radio-communication scenarios (e.g., [7] and the references

* Work of the U.S. government, not subject to copyright in the U.S.

cited therein), such as those required in many emergency-responder scenarios.

In addition to supplying standards-development organizations with real-world data available in the open literature, one of the goals of this program is to provide data for verification of network simulations of emergency responder radio links. The oil refinery was chosen because it is an environment that is similar to the chemical plant explosion scenario described in the SAFECOM Statement of Requirements (SoR), 2nd revision [8]. We anticipate that these data may also be used directly by system designers and researchers, and by end users, including public-safety practitioners.

3. Overview of Oil Refinery Measurements

The Suncor oil refinery* is an outdoor facility covering many hectares with several intricate, multi-story metallic piping systems, as shown in Fig. 1(a) and (b). The complex is several hundred meters long. The tower in Fig. 1(a) is nine stories high. In certain areas, the dense overhead piping forms a tunnel-like structure, Fig. 1(c), that can impede radio communications.

We carried out three types of radio transmission tests in this environment: (1) narrowband received-power measurements by use of a calibrated communications receiver, (2) wideband excess-path-loss measurements by use of a synthetic-pulse system based on a vector network analyzer, and (3) modulated-signal measurements of the spectrum using a vector signal analyzer. A more detailed account of these measurements can be found in [5].

3.1 Narrowband received-power measurements:

We collected single-frequency (unmodulated, carrier only) received-power data at frequencies near public-safety and cell-phone bands as well as in the unlicensed Industrial, Scientific, and Medical (ISM) and wireless local-area network (WLAN) bands (approximately 50 MHz, 150 MHz, 225 MHz, 450 MHz, 900 MHz, and 1.8 GHz).

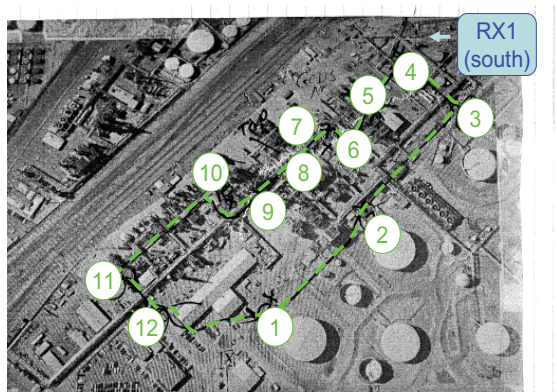
The radios were similar to those of first responders, except they were placed in ruggedized cases and were modified to transmit continuously. An example can be seen in Fig. 1(c) in the left hand of the NIST researcher on the left.

We carried the radio transmitters throughout the oil refinery, along the path shown in Fig. 1(b), while recording the received signal at a fixed receiver site located approximately 30 m from the piping structure

(labeled RX1). The receiving equipment was placed in a van (Fig. 2) made available for NIST use by the Institute for Telecommunication Sciences (ITS), a sister Department of Commerce organization at the Boulder Laboratories Site. Omnidirectional discone receiving antennas were mounted on masts on top of the van, as shown in the figure.



(a)



(b)



(c)

Figure 1: Oil refinery near Denver, Colorado. (a) Overview of the site. (b) Aerial view of the facility including the path taken for the received-power measurements. (c) Dense piping makes a tunnel-like propagation environment in certain areas.

* This company is identified solely for completeness of description, and such identification constitutes no endorsement by the National Institute of Standards and Technology.

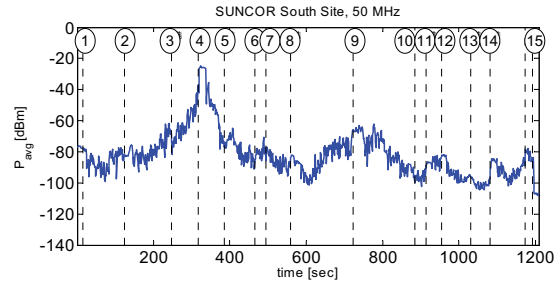
We used a narrowband communications receiver. This instrument, when combined with NIST-developed post-processing techniques [9], provides a high-dynamic-range measurement system that is affordable for most public safety organizations. Part of our intent was to demonstrate a user-friendly system that could be utilized by public-safety organizations to assess their own unique propagation environments.



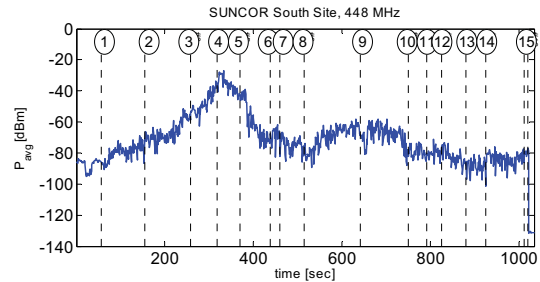
Figure 2: The receiver was located inside a van with antennas top-mounted on a mast approximately 7.5 m (25 feet) above the ground.

The dashed line in Fig. 1(b) represents the path where the transmitters were carried by foot through the refinery. The path wound through the center of the processing section. In many places we encountered dense piping both to the side and overhead. Tunnel-like corridors through the piping are approximately five meters in width. As mentioned above, in most cases the piping extended several stories into the air. Fig. 1(c) shows NIST personnel carrying a portable transmitter through such a corridor.

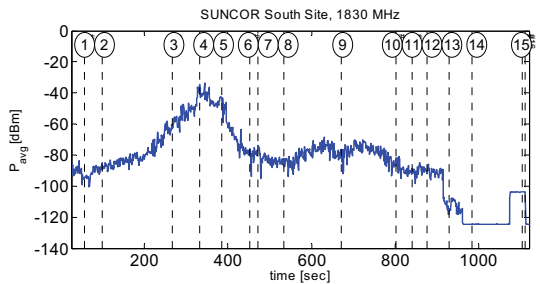
Fig. 3 shows three representative sets of received data gathered while the transmitters were carried by foot through the facility. The numbered points on the graph correspond to those labeled in Fig. 1(b), with the exception of point 13 – 15, which were located below the lower edge of the photo. For a 50 MHz carrier frequency, we see in Fig. 3(a) that the received signal levels decrease rapidly as the transmitter moves from a nearby, line-of-sight location (position 4) to a location having line-of-sight but deep inside the piping structure (for example, position 8). This rapid attenuation is due to a waveguide-below-cutoff effect described in [5] and the references therein. The received power for the 448 MHz carrier frequency (Fig. 3(b)) has, on average, a slightly higher level than the 1830 MHz carrier frequency (Fig. 3(c)), but the rapidity of the changes are very similar with position (or time).



(a)



(b)



(c)

Figure 3: Received-power measurements collected as transmitters were carried by foot throughout an oil refinery complex for carrier frequencies of (a) 50 MHz, (b) 448 MHz, and (c) 1830 MHz. The highest received signal level is nearest to the receiver. The second-highest level is located at the top of a tall tower.

3.2 Excess-path-loss measurements: We studied excess path loss over a wide frequency band at specific locations within the oil refinery. These locations were confined to the path between points 7 and 9 in Fig. 1(b) for logistical reasons. The excess-path-loss measurements provide the received signal strength relative to a direct-path signal over a frequency band from 25 MHz to 18 GHz for the system we used.

Our synthetic-pulse, ultrawideband system is based on a vector network analyzer (VNA). The post-processing and calibration routines associated with it were developed at NIST [10]. In the synthetic-pulse system, the VNA acts as both transmitter and receiver. The transmitting section of the VNA sweeps over a wide range of frequencies, a

single frequency at a time. The transmitted signal is amplified and fed to a transmitting antenna. We used directional horn-type transmitting and receiving antennas at frequencies between 1 GHz and 18 GHz.

The received signal is picked up over the air by the receiving antenna and sent back to the VNA via a fiber-optic cable. The fiber-optic cable phase locks the received signal to the transmitted signal enabling reconstruction of the time-domain waveform associated with the received signal in post processing. Because the wideband transmitted signal corresponds to a short-duration pulse in the time domain, this system allows us to quantify the effects of the propagation environment, including losses and multipath reflections.

We carried out measurements at 13 positions (a subset of the receiver positions) in the oil refinery that were located in an area of very dense piping. We rolled the receiving antenna along the path on a mobile cart. The VNA was located in the ITS mobile test van. The vertically polarized transmitting antenna was located on top of this van.

Figure 4 shows excess path loss for frequencies between 1 GHz and 18 GHz at various positions in the oil refinery. The top curve represents the received power levels relative to the reference value, and the bottom curve represents the noise floor of the measurement system.

At a line-of-sight position shown in Fig. 4(a), the spectrum is quite flat with frequency. The peaks in the spectrum correspond to peaks in the instrumentation noise floor. Once the transmitting antenna is within the piping corridor, the spectrum starts to show significant frequency dependence, caused by strong reflections, as shown by the nulls and peaks in Fig. 4(b). Then, as the transmitting antenna turns the corner and proceeds even further down the piping corridor, the signal drops off rapidly and is almost lost in the noise, Fig. 4(c). The higher frequency bands show greater attenuation with distance than do the lower frequency bands. The complete set of UWB excess-path-loss data is given in [5].

3.3 Modulated-signal spectra: We also conducted measurements of representative broadband digitally modulated signals at carrier frequencies of 2.4 GHz and 4.95 GHz. We used a vector signal analyzer (VSA) to measure the signals. The VSA maintains the relative phase of the measured frequency components and enables laboratory-grade measurements of distortion in digitally modulated signals. The transmitter consisted of a vector signal generator, power amplifier, and omnidirectional antenna mounted on a cart. The VSA receiver was located in the ITS van.

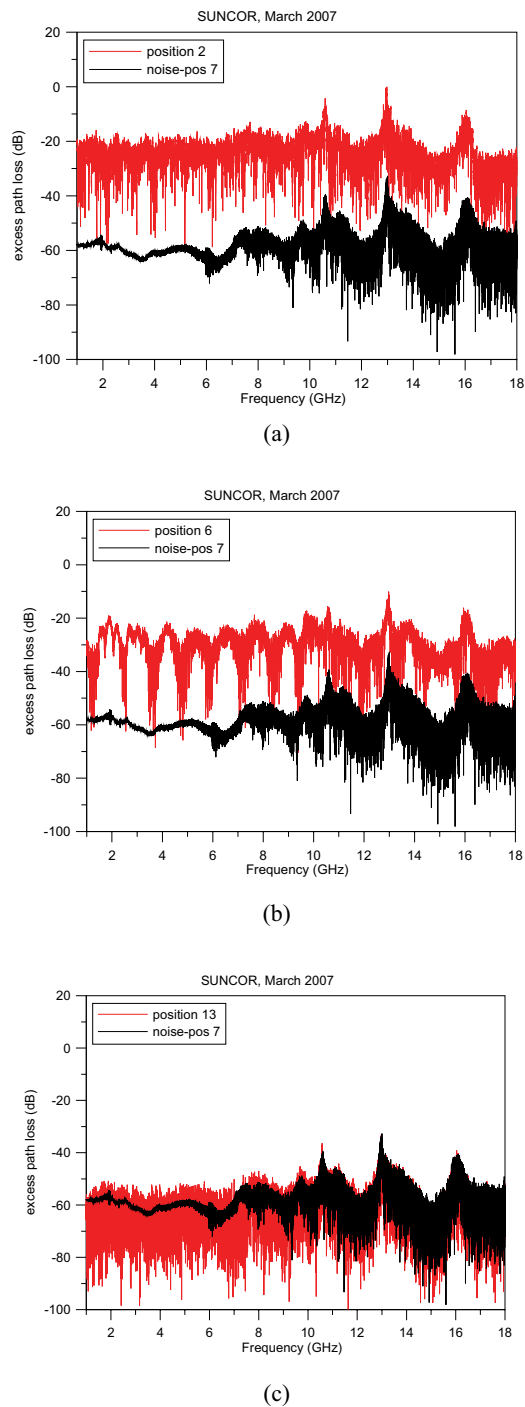


Figure 4: Excess-path-loss measurements at an oil refinery for (a) line-of-sight, (b) down piping corridor, and (c) non-line-of-sight positions for frequencies from 1 GHz to 18 GHz. The path was located outdoors but under dense piping several stories high, at 13 positions between points 7 and 9 shown in Fig. 1(b).

The modulated signal used as excitation was based on the orthogonal frequency-division multiplexing (OFDM) multiple access scheme, as specified by the

IEEE 802.11aTM-1999 standard [11-12]. OFDM is used in wireless local-area networks (WLANs), in dedicated short-range communication (DSRC) systems for tracking and observing loads in commercial vehicles, and in the public-safety band at 4.95 GHz. In the latter, OFDM signals are often transmitted in a 10 MHz wide channel using the 802.11j standard, instead of the 20 MHz wide channel utilized in 802.11a. The demodulator that we used was able to measure only the 802.11a standard, as reported below.

We also made measurements of multisine signals designed to simulate the statistical properties of digitally modulated signals [13]. Multisines are collections of simultaneously generated sine waves whose amplitudes and relative phases are engineered to transmit a waveform having properties similar to the digitally modulated signal, but in a more efficient and easier-to-characterize fashion.

We made measurements at the same positions where the synthetic-pulse VNA measurements were made. Figs. 5(a)–5(c) show measured bandpass spectra for a digitally modulated quadrature-phase-shift-keyed (QPSK) signal and for a multisine signal designed to simulate it. Fig. 5(a) shows a measurement where the transmitter and receiver were located approximately three meters from each other in a low-multipath environment. This undistorted signal may be used for comparison to the distorted signals described below.

In Fig. 5(b), the transmitter has just entered into the metallic piping structure and there is still a good line of sight between the transmitter and receiver. Still, the figure shows much frequency-selective distortion, indicated by the deep nulls across the modulation band of the signal. This could impair accurate decoding of the signal. The 2.41 GHz carrier signal is more strongly affected than the 4.95 GHz carrier one. We suspect this is due to the physical dimensions of objects within the piping structure.

In Fig. 5(c), the transmitter has proceeded down the piping corridor to the same location shown in Fig. 4(b). The signals at both carrier frequencies are attenuated and again, significant frequency-selective wideband fading is seen. We were unable to receive the digitally modulated signal in the non-line-of-sight location due to the limited dynamic range of the VSA system we used.

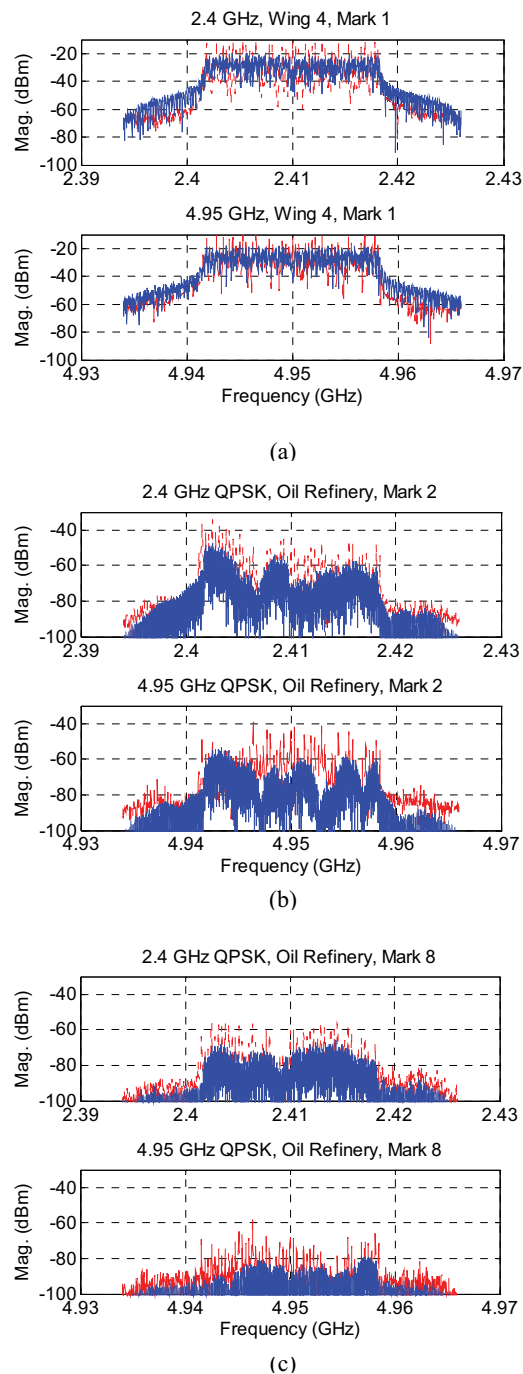


Figure 5: Bandpass spectra measured using the vector signal analyzer showing received QPSK digitally modulated OFDM signals at carrier frequencies of 2.41 GHz (top graphs) and 4.95 GHz (bottom graphs). The dashed lines correspond to multisine signals designed to simulate the modulated signals. (a) Undistorted received signals. (b) Line-of-sight path between transmitter and receiver in the oil refinery. (c) Down the piping corridor, still line of sight.

4. Conclusion

We have presented a variety of measured data collected in a high-multipath, outdoor environment. The intent of this work is to improve radio communications for emergency responders when they transmit wideband, digitally modulated signals.

Results showed waveguide-below-cutoff attenuation effects at the lower carrier frequency of 50 MHz. We saw frequency-dependent behavior in the channel due to strong multipath reflections and attenuation within the piping structures. In non-line-of-sight conditions, we saw classic Rayleigh noise-like signals. In digitally modulated signals, significant distortion occurred in the bandwidth of the signal. This indicates significant wideband fading that may impair wireless transmissions. It is hoped that these data will prove useful in standards development, as well as improved technology and system design for the emergency-responder community.

Acknowledgement

This work was funded by the Department of Justice Community Oriented Policing Services (COPS) through the NIST Office of Law Enforcement Standards, Dereck Orr Program Manager for Public Safety Communications.

References

- [1] C.L. Holloway, G. Koepke, D. Camell, K.A. Remley, D.F. Williams, S.A. Schima, S. Canales, D.T. Tamura, "Propagation and Detection of Radio Signals Before, During, and After the Implosion of a 13-Story Apartment Building," *Natl. Inst. Stand. Technol. Note 1540*, May 2005.
- [2] C.L. Holloway, G. Koepke, D. Camell, K.A. Remley, D.F. Williams, S.A. Schima, S. Canales, D.T. Tamura, "Propagation and Detection of Radio Signals Before, During, and After the Implosion of a Large Sports Stadium (Veterans' Stadium in Philadelphia)," *Natl. Inst. Stand. Technol. Note 1541*, October 2005.
- [3] C.L. Holloway, G. Koepke, D. Camell, K.A. Remley, S.A. Schima, M. McKinley, R.T. Johnk, "Propagation and Detection of Radio Signals Before, During, and After the Implosion of a Large Convention Center," *Natl. Inst. Stand. Technol. Note 1542*, June 2006.
- [4] C.L. Holloway, W.F. Young, G. Koepke, K.A. Remley, D. Camell, Y. Becquet, "Attenuation of Radio Wave Signals Coupled Into Twelve Large Building Structures," *Natl. Inst. Stand. Technol. Note 1545*, Feb. 2008.
- [5] K.A. Remley, G. Koepke, C.L. Holloway, C. Grosvenor, D. Camell, J. Ladbury, D. Novotny, W.F. Young, G. Hough, M.D. McKinley, Y. Becquet, J. Korsnes, "Measurements to Support Broadband Modulated-Signal Radio Transmissions for the Public-Safety Sector," *Natl. Inst. Stand. Technol. Note 1546*, Apr. 2008.
- [6] P. Papazian, "Basic transmission loss and delay spread measurements for frequencies between 430 and 5750 MHz," *IEEE Trans. Antennas Prop.*, vol. 53, no. 2, Feb. 2005, pp. 694-701.
- [7] J.R. Hampton, N.M. Merheb, W.L. Lain, D.E. Paunil, R.M. Shurfor, And W.T. Kasch, "Urban propagation measurements for ground based communication in the military UHF band," *IEEE Trans. Antennas Prop.*, vol. 54, no. 2, Feb. 2006, pp. 644-654.
- [8] SAFECOM Statement of Requirements, vol. 1, v. 1.2, http://www.safecomprogram.gov/NR/rdonlyres/8930E37C-C672-48BA-8C1B-83784D855C1E/0/SoR1_v12_10182006.pdf, Oct. 2006. Section 3.3 is the residential fire, and Section 3.5 is the explosion at the chemical plant.
- [9] M. Rütshlin, K. A. Remley, R. T. Johnk, D. F. Williams, G. Koepke, C. Holloway, A. MacFarlane, and M. Worrell, "Measurement of weak signals using a communications receiver system," *Proc. Intl. Symp. Advanced Radio Tech.*, Boulder, CO, March 2005, pp. 199-204.
- [10] B. Davis, C. Grosvenor, R.T. Johnk, D. Novotny, J. Baker-Jarvis, M. Janezic, "Complex permittivity of planar building materials measured with an ultra-wideband free-field antenna measurement system," *NIST Journal of Research*, Vol. 112, No. 1, Jan.-Feb., 2007.
- [11] IEEE Standard for Wireless LAN Medium Access Control (MAC) and Physical Layer (PHY) Specifications: High-Speed Physical Layer in the 5 GHz Band, *IEEE Standard 802.11aTM-1999*.
- [12] IEEE Standard for Wireless LAN Medium Access Control (MAC) and Physical Layer (PHY) Specifications: Higher-Speed Physical Layer Extension in the 2.4 GHz Band, *IEEE Standard 802.11b-1999*.
- [13] K.A. Remley, "Multisine excitation for ACPR measurements," *IEEE MTT-S Int. Microwave Symp. Dig.*, June 2003, pp. 2141-2144.

New Challenges In The Understanding Of Surface Wave Propagation

Les Barclay
Barclay Associates Ltd
Lancaster University

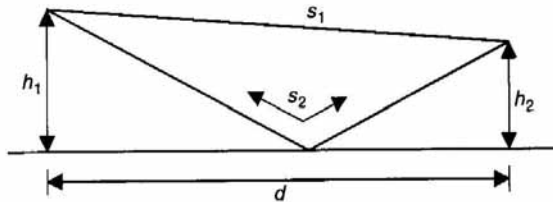
Abstract

Theories of surface wave propagation, of importance at lower frequencies, notably for broadcasting at MF and LF, were first developed 100 years ago and have become well established. Methods are available for propagation over a homogeneous smooth earth, over paths of mixed ground conductivity and over irregular terrain. However, results have been reported showing a correlation with temperature, and this has not been explained using the accepted theory.

Also, there is a growing interest in the introduction of digital modulation for MF broadcasting and better predictions are needed for propagation in city areas. Such propagation has been shown to be subject to significant excess attenuation, but more work is needed to develop this understanding to provide a prediction procedure.

1. Introduction

The ray path treatment for propagation between two elevated antennas above a plane earth is well known, Figure 1.



Two-ray reflection
Figure 1

The resultant field strength at the receiving antenna is obtained by the vector summation of the direct and ground-reflected components¹:

$$V = QI \left\{ Q_1 \cdot \frac{\exp(-jks_1)}{r_1} + Q_2 \cdot \frac{\exp(-jks_2)}{r_2} \right\}$$

where: Q is a constant
I is the current in the transmitting antenna
Q₁ and Q₂ depend on the antenna polar diagrams
and R is the ground reflection coefficient

This relationship is quite sufficient at VHF and higher frequencies, but it turns out that a complete description of the field, to satisfy Maxwell's equations, also requires an additional component:

$$V = QI \left\{ Q_1 \cdot \frac{\exp(-jks_1)}{r_1} + Q_2 \cdot \frac{\exp(-jks_2)}{r_2} + S \frac{\exp(-jks_2)}{r_2} \right\}$$

where S is a factor which depends on the electrical properties of the ground, the polarisation, frequency and terminal locations.

As the antenna heights are reduced, r₁ and r₂, become more equal and the reflection coefficient approaches -1, so that when the antennas are on the ground, the only term left is the third term – the surface wave.

2. Terminology

The terminology used to name this propagation mode is confusing. In the past some authorities have defined the ground wave as comprising all three of the components identified above:

$$\text{ground wave} = \underbrace{\text{direct wave} + \text{reflected wave}}_{\text{space wave}} + \text{surface wave}$$

Here the two components of Figure 1 are collectively described as the space wave and the third component as the surface wave. I suppose that this way of grouping the components has partly fallen out of use with the introduction of satellite communication and the consequent extra confusion.

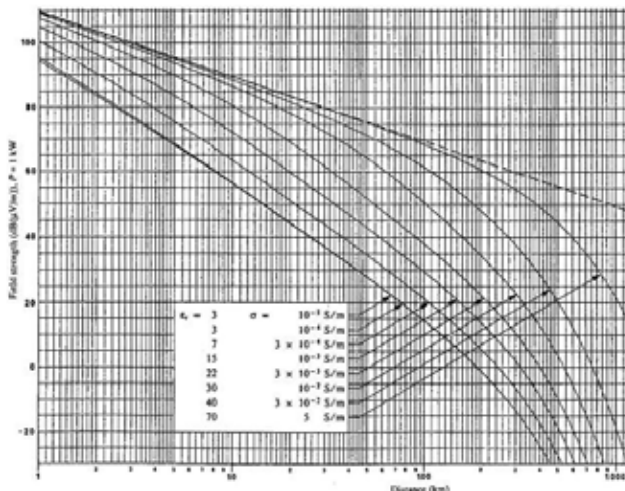
Calling the third component the *surface wave*, or the *Norton surface wave* after the author who made the calculations tractable, is perhaps better, but the term

ground wave is often used just for the surface wave component - with some ambiguity as the antennas are elevated.

Note also that there is another surface wave mode, the *Zenneck wave*, first described in 1907. But there is still confusion about the relevance of this mode, which may refer to propagation in a surface and not to propagation in the space above a surface².

3. Ground Wave Theory

The first analysis of ground wave propagation was probably the flat earth theory of Sommerfeld³ (which had a sign error, later corrected). Van der Pol and Bremmer⁴ presented the theory in a form more amenable to calculation. These methods did not include the atmosphere and it is the work of Rotheram⁵, which includes an exponential atmosphere, which is now used for the field strength curves of ITU-R Recommendation 368. An example from the Recommendation is shown in Figure 2.



Surface wave propagation at 1 MHz for various values of ϵ and σ , for ITU-R Recommendation P.368
Figure 2

Rotheram also wrote the computer code GRWAVE, which is available on the ITU-R web site and which includes the case of elevated antennas.

These methods are all complicated, and Norton⁵ provided a practical graphical method of treating the ground wave by means of a complex attenuation function. For the case of the pure surface wave, when both antennas are on the ground, it turns out that there are both vertical and radial components of the

electric field, so that the wavefront is tilted forward in the direction of propagation, giving rise to attenuation in the ground. The ratio of the radial to vertical components is $1/\sqrt{K}$, where K is the complex electrical characteristic of the ground. At lower frequencies the main term in this is usually due to the conductivity.

Thus we have a stable surface wave where field strengths attenuate as they propagate around the earth; the attenuation depending only on the frequency and on the relative permittivity and the conductivity of the ground. At these frequencies there will also be a propagation mode utilising reflection from the ionosphere, but that is not considered here.

4. Non-homogeneous, imperfect ground

4.1 Stratified ground

The basic theory is for propagation over a smooth spherical earth having homogeneous electrical constants. Where the sub-soil is stratified, for example with top soil overlying rock, predictions may be made using effective values for the ground constants which take account of the penetration of the radio waves into the ground. The effective constants may be found by making measurements of the forward wave tilt (a difficult measurement), or of the attenuation of signals with distance, relating this to the curves for the expected variation for different ground conditions. With experience an estimate may be made from geological maps. Maps of ground conductivity for many countries may be found in ITU-R Recommendation P.832; two sets of maps are given, for VLF and for MF, to take account of the differing penetration depths.

4.2 Changes in conductivity along the path

Changes in conductivity along a propagation path, particularly when crossing a land/sea boundary, may be very significant. A full analysis of this situation has been undertaken by several workers, but the empirical method developed by Millington⁷, which entails piecing together parts of the field strength distance curves for the appropriate conductivities, doing this for propagation in both directions along the path and then forcing reciprocity by taking the geometric mean, has proved to be very satisfactory. It is described in an annex to ITU-R Recommendation P.368. The method was first tested at VHF, and then at MF on a path across the English Channel⁸.

Although the results have been proved experimentally, the increase in the signal as the path

moves across the shore line and over sea may not be expected and it may be necessary for a planner to undertake further measurements to remove his “doubts about the existence of the recovery effect”⁹.

measured (dashed line) and predicted (solid line) field strengths across a land/sea path in the Baltic sea at 3.9 MHz.

Figure 3

In this case doubts were resolved in a most commendable way, Figure 3, but it highlights a general danger for well established topics where substantial past studies may not be fully appreciated and where it may become important to safeguard against changes proposed on the basis of limited new work.

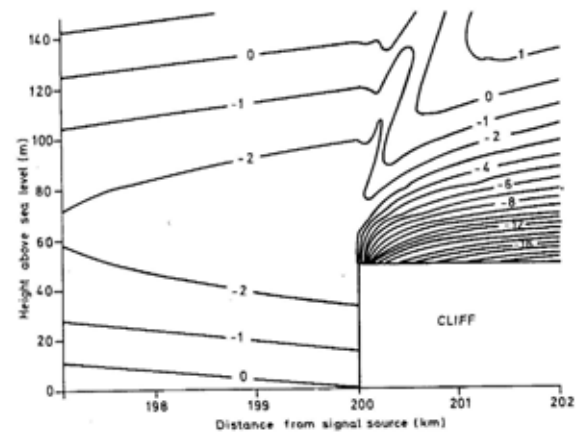
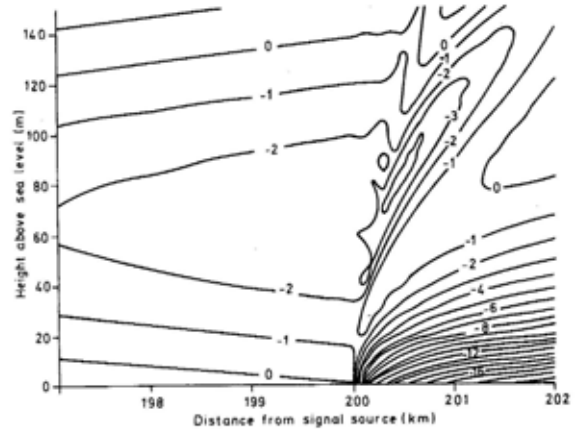
4.3 Ground height irregularities

The methods discussed so far, taking account of frequency, ground conductivity and changes in conductivity along the path, are probably sufficient for most requirements for LF and MF coverage planning. There do not seem to be any methods, practical for frequency assignment planning, which take account of ground height irregularities.

Hufford¹⁰ developed an integral equation theory for undulating paths, and Ott¹¹ published a program for evaluation of the method. However at MF and lower frequencies, where ground height irregularities are most often less than one wavelength high, the effects, except close to a large abrupt height change, seem to be of minor importance, particularly when taking into account the accuracy with which the actual ground conductivity will be known prior to the installation of the radio station.

Furutsu¹² developed a theory for paths of mixed conductivity with sections at different heights. With some restrictions this method may be used for propagation near to cliffs. Pielou et al¹³ studied the

Furutsu method and found that, near to the cliff edge, differences due to changes in cliff height are small. Pielou developed a simple procedure for estimating “site gain” near to a cliff, see Figure 4.



relative field strength (dB) at 10 MHz for propagation on a 200 km overseas path, reaching land with and without a 50 m cliff

Figure 4

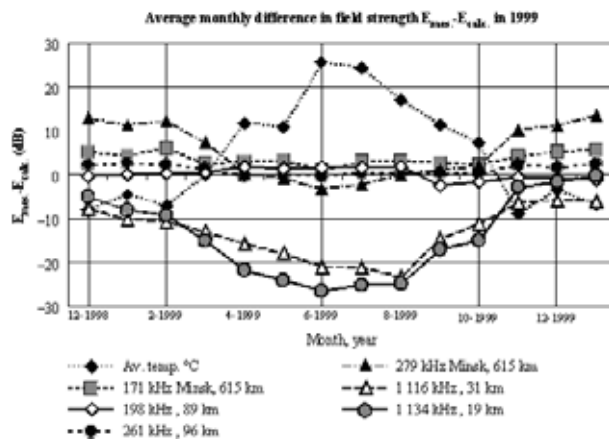
5. New Challenges for ground wave propagation

This paper so far has reported the well recognised and long established methods for dealing with the surface wave. These are based on the analyses by Van der Pol and Bremmer and of Norton and have proved their value over many years. There is sufficient known information and there are established methods which will, for example, be adequate to provide guidance on the ground wave propagation issues in relation to agenda item 1.15 of the World Radiocommunication Conference, 2011.

There are however two issues which may affect the understanding of ground wave propagation and where further studies are needed. The first of these is the report of correlation between ground wave field strength and temperature. The second, which may be of considerable importance for the re-engineering of the MF broadcast band for digital modulation, is the problem of propagation across cities.

5.1 Variation with temperature

From the earliest days of broadcasting there have been reports of changes of ground wave field strength. These are listed in a paper from the Russian Federation¹⁴. In some cases these variations may be accounted for by changes in atmospheric refractivity and by changes in ground conductivity – e.g. by seasonal changes in sub-surface water content. However the paper emphasises substantial increases in field strength at low temperatures on paths of moderate length. An earlier paper¹⁵ gives more information regarding some of the Russian results, Figure 5.



monthly differences in MF field strength in Russia
Figure 5

These results are puzzling, since temperature is not a direct parameter in the theory of ground wave propagation. Further work is needed to repeat such measurements in other geographic regions and to explain the results. Possible explanations may be in terms of ground freezing. It is well known that ice is low loss dielectric¹⁶ but less may be known about frozen earth. However it might be expected that ground freezing would show a time lag when correlated against temperature. Other explanations may relate to sap in trees having a seasonal effect, or to tree and ice cover on trees. It seems that it may be an effect of importance only to countries which experience sub zero temperatures. In the UK we have

proposed a measurement campaign for this purpose, involving seasonal measurements in both the UK and in Svalbard, but unfortunately this has not attracted funding.

ITU-R Recommendations are intended to “Recommend” and to give clear guidance to the user. Unfortunately ITU-R Recommendation 368-9, in its latest revision, includes a sentence within a note: “The average annual difference between winter and summer monthly median field strengths, for 500-1 000 kHz, ranges between 5 dB (where the average Northern Hemisphere January temperature is +4°) and 15 dB (where the average Northern Hemisphere January temperature is –16°)”. This sentence does not give clear guidance: it is very general, relating to the whole of the northern hemisphere where there are appropriate temperatures but has not been tested in other geographic regions; it seems to apply at all ranges; and it does not indicate the transition from this temperature regime to adjacent regions with less extreme conditions.

5.2 Surface wave propagation in cities.

When commercial broadcasting was introduced into the MF band in the UK, extensive studies and planning exercises were undertaken to fit a significant number of low power transmitters into an already crowded band governed by an international treaty. Measurements of existing stations confirmed the methods for use over paths of mixed conductivity. However measurements across cities showed lower field strengths than expected, and these could not be accounted for by assuming that cities would be of, for example, low conductivity. Regrettably results obtained then are not now available. However Causebrooke¹⁵ was much better organised. He made similar measurements at about the same time and he went on to develop an explanation for the effect.

At the present time some trials are being made of digitally modulated broadcasting in the MF band. Digital systems are less tolerant of poor signal to noise ratios, so that services will fail while a comparable analogue service will degrade to poorer quality. Moreover the introduction of new technology in the band is likely to stimulate use of the band, and additional low power stations are likely to be introduced. Thus it is important to understand the reasons for low signal levels in city areas and to develop a prediction procedure for the planning of such stations.

Some of Causebrooke's measurement results are shown in Figure 6 for a path across London from a transmitter location on the northern edge of the city area for three frequencies. The shorter range part of the measurements shows an almost constant field, followed by a rapid decrease to a minimum and a subsequent increase. This variation of field strength with distance cannot be reproduced from the material in Recommendation P.368 and the use of Millington's mixed path method.

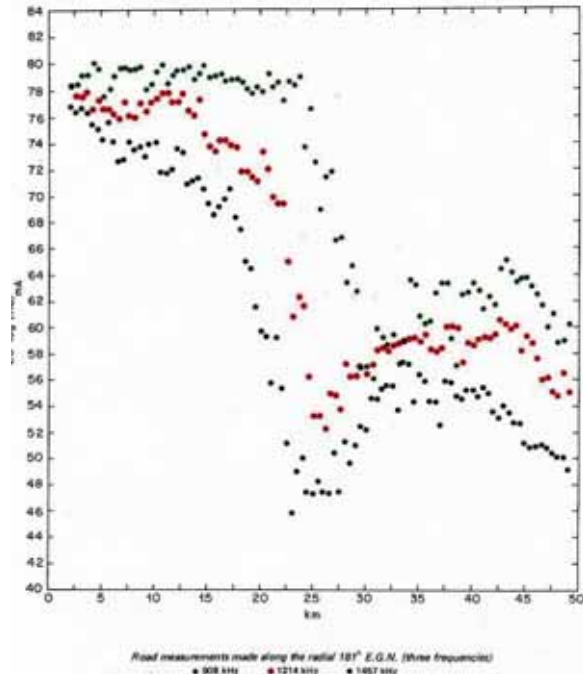


Figure 6

Causebrooke found an explanation in an examination of the Sommerfeld's attenuation function, and its graphical representation by Norton. Simplified for the surface wave only:

$$A = 1 - j\sqrt{\pi\rho} \cdot \exp(-\rho) \operatorname{erfc}(j\sqrt{\rho})$$

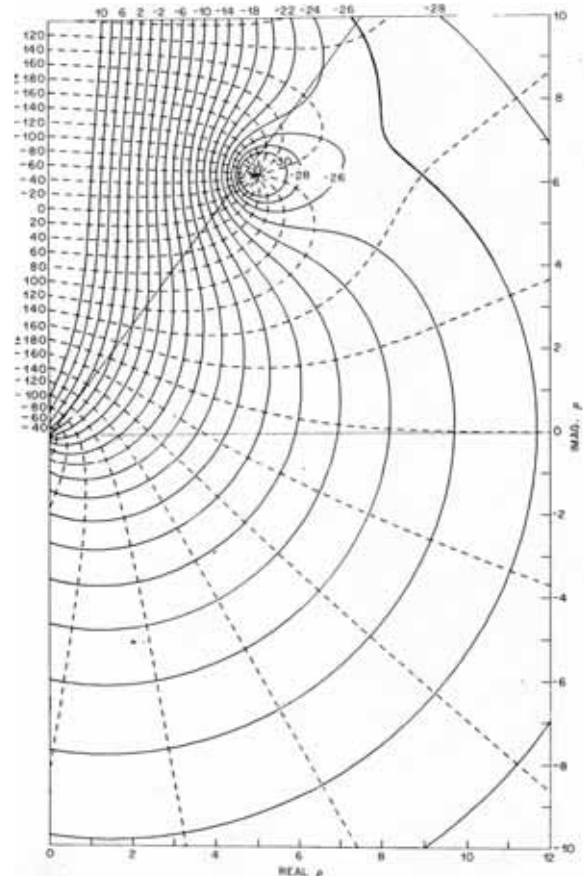
where $\rho = -j\pi\eta^2 r/\lambda$

and the relative surface impedance, η , is:

$$\eta = \frac{(\epsilon - j60\sigma\lambda - 1)^{1/2}}{\epsilon - j60\sigma\lambda}$$

ϵ and σ are the relative permittivity and the conductivity of the surface.

He computed the attenuation factor in the complex plane of ρ , see Figure 7. At low frequencies the attenuation of naturally occurring surfaces lie more or less along the real axis in this plane, with attenuation increasing for greater values of ρ . However for surfaces with electrically conducting vertical structures on them the results are in the upper half of the map, where the attenuation factor has a minimum.



mapping of ground wave attenuation on an argand diagram of the parameter, ρ

Figure 7

Causebrooke went on to find an empirical fit to his results in terms of the height of the man-made structures, the fraction of the area covered with buildings and the surface impedance of the underlying ground.

So here there is the basis of a method for predicting the field strength in cities. But more work needs to be done to establish a procedure for paths which are partly in open country and partly in built up areas, and where building heights vary. This kind of modelling needs measurement programmes across towns and cities of various configurations, but will be

greatly facilitated now by the availability of detailed mapping now available.

One further aspect needs more study. Most domestic MF broadcast receivers use magnetic antennas, as do the usual field strength measuring instruments, but car antennas are generally electric. Experience has shown that the magnetic field is more stable than the electric field in obstructed situations, and the ground wave environment is clearly one where the wave impedance differs from that in free space. Yet, conventionally, field strengths are usually quoted in measurements and in predictions in terms of the electric field. This needs to be considered further to ensure that the most useful information is given.

6. Conclusion

Surface wave, or ground wave, propagation has been considered to be fully understood, with stable ITU-R Recommendations for the prediction of the performance of ground wave systems. However some issues are outstanding which may be very important for the future development of use of these bands, particularly the introduction of digital broadcasting. Reports of a correlation of field strength with temperature need further study. The reason for the unexpected variations in field strength across city areas has been established, but a full measurement and modelling campaign is necessary before a usable prediction procedure can be developed.

7. References

1. J D Milsom "Surface waves and sky waves below 2 MHz" in "Propagation of Radiowaves" ed. L Barclay; IEE 2003
2. V N Datsko & AA Koplov "On surface electromagnetic waves" Physics – Uspekhi Vol 51, p 101, 2008
3. A Sommerfeld "The propagation of waves in wireless telegraphy" Ann. Phys, V28, p665, 1909
4. B Van der Pol & H Bremmer, "The diffraction of electromagnetic waves from an electrical point source round a finitely conducting sphere" Philos.Mag Ser 7 V24 p 141 1937; V24 p 825, 1937; V25 p817, 1938; V26 p261, 1939
5. S Rotheram, "Ground wave propagation" Part 1 "Theory for short distances" IEE Proc F, V128, p275, 1981; Part 2 " Theory for medium and long distances and reference propagation curves" IEE Proc F, V128 p285, 1981
6. K A Norton " The propagation of radio waves over the surface of the earth and in the upper atmosphere" Part 1 Proc IRE V24 p1367, 1936; part 2 Proc IRE V25 p1203, 1941
7. G Millington "Ground wave propagation over an inhomogeneous smooth earth" part 1, Proc IEE, V96 p53, 1949
8. G Millington and G A Isted "Ground wave propagation over an inhomogeneous smooth earth" part 2, Proc IEE, V97 p209, 1950
9. Th Damboldt "HF ground wave field-strength measurements on mixed land-sea paths" IEE second conference on antennas and propagation, York, 1981
10. G A Hufford "An integral equation approach to the problem of wave propagation over an irregular surface" Quart. Appl. Math V9, p391, 1952
11. R H Ott AGARD Lecture series 131, 1983
12. K Furutsu. Rad. Sci. V17, p1037, 1982
13. J M Pielou, J D Milsom & R N Herring "HF Ground wave propagation from a cliff top site", IEE Conf ICAP87, p103, 1987
14. Russian Federation "The climatic control of intensity of a field strength terrestrial wave on communications lines in an MF band" ITU-R document 9C/17, 2004
15. J H Causebrooke "Medium wave propagation in built-up areas" Proc IEE V125 p804, 1978

Polarization and Space Diversity Antenna Using Two Inverted-F 1x2 Sub-Arrays for RFID Reader Applications

Jong-Sung Kim

Department of Communications Engineering
Kyungsoong University, Pusan, Korea

ABSTRACT: *An orthogonal antenna is presented for reader applications of radio frequency identification (RFID) at 433 MHz. The antenna is composed of two 1x2 sub-arrays orthogonally placed on a ground plane. Two different feeding networks are introduced to control horizontal and vertical radiation current flows for each sub-array, respectively. An inverted-F structure is used as a radiation element with vertical and horizontal currents flowing on the radiator, thereby obtaining two linear polarizations.*

Keywords: RFID, reader, tag, inverted-F antenna, diversity

1. Introduction

Radio frequency identification (RFID) has been rapidly applied as its cost comes down and its benefits are recognized in many application areas. Recently, one of the most famous RFID applications is that of the active RFID part of ISO-18000-7, which has the allocated channel bandwidth of 500 kHz at 433 MHz for logistics entrance and transportation in a harbor or an airport [1]. In a port where large metal container boxes with a uniform size are stacked or moved, each container is tagged and automatically identified within detection ranges of 100 m or more by readers installed in specific areas and information about locations, quantities, types, or contents of each container are electrically read at any time. For the stable and reliable RFID services in a port environment surrounded by metal objects with total reflections and no penetrations, an RFID reader antenna with a compact size and a good performance is needed for enhancing high recognition rates.

The use of polarization and space diversities at the transmitter and/or receiver was found to reduce the error rate by about two to four orders of magnitude in most cases, thus leading to the higher detection capability of RFID tags [2]. One of the most popular polarization diversity antennas is the 45° dual-polarized antenna, in which a square patch is coupled to a pair of microstrip lines through either two separated offset orthogonal slots or two centered crossed slots to match the antenna [3][4]. With the optimum choice of the feed lines and aperture geometry, its decoupling and radiation characteristics are preferred to antenna designers, but its radiation direction is limited to the broadside direction of the microstrip patch.

In this draft, we propose a polarization and space diversity antenna for an RFID reader application by the use of an inverted-F antenna (IFA), which is very popular in portable handsets of mobile communications, particularly in planar types due to

its simple design, flexibility, low cost and reliable performance. It consists of a ground plane, a feed line, and a shorting conductor that connects the top conducting patch to the ground plane. The shorting operation leads to a quarter wavelength resonator; that is, the patch length can be reduced to at least 50% in comparison to the conventional half wavelength patch. However, the use of the IFA array has been rare, in contrast to the explosive use of PIFA in wireless handsets. An IFA array for gain increase of CDMA systems and a two-element array for antenna diversity of portable devices were reported in [5][6]. The IFA array structure has many design parameters, which can be used to generate the desired antenna performance. It can also be used for the base station in highly scattered downtown areas.

2. Antenna Design

Fig. 1 shows a dual-feed 1x2 inverted-F array in which each sub-array is located horizontally and vertically on a circular ground plane with a diameter of 320 mm. Two input ports are made through the ground plane by SMA connectors and feed networks, denoted by slant lines, provide input signals to radiators with proper amplitude and phase. The input signal of port 1 is equally divided in two IFAs with the same phase, while two IFAs of the sub-array 2 are excited by two signals with the same amplitude and opposite phase by the corresponding propagation delay of feed network from port 2. All vertical shorting lines in the patch of four IFAs are placed near the outer boundary of the circular ground plane. The side views of sub-arrays 1 and 2 with a radome cover, which has a permittivity of 3.2 and a thickness of 5 mm, are drawn at the right and bottom sides of Fig. 1, respectively. The optimized dimensions of the IFA at the operating frequency of 433 MHz are : $L=108$ mm, $W=20$ mm, $h=53$ mm, $s_1=12$ mm, and $w_r=7.4$ mm. A copper sheet with a thickness of 0.5 mm is used to implement the antenna. The distances between two IFAs in each sub-array are chosen as a quarter wavelength to obtain the desired space and polarization diversity in an RFID reader. The current distributions on each sub-array in Fig. 1 are drawn in Fig. 2 as arrow lines with the corresponding phases of the horizontal and vertical conductors, separately shown, for sub-arrays 1 and 2.

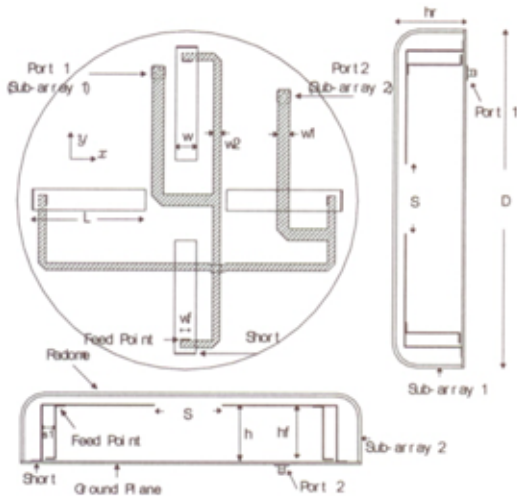


Fig. 1. Geometry of the proposed Antenna

Table I Dimensions of the proposed antenna

Parameters	Values [mm]	Parameters	Values [mm]
W	20	h_r	50
L	108	S	66
w_r	7.4	s_1	12
D	320	w_1	11
h	53	w_2	6.8
h_r	67		

Table II lists three different factors of distance, feed phase and angular orientation between two IFAs of each sub-array. The distances between two horizontal/vertical conductors are d_h and d_v , respectively. The angular orientation between the two horizontal conductors has a difference of 180° , while that between the two vertical conductors is the same. The feed networks of two sub-arrays are made in

such a way that the feed phase differences between two elements in two sub-arrays become 0° and 180° , respectively. By th Table II. Three phase factors between two IFAs of each sub-array

ese three different factors of the array structures, vertical currents in sub-array 1 and horizontal currents in sub-array 2 play dominant roles in generating their corresponding far field radiation patterns, thus leading to the production of polarization and space diversities. Isolation between two ports, which is one of key factors characterizing diversity antennas, can be obtained by the chosen feed lines.

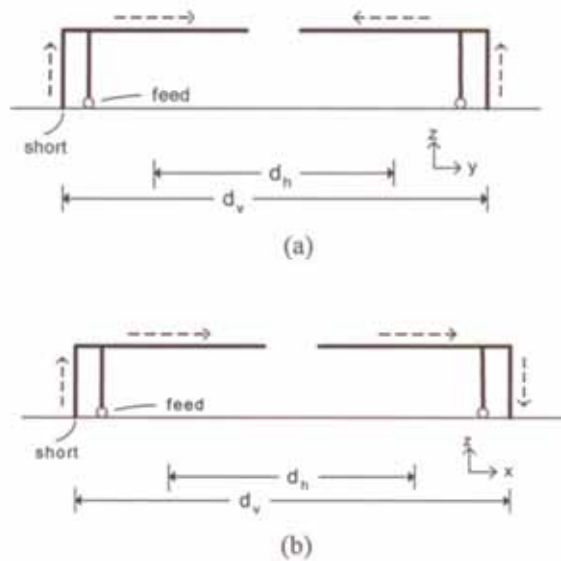


Fig. 2. Current flows of (a) sub-array 1; (b) sub-array 2

Table II. Three phase factors between two IFAs of each sub-array

Sub-Arrays	Currents	Distance Difference	Angular Orientation	Feed Phase Difference
1	horizontal	d_h	180°	0°
	vertical	d_v	0°	0°
2	horizontal	d_h	180°	180°
	vertical	d_v	0°	180°

3. Measurement Results

Fig. 3 shows the proposed antenna and radome made to the dimensions listed in Table I. Fig. 4

shows the simulated and measured return losses and isolation at two input ports of the antenna. Simulation data were obtained, to validate the proposed design, using the available electromagnetic simulator, CST Microwave Studio, based on the finite integration method [7]. It can be observed that the antenna exhibits excellent impedance matching to 50Ω . Also, isolation greater than 27 dB throughout the indicated RFID channel bandwidth specifications is observed. The unbalance in VSWR bandwidth of two sub-arrays is originated from an asymmetric feeding phase in the two IFAs of the sub-array 2. The slight discrepancy between the numerical and measured return losses may be attributed to both fabrication tolerances and numerical limitations in the precise modeling of metal edges and thickness in the computer model.

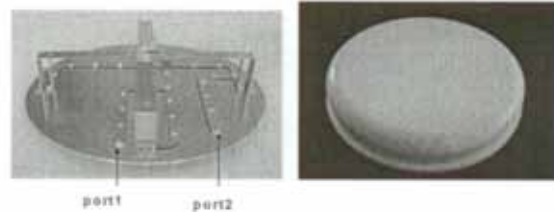


Fig. 3. Photograph of the fabricated antenna and radome

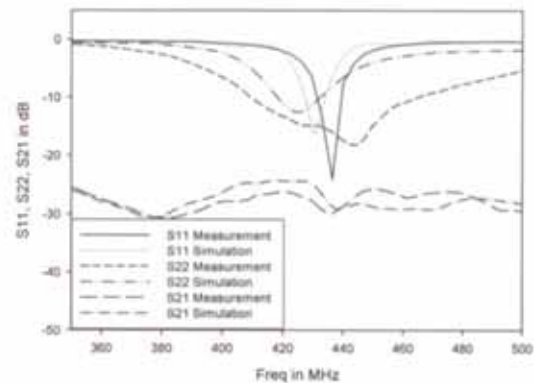


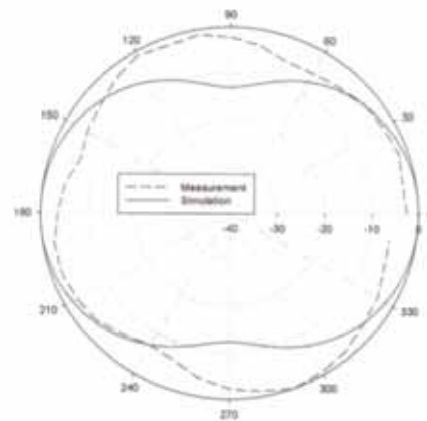
Fig. 4. Scattering parameters of the proposed antenna

The far field patterns at the E and H planes for the proposed antenna are obtained at the yz and xy planes for the sub-array 1 and the xz and yz planes for the sub-array 2. While obtaining the radiation patterns in

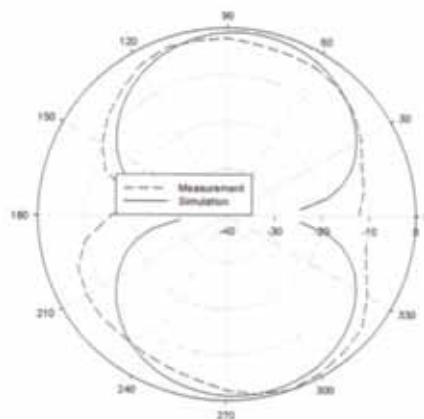
the E and H planes due to port 1, port 2 was terminated in its system impedance and vice versa. The computed radiation patterns in the E and H planes are plotted together to validate the proposed antenna design. Fig. 5 shows the radiation patterns at the E- and H-planes of two sub-arrays. For the sub-array 1, maximum and minimum radiations exist in the x - and z -axis respectively, as shown in Fig. 5(a). It is due to the fact that two z -directed vertical currents with the same phases in Fig. 2(a) are placed along the y -axis. Fig. 5(b) gives the plot of radiation pattern at the H plane of the sub-array 1. Note that the radiation of x -direction is greater than that of y -direction due to the array factor for in-phase vertical current sources along the y -axis. In contrast to the sub-array 1, while the current distributions on two horizontal conductors are in-phase with each other for the sub-array 2, the vertical currents are out-of-phase. For radiation patterns for the sub-array 2 in Fig. 5(c) and (d), there are maximum and minimum radiations in the z - and x -direction, respectively, opposite to the sub-array 1. The sub-array 1 and 2 generate the maximum gains of 3.71 dBi and 3.43 dBi in the x - and z -direction, respectively and the y -direction has a radiation with polarization diversity by both sub-arrays, thereby obtaining an omnidirectional antenna in hemisphere areas like a streetlight in a port or a harbor.

From the viewpoint of antenna configurations and radiation characteristics, the proposed antenna design resembles the circular orthogonal two thin-wire loops in [8]. The antenna consisting of two collocated orthogonal thin-wire circular loops of one wavelength in perimeter is considered as a model for a polarization diversity antenna. It was found that no coupling occurs when the terminals of each loop cross the other loop. Two orthogonal loops produce orthogonal radiations normal to their corresponding

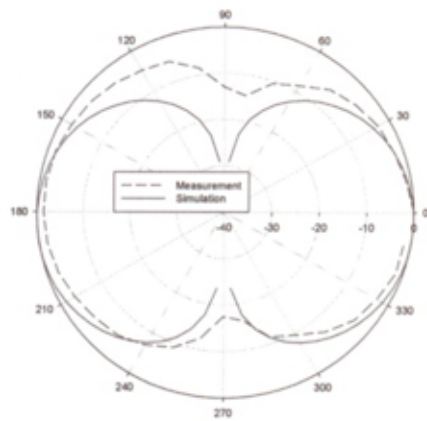
loop planes, thus leading to space and polarization diversities. It is shown in chapter 5 of [9] that a one-wavelength loop corresponds to two line sources spaced with a quarter wavelength, similarly to either vertical or horizontal currents shown in Fig. 2. Obtaining the desired isolation by difference in feed phase and orthogonal orientation of our two sub-arrays are similar to no coupling at cross points of two loops. The proposed IFA array on the circular ground plane can overcome the inherent mechanical drawback of two orthogonal loops in free space. We anticipate that IFA geometrical configurations with vertical and horizontal currents, other than our proposed IFAs, can generate many antenna features, as there are similarities between the IFA array and the orthogonal loop antennas.



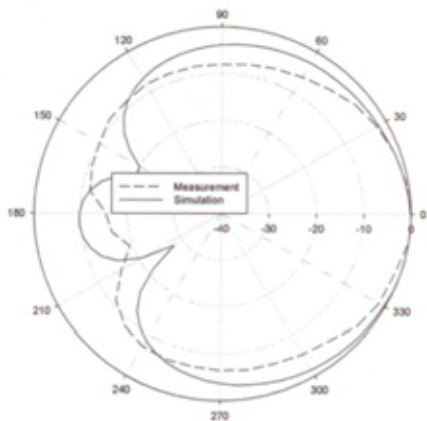
(a) E -plane of Sub-Array 1 (zx plane)



(b) H -Plane of Sub-Array 1 (xy plane)



(c) *E*-Plane of Sub-Array 2 (*zx* plane)



(d) *H*-Plane of Sub-Array 2 (*yz* plane)

Fig. 5. Radiation Patterns of the Proposed Antenna

4. Conclusions

Two inverted-F antenna (IFA) sub-arrays are proposed as a space and polarization diversity antenna in RFID applications. Two 1x2 IFA sub-arrays orthogonally placed on a ground plane can produce horizontal and vertical radiation current flows on radiating conductors of IFAs of each sub-array. It is proposed that return losses and radiation patterns of two sub-arrays may improve the detection rates of RFID tags in port or harbor environments.

References

1. ISO/IEC 18000-7, International Standards,

2004.4.8

2. N. Serikin, M. Jorgenson, K. W. Moreland, S. Chow and T. Willink, "Polarization Diversity in High Frequency Radio Data Systems," *Electron. Lett.*, 1996, 32, (12), pp. 1824-1826
3. A. Adrian and D. H. Schaubert, "Dual Aperture-Coupled Microstrip Antenna for Dual or Circular Polarization," *Electron. Lett.*, Vol.23, pp. 1226-1228, Nov., 1987
4. C. H. Tsao, Y. M. Hwang, F. Kilburg, and F. Dietrich, "Aperture-Coupled Patch Antennas with Wide-bandwidth and Dual-Polarization Capabilities," "in *Proc. IEEE Antennas Propagat. Symp. Dig.*, Syr., New York, June 1988, pp.936-939
5. Y. Gao, C. C. Chiau, X. Chen and C. G. Parini, "Modified PIFA and its array for MIMO terminals," *IEE Proc.-Microw. Antennas Propag.*, Vol.152, No.4, pp.255-259, Aug., 2005
6. S. Arismar Cerqueira, Jr. and L. C. Kretly, "Experimental Analysis of a CDMA Adaptive System Performance," *IEEE Antennas and Wireless Propagation Letters*, Vol.2, pp.356-359, 2003
7. "Computer Simulation Technology (CST) Microwave Studio," ver.4.2, Available : www.cst.com
8. Yikun Huang, Arye Nehorai, and Gary Friedman, "Mutual Coupling of Two Collocated Orthogonally Oriented Circular Thin-Wire Loops," *IEEE Trans. Antennas and Propagation*, Vol. 51, No.6, pp.1307-1314, June, 2003
9. W. L. Stutzman and G. A. Thiele, "Antenna Theory and Design," 2nd ed., John Wiley & Sons, Inc., New York, USA, 1998

Modeling and Analysis of the Interference Potential of Cognitive Radio Devices to Wireless Microphones Operating in TV bands

Ramandeep S Dhillon, Timothy X Brown
Interdisciplinary Telecommunication Program
Electrical and Computer Engineering Department
University of Colorado Boulder, CO 80309-0530
Email: {dhillon, timxb}@colorado.edu

Abstract—The FCC is considering unlicensed spectrum access by cognitive radio devices in licensed bands. The licensed spectrum holders in the TV bands are concerned about the interference potential of these proposed unlicensed devices to the operation of incumbent devices such as TV receivers and wireless microphones. This paper presents an analysis of possible interference to wireless microphones and presents a model for interference based on the concept of an interference contour. The paper also illustrates some of the key interference scenarios based on the proposed interference contour model.

1. Introduction

The FCC is considering allowing unlicensed spectrum access to the licensed bands by new smart radio devices called cognitive radios (CRs) [1]. A CR can operate on licensed bands if they are not being used by licensed users. The FCC is looking at the TV bands as the first set of licensed spectrum bands to be opened up for unlicensed access using CR devices. However, the TV broadcasters have raised concerns over the possibility of CR devices interfering with signal reception on TV receivers as well as wireless microphone systems used in the TV bands. Thus, unlicensed users must show that their devices do not interfere with the licensed devices operating in the TV bands.

While the potential for harmful interference to TV receivers due to the operation of CR devices has been analyzed before in [2], a different analysis is required to ascertain the interference potential to wireless microphones operating in TV bands. Wireless microphones are designed for low power operation as compared to TV broadcast towers and typically utilize bands unoccupied by TV broadcasters in a given geographical region. The wireless microphones are utilized by staff of TV broadcast stations, organizers and performers in concerts and other stage events, commentators and managers at sports events, film production crews, educational institutions, and the agencies of the Federal government. While it is easy to obtain information on VHF-UHF frequencies in use for TV broadcasts in a given region from FCC databases, information on the frequencies used by the wireless microphones are difficult to obtain due to the ephemeral nature of wireless microphone use. This situation requires an analysis of the impact of CR device operation to wireless microphone systems.

In this paper, we develop a model for analyzing the extent of interference to the wireless microphone sys-

tems due to operation of CR devices in their vicinity. The usefulness of the proposed interference model is twofold: first, the model provides a measure of the reduction in the operational area of wireless microphones due to the presence of CR interferers; and second, the model helps in defining signal detection capabilities for CR devices that are required to keep potential interference below a certain threshold.

Section 2 presents the interference model for a coexistent wireless microphone system and an interfering CR device. Section 3 presents an analysis of the various interference scenarios considering the incumbent detection capabilities of the CR interferer and the original communication range of the wireless microphone system in the absence of the interferer. Section 4 describes and analyzes the wireless interference tests that were carried out to ascertain the extent of degradation to wireless microphone operation due to a wideband interferer operating in the same TV band as the wireless microphone. Section 5 presents the concluding remarks on the entire discussion.

2. Interference Model

In this section, we present a model for analyzing interference to wireless microphone systems from nearby CR devices operating in the same TV bands as the microphone systems. The model is based on a geometric analysis of the positions of the wireless microphone and the CR interferer relative to the wireless receiver. Further, the model is presented for noise limited as well as shadow faded scenarios.

2.1 Basic interference contour model

Figure 1 illustrates the concept of interference contour for the operation of a CR device in a region of wireless microphone operation. This model of wireless interference is based on the outage contour models discussed in

[3], [4] and [5]. The analysis here differs in that a CR interferer can carry out sensing of the wireless spectrum to detect and avoid channels used by wireless microphones.

The interference model reflects the relationships of three entities: the wireless microphone which is a licensed transmitter, the receiver of the wireless microphone system which is a licensed receiver, and a cognitive radio interferer. The wireless microphone and the licensed receiver are denoted by T and R and placed at locations (x,y) and $(0,0)$ respectively. The interferer I is placed at a distance S from R on the y-axis i.e. at location $(S,0)$. The licensed receiver is in a fixed location, however the wireless microphone is mobile and as such is assumed to be at an arbitrary location (x,y) . Typically, the interferer is also mobile but we consider a specific moment of time. The path loss exponent experienced by signals transmitted by the wireless microphone and the CR interferer is assumed to be the same at the licensed receiver. As well, all radios are assumed to be placed at the same height from the surface of the earth and as such the antenna height factors cancel out while computing signal to interference (SIR) ratios.

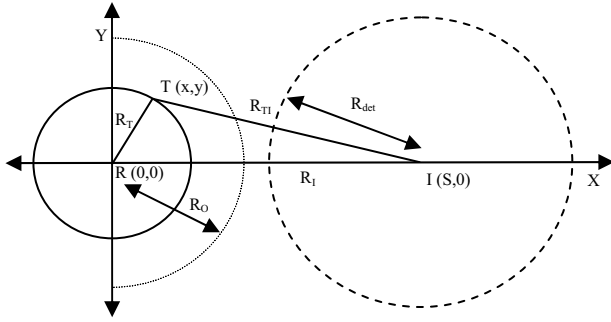


Figure 1 Interference contour model for a single interferer and a single licensed device pair i.e. a wireless microphone system

The following denote the distances between different entities described above:

- R_T is the distance between the wireless microphone and the licensed receiver
- R_I is the distance between the CR interferer and the licensed receiver
- R_{TI} is the distance between the wireless microphone and the CR interferer
- R_{det} is the signal detection range of the CR interferer
- R_O is the communication range of the wireless microphone and the licensed receiver when the interferer is not present

For an acceptable quality of licensed device operation i.e. acceptable quality of audio in wireless microphone

operation, a certain minimum SNIR ratio, Z , needs to be achieved.

$$SINR = \frac{S}{I + N} = \frac{P_T(R_T)}{P_I(R_I) + N} \geq Z \quad (1)$$

where

$P_T(R_T)$ is the wireless microphone power at range R_T .

$P_I(R_I)$ is the interferer power at range R_I .

N is the background noise power.

Assuming there is no interference, $P_I = 0$ and that the wireless microphone is at the edge of the communication range R_O , then (1) reduces to:

$$\frac{P_T(R_O)}{N} = Z \Rightarrow N = \frac{P_T(R_O)}{Z} \quad (2)$$

Substituting N into (1) and following the analysis in [3], [4] and [5], the following relation can be established:

$$R_T = R_I \frac{K^{1/n}}{\left[K \left(\frac{R_I}{R_O} \right)^n + 1 \right]^{1/n}} \quad (3)$$

where

$$K = \frac{P_i G_r W_i L_s}{Z P_t W_t} \quad (4)$$

and

- P_t is the wireless microphone power
- P_i is the CR interferer power
- W_i is the bandwidth of interferer signal
- W_t is the bandwidth of wireless microphone signal
- L_s indicates the system loss factor
- G_r is the net antenna gain between the CR interferer and the licensed receiver
- Z is the threshold / protection ratio of the licensed receiver
- n is the path loss exponent

From (3) we get,

$$R_T = (x^2 + y^2)^{1/2} \leq \frac{S K^{1/n}}{\left[K (S / R_O)^n + 1 \right]^{1/n}} \quad (5)$$

Equation (5) defines a circle that forms the interference contour for T-R communication in the face of an interferer located at a distance S from the receiver. A family of interference contours can be derived for different power levels of the licensed transmitter and the interferer, intended threshold or protection ratio Z and signal bandwidths W_i, W_t .

The new and important aspect of this interference model is the incumbent signal detection capabilities of the CR interferer device as well as the device's ability to avoid using channels where licensed signals have been detected. Considering the path loss, a certain minimum signal power of the wireless microphone is needed at the interferer for the interferer to detect and infer the presence of the licensed device on a certain channel.

$$P_{ii} = \frac{P_t G_t G_i}{(R_{det})^n} > \tau \quad (6)$$

where

τ indicates the threshold of detection
 R_{det} is the minimum distance for detection of wireless microphone signal

If,

$$R_{det} \geq R_{TI} = \left((x-S)^2 + y^2 \right)^{1/2} \quad (7)$$

the CR interferer can successfully detect the wireless microphone signal and so the CR interferer does not transmit thus avoiding interference to an ongoing wireless microphone transmission. Further (7) defines the equation of a circle that indicates the CR detection contour.

Thus, if a wireless microphone falls within the interference contour (5) or detection contour (7), there is no potential for interference to the licensed receiver. However, when the CR interferer transmits the effective communication range for the wireless microphone is reduced to R_T . Thus only a fraction R_T^2 / R_O^2 of the original area can now be used for the licensed service.

2.2 Incorporating fading effects

Next we incorporate the effects of fading into the propagation characteristics of our interference model. In a wireless channel, fading can potentially reduce the communication potential by reducing the signal strength at the receiver. The fading can be essentially of two types: fast fading due to multi-path and slow fading due to obstacles in the path of the signal. The slow shadow fading in particular is important in indoor environments where obstacles in the path of the signal can result in a deep fade that remains for the entire duration of a transmission. Shadow fading is often modeled as a multiplicative factor, S_σ , that in decibels has zero mean and standard deviation σ and scales the received power [10]. Incorporating S_σ into (4) we get

$$K = \frac{P_t G_r W_i S_{\sigma_i} L_s}{Z P_i W_t S_{\sigma_t}} \quad (8)$$

where

S_{σ_i} is the shadow fading factor for the interference signal received at the licensed receiver
 S_{σ_t} is the shadow fading factor for the wireless microphone signal received at the licensed receiver
 $S_{\sigma_{ti}}$ is the shadow fading factor for the wireless microphone signal received at the CR interferer and affects the incumbent signal detection capabilities of the CR device.

The shadow fading factors affect (3) as K now becomes dependent on the separation between the wireless microphone, licensed receiver and the CR interferer. For each value of R_i , the shadow fading factors result in a different K and impact R_T .

3. Interference Analysis

This section presents an analysis of the potential interference to the wireless microphone system on the basis of the interference-detection contour model developed in Section 2. First we utilize a set of geometric scenarios based on the location of the wireless microphone and the CR interferer relative to the licensed receiver to determine the impact of interferer's location. Next, we analyze the loss of operational area of the wireless microphone system due to the presence of the interferer. Lastly, we utilize our analysis to define the operating characteristics of a CR device for it to avoid interference to wireless microphone systems.

3.1 Analysis of interference scenarios

The interference contour model as described in Section 2 indicates that as the CR interferer moves closer to the licensed receiver, the effective communication range of the wireless microphone decreases. However, if the wireless microphone is within the detection range of the CR interferer, the interferer would choose another channel for communication and as such would not interfere with the wireless microphone system. A geometric analysis of the interference model presents four different scenarios based on the positioning of the interference contour (R_T), the detection range (R_{det}) and the original communication range (R_O) of the wireless microphone system. The four scenarios are as follows: (a) the detection range of the CR interferer does not intersect the original communication range of the wireless microphone system; (b) the detection range of the CR interferer intersects the original communication range but not the interference contour; (c) the detection range of the CR interferer intersects the interference contour; (d) the detection range of the CR interferer encompasses the original communication range of the wireless microphone system.

Figures 2 (a), (b), (c), (d) illustrate the four scenarios, where the shaded areas indicate the lost coverage of the

wireless microphone system due to interference from the CR device. The interference contour in the figures below is indicated using a solid circle, the incumbent signal detection range of the CR interferer is indicated using a dashed circle, while the communication range of the wireless microphone system (i.e. the licensed T-R pair) in the absence of an interferer is indicated using a dotted circle. Next we discuss each of the four scenarios and their implications on the operation of the wireless microphone system as well as the CR device.

Figure 2 (a) illustrates the scenario where the incumbent signal detection range of the CR interferer does not intersect the original communication range of licensed T-R pair. In such a situation, the CR device causes interference at the licensed receiver resulting in some reduction of the original communication range. The extent of interference and corresponding loss in licensed communication area would depend upon the transmitter power levels of the interferer and the distance between the interferer and the receiver. If the interferer power levels are low or if the separation between the interferer and receiver is large, the resulting interference may not be perceived as harmful by the licensed incumbents.

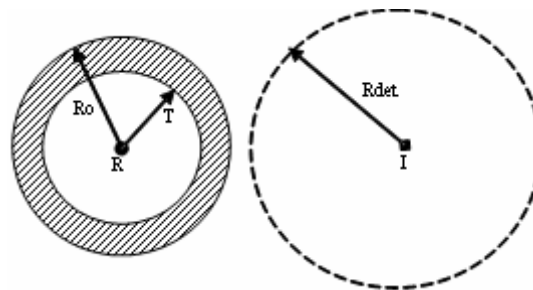


Figure 2 (a) No intersection of R_O and R_{det}

Figures 2 (b) and 2 (c) illustrate the scenarios where the incumbent signal detection range of the CR device intersects the original communication range and the interference contour of the licensed T-R pair respectively. As the interferer moves closer to the licensed receiver the interference causes greater loss of communication area for the licensed T-R pair. However, as the detection range intersects with the original communication range, the effective loss of communication area reduces as the area common to the detection range and the communication contours increases. On the contrary, the intersection of the detection range and the interference contour provides no additional benefits in terms of area loss reduction. Nevertheless, the scenarios (b) and (c) present a better situation for the wireless microphone systems as a microphone located within the detection range of a CR interferer induces the interferer to refrain from transmitting thus avoiding any interference to the licensed receiver.

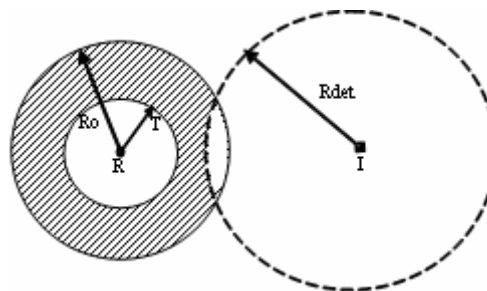


Figure 2 (b) Intersection of R_O and R_{det}

Figures 2(d) illustrates the best case scenario for CR device operation where the detection range of the CR completely encompasses the original communication range of the licensed T-R pair. Now, the CR device will almost always detect the presence of the wireless microphone and then refrain from transmitting at the spectrum band that the microphone is using thus avoiding interference to the licensed receiver. However, for this scenario to be predominant in a CR network deployment, it is imperative that a CR device have a highly sensitive detector.

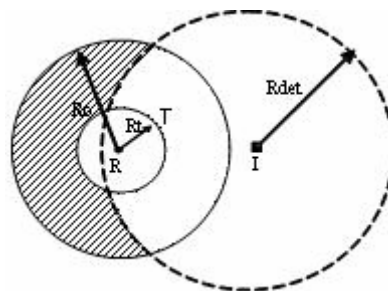


Figure 2 (c) Intersection of R_T and R_{det}

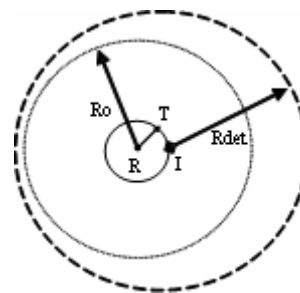


Figure 2 (d) R_{det} overlaps R_O

3.2 Loss of operational area due to interference

The interference caused by the CR device reduces the effective communication area of the licensed T-R pair, i.e. it reduces the coverage of the wireless microphone system. This loss in area can be used to justify or refute the deployment of any set of CR devices as well as to determine the transmission parameters of CR devices when they are operating in the licensed TV bands. We determine the potential area loss by simulating the interference scenarios discussed in Section 3.1. For the simulation, we developed an interference modeling software in C++ and carried out a geometric analysis of the four possible scenarios for potential area loss (see details in Appendix A). Figure 3 illustrates a set of scenarios comparing the loss of operational area of a wireless microphone system caused by interference from a CR device and a traditional radio.

Figure 3 (a) and (b) compare the traditional area loss (i.e. for an interferer without spectrum sensing capabilities) with the area loss caused by a CR interferer with different detection capabilities (R_{det}). The plots are for the following parameters: $R_O = 39.24$ m, $K = 3.16$, $Z = 10$ dB, $n = 2$ for Figure 3 (a), $n = 4$ for Figure 3 (b), $W_i = 100$ kHz, $W_i = 1$ MHz (i.e. a wideband interferer) and represent the typical values for a wireless microphone system. We ignore the impact of shadow fading in these plots for the sake of simplicity (shadow fading is separately addressed in 3 (e)).

Figure 3 (a) and (b) indicate that as a traditional interferer (i.e. one without CR capabilities) moves closer to the licensed receiver it increasingly causes greater loss of operational area and eventually reduces the operational area to zero. However, unlike the traditional interferer, a CR interferer reduces the loss of operational area to a wireless microphone system as it moves closer to the licensed receiver. Initially, as the CR moves closer to the licensed receiver, the area loss increases as the wireless microphone is potentially outside the detection range of the CR device. However, once the detection range intersects the original communication range of the wireless microphone or the interference contour (Figure 2 (b), (c)), the area loss starts decreasing and eventually reduces to zero (0% loss). Further, as the detection range of the CR device is increased, the CR causes considerably less interference to the wireless microphone system. This reinforces the need to define the detection capability of the CR device as one of the most important design considerations for avoiding interference to licensed devices.

Figure 3 (c) and 3 (d) illustrate the loss of operational area due to interference caused by a CR device and a traditional radio respectively for different values of K as determined from (4). The values of K used in the plots were obtained by varying the value of Z while the rest

of the parameters were kept the same as in 3 (a). The value $K = 3.16$ is typical for an interference scenario involving a wireless microphone system ($P_i = 15$ dBm), a low power interferer ($P_i = 20$ dBm) and a protection ratio of $Z = 10$ dB. As can be seen in the plots, for small separation between the interferer and the licensed receiver (R_i), the amount of interference is identical irrespective of the value of K . However, as the interferer moves away from the licensed receiver different K values result in different amounts of interference to the wireless microphone system. As the value of K increases, the interferer causes lesser loss of operational area for the wireless microphone system. This situation reflects the importance for a system design that increases the value of K i.e. higher the value, lesser is the loss of operational area due to interference. Further, the CR interferer performs significantly better than a traditional radio as it can vacate the licensed band on detecting wireless microphone transmission.

Figure 3 (c) further illustrates that even the CR device causes significant interference at small values of K . This situation indicates that large detection ranges of CR devices may not be enough to prevent interference to wireless microphone systems. As such a strict bound on the value of K is needed for a typical interference scenario consisting of a CR device and a wireless microphone system. Since the onus of avoiding interference is with the CR device, it needs to ensure either a large W_i or a small P_i in (4) in order to keep a lower bound on the value of K .

Figure 3 (e) incorporates the shadow fading factors into the interference model based on (8). The plot illustrates the variation in area loss in both traditional and CR interferer scenarios due to variations in S factors at every new value of R_i (and hence a different K value at each new location). This situation indicates that the area loss could be more severe or on the other hand less intense as compared to the loss predicted by a model without shading fading.

Figure 3 (f) plots the incumbent signal detection range of a CR device that is needed to ensure that the loss of operational area of the wireless microphone system remains within a certain threshold (maximum allowed area loss). The plot compares the interference scenarios for $n=2$ (free space) and $n=4$ (typical indoor environment) for $K=3.16$. The plot provides us a useful tool to devise the detection range of a CR device required to keep the interference within the acceptable limits. However, any CR system design intending to reduce interference would be eventually a combination of R_{det} and K factors.

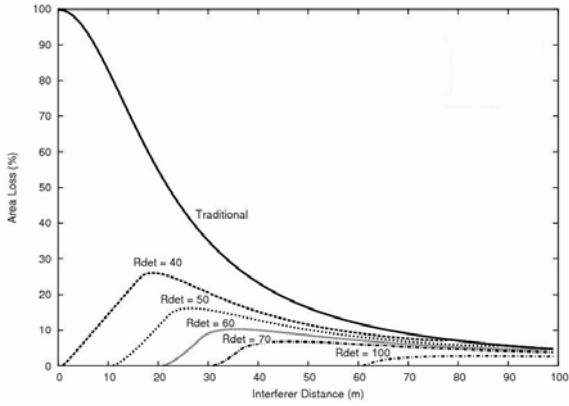


Figure 3 (a) Operational area loss versus distance to interferer, $n=2$, $K=3.16$

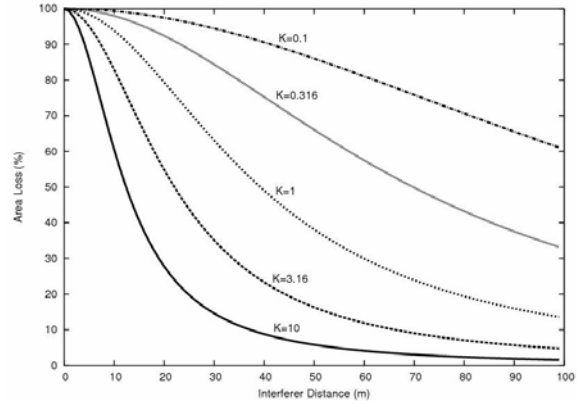


Figure 3 (d) Traditional radio for different values of K , $n=2$

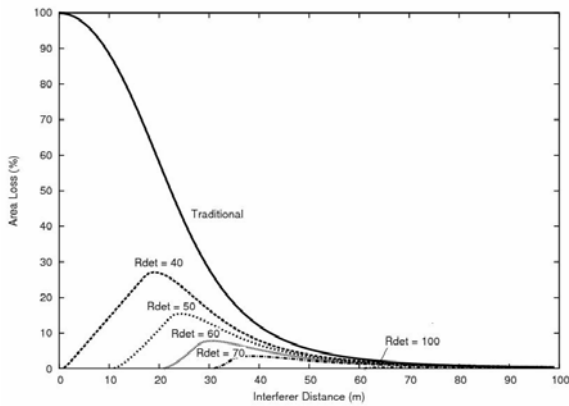


Figure 3 (b) Operational area loss versus distance to interferer, $n=4$, $K=3.16$

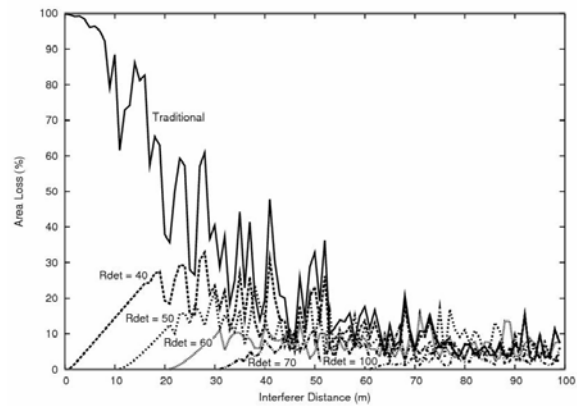


Figure 3 (e) Operational area loss versus distance to interferer impacted by shadow fading, $n=2$

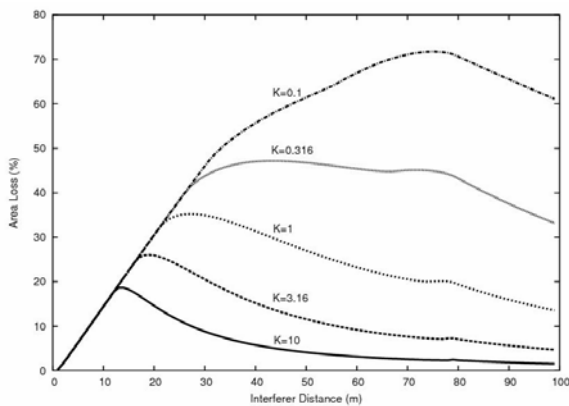


Figure 3 (c) CR for different values of K , $n=2$, $R_{det}=40$ m

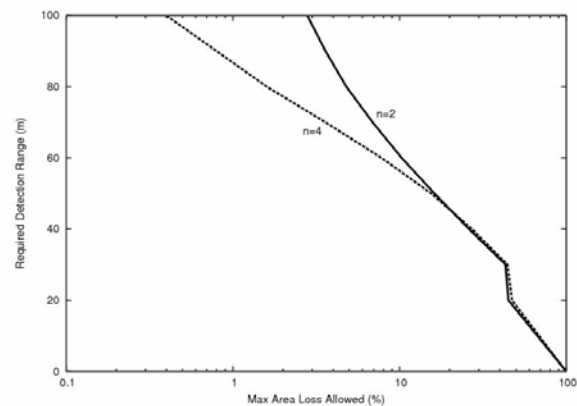


Figure 3 (f) Required detection range for specified maximum allowed area loss

3.3 CR device characteristics for reducing interference

Based on our analysis of potential interference caused by a CR device to a wireless microphone system, we can define the typical characteristics of a CR device needed to reduce or avoid interference. The required characteristics are as follows:

- (a) The CR device needs to have a detection range that ensures that the worst case operational area loss remains below a certain threshold for different values of K and n . In order to ensure a large detection range, the CR device requires a highly sensitive RF front end.
- (b) The CR device needs to ensure that its transmissions do not exceed the protection ratio at the licensed receiver. This requirement translates into either the use of low power CR (i.e. lower K) devices or the utilization of an appropriate power control mechanism on the CR device.
- (c) The CR device can reduce the interference potential to wireless microphones by using wideband transmissions or by employing appropriate modulation schemes, in effect increasing K . The discussion of these techniques is out of scope of the current paper.

3.4 Analysis of shadow fading

The shadow fading factors S_{oi} and S_{oi} (as defined in section 2.2) indicate that the interference model when applied to the same set of wireless microphone and CR devices with the same set of transmission parameters and separation distances (R_T , R_I) would result in different levels of interference due to the randomness of the physical environment. A third shadow fading factor S_{oi} indicates the signal fade between the wireless microphone and the CR interferer, and affects the signal detection capability of the CR device.

A certain level of correlation can be established between the three factors: S_{oi} and S_{oi} would have a positive correlation if an obstacle exists in the line of sight of the licensed receiver, S_{oi} and S_{oi} would have a positive correlation if the CR device is in the non-line-of-sight configuration with respect to the wireless microphone system, and the S_i and S_{oi} would have positive correlation if the wireless microphone signal faces shadowing fading. Typically, the wireless microphone is operated close to the licensed receiver and as such has a line-of-sight path to the receiver. This situation indicates that the most significant correlation would exist between S_{oi} and S_{oi} based on the location of the CR interferer. This correlation is desirable as it indicates that a CR device that is less likely to detect the wireless microphone signal is less likely to cause interference on the licensed receiver. This result follows from the fact that the de-

tection range of the CR device would be greater than the minimum interferer distance R_I that can cause harmful interference on the receiver.

4. Interference Tests

In this section we describe the set of interference tests that we carried out to determine the impact of wideband interference on a wireless microphone system. These interference tests allow us to verify the assumptions in defining our interference model.

4.1 Interference tests

We carried out a set of interference tests for a SennHeiser eW 100 G2 wireless microphone system as shown in Figure 4 below. The wireless microphone system consisted of a lavalier microphone with a body-pack transmitter and a true diversity receiver with two antennas and two radio chains [9]. The system worked on Frequency Modulation (FM) with a bandwidth of 100 kHz and peak transmitter power of 30 mW (15dBm) [9]. We operated the microphone system on TV channel 5 with a subchannel frequency of 542.350 MHz.



Figure 4: SennHeiser Wireless Microphone System

An interference source was constructed using a Hewlett Packard E4400B Signal Generator. This interferer behaved like a traditional radio and did not have the incumbent signal detection capabilities of a CR device. The interferer generated a 1 MHz wide FM signal using a noise-like modulation source. This noisy wideband FM signal represents a spread spectrum CR signal that can potentially interfere with the microphone system.

Figure 5 below illustrates the setup for the interference experiments. Both the wireless microphone and the interferer were placed equidistant (3 meters each) from the receiver in a line-of-sight configuration. This placement is in accordance with the interference contour model discussed in Section 2 where a wireless microphone acts as the licensed transmitter and wireless receiver acts as the licensed receiver. Further the placement ensures that the signals generated by both the

microphone and the interferer experience the same free space path loss while reaching the wireless receiver.

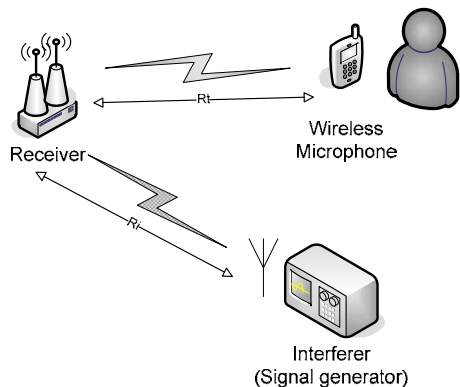


Figure 5: Interference Test Setup

The experimental procedure consisted of generating different levels of interference by varying the amplitude of the interference signal while using the wireless microphone system for voice recording. We varied the interferer signal amplitude in the range -100 dBm to +20 dBm using increments of 10 dBm each. Further, we analyzed the quality of the voice recording based on human perception of acceptable “pleasant-to-the-ears” audio. Subsequently, we identified a range of interest of the interference signal to narrow down the scope of interference tests for finer variations of interferer signal amplitude. In this range of interest we carried out interference tests using amplitude variations of 2 dBm each for the interferer signal. We repeated the set of interference tests 5 times.

4.2 Test Results

Based on the first set of interference tests we identified a range of interest between 0 dBm to 20 dBm of interferer signal amplitude. The test results within this range indicated a significant degrade in the audio quality when the interferer signal amplitude exceeded 10 dBm. Since the wireless microphone transmits at 15 dBm, the above result indicates that a minimum signal to interference (SIR) ratio of 5 dB is required for bearable audio quality. Even though at 10 dBm interference the audio quality was comprehensible from a human perspective, considerable amount of “hissing” noise was heard in the silent periods between voice transmissions. This quality of sound would be unacceptable to audiences of concerts and sports events especially when aired on loud broadcast systems.

The interferer signals of 14 dBm or higher completely overwhelmed the wireless receiver and a speaker’s voice was barely audible and comprehensible in the midst of noise. However, on the lower end of interference, the audio was loud and clear when the interferer signal was restricted to 6 dBm or lesser. The audio

quality at 6 dBm interference indicated that a minimum SIR ratio of 9 dB would be needed for wireless microphone operation in the face of CR interferers.

4.3 Interference contour analysis

Based on the interference contour model discussed in Section 2, we use (3) and (4) to analyze the experimental results of Section 4.2. We first determine the value of K as given in (4) for the given set of microphone and interferer devices and then utilize this value to predict the interference contour for the wireless microphone. The wireless microphone under test transmitted at 15 dBm. The threshold SIR ratio for acceptable audio quality was experimentally determined to be 9 dB. We utilize a 10 dB value of SIR for further protection. The path loss exponent n is assumed to be 2 for free space propagation and 4 for indoor environments. A typical wireless microphone system utilizes a bandwidth of 100 kHz while we assume 1 MHz interferer bandwidth. Based on the above discussion we change interferer power to obtain different values of K .

Figure 6 below illustrates the change in interference contour with increase in interferer power. For this plot, we only consider the interferer power of 0 dBm to 20 dBm as identified as the range of interest in Section 4.2. As the interference power exceeds the wireless microphone transmit power, the interference contour decreases sharply till it becomes impossible for the wireless microphone to communicate with the receiver. For example, for an interferer placed 40 meters from the receiver, the wireless microphone needs to be within 2.25 meters of the receiver for an interferer power level of 20 dBm for $n=4$. Such a situation makes it very difficult for any unlicensed devices to operate close to the wireless receivers without causing significant interference.

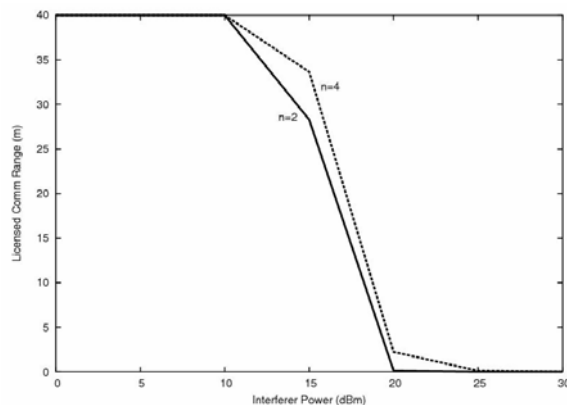


Figure 6: Change in interference contour for wireless microphone with increasing interference

The situation discussed above eliminates the use of any unlicensed devices in most concert halls and sports stadiums close to the presenters using the wireless microphones. However, a device with CR capabilities considerably improves the situation in this regard by increasing the operational area of a microphone system beyond the interference contour (as discussed in Section 3). Thus, the use of CR devices can remedy the interference scenario presented in Figure 6.

5. Conclusion

In this paper we carried out an analysis of the potential of interference to wireless microphones due to the operation of cognitive radio devices in licensed TV bands. We observe that irrespective of the licensed signal detection and protection capabilities of the CR devices, these devices will cause some interference to the wireless microphone systems, i.e. it is not possible to eliminate interference altogether by using cognitive spectrum sensing techniques.

We presented a model for assessing the interference potential to wireless microphones based on the concept of an interference contour and a signal detection contour of a CR device. The simulation results based on the model indicate that the interference can be reduced to less than 30% of that caused by traditional radio devices. These results require an appropriate selection of radio parameters such as the detection range of the CR device and the use of power control techniques. We also carried out interference tests with wireless microphone equipment and obtained a minimum protection ratio of 10 dB for CR interference to microphone systems.

The interference model in its current shape has several limitations: (a) the model considers interference to a wireless microphone system from only one CR device which will not be the case in an actual CR network (i.e. multiple CR interferers need to be considered), (b) the model does not account for the signal modulation techniques that could reduce the interference potential of the CR devices, (c) the model assumes circular antenna patterns which is an approximation of actual omnidirectional patterns. All the above limitations of the model present opportunities for further research.

Appendix A: Simulation Methodology

The appendix describes the simulation methodology used for evaluating the interference potential of CR devices to wireless microphone systems based on the interference model developed in the paper (Section 2, 3). The simulations were carried out by building a simulation tool in the C++ programming language. The pseudo-code is presented here in the form of an algorithm used for evaluating loss of operational area of a wireless microphone system due to a CR interferer.

User Inputs:

- R_{det} : the detection range of the CR device in meters
- R_{I-max} : the maximum distance separating the CR interferer from the licensed receiver
- Z : the protection ratio of the licensed receiver in terms of the signal to interference ratio
- n : the path loss exponent to be used

Algorithm

Step 1: Compute R_O i.e. the original communication range of the CR device.

Step 2: For each value of R_I in the range 0 to R_{I-max} :

- Generate random values for S_{oi} and S_{ot} .
- Compute the value of K using the input parameters and values described in Section 3.2.
- Compute the value of R_T for the current values of R_I and K as described in Section 2.
- Determine if R_O and R_{det} overlap and assign a value to constant C1 accordingly:

$$C1 = 0 \quad \text{if } (R_I < \| R_O - R_{det} \|) \text{ i.e. the circles overlap}$$

$$C1 = 1 \quad \text{otherwise}$$
- Determine if R_O and R_{det} intersect and assign a value to constant C2 accordingly:

$$C2 = 0 \quad \text{if } (R_I > (R_O + R_{det})) \text{ i.e. the circles do not intersect}$$

$$C2 = 1 \quad \text{otherwise}$$
- If $C2 = 1$ i.e. the circles intersect: Find the common area between the two circles (R_O and R_{det}) i.e. the area of the football shaped common area between the two circles (as obtained in Calculation 1 below). Denote it as $A_{ro} + A_{rdet}$.

If $C1 = 1$ i.e. the circles do not overlap:

Determine if R_T and R_{det} overlap:

if $(R_I < \| R_T - R_{det} \|)$ then the circles overlap and then the common area between the two circles is simply the area of the circle R_T (utilize an approach similar to Calculation 1). Denote it as A_{rt} .

else if circles do not overlap, determine if they intersect:

if $(R_I < (R_T + R_{det}))$ the circles intersect and then determine the common area between the two circles (utilize an approach similar to Calculation 1). Again denote it as A_{rI} .

Step 3: Determine the area common area between R_O and R_{det} that does not include common area between R_T and R_{det} . Denote it as A_c . $A_c = A_{ro} + A_{rdet} - A_{rI}$.

Step 4: Determine the loss of operational of the wireless microphone system as follows:
Area loss, $A_l = C1 * (\pi (R_O^2 - R_T^2)) - C2 * A_c$

Step 5: Determine original communication area of the wireless microphone systems as $A_o = \pi * R_O^2$

Step 6: Determine % of area loss using A_l / A_o .

Step 7: Compare the area loss due to CR with area loss due to traditional interferer. The area loss of traditional interferer is given by $A_{trad} = \pi (R_O^2 - R_T^2)$

Calculation 1: Here we describe the procedure to calculate the common area between the circles of radius R_O and R_{det} . Figure 7 below illustrates the key concepts utilized in the calculation.

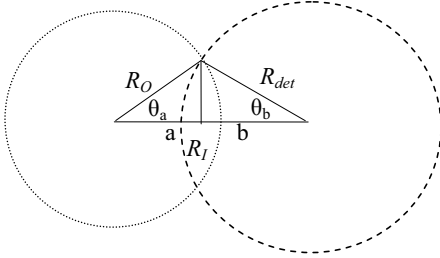


Figure 7: Intersection of R_{det} & R_O circles

From Figure 7 we obtain the following:

$$a = \left(\frac{R_O^2 - R_{det}^2 + R_I^2}{2R_I} \right)$$

$$b = \left(\frac{R_{det}^2 - R_O^2 + R_I^2}{2R_I} \right)$$

$$\theta_a = 2 \cdot \cos^{-1}(a / R_O)$$

$$\theta_b = 2 \cdot \cos^{-1}(b / R_{det})$$

$$A_{ro} = \frac{R_O^2}{2} (\theta_a - \sin(\theta_a))$$

$$A_{rdet} = \frac{R_{det}^2}{2} (\theta_b - \sin(\theta_b))$$

The common area between the two circles is given by $A_{ro} + A_{rdet}$.

References

- [1] Federal Communications Commission, "Facilitating Opportunities for Flexible, Efficient, and Reliable Spectrum Use Employing Cognitive Radio Technologies", *Notice of Proposed Rule Making and Order, Docket No. 03-108*, Dec 30, 2003.
- [2] Timothy X Brown, "A harmful interference model for unlicensed device operation in licensed service bands", *Journal of Communications*, Vol. 1, No. 1, April 2006.
- [3] IEEE LAN/MAN Standards Committee, "Part 22.1: Enhanced Protection for Low-Power, Licensed Devices Operating in Television Broadcast Bands", *IEEE Standard for Information technology - Telecommunications and information exchange between systems -Local and metropolitan area networks - Specific requirements*, 2007.
- [4] B.C. Jones and D.J. Skellern, "Interference Modelling and Outage Contours in Cellular and Microcellular Networks", *2nd MCRC International Conference on Mobile & Personal Communication Systems*, pp 149--158, Adelaide, Australia, 10-11 April 1995.
- [5] Cook, C., "Modeling Interference Effects for Land-Mobile and Air-Mobile Communications", *Communications, IEEE Transactions on*, vol.35, no.2, pp. 151-165, Feb 1987.
- [6] Cook, C., "Optimum Deployment of Communications Relays in an Interference Environment", *Communications, IEEE Transaction on*, vol.28, no.9, pp. 1608-1615, 1980.
- [7] Iyer, A., Rosenberg, C., and Karnik, A. 2006. "What is the right model for wireless channel interference?", *In Proceedings of the 3rd International Conference on Quality of Service in Heterogeneous Wired/Wireless Networks* Waterloo, Ontario, Canada, August 07 - 09, 2006.
- [8] Hartman A., and Reihl E., "Mitigating the Effects of Unlicensed Devices on Wireless Microphones", *IEEE 802 Plenary Tutorials*, November 14-18, 2005, Vancouver, B.C., Canada, Tutorial #2, Nov 14, 2005.
- [9] Sennheiser, "evolutionwireless G2 100 Series Product datasheet", <http://www.sennheiserusa.com/newsite/>.
- [10] Rappaport T.S., "Wireless Communications: Principles and Practice," *Prentice Hall Communications Engineering and Emerging Technologies Series, 2nd Edition*, 2002.
- [11] Gudmundson, M., "Correlation model for shadow fading in mobile radio systems," *Electronics Letters*, vol.27, no.23, pp.2145-2146, 7 Nov 1991.

High-Resolution Propagation Measurements using Conventional EMC Test Antennas—A Numerical Study

Robert T. Johnk, Senior Member, IEEE
Institute for Telecommunication Sciences (NTIA/ITS)
Theory Division (ITS.T)
325 Broadway
Boulder, Colorado USA
Contact: bjohnk@its.bldrdoc.gov

Abstract: *This paper explores the possibility of using common types of electromagnetic compatibility (EMC) test antennas to perform high-resolution time-domain propagation measurements. The objective of this research is to provide wireless engineers with a tool to perform propagation measurements using a combination of commercial-off-the-shelf EMC test antennas and a stepped-frequency measurement system such as a vector network analyzer. Numerical simulations are used to model propagation path transmission with biconical antennas, log-periodic dipole arrays, and dipoles. A two-step measurement procedure and an efficient data processing sequence are used to generate high-resolution time-domain waveforms. The results are promising, and demonstrate that high-resolution waveforms can be obtained using models of conventional, low-frequency EMC antenna types.*

1. Introduction

Time-domain measurements have been used to characterize short-range propagation characteristics of electromagnetic compatibility (EMC) radiated emissions test sites [1]–[3] in the frequency range of 30 to 1000 MHz. Phase-linear transverse electromagnetic (TEM) horn antennas were used to obtain high-resolution transmission data that permitted the isolation of nearby scattering events, and the assessment of site quality. While TEM horns have optimized time-domain impulse response characteristics, one significant drawback is limited commercial availability.

A question that naturally arises is: can high-resolution time-domain measurements be carried out using commercial off-the-shelf (COTS) EMC antennas, such as biconical dipoles, log-periodic dipole arrays (LPDA), and dipoles? The answer to this question is not simple. These antenna types are not optimized for time-domain measurements, and they have temporally-extended impulse responses that prevent the separation and identification of reflections from nearby scatterers. To achieve a high-resolution capability that enables separation of these reflections, we must reduce the duration of the antenna impulse response.

One way to reduce the duration of the impulse response is to use a combination of either a free-space or a quasi-free space reference and signal processing. A free-space reference is obtained from a transmission measurement between a pair of antennas without reflections from nearby scatterers, such as ground, buildings, or trees. Advances in EMC antenna metrology [4] show it is possible to obtain a quasi-free space transmission over an open-area test site using a vector network analyzer (VNA), stepped-frequency measurements, low-reflectivity polyvinyl chloride (PVC)

pipe towers, and time-domain signal processing. Given the stability and precision of VNA measurements, we might be able to use the free-space reference data in combination with our in-situ propagation measurements to obtain high-resolution waveforms that permit the identification and location of nearby scatterers.

To simulate the proposed measurement procedure, Numerical Electromagnetics Code (NEC-2) [5] is used to simulate a two-antenna transmission in both free space and over a metallic ground plane. NEC-2 is a public-domain electrodynamics modeling software package based on method-of-moments (MoM) code. We simulate a VNA measurement by stepping the transmitted frequency over a wide range, and compute the magnitude and phase of the resulting s-parameters. The resulting transmission data is post-processed to produce high-resolution time-domain waveforms. Three antenna types are investigated: 1) a biconical dipole, 2) a dipole, and 3) a log-periodic dipole array. The simulations look promising, and demonstrate that high-resolution time-domain waveforms can be obtained using all three antenna types.

2. NEC Antenna Models

Three different wire antenna models were constructed as shown in Figure 1.

The first model, labeled a), is a biconical antenna. This model closely approximates the dimensions of commercially available biconical antennas. A pair of identical antennas is used to model the transmission measurements. A delta-function voltage gap source is used with a 200-Ohm source resistance on the transmit side, and

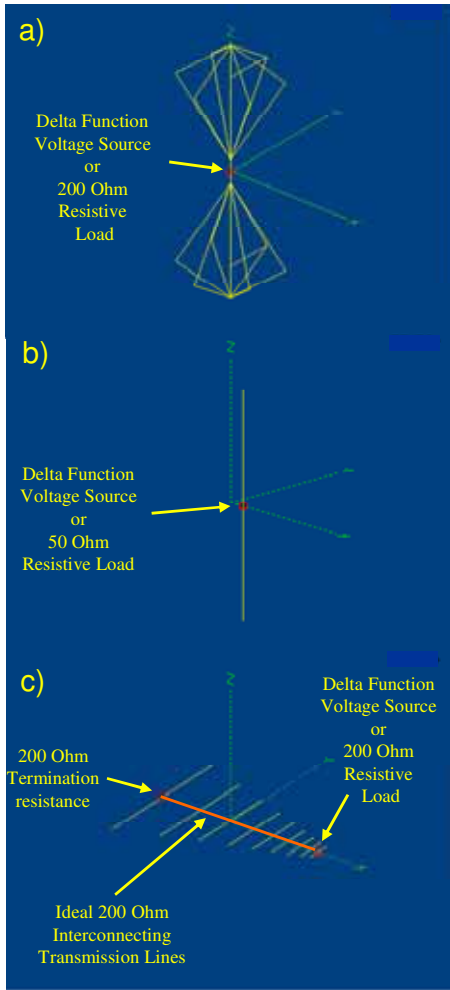


Figure 1. NEC MoM models for three antenna models: a) biconical, b) dipole, and c) log-periodic dipole array.

a 200-Ohm load resistance at the receive antenna termination. Balun effects are not incorporated in this study.

The second antenna model, labeled b) in Figure 1, is the dipole. This antenna has 50-Ohm source and termination resistors, and it has a length of 1 m and a diameter of 6.4 mm.

The third antenna model, labeled c) in Figure 1, is a log-periodic antenna. This antenna is designed to operate over the frequency range of 200 to 1000 MHz. This model approximates the behavior of commercially-available LPDA antennas. The antenna was designed using LPCAD (log-periodic dipole array software) [6], which is a freeware package for the design of log-periodic antennas. The resulting array is 0.9-m long and has 9 dipole elements. The elements are center-fed with ideal, 200-Ohm transmission lines. The interconnections are transposed at each element for correct phasing. Transmission line interconnection is a standard NEC-2 feature [7].

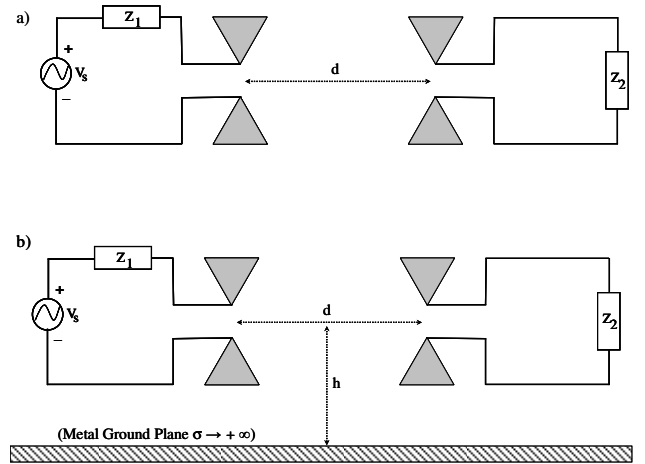


Figure 2. Two antenna setups. a) Free-space environment. b) Over an infinite, perfectly conducting ground plane.

3. Simulation Geometries

Figure 2 shows the configuration geometries for the two-step simulation procedure that is carried out. In the first configuration, labeled a), the antennas are placed in a free-space environment with the antennas aligned in the same plane at a separation d . In the second configuration, labeled b), the antennas are placed at a height h over a perfectly conducting ground plane of infinite extent.

NEC is configured to step the source frequency over a user-specified range, and the voltages and currents at the transmitting and receiving antenna ports are computed at each of the stepped frequencies and stored for post-processing.

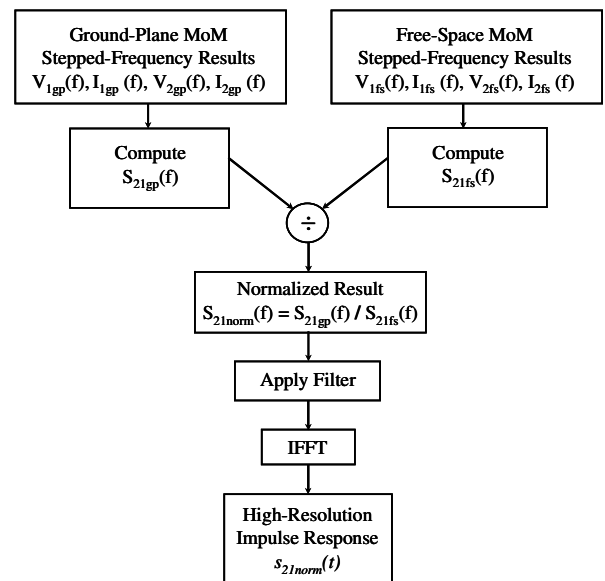


Figure 3. Signal processing sequence to obtain high-resolution time-domain waveforms.

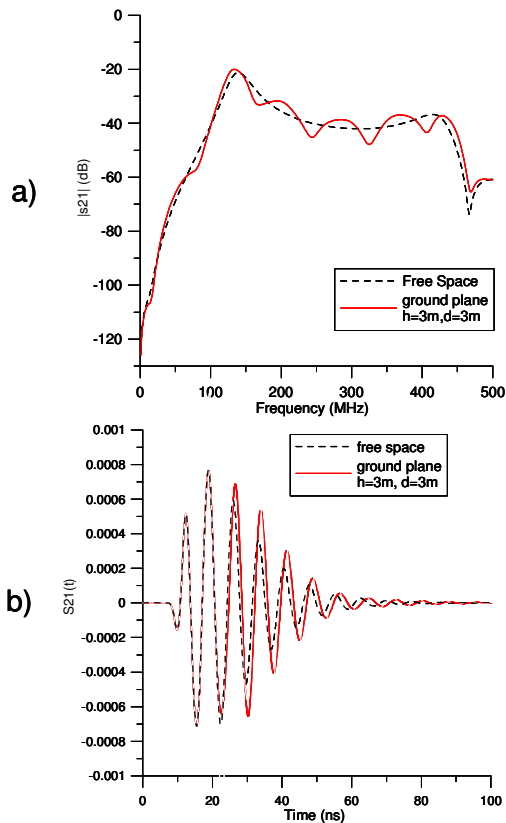


Figure 4. a) Free-space and ground-plane transmission results for two dipoles with $h=d=3$ m. b) Transformed time-domain responses.

4. Signal Processing

Figure 3 shows the signal processing sequence used to generate high-resolution time-domain waveforms. The first step consists of taking the stepped-frequency port voltages and currents obtained from the two simulations, and converting them to s-parameters using equations provided in [8]. In the second step, the ground-plane s-parameters are divided by the free-space s-parameters yielding a normalized result $S_{21norm}(f)$. This division is deconvolution [9]; and, as will be seen, it significantly reduces the effect of the antennas. Next, a Kaiser-Bessel window [10] provides an amplitude taper to the normalized s-parameters to reduce Gibb's ringing. In the final step, an inverse fast Fourier transform (IFFT) is applied to $S_{21norm}(f)$ to yield a high-resolution time-domain waveform $s_{21}(t)$.

Figures 4 and 5 illustrate this process. Figure 4 shows the magnitude of S_{21} between two dipoles with a separation of 3 m in free space, along with corresponding results 3 m above a ground plane. The ground plane introduces amplitude scalloping that is a result of interference between the direct antenna-to-antenna coupling and the ground reflection.

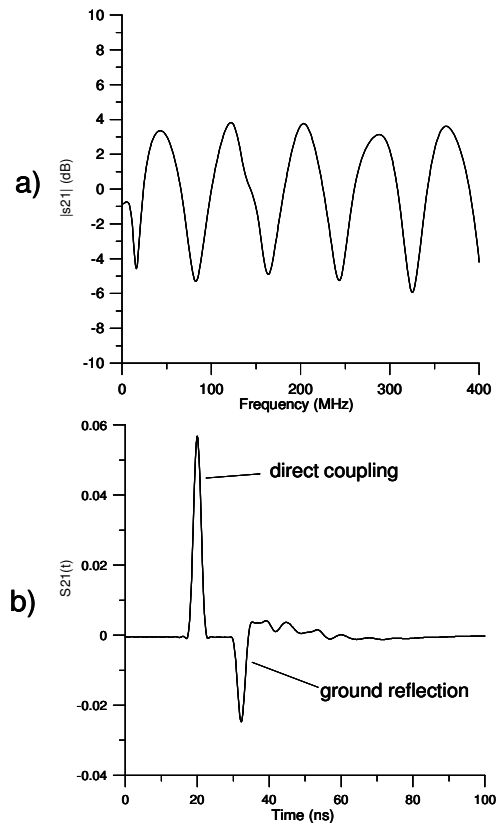


Figure 5. a) $|S_{21norm}|$ for two dipoles with $h=d=3$ m. b) Transformed time-domain response with a 20-ns time delay added.

The time-domain responses are identical until the ground bounce arrives 12 ns after the onset of the waveforms. The free-space and ground-plane cases have similar responses with a single packet that initially rises to a maximum amplitude, and decays afterwards. The direct and ground bounce components are not separable in the time domain. This is due to the extended impulse response of the dipoles.

If we now divide the ground-plane transmission with the free-space results, we obtain the amplitude spectrum shown in Figure 5 a). The normalization removes most of the antenna effects and “flattens” the amplitude spectrum. Prior to normalization, the transmission amplitude exhibits 100-dB variations. The normalization reduces the variation to approximately 10 dB.

Figure 5 b) shows the dramatic improvement in resolution that results from normalization. The direct and ground-reflected components are distinct and separable. The polarity of the ground-reflected component is reversed, which is expected for horizontally-polarized dipoles over a metal ground plane.

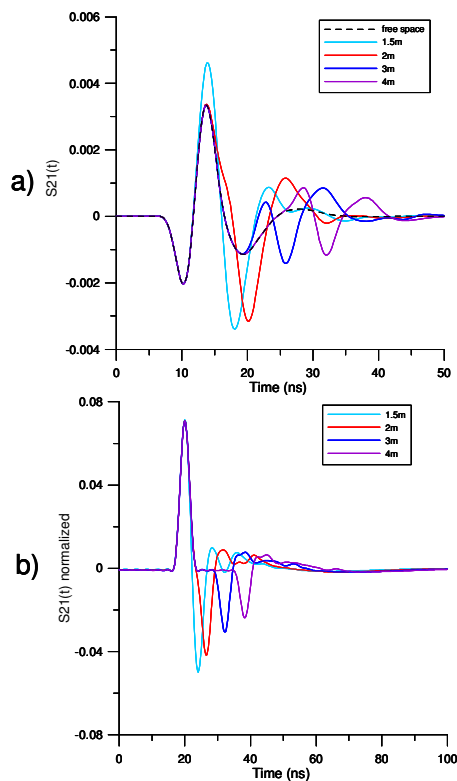


Figure 6. a) Free-space and ground-plane impulse responses for horizontally-polarized biconical antennas with $d=3$ m and $h=1.5$ m, 2 m, 3 m, and 4 m. b) Normalized results with a 20-ns time delay.

5. Results

Figures 6 through 11 summarize time-domain results obtained for the three types of antennas. For the results presented here, a separation distance of 3 m is used since it is common in radiated electromagnetic interference (EMI) test facilities. The antennas are placed in free-space and over an infinite ground plane at heights of 1.5 m, 2 m, 3 m, and 4 m. The ground plane is a highly reflective, broadband surface, and it is a good test of the procedure.

Figures 6 and 7 depict the horizontally- and vertically-polarized biconical antenna results. The raw time-domain waveforms are obtained by windowing and then inverse-Fourier-transforming the S_{21} data. The frequencies are stepped from 1 to 300 MHz in 1-MHz steps. The free space time-domain response has a distinct “triplet” signature with a duration of approximately 20 ns. Reflections from the ground plane are visible, particularly in horizontal polarization, but are not separable from the direct coupling. When a free-space normalization is applied, the direct-coupling and ground-reflected components are clearly separable at all of the antenna heights for horizontal polarization and 2 to 4 m for vertical polarization.

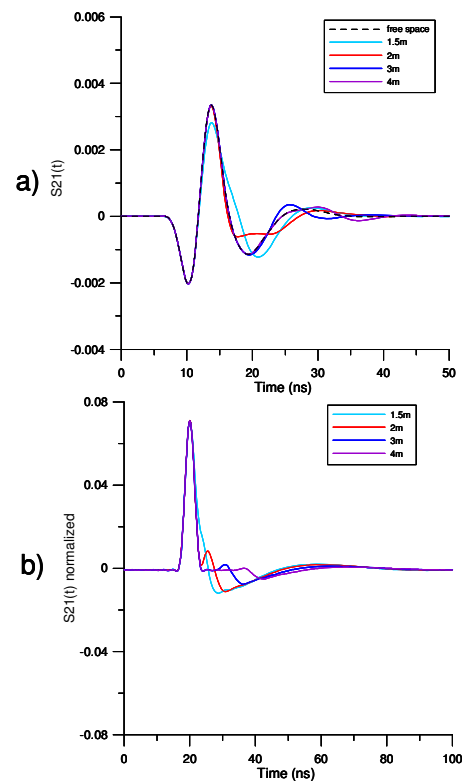


Figure 7. a) Free-space and ground-plane impulse responses for vertically-polarized biconical antennas with $d=3$ m and $h=1.5$ m, 2 m, 3 m, and 4 m. b) Normalized results with a 20-ns time delay.

A polarity reversal is noted for horizontal polarization—a result consistent with plane-wave theory. These reflections are strong and well-defined. The vertically polarized ground reflections, however, are much weaker and spread in time. This is caused by the combination of a pattern that more weakly illuminates the ground-plane and frequency dispersion in the pattern characteristics. The polarity of the ground reflection is the same as the direct coupling which is also consistent with plane-wave theory. As a result of these effects, the ground reflection is not separable at $h=1.5$ m for vertical polarization. Low-frequency “tails” are seen in all of the normalized results, and are caused by residual low-frequency components in the normalization process.

The dipole time-domain results are shown in Figures 8 and 9 for the same combination of parameters and antenna geometries. In this case, the range of stepped-frequencies is 1 to 400 MHz in evenly-spaced 1-MHz steps. Due to the resonant behavior, the impulse responses of the dipoles are considerably longer (90 to 100 ns) than those obtained with the biconical antennas. The normalized results exhibit similar trends to those of the biconical antennas. The resolution is improved due to the wider frequency range covered. Distinct ground-reflection components are seen at all heights.

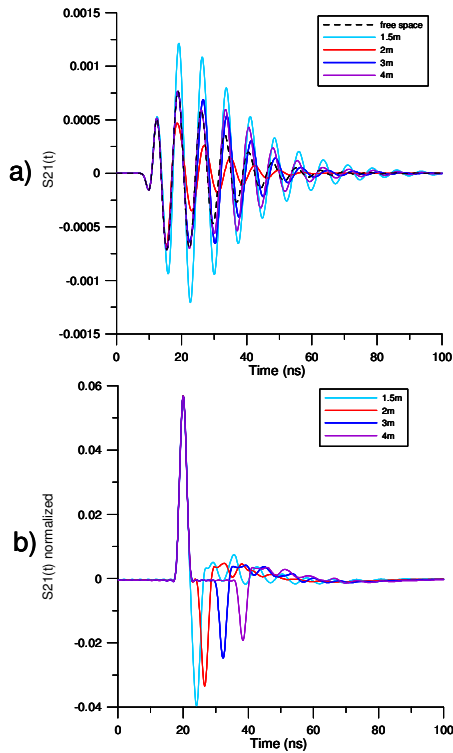


Figure 8 a) Free-space and ground-plane impulse responses for horizontally-polarized dipole antennas with $d=3$ m and $h=1.5$ m, 2 m, 3 m, and 4 m. b) Normalized results with a 20-ns time delay.

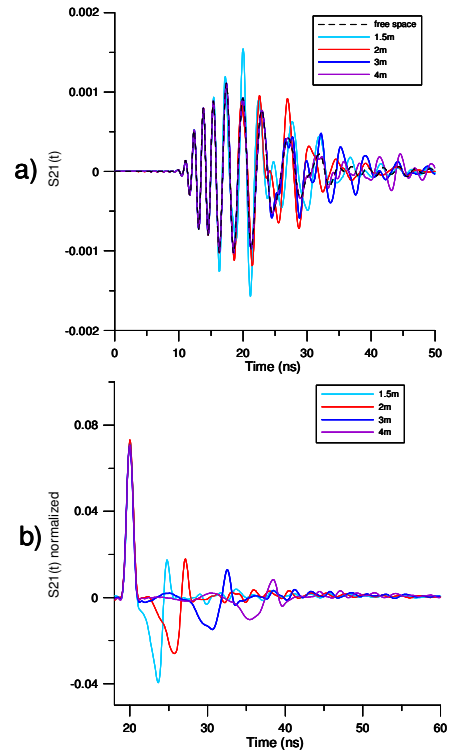


Figure 10 a) Free-space and ground-plane impulse responses for horizontally-polarized LPDA antennas with $d=3$ m and $h=1.5$ m, 2 m, 3 m, and 4 m. b) Normalized results with a 20-ns time delay.

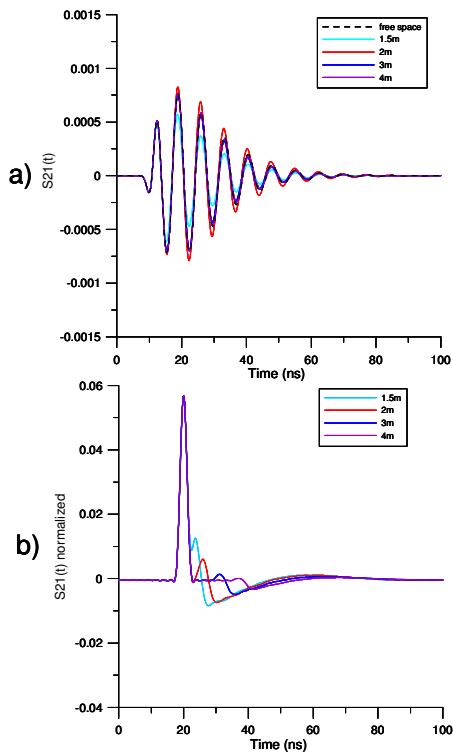


Figure 9 a) Free-space and ground-plane impulse responses for vertically-polarized dipole antennas with $d=3$ m and $h=1.5$ m, 2 m, 3 m, and 4 m. b) Normalized results with a 20-ns time delay.

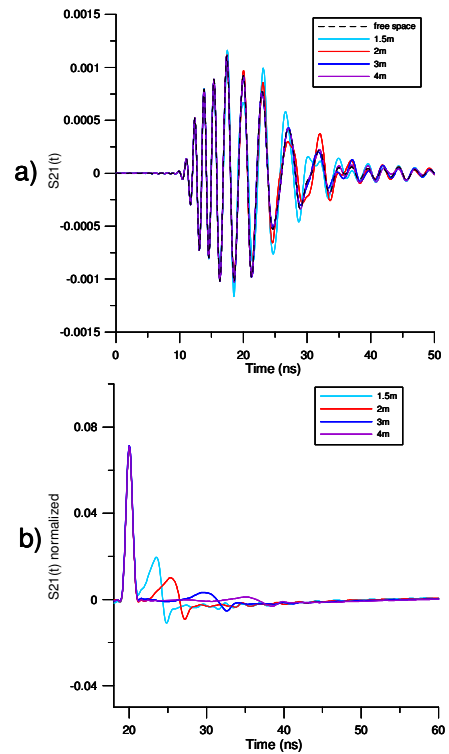


Figure 11 a) Free-space and ground-plane impulse responses for vertically-polarized LPDA antennas with $d=3$ m and $h=1.5$ m, 2 m, 3 m, and 4 m. b) Normalized results with a 20-ns time delay.

Waveforms for the log-periodic dipole arrays are shown in Figures 10 and 11. The raw impulse response waveforms have a distinctive downward chirping in frequency after the onset of the waveform. The source frequency is stepped over a range of 1 to 1000 MHz in 1-MHz steps. The duration of the impulse responses are also longer than the biconical antennas, and significant waveform activity is seen for 50 to 60 ns. Once again, stronger ground-plane reflections are seen for horizontal polarization. Normalizing the results provides separable direct- and ground-reflected components. The reflected components have a distinctive “doublet” signature due to the signal processing and pattern characteristics.

6. Conclusions

The results of this numerical study are quite promising. It demonstrates that high-resolution time-domain waveforms can be obtained using several types of EMC test antennas: 1) a biconical antenna, 2) a dipole, and 3) a log-periodic dipole array. The study also shows that a combination of a free-space reference and an efficient signal processing sequence yields time-domain waveforms that can resolve nearby scatterers. The level of measurement fidelity obtained indicates that this procedure will be useful for high-resolution, short-range, indoor propagation measurements. A comprehensive series of experiments is currently being planned to validate this proposed method using COTS EMC antennas.

7. References

- [1] R. Johnk, D. Novotny, C. Grosvenor, N. Canales, J. Graham, D. Martin, S. Yencer, D. Hibbard, T. Roach, L. Nagy, “An electric-field uniformity study of an outdoor vehicular test range,” *Electromagnetic Compatibility*, 2006. EMC 2006. 2006 IEEE International Symposium on, Volume 2, 14–18 August 2006, pp. 404–409.
- [2] D. Camell, R.T. Johnk, B. Davis, M. Taylor, “Verification of an EMC Facility Retrofit by Time-Domain and Field Uniformity Measurements,” *Electromagnetic Compatibility*, 2007. EMC 2007. IEEE International Symposium on, 9–13 July 2007, pp. 1–5.
- [3] R.T. Johnk, D. R. Novotny, C.M. Weil, M. Taylor, T.J. O’Hara, “Efficient and accurate testing of an EMC compliance chamber using an ultra-wideband measurement system,” *Electromagnetic Compatibility*, 2001. EMC 2001, IEEE International Symposium on, Volume 1, 13–17 August 2001, pp. 302–307.
- [4] D. Camell, R. Johnk, D. Novotny, C. Grosvenor, “Free-space antenna factors through the use of time-domain signal processing,” *Electromagnetic Compatibility*, 2007. EMC 2007, IEEE International Symposium on 9–13 July 2007, pp. 1–5.

[5] Unofficial NEC2 home page web address: <http://www.NEC2.org/>.

[6] LPCAD log-periodic antenna design software download site web address: <http://www.wb0dgm.com/>.

[7] L.B. Cebik, R.D. Straw, *ARRL Antenna Modeling Course*, American Radio Relay League, Newington, CT, 2002.

[8] K.C. Gupta, *Computer-Aided Design of Microwave Circuits*, Artech House, Dedham, MA, 1981.

[9] N.S. Nahman and M.E. Guillaume, “Deconvolution of time-domain waveforms in the presence of noise,” National Bureau of Standards (U.S.) Tech. Note 1047 (1981).

[10] R.T. Johnk, B. Archambeault, D. Novotny, “Using joint time-frequency analysis to enhance time-domain numerical EMC simulations,” *Interference Technology*, 2003.

CW VITAL SIGNS DETECTION WITH RANGING CAPABILITY.

A. Wiesner

Wiesner Associates, Postfach 301562, Berlin, Germany.

email: Sig346@netscape.net

This paper sets up to discuss further development of radio frequency based Continuous Wave (CW) living bodies' vital signs detection and to add a ranging capability by shifting from a true CW to step-frequency and slow frequency hopping interrogating signal. The paper summarizes preliminary experimental results obtained with the proposed vital signs detection and ranging method.

The use of interaction between electromagnetic field and human body to detect its presence within area of interest is known at least since 1924, when Leon Theremin proposed a radio frequency movement sensor [1], and the use of radio frequency radiation to detect a living body through extracting information on its breathing and heartbeat is known at least since Lipkin et al proposed a microwave respiration monitor at Carnahan Conference on Crime and Countermeasures in 1979 [2]. The first generation of commercially available radio frequency (RF) based system purposely designed for detecting the presence of persons in visually obstructed areas was released in Mai 1991 [3, 4], the second generation followed in 1998 [5], it also has been the first RF system which documented use led to rescue of two persons out of debris in an earthquake area Niigata in Japan [6].

These systems, as they are known at present, constitute three groups depending on the type of interrogating signal and associated signal processing algorithms used to extract vital signs (breathing and heartbeat) signature, and they are single frequency (monochromatic) continuous wave (CW), linear frequency modulation (LFM) and ultrawideband (UWB) systems [4,6,7].

Continuous wave systems are still attractive for many applications because of their minimal RF spectrum requirements due to narrowband nature of the interrogating signal, their very high sensitivity, moderate level of radiated RF power and ease of technical implementation. This paper sets up to discuss further development of radio frequency based CW living bodies detection systems and to add a ranging capability without dramatically enhancing RF spectrum requirements by transition to a step frequency (SF) or a slow frequency hopping (SFH) interrogating signal.

A basic block diagram of a living bodies detecti-

on system is shown in Fig.1.

Assuming that a monochromatic interrogating signal of angular frequency ω is directed at the target of interest, the return signal U_R , reflected from the target can be represented as

$$U_R(t) = \sigma_1 A \sin \omega(t - T), \quad (1)$$

where σ_1 represents aggregate path loss, A is amplitude of the interrogating signal, and parameter T represents round trip time delay.

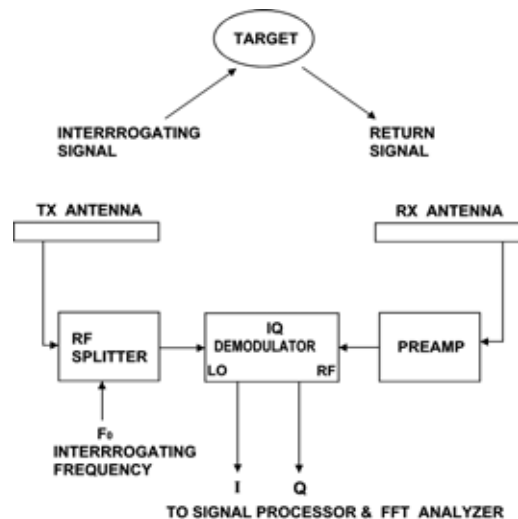


Fig.1 Basic Block Diagram.

Quadrature mixing of the return signal $U_R(t)$ with the interrogating signal $A \sin \omega t$, $A \cos \omega t$ yields the following output after removing high frequency components:

$$\begin{aligned} U_I &= \frac{1}{2} \sigma_1 \sigma_2 \cos \omega T, \\ U_Q &= \frac{1}{2} \sigma_1 \sigma_2 \sin \omega T, \end{aligned} \quad (2)$$

where σ_2 denotes aggregate conversion loss in splitters and mixers.

For a static target $T = \text{const}$ and mixing produces direct current components. Minute movements of a living body's surface due to respiration and heartbeat lead to periodic variations in round trip range R , it becomes time-variant $R(t)$, hence, round trip delay becomes also time variant $T(t) = 2R(t)/c$. Substituting T with $2R(t)/c$ and ω with $2\pi c/\lambda$ the equations for quadrature components can be written as:

$$\begin{aligned} U_I &\sim \cos \frac{4\pi R(t)}{\lambda}, \\ U_Q &\sim \sin \frac{4\pi R(t)}{\lambda}, \end{aligned} \quad (3)$$

where λ denotes interrogating signal wavelength.

For reasonably calm target $R(t)$ can be written as

$$R(t) = R_0 + R_V(t), \quad (4)$$

where R_0 - median range to the target
 $R_V(t)$ - time variable resulting from living body's minute movement due to respiration and heartbeat.

Combining (3) and (4) after simple trigonometrical transformations yields:

$$\begin{aligned} U_I &\sim \cos \frac{4\pi}{\lambda} R_0 \cos \frac{4\pi}{\lambda} R_V(t) - \sin \frac{4\pi}{\lambda} R_0 \sin \frac{4\pi}{\lambda} R_V(t), \\ U_Q &\sim \frac{4\pi}{\lambda} R_0 \cos \frac{4\pi}{\lambda} R_V(t) + \cos \frac{4\pi}{\lambda} R_0 \sin \frac{4\pi}{\lambda} R_V(t), \end{aligned} \quad (5)$$

It can be seen from (5) that quadrature output signals representing information of interest $R_V(t)$ are periodical functions of the median range to the target R_0 and at $R_0 = \lambda/8, 3\lambda/8, 5\lambda/8$ etc.
 $R_0 = (2k - 1)\lambda/8$ ($k = 1, 2, 3, \dots$)

$$\begin{aligned} U_I &\sim -\sin \frac{4\pi}{\lambda} R_V(t), \\ U_Q &\sim \cos \frac{4\pi}{\lambda} R_V(t), \end{aligned} \quad (6)$$

and at $R_0 = 2k\lambda/8$ ($k = 1, 2, 3, \dots$)

$$\begin{aligned} U_I &\sim \cos \frac{4\pi}{\lambda} R_V(t), \\ U_Q &\sim \sin \frac{4\pi}{\lambda} R_V(t), \end{aligned} \quad (7)$$

If RF wavelength is much longer than amplitude of the movements associated with respiration and heartbeat, $\lambda \gg |R_V(t)|$ cosine term in (6,7) denotes positions where output is at minimum and sine

term denotes positions where output is at maximum. For a sign-variable $R_V(t)$, say $R_V = A_V \sin 2\pi F_V t$, where A_V and F_V are respectively amplitude and frequency of breathing or respiration signature, the cosine term produces no output on the frequency F_V , while sine term produces maximum output signal on F_V .

The relationship between U_I, U_Q and R_0 is periodic with a period of $\lambda/4$, and amplitude of both components are equal at $R_0 = (2k - 1)\lambda/16$, $k = 1, 2, 3$ (odd integer sixteenth wavelength), giving distance between two adjacent positions with equal amplitude of I and Q component equal to $\lambda/8$. This fact is used in proposed here ranging method [8] for distance calibration as a calibrated range measure, although it cannot be used directly for ranging because of unavoidable ambiguity. To get absolute distance to the target proposed ranging method employs electrical shift of target position by way of changing the frequency of the interrogating signal as described below.

Aggregate phase shift of the RF signal depends on its frequency and propagation path length. Thus, any change in propagation path length can be compensated by a frequency shift to maintain the same phase relationship, and accordingly, every frequency shift leads to an equivalent propagation path change. A very simple relationship exists between frequency shift ΔF and equivalent path change ΔR_0 :

$$\Delta F = \frac{300}{(\lambda/\Delta R)R_0}. \quad (8)$$

Thus, solving (7) against R_0 yields the range to the target if a required frequency shift ΔF to compensate the known range shift ΔR is known.

Obviously, calculating the range R_0 requires some reference to determine range shift ΔR and some method of measuring the phase relationship in signal path to determine as to whether frequency shift ΔF compensates for range shift. As a reference for ΔR the proposed ranging method employs frequency shift which corresponds to two consecutive conditions in the return signal with equal I and Q components, as shown above these two positions are equal to a range shift of $\lambda/8$. Solving (8) against R_0 $\Delta R = \lambda/8$ yields

$$R_0 = \frac{300}{8 \Delta F}. \quad (9)$$

Fig.2 illustrates changes in IQ output signal by switching the operating frequency between

1292.0MHz and 1297MHz, and Fig.3 represents consecutive waterfall diagrams for 5 frequencies starting 1292.4MHz to 1296.4MHz with increment 1MHz. The spectral plots and waterfall diagrams were obtained using radar calibration unit (RCU) as a target simulator. RCU employed a membrane with a respiration radar cross section (RCS) equal to that of a human body and displacement amplitude 5mm at frequency 2.5Hz. FFT input size was set to 65536 at 16 bit per sample.

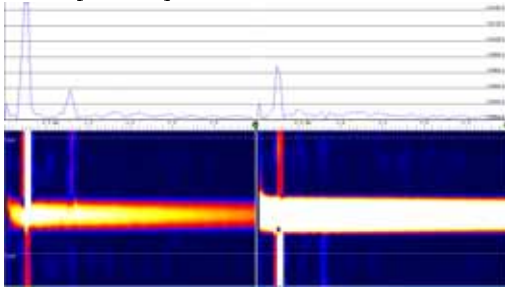


Fig.2 I & Q Outputs For Two Consecutive Frequencies.

Exact number of frequencies used for ranging depends on required measurement range and acceptable ranging error. For most practical applications a set of 16 frequencies with frequency step 1MHz will be sufficient for estimating the range from 2m to 10m.

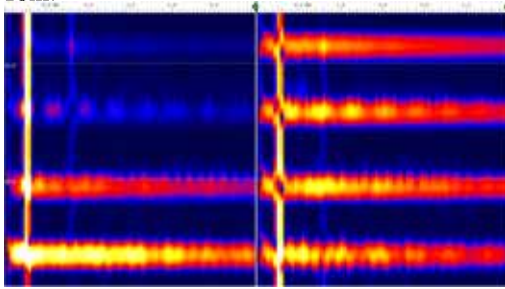


Fig.3 I & Q Outputs For Five Consecutive Frequencies.

Since changing the frequency of the interrogating signal may be not practical because of making detection time too long, other alternatives have been experimentally tested.

One of them is employing step-frequency interrogating signal and separate IQ mixing on every frequency $F_1 \dots F_N$, as shown in Fig.4. Since the number of frequencies N is small ($N < 16$), commercially available RF splitters and high isolation switches were used in experimental setup.

Another option is employing slow frequency hop-

ping interrogating signal and demultiplexing every frequency to a separate IQ mixer. This option was implemented with the same set-up as shown in Fig.4 by changing control algorithm (pseudo-random sequence instead of consecutive switching). Implementing the latter option can avoid potential collisions when deploying more than one detecting system on a site if all systems use the same set of frequencies.

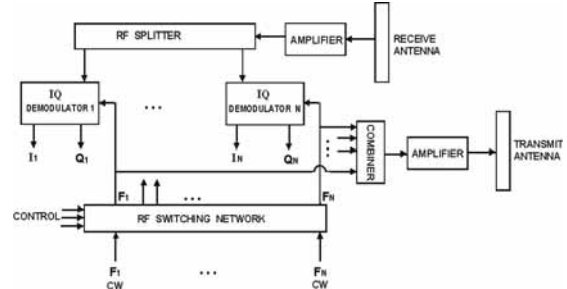


Fig.4 Coherent Step-Frequency RF Processor.

It should be noted, that a reliable ranging is only possible when signal to interference ratio in demodulated vital sign signature is sufficient to determine frequencies where IQ balance occurs, and detection range with ranging may be shorter as compared to detection on a single frequency without ranging, since duty factor on every frequency is less than 1 in ranging mode.

The range obtained by (9) is an apparent electrical path length which may exceed actual path length due to time delay in RF circuitry of the transmitter, receiver and RF cables. These factors can be excluded by a proper calibration of the circuit using RCU, provided they remain reasonably constant after calibration. The latter is easily to achieve in a constellation with transmit and receive antenna being integral part of a single mechanical structure or using a common antenna and high isolation splitter for transmit and receive paths.

To illustrate the proposed ranging method a multistrip spectral plot and partial waterfall diagram represented in Fig.5 for a step frequency interrogating signal spanning 12 frequencies from 1282 to 1294MHz with frequency step 1MHz and dwell time 12ms. As can be seen from Fig.5 two consecutive frequencies where IQ balance occurs are 1284MHz and approximately 1294MHz, corresponding to frequency shift 10MHz, yielding the range to the target $R_0 = 300/(8 \Delta F) = 3.75m$ (actual range was 3.5m). Arrangement of Fig.4, modified for a single transmit-

receive antenna was used for the measurements.

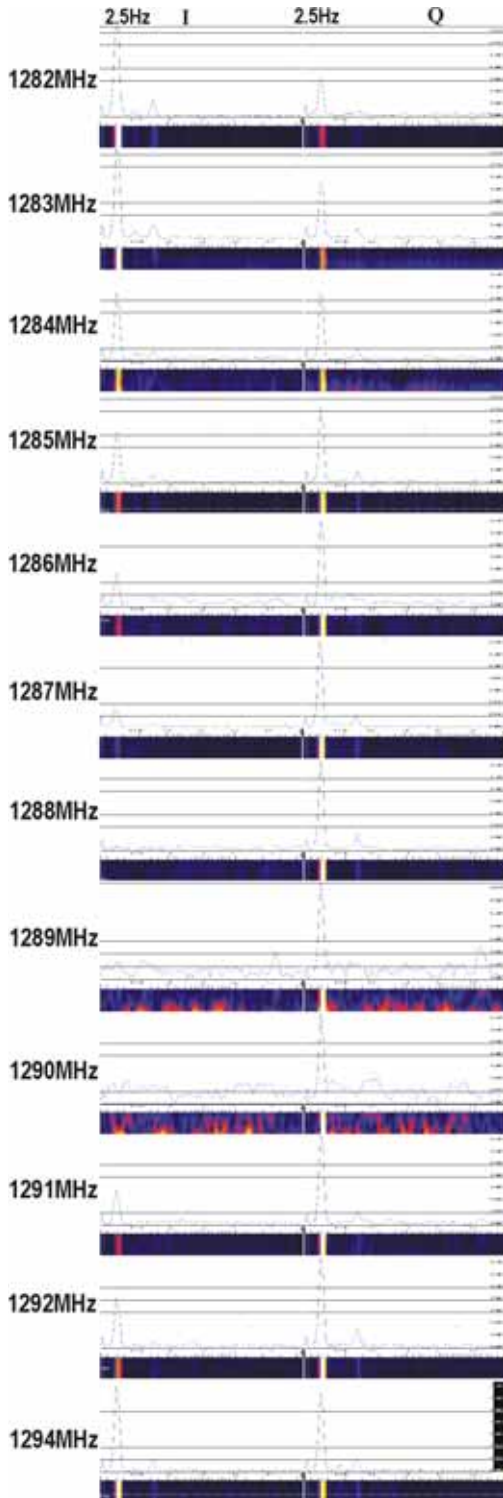


Fig.5 Measured I & Q Signals for 12 Frequencies.

In a bistatic configuration the proposed ranging method ensures two-dimensional target positioning using triangulation. Both sites may share the same set of frequencies $\{F_1 \dots F_N\}$ with time division or code division control algorithm. In its simplest implementation a bistatic detection system two equal sites with a common transmit-receive antenna on each site, each site being driven by the same set of frequencies $\{F_1 \dots F_N\}$ and the same switching sequence with a relative shift of 1 bit.

Range readings R_1 and R_2 of two sites yield azimuth angle to the target α within radiation pattern of the antenna:

$$\alpha \cong \frac{R_1^2 + B^2 - R_2^2}{2R_1 B}, \quad (10)$$

where B is a distance between site's antennas (interferometric base).

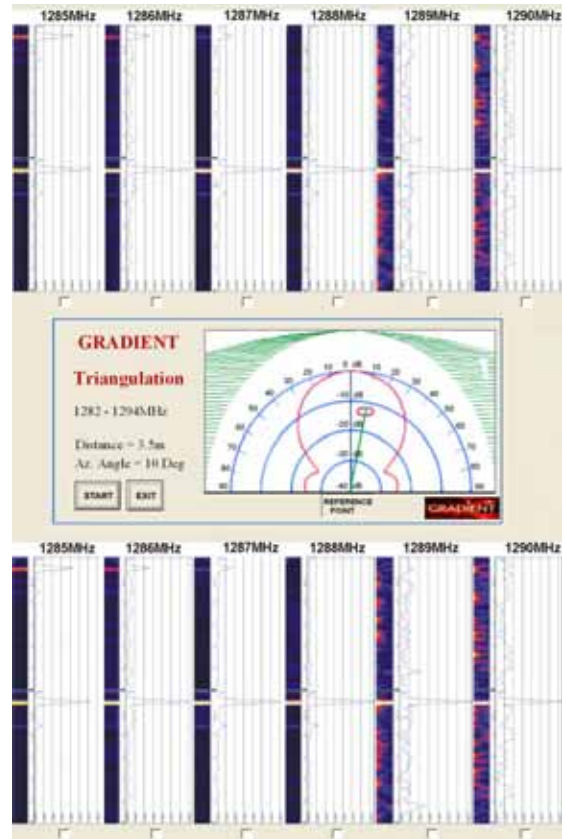


Fig.6 Triangulation Software Interface.

Quadrature FFT Signal analysis, ranging and triangulation can be incorporated into a single software package using operator's environment as shown in Fig.6. The operator must check the box next to

the respective plot with equal I and Q levels on both stripes representing returns from Site1 and Site2 and the box "START" in the triangulation window.

For initial detection of vital signs in a visually obstructed area the system can be switched to a single frequency CW mode, thus enhancing effective radiated RF power by N , and, therefore enhancing overall system sensitivity.

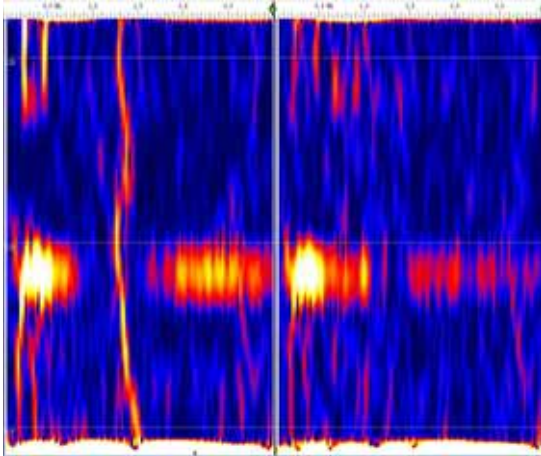


Fig.7 Waterfall Diagram of a real Person's return at 1287MHz. Note, the breathing had been held for 40 seconds at 16:28:00 for test purposes.

Fig.7 represents a single channel (CW, 1282MHz) waterfall diagram of a real person's breathing and heartbeat at 2m behind a 27cm thick brick wall obtained with the same setup, a common transmit-receive antenna was placed approximately 1m from the wall.

Fundamental and second harmonic breathing frequency are seen at approximately 0.24Hz and 0.48Hz, while a clear heartbeat signal is seen at 1.2 to 1.4Hz.

The proposed ranging method is invariant to the operating frequency. Nevertheless, the overall system performance (operating range in detection mode and ranging accuracy in ranging mode) may strongly depend on operating frequency, hence, more than one frequency band may be required to cover a wider range of applications (security, rescue, medical).

European Radio Frequency Spectrum Allocation provides two frequencies for vital signs detection used by Rescue Services: around 433.150MHz

and around 1299MHz. Switching to lower UHF (433MHz) may be advantageous in dense RF-lossy environments, when detecting through thick walls, etc., despite obvious reduction of human body's radar cross section. To illustrate this fact, Fig. 8 represents return signal from a person approximately 4.9m from the antenna in a densely occupied laboratory behind 27cm thick brick wall, obtained on the frequency 433MHz. Both respiration and heartbeat signals are clearly visible on the spectrogram. Return signal on 1299MHz in the same environment contained no heartbeat signals and much weaker respiration signal.

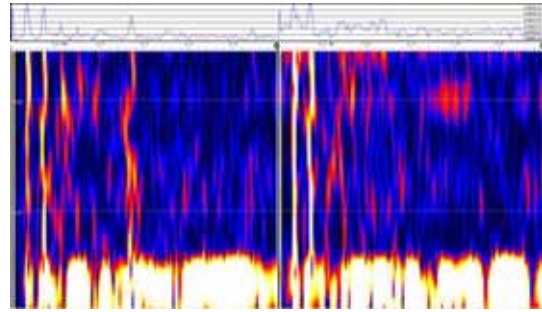


Fig.8 433MHz real person's return.

Fig.9 represents returns from a real person 5.5m from the antenna with two walls inbetween: a 27cm brick wall and a 10cm wooden wall obtained on two frequencies, 433MHz (a) and 1299MHz (b). A clear respiration signal can be seen on 433MHz spectrogram, while 1299MHz return contained no vital signs.

Range calibration as it is known in conventional radar technology can not be used for calibration of the proposed method, since only a component containing vital signs signature in return signal is used for ranging, and not reflected RF signal as such, and even not necessarily the strongest component in the return signal. A simple arrangement for range calibration using an arbitrary waveform generator, e.g. TGA1201, a DC-coupled sub-audio amplifier and a loudspeaker, acting as a moving membrane, simulating breathing and heartbeat has been used as an RCU in experiments presented here.

Range reading depends on the propagation media and, since interrogating and return signal propagate through walls, debris and the like, rather than in a free space, a correction coefficients must be integrated into a processing software. And since a

very little may be known about electrical properties of the propagation media, some errors are unavoidable. Nevertheless, the proposed method ensures ranging with 20-30% uncertainty, which is adequate for many practical applications.

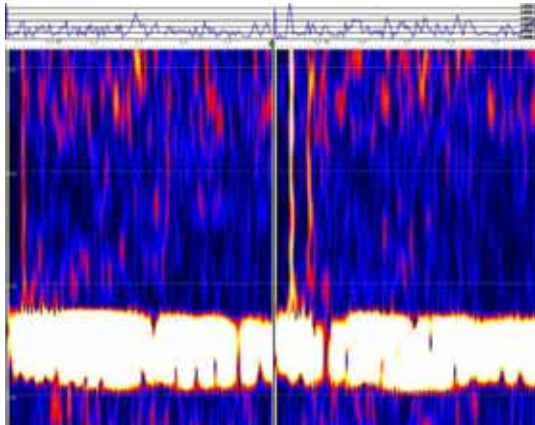


Fig.9a 433MHz long range return

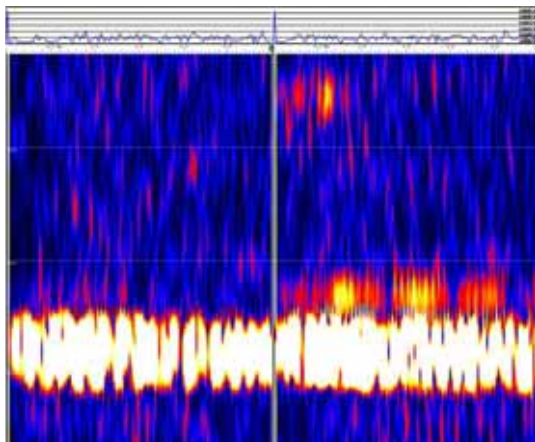


Fig.9b 1299MHz return, same conditions as Fig.9a.

Apparently, adding ranging capability requires

an interrogating signal with more than one frequency in its spectrum, this may require two modes of operation: single-frequency detection and multi-frequency ranging. But even in ranging mode a SF or SFH system, employing a set of a few frequencies requires less RF spectrum resources as compared with a short pulse based systems.

References:

1. L.S. Theremin, German Patent No. 449075
2. Y. Lipkin et al., Microwave Respiration Monitor. Carnahan Conference on Crime and Countermeasures, 1979, May 16-18, Lexington, Kentucky, pp. 53-56.
3. German Federal Ministry for Research and Technology, Project No. 13 RG 9008 Selectronic GmbH, May 1991.
4. G. Schmidt. European Patent No. EP0740800.
5. A. Wiesner, G. Schmidt et al. Report on Project No SWE 236, Ministry for Development and Industry of Federal State Brandenburg, Selectronic GmbH, Werder-Havel, Sept 1998.
6. Rescue Mission At Niigata Mid Area Eathquake: Rescue Team and Sirius. Tokyo Daily, 28 Oct. 2004, <http://web-japan.org/nipponia/nipponia33/en/feature/feature03.html>
7. E.F. Greneker. Radar Sensing of Heartbeat and Respiration at a Distance With Security Applications. Proceedings of SPIE, Radar Sensing Technology, Vol. 3066, Orlando, Florida, 1997, pp. 22-27.
8. A. Wiesner. Method and System for Vital Sign Detecting of living bodies. US Patent Application No 61024546.

Design and Implementation of a Portable Software Radio

Brian P. Dunn, Michael L. Dickens, and J. Nicholas Laneman

University of Notre Dame
Department of Electrical Engineering
Notre Dame, IN 46556
{bdunn2, mdickens, jnl}@nd.edu
Vox: 574-631-8034
Fax: 574-631-4393

Abstract — We describe the design and development of a portable software radio prototype device built primarily using commercial off-the-shelf components and open-source software. The device components include a general-purpose processor (GPP) on a small-form-factor motherboard, radio hardware, touchscreen and LCD, audio microphone and speaker, and an internal battery enabling hours of mobile operation. This device demonstrates that a GPP-based software radio can be implemented in a portable-form-factor using current technology. We describe the design and selection of hardware components, identification and modification of the operating system, and installation of the selected radio software. We discuss trade-offs in the selection of hardware and software, decisions that proved to be stable throughout the lifetime of the project, issues that arose, and lessons learned along the way.

1 Introduction

This article describes the design and development of a portable software radio prototype that uses as much open-source-hardware and -software as possible, and leverages commercial off-the-shelf (COTS) components. The device is shown in Figure 1, and operates using GNU Radio software for signal processing on a small-form-factor GPP-based computer and an Ettus USRP for the air interface. The prototype offers the same capabilities as GNU Radio running on a desktop computer with an Intel Core 2 Duo CPU running at 2 GHz with an Ettus USRP attached. A single device can fit inside a box approximately 29 x 10.5 x 21 cm and has roughly 2 hours of runtime off of a single battery charge. Although functionally similar software radios currently exist, they are almost entirely designed by a single manufacturer. To the best of our knowledge, this is the first portable software radio built primarily using COTS components.

The functionality of traditional hardware-based radios is limited to the capabilities present in the initial design, e.g., broadcast AM reception or analog cell-phone communications. Such devices cannot be reconfigured in any significant capacity, e.g., as an FM radio or with digital cell-phone service. An emerging architecture generally referred to as *software radio* shifts much of the signal processing into software and reprogrammable

hardware, enabling devices that can be reconfigured after deployment – including augmenting their functionality. In this article, we use the term “software radio” to refer to all types of radios that are substantially defined in software and can significantly alter their physical layer behavior through changes to their software [1, Page 2].

The concept of a software radio is credited to Dr. Joseph Mitola III in the early 1990’s [2], and refers to a class of radios that can be reprogrammed and thus reconfigured via software. The first open-source software for radios is credited to Dr. Vanu Bose in 1999 in his dissertation at MIT [3]. Dr. Bose was a member of the SpectrumWare project at MIT, which developed the original Pspetra code described in his dissertation. This code was the basis for both the Vanu Software Radio [4] – the most prominent industrial product utilizing software radio – as well as the GNU Radio open-source project [5].

Although hardware devices outperform software-based devices, the limited presence of software radios is more so an artifact of the conventional wisdom that the cost of reconfigurability is too great. There are, however, certain applications that necessitate reconfigurability, such as when device interoperability is critical, when the lifetime of a product greatly exceeds that of the devices with which it needs to communicate, or when conduct-



Figure 1. Highly reconfigurable portable software radio prototype implemented using open-source software and predominantly COTS hardware, providing dynamically configured multi-channel and full-duplex communications in most frequency bands from 50 MHz to 900MHz.

ing wireless research and development. There are also increasing numbers of applications for which software-based processing is more than adequate to meet performance requirements, and the reconfigurability provided by the use of software is highly desirable. Given the growing application-range for software radios, and the lack of industrial adoption of this technology, we set out to show that current technology is ready for, and capable of, implementing a portable-form-factor GPP-based software radio.

In the following section we give more specific objectives, motivate the decision to use GNU Radio as the software framework for the prototype, and discuss several alternative platforms that offer similar functionality. In Section 3 we detail what went into the selection and design of each hardware component along with their integration into the prototype. In Section 4 we do the same for software, discussing the lessons learned at the end of both of these sections. We conclude in Section 5 with a summary of our work on the prototype, and a discussion of some broader implications of this work and software radio as a whole.

2 Core Platform Selection

We had two primary goals. First, we wanted to create a device that could be used as a wireless research platform to quickly try out new ideas and provide a more concrete basis for what would otherwise be purely theoretical work. A key metric of success for this goal is minimizing the learning curve and development time often associated with algorithm development and experimental work in communications. Second, we set out to demonstrate that comprehensive protocol agility through software-based processing on a mobile device

is not just a technology of the future, but a viable alternative today.

Primary options for the core processor in a software radio include a field-programmable gate array (FPGA), digital signal processor (DSP), or general purpose processor (GPP). This list is roughly in decreasing order of signal processing performance, required programmer / programming specialization, and power efficiency. The list is also in increasing order of computational latency, code portability and reusability, simplicity of live-reconfiguration, and ease of processor upgradability.

Processor selection was based on the anticipated uses of the prototype, e.g., by researchers without specialized programming expertise. GPP-based software requires the least programming specialization, provides the best code-reuse, and can also be readily modified to include new or additional functionality, e.g., upgrading software from a draft to accepted wireless standard. Another argument for using a GPP is the upgrade path to newer, more capable processors via direct replacement of the processor or the motherboard on which the processor resides. A faster processor allows current code to run faster – possibly even in real-time – and for more sophisticated algorithms to be implemented, simply by recompiling for the new hardware. The advantages of using a GPP outweighed the limitations, and thus we decided to require GPP-base signal processing, but still had to decide on the hardware type – proprietary or COTS.

Proprietary hardware and software have traditionally been required when building a software radio in order to overcome some fundamental limitations including radio frequency (RF) access range, digital data-transport bandwidth, and signal processing capabilities. Commercially-available advances in the myriad radio hardware technologies – antennas and the RF front end, ADCs and DACs, data transport protocols and hardware, signal processors and small-form-factor computers, and power management systems and batteries – and the maturity of freely-available open-source radio software have significantly mitigated these limitations. Accordingly, we adopted requirements to use as much open-source software and COTS hardware as possible. The use of open-source software and a GPP for signal processing are key to both goals, by controlling device costs, providing a processor upgrade path, and allowing users to modify the original source for research purposes.

Several baseline requirements were identified to show that a GPP-based software radio could be built in a portable-form-factor offering reasonable runtime while powered from an internal battery. It was important that the system be capable of handling multiple 25 kHz voice channels with typical voice encoding, and data

transmission up to a few hundred kilobits per second with QAM, PSK, or OFDM modulation. With respect to software architecture requirements, we needed cross-platform support for Unix-like operating systems including Linux and Mac OS X, critical code written primarily in a compiled, standardized, operating-system independent programming language such as Fortran, C, or C++, and software-based control down to the physical layer. Finally, the hardware had to be economically priced, while still offering processing performance on par with currently-available desktop computers.

It was initially unclear whether we could leverage an existing software radio platform, or if it would be necessary to develop a new platform specific to our needs. To build from an established platform, we looked for mature open-source projects focusing on software-based signal processing independent of any specific operating system. There were a variety of projects that offered some of the features we needed. Those best aligned with our goals include:

- CalRadio [6]
- GNU Radio Software [5] and Ettus USRP hardware [7]
- High Performance SDR [8]
- KU Agile Radio [9]
- Rice WARP [10]
- Lyrtech Small Form Factor SDR [11]
- University of Texas HYDRA
- Virginia Tech Chameleon Radio [12]
- Virginia Tech Cognitive Engine [13]
- Virginia Tech OSSIE [14]

There were benefits and drawbacks to each of the candidate platforms. Several were too expensive while several were overly bandwidth-constrained, limiting their usefulness to voice and audio transport. Others relied exclusively on hardware for signal processing (FPGA-based) or were not sufficiently open-source. We found the combination of GNU Radio and USRP to be the best candidate, and considered the platform to be sufficiently mature to use in our devices. In the following sections we discuss the trade-offs involved with selecting this platform and describe the hardware and software development specific to the prototype. A conceptual drawing of the functionality of our chosen platform is shown in Figure 2. The discussion is structured such that readers who may have different requirements, constraints, or other considerations may readily map our decision processes and lessons learned to their environments.

3 Hardware Integration

The prototype device's hardware is comprised of a reconfigurable radio enabling communication in multiple

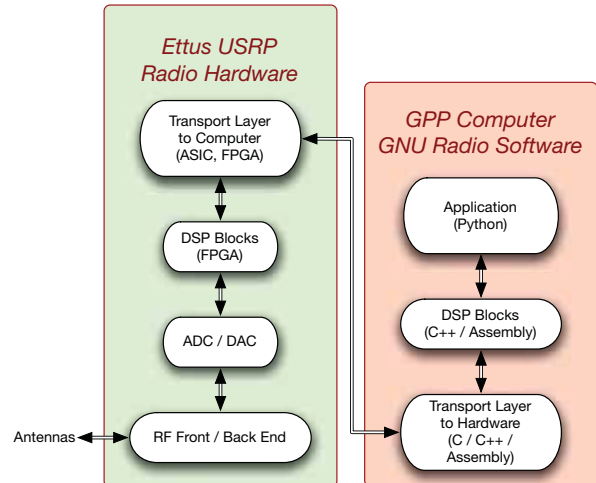


Figure 2. Block diagram depicting the functional relationship between the Ettus USRP hardware and GNU Radio software.

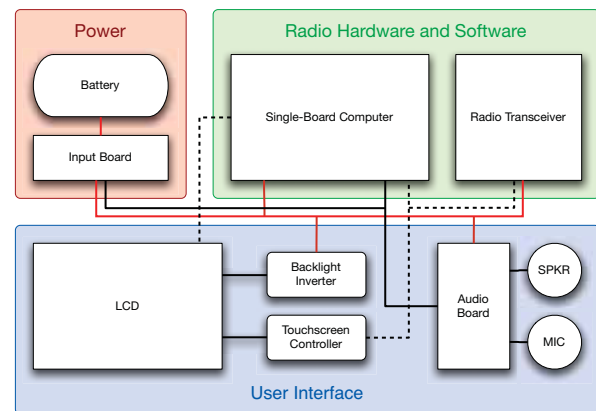


Figure 3. Block diagram of the prototype's major hardware elements, including power, LVDS, and USB connectivity.

frequency bands, a host computer to control the entire system and to perform signal processing, a touchscreen LCD and audio interface for display and user-control, and a rechargeable battery for portable operation. The block diagram in Figure 3 illustrates the system's architecture and depicts interfaces between components within the system. In the following sections, we discuss the design and integration of each hardware component and key interfaces, highlighting the challenges encountered throughout the process.

3.1 Enclosure

Three options were considered for the enclosure: sheet metal, machined aluminum, and stereolithography (SLA). SLA is the most widely-used rapid-prototyping technique for producing three-dimensional parts quickly and efficiently – the process itself takes on the order



Figure 4. Internal view of the prototype showing the touchscreen LCD, backlight inverter, and audio interface on the left; the single-board computer and rechargeable battery in the middle; and, with the RF shield removed, the Ettus USRP, input board, and touchscreen controller on the right.

of hours to complete. SLA fabrication works by laser-hardening light-sensitive plastic in consecutive cross-sectional layers of the part being fabricated. Although SLA can be more expensive than some alternatives, we chose to fabricate the enclosure using SLA because a more customized enclosure could be delivered as a turn-key solution in the shortest amount of time. Two key factors in determining the device’s form-factor were the use of a commercial off-the-shelf single-board computer (SBC) and the inclusion of an LCD, both discussed below. The enclosure design is a “clam-shell” with the computer and user interface (LCD, microphone, and speaker) on the top half, and the USRP in the bottom. The open clam-shell with internal components is shown in Figure 4. The top and bottom halves are separated by a grounded sheet of aluminum that helps shield electromagnetic interference between the top and bottom of the enclosure and provides a mechanical connection for several components.

3.2 Host Computer

A number of vendors offer embedded processing boards intended for OEM integration. Taking full advantage of the existing GNU Radio software and the USRP transceiver required a SBC with a high-end chipset that was in common use. A lower-end Intel Celeron processor would have been sufficient for most applications, but an Intel Core 2 Duo offered superior performance with only a modest increase in power consumption, if any, over the Celeron. We chose the Commell LS-371 SBC because it incorporates all of the required peripherals and has one of the best performance-to-size ratios among the SBCs we evaluated. For the purposes of building a few prototypes, a commercially available SBC can provide flexible and powerful processing with little capital investment or development time. The LS-371, like most modern computers, can boot from almost any data-transport mechanism, including USB, IDE, SATA, ENET, and compact flash (CF). In order to

simplify the enclosure design and save space, we opted to use the CF memory-slot on the bottom of the board, recognizing that the throughput would likely be slower than other boot device connections.

3.3 Graphics Display

The device includes a full-resolution display and touchscreen interface that substantially enhances the platform’s functionality. However, incorporating the graphics display was the source of several unanticipated challenges, and increased the design complexity. A simpler approach would have been to use a character LCD, but that would have limited the user interface options and made on-device development overly challenging. The ideal solution was a small computer display that interfaces directly to the LS-371 and a touchscreen that emulates mouse clicks.

The main difficulties stemmed from the fact that LCDs are usually designed for a specific product, and touchscreen overlays are typically LCD-specific. Additionally, there are a variety of signaling formats used for internal video transport, further limiting what off-the-shelf display devices would work for this application. LCDs smaller than 8.4 in. usually have parallel TTL-level inputs, whereas many SBCs only provide video output over a high speed serial interface using low-voltage differential signaling (LVDS). For simplicity, we chose to use the AUO G065VN01 6.5” VGA (640x480) LCD – the smallest readily available with an onboard LVDS interface. Because the G065VN01 does not have an integrated touchscreen, we incorporated a resistive touch overlay that was designed for a similarly-sized LCD. The overlay’s output is encoded by a touchscreen controller – which are readily available using a variety of interfaces such as RS-232, PS/2, and USB. Developing the Linux software drivers for the USB controller we chose presented some additional challenges, which are further discussed in Section 4.

3.4 Power System

It was essential that the system be portable, necessitating an internal power source with enough capacity for running useful experiments in the field. However, the computationally-intensive signal processing of the SBC and USRP requires a sizable amount of power. Because weight was also of importance, heavier batteries such as lead-acid were inadequate. Lithium-ion (Li-ion) batteries, and more recent successors such as lithium-polymer (LiPo) batteries offer one of the best energy-to-weight ratios and lowest self-discharge rates available today. LiPo technology offers several additional benefits over Li-ion such as improved robustness, increased energy density, and flexible housing that enable more cus-

tomized form-factors. These benefits led to the decision to use a LiPo battery pack (with internal protection circuitry) constructed from four 3.7 V cells, which together weigh about one pound and provide a capacity of over 6 Ah at 14.8 V.

The LS-371 provides the 5 V and 12 V power supplies needed for the USRP, LCD backlight inverter, and audio amplifier. Although using the same power supply for the radio and digital boards results in increased RF noise, the overall design is much simpler and we found this solution to be acceptable for many applications. For fixed operation, an external power supply can be used via a standard 2.1 mm center pin DC jack on the back of the device.

3.5 Audio Interface

The easiest way to provide the necessary audio peripherals while interfacing with the LS-371 was to design a simple audio board specific to the prototype's needs. The audio board connects directly to the LS-371's audio header and is powered by its 5 V supply. It is mounted to the top-front of the enclosure and contains a built-in microphone, amplifier for the audio signal to an internal speaker, and logic for an externally-accessible audio port. The audio port provides 3.5 mm stereo line input and output jacks that are automatically selected when a plug is inserted or withdrawn. A low-noise adjustable gain amplifier can be switched in and out of the audio signal path to provide gain for low-level input signals, such as from an external electret microphone. All of these features are configured via an onboard DIP switch, allowing audio operation tailored for varied applications.

3.6 Lessons Learned

At the outset, it did not seem necessary to explicitly define electrical and mechanical interfaces between components, thinking that doing so would take too much time and reduce design flexibility as the project evolved. In retrospect, a more rigorous approach would have been more amenable to changes in human and capital resource allocation, allowed multiple tasks to proceed in parallel, and ultimately saved time.

Many of the challenges we encountered were caused by minor differences between our test-bench setup and the final system components. For example, something as simple as interfacing all of the components together required about fifteen different cables that collectively occupy a significant amount of space. It was difficult to recognize the importance of this issue until all of the final components were in place. The need for consistency between a test setup and the final deployment is also highlighted by problems encountered with establishing a cross-platform software development environment,

which we discuss further in the following section.

4 Software Integration

Even with the decision to use GNU Radio software for the radio, there were a number of software issues to address including selection of the operating system for the SBC, integration of drivers for hardware interfaces, and installation of the GNU Radio software and its prerequisites. This section discusses the choices and implementation of software, issues that arose and how they were resolved, and lessons learned during the integration process.

4.1 Operating System

In the spirit of keeping the project open-source, we focused on Linux for the host operating system. As the SBC we chose was quite new, we had to investigate several Linux distributions before one was found that functioned reliably. Among the free mainstream distributions that booted the SBC, Ubuntu 6.10 was the only one that functioned correctly. After choosing Ubuntu as the de-facto host operating system, we had to integrate USB-based touchscreen software and deal with boot issues created by our choice of CF storage.

4.1.1 Touchscreen Drivers

The kernel-space extension (“kext”) for USB-based touchscreens could not provide orientation parameters for our selected touchscreen; this kext is not designed for calibration. To make use of the touchscreen, we modified the USB touchscreen kext to add user-space options for swapping the X and Y coordinates and inverting the resulting X or Y axis – all independent of each other. For calibration of the incoming touchscreen data with the LCD, we chose the Evtouch X.Org event driver [15], as it was the first solution that compiled with minimal changes – even though at the time it wasn't designed specifically for Ubuntu Linux.

4.1.2 Boot Disk Issues

Compared with booting from an IDE hard drive, booting from CF was around 4 times slower at roughly 4 minutes. After reviewing the output of “dmesg” it was clear that a direct memory access timeout was stalling the boot process. A search of the particular error in the Ubuntu web forums resulted in a fix via adding the boot parameter “ide=nodma” to the GRUB “menu.lst” file for each boot command. This addition reduced the boot time to around 2.5 minutes.

4.2 Radio Software

GNU Radio provides basic building blocks for a “simple” analog repeater as well as a “complex” HDTV receiver; users can also create their own blocks. The

software package as a whole provides a framework for experimentation, testing, and evaluation of new communications protocols. Not all tasks can be done in “real-time” or “live” when using GNU Radio due to constraints inherent to the radio hardware, the host computer’s CPU, the data transport between the radio and host computer, and even the radio software itself. The demos that we developed for the prototype use GNU Radio as the underlying software framework.

There are a significant number of required packages (“pre-requisites”) that must be available before GNU Radio can function. Some of the pre-requisites are solely for compilation, while others are for runtime. Our choice of software development operating systems – Ubuntu 6.10 Linux and Mac OS X 10.4 – have different means for installing pre-requisites. As GNU Radio also requires minimum versions of some of the pre-requisites, and not all of the versions were available as pre-compiled binaries or installable packages, for both platforms some of the pre-requisites had to be installed from source. In order to ease the installation burden for each developer, we created executable scripts to handle the installation of the pre-requisites. Because we controlled what was already installed on the computers, these scripts worked reliably; on developer’s personal computers, the scripts often encountered issues due to unexpected already-installed packages.

GNU Radio software can be obtained as pre-compiled packages for some operating systems, or as an archive or repository check-out that can be compiled and installed locally. As with any rapidly-evolving open-source multi-contributor project, important bug fixes are placed in the “trunk” of the repository and not integrated into a pre-compiled package until the next release – which may be a few days, weeks, or months away. The trunk is “bleeding edge” and although it is supposed to always compile and execute properly, reality is that it doesn’t always. Hence we chose to use the trunk for the newest fixes, but to test it out with our demos before committing to a particular set of fixes. Compiling and installing GNU Radio is well-documented on their Wiki, for Ubuntu, MacOS X, and a variety of other operating systems.

4.3 Lessons Learned

During our software development efforts, we learned quite a bit about Linux, project management, software development, and participating in software projects’ lists and forums.

4.3.1 Linux Compatibility

“Linux Compatibility” in a generic sense does not necessarily mean specific Linux-distribution compatibility. Before picking a distribution, investigate any additional

required software and look for a distribution that is known to be compatible with the majority of that software.

4.3.2 Up-Front Time to Save Time Later

We wasted a lot of time waiting for the prototype to boot or reboot – which was often required during the early stages of development, especially when trying to get the touchscreen software to function. In retrospect, we should have invested more up-front time into speeding up the CF boot, and / or more thoroughly investigated other boot methods in order to reduce this waiting time.

4.3.3 Prototype Software Installs

Expect up-front to have two types of software installs: one for the *development* platform, using a fast boot interface (e.g., IDE, SATA, or USB) and another for the *testing* platform. For either storage, get a device with plenty of extra space since as software progresses it usually increases in the size of both source code and installed files.

4.3.4 Revision Control

Keeping track of the various installs of GNU Radio was difficult at best and often-times confusing. Create a local source repository with revision control (e.g., CVS, SVN, git) to hold the multiple required versions of the software being used: a *stable* branch from which most development happens; a *testing* branch with which locally-developed software can be checked for correct functionality against the latest changes of GNU Radio; and a *personal* branch for each programmer. Although the use of multiple branches in a separate repository requires some effort on all programmers’ parts, it is much easier to keep track of than each programmer maintaining a separate branch.

4.3.5 Finding and Providing Information

A major benefit of open-source software over proprietary code is the ease of access to the original source code. One can use the source code to determine how to make function calls if help files are not accurate or descriptive enough, or what a function really does via comments placed in the code, or by reviewing the code itself.

Most online software projects, and especially open-source ones, provide at least one venue in which users of all experience levels can participate – for example an email list or a web forum. These discussion venues are amazing resources for gaining knowledge about and an understanding of the project and its participants. Most are archived, and that information made available for searching.

Most software projects have multiple users, who often keep information they have learned on their personal website. Sometimes information is posted on multiple

websites, with some updated regularly while others aren't at all. While this can make gleaning information more difficult, rely on the most recent version of any information since it is the most likely to be correct.

5 Conclusions

Significant progress has been made towards making portable software radios commercially-viable, and our efforts support this endeavor. Given the ever-increasing computational power of GPPs, as well as continually increasing interest and funding for software radio and related projects, we believe that GPP-based software radio will soon provide the processing power, scalability, and reconfigurability required by today's communications problems.

The presence of an easily programmable and reconfigurable wireless platform in the research arena has the potential to accelerate innovation and stimulate more rapid deployment of new wireless protocols and platforms. Beyond the academic setting, there are several successful startup companies focusing solely on software radio. With increased attention and collaboration, we feel software radio has the potential to develop into a new technology ecosystem, similar to that emerging in the operating system market with the development of Linux by companies such as Red Hat. Coupling university research to such an ecosystem would greatly accelerate technology transfer and positively impact real-world communication systems.

6 Acknowledgments

The authors thank Phil McPhee for mechanical engineering design work, Brynnage Design

(brynnage.com) for next-day SLA fabrication of the enclosure, and our Software Defined Radio Group for their continuing efforts, including Neil Dodson, Andrew Harms, Ben Keller, Marcin Morys, and Yaakov Sloman.

This work has been supported in part by the US National Institute of Justice (NIJ) through grant 2006-IJ-CX-K034 and the US National Science Foundation (NSF) under grant CNS06-26595.

References

- [1] Jeffrey H. Reed, *Software Radio: A Modern Approach to Radio Engineering*, ser. Prentice Hall Communications Engineering and Emerging Technologies Series. Prentice Hall PTR, May 2002.
- [2] Mitola, J., III, "Software Radios - Survey, Critical Evaluation and Future Directions," *IEEE National Telesystems Conference, NTC-92*, pp. 13/15-13/23, 19-20 May 1992.
- [3] Bose, Vanu G., "Design and Implementation of Software Radios Using a General Purpose Processor," Ph.D. dissertation, MIT, 1999.
- [4] "Vanu Software Radio." [Online]. Available: www.vanu.com
- [5] "GNU Radio Software." [Online]. Available: www.gnuradio.org/trac
- [6] "CalRadio." [Online]. Available: calradio.calit2.net
- [7] "Ettus USRP Hardware." [Online]. Available: www.ettus.com
- [8] "High Performance SDR." [Online]. Available: hpsdr.org
- [9] "KU Agile Radio." [Online]. Available: agileradio.ittc.ku.edu
- [10] "Rice WARP." [Online]. Available: warp.rice.edu
- [11] "Lyrtech Small Form Factor SDR." [Online]. Available: www.lyrtech.com
- [12] "Virginia Tech Chameleon Radio." [Online]. Available: www.ece.vt.edu/swe/chamrad
- [13] "Virginia Tech Cognitive Engine." [Online]. Available: www.cognitiveradio.wireless.vt.edu
- [14] "Virginia Tech OSSIE." [Online]. Available: ossie.wireless.vt.edu/trac
- [15] "Evtouch X.Org Event Driver." [Online]. Available: www.conan.de/touchscreen/evtouch.html

Using rain microstructure information from 2-D video disdrometer for propagation predictions at 20 GHz

M. Thurai, V. N. Bringi and G.J. Huang

Dept. of Electrical Engineering, Colorado State University, Fort Collins, Colorado, USA

e-mail: bringi@engr.colostate.edu, merhala@engr.colostate.edu

Abstract

Individual drop images in natural rain from the 2-dimensional video disdrometer (2DVD) have been processed to obtain their shapes and orientation angles, which in turn have been used to derive their complex forward scattering amplitudes at 19.701 GHz. Using these calculations, the cross-polar discrimination versus co-polar attenuation variation has been derived for a simulated experimental link. The variation is compared with 1-year of beacon data and shown to give rise to significantly higher XPD spread than the previous computations which used mean shapes and orientation models for the measured drop sizes. Also derived from the 2DVD data (taken from several locations) are the 20 GHz specific attenuations for horizontal and vertical polarizations. When compared with predictions from ITU-R Recommendation P. 838-3, our calculations consistently show lower values for a given rainfall rate. Reasons for these discrepancies are several, but the main one is related to the inherent assumptions in the drop size distributions used in developing the Rec. P. 838-3 prediction method.

1. Introduction

It has been shown in the recent past [1] that the 2-dimensional video disdrometer (2DVD) is capable of providing rainfall microstructure information, in terms of (a) drop size distribution (DSD), (b) drop shapes, (c) drop orientation angles and (d) fall velocities, all of which are required to evaluate (i) the specific attenuation in rain and its dependence on rainfall rate and (ii) cross-polar effects for earth-space systems operating with orthogonal polarizations at microwave and millimeter wave frequencies. The unique feature of the 2DVD measurement is that it provides size, shape, orientation and fall velocity of each individual hydrometeor falling within its sensor area.

In this paper, we present (and compare) such rain-microstructure data obtained from several, climatically different locations, such as Alabama (USA), Okinawa (Japan), Ontario (Canada) and west Sumatra (Indonesia). Drop shapes and orientations have been derived from the individual images obtained using the two orthogonally placed fast line scan cameras of the 2DVD. We report examples of results from the various locations and compare with the shape and orientation angle distributions derived from an artificial rain experiment, conducted under calm wind conditions. The individual drop-by-drop data from natural rain in the four above mentioned locations are then used to calculate the probable variation of the XPD versus CPA (i.e. cross-polar discrimination versus co-polar attenuation) for a simulated earth-space scenario at 20 GHz, which in turn are compared with 1-year of beacon measurements [2]. Also calculated from the drop-by-drop measurements is the 20 GHz specific attenuation for horizontal and vertical polarizations. The calculations are compared with the predictions from the ITU-R Recommendation 838-3 [3].

2. Processing 2DVD images

The 2DVD records the images of each individual drop falling through its sensor area. Details of the instrument are given in [1], [4] and [5]. It has two, orthogonally placed line scan cameras which give two ‘views’ of the raindrop as it passes through the sensor area. Normally the drops fall through the sensor area with a finite horizontal velocity and hence the shape appears distorted which can easily be corrected for if there is no tilt of the symmetry axis, i.e., in radar/propagation terminology the ‘intrinsic’ canting angle is zero. If in addition to finite horizontal velocity there is a finite ‘intrinsic’ canting angle then the images of individual drops are again distorted

but can be ‘de-skewed’ using the algorithm described in [6] to derive the so-called ‘canting angles’ from each image from the two cameras. Here, the term canting angle is used (even though it is defined for propagation applications) since each camera ‘view’ can be thought of as being in the ‘polarization’ plane of a propagation path at zero elevation angle. As such, two canting angles are derived for each drop (the angle being defined from the vertical line which is perpendicular to the light planes). Recently, Huang et al. [7] have described in detail the procedure (based on Schoenhuber et al 2000) for estimating the orientation angles on a drop-by-drop basis and derived the canting angle distributions for the artificial rain experiment [8] conducted under calm conditions and where the drops were allowed to fall a distance of 80 m. Fig. 1 shows these distributions derived after processing the two camera images. The shapes of the canting angle histograms are similar to each other and moreover are approximately Gaussian with mean equal to $\sim 0^\circ$ and standard deviation of around 7° . It was also found that the larger drops were generally more stable. Fig. 2 shows the standard deviation of the canting angle distribution derived for the various drop diameters (D_{eq}). A noticeable reduction with increasing D_{eq} can be seen. These results support previous studies using dual-polarized radar observations [9] in a summer-time convective rain storm in Colorado using the CSU-CHILL radar, the inference being that it “.. reflects the fact that larger drops are more stably oriented as compared to small-sized drops”.

Thurai et al [10] derived the drop shapes for the various drop diameters for the same artificial rain experiment. From the images of over 115,000 drops, the ‘most probable’ shapes were derived; fig. 3 shows the shapes for D_{eq} ’s of 1, 2, 3, 4, 5 and 6 mm. They show remarkable resemblance to the contours from the numerical model of Beard-Chuang ([11]; (refer to their Fig. 7), except for the larger sizes (6 mm) which appeared to have somewhat flatter base than the model prediction. Note however, both the Beard-Chuang model and the 2DVD images based contours show more pronounced deviation from the oblate spheroid shapes for the 5 and 6 mm cases.

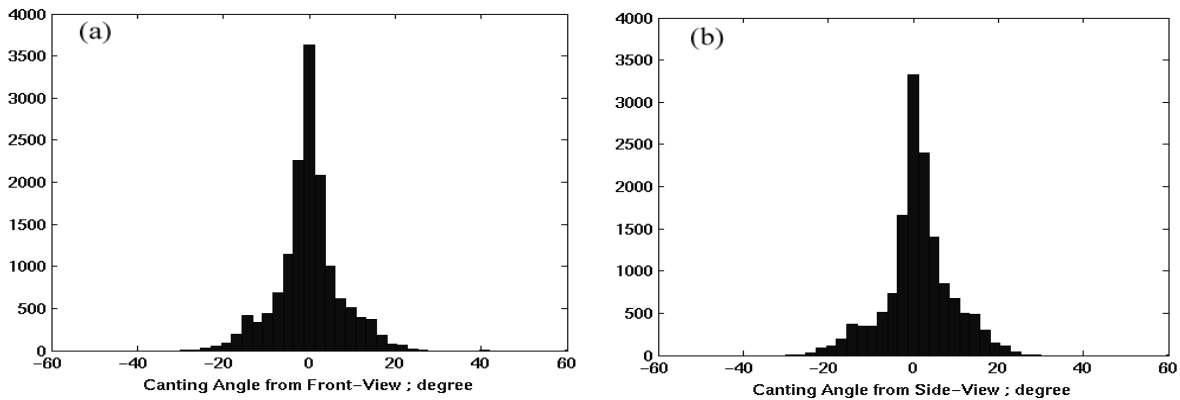


Fig. 1: Drop canting angle histograms, from the 2 orthogonal cameras (a and b), independent of each other

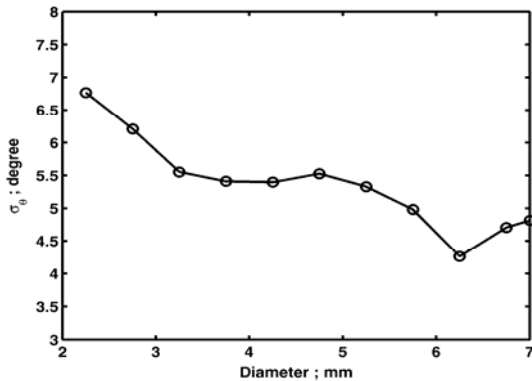


Fig. 2: Standard deviation of canting angle distributions for various drop diameter intervals

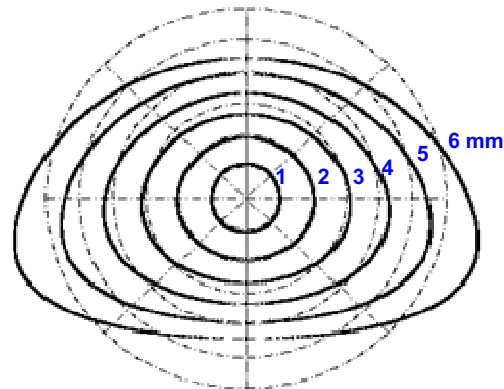


Fig. 3: Drop mean shapes derived from 2DVD images for various drop diameters

The 2DVD has been used in several field campaigns in various locations, and with precise calibration of each instrument, it has been possible to derive drop shapes in natural rain. Fig. 4 shows a sample of processed images from 3 locations, viz: Okinawa (Japan), West Sumatra (Indonesia) and Alabama (USA). For the first 2 locations, drops in the 3 - 3.25 mm and in the 4 - 4.25 mm range are shown, and for the third location, drops in the 4 - 4.25 and 5 - 5.25 mm range are shown. The color scale represents the probability values, and as such, indicates the shape variations due to drop oscillations etc. Superimposed on these plots as black lines are the ‘most probable shapes’ derived from the artificial rain experiment (given in Fig. 3) corresponding to the various drop diameters. In all cases, the black contours seem to represent the most probable shapes, but in the case of Okinawa and Alabama, the 4 - 4.25 mm drops appear to show somewhat more ‘conicity’, with the variation at the top of the drops being marginally higher than the base. Note also that this is the first time the flattening at the base with increasing D_{eq} has been demonstrated with sufficient number of recorded images in natural rain (the 5 mm data from Alabama), as was the case with the artificial rain data [10].

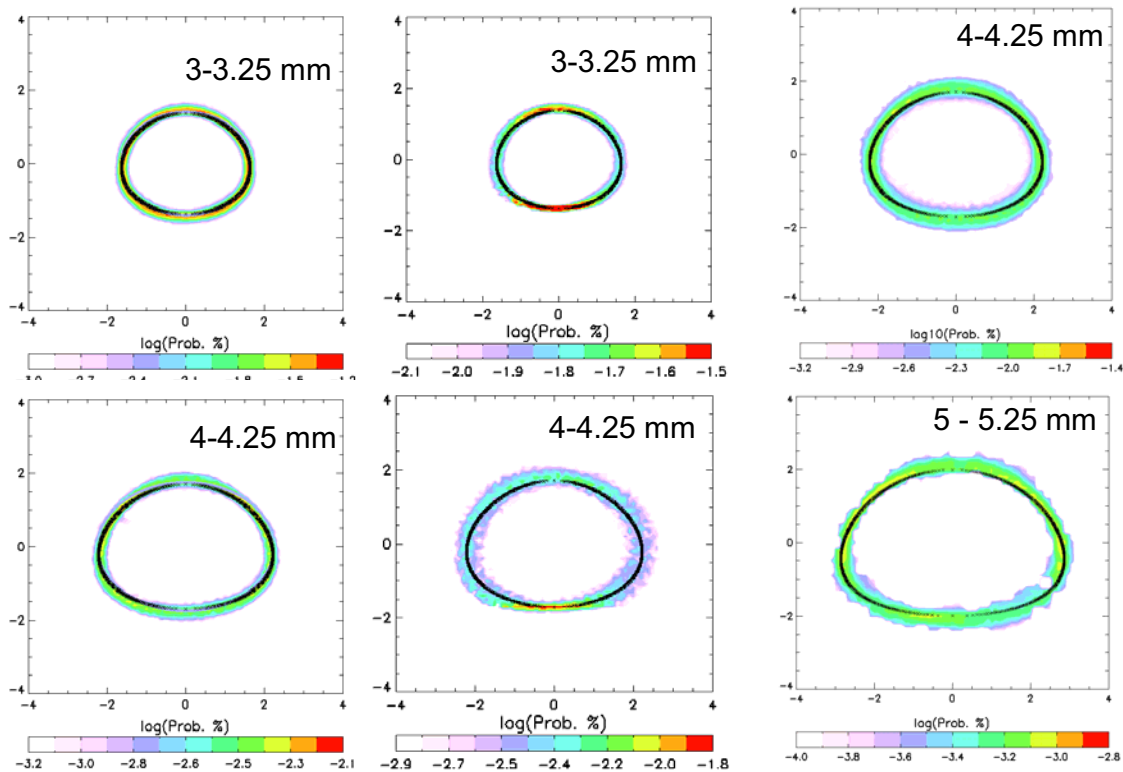


Fig. 4: Drop shape ‘probability contours’ for various diameters and for three locations, namely, Okinawa (left panels), west Sumatra (middle panels) and Alabama (right panels). The color scale is in log (probability). The solid black curves represent the conical fit to the ‘most probable’ drop shapes from the 80 m fall experiment (see Fig. 3).

3. Calculating propagation (fundamental) parameters

The propagation parameters such as the specific attenuation are fundamentally governed by the scattering matrix of the individual hydrometeors along the propagation path. When calculating these individual contributions, information on each hydrometeor is input in terms of its shape (assuming rotational symmetry about one axis for the case of raindrops) and its orientation defined by its polar (or zenith) angle and its local azimuth angle. Huang et al. [7] have shown that the individual drop orientation can be derived from the pair of canting angles derived from the two cameras for each drop. The same procedure was applied to the images of each individual drops in natural rain to derive their shape and the orientation, and the scattering matrix was calculated on a drop-by-drop basis. If we denote

the complex forward scattering amplitudes for horizontal and vertical polarizations as \bar{f}_H and \bar{f}_V respectively, then for each drop, the corresponding elemental contribution to the specific attenuation (γ_H) and the specific differential attenuation (γ_{HV}) as well as the specific differential phase (K_{DP}) were calculated from:

$$\gamma_h^{nth\ drop} = -8.686 \lambda 10^3 \text{Im}(\bar{f}_H) ; \text{dB/km} \quad (1a)$$

$$\gamma_{hv}^{nth\ drop} = -8.686 \lambda 10^3 \text{Im}(\bar{f}_H - \bar{f}_V) ; \text{dB/km} \quad (1b)$$

$$K_{DP}^{nth\ drop} = \frac{180}{\pi} \lambda 10^3 \text{Re}(\bar{f}_H - \bar{f}_V) ; \text{deg/km} \quad (1c)$$

where λ is the wavelength in m and \bar{f}_H and \bar{f}_V are in units of m and the drop concentration is assumed to be 1 per m^3 . Further, using the fact that the complex forward scattering amplitudes sum coherently, the individual drop contributions can be summed over a finite time period and normalized with respect to the drop concentration.

An example of the calculations at 20 GHz is shown in Fig. 5 as time series for an event recorded in Okinawa. The magenta curves in both (a) and (b) show γ_H and γ_{HV} (respectively) determined over a time interval of 60 seconds using the drop-by-drop data. Superimposed in blue are the corresponding estimates using the 60 second drop size distribution (DSD) and assuming the mean drop shapes and a standard model for the drop orientation (i.e. Gaussian distribution with 0° mean and 7° standard deviation). The rainfall rate for the event is shown in the lowest panel, and is a sample of the same event used in a previous study [12]. The comparisons in Fig. 5 (a) and (b) show that it is not necessary to utilize the rainfall microstructure (drop-by-drop) information for calculating γ_H and γ_{HV} , and that it is sufficient to use 60 second DSD and bulk assumptions regarding drop shapes and orientations.

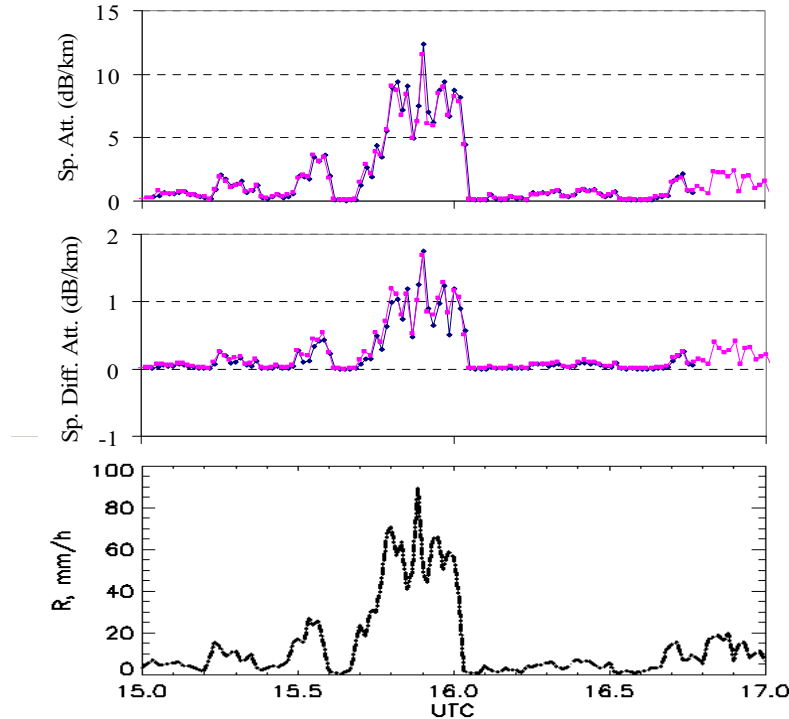


Fig. 5: 20 GHz specific attenuation calculations for H polarizations (top panel) , the specific differential attenuation (middle panel) and rainfall rate (bottom panel), given as time series, calculated using 2DVD data. The magenta curve uses the rain microstructure information on a drop-by-drop basis and the blue curve makes ‘bulk assumptions’.

4. Cross-polar effects

Next we consider rain-induced depolarization. This is of relevance to fixed satellite systems using orthogonal polarizations which require information on cross-polar effects along their propagation paths. For systems operating at 10 GHz or higher, rain-induced depolarization will become increasingly significant (as will rain attenuation), and their effects are often quantified in terms of the variation of cross-polar discrimination with co-polar attenuation (XPD – CPA variation, as in [13]).

An earlier study utilized the Okinawa data to derive the XPD-CPA variation for a simulated earth-space scenario at 20 GHz. That study assumed that the ‘point-to-path scaling’ would be the same for the co-polar signal and the cross-polar signal at any given time. This is a reasonable assumption to derive the XPD-CPA variation (but not valid for deriving CPA or XPD statistics).

The study also used 2DVD data as the basic input to the calculations. Fig. 6 shows the step-by-step procedure, with the input used in the first study given in blue. The 1-minute DSDs and the mean drop shapes together with model based assumptions on drop orientations were used for the scattering (T-matrix) calculations.

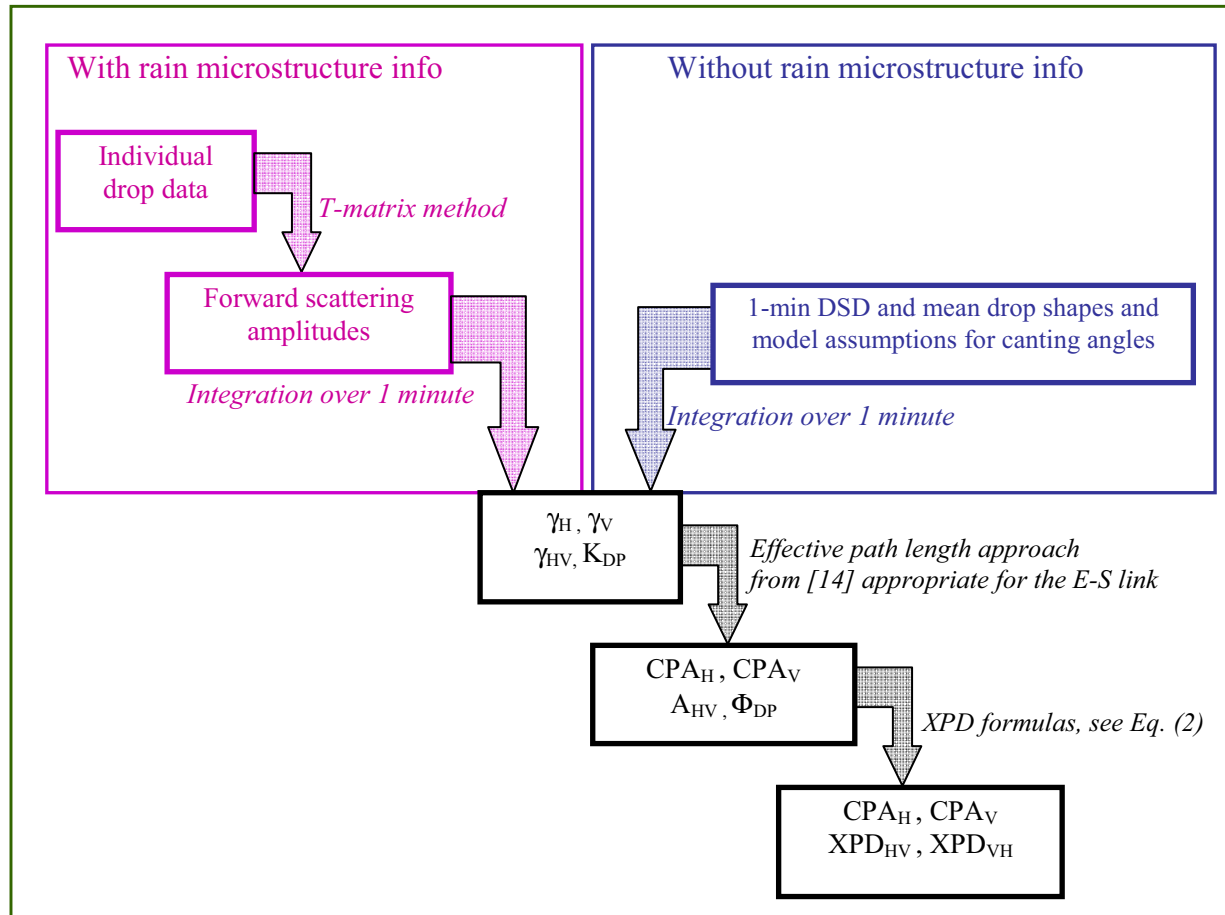


Fig. 6: Calculation procedure for deriving the XPD-CPA variation. The blue input represents the standard approach and the pink input represents the calculations using the (drop-by-drop) rain microstructure data.

Values of γ_H and γ_{HV} as well as K_{DP} were derived for a nominal temperature of 20 °C. An effective path length approach, based on the ITU-R Recommendation P. 618-9 [14], was used for point-to-path scaling to derive the co-polar attenuation (CPA_H) for the H polarization, the differential attenuation (A_{HV}) and the differential phase (Φ_{DP}) for the entire path in rain. Finally using the approach given in Kamp [15], based on the earlier work by Oguchi et al., [16], it was possible to derive the XPD from the calculated CPA_H , A_{HV} and Φ_{DP} via the equation:

$$\text{XPD} = 20 \log_{10} \left| \frac{\chi_{\text{rain}} + \tan^2(\phi - \delta)}{(\chi_{\text{rain}} - 1) \tan(\phi - \delta)} \right| \quad \text{where} \quad \chi_{\text{rain}} = \exp - \left\{ \frac{A_{\text{HV}} \ln 10}{20} + j \Phi_{\text{dp}} \frac{\pi}{180} \right\} \quad (2)$$

and $\phi - \delta$ is the canting angle of symmetry axis of the medium relative to the polarization direction, with δ being the polarization angle and ϕ being the canting angle of the rain drop.

For the drop-by-drop calculations, we simply replace the 2DVD input data by the drop shape and orientation of each individual drop and integrate over say 1 minute time interval (bearing in mind that the calculations need to be normalized with respect to the drop concentration). The input is shown in pink in Fig. 6.

The two calculation procedures are compared in Fig. 7 for an earth-space scenario with the link parameters given in Table 1. The parameters represent a beacon experiment [2] conducted in Aveiro, Portugal, and the color intensity in Fig. 7 represents the XPD-CPA variation derived from 1-year of beacon measurements. Note, the input 2DVD data used for the calculations (shown as pink circles) were obtained from Okinawa, a region climatically similar (at least in rainfall microstructure terms) to the earth-station location.

Table 1: Parameters used for the XPD-CPA calculations for the 20 GHz beacon experiment [2]

Transmit signal:	19.701 GHz from Eutelsat Hotbird-6, H-polarisation, tilt = 23°
Receiver:	1.5 m antenna, elevation = 38° Co-polar and XPD (complex) measurements
Lat and Long:	40° 38'N and 8° 39'W
Calculated effective path length for point-to-path scaling	3.96 km, assuming the annual mean rain height to be 2.4 km

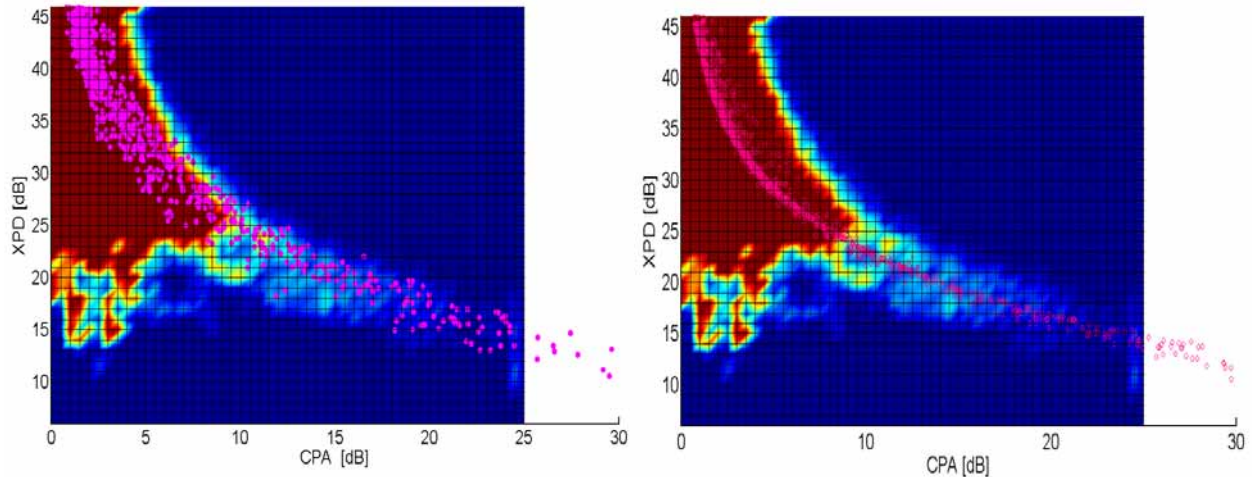


Fig. 7: XPD-CPA variation (shown as pink circles) calculated for the 19.701 GHz experimental scenario in Portugal, compared with the beacon measurements taken over a year [2] shown as colour intensity plot. The left panel shows the model calculations using the drop-by-drop method, and the right panel shows the calculations using the mean shape and orientation distribution models as in the previous study [12].

Both sets of calculations superimpose well on the beacon data derived variation, but the ‘drop-by-drop’ based calculations, given in fig. 7(a), shows significantly more spread in XPD for a given CPA level compared to the ‘shape/orientation model based approach’ given in fig. 7(b). For CPA < 10 dB, the beacon data will contain substantial contributions from ice depolarization - as seen from the color intensity plots - but even in this region, the spread in the rain contribution is noticeable as in Fig. 7a. For CPA > 10 dB, much of the XPDs arise due to rain and in this region, the drop-by-drop based calculations capture most of the spread in the experimental data. This spread is due in most part to the variance of drop shapes (i.e., due to drop oscillations) which is not captured when mean shapes are used.

5. Specific attenuation calculations and ITU-R Rec. P. 838-3

ITU-R Recommendation P. 838-3 (abbreviated to P. 838-3 hereafter) has a power-law approximation to relate the rainfall rate with the specific attenuation [3]. The relationship is of the form:

$$\gamma_{H,V} = a_{H,V} R^{b_{H,V}} \quad (3)$$

R being the rainfall rate in mm/h and the units of γ_H and γ_V being dB/km. In this section we examine the accuracy of the predictions using the 2DVD measurements in several different locations.

Fig. 8 shows the calculated specific attenuations (grey points) for 20 GHz using 2DVD data taken a long duration event in Okinawa for (a) H and (b) V polarizations. For comparison, the predicted curves from P. 838-3 are included (as solid lines). The calculations shown here were performed using the somewhat ‘simpler’ approach (corresponding to the magenta curve in Fig. 5); however, as noted in section 3 earlier, this is not different from the computed γ_H and γ_V using the drop-by-drop calculations. The spread in the calculated points in Fig. 8 hence reflects the variations in the DSDs and the shape of their distributions (e.g. gamma DSD with different ‘shape’ parameter μ). Despite this, the calculations are consistently lower than the P. 838-3 predictions both for H and for V polarizations.

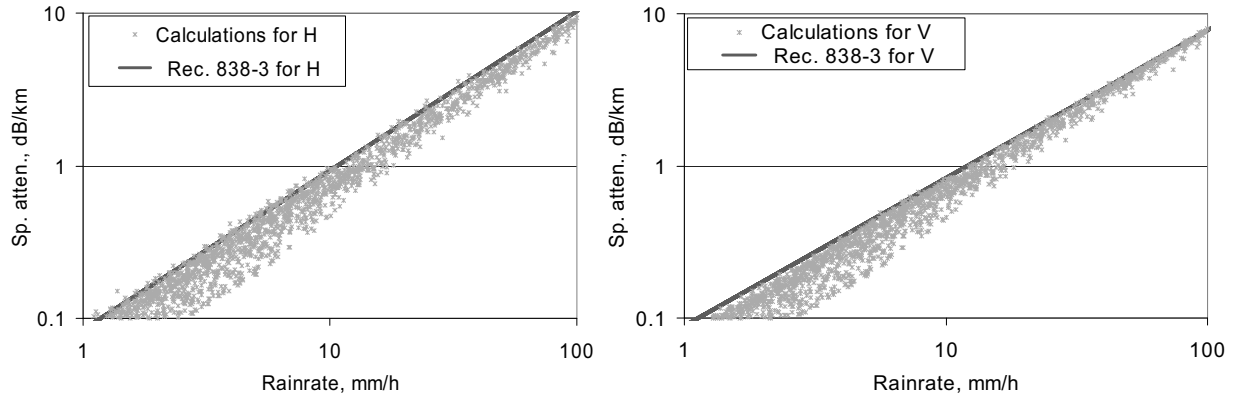


Fig. 8: 20 GHz specific attenuation versus rainfall rate using 2DVD data, compared with P. 838-3 predictions

The power-law coefficients fitted to the data are compared with those from P.838-3 for 20 GHz in Table II. Also included are calculations for other locations for a number of selected events. As seen, there are consistent differences. The main reason for the discrepancy between the calculations and the P. 838-3 predictions is the assumed DSDs in the latter case. More specifically, the coefficients given in version 3 of P. 838 were based on a variety of theoretical distributions, whereas our calculations are based on measured DSDs taken under a variety of rain climate and conditions and are more realistic and more representative of the DSDs on a statistical and global basis. The other reasons for the discrepancy could be (i) the upper limit of the drop diameter required for the scattering calculations (set to 3 times the median volume diameter in our calculations) and (ii) the assumed oblateness for drop shapes in P. 838-3 compared with the most probable (non-oblate) shapes used in our calculations.

TABLE II. Fitted coefficients for equation (3) from the 20 GHz calculations using 2DVD measurements from selected locations and events, compared with the Rec. P. 838-3 coefficients

Location	a_H	b_H	a_V	b_V	Selected events	Year and / or season
Colorado	0.05428	1.0521	0.05183	1.0468	Seasonal ‘Baiu’ event	June 2004
Okinawa	0.06958	1.0872	0.06708	1.0652	Rain only events	Summer 2005
Toronto	0.0590	1.0802	0.0562	1.0680	Stratiform precip.	November 2006
Sumatra	0.0664	1.0591	0.0622	1.0498	Pre SW monsoon	April 2007
P. 838-3	0.09164	1.0568	0.09611	0.9847		

6. Conclusions

We have demonstrated that the 2DVD can provide information on rain microstructure in terms of shapes and orientations of individual drops, which are pertinent for evaluating propagation effects at 20 GHz. Our calculations have suggested that the individual drop information is particularly useful in predicting the XPD spread for a given level of CPA. The drop-by-drop measurements contain information on drop oscillations as well as their orientations. We expect these computations to be more ‘realistic’ as compared with those using mean shapes and model-based orientation angle distributions. When compared with the 19.7 GHz beacon measurements over 1 year, the individual drop-based calculations better isolate the rain component of the XPD variability, particularly for the lower CPA levels (<10 dB) where additional XPD contributions due to ice aloft are well known to frequently occur.

Regarding specific attenuation, it appears that the predictions by ITU-R Rec. P.838-3 are overestimated for a given rainfall rate. The 2DVD data from several locations have been used in our computations and have consistently given lower estimates for γ_H and γ_V at 20 GHz. The discrepancies are attributed to a number of factors, the main one being that the DSDs used in the development of P. 838-3 (i.e. version 3), which are theoretically based, are biased towards higher values of median diameters (for a given rainfall rate) as compared with our measured DSDs which show drop median diameters to be less for the same rainfall rate. Two additional factors also contribute, namely the oblate approximation used in the P. 838 3 predictions and the maximum diameter used in the scattering calculations.

Acknowledgements

This work was supported by the National Science Foundation via grant ATM-0603720. We would also like to thank our collaborators in the various Institutes who have kindly contributed the 2DVD data, in particular Dr. K. Nakagawa of NiCT, Japan, for the Okinawa data and Prof. T. Kozu and Dr. T. Shimomai of Shimane University, Japan for the Sumatra data. We also wish to thank Dr. D. Hudak et al. (Environment Canada) for collaborating with us in the Toronto campaign and Dr. W. Petersen (University of Alabama, Huntsville), for collaborating with us in the Alabama campaign. Finally, we wish to thank Dr. M. Schönhuber for the assistance with the 2DVD image analyses and to Günter Lammer (both of Joanneum Research, Austria) for all the hardware assistance with the various 2DVD installations.

References

- [1] Schönhuber M., G. Lammer and W.L. Randeu, ‘One Decade of Imaging Precipitation Measurement by 2D-Video-Distrometer’, *Advances in Geosciences*, 10, pp. 85–90, 2007.
- [2] Rocha, A., R. Teixeira and J. Neves: “One year Fade Dynamics Statistical Results for an Earth-Satellite Path at 20 GHz”, Proceedings of the 3rd International Workshop of COST Action 280 on Propagation Impairment Mitigation for Millimetre Wave Radio Systems, Prague, Czech Republic, June, 2005.
- [3] International Telecommunication Union Recommendation ITU-R. P. 838-3, “Specific attenuation model for rain for use in prediction methods”, Geneva, 2005.
- [4] Kruger, A. and W.F. Krajewski, “Two-Dimensional Video Disdrometer: A Description”, *J. Atmos. Ocean. Tech.*, 19, pp. 602-617, 2002.
- [5] Schönhuber, M., G. Lammer and W.L. Randeu, 2008: “The 2D-Video-Distrometer”, Chapter 1 in “*Precipitation: Advances in Measurement, Estimation and Prediction*”, Michaelides, Silas (Ed.), Springer, 2008, ISBN: 978-3-540-77654-3
- [6] Schönhuber, M., W.L. Randeu, H.E. Urban and J.P.V. Poyares Baptista, “Field Measurements of Raindrop Orientation Angles”, Proceedings of the IEE Millennium Conf. Ant. Prop., Davos, Switzerland., 2000.

- [7] Huang, G.J., V. N. Bringi and M. Thurai, "Orientation Angle Distributions of Drops after 80 m fall using a 2D-Video Disdrometer", *J. Atmos. Oc. Tech.*, Early online release, 2008, DOI: 10.1175/2008JTECHA1075.1
- [8] Thurai, M. and V.N. Bringi, "Drop Axis Ratios from 2D Video Disdrometer, *J Atmos. Ocean. Tech*, 22, pp. 963-975, 2005.
- [9] Huang G. J., "Evaluation and Application of Polarimetric Radar Data for the Measurement of Rainfall". *Ph. D. Dissertation*, Colorado State University, USA.
- [10] Thurai, M., G.J. Huang, V.N. Bringi, W. L. Randeu, M. Schönhuber: "Drop Shapes, Model Comparisons and Calculations of Polarimetric Radar Parameters in Rain", *J. Atmos. Ocean. Tech. of the Am. Met. Soc.*, 24 (6), pp. 1019-1032, 2007.
- [11] Beard, K.V. and C. Chuang. "A New Model for the Equilibrium Shape of Raindrops", *J. Atmos. Sci.*, 44, pp. 1509-1524, 1987.
- [12] Thurai, M., V.N. Bringi and A. Rocha.: "Specific Attenuation and Depolarization in Rain from 2-Dimensional Video Disdrometer data", *IET Microwaves, Ant. and Prop.*, 1, pp. 373-380, 2007.
- [13] COST Action 255 Final Report, "Radiowave Propagation Modeling for New Satellite Communication Services at Ku-band and above", Chapter 2.4: Rain and Ice Depolarisation, *ESA publications Division*, 2002.
- [14] International Telecommunication Union Recommendation ITU-R. P. 618-9, "Propagation Data and Prediction Methods Required for the Design of Earth-Space Telecommunication Systems", Geneva, 2007.
- [15] van der Kamp, M. M. J, "Separation of Simultaneous Rain and Ice Depolarization", *IEEE Trans. Antennas and Propagation*, 52(2), pp. 513-523, 2004.
- [16] Oguchi, T., "Scattering Properties of Pruppacher-and-Pitter Form Raindrops and Cross Polarization due to rain: Calculations at 11, 13, 19.3 and 34.8 GHz", *Radio Science*, 12 (1), pp. 41-51, 1977.

Four-Year Rain Attenuation Statistics of Ku-Band Up and Down Links Simultaneously Observed in Japan and Indonesia

Yasuyuki Maekawa, Yoshiaki Shibagaki⁽¹⁾, Toru Sato⁽²⁾,
Mamoru Yamamoto, Hiroyuki Hashiguchi⁽³⁾ and Shoichiro Fukao^{(3),(4)}

⁽¹⁾Osaka Electro-Communication Univ., 18-8 Hatsucho, Neyagawa, Osaka 572-8530, Japan
E-mails: maekawa@maelab.osakac.ac.jp, sibagaki@maelab.osakac.ac.jp

⁽²⁾Dept. of Communications and Computer Engineering, Kyoto Univ., Kyoto 606-8501, Japan
E-mail: tsato@kuee.kyoto-u.ac.jp

⁽³⁾Research Institute for Sustainable Humanosphere, Kyoto Univ., Uji, Kyoto 611-0011, Japan
E-mails: yamamoto@rish.kyoto-u.ac.jp, hasiguti@rish.kyoto-u.ac.jp, fukao@rish.kyoto-u.ac.jp

⁽⁴⁾Research Institute of Science and Technology, Tokai Univ. Tokyo 151-0063, Japan

Abstract

Four-year rain attenuation statistics are obtained for both up (14GHz) and down (12GHz) links of Japan's Ku-band satellite (Superbird C, 144E), which connects the earth stations in West Sumatra, Indonesia and Kyoto, Japan. Their long-term statistics agree well with the ITU-R predictions except for high attenuation range in Indonesia. A year-to-year variation of the worst month statistics is larger in Japan, while that of the attenuation ratio of up to down links is larger in Indonesia. This ratio is found to be inversely correlated with the equivalent path lengths at both stations. A very large daily variation of the attenuation statistics is found in Indonesia, indicating the decrease and increase of the time percentages by more than two orders in the morning and the afternoon, respectively. Also, "worst hour statistics" calculated on hourly basis show much larger difference from the yearly average statistics than the worst month statistics.

1. Introduction

It is known that rain attenuation of radio wave is significant in satellite communications using frequencies of higher than 10 GHz. Rain attenuation may become very severe even for Ku-band (14/12 GHz) radio waves in heavy rain regions like the equatorial region. The Ku-band radio wave signals tend to be attenuated by rain more significantly than those of C-band (6/4 GHz) that has long been used in these regions up to now. However, demand for satellite communications with high data transmission rate capacity is recently increasing in newly developing areas such as South-East Asia, which is one of the heaviest rain regions in the world [1], [2]. Therefore, characteristics of the rain attenuation at Ku band need to be investigated in more detail in the equatorial region.

This study presents four-year rain attenuation statistics obtained from September 2002 to September 2006 for both up (14GHz) and down (12GHz) links of Japan's Ku-band satellite (Superbird C, 144E), which connects the Equatorial Atmosphere Radar (EAR; 0.2S, 100.3E) in West Sumatra, Indonesia and Research Institute for Sustainable Humanosphere (RISH; 34.9N, 135.8E), in Kyoto, Japan [3], [4]. First, the up- and down-link rain attenuation statistics observed at both stations are compared with the predictions of recent ITU-R recommendations [5]. Then, yearly variations of the attenuation statistics such as worst month statistics, attenuation ratio of up to down links, and equivalent path lengths are investigated at both stations in Japan and Indonesia. Also, the effect of the daily cycle of rainfall that is more conspicuous in Indonesia is discussed in terms of daily variation and local time dependence of the attenuation statistics. Finally, a concept of "worst hour statistics" analogous to the traditional worst month statistics is introduced, and their statistical features are compared between Japan and Indonesia.

2. Observation systems

The satellite links that connect RISH and EAR uses Superbird C. At RISH, the up-link transmission carrier frequency is 14.1292GHz and the down-link receive carrier frequency is 12.4198GHz. At EAR, on the other hand, the up-link transmission carrier frequency is 14.1498GHz and the down-link receive carrier frequency is 12.3992GHz. At both stations, the up-link radio waves use the vertical linear polarization, while the down-link radio waves use the horizontal linear polarization. The elevation angle is about 39 deg at EAR, while it is about 49 deg at RISH. For our data acquisition systems, personal computers (PCs) equipped with 16-bit A/D converter boards are used at both EAR and RISH stations, to measure Automatic Gain Control (AGC) voltage of the In Door Unit (IDU) of the VSATs that indicates the received signal level [6]. The measured data is stored in their internal hard disk drives every second. The measurements started in September 2002 and January 2003 at RISH and EAR, respectively. In this experiment, the up-link attenuation is estimated from the down-link signal level received at the opposite site in fair weather conditions, since both terminals use an SCPC signal linearly amplified by the satellite transponder without saturation [7]. An Optical Rain Gauge (ORG) was installed at EAR by a Shimane University group and we can utilize their 1-min rainfall rate data for this study. At the RISH station, we installed a rain gauge with 0.1 mm tipping buckets and started measurements of 1 min rainfall rates in 2004.

3. Four-year cumulative time percentages

Figure 1 shows cumulative time percentages of the up- and down-link rain attenuation and the rainfall rates observed during four years at (a) RISH in Japan and (b) EAR in Indonesia, respectively. The rainfall rates in 2002 and 2003 are substituted by those obtained at OECU in Osaka [8], which is located about 20 km west-south from RISH. In Fig.1 the prediction values for up- and down-link attenuation based on the recent ITU-R recommendations are shown by dashed (14 GHz) and dashed-dotted (12 GHz) lines, respectively. The rainfall rates for the cumulative time percentages of 0.01% used in these predictions are 60 and 85 mm/h at RISH and EAR, respectively. We can find good agreement between the measurements and predictions. At RISH in Japan, the time percentages of both up- and down-link attenuation values fairly well follow the prediction up to 20 dB. At EAR in Indonesia, to contrast, they become much smaller the predictions and rapidly decrease to 0.001% as the attenuation exceeds about 13 dB. This may represent a fairly localized structure of convective clouds along the slant path in the tropics for such heavy rainfall [4].

Figure 2 shows the relationship between worst month statistics and yearly average statistics of the rainfall rate obtained during three years from 2004 to 2006 at (a) RISH and four years from 2003 to 2006 at (b) EAR, respectively. The worst month statistics are also averaged during these years. We can see linear relationships between them in a logarithmic scale at both stations, so the relationships are expressed by $P = a P_w^b$, where P_w and P are the worst month and yearly average statistics, respectively; a and b are co-efficients for the least RMS (Root Mean Square) fitted approximation lines shown by the dashed lines in Fig.2. These best fitted parameters are given by $a=0.32$, $b=1.14$ at RISH in Japan; $a=0.57$, $b=1.19$ at EAR in Indonesia, respectively. In Japan these parameters show the values quite similar to the ITU-R predictions of $a=0.30$, $b=1.15$ [5]. In Indonesia, however, their values are larger than the prediction especially for a . This is probably due to longer period of the rainy season and smaller variation of the ground temperature compared to Japan [4].

The yearly variations of the worst month statistics are then investigated at both stations in Japan and Indonesia. Figure 3 depicts the yearly values of the coefficients a and b obtained for the up- and down-link attenuation and the rainfall rates at (a) RISH and (b) EAR, respectively. In Japan these yearly values obtained for the attenuation of CS (20 GHz) and BS (12 GHz) and the rainfall rate at OECU are also indicated by dashed lines from 2000 to 2006. In Fig.3 larger yearly variations are found in Japan than in Indonesia, although the annual rainfall as such was larger in Indonesia. This larger variability is related to larger year-to-year variation of the annual rainfall in Japan. It should be noted that similar variability is also found in OECU which is 20 km apart from RISH. This indicates that the effects of annual rainfall statistics are quite similar between the nearby two stations in Japan.

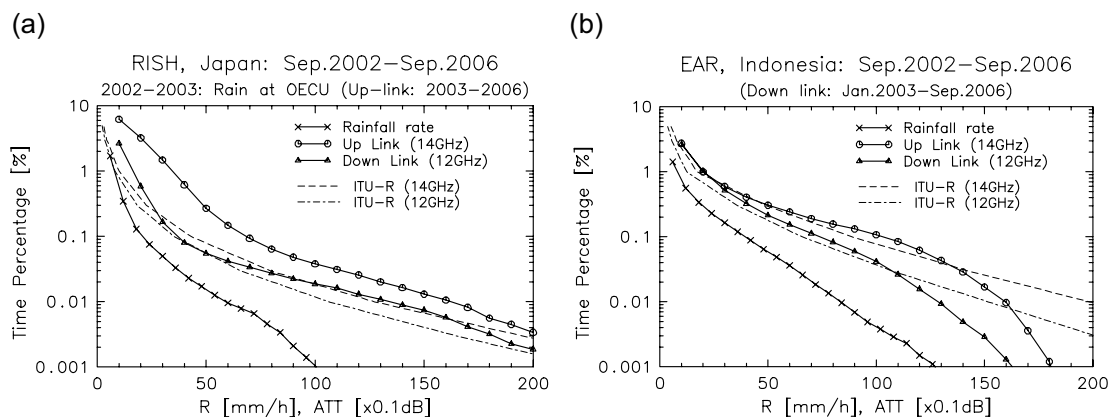


Figure 1. Cumulative time percentages of the up- and down-link rain attenuation and the rainfall rates observed during four years at (a) RISH in Japan and (b) EAR in Indonesia, respectively.

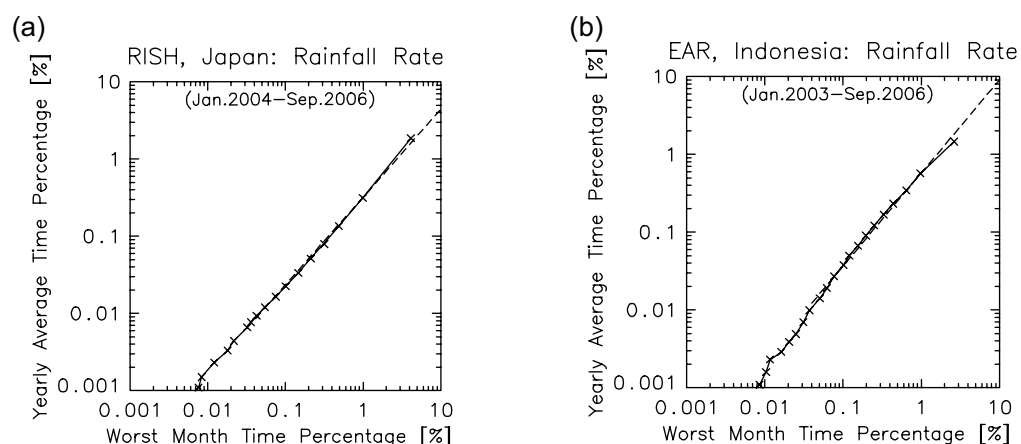


Figure 2. Relationship between worst month statistics and yearly average statistics of the rainfall rate obtained at (a) RISH and (b) EAR, respectively.

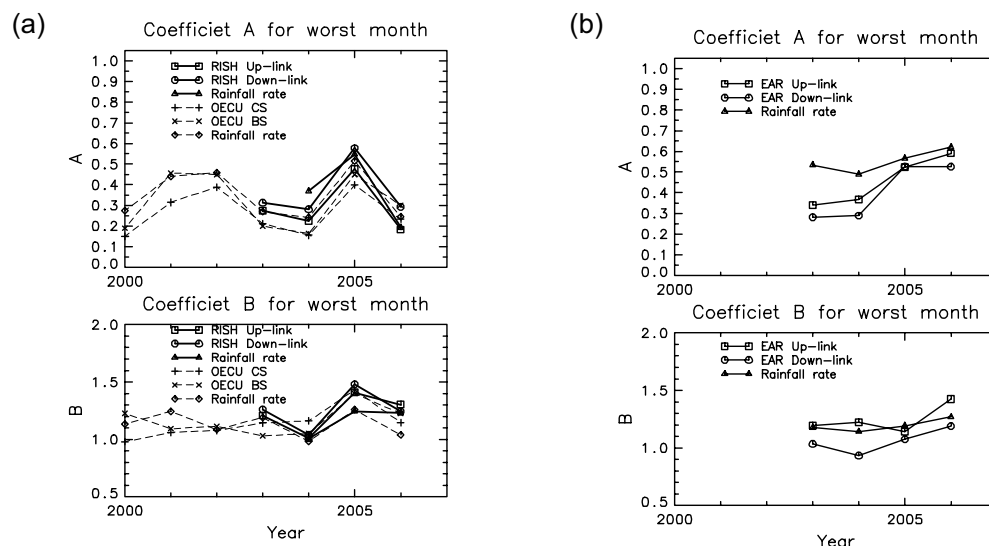


Figure 3. Yearly values of the coefficients a and b obtained for the up- and down-link attenuation and the rainfall rates at (a) RISH and (b) EAR, respectively.

4. Equi-probability relationships

4.1. Equivalent path lengths

In this section, equivalent path lengths are investigated at both stations in Japan and Indonesia in each year, based on the equi-probability relationships between rainfall rates and up- and down-link attenuation values. Figure 4 shows equi-probability values of the down-link attenuation against the rainfall rates obtained at (a) RISH and (b) EAR in each year from 2003 to 2006, respectively. The rainfall rates at RISH in 2003 are similarly substituted by those of OECU. Solid and dashed lines indicate theoretical relationships between attenuation and rainfall rates for equivalent path lengths of 2-6 km. In these calculations, the raindrop size distribution (DSD) is based on the Marshall-Palmer type. At RISH in Japan (a), the equivalent path lengths estimated from Fig.4 in each year remain more than about 4 km up to the rainfall rate of 60 mm/h, whereas they slightly decrease down to 3 km as the rainfall rate exceeds 60 mm/h. Also, the equivalent path lengths are found to have fairly large year-to-year variations in Japan. At EAR in Indonesia (b), on the other hand, the equivalent path lengths rapidly decrease down to around 2 km in each year as the rainfall rate exceeds 60 mm/h, although they remains more than 3 km below 60 mm/h. This also suggests a localized structure of convective precipitating clouds in the equatorial region. The equivalent path lengths, however, do not seem to have so much year-to-year variations in Indonesia as in Japan.

4.2. Attenuation ratios of up to down link

The ratios of up- to down-link attenuation are statistically examined in each year based on their equi-probability relationships in Japan and Indonesia. Figure 5 shows the equi-probability values of the up-link attenuation against the down-link attenuation obtained at (a) RISH and (b) EAR in each year from 2003 to 2006, respectively. Three thin lines are theoretical relationships of the frequency scaling between up- and down-link attenuation at each station. These theoretical values are based on the three typical kinds of raindrop size distributions such as Joss-drizzle (Jd), Marshall-Palmer (MP) and Joss-thunderstorm (Jt) types [9], assuming homogeneity of rain along the path. The equivalent path lengths needed for this theoretical calculation are, on an average, assumed to be 4 and 3 km at RISH and EAR, respectively, for the large attenuation range of more than 10 dB, as was shown in Fig.4. In Fig.5, the equi-probability relationships obtained at both stations in each year are found to exist around these three theoretical values, although they also show considerable year-to-year variations. For example, the ratio of up- to down-link attenuation estimated from their equi-probability relationship at RISH (a), as a whole, indicates slightly smaller values in 2005 (triangles), while that obtained at EAR (a) indicates considerably larger values in 2005. Note that the equivalent path lengths shown in Fig.4, to contrast, indicate larger and smaller values at RISH and EAR in 2005, respectively, compared to the other years.

The yearly average values of attenuation ratios and equivalent path lengths are then compared in Fig.6. These yearly values are obtained from the equi-probability values averaged over the attenuation range of more than about 10 dB, which were shown in Figs.4 and 5. The equivalent path lengths are averaged over both up and down links at each station. Also, attenuation ratio of Ka to Ku bands and equivalent path lengths similarly obtained at OCEU are indicated by dashed lines from 2000 to 2006. It is found that the attenuation ratios show fairly large variations at both stations in Japan and Indonesia, ranging from 1.1 to 1.4 even for the Ku band (14/12 GHz). The attenuation ratios are also found to be inversely correlated with the equivalent path length in each station. The magnitude of the variation is, however, much larger in Indonesia than in Japan compared to the variation of their equivalent path lengths, possibly indicating larger variability of raindrop size distribution (DSD) for the tropical convective clouds in Indonesia that may contain rather smaller DSD as was discussed in our previous study [4]. It is also noted that these yearly variations of the attenuation ratios and equivalent path lengths do not indicate so much correlation between RISH and OECU in Japan, although their distance is only 20 km. Thus, the annual statistics of the attenuation ratios and the equivalent path lengths show characteristics quite different from those of the worst month statistics which are simply explained by the similarity of their annual rainfall statistics between the nearby two stations.

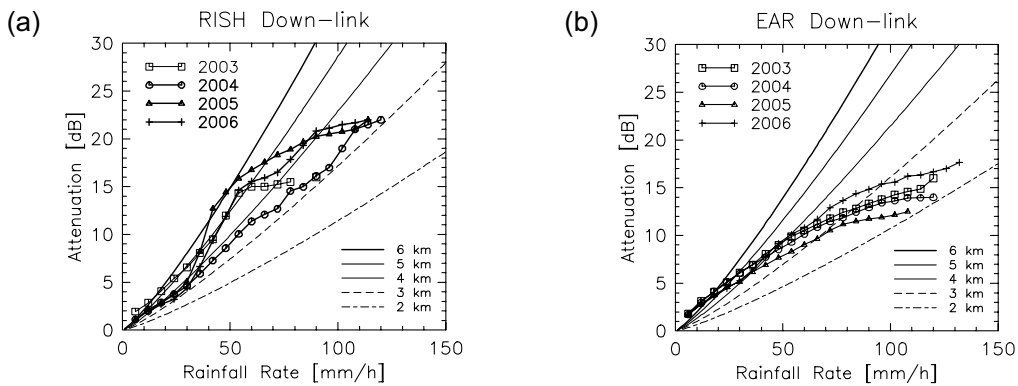


Figure 4. Equi-probability values of the down-link attenuation against the rainfall rates obtained at (a) RISH and (b) EAR, respectively, in each year.

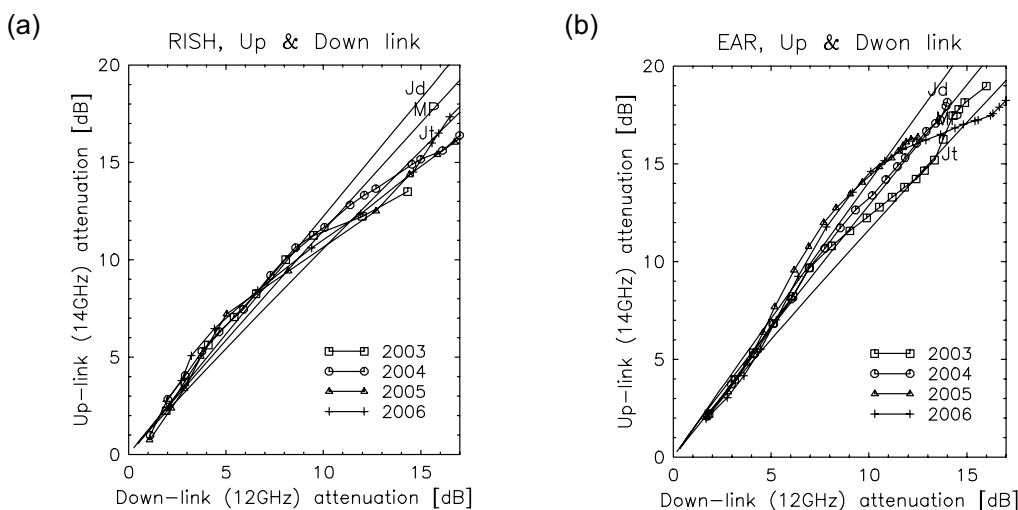


Figure 5. Equi-probability values of the up-link attenuation against the down-link attenuation obtained at (a) RISH and (b) EAR, respectively, in each year.

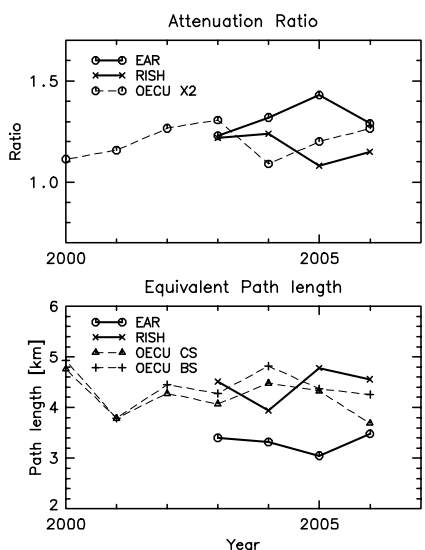


Figure 6. Yearly average values of attenuation ratios and equivalent path lengths.

5 .Local time dependence

In tropical region, rainfall usually shows large local time dependence, and at EAR in Indonesia, the rainfall is primarily concentrated in 13-19 LT all the year round. Also in Japan, we often observe showers in these afternoon hours in summertime. To evaluate the effects of such daily cycle of the rainfall at both locations, the cumulative time percentages of each rain attenuation levels from 1 to 20 dB are calculated according to local time on hourly basis. Figure 7 shows examples of the local time dependencies for both up- and down-link attenuation of 7 dB at (a) RISH in Japan and (b) EAR in Indonesia, respectively. The corresponding time percentages are plotted by their three-hour average values. At both stations, the time percentages are increased in the afternoon hours, and this tendency is quite conspicuous at EAR (b), demonstrating the increase and decrease of time percentages by more than two orders before and after the noon.

In order to estimate the enhancement of local time dependence statistically, cumulative time percentages are then calculated according to each local time at one hour interval during every year, and “worst hour statistics” analogous to worst month statistics are evaluated, combining the cumulative time percentages at every attenuation level in each year. The results of their down-link attenuation over the whole observational period are shown in Fig.8 compared with the yearly average statistics in a logarithmic scale at (a) RISH and (b) EAR, respectively, together with the worst month statistics.

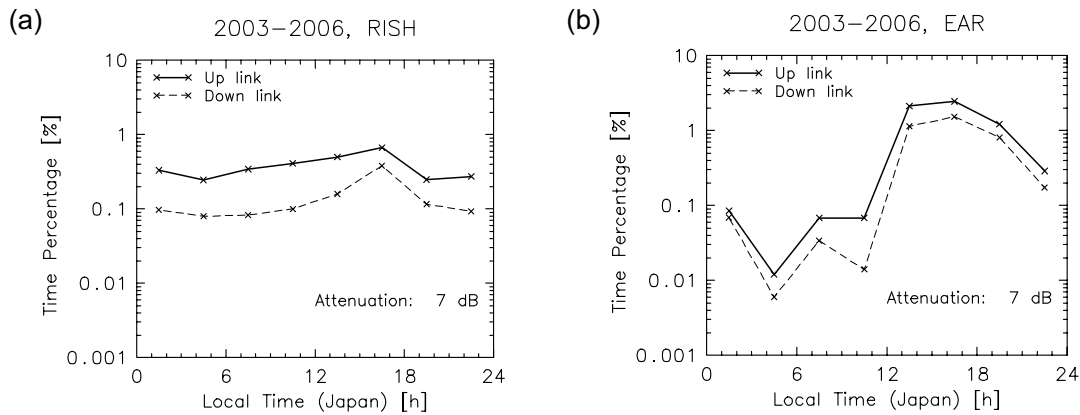


Figure 7. Local time dependencies for both up- and down-link attenuation of 7 dB at (a) RISH in Japan and (b) EAR in Indonesia, respectively.

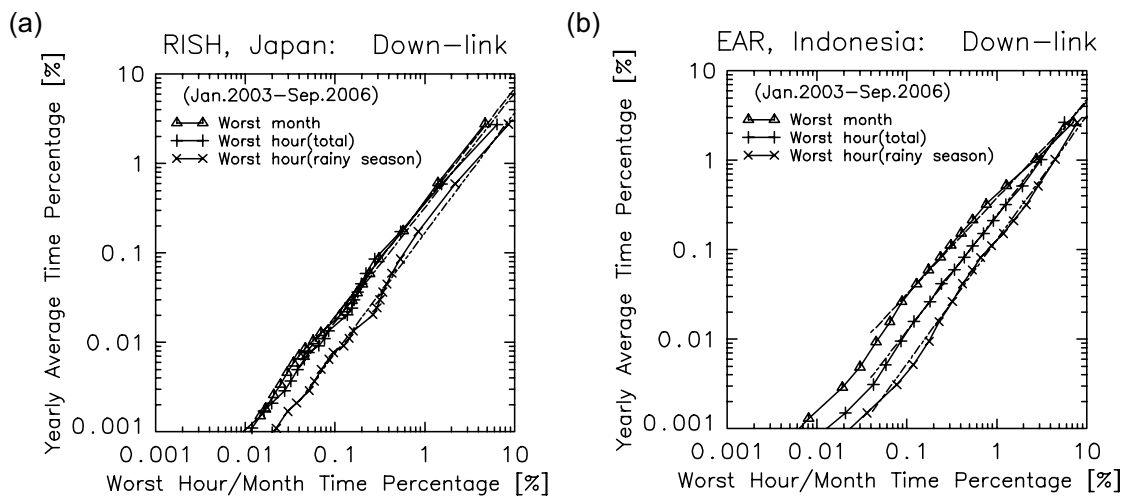


Figure 8. Relationship between worst hour statistics and yearly average statistics of the down-link attenuation obtained at (a) RISH and (b) EAR, respectively, together with worst month statistics.

Moreover, the worst hour statistics are demonstrated for the two cases: those for all the year and those for the rainy season only at both stations. At RISH in Japan (a), the worst hour statistics for all the year are found to have similar tendencies and are not very much enhanced compared to the worst month statistics. When they are confined during the rainy season from May to October, however, their time percentages are shown to be slightly increased, giving rise to the coefficient of $a=0.17$, $b=1.34$ compared to those of $a=0.35$, $b=1.24$ for the original worst month statistics. At EAR in Indonesia (b), on the other hand, the worst hour statistics for all the year are even shown to be largely increased and those for the rain season are found to be further enhanced: their coefficients are $a=0.24$, $b=1.29$ and $a=0.13$, $b=1.38$, respectively, compared those of $a=0.38$, $b=1.07$ for the original worst month statistics.

6 .Conclusions

This study has discussed fairly long-term rain attenuation statistics for both up (14GHz) and down (12GHz) links of Japan's Ku-band satellite (Superbird C, 144E), which connects the Equatorial Atmosphere Radar (EAR; 0.2S, 100.3E) in West Sumatra, Indonesia and Research Institute for Sustainable Humanosphere (RISH; 34.9N, 135.8E), in Kyoto, Japan. The yearly average rain attenuation statistics are first obtained for Ku-band up and down links at both earth stations during the whole observation period from September 2002 to September 2006. Compared with the recent ITU-R predictions, these four-year statistics indicate fairly good agreement with the predictions for both locations and frequencies, except for the attenuation range of more than about 13 dB with time percentages of less than 0.03% in Indonesia. For the worst month statistics, a large year-to-year variation is found in Japan than in Indonesia, although the annual rainfall as such is larger in Indonesia during the four years. This larger variability is primarily caused by the year-to-year variation of rainfall which is more conspicuous in Japan.

The attenuation ratio of up to down links is found to show fairly large variations at both stations in Japan and Indonesia. This ratio is, as a whole, inversely correlated with the equivalent path lengths at both stations. The magnitude of the variation is, however, much larger in Indonesia than in Japan compared to the variation of their equivalent path lengths, possibly indicating larger variability of raindrop size distribution (DSD) for the tropical convective clouds in Indonesia that may contain rather smaller DSD.

For the daily variation of the attenuation statistics, on the other hand, very large local time dependence is found in Indonesia, since the rainfall is especially concentrated in 13-19 LT all the year round. The cumulative time percentage of a specified attenuation level is shown to be increased and decreased by more than two orders before and after the noon. Moreover, the "worst hour statistics" calculated according to each local time at one hour interval are found to indicate much larger difference from the yearly average statistics than the worst month statistics especially in the rainy season. In Japan, however, the hourly attenuation statistics do not show so much local time dependence except for summertime.

Acknowledgements

The authors deeply thank the staff of Equatorial Atmosphere Radar for assisting our study and observations.

References

- [1] H.Minakoshi, K.Igarashi, T.Boonchauk, N.Hemmakorn, A.Yagasena, S.I.Hassan, J.Suryana, U.Sastrokusumo, S.C.N.Monje, and R.Reyes, "Rain Attenuation Measurements in Ku-band Satellite Communication in the East-Asiam Region under the POST-PARTNERS Project," *2001 Asia-Pacific Radio Science Conference, Digest*, Vol.1, 153p., 2001.
- [2] Q. W. Pan, and J. E. Allnutt, "12-GHz fade durations and intervals in the tropics," *IEEE Trans. Antennas and Propagat.*, Vol.52, pp.693-701, 2004.
- [3] S. Fukao, H. Hashiguchi, M. Yamamoto, T. Tsuda, T. Nakamura, M.K. Yamamoto, T. Sato, M. Hagio, and Y. Yabugaki,"The Equatorial Atmosphere Radar (EAR): System Description and First Results," *Radio Sci.*, Vol.38, No.4, 1053, doi:10.1029/2002RS002767, 2003.
- [4] Y. Maekawa, T. Fujiwara, Y. Shibagaki, T. Sato, M. Yamamoto, H.Hasiguchi, S. Fukao, "Effects of tropical rainfall to the Ku-band satellite communications links at the Equatorial Atmosphere Radar Observatory," *J. Meteor. Soc. Japan*, Vol. 84A, pp.211-225, 2006

- [5] ITU-R, "P837-1 Characteristics of precipitations for propagation modeling," *ITU-R Recommendations*, 2003.
- [6] Y. Maekawa, T. Fujiwara, Y. Shibagaki, T. Sato, M. Yamamoto, H. Hashiguchi, and S. Fukao, "First year results on rain attenuation characteristics of satellite links at equatorial atmospheric radar," *2004 IEEE AP-S/URSI Symposium*, Vol.2, pp.1660-1663 (Paper #65.9), Monterey, California USA, June 2004.
- [7] K.Hatsuda, Y.Aoko, H.Echigo, F.Takahata, Y.Maekawa and K.Fujisaki, "Ku-band long distance site-diversity (SD) characteristics by using new measuring system," *IEEE Trans. Antennas and Propagat.*, Vol.52, No.6, pp.1481-1491, 2004.
- [8] Y. Karasawa, and Y. Maekawa, "Ka-band earth-space propagation research in Japan," *Proc. IEEE*, Vol.85, pp.821-842, 1997.
- [9] T.Iida, *Satellite Communications (in Japanese)*, Ohmusha, pp.236-238, Tokyo, 1997.

A Unified Method for the Prediction of Rain Attenuation in Slant Paths and Terrestrial Links Using the Full Rainfall Rate Distribution

L. A. R. da Silva Mello and M. S. Pontes

CETUC-PUC/Rio and INMETRO

Rua Marquês de S. Vicente, 225 – Rio de Janeiro – 22453-900 – Brazil

smello@cetuc.puc-rio.br

mspontes@cetuc.puc-rio.br

Abstract

A semi-empirical method for the prediction of rain attenuation in slant paths and terrestrial links is proposed. The method uses the same simplified model of equivalent rain cell that are the basis for the ITU-R rain attenuation prediction methods but, additionally, the concept of an effective rain rate is introduced. This allows the use of the full rainfall rate distribution for the prediction of the rain attenuation distribution and the unification of the slant path and terrestrial links prediction algorithms. The numerical coefficients in the expressions were derived by multiple non-linear regressions using the experimental data currently available in the ITU-R data banks. Test results indicate that the proposed method provides significant improvement over the current ITU-R methods.

1. Introduction

The methods for the prediction of rain attenuation in slant path links and terrestrial links currently recommended by the ITU-R were originally developed based on simplified models for the rain field affecting the propagation path. The basic assumption in these methods is that an equivalent cell of uniform rainfall rate can model the non-uniform rainfall along the propagation path.

The terrestrial prediction method, given in Rec. ITU-R P.530-12 [1], assumes that an equivalent cylindrical cell of uniform rain can intercept the link at any position with equal probability. An effective path length is calculated as the average length of the intersection between the cell and path. It is a result of these assumptions that the effective path length is always smaller than the actual path length, leading to the definition of a path reduction factor. In the slant path prediction method, given in Rec. ITU-R P.618-12 [2], both a horizontal and a vertical reduction factors are employed to take into account the spatial and temporal variability of the rain field.

One limitation of the current ITU-R methods is that the attenuation is predicted using only the measured rainfall rate exceed at 0.01% of the time. For other percentages of time, the attenuation is obtained using extrapolation functions. Another important limitation is that, tested against the experimental data now available, the terrestrial prediction method shows significant underestimation of the measured attenuations. Also, the slant path and terrestrial methods are not consistent, as different expressions for the horizontal path reduction factor are used in each case.

An alternative, semi-empirical method for the prediction of rain attenuation in terrestrial links was recently proposed [3], which addresses the problems observed in the current ITU-R method. The concept of an effective rainfall rate was introduced, in order to avoid path correction factors larger than 1. The numerical coefficients in the method were derived by multiple non-linear regressions using the experimental data on rain attenuation in terrestrial links currently available in the ITU-R data bank.

In the present paper, the method proposed for terrestrial links is extended for slant path links, by the introduction of a vertical path reduction factor. The expression for this factor is derived using the experimental data on rain attenuation in slant path links currently available in the ITU-R data bank. Although this type of approach is not new, in our case the horizontal path reduction factor previously obtained from terrestrial measurements is kept. It ensures that the general method reduces itself to the terrestrial method when the elevation angle tends to zero.

This unified method is simple to apply and uses the full rainfall rate distribution to predict the attenuation distribution, avoiding extrapolations functions dependent on the percentage of time and frequency. Test results indicate that the proposed method provides significant improvement over the current ITU-R methods, in both the terrestrial and slant path cases. The method retains the concept of an equivalent rain cell, which is the basis of the current ITU-R method. Also, the expressions for the slant path and terrestrial cases are fully consistent.

2. Prediction of rain attenuation in terrestrial links

2.1. The ITU-R prediction method

The method for the prediction of rain attenuation in terrestrial links, given in Recommendation ITU-R P.530 [1], was originally developed based on a simplified model for the temporal and spatial random variations of rain field causes the attenuation. The basic assumption in the method is that an equivalent cell of uniform rainfall rate and length d_0 , randomly position in the great circle plane can represent the effect of the non-uniform rainfall along the propagation path.

Assuming that this equivalent rain cell may intercept the link at any position with equal probability, the expression for an effective path length is calculated. The effective path length is the average length of the intersection between the cell and path, given by:

$$d_{\text{eff}} = \langle L \rangle = \frac{1}{d_0 + d} \int_{-d_0}^d L(x) dx = r \cdot d = \frac{1}{1 + d/d_0} \cdot d \quad (1)$$

The variables involved in the calculation are indicated in Figure 1.

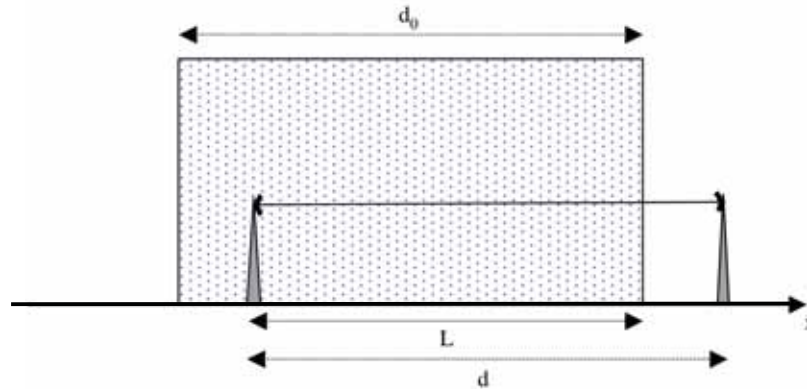


Figure 1: Equivalent rain cell

The diameter d_0 of the equivalent cell is empirically derived from experimental data. It depends on the long-term point rainfall rate measured in the region. In the current model, d_0 is an exponentially decaying function of the point rainfall rate R (mm/h). The function parameters were adjusted using experimental data available some years ago.

Using this model, the rainfall rate exceeded at 0.01% of time ($R_{0.01}$) is used to predict the corresponding value of rain attenuation ($A_{0.01}$).

$$A_{0.01} = \gamma_{0.01} \cdot d_{\text{eff}} = k(R_{0.01})^\alpha \cdot \frac{d}{1 + d/d_0(R_{0.01})} \quad (2)$$

where γ (dB/km) is the specific attenuation, calculated using the frequency and polarization dependent parameters k and α , given in Recommendation ITU-R P. 838 [4] and d is the actual path length.

To calculate the attenuation exceeded at other percentages of time between 1% and 0.001% an extrapolation formula is used [1]. This represents a shortcoming of the method, as in two regions with different distributions of point rainfall rate but similar values of $R_{0.01}$, the same behaviour for the attenuation will be predicted. Also, empirical evidence [4] based on measured data now available indicates that this model may significantly underestimate the cumulative distribution of rain attenuation, particularly for region with severe rain regimes.

Some attempts to modify the ITU-R method to improve the accuracy have been recently made [5-8]. It is usually found that, to correct the underestimation simply by refitting the method against the experimental data now available, it would be necessary to allow for effective path lengths longer than the actual path length. However, as it can be seen from Equation (1) that the effective path length d_{eff} is always smaller than the actual path length d , leading to the definition of a path reduction factor $r = d_{\text{eff}}/d_0$.

2.2. Modified prediction method for terrestrial links

A modified method has been proposed [3], which addresses some of the problems found in the current ITU-R method but retains the general expression for d_{eff} , which is the basis of the model, and uses the full rainfall rate distribution at the links region as input for the prediction of the cumulative distribution of rain attenuation.

As a starting point, the dependence of the reduction factor on link parameters was investigated, using experimental data from concurrent long-term measurements of point rainfall rate and rain attenuation in terrestrial links available in the ITU-R databanks [9]. A correction factor r_p was calculated not only for 0.01% of time, but for all percentages of time for which data is available, using Equation (3).

$$r_p = \frac{A_p}{kR_p^\alpha \cdot d} \quad (3)$$

where A_p and R_p are the rain attenuation and the point rainfall rate exceeded at $p\%$ of the time, respectively. It was found that r_p decreases with the path length and the point rainfall rate, as depicted in Figures 2 and 3.

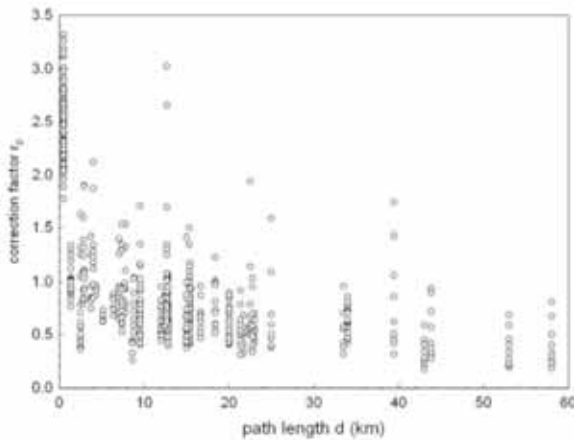


Figure 2. Correction factor vs. path length

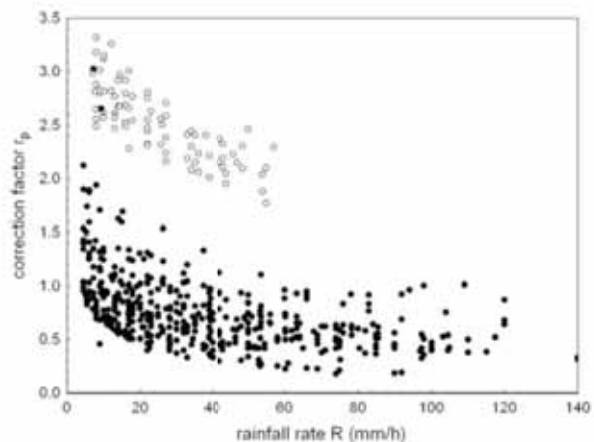


Figure 3. Correction factor vs. rainfall rate $d > 1\text{km}$ (black) and $d < 1\text{km}$ (hollow)

In Figure 3, a very distinct behaviour is observed for links shorter than 1 km. Although unexpected, it explains why it is necessary to allow for correction factors larger than 1 to improve the methods accuracy in refitting the current ITU-R method.

To avoid inconsistencies and retain the general expression for d_{eff} given by (1), the concept of an effective rainfall rate is introduced. The cumulative distribution of rain attenuation is obtained from the distribution of rainfall rate in the links region by

$$A_p = \gamma_p \cdot d_{\text{eff}} = k \left[\left(R_{\text{effT}}(R_p, d) \right)^\alpha \cdot \frac{d}{1 + d / d_0(R_p)} \right] \quad (4)$$

where R_{effT} is the effective rain rate for terrestrial links. The empirical expression obtained for this effective rainfall rate in given by Equation (5). The behaviour of R_{effT} with R , for different values of d , is shown in Figure 4.

$$R_{\text{effT}} = 1.763R^{0.753+0.197/d} \quad (5)$$

For the equivalent cell diameter d_0 , it was found that a power-law could provide better results than the exponential law used in the current ITU-R method. The expression obtained is given in Equation (6). The behaviour of d_{eff} with R , for different values of d , is shown in Figure 5.

$$d_0 = 119 \cdot R^{-0.244} \quad (6)$$

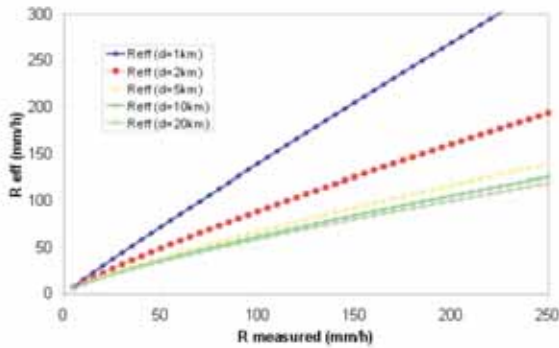


Figure 4. Effective rainfall rate (terrestrial links)

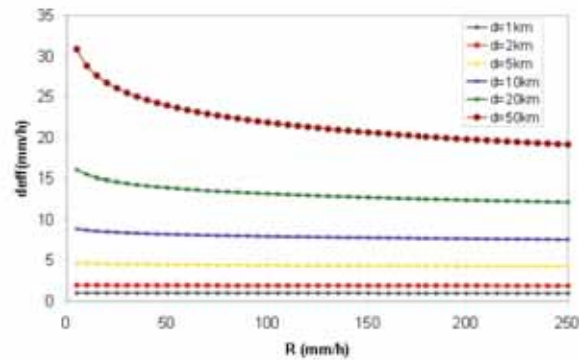


Figure 5. Effective path length (terrestrial links)

3. Unified method for slant paths and terrestrial links

3.1. Effective path length for slant paths

The model for the effective path length, represented by equation 1 and figure 1, can be extended for the slant path case by considering the rain height. The rain height is defined as a function of the zero degrees isotherm height, which is mapped all over the world and given in Rec. ITU-R P.839-3 [9]. For a slant path with an elevation angle θ , the effective path length will be given by

$$L_{\text{eff}} = \langle L \rangle = \frac{1}{L_0 + L_S \cos \theta} \int_{-L_0}^{L_S \cos \theta} L_S(x) dx = \frac{1}{1 + \frac{L_S \cos \theta}{L_0}} \cdot L_S \quad (7)$$

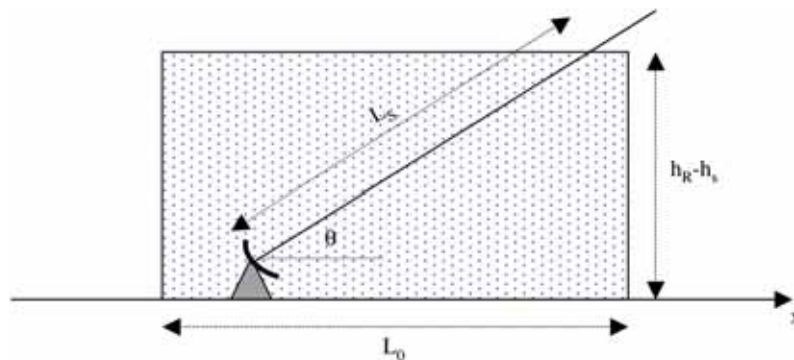


Figure 6. Equivalent rain cell for slant paths

3.2. General method for rain attenuation prediction

To obtain a more general prediction method that includes the slant path case but is still consistent with the terrestrial case, the rain attenuation cumulative probability distribution will be calculated by

$$A_p = \gamma_p \cdot L_{\text{eff}} = k \left[\left(R_{\text{eff}}(R_p, L_s, \theta) \right)^\alpha \right] \cdot \frac{L_s}{1 + L_s \cos \theta / L_0} \quad (8)$$

For the slant path case $L_s = (h_R - h_s) / \sin \theta$, where h_R is the rain height, h_s is the antenna height above mean sea level and θ is the elevation angle. For the terrestrial case, the elevation equals zero, $L_0 = d_0$ and L_s becomes the terrestrial path length d .

The dependence of the effective rain rate on link parameters was investigated, using experimental data from concurrent long-term measurements of point rainfall rate and rain attenuation in slant path links available in the ITU-R databanks [10]. Only data from beacon measurements (not data from radiometer measurements) with concurrent measurements of rainfall rate were considered. The values of R_{eff} were obtained from the measured distribution of attenuation and rainfall rate by

$$R_{\text{eff}} = \left(\frac{A_p}{k \cdot \frac{L_s}{1 + L_s \cos \theta / L_0}} \right)^{1/\alpha} \quad (9)$$

The dependence of the effective rainfall rate with the point rainfall rate, the slant path length the elevation angle and the rain height found in the experimental data is shown in figures 7 to 10.

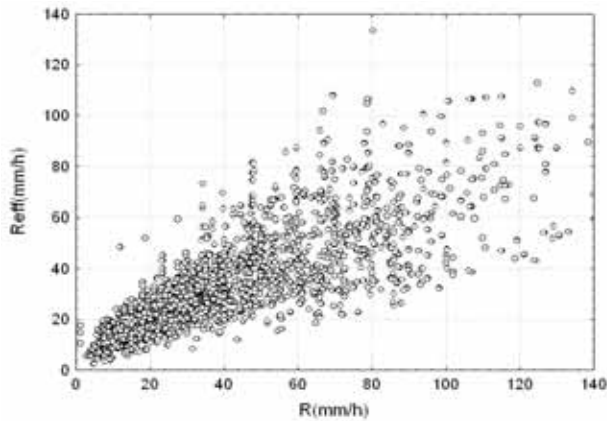


Figure 7. Effective rain rate vs. point rainfall rate

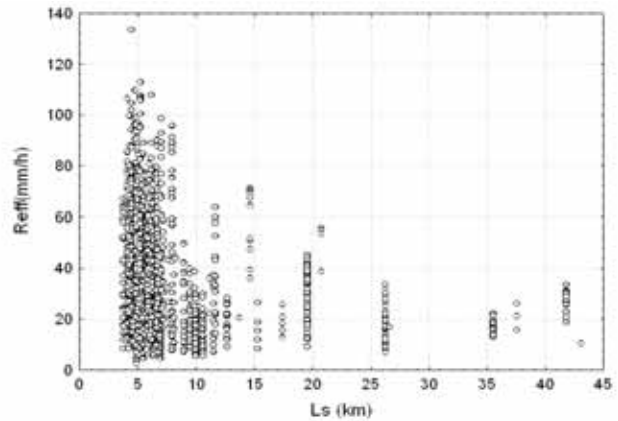


Figure 8. Effective rain rate vs. slant path length

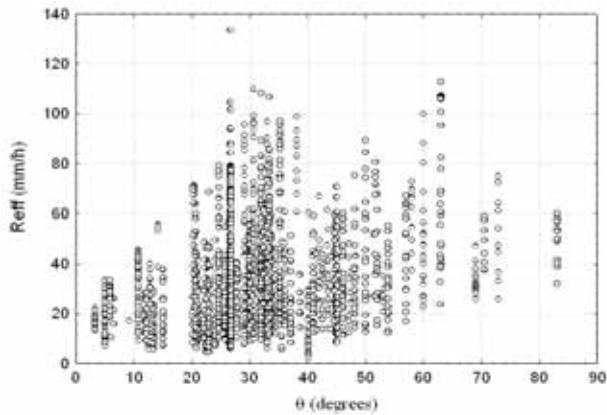


Figure 9. Effective rain rate vs. elevation angle

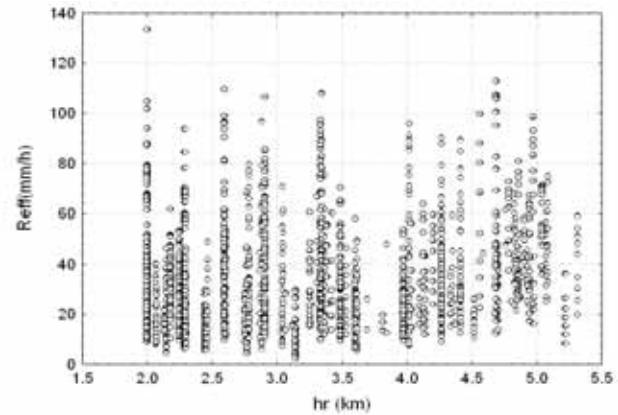


Figure 10. Effective rain rate vs. rain height

It can be observed that the effective rain rate is strongly dependent of the point rainfall rate as should be expected. It also decreases with the slant path length and shows a moderate increase with the elevation angle. The dependence on the rain height is found to be weak. Based on these observations, and after a series of trials of different functions, the following expression was chosen to fit R_{eff} .

$$R_{\text{eff}}(R_p, L_S, \theta) = R_{\text{effT}} \left(\cos \theta + a_1 \cdot R^{a_2 + a_3 / L_S \cos \theta} \cdot L_S^{a_4} \cdot \sin \theta \right) \quad (10)$$

The combination of two terms depending on $\cos \theta$ and $\sin \theta$ was used to ensure the consistence with the terrestrial case. Fitting this expression to the values obtained from the experimental data provided the values for a_1 to a_4 . From equations (8) and (10), with R_{effT} given by equation (5) and $L_0 = d_0$ given by equation (6), the general expression for rain attenuation prediction is

$$A_p = k \left[1.763 R^{0.753 + 0.197 / L_S \cos \theta} \cos \theta + \frac{203.6}{L_S^{2.455}} R^{0.354 + 0.088 / L_S \cos \theta} \sin \theta \right]^\alpha \frac{L_S}{1 + \frac{L_S \cos \theta}{119 R^{-0.244}}} \quad (11)$$

For the terrestrial case $L_S = d$, the second term in brackets vanishes ($\theta = 0$) and the expression reduces to

$$A_p = k \left[1.763 R^{0.753 + 0.197 / L_S \cos \theta} \right]^\alpha \frac{d}{1 + \frac{d}{119 R^{-0.244}}} \quad (12)$$

4. Comparative tests of prediction methods

The proposed method was tested against the ITU-R methods and other methods proposed in the technical literature, using the test variable recommended by the ITU-R [11]. This test variable is the weighted natural logarithm of the ratio between the predicted and measured values of the attenuation exceeded at a given percentage of time. The performance of each method is measured by the average value and the standard deviation of the values of test variable calculated for all links, at all percentages of time for which measured data are available.

For the terrestrial case, the data used to test the prediction methods includes concurrent measurements of rainfall rate and rain attenuation available in the ITU-R databank [10], a total of 74 year-stations from 64 links in 15 countries. The tests included the proposed method, the current ITU-R method [1], the UK method [5], the Australian method [6] and the China method [7]. Table 1 shows the average values, standard deviations and the r.m.s. values of the test variable for each method, which are depicted in figures 11 to 13.

The test results indicate that, for the terrestrial case, the proposed method provides a large improvement over the method currently recommended by the ITU-R. The only other method that provides similar results is the China's method, which uses one single point of the rainfall rate distribution to predict the attenuation distribution. The path reduction factor and the extrapolation function used in this method show frequency dependency, that should be restricted to k and α .

Table 1. Prediction error – terrestrial links

p (%)	AVERAGE VALUE					STANDARD DEVIATION					RMS VALUE				
	ITU-R	UK	AUS	China	Prop.	ITU-R	UK	AUS	China	Prop.	ITU-R	UK	AUS	China	Prop.
0.001	-0.11	-0.11	0.07	0.04	0.09	0.37	0.37	0.44	0.24	0.23	0.38	0.38	0.44	0.24	0.24
0.002	-0.13	-0.11	0.06	0.03	0.06	0.35	0.36	0.42	0.22	0.22	0.37	0.38	0.43	0.22	0.23
0.003	-0.16	-0.14	0.05	0.02	0.03	0.34	0.36	0.43	0.21	0.21	0.36	0.38	0.43	0.21	0.21
0.006	-0.17	-0.13	0.05	0.01	0.01	0.35	0.34	0.42	0.20	0.21	0.39	0.37	0.43	0.20	0.21
0.01	-0.17	-0.12	0.05	0.00	0.01	0.36	0.36	0.44	0.20	0.22	0.40	0.37	0.44	0.20	0.22
0.02	-0.20	-0.13	0.03	-0.02	-0.02	0.38	0.37	0.44	0.23	0.25	0.43	0.39	0.44	0.23	0.25
0.03	-0.22	-0.13	0.02	-0.03	-0.04	0.40	0.37	0.46	0.25	0.26	0.46	0.40	0.46	0.25	0.26
0.06	-0.27	-0.18	-0.04	-0.05	-0.09	0.43	0.36	0.47	0.27	0.27	0.51	0.41	0.47	0.28	0.29
0.1	-0.32	-0.24	-0.10	-0.15	-0.12	0.45	0.36	0.49	0.31	0.30	0.55	0.43	0.49	0.34	0.32

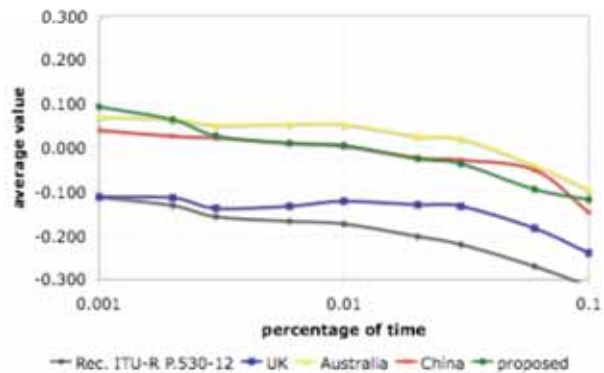


Figure 11. Average error – terrestrial links

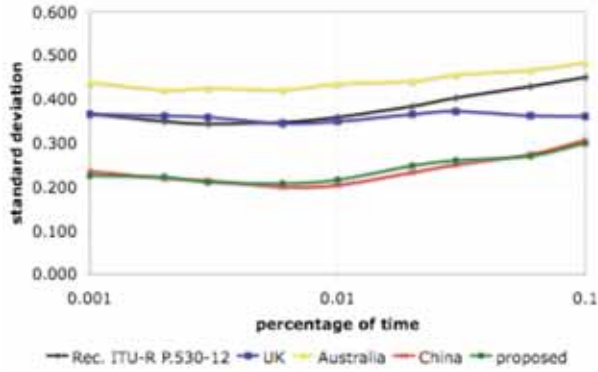


Figure 12. Standard deviation – terrestrial links

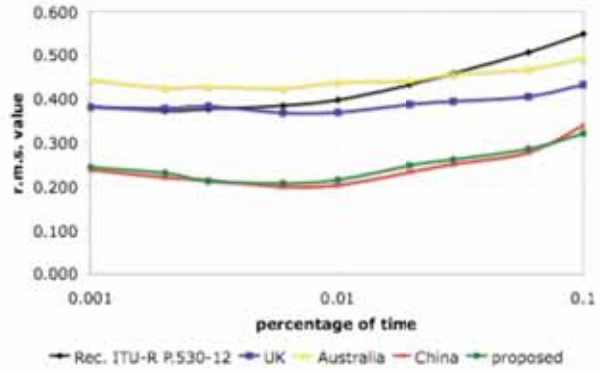


Figure 13. R.m.s value – terrestrial links

For the slant path case, the data used to test the prediction methods includes concurrent measurements of rainfall rate and rain attenuation in received satellite beacon signals, also available in the ITU-R databank [10], comprising a total of 280 year-stations from 68 sites in 24 countries. The tests included the proposed method, the current ITU-R method [2], the UK method [12], the Australian method [13] and the China method [14]. Table 1 and figures 14 to 16 show the average values, standard deviations and the r.m.s. values of the test variable for the slant path links.

Table 2. Prediction error – slant path links

p (%)	AVERAGE VALUE					STANDARD DEVIATION					RMS VALUE				
	ITU-R	UK	AUS	China	Prop.	ITU-R	UK	AUS	China	Prop.	ITU-R	UK	AUS	China	Prop.
0.001	0.06	-0.05	0.02	0.08	0.004	0.32	0.32	0.31	0.34	0.31	0.33	0.32	0.31	0.35	0.31
0.002	0.00	-0.05	-0.01	0.00	-0.01	0.33	0.31	0.33	0.34	0.30	0.33	0.32	0.33	0.34	0.30
0.003	-0.03	-0.05	-0.04	-0.04	-0.03	0.31	0.30	0.31	0.32	0.29	0.32	0.31	0.32	0.32	0.29
0.005	-0.06	-0.05	-0.07	-0.06	-0.04	0.29	0.30	0.32	0.29	0.28	0.29	0.30	0.32	0.30	0.28
0.010	-0.08	-0.03	-0.07	-0.07	-0.03	0.29	0.29	0.30	0.29	0.28	0.30	0.29	0.31	0.30	0.28
0.020	-0.08	0.00	-0.11	-0.05	-0.02	0.27	0.27	0.30	0.27	0.27	0.28	0.27	0.32	0.27	0.27
0.030	-0.08	0.03	-0.12	-0.02	0.00	0.26	0.27	0.29	0.26	0.27	0.27	0.27	0.31	0.26	0.27
0.050	-0.08	0.04	-0.15	0.01	0.01	0.25	0.27	0.31	0.26	0.27	0.26	0.27	0.34	0.26	0.27
0.100	-0.10	0.05	-0.20	0.02	0.03	0.28	0.30	0.36	0.28	0.30	0.30	0.30	0.41	0.28	0.30

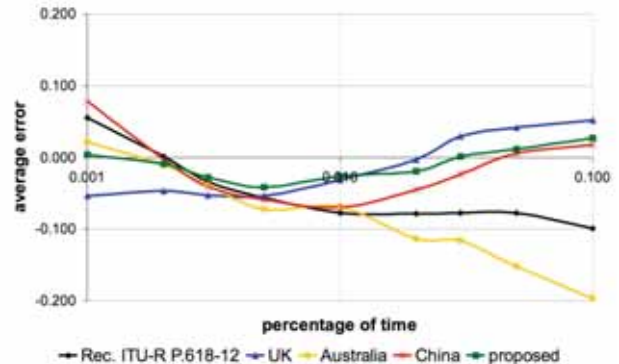


Figure 14. Average error – slant path links

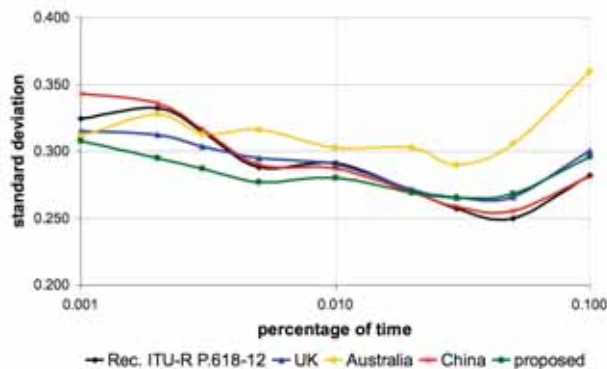


Figure 15. Standard deviation – slant path links

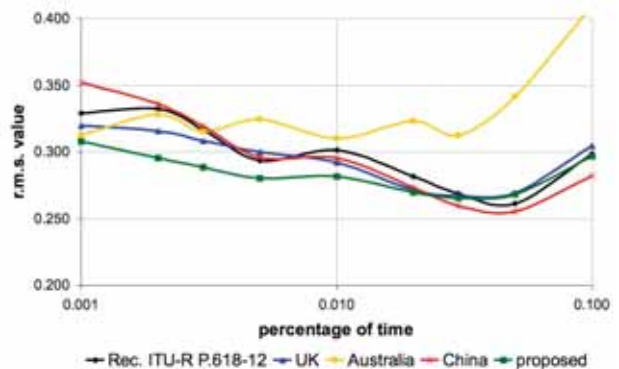


Figure 16. R.m.s value – slant path links

The test results indicate that, for low percentages of time, the proposed method provides a significant improvement over the method currently recommended by the ITU-R. For percentages of time between 0.03 and 0.1% the two methods are approximately equivalent. In this time percentage range, the China's method provides slightly better results than the other methods.

5. Conclusions

The proposed method for the prediction of rain attenuation in terrestrial and slant path simple to apply and uses the full rainfall rate distribution to predict the attenuation distribution, avoiding the extrapolation function dependent on the percentage of time.

The concept of an equivalent rain cell, which is the basis of the original ITU-R methods, is retained in the new method and the attenuation dependence on frequency is completely described by the parameters k and α , as should be expected from the physical point of view. Consistency between the terrestrial and the slant path cases was also achieved.

Test results indicate that the proposed method provides a large improvement over the method currently recommended by the ITU-R in the case of terrestrial links. A significant improvement is also obtained for low percentages of time in the case of Earth-space links.

6. References

- [1] ITU-R Recommendation P.530-12: 'Propagation data and prediction methods required for the design of terrestrial line-of-sight systems', International Telecommunication Union, 2006.
- [2] ITU-R Recommendation P.618-12: 'Propagation data and prediction methods required for the design of Earth-space systems', International Telecommunication Union, 2006.
- [3] Silva Mello, L.A.R., Pontes, M.S., Souza, R. M. and Pérez-Garcia, N. A., 'Prediction of rain attenuation in terrestrial links using the full rainfall rate distribution', *Electronics Letters*, v. 43, p. 1442-1443, 2007.
- [4] ITU-R Recommendation P.838-3: 'Specific attenuation model for rain for use in prediction methods', International Telecommunication Union, 2006.
- [5] Doc. 3M/28, 'Proposed modification to Recommendation ITU-R P.530-10 - Propagation data and prediction methods required for the design of terrestrial line-of-sight systems', UK.
- [6] Doc. 3M/27 (Study Period 2000-2003), 'Proposed amendment to Recommendation ITU-R P.530-9 - Rain attenuation effective path length', Australia.
- [7] Doc. 3M/107, 'Proposed modification to Recommendation ITU-R P.530-10 - An improved prediction method of rain attenuation for terrestrial light-of-sight path', China (Peoples Republic of).
- [8] L. A. R. Silva Mello, E. P. O. Costa, R. S. L. Souza, 'Improved Method for the Prediction of Rain Attenuation in Terrestrial Links', *Electronics Letters*, Londres, UK, v. 40, n. 11, p. 683-684, 2004.
- [9] ITU-R Recommendation P.839-3: 'Rain height model for prediction methods', International Telecommunication Union, 2001.
- [10] ITU-R Databank DBSG3, <http://www.itu.int/pub/R-SOFT-SG3/en>.
- [11] ITU-R Recommendation P.311-12: 'Acquisition, presentation and analysis of data in studies of tropospheric propagation', International Telecommunication Union, 2006.
- [12] Doc. 3M/134, 'Proposed modifications to Recommendation ITU-R P.618-8 - Propagation data and prediction methods required for earth-space telecommunication systems', UK.
- [13] Doc. 3M/20 (Study Period 1996-1997), 'Proposed amendment to Recommendation ITU-R PN.618 - Prediction of Rain Attenuation', Australia.
- [14] Doc. 3M/108, 'Proposed modification to Recommendation ITU-R P.530-10 - The prediction method of rain attenuation along Earth-space path', China (Peoples Republic of).

Angular Dependence of Satellite Diversity Effects on the Attenuation Statistics Obtained from Ku and Ka Band Signals of the Geostationary Satellites in Japan

Yasuyuki Maekawa⁽¹⁾ and Takeshi Hatsuda⁽²⁾,

⁽¹⁾Osaka Electro-Communication Univ., 18-8 Hatsucho, Neyagawa, Osaka 572-8530, Japan
E-mails: maekawa@maelab.osakac.ac.jp

⁽²⁾Hokkaido Institute of Technology, 4-1, 7-15, Maeda, Teine, Sapporo 007-8585, Japan
E-mail: hatsuda@ieee.org

Abstract

Angular dependence of the satellite diversity effects on Ku- and Ka-band rain attenuation is investigated using the radio wave signal levels obtained from Japan's domestic geostationary satellite, JCSAT, SCC, BS, and CS-3 (N-STAR), in 1995-1998 and 2003-2007 at Osaka Electro-Communication University (OECU) in Osaka, and in 2005-2007 at Kyoto University in Kyoto, Japan. The improvement factor of the satellite diversity is increased, as the azimuth angle separation of the propagation paths is increased. The improvement factor is, however, slightly decreased as the elevation angles separation is increased. These angular characteristics are well described as a simple exponential function of their differences. The improvement factor does not exceed a factor of 2 or 3, as far as the time percentages are greater than 0.01%, while it may exceed a factor of 10 as the time percentages become smaller than 0.01% with the Ku-band attenuation of greater than about 10 dB.

1. Introduction

High frequency bands such as Ku and Ka bands now start to be used in satellite communications links. The effects of rain attenuation are, however, significant in the frequency range of higher than 10 GHz. Some countermeasures against the rain attenuation, such as site and satellite diversity techniques are then required to maintain reliable satellite communications links. So far, the site diversity techniques have been investigated by a number of rain attenuation measurements, and the prediction methods for site diversity effects using the distance between two stations are well established in terms of the improvement of the joint cumulative time percentages between them [1]. However, there has not been much discussion on the effects of satellite diversity techniques and observational data is not sufficiently accumulated for detailed examinations of them.

In this study, the satellite diversity effects are numerically estimated using the observational data of the rain attenuation continuously obtained for the four years of 1995-1998 at Osaka Electro-Communication University (OECU), from Ku-band up and down links of Japan's domestic communications satellite (JCSAT-1, 14/12 GHz band), Ku band broadcasting satellite (BS, 12 GHz band), and Ka-band beacon signal (N-STARa, 20 GHz band) [2]-[4]. The orbital positions of JCSAT-1, BS, and N-STARa are 150 °, 110 °, and 132 ° E, respectively. The received signal levels of these three satellites are converted by frequency scaling methods into the same Ku or Ka band frequencies with the right-hand circular polarization. Then, the improvement of joint cumulative time percentages of rain attenuation due to the satellite diversity techniques are numerically simulated among the three satellite orbital positions for the attenuation range of time percentages of 0.1-0.01%.

In 2003-2007, the Ka-band beacon signal (N-STARa, b: 132 °, 136 ° E), the Ku-band broadcasting signal (BS: 110 ° E), and the signals from several Ku-band communication satellites (Superbird-C: 144 ° E, Superbird-A: 158 ° E, JCSAT-3: 124 ° E) are measured. Using various kind of combinations of their propagation paths, the satellite diversity effects are further examined for azimuth angle separations from 10 to 70 deg in time percentages of 0.1-0.01%. Moreover, their characteristics are investigated in higher attenuation range of Ku band with time percentages of less than 0.01%, which are recently observed from the combination of the Ku-band satellite signals at OECU and Kyoto University, in Uji, Kyoto [5].

2. Observation systems

The data sets of the Ku-band and Ka-band satellite signals obtained at OECU in Japan for the estimation of satellite diversity effects are as follows, where * indicates the Ka-band satellite and the numbers in the parenthesis are the difference of azimuth and elevation angles (deg) between the relevant satellites [2]-[5].

- (1) Satellites: BS, CS-3a(N-STARa)*, JCSAT-1
Period: March 1995 – December 1998
Angular difference: BS – CS-3a (33.7, 8.1), JCSAT-1 – CS-3a (30.5, 2.6), BS – JCSAT-1(64.3, 5.5)
- (2) Satellites: BS, N-STARa*, Superbird-C (SCC-C)
Period: September 2003 – March 2005
Angular difference: BS N-STARa (33.7, 8.1), N-STARa SCC-C (20.8, 1.1), BS SCC-C (54.6, 7.3)
- (3) Satellites: BS, N-STARa*, Superbird-A (SCC-A)
Period: April 2005 – August 2005
Angular difference: BS N-STARa (33.7, 8.1), N-STARa SCC-A (42.2, 6.5), BS SCC-A (75.9, 1.8)
- (4) Satellites: BS, N-STARb*, Superbird-C (SCC-C)
Period: January 2006 – December 2006
Angular difference: BS N-STARb (40.7, 8.3), N-STARb SCC-C (13.8, 1.0), BS SCC-C (54.6, 7.3)

Also, the data sets listed below, which are observed at OECU and Kyoto University using the Ku-band satellites, are used to analyze the satellite diversity effects in high attenuation range of greater than 10 dB with time percentages of less than 0.01%.

- (5) Satellites: BS, JCSAT-3, Superbird-C (SCC-C)
Location: Osaka Electro Communication University (OECU), Osaka
Period: November 2003 – March 2005, July 2006 – August 2007
Angular difference: BS JCSAT-3 (26.9, 7.5), JCSAT-3 SCC-C (27.7, 0.2), BS SCC-C (54.6, 7.3)
- (6) Satellites: BS, Superbird-C (SCC-C)
Location: Kyoto University, Uji, Kyoto
Period: August 2005 – September 2006
Angular difference: BS SCC-C (54.6, 7.3)

As concerns the data set (1), the signal level observation of JCSAT-1 is conducted from 1995 to 1998 by the VSAT system at Osaka Electro-Communication University (OECU), Neyagawa, Osaka, which has a 1.8 m diameter offset parabola dish. The up link uses the frequency of 14.00 GHz with horizontal polarization, while the down link uses the frequency of 12.26 GHz with vertical polarization. The received signal level of JCSAT-1 is detected by the AGC voltage obtain from the IDU of the VSAT system, which is corrected by signal levels indicated on the front panel of the IDU in dBm. The BS signal that has the frequency of 11.84 GHz with right hand circular polarization is received by a 1.2 m diameter offset parabola dish, and detected by the AGC voltage of a BS tuner, which is also corrected by a signal level meter. The beacon signal of CS-3a (N-STARa) that has the frequency of 19.45 GHz with right hand circular polarization is received by a 5-m diameter Cassegrain antenna, and detected by the beacon receiver of the earth station.

As for the data sets (2)-(6) obtained after 2003, the Ka-band beacon signal of N-STARa and N-STARb is similarly received by the 5-m diameter Cassegrain antenna, while the Ku-band BS signal is received by a 45 cm diameter offset parabola dish. Also, several kinds of Ku-band signals are received from JCSAT-3, SCC-C and SCC-A using 60 cm diameter offset parabola dishes. The signal out puts of these satellites are simultaneously sampled at 1 sec interval by a personal computer (PC) equipped with a 12-bit A/D converter. For the estimation of attenuation statistics and their diversity effects, these observed data are further averaged over 1 min.

3. Satellite diversity effects

In order to investigate the satellite diversity effects on the Ku-band and Ka-band propagation paths, each attenuation level of the measured satellite signals with various frequencies, polarizations, and elevation angles should be once converted into their specific values. In this study, the attenuation values of these satellites are transformed into those of the representative Ku- and Ka-band satellites, i.e., BS (11.84 GHz, RHCP, EL=41.3 deg) and N-STAR (19.45 GHz, RHCP, EL=49.5 deg), respectively. This transformation of the attenuation is conducted by frequency scaling methods, taking into consideration the difference of raindrop size distribution (DSD) in each rainfall event [6].

The attenuation ratio of N-STARa to BS is here compared with that of N-STARa to JCSAT-1's down link, or JCSAT-1's up-and-down link to BS, for each corresponding rainfall event during 1995-1998 in the data set (1). Fig.1 (a) and (b) show scatter plots for the ratio of N-STARa to JCSAT-1's down link and JCSAT-1's up-and-down link to BS, against that of N-STAR to BS, respectively. The number of rainfall events obtained during 1995-1998 is 21 and 34 for Fig.(a) and (b), respectively. The bold crosses (+) denote the theoretical values based on the three typical kind of DSD's, such as Joss-drizzle (Jd), Marshall-Palmer (MP), and Joss-thunderstorm (Jt) types, at the average rainfall rate of 14 mm/h. It is found in Fig.1 that the rain attenuation that occurred in the three different slant paths separated from about 30 to 60 deg in azimuth angle each other, are similarly affected by DSD's with comparatively high correlations between them. In the present frequency scaling methods, the relevant DSD nearest to the observation is thus chosen from these three typical DSD's using Fig.1 in each event. The kind of DSD is similarly determined in very rainfall event of the data sets (2)-(6). The validity of DSD has also been confirmed by the ground measurements for almost all rainfall events using instruments with optical sensor.

Figure 2 shows the results for the numerical simulations of the satellite diversity effects in the form of the reduction of unavailable time percentages of the rain attenuation with specific time percentages. These calculations are conducted for every combination of the satellite signals of both Ka and Ku bands using the data sets of (1)-(4) as shown by their observational periods. The reductions of the unavailable time percentages are depicted for 0.1 and 0.02% in Fig.2(a) and for 0.05 and 0.01% in Fig.2(b), respectively. Then, they are plotted against the difference of azimuth angles between the two selected satellites. It is seen from Fig.2 that as the difference of the azimuth angles increase, the unavailable time percentages tend to decrease due to the satellite diversity effects for all the data sets of (1)-(4). Note that the unavailable time percentage of 0.01 % corresponds to the attenuation of about 25 dB and 10 dB for the Ka- and Ku-band satellite signals. In such a case, the azimuth angle separation of more than 50 deg is found to reduce the unavailable time percentages down to less than 50%..

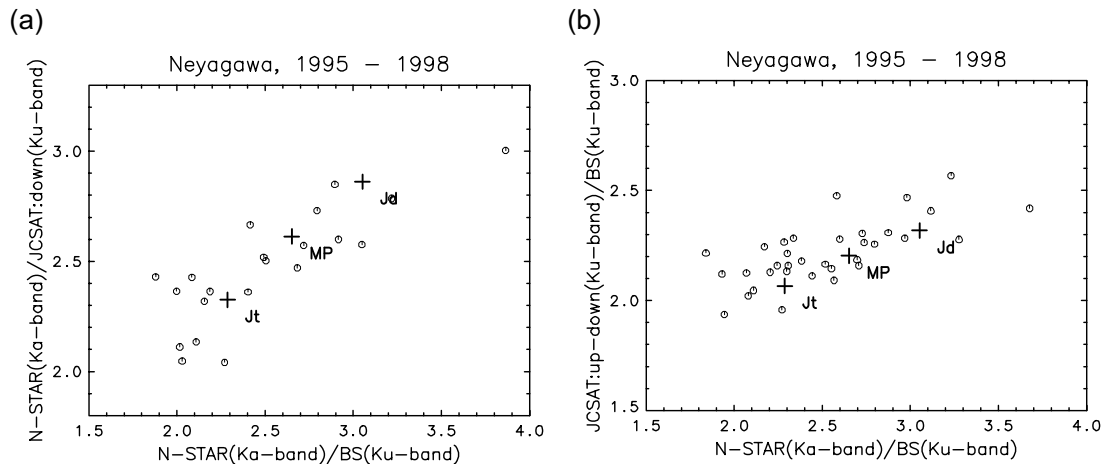


Figure 1. Scatter plot between average attenuation levels of each satellite signal obtained in rainfall events during 1995-1998. Crosses (+) denote the theoretical values using the three typical kinds of DSD's.

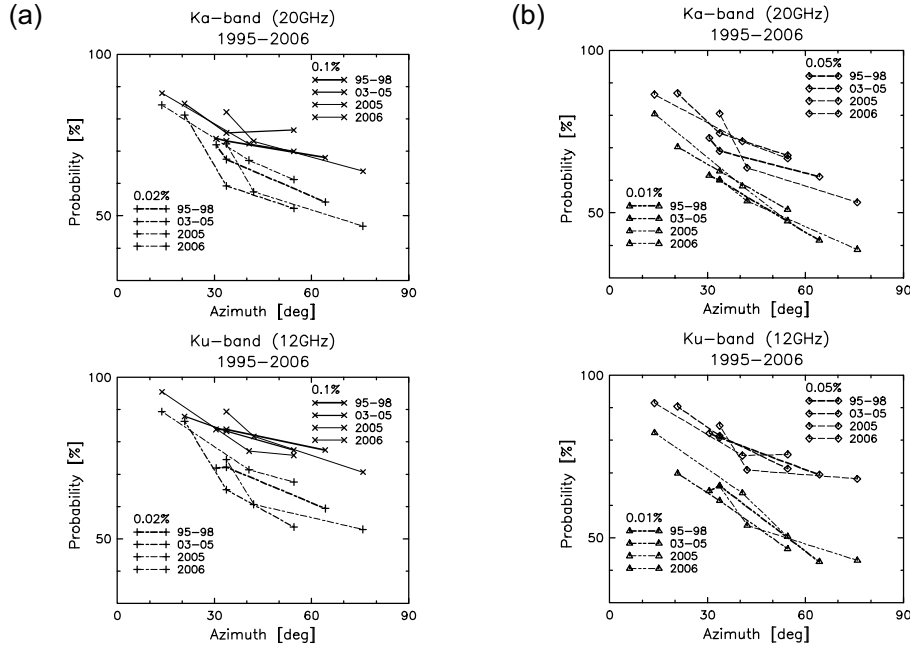


Figure 2. Reduction of unavailable time percentages due to the satellite diversity effects numerically calculated for the rain attenuation with time percentages of (a) 0.1 and 0.02% and (b) 0.05 and 0.01%.

4. Improvement factor of satellite diversity

4.1. Azimuth angle dependence of the improvement factor

In this section, the improvement of the unavailable time percentages are represented by the reciprocal of the reduction presented in Fig.2, as the improvement factor of the satellite diversity. Figure 3 shows the azimuth angle dependence of the improvements due to the satellite diversity for the Ka-band (a) and Ku-band (b) signals, respectively. In Fig.3, the data points at the same azimuth angle are averaged. Thin or dashed lines are the least RMS (Root Mean Square) fitted approximation lines, using an exponential function:

$$I = p_1/p_2 = \exp(a_K \phi) \quad (1)$$

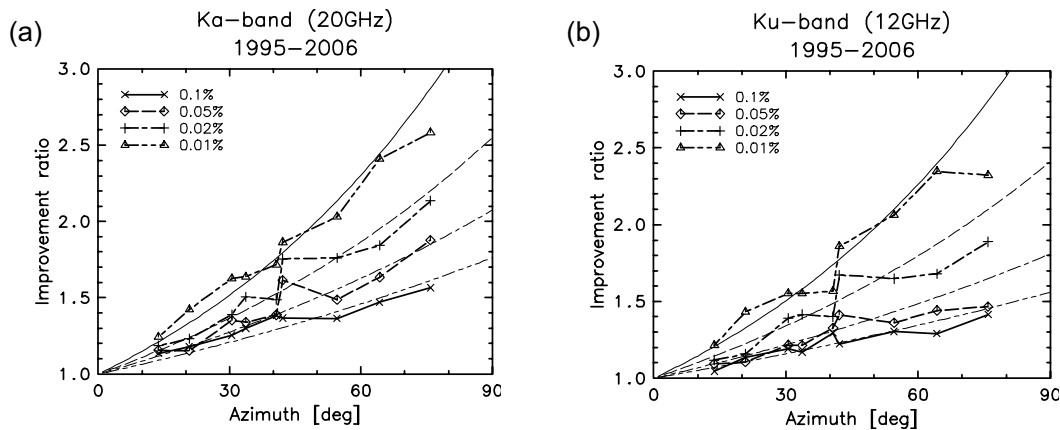


Figure 3. Azimuth angle dependence of the improvement factor of the satellite diversity for (a) Ka and (b) Ku band.

where p_1 is the cumulative probability of the single satellite path attenuation, p_2 is the joint cumulative probability due to the improvement of the satellite diversity, and ϕ is the difference between their azimuth angles. a_K [deg^{-1}] is the coefficient given by the equation (1) that is best fitted to the observed data at each frequency band and each cumulative probability. These coefficients obtained for the Ka-band signals (a_{Ka}) and the Ku-band signals (a_{Ku}) are summarized in Table 1.

Table 1. Coefficients for azimuth angle dependence

p_1 (%)	a_{Ka} (deg^{-1})	a_{Ku} (deg^{-1})
0.01	0.0139	0.0136
0.02	0.0104	0.00977
0.05	0.00811	0.00659
0.1	0.00630	0.00494

Then, the dependence of these coefficients a_K on the cumulative probability p_1 is approximately expressed for both Ka and Ku bands by,

$$a_{Ka} = 0.00285 p_1^{-0.344} \quad (2)$$

$$a_{Ku} = 0.001795 p_1^{-0.440} \quad (3)$$

Thus, the improvement factor of the satellite diversity I for each frequency band is given by,

$$I_{Ka} = p_1 / p_2 = \exp(0.00285 p_1^{-0.344} \phi) \quad (4)$$

$$I_{Ku} = p_1 / p_2 = \exp(0.001795 p_1^{-0.440} \phi) \quad (5)$$

where $0.01 \leq p_1 \leq 0.1$ [%] and $\phi < 70$ [deg]. Also, the elevation angle of all the satellites is assumed to be 49.5 deg for the Ka band and 41.3 deg for the Ku band, which are equivalent to those of N-STAR (19.45GHz) and BS (11.84GHz), respectively.

4.2. Elevation angle dependence of the improvement factor

In the previous section, the elevation angle of all the satellites is set to the same specified value, to deduce the azimuth angle dependence of the improvement factor independently. In the actual satellite propagation paths, however, there are slight differences between their elevation angles as listed in Chapter 2, giving rise to discrepancies of their path lengths and cumulative time percentages. This leads to slight reduction of the improvement factor of the satellite diversity. In this section, the satellite diversity effects are again numerically estimated for every combination of the satellite signals of both Ka and Ku bands, keeping each elevation angle in their original orbital position. In this calculation, their frequency and polarization are similarly converted into those of N-STAR and BS for Ka and Ku bands, respectively, using the above-mentioned frequency scaling methods using DSD in each event. Their elevation angle, however, is not changed from each original value to that of N-STAR or BS. Thus, the elevation angle dependence is deduced from the difference of their diversity effects compared to those of the same elevation angle as N-STAR or BS.

Figure 4 shows the difference between these satellite diversity effects as reduction of the improvement factor against the difference of elevation angle. The results are shown for both Ka and Ku bands, indicating similar tendencies. As marked by a dashed line in Fig.4 the reduction of the improvement factor is approximated by an exponential function in the sense of the least RMS, including both Ka and Ku bands:

$$r = \exp(-0.00156\theta) \quad (6)$$

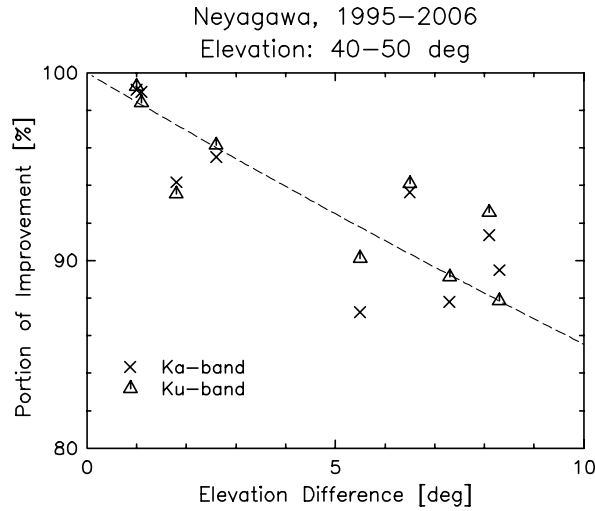


Figure 4. Reduction of the improvement factor of the satellite diversity due to the difference of elevation angle.

where θ [deg] is the difference of elevation angle. Therefore, the improvement factor of the satellite diversity I' is given by the following expressions for the Ka and Ku bands, respectively, when the difference of the elevation angles exists between their actual propagation paths:

$$I'_{Ka} = I_{Ka} \exp(-0.0156\theta) = \exp(0.00285 p_1^{-0.344} \phi) \exp(-0.0156\theta) \quad (7)$$

$$I'_{Ku} = I_{Ku} \exp(-0.0156\theta) = \exp(0.001795 p_1^{-0.440} \phi) \exp(-0.0156\theta) \quad (8)$$

where $0.01 < p_1 < 0.1$ [%], $\phi < 70$ [deg], and $\theta < 10$ [deg].

5 .Improvement factor in high attenuation range

In Chapter 4, the improvement factors of satellite diversity are presented for both Ka- and Ku-band signal attenuation statistics for almost all geostationary satellite orbits currently available in Japan. Their unavailable probability is, however, limited down to 0.01%, and the resulting improvement factor does not exceed two or three. Also, the attenuation level equivalent to the cumulative time percentage of 0.01% remains 10 dB or so in Ku band, while it amounts to about 25 dB in Ka band. So we need to further investigate the improvement factor of satellite diversity in higher attenuation range with time percentages of less than 0.01% especially in Ku band. In this chapter, the data sets of (5) and (6) listed in Chapter 2, which are dedicated to the Ku-band satellite signal measurements for comparatively long periods, are analyzed for the satellite diversity effects in attenuation range of higher than 10 dB with time percentages of less than 0.01%

Figure 5 shows the cumulative time percentages of the Ku-band attenuation of the data set (5), together with the results of the satellite diversity effects on each of the two paths, obtained at OECU during 2003-2007. In these calculations, the attenuation values of JCSAT-3 and SCC-C are transformed to those of BS (11.84 GHz, RHCP, EL=41.3 deg), considering the difference of DSD's in each rainfall event. The attenuation levels of these three satellites are all detected down to 20 dB similarly, with the cumulative time percentages of down to 0.001%. Moreover, their satellite diversity effects are detected even down to the time percentages of 0.0001%. It is found in Fig.5 that the cumulative time percentages begin to decrease more rapidly when the attenuation exceeds 10 dB. Also, those of the satellite diversity effects seem to decrease even more rapidly in this high attenuation range, yielding a larger improvement factor of the satellite diversity. Actually, it is seen to become a factor of more than 10, as the unavailable time percentage of the single satellite becomes as low as 0.002%.

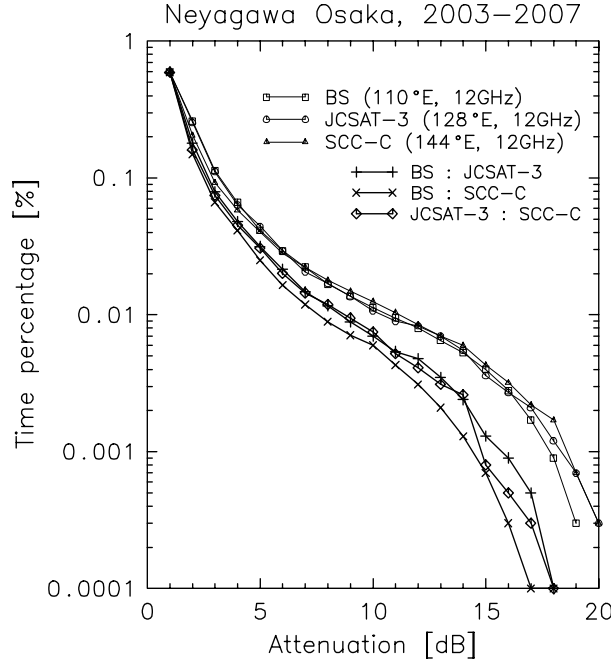


Figure 5. Cumulative time percentages of the Ku-band attenuation for the three satellites and their satellite diversity effects on each of the two paths obtained at OECU during 2003-2007.

Using these measurements and numerical simulation results of the Ku-band long-term data sets (5) and (6), the improvement factor of the satellite diversity for Ku-band higher attenuation range are calculated in the same manner as was done in the previous chapter. Also, the reduction of the improvement factors due to the difference of elevation angles between their actual orbital positions are similarly estimated for the time percentages of less than 0.01%, and it is confirmed to become two or three times larger than for the time percentages of greater than 0.01% [7]. Then, the improvement factor of the satellite diversity I'' is given by the following expression for the Ku-band high attenuation range of 10-20 dB:

$$I''_{Ku} = \exp(0.0001380 p_1^{-0.997} \phi) \exp(-0.0415\theta) \quad (9)$$

where $0.002 < p_1 < 0.01$ [%], $\phi < 70$ [deg], and $\theta < 10$ [deg].

6 .Conclusions

Angular dependence of the satellite diversity effects on Ku- and Ka-band rain attenuation is presented for both azimuth and elevation angles, using the radio wave signal levels obtained from Japan's domestic geostationary satellite, JCSAT, SCC, BS, and CS-3 (N-STAR), in 1995-1998 and 2003-2007 at Osaka Electro-Communication University (OECU) in Osaka, and in 2005-2007 at Kyoto University in Kyoto, Japan. First, the azimuth angle dependence is evaluated, converting the frequencies, polarizations, and elevation angles of each satellite into those of N-STAR and BS for Ka and Ku bands, respectively, by the frequency scaling methods including the kinds of DSD's. Then, The satellite diversity effects are numerically calculated for about ten kinds of azimuth angle separations from 10 to 70 deg, using the combination of two propagation paths taken from all the satellites, assuming the same frequency, polarization, and elevation angle. Next, the satellite diversity effects are similarly estimated, taking into account the difference in elevation angles between their original orbital positions. Thus, the elevation angle dependence is deduced from the difference of their improvement factors compared to those of the same elevation angle.

In both Ku and Ka bands, the improvement factor of the satellite diversity is increased by a factor of 2 or 3, as the azimuth separation of the propagation paths is increased up to 70 deg. The improvement factor is decreased by 10 or 20 % as the difference of elevation angles is increased up to 10 deg. These characteristics of azimuth and elevation angle dependence are well described as a simple exponential function of their differences. The improvement factor, however, does not exceed a factor of 2 or 3, as far as the cumulative time percentages of the single satellite paths are greater than 0.01%. On the other hand, recent observations dedicated to the Ku-band satellite signals at OECU and Kyoto University in 2003-2007 demonstrate that it may exceed a factor of 10, as the time percentages become smaller than 0.01% with the attenuation exceeding 10 dB. Thus, the satellite diversity technique seems to be fairly effective as a rain fade mitigation method in such a high attenuation range.

References

- [1] ITU-R, "P837-1 Characteristics of precipitations for propagation modeling," *ITU-R Recommendations*, 2003.
- [2] Y. Karasawa, and Y. Maekawa, "Ka-band earth-space propagation research in Japan," *Proc. IEEE*, Vol. **85**, pp.821-842, 1997.
- [3] Y. Maekawa, "A study on the effects of satellite diversity on Ka-band rain attenuation in three earth-space paths," *XXVIIth General Assembly of International Union of Radio Science*, Maastricht, Netherlands, Aug. 2002.
- [4] Y. Maekawa, T. Fujiwara, Y. Shibagaki, T. Sato, M. Yamamoto, H. Hashiguchi, and S. Fukao, "First year results on rain attenuation characteristics of satellite links at equatorial atmospheric radar," *2004 IEEE AP-S/URSI Symposium*, Vol.2, pp.1660-1663 (Paper #65.9), Monterey, California USA, June 2004.
- [5] K.Hatsuda, Y.Aoko, H.Echigo, F.Takahata, Y.Maekawa, and K.Fujisaki, "Ku-band long distance site-diversity (SD) characteristics by using new measuring system," *IEEE Trans. Antennas and Propagat.*, Vol.52, No.6, pp.1481-1491, 2004.
- [6] Y. Maekawa, and T. Hatsuda, "Azimuth angle dependency of the satellite diversity Characteristics of rain attenuation in Ku and Ka band satellite communications links," *IEICE Tech. rep.*, A P2007-49, 2007.
- [7] Y. Maekawa, and T. Hatsuda, "Azimuth and elevation angle dependency of the satellite diversity Characteristics of rain attenuation in Ku and Ka band satellite communications links," *IEICE Tech. rep.*, A P2008-1, 2008.

Implementing Adaptive Transmit Power Control in Fixed Terrestrial Links: Spectrum Management and Interference Issues

S. A. Callaghan,
STFC – Rutherford Appleton Laboratory
Chilton, Didcot, OX11 0QX, United
Kingdom

Email: s.a.callaghan@rl.ac.uk
Telephone: +44 1235 445770
Fax: +44 1235 446140

I Inglis, P Hansell
Aegis Systems Ltd,
Cobham, Surrey KT11 2LA, United
Kingdom

Abstract

Adaptive transmit power control is proposed as a method to improve the spectrum efficiency of terrestrial point to point fixed links by limiting the transmit power to that required to maintain a constant bit error rate (BER) regardless of the propagation conditions. This results in a reduced transmit power being used during clear sky conditions, lowering the interference resulting from the ATPC link, and allowing neighbouring links to be closer in geographical space. This also improves the frequency reuse factor associated with a given band and geographic area, and provides a spectrum efficiency gain. This paper describes a project funded by the UK's Ofcom as part of its Spectrum Efficiency Scheme, which aimed to determine the spectrum efficiency gains resulting from implementing ATPC in the 38 GHz fixed terrestrial link band.

1. Introduction

The UK's Ofcom (Office of Communications) recently funded a Spectrum Efficiency Scheme (SES) with the aim of investigating novel methods of improving spectrum efficiency in congested frequency bands. The work reported in this paper was funded by the SES, with the intention of investigating the spectrum efficiency benefits resulting from implementing Adaptive Transmit Power Control (ATPC) in the 38GHz fixed terrestrial link band.

ATPC can be used to improve the spectrum efficiency of fixed links by limiting the transmit power to that required to maintain a constant bit error ratio (BER) regardless of the propagation conditions. This results in a reduced transmit power being used during clear sky conditions, meaning that the interference resulting from the ATPC link is correspondingly lower. This improves the frequency reuse factor associated with a given band and geographic area, providing a spectrum efficiency gain.

However, it is vital to emphasise that ATPC should only be used to combat temporary fading of the wanted link rather than interference from the unwanted link(s). Otherwise, a situation could arise where two ATPC systems repeatedly increase their transmitter power in response to each other's interference until both are transmitting at their maximum power. This situation would then reduce to the non-ATPC case, completely negating any spectrum efficiency benefits gained as a result of employing ATPC in the first place. To avoid this situation, ATPC links must be designed and deployed correctly to take into account the interference generated by neighbouring links so that ATPC is used to combat fading, rather than interference.

For systems operating at frequencies of above 10GHz, the primary propagation impairment is rain. The spatio-temporal distribution of rain fields determines whether interfering links are attenuated in similar proportion to wanted links, thereby indicating if the implementation of ATPC will result in increased levels of interference. To accurately determine this, the frequency assignment plans created using different ATPC penetration values (e.g. 50% ATPC, 50% non-ATPC links) were exposed to measured and simulated rain rate fields.

2. Application of adaptive power control techniques in congested spectrum

The assignment criteria used by Ofcom to determine whether a new frequency assignment can be made to a point-to-point link without receiving or generating unacceptable interference address two different situations:

- The wanted path is in its faded state (i.e. at the Receiver Sensitivity Level, RSL) and the interfering path is in a state that gives rise to its median received signal level, as modelled using ITU-R Recommendation 452.[1]
- The wanted path is in an unfaded state, as represented by the median received signal level, and the interfering path is enhanced, once again as modelled using ITU-R Recommendation 452.

The RSL and median received signal level are known a priori and the relationship between them is the margin (M) as calculated using ITU-R Recommendation 530 [2].

In both of these situations it is necessary to satisfy a given wanted to unwanted signal ratio (W/U). Co-channel W/U values may be calculated from first principles and are based on a noise limited frequency assignment methodology where aggregate interference and individual sources of interference are limited to specified levels below an allowance for receiver noise. In practice, at the present time, co-channel and first adjacent channel values are taken from ETSI Standards [3] and modified in order to take account of multiple interferers (this approach is under review and a return to calculation from first principles is envisaged). Offset W/U values, beyond the first adjacent channel, are based on the co-channel value, the Net Filter Discrimination (NFD) associated with the relative bandwidths of the wanted and unwanted signals, the out of band emissions of the interfering signal (transmit mask), the out of band discrimination of the receiver (receive mask) and the frequency offset of the two signals.

The implications of ATPC for this assignment process are shown in figure 1. It should be noted that this does not show all of the complexities. For example, outages are treated as instantaneous at peak fade or enhancement points—outage times are therefore not completely represented. Also, the schematics are not meant to be to scale, but it can be assumed that the power increase during a fade on the unwanted link gives rise to no more interfering power than the baseline case (i.e. no ATPC).

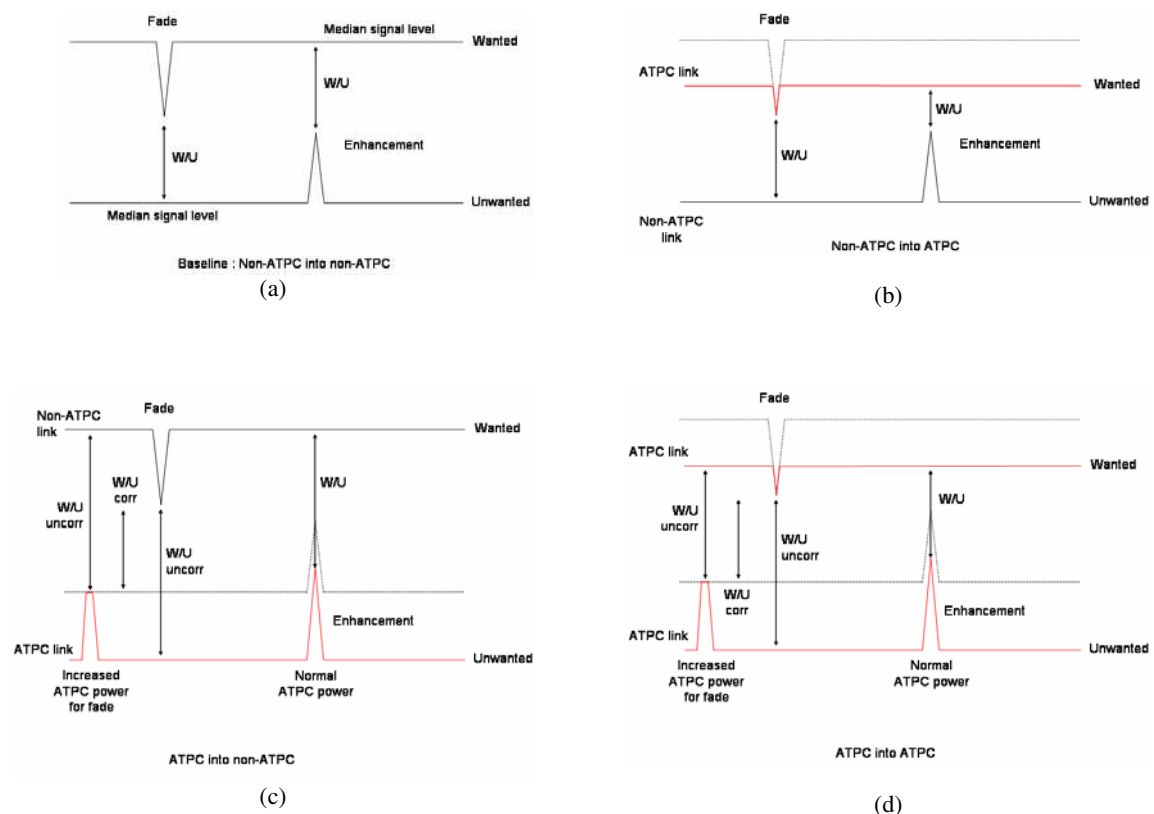


Figure 1: Schematic example of the W/U for
(a) a non-ATPC system interfering with another non-ATPC system (baseline case. (b) a non-ATPC system
interfering with an ATPC system (c) an ATPC system interfering with a non-ATPC system (d) an ATPC
system interfering with an ATPC system

3. ATPC implementation tool

The effects of implementing ATPC in the 38GHz band has been investigated by the use of a simulator developed for the purpose of this study. The simulator has two parts: a planning tool, which plans a set of links using standard planning assumptions, and an analysis tool, which takes a plan produced by the first tool and examines the response of the links to a sequence of rain fields.

3.1. Planning tool

The planning tool takes an existing plan and re-plans it, subject to a number of assumptions:

- the mix of ATPC and non-ATPC links
- the type of ATPC in use.

The statistics of the new plan are then calculated to estimate changes in band efficiency.

The initial plan was based on the existing 38 GHz band plan supplied by Ofcom. Figure 2 shows the spatial distribution of these links across the UK. The 13,949 links in the initial plan were filtered to remove links for which the data appeared to be incorrect (76 links), for which antenna patterns could not be found (165 links) or which failed the Fresnel zone test (52 links)—leaving 13,656 links, located throughout the UK; one link is one-way, the remainder are two-way; all links are vertically polarised.

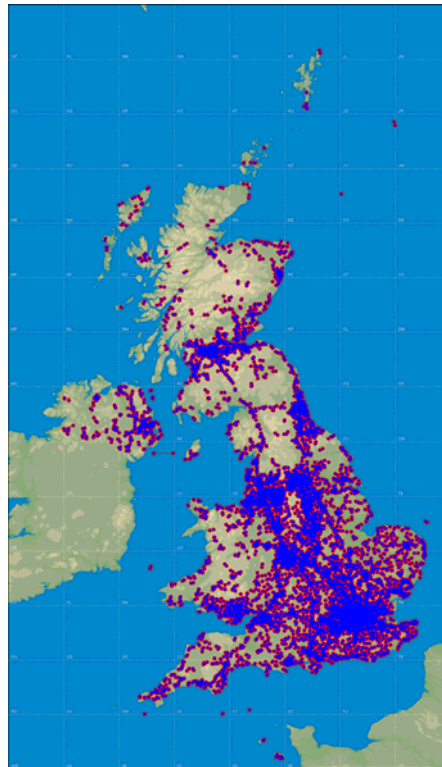


Figure 2: Link distribution in the UK in the 38 GHz band

The planning process follows OfW 42 [4], with some exceptions:

- the links are not checked against the ‘minimum path length policy’
- there is no 6 dB EIRP uplift for obstructed paths
- antenna pointing is calculated by the application—the plan value is discarded.

Figure 3 shows the currently existing assignments in the 38GHz band. As can be seen, there are a lot of legacy assignments, and the band has not had a consistent planning algorithm applied to it. For this reason it is difficult to determine the actual amount of congestion in the band. Also, in order to provide a valid baseline for comparison, the band was re-planned without the use of ATPC, using a lowest-first frequency assignment criterion.

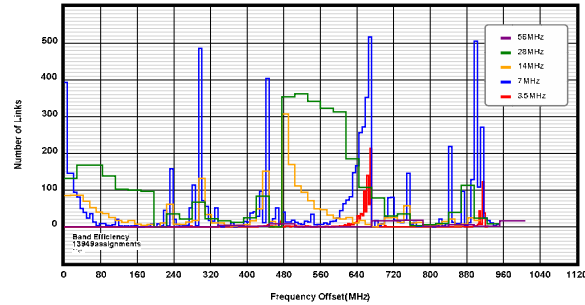


Figure 3: Existing assignments in the 38 GHz band

Plans have been run using the following two ATPC methods:

- assigned EIRP is offset by a constant positive amount (known as the remote fade margin) from $EIRP_{non-ATPC} - FM$. This method assumes the ATPC equipment is capable of covering the difference between the remote fade margin and the fade margin.
- assigned EIRP is offset by a variable negative amount (normally the ATPC range: however, the reduced EIRP is constrained to provide the required remote fade margin) from $EIRP_{non-ATPC}$.

Plans have also been run for two orderings of the link data—forward and reverse—which tests the stability of the results against assumptions about link geometry.

In practice, the automatic planning software was unable to assign every link because of high-low clashes. The number of such clashes was, however, greatly reduced by grouping links that share masts into pseudo-networks before frequencies were assigned. For example, the total number of assigned links increased from 12,781 to 13,500 for the non-ATPC plan, and from 12,805 to 13,527 links for an all-ATPC plan with a remote fade margin of 5 dB. The supplied database does not contain any information about actual networks.

The effect of re-planning the band with the automated planning application results in a contraction of the assignments to the lower end of the band (see figure 4). The band was re-planned using a lowest-first frequency assignment algorithm.

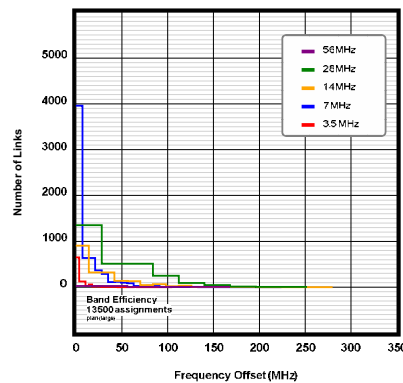


Figure 4: Automated re-plan (no ATPC)

The effect of introducing ‘ideal’ ATPC on all links is apparent when comparing figures 5 and 6 (RFM is 5 dB): both the number of assignments in the first channel and the maximum bandwidth are significantly improved. The number of links assigned to the first channel rises from 51% to 75%; the maximum bandwidth decreases from 280 MHz to 168 MHz.

A more realistic method of modelling ATPC was also considered, in which the non-ATPC EIRP was backed-off by a constant offset (i.e. the ATPC range), subject to satisfying the RFM. The following plan (figure 7) was produced for an assumed ATPC range of 10 dB and an RFM of 5 dB: the result of imposing the constraining effect of a limited ATPC range is to reduce the plan efficiency as compared with the ‘ideal’ case (figure 6).

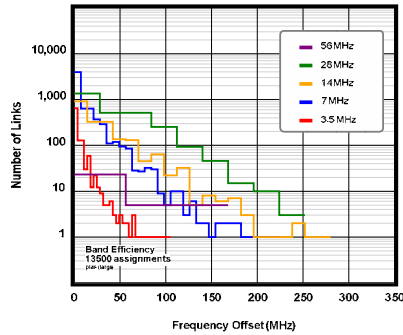


Figure 5: Automated re-plan (no ATPC)—log scale

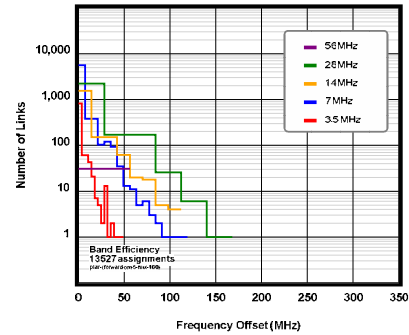


Figure 6: Automated re-plan (all ATPC, RFM = 5 dB)—log scale

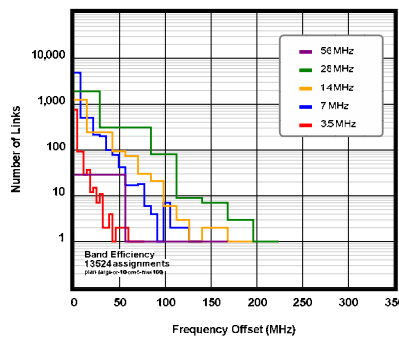


Figure 7: Automated re-plan (all ATPC, range = 10 dB, RFM = 5 dB)—log scale

3.2. Analysis tool

The analysis tool takes a plan generated by the planning tool (or by another process) and applies a sequence of rain fields, evaluating system performance as measured by outage probabilities. For each rain field, the fade on each link is calculated, which then allows the EIRP uplift to be determined for each ATPC link. Every link is then tested in turn against all interfering paths, for all rain fields, and the number of outages is recorded (distinguishing between those outages directly caused by a rain fade and those outages caused by ATPC-enhanced interference). The ATPC-induced outage counts reported here are ‘extra’ outages (i.e. those outages occurring in a link that is not also in outage because of a rain fade that exceeds its fade margin).

The rain fields used in this analysis were a combination of measured and simulated rain fields. The measured fields were recorded at Chilbolton, in the south of England, and cover an area of 56.4 km square (188 pixels of 300 m). Three types of measured rain data were used (convective, stratiform and frontal), as well as two types of simulated rain data (convective and stratiform). The measured rain data forms a sequence of rain fields in which a clear time progression is apparent, with a time step of 2 minutes between radar rasters, whereas each field in the simulated sequence is independent and time is not a consideration.

The maximum rainfall rates for the measured convective, stratiform and frontal rain data were 52.5, 45.7 and 95.5 mm/hr respectively. The maximum rainfall rate for the measured stratiform event is somewhat misleading: the effective maximum is ~30 mm/hr, which is the same as the simulated data.

As there was not enough measured rain radar data to reproduce the behaviour of the system over an average year, simulated rain fields were used to investigate the longer-term statistics. The simulated fields were created

according to the method presented in [5] and were scaled to 45 mm/hr for convective and 30 mm/hr for stratiform events. This meant that these values were the maximum rain rate experienced in the simulated arrays.

In order to avoid edge effects, the analysis of link performance is not performed on the whole area, but on a smaller ‘test’ area. Interference, however, is considered from links throughout the entire area (the ‘background’). Simulations using the measured data were run using a square 35 km test area set in the centre of the 56.4 km background area. The simulated rain fields had somewhat larger area coverage, which allowed the test area size to be increased to include more links. Simulations were run with a test area of 35 km (background 56.4 km) and 50 km (background 70 km). The pixel size for the simulated rain data was 100 m.

The number of detected outages will depend upon the severity and distribution of the rain. The distribution of rain fades can be seen in figure 8.

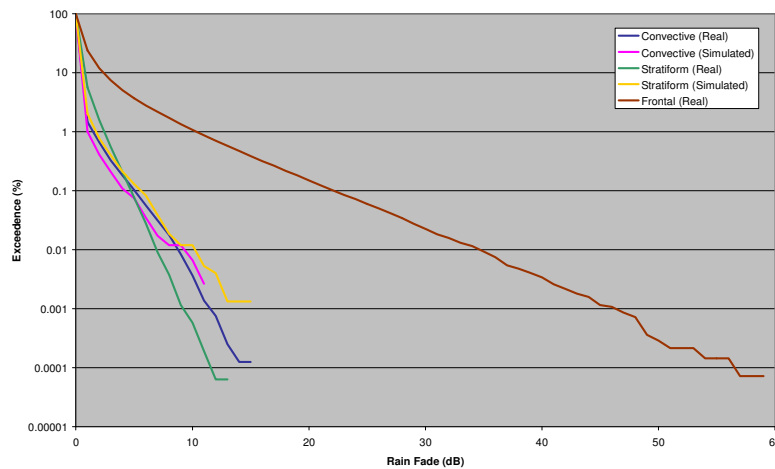


Figure 8: Rain fades for various rain types

The rain will directly cause an outage in a link if the fade exceeds the link’s fade margin (whether or not the link uses ATPC)—in other words, when the ‘signal excess’ ($fade - FM$) exceeds 0 dB. The following figure shows the distribution of signal excess for each of the rain types, and for simulations with and without ATPC. It is clear from the results that the convective and stratiform rain will not directly cause any significant number of outages, although the measured convective rain data set does in fact cause four outages for the ATPC plan considered here (ATPC range = 10 dB, RFM = 5 dB). The frontal rain will cause a significant number of outages.

The effect of introducing ATPC is apparent in figure 9, in which the number of extra, ATPC-induced outages rises as the proportion of ATPC links increases. The graph plots the number of outages, rather than the percentage, to avoid mistakenly interpreting the results as annual statistics—the probability of each rain event is not known and the results cannot therefore be compared directly with planned unavailability.

In the example shown, the number of extra outages is 12% of the total. The number of outages directly caused by rain also increases with ATPC penetration, even though ATPC does not, in itself, reduce the protection a link has against rain fading. This rise is caused by the progressive withdrawal of ‘excessive’ fade margin as non-ATPC links with the 10 dB minimum fade margin are replaced by ATPC links with a lower fade margin (e.g. an RFM of 5 dB). If the remote fade margin is increased to 10 dB, the number of direct outages then remains constant as the ATPC penetration increases.

The results also show the trade-off introduced by assumptions about ATPC equipment capability: a larger ATPC range results in a more efficient plan because EIRPs are minimised. However, if the ATPC range is smaller than typical $FM - RFM$ values then some links will have ‘excessive’ RFM—and will be better protected against interference. For example if the fade margin for a link is 25 dB and the ATPC range is 10 dB, then the link will operate at $25\text{ dB} - 10\text{ dB} = 15\text{ dB}$ above RSL, even if the required RFM is only 5 dB. Matching the ATPC range and remote fade margin appears to be a very effective method of reducing ATPC-induced outages.

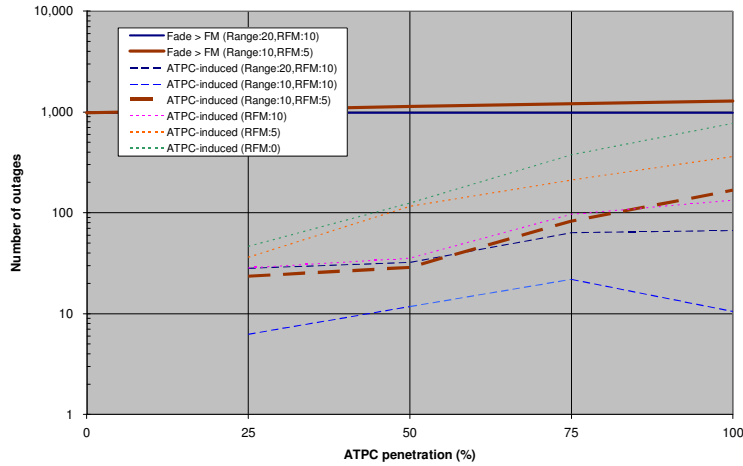


Figure 9: Number of extra outages

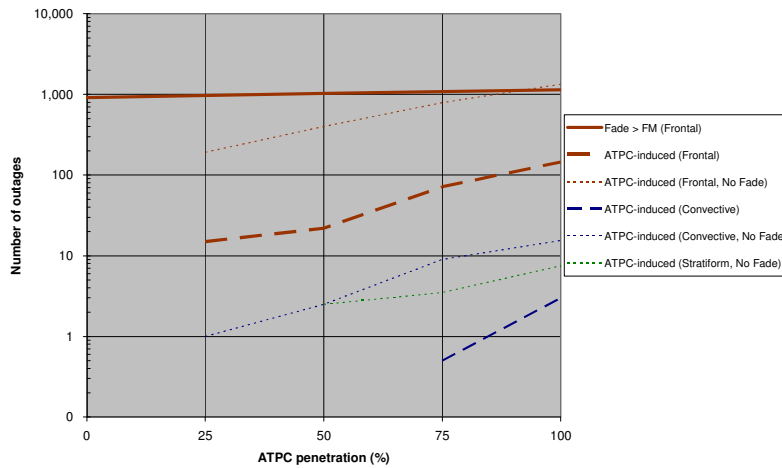


Figure 10: Mitigating effect of interfering path fades

Figure 9 shows the effect of testing an automated plan with measured rain fields, and the resulting ATPC-induced outages. Depending on the characteristic spatial distribution of the rain, an aggravating factor causing these outages is the correlation between power increases on the interfering link with fading on the victim link. A mitigating factor is expected to be the presence of correlation between the rain fades on the interfering and victim links and rain fading along the interfering path. A brief investigation has been performed to illustrate the extent of this mitigation, by suppressing the rain fades on all interfering paths and noting the increase in the number of ATPC-induced outages. These results are shown in figure 10.

When the rain fades on interfering paths are artificially removed, then the number of ATPC-induced outages increases dramatically: for the frontal rain event, the number of extra outages actually exceeds the number of direct outages in the all-ATPC case, and outages are now present in the relatively less intense convective and stratiform rain events. It is clear from this limiting case that correlated fading on the interfering path acts as a significant mitigating factor for ATPC-induced outages.

3.3. Mitigation of ATPC-induced outages

It has been shown earlier that improvements in band efficiency result from the introduction of ATPC, but that additional outages then occur (during intense rain). The question then arises of whether changes to the planning

process could be made that retain the efficiency gains but reduce the number of ATPC-induced outages. Three such adjustments have been investigated:

1. Increasing the fade margin for all links.
2. Increasing (or decreasing) the required W/U ratios for all links.
3. Increasing the interference margin.

The effect of increasing the fade margin (i.e. EIRP) of all links was shown to be not effective. As expected, the band efficiency is reduced somewhat, but this didn't reduce the number of ATPC-induced outages. As the fade margins increase the total number of outages decreases because of the extra protection against direct rain outages, but those links affected by a nearby ATPC link receive no specific protection. An increase of 1 dB in fade margin 'cancels' the extra outages caused by ATPC during the frontal rain event (for an ATPC range of 10 dB and an RFM of 5 dB).

The second mitigation approach was to vary the W/U ratios used in planning, in the expectation that this would specifically provide extra protection against interference. Adjusting the W/U ratios in the planning process and then using the same adjusted values to judge whether an outage occurs in the rain analysis produces the paradoxical result that increasing the W/U ratios actually increases, not decreases, the number of outages. The explanation for this that in a relatively efficient plan, there will always be a large number of interfering paths with small clash test excesses, 'ready' to cause interference. Band efficiency, however, behaves as expected—increasing the required W/U results in a relatively less efficient plan; decreasing the required W/U results in a relatively more efficient plan.

In practice, a better definition of a simulated outage might be to adjust W/U when planning, but to assume the original W/U values when performing the rain analysis. The results are then as expected: increasing W/U now removes some, but not all, of the ATPC-induced outages; similarly, reducing the W/U protection increases outages. Note that adjusting W/U, while leaving RSL unchanged, has no effect on the number of direct outages.

The final approach is to adjust the interference margin. As expected, increasing the interference margin increases efficiency (though with diminishing effect), whereas there is effectively no change in the number of ATPC-induced outages.

In summary, adjusting W/U in the planning process is a more effective technique for reducing ATPC-induced outages than adjusting the fade margins or interference margin. However, it is evident that none of these band-wide mitigation techniques targets the ATPC-induced outages very effectively.

3.4. Example outage event

An example outage event is shown in figure 11. Three variables are plotted for each of the 231 rain fields in the frontal sequence (with two supplementary variables):

- *Interfering Link*. The change in EIRP on the interfering link. The interfering path is very short in this example and the correspondence between EIRP increases on the interfering link and fading on the wanted link is very close. A second variable shows the change in EIRP including the effect of rain fading on the interfering path: however, there is no significant fading on this particular interfering path.
- *Wanted Link*. The 'signal excess' (*fade-FM*); a second variable shows the effective signal excess, taking into account the effect of ATPC. When the signal excess becomes positive, then the wanted link is in outage.
- *Wanted Link and Interfering Link*. The clash test excess. When the clash test excess becomes positive, then the wanted link has an interference-induced outage. Note that the second outage (at sequence number 66) is not an 'extra' outage, as the clash test excess and the signal excess are both positive.

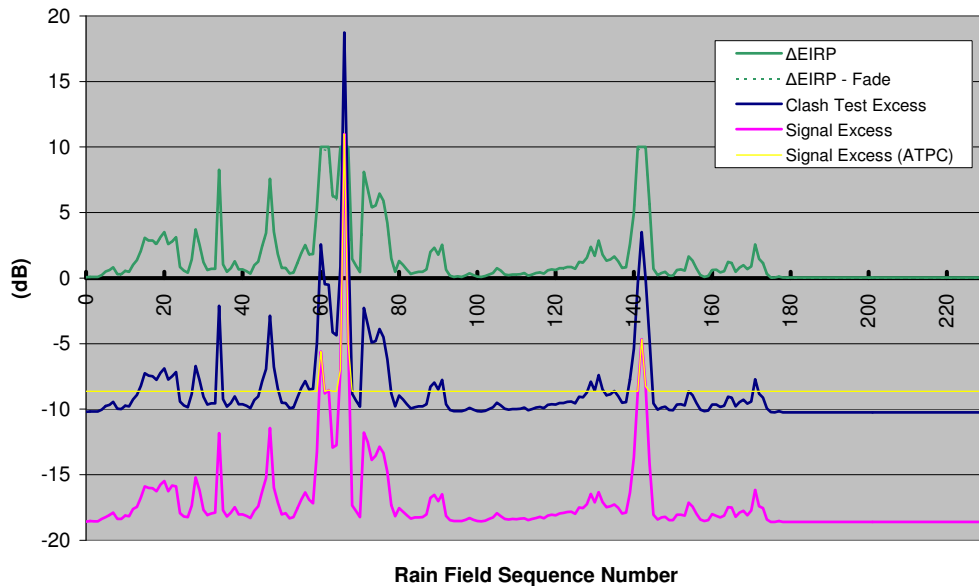


Figure 11: Trace of simulated excesses for a single link

3.5. Outage rate in a standard plan exposed to annualised rain

Callaghan [6] has described the generation of a database of rain fields which can be used to expose fixed link plans to simulated annualised rain. An important step in gaining confidence in the annualised outage percentages obtained from runs of the fixed link planning simulator is to show that the simulator does indeed produce outages at the planned rate for a plan constructed under standard planning assumptions (i.e. no novel technologies).

An exercise has therefore been conducted to examine the performance of the simulator. Firstly, the simulator was tested with a series of uniform rain fields to check whether rain attenuation is calculated the same way in the outage assessment software as in the planning software. Secondly, a standard plan was constructed and the outage rate measured in response to a sample of annualised rain fields.

The results show that a plan constructed with the objective of achieving a 0.01% unavailability has, when exposed to simulated annualised rain, a measured unavailability of 0.008%. This is close enough to demonstrate the general method. However, it is probable that further improvements to the simulated rain might improve the ability of that rain to provoke the expected unavailability. Any user of the data should also be aware that the various biases in the planning process mean that link outages may occur at only half the planned rate. In other words, the planning process at 38 GHz is, in this limited respect, conservative.

4. CONCLUSIONS AND FURTHER WORK

The following conclusions regarding the spectrum efficiency gains resulting from the implementation of ATPC have been identified by this study:

1. The implementation of ATPC in the 38 GHz band gives significant improvements in spectrum efficiency as measured by the increase in the number of links assigned to channel 1 (from ~50% to ~70%) and the decrease in the maximum bandwidth used (from ~300 MHz to ~180 MHz). The introduction of ATPC does give rise to a number of additional outages in the presence of intense rain (~10% increase in frontal rain). These additional outages can be mitigated to some extent by bandwidth changes to the planning process and by matching the ATPC range with the remote fade margin; however, the outages cannot be wholly eliminated by the methods examined here.

2. Adjusting W/U in the planning process is a more effective technique for reducing ATPC-induced outages than adjusting the fade margins or interference margin. However, it is evident that none of these band-wide mitigation techniques targets the ATPC-induced outages very effectively.
3. Based on the similarity of average fade margins between the 38 GHz band and other high frequency fixed link bands, gains in spectrum efficiency should equally be possible in those other bands.

Previous work attempting to assess the impact of new assignment methods or technologies on planned link availabilities was restricted to relative comparisons because annual outage rates could not be determined. This study sought to remove this issue by using sequences of simulated rain fields that, together, represent annual rain statistics. This allows simulated link availabilities to be compared directly with planned availabilities. The method relies on the generation of simulated stratiform and convective rain fields, which are then scaled to fit the tail of the ITU-R P.837 [7] rain rate distribution and combined in proportions appropriate to annual rain statistics. The method has been proved by generating a plan with known link availabilities and then testing to see whether the links respond in the appropriate way to the scaled, mixed, annualised collection of rain fields.

The results from this test show that a plan constructed with the objective of achieving a 0.01% unavailability has, when exposed to simulated annualised rain, a measured unavailability of 0.008%. This is close enough to prove the concept, and it is anticipated that further developments in the rain field model will improve the ability of the simulated rain to provoke the expected unavailability.

The final report of this project [8] is available on-line at <http://www.ofcom.org.uk/research/technology/overview/ese/atpc/atpcfinal2.pdf>

5. ACKNOWLEDGMENT

The research presented in this paper was funded by the UK's Ofcom as part of the Spectrum Efficiency Scheme.

6. REFERENCES

- [1] ITU-R Recommendation P.452 "Prediction procedure for the evaluation of microwave interference between stations on the surface of the Earth at frequencies above about 0.7 GHz"
- [2] ITU-R Recommendation P.530 "Propagation data and prediction methods required for the design of terrestrial line-of-sight systems"
- [3] ETSI TR 101 036-1 v1.3.1 2002-8
- [4] OfW 42 "Technical Frequency Assignment Criteria for Fixed Point-to-Point Radio Services with Digital Modulation Operating in the Frequency Ranges 32.319 to 32.571 GHz paired with 33.131 to 33.383 GHz and 37.0 to 38.178 GHz paired with 38.318 to 39.50 GHz" Version 3 November 2006 http://www1.bsc.org.uk/radiocomms/ifi/tech/tfacs/tfac_ofw42.pdf
- [5] Callaghan, S.A, Vilar, E., "Fractal Generation of Rain Fields: Synthetic realisation for radio communication systems", IET Microwaves, Antennas and Propagation, Vol. 1, Number 6, 1204-1211, December 2007
- [6] Callaghan, S.A., "Generating Year-Equivalent Databases of Fractally Synthesised Rain Rate Fields" ClimDiff, 2 – 4 June 2008, Boulder, Colorado, USA.
- [7] ITU-R Recommendation P.837-4 "Characteristics of precipitation for propagation modeling"
- [8] Callaghan, S.A., Hansell, P., Inglis, I., "Impact of introducing Automatic Transmit Power Control in P-P Fixed Service Systems operating in bands above 13 GHz" Final report for Ofcom, 19th December 2005

Preliminary Analysis of Radiowave Propagation Data Using a Gigabit Radio Link Operating at 83.5 GHz Close to Oslo in Norway

Terje Tjelta and Tor Ove Breivik
Telenor R&I, Snaroyveien 30, 1331 Fornebu, Norway
terje.tjelta@telenor.com and tor-ove.breivik@telenor.com

Abstract

Radio links continue to play an important role in many telecommunications and broadcasting networks. As the total traffic grows the demand for flexible high capacity solutions exists in all parts of the network, from the access to the core. Millimetre frequency technology is now commercially available with links that can deliver gigabit capacity to be used for access or backhaul applications. The ITU-R Recommendations provide radiowave propagation guidance and models, but at the frequencies above 40 GHz there are very few data sets available for testing, validating, and improving the prediction methods. This paper presents preliminary results from an experimental link with nine months data for discussion of the prediction of hydrometeor precipitation caused attenuation and some other propagation effects.

1. Introduction

Radio links continue to play an important role in many telecommunications and broadcasting networks. The total traffic has been growing for many years. The capacity demand in the access network increases with a doubling rate close to two years. Digital broadcast networks are installed at an increasing rate with further demand for efficient and flexible backhaul. Links providing gigabit capacities are indeed needed already, e.g., for backhauling digital subscriber line access multiplexer (DSLAM).

During the recent years several vendors have developed gigabit radio links operating in the 60 to 90 GHz frequency range. The commercial products seem to reach a price making them competitive with alternative solutions. The technology is well established and develops further, and the modulation robust giving at least the 70 to 90 GHz links a reasonable range.

With respect to dimensioning outdoor links operating in the 70 to 90 GHz bands, clearly attenuation due to rainfall becomes a limiting factor. However the gaseous absorption is limited and these bands offer an interesting opportunity for high capacity links with the scope of several Gbit/s. The current guidance for dimensioning links in the frequency range is limited to a few propagation experiments in the past, and the ITU-R does not guarantee the rain attenuation prediction method valid to more than about 40 GHz. It is therefore necessary to collect data both for validation purposes and model improvement for a more secure design of this type of links.

This paper is organised in 4 main sections where Section 2 presents the Telenor experimental gigabit link in the 70/80 GHz band, Section 3 presents measured results, a brief discussion is given in Section 4, and finally Section 5 with a summary and conclusions.

2. Experimental link and measurement setup

Telenor R&I has since June 2007, conducted an experiment using a 1 Gbit/s radio link operating in the 70/80 GHz band. The path and terrain profile are shown in Figure 1a, The link is 3.45 km long and located at 10.6° West and 59.9° North. The data collection equipment is located at Telenor R&I's premises at Fornebu where the vertical polarised 83.5 GHz link is terminated. Collected data include attenuation and meteorological data such as air pressure, temperature, rainfall, relative humidity, and wind, see list in Figure 1b. The link has 60 cm reflector antennas resulting in a very narrow beam. The system gain is about 80 dB for the actual equipment used, with respect to a bit error ratio of 10^{-6} .

The normal yearly precipitation height in Oslo is somewhat less 800 mm, but last year (April 2007 through March 2008) it was close to 1000 mm [1]. The precipitation during winter periods will normally be a mixture of rain and snow, or wet snow. The link is located close to the Oslo fjord and there is a certain risk of fog. During the period covered by the experiment there has been more precipitation than normal.

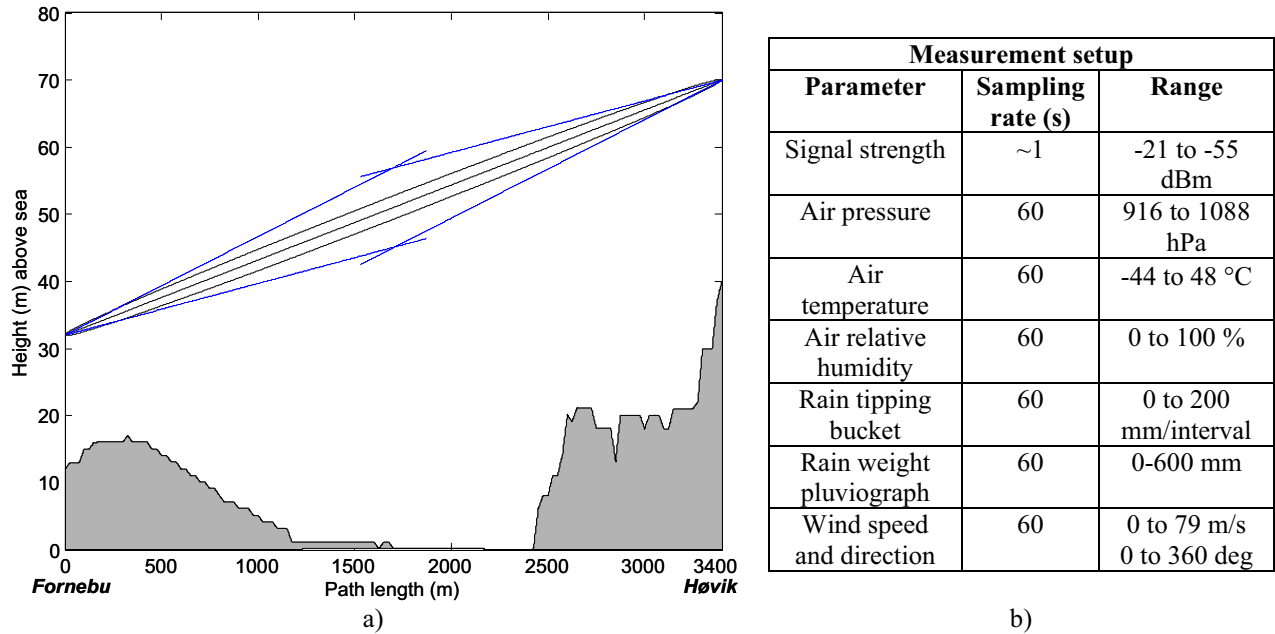


Figure 1. a) Terrain profile and path indicating the first Fresnel zone and antenna 3 dB beam width common volume and b) the measurement setup key data

3. Measured events and distributions

The measured signal strength has been fairly stable over the nine month measurement period performed so far. However, a long term deviation has been observed, perhaps caused by antenna misalignment increasing with time, or an equipment temperature dependency. The long term variation has not been investigated in this paper.

3.1. Some measurement events

The measurements cover many events, from which four have been selected Figure 2 and Figure 3, where each represents a propagation phenomenon that might be considered in developing or improving radio link dimensioning rules. The rain attenuation event on 20 June 2007 given in Figure 2a, shows that the signal is deeply attenuated (top curve in black) at the same time as a heavy shower of up to 60 mm/h maximum (bottom curve in blue) at the end of the link. However, the 31 January 2008 event in Figure 2b shows equally deep fading but for insignificant rainfall rate. The latter precipitation event is much more likely wide-spread than the first event. The bottom curve here (in pink) shows the rainfall weight pluviograph measuring an increase in total rainfall of about 12 mm over about 6 hours with a rainfall rate maximum in the order of 2-4 mm/h. Together with the temperature close to zero (from top second curve in red), and high humidity (from top third curve in cyan) it suggests a wet snow effect, known to easily increase attenuation by several times compared to rainfall of the same intensity. The other data plotted in the third group from top of figure are rainfall rate measured by the tipping bucket (TP) sensor (in blue) and the differential of rainfall weight pluviograph (WP) (in pink). The TP measurement is not operated during winter time; there is no heating installed, and the curve actually coincides with the abscissa when there is no data.

Figure 3a and Figure 3b show two events, suggesting effects of dry snow and fog. The dry snow event on 5-6 January does not lead to any attenuation, in contrast to the event shown in Figure 2b for a similar precipitation rate. The possible reasons for signal strength change around 18h has most likely nothing to do with the precipitation in the air. It needs further investigations if it is to be linked to propagation conditions. On 13 February 2008 there was a situation with fog with a visibility subjectively estimated to 100-150 m. The attenuation seems to be one to two dB for the period.

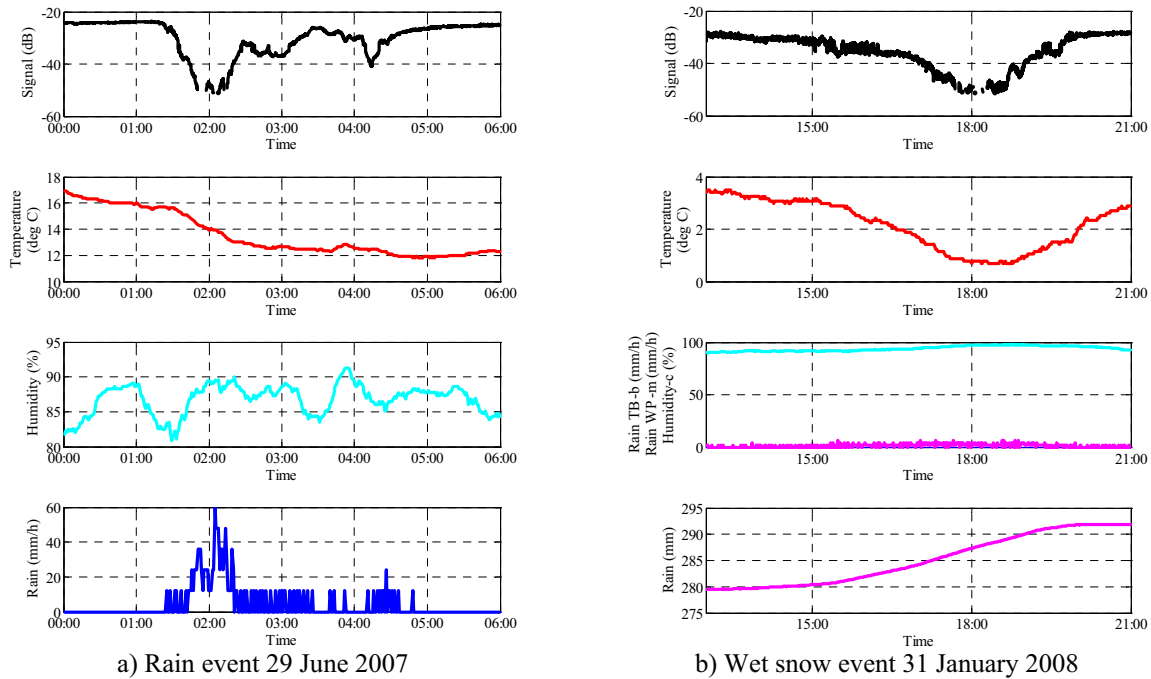


Figure 2. Events due to a) rain and b) probably wet snow

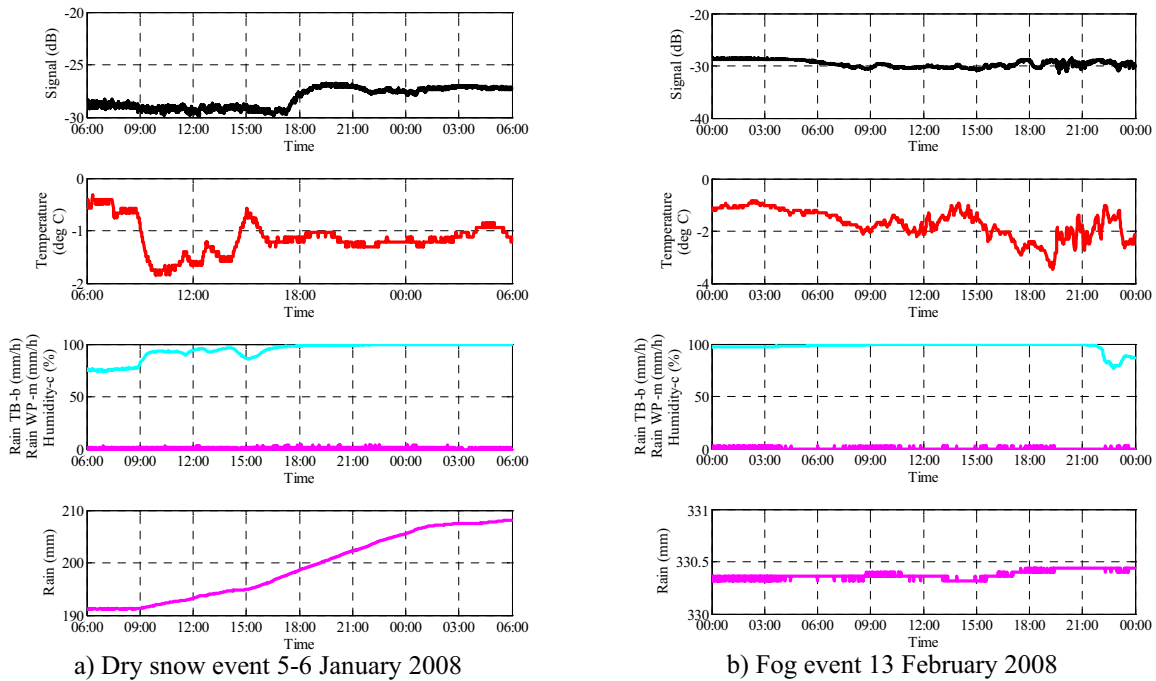


Figure 3. Events suggested due to a) dry snow and b) fog

3.2. Monthly attenuation distributions

The calendar month attenuation distributions and the average distribution are shown Figure 4 along with average year and worst month predictions. The monthly median values have been removed from the signal strength histograms. The colour and line-type codes are given in the legend along with available data for each month. The

interpretation is percentage of time the attenuation exceeds the values on the abscissa. For month with little available data, e.g., July and October, it is not sure whether this is a conservative or optimistic estimate. A more careful analyse of weather data, as their time series are longer, and such data from other sources, will help in judging whether the attenuation data should be normalised using a different period than the attenuation measurement period.

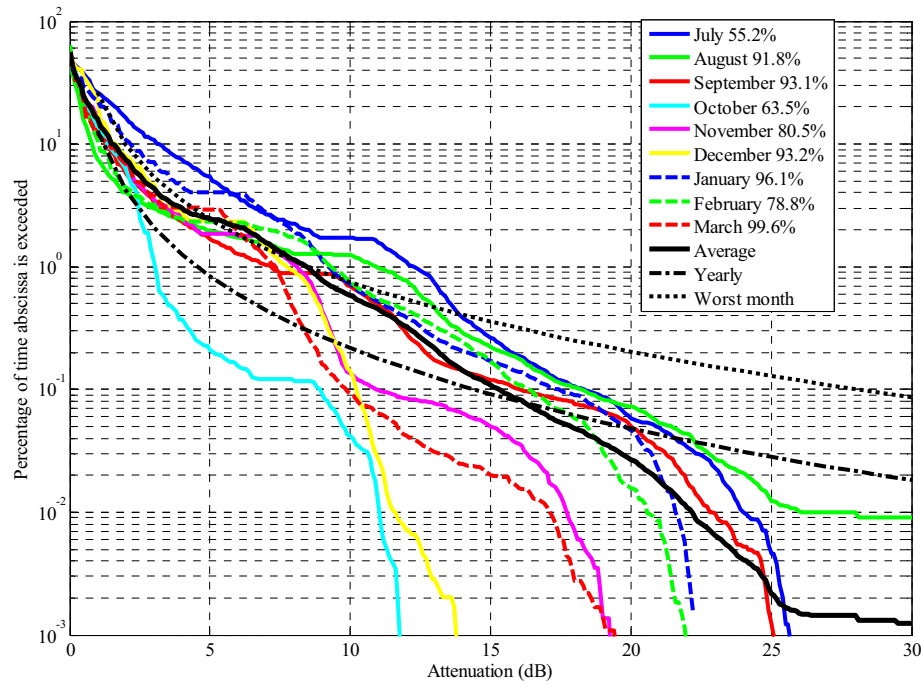


Figure 4. Attenuation distributions showing percentage of measured time the attenuation exceeds abscissa values compared to average year and worst month predictions. The monthly median values have been used as reference for the attenuation. The total available measured time per month is shown in the legends

4. Discussion of measurement results

The measurements have been compared with ITU-R predictions, noting that the terrestrial link precipitation attenuation prediction method has only been validated up to about 40 GHz due to lack experimental data. The nine month average shown in Figure 4, suggests less attenuation than the ITU-R rain attenuation prediction method from 16 dB attenuation and beyond, for about 0.08 % of the period. This means that for availability requirements for example from of 99.99 % or higher, the ITU-R prediction method might be considered conservative for this link. However, at shallower attenuation level considerably higher attenuation is observed, than predicted by rain only.

It is not straight forward to identify reasons for the observed longer periods of shallower attenuation than predicted. As there have been few data published it is yet not clear whether this is an effect for the higher frequency. But earlier studies of specific attenuation from this region has pointed in the same direction [2], in fact also at a number of other sites from different parts of the world regarding millimetre wave rain attenuation referenced in [2].

Two possible reasons for the deviations are gaseous absorption and attenuation due to fog and clouds. As the attenuation is taken to represent the difference between signal strength and the monthly median the gaseous absorption will contribute both to positive and negative attenuation levels. Anyway, the analyses using air pressure, temperature and relative humidity [3][4] it seems clear that the gaseous absorption is within 3 dB for all months and less than 2 dB for the winter months. The histogram for the August 2007 data is shown in Figure 5. It is then obvious that gaseous absorption does not explain the additional attenuation observed compared to rain

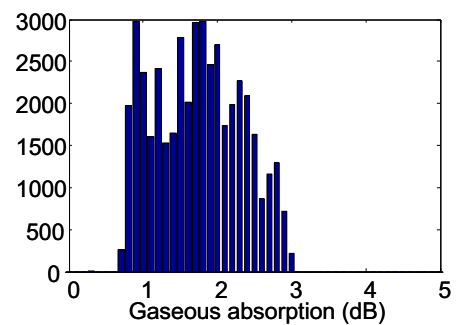


Figure 5. Histogram of gaseous absorption August 2007

attenuation predictions. Similarly, the attenuation in fog and clouds [5], although a couple of dB is possible, can neither explain the distribution form.

One possible cause is wet snow. As heavy attenuation has been observed during periods with low rainfall, it cannot be ruled out. But the deep fade examples as the one shown in Figure 2b, will affect at the tail for the deep attenuation range. With respect to the shallower fading region it is not obvious that wet snow is the cause, but it can be.

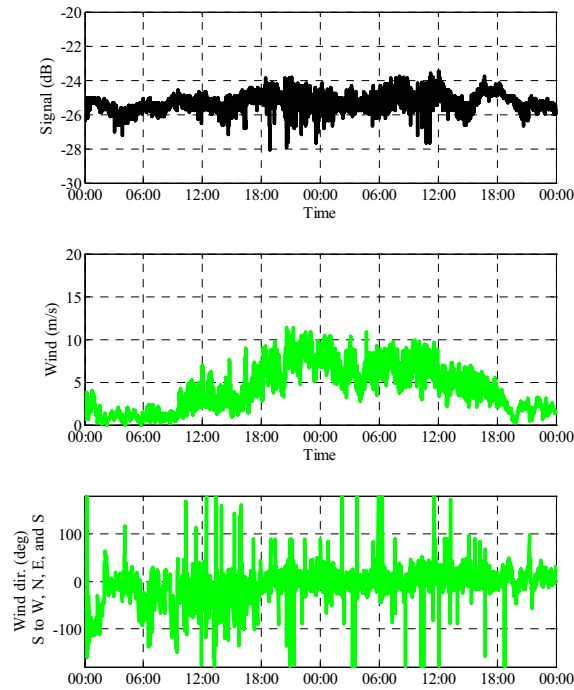


Figure 6. Scintillation 3 and 4 September 2007

However, the recent adopted method for combined rain and wet snow distribution predicts an insignificant increase for this particular link [6].

At high frequencies the scintillation amplitudes will increase as well. On the other hand the very small common volume reduces the scintillation on the link. Some examples of time series data show higher signal variability with increased wind speed, but not to the extent that it can explain he increased shallow attenuation compared to the predicted. One two-day event is given in Figure 6 clearly showing that the scintillation is increasing with wind, up to about 4 dB peak-to-peak. If the effect is caused by refractive index variability within the common volume, these events will not influence the precipitation attenuation distributions in the shallow region beyond a couple of dBs. However, if the variation seen is caused by antenna vibration or movement it may have an effect even during periods with rain.

The most likely problem seems to be that the predicted attenuation distribution may not be accurate enough for the frequency range under consideration. The current ITU-R method uses only one point from the rainfall distribution to derive the full attenuation distribution. If the full rainfall distribution was used it might be easier to obtain a more accurate prediction.

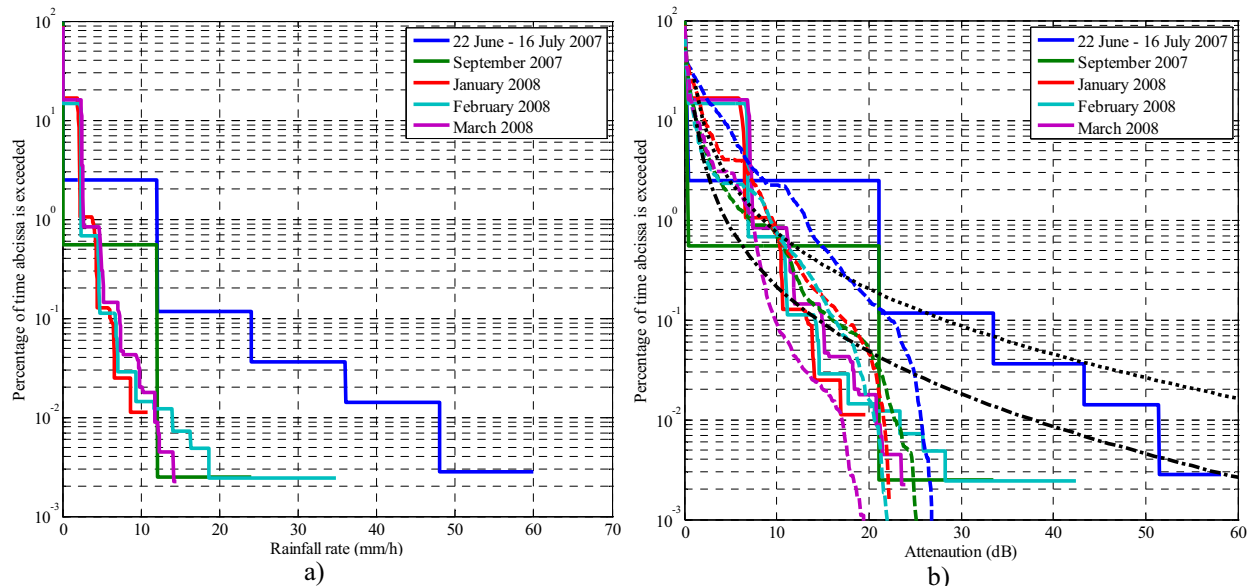


Figure 7. Five periods showing a) rainfall rate and b) attenuation derived from rainfall rate (colour solid lines) together with observed data (coloured broken lines) and predicted average year and worst month (black dash dot and dot lines, respectively)

To investigate the impact of the actual rainfall distribution in looking for an explanation for the attenuation prediction deviation the periods with available rainfall rate measurements have been studied, i.e., five periods as

indicated in the legend of the analysed rainfall rate distributions in Figure 7a. The two first periods a tipping bucket type of measurements is used, it tips for each 0.2 mm rainfall and the tipping number is recorded each minute. This is the reason for the quantized plot in 12 mm/h steps. It is observed in the first period, that there is just one significant event of 60 mm/h in the period 22 June through 16 July, i.e., one count in one minute. The latter three periods the weight pluviograph is used having smaller quantization steps.

In Figure 7b the rainfall rate data have been used to calculate the attenuation to be expected on the 3.45 km link using the rainfall rate path reduction model in [6]. The results are shown with solid coloured line, colour code in the legend. The distribution of the observed data from the same period, are shown with the same colour code, but using broken lines. Finally, Figure 7b also shows the average year and worst month predictions, in black with line style dash dot and dot, respectively.

For an exact comparison concurrent data is preferred. For the five periods shown this is the case for the periods in 2007 and March 2008. In January 2008 a small portion of radio data are missing compared to the period for the meteorological data, whilst in February about 6 days of radio data are missing.

The graphs in Figure 7b suggest that using the full rainfall rate distribution a more exact attenuation prediction can be developed. The June/July 2007 period does not quite show this for the deep fading range. However, it should be noted that the 60 mm/h event was a single and rare event for the region and it may have been just at the end of the path. Anyway, the concern with the accuracy of the prediction seems to be at the shallower part where the current ITU-R method is significantly under-predicting the observed attenuation.

5. Summary and conclusion

The results from the first 9 months operating a 1 Gbit/s radio link at 83.5 GHz show that it is hydrometeor precipitation that causes the most severe attenuation. Other effects play a smaller role, where gaseous absorption seems to be the most significant factor. Also fog may play a similar role as the atmospheric gases, but being more likely during cold periods, the attenuation maximum caused by fog plus gaseous absorption may not be more than what gaseous absorption causes on its own. For an exact evaluation of the gaseous effects and the impact on the attenuation distribution another reference level than the monthly median has to be used, or the estimated gaseous absorption have to be removed from the radio time series data before the analysis of rain attenuation effects.

The preliminary analysis shows that

- the time attenuation up to 25-30 dB caused by precipitation is significant less than predicted by the ITU-R method, the ITU-R method gives a pessimistic estimate
- the time with shallower attenuation, say less than 16 dB, the ITU-R method provides an optimistic estimate
- other propagation effects than precipitation, such as gaseous absorption, fog attenuation and perhaps scintillation, in part explain the possible deviation in the shallower fading range
- a more accurate prediction method can be obtained if the full rainfall rate distribution is used.

The experiment will be continued to collect longer time series data and further analyses will be done.

6. Acknowledgments

The authors want to acknowledge colleagues Trond Berrefjord, Torbjørn Tanem, Tore Scharning, and Pål Grønsund for many valuable discussions, help with the link installation and set-up, and the data collecting software.

7. References

- [1] Norwegian Meteorological Institute, "eKlima. External access to climate data from Norwegian Meteorological Institute", URL: <http://sharki.oslo.dnmi.no>, April 2008
- [2] Aasen, W. and T. Tjelta, "A novel method for predicting site dependent specific rain attenuation of millimeter radio waves", *IEEE Transactions and antennas and propagation*, vol. 51, no. 10, pp. 2987-2999, October 2003
- [3] ITU-R, "Recommendation P.676-7. Attenuation due to atmospheric gases", International Telecommunication Union, Geneva, Switzerland, 2007
- [4] ITU-R, "Recommendation P.453-9. The radio refractive index: its formula and refractivity data", International Telecommunication Union, Geneva, Switzerland, 2003
- [5] ITU-R, "Recommendation P.840-3. Attenuation due to clouds and fog", International Telecommunication Union, Geneva, Switzerland, 1999
- [6] ITU-R, "Recommendation P.530-12. Propagation data and prediction methods required for the design of terrestrial line-of-sight systems", International Telecommunication Union, Geneva, Switzerland, 2007

Micro Rain Radar Measurements of Rainfall in Madrid: First Results

Pilar García-Vila, Ana Benarroch, Pedro García, José M. Riera
Universidad Politécnica de Madrid, Spain
e-mail: ana@grc.ssr.upm.es

Abstract

A vertically pointing Doppler radar at 24.1 GHz, or Micro Rain Radar, has been recently installed at Universidad Politécnica de Madrid as part of the experimental set-up for propagation measurements. Additional meteorological equipment, such as a tipping-bucket rain gauge and a disdrometer, is available at the site, allowing the comparison of rain rate statistics derived from the various instruments. The first results of the analysis of the radar data, including the time series of rain rate and drop number and size parameters, as well as profiles and sodargrams of radar reflectivity, are presented in this paper.

1. Introduction

The knowledge of rainfall characteristics is necessary for the design of microwave and millimetre-wave radio communication systems. The statistical distribution of rainfall rate in the region of interest is required for the application of various rain attenuation prediction models. Therefore, reliable rain data must be used to perform model calculations. Furthermore, the development and operation of many Propagation Impairment Mitigation Techniques (PIMT's) relies on the availability of information on time and space variability of rainfall rates [1].

The Group of Radiocommunications of the Universidad Politécnica de Madrid has been performing various propagation measurements for a number of years. The present experimental set-up includes:

- Eutelsat HB-6 Ka-band 19.7 GHz beacon receiving station with associated radiometer.
- 38 GHz radio-link, length 1 km, in operation since 2005.
- 75 & 85 GHz radio-link (Gigabeam Wifiber), length 1 km, installed in 2008.
- METEK MICRO RAIN RADAR MMR-2, installed in 2007.
- THIES Disdrometer, installed in 2008, borrowed from Universidad de León.
- Tipping-bucket rain gauge, in operation since 1999.
- Automatic meteorological station, in operation since 1999.

The meteorological equipment and the propagation receivers are co-located and record data simultaneously, so that the meteorological conditions producing a given propagation event can be identified. The availability of rain data from a Doppler radar, a disdrometer and a tipping-bucket rain gauge, which are instruments useful to investigate rainfall characteristics, will allow a more complete and detailed analysis of the rain effects on the propagation data gathered with the EUTELSAT satellite experiment and the set of millimetre-wave radio-links. The radar data are particularly interesting to look into the effects of rainfall on the satellite propagation path. Cloud features, such as the melting zone, may be detected as well with this radar.

The MRR is a vertically pointing Doppler radar at 24.1 GHz [2]. The measured Doppler spectra are converted into drop size density distributions. Profiles of radar reflectivity, liquid water content, rainfall rate and terminal velocity are also provided by the radar. The height resolution can be adjusted between 35 and 200 m, detecting up to 30 levels, which amounts to a maximum height that may be changed from 1050 to 6000 m. The integration time can be also selected starting from 10 seconds, although this parameter has been chosen equal to 1 min. in most cases.

The radar data recorded during 5 months are being used to obtain various statistics so that single events as well as long term statistical distributions can be analyzed. Since a tipping-bucket rain gauge and a disdrometer are also available, the rain data statistics derived from their measurements are being compared with the radar results. The first outcomes of this study are discussed below.

2. Parameters derived from radar measurements

Drop size distributions (DSD), $N(D)$, are derived from the Doppler spectra. The analytic fit of Atlas et al. [3] to the data of Gunn and Kinzer [4] is used to determine the drop diameters, D , that correspond to terminal velocities, as measured directly by the radar. The characteristic falling velocity is obtained calculating the first moment of the Doppler spectra. The DSD is used to calculate reflectivity, Z , and rainfall rate intensity, R , according to:

$$Z = \int_0^{\infty} N(D) D^6 dD \quad (1)$$

$$R = \frac{\pi}{6} \int_0^{\infty} N(D) D^3 v(D) dD \quad (2)$$

where $v(D)$ is terminal velocity.

The total concentration of drops in number/mm³, N_T , and the average mass-weighted drop diameter in mm [5], \bar{D}_m , have also been calculated using:

$$N_T = \int_0^{\infty} N(D) dD \quad (3)$$

$$\bar{D}_m = \frac{\int_0^{\infty} N(D) D^4 dD}{\int_0^{\infty} N(D) D^3 dD} \quad (4)$$

3. Experimental results

Since only a few months of radar data are available, long term statistics have not been derived yet. Various single events have been analyzed to investigate the behaviour of the set of parameters provided by the radar, as discussed above, using an integration time of 1 minute. The events chosen to illustrate the variability of these parameters correspond to a light to moderate rain event associated to a weather front, which occurred on April 19th, and to a heavy convective rain event that was observed on April 7th.

The time series of the rainfall rate measured by the radar at the first height levels, 100 and 200 m, during the April 19th event are compared to the rain rate measured simultaneously by the rain gauge and the disdrometer in figure 1. This event starts with a peak of moderate intensity that was detected by all three instruments and lasted less than 5 min. Afterwards, the rain gauge and the disdrometer show several smaller peaks between 5 and 8 mm/h. The event continues with an interval of lower rain rates. The differences between the rain gauge and the disdrometer rain rates can be attributed to the peculiarities of each instrument. The corresponding time series appear, in general, above the rainfall rate plots obtained from the radar data. The time series of the radar data have also been plotted separately in figure 2, showing larger values for the highest level considered.

The total concentration of drops and the mass-weighted drop diameter derived for the April 19th event are presented in figure 3. A peak above 60000 drops/m³ is detected in coincidence with the rain rate maximum. The concentration of drops stays between 1000 and 3000 drops/m³ during the rest of this event. The average mass-weighted drop diameter does not present any significant effect when the rain rate maximum is detected, varying between 1 and 2 mm during most of the event.

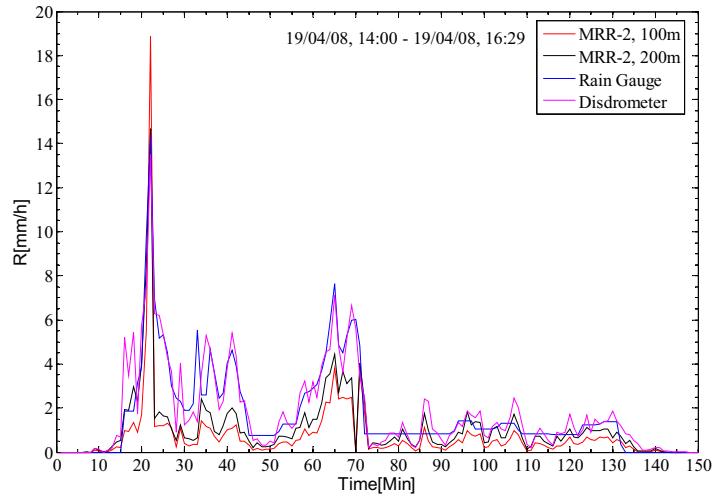


Figure 1. Time series of the rainfall rate measured by the rain gauge, the disdrometer and the radar during the April 19th event.

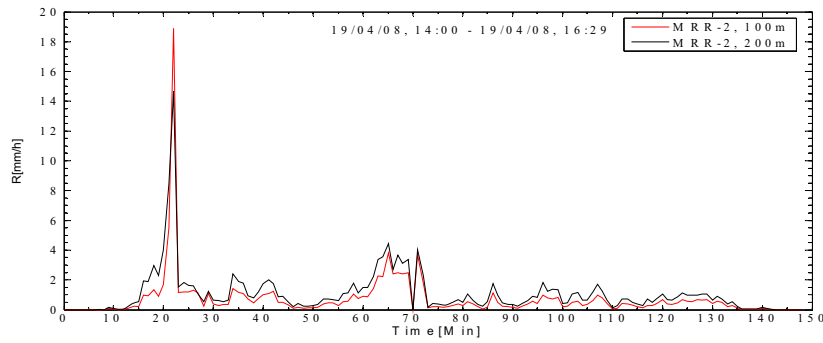


Figure 2. Time series of the rainfall rate measured by the radar (April 19th event).

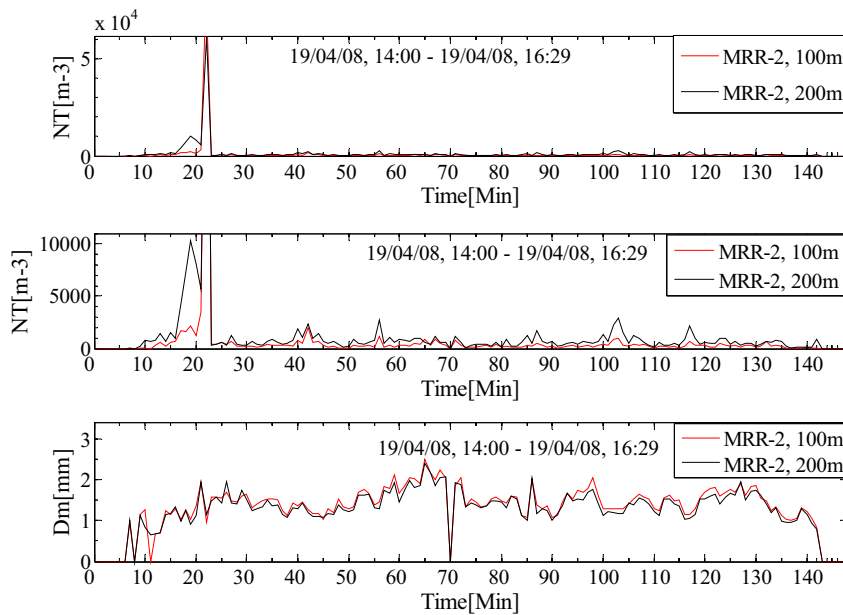


Figure 3. Total concentration of drops and mass-weighted drop diameter (April 19th event)

The radar reflectivity profiles measured during this event are shown in figure 4 and 5 for two intervals that correspond to intermediate and low rain rate, so that the different characteristics of the profiles can be observed. During the first 5 minutes the reflectivity values are relatively high, above 35 dBZ, which coincides with the rain rate maximum discussed above, decreasing later, when the rain rate is also diminishing. Reflectivity variations with height are also affected by such changes in precipitation behaviour. The graphs in figure 5 show similar patterns up to 1500 m that are clearly different from the ones in figure 4. The reflectivity peak at about 1200 m could be attributed to the existence of a melting zone. The zero degree isotherm extracted from the closest (Madrid Airport) radiosonde measurements available for the same day has been found at approximately that same height. A steady, low rate rainfall is observed in the time interval selected for figure 5, as can be seen in the time series in figure 1.

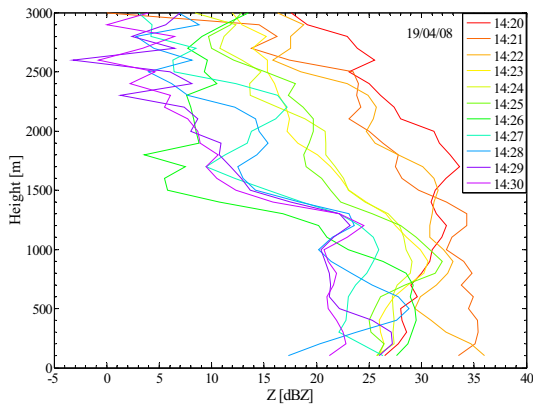


Figure 4. Radar reflectivity profiles for an intermediate rain rate interval (April 19th event)

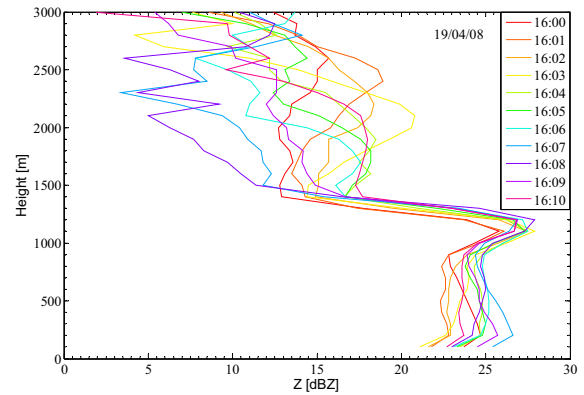


Figure 5. Radar reflectivity profiles for a low rain rate interval (April 19th event)

The time series for all three instruments are depicted in figures 6 and 7 for the April 7th event. A high rain rate maximum is detected at the beginning of this event that presents different values depending on the measuring equipment. The rain gauge gives a maximum of about 65 mm/h while the disdrometer yields a value over 90 mm/h. As in the previous case, during most of the event, rain rate values derived from the radar measurements are below the rain gauge and disdrometer values, which are almost coincident except for the high intensity peak.

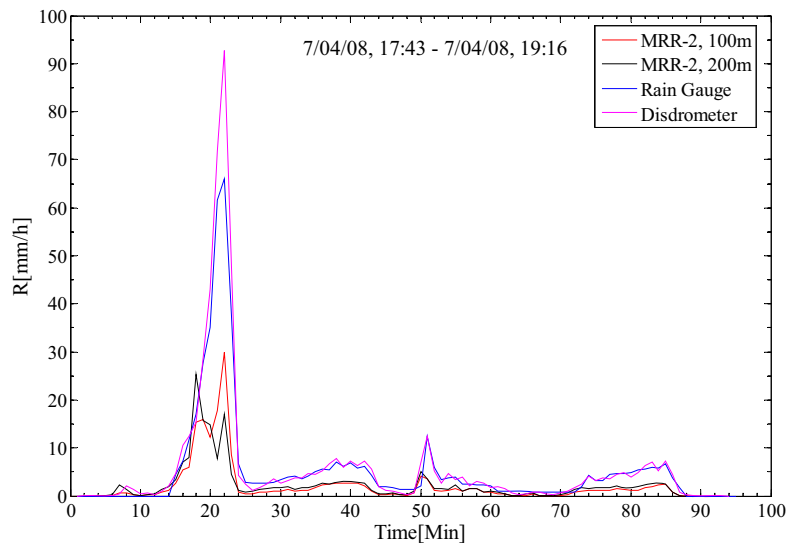


Figure 6. Time series of the rainfall rate measured by the rain gauge, the disdrometer and the radar during the April 7th event.

The total concentration of drops and the mass-weighted drop diameter for this event are shown in figure 8. A very large maximum value, above 100000 drops/m³ is obtained when the rain rate reaches its peak in this event. Afterwards, drop concentration stays below 2000 drops/m³ and even below 1000 drops/m³ most of the event. The heavy rain part of the event is also reflected in a maximum value of 4.3 mm of the the average mass-weighted drop diameter. This parameter gives larger values than in the previous case, being between 2 and 3 mm most of the event.

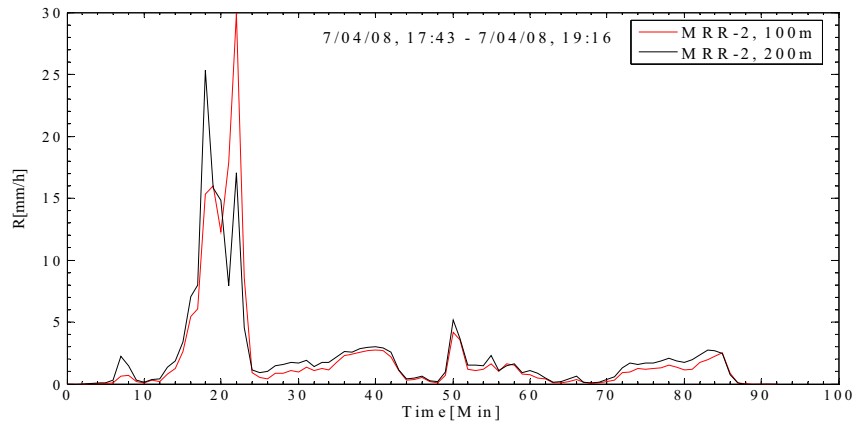


Figure 7. Time series of the rainfall rate measured by the radar (April 19th event).

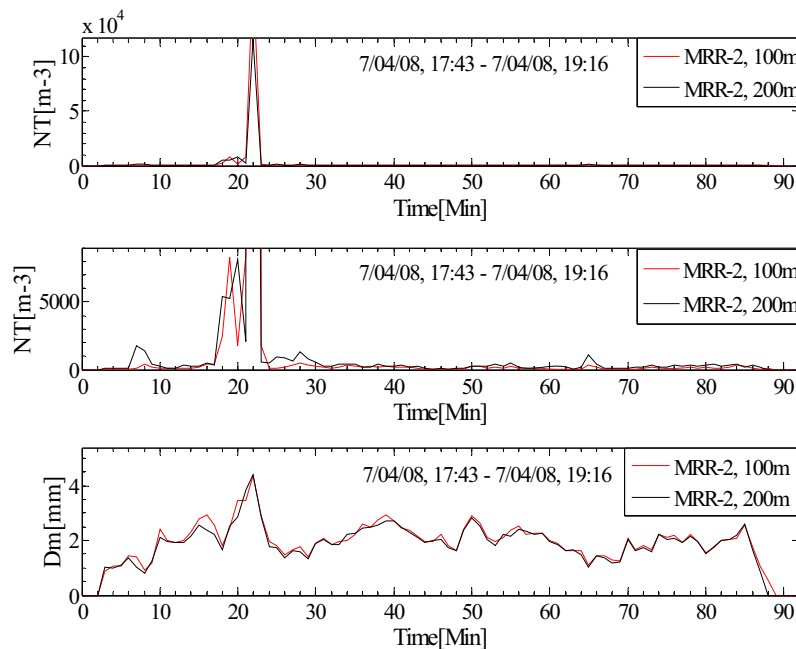


Figure 8. Total concentration of drops and mass-weighted drop diameter (April 19th event)

Two different intervals of this event have been selected to plot the profiles of radar reflectivity that are presented in figures 9 and 10. Relatively high values, of around 40 dBZ, were detected close to the ground during the peak that reached 65 mm/h measured with the rain gauge. Reflectivity values over 30 dBZ are observed in the profiles derived for the first minutes of the second interval. Although the lapse of time between both profile series is relatively short (only several minutes), their shape has changed significantly. As in the previous case, a maximum of reflectivity is detected at a height of 1500 m, which is approximately the height of the zero degree isotherm obtained from radiosonde measurements performed the same day.

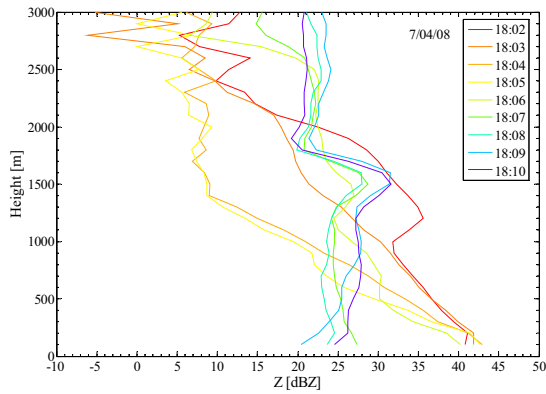


Figure 9. Radar reflectivity profiles for a high rain rate interval (April 7th event)

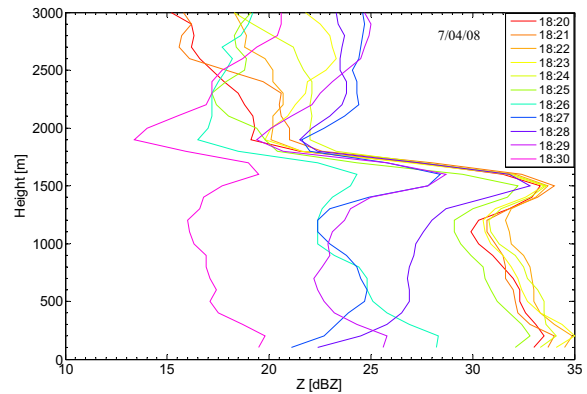


Figure 10. Radar reflectivity profiles for a low rain rate interval (April 7th event)

The variability of radar reflectivity for both events is depicted in the sodagrams of figures 11 and 12. The area of precipitation is clearly marked with brighter colors, extending from the ground to approximately 1500 m, except for several intervals of higher reflectivity. In both cases, such intervals correspond to the peaks observed previously in the time series of rain rate. Some of the stretches presenting a high reflectivity at an approximate height of 1200 or 1500 m, for each of the events, could be attributed to the existence of a melting zone, usually detected during stratiform events. However, the regions of higher reflectivity around the rain rate peaks, in particular for the April 7th event, show convective characteristics.

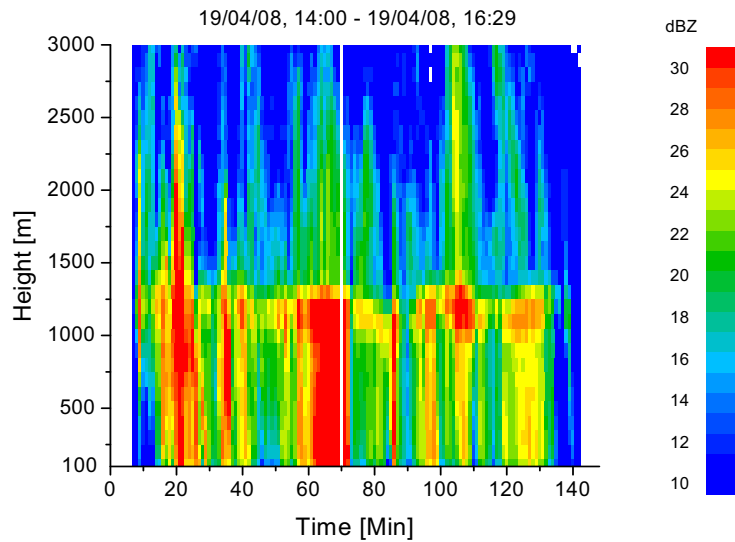


Figure 11. Time variability of reflectivity (April 19th event)

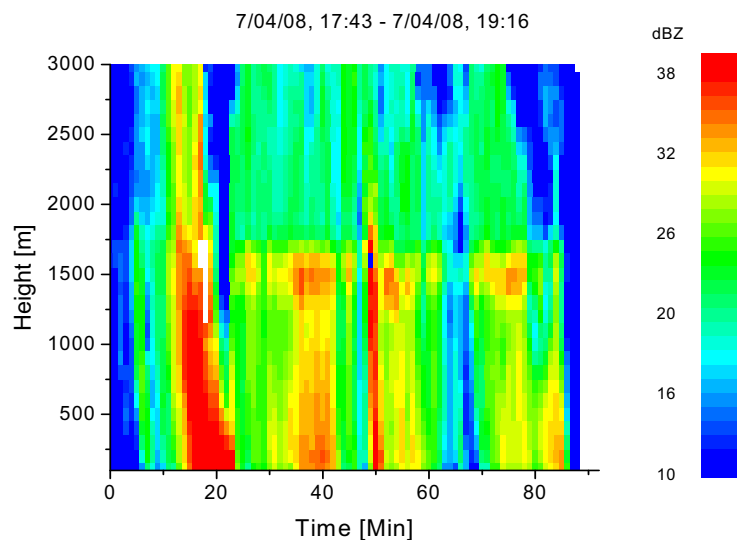


Figure 12. Time variability of reflectivity (April 7th event)

4. Conclusions

The first results derived from the radar measurements show that, in general, the various parameters of interest exhibit consistent behaviour. However, larger amounts of radar data must be analysed to understand the effects displayed in the statistics obtained from them. In this way, such results will be useful to investigate rain effects on propagation measurements performed with the satellite beacon receiver or with the radiolinks.

5. References

- [1] COST Action 280, “Propagation Impairment Mitigation for Millimetre Wave Radio Systems”, Final Report, in preparation.
- [2] Peters, G., B. Fischer, and T. Andersson, “Rain observations with a vertically looking Micro Rain Radar”, *Boreal Environment Research*, 7(4), pp. 353–362, 2002.
- [3] Atlas, D., R. Srivastava, and R. Sekhon, “Doppler radar characteristics of precipitation at vertical incidence”, *Rev. Geophys. Space Phys.*, 11, pp.1-35, 1973.
- [4] Gunn, R. and G. Kinzer, “The terminal velocity of fall for water droplets in stagnant air”, *J. Meteor.*, 6, 248-248, 1949.
- [5] Clemens, M, G. Peters, P. Winkler, “Spectral and integral modes in measured raindrop size distributions”, Proceedings of the Fourth European Conference on Radar in Meteorology and Hydrology (ERAD), pp. 183-186, Barcelona, 2006.

A Study on Formulating the Statistical Characteristics of the Rain Rate Duration

Akio SATO

Tokyo University of Technology
1404-1 Katakura, Hachioji, Tokyo 192-0982 JAPAN
Fax +81 426 37 2519, E-mail: asato@cs.teu.ac.jp

Abstract

This paper presents results of the applicability of exponential types of formula to estimate the number of rain events for a temperate climatic zone. As a generalized exponential distribution, the Weibull distribution is also examined. First, the applicability of the lognormal formula to a tropical area is reconsidered. Then the applicability of the exponential type of formula, which includes the Weibull distribution, is studied using measured data obtained in a temperate climatic zone. The results indicate that the exponential type of formula can be applied to estimate the annual number of rain events in a range including tropical to temperate climate zones. A solution is also proposed that employs a lognormal formula to avoid the inconvenience caused by a peak in the estimated values.

1. Introduction

The rain rate duration is a fundamental parameter for evaluating the dynamic effects of rain attenuation. Studies are continuing in Working Party 3J of ITU-R Study Group 3. Recent results were summarized in the chairman's report [1]. In this study, the annual number of events that exceed a time duration is expressed by a lognormal formula. A lognormal formula exhibits good accuracy in estimating the annual number of rain events that exceed a time duration for a temperate climatic zone. During the last meeting, new study results were discussed and the use of the Weibull distribution was suggested to express statistical characteristics of the duration [2]. These new results were obtained from measurements in a tropical climate zone. In a tropical climatic zone, it is reported that an exponential formula is superior to the lognormal formula. This paper presents study results of the applicability of the Weibull distribution to the estimation of the annual number of events that exceed a time duration in a temperate climate zone.

2. Existing formula and its key aspects

In order to express the annual number of events that exceed a time duration, a lognormal model has been used [3-5]. Equation (1) is proposed for estimating the number of rain rate events that exceed rain rate R and duration D , $N_R(D/R)$. This type of formula shows a good fit to the measured data by using a part of the curve of this formula.

$$N_R(D/R) = N_0 \exp\left\{-\frac{(\ln D_R - \mu)^2}{2\sigma^2}\right\} \quad (1)$$

Although this equation appears similar to a so-called lognormal distribution, it represents neither a probability distribution nor a frequency distribution because it is not a formal statistical distribution because it lacks a fraction term, i.e., $1/D_R$ just before the exponential term. It is used only to approximate changes in the measured data of the rain rate duration and good approximations are obtained in several cases.

However, this method is inconvenient when comparing several estimated results in a certain range of the duration. Figure 1 shows three curves for the estimated number of events according to the method in the chairman's report. In the case of Norway, the curve has a peak value because the curve was fit using data in a range that exceeds 120 seconds. In such a case, the applicable range of the duration, D , must be restricted to avoid a decrease in the estimated number of events in a narrow range of D . In the cases of Japan and the UK, the peaks of the estimated values are shifted in a range of less than 10 seconds because the minimum duration data that is used to fit the curve is 60 seconds. Since the annual number of events that exceed a time duration is a cumulative distribution, it is better to

express this cumulative distribution using a monotone function.

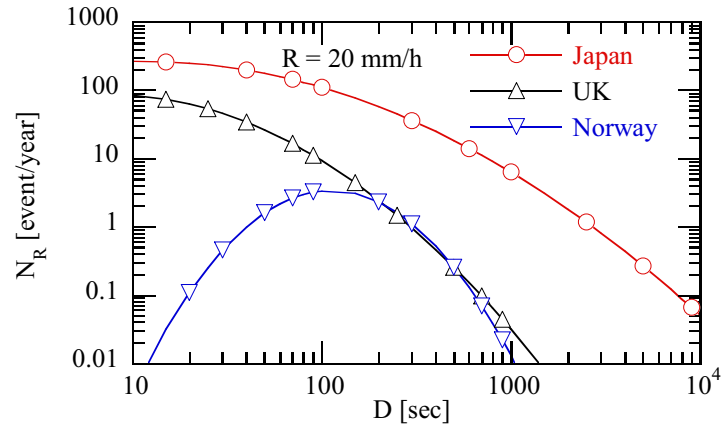


Fig. 1 Inconvenience of the existing method

3. Approximation using Weibull distribution

3.1. Reconsideration of the data in a tropical climate zone

According to [2], a cumulative distribution function of the Weibull distribution was studied. The Weibull distribution has two main parameters, α and β . The probability density function and the cumulative distribution function of the Weibull distribution are expressed as Eqs. (1) and (2), respectively. Parameter β is expressed by the standard deviation, σ , the mean value of x , and the Gamma function which contains the other parameter, α . The relationships among these parameters are expressed as Eqs. (3) to (5). The Weibull distribution is well known as a generalized exponential distribution. In the case where α equals 1, Eq. (1) becomes an exponential distribution. If α is 2, Eq. (1) becomes a Rayleigh distribution.

$$f(x) = \frac{\alpha}{\beta^\alpha} \cdot x^{\alpha-1} \cdot \exp\left\{-\left(\frac{x}{\beta}\right)^\alpha\right\} \quad (1)$$

$$F(x) = \int_x^\infty f(t)dt = \exp\left\{-\left(\frac{x}{\beta}\right)^\alpha\right\} \quad (2)$$

$$\beta = \sqrt{\frac{\sigma^2 + (\bar{x})^2}{\Gamma(1+2/\alpha)}} \quad (3)$$

$$\bar{x} = \beta \cdot \Gamma\left(1 + \frac{1}{\alpha}\right) \quad (4)$$

$$\sigma = \sqrt{\beta^2 \cdot \left[\Gamma\left(1 + \frac{2}{\alpha}\right) - \left\{ \Gamma\left(1 + \frac{1}{\alpha}\right) \right\}^2 \right]} \quad (5)$$

The results on Brazil point out graphically that the distributions of the event durations can be well approximated by using an exponential type of formula [2]. It also indicates that the statistics of the number of events can be expressed by the Weibull or exponential type of formula, but these results are not clearly illustrated. In this section, the statistics of the number of events that exceed a certain duration time is verified.

Figure 2 shows the measured results of the number of events that exceed a certain duration. These numbers are expressed by cumulative distributions normalized by the total number of events. These data are mean values derived from three sets of the data measured at Belem, Manaus, and Ponta das Lages. The averaging procedure for the

measured data obtained at these three cities is also used in the study of the event duration. There are five sets of data corresponding to five kinds of rain rates. The symbols in Fig. 2 represent the measured values and the solid lines represent the regression curves using an exponential function. In the cases of heavy rain rates such as 75 mm/h and 100 mm/h, the exponential formula matches the measured data well. In the cases of a medium rain rate range such as 50 mm/h to 10 mm/h, some differences are observed outside the duration range of 5 minutes to 20 minutes. However, it is obvious that the tendency of the relationship between the number of events and the duration time can be expressed by an exponential formula. In [2], the exponential model is formulated using Eq. (6). This model refers to the values at 1 minute.

$$S(D) = \exp\{k_0(R) \cdot (D - 1)\} \quad (6)$$

The k_0 coefficient expresses the inclination of the curve according to duration D as a function of rain rate R . Figure 3 shows the $k_0(R)$ graph. The linear fit is found to agree well and the expression obtained is as follows.

$$k_0(R) = -0.0037 \cdot R - 0.0468 \quad (7)$$

The results indicate that the statistics of the number of rain events that exceed a certain duration time can be approximated by using an exponential type of formula as well as the distributions of the event durations.

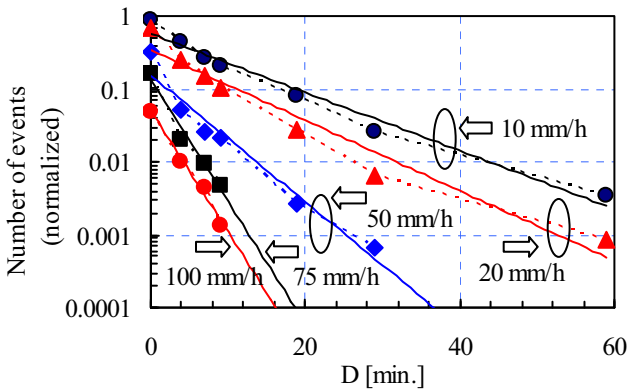


Fig. 2 Probability distribution function of number of events

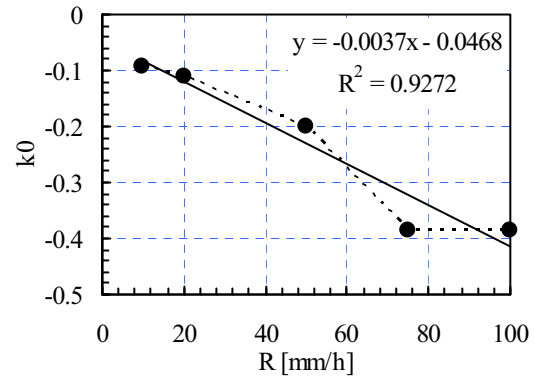


Fig. 3 Linear fit of k_0

The exponential distribution is one of the Weibull distributions in which parameter α equals 1. In other words, an exponential distribution has only one degree of freedom because one of two parameters of the Weibull distribution is set to one. If we can use two parameters, α and β , the accuracy of the approximation can be improved.

Figure 4 shows trial results of curve fitting using three different formulas. The red straight lines are approximated results using an exponential formula. The black curves represent Weibull distributions. The blue curves are obtained using an approximation of a lognormal model that is formulated using Eq. (1). Since the Weibull and lognormal models have two degrees of freedom, the approximate accuracy of these models is improved. The residuals of these approximations are tabulated in Table I. The table shows that the Weibull model yields the best match to the measured data in the middle range of the rain rate.

It is confirmed that the number of events that exceed a certain duration time measured in a tropical region in Brazil can be approximated by an exponential model. The applicability of the Weibull model is studied and its improvement is also clarified. An exponential model can simply and easily formulate an approximation because of its single parameter, but the effectiveness of the two degrees of freedom of both the Weibull and the lognormal models suggests further improvement.

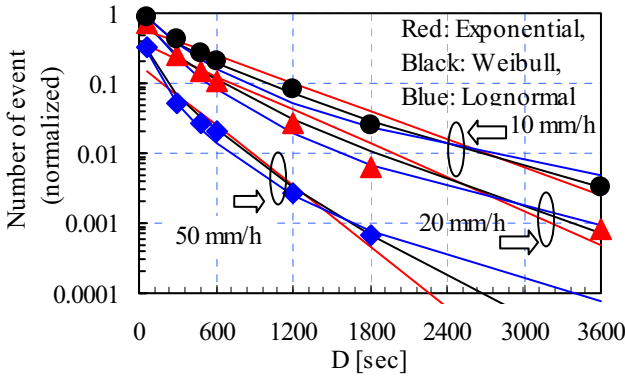


Fig. 4 Comparison of curve fitting models

Table 1 Residuals of three types of approximation

		Residuals		
		Exponential	Weibull	Lognormal
R [mm/h]	10	0.895	0.996	0.993
	20	0.773	0.999	0.996
	50	0.726	0.995	0.984
	75	0.971	0.997	0.983
	100	0.999	0.995	0.982

3.2. Applicability of the Weibull distribution to a temperate climate zone

The existing formula for estimating the annual number of events that exceed a time duration is to employ a lognormal model as in Eq. (1). Three parameters, N_0 , μ , and σ depend on the climatic zone and they are deeply related to rain rate R [mm/h]. The parameters are tabulated for several countries such as Norway, the U.K., and Japan in [1]. All countries in the table belong to temperate climatic zones. In this section, the applicability of the Weibull model to a situation in which the lognormal model has a good agreement is studied.

First, the applicability of the Weibull distribution as a probability distribution function is considered. It is treated as a formal statistical distribution and not as an approximation model. Therefore, statistical parameters such as the mean value and standard deviation are required. Reference [5] proposes the number of events per year, N_0 , the mean duration, $x(R)$, and the standard deviation, $\sigma(R)$, as measured parameters in the Tokyo area. They are expressed as follows.

$$N_0 = 2.32 \cdot 10^4 \cdot R^{-1.49} \quad (8)$$

$$\overline{x(R)} = 535.1 \cdot R^{-0.2651} \quad (9)$$

$$\sigma(R) = 1768.1 \cdot R^{-0.5637} \quad (10)$$

On the basis of these equations, cumulative distributions of the Weibull distribution can be calculated. In the case of the Weibull distribution, Eq. (9) corresponds to Eq. (4) and Eq. (10) corresponds to Eq. (5). Then we can have two values for Eqs. (4) and (5). However, it is difficult to derive explicitly parameters α and β from these values because α is contained in the Gamma function. Therefore, β is calculated using Eq. (3) by assuming that α is in a specified range. After obtaining several sets of α and β , the mean and the standard deviation are calculated based on Eqs. (4) and (5) for those sets. By comparing the calculated sets of the mean and the standard deviation and the original mean and standard deviation obtained using Eqs. (9) and (10), a suitable set of α and β can be selected. Once the set of α and β is obtained, Eq. (2) is used to calculate the cumulative distribution. Finally, multiplying the N_0 from Eq. (8) with the results of Eq. (2) yields the annual number of events N_R .

Figure 5 illustrates two types of curves for N_R obtained from one probability distribution and one approximation. The parameter is the rain rate and is 20 mm/h as a medium intensity rain and 90 mm/h as a heavy rain. The approximation is formulated by Eq. (1), which is a good fit to the measured data. In this figure, curves for “Tokyo 20” and “Tokyo 90” are the calculated results from Eq. (1) and they are targets for the estimation of N_R . Curves “Weibull 20” and “Weibull 90” are the calculated results of the Weibull distribution expressed by Eq. (3). The calculation method for the Weibull distribution is mentioned above. There are large differences between the lognormal approximation and the Weibull distribution. This result indicates that the statistical parameters derived from Eqs. (9) and (10) do not work well to estimate the cumulative distribution of the number of events by substituting directly into the Weibull distribution expressed as Eq. (3). In order to overcome this problem, the estimated results calculated from the Weibull distribution are contrived to be attuned to the calculated results using the lognormal model.

Figure 6 shows a comparison of the results between the lognormal approximation and the modified Weibull distribution. The solid and dashed lines represent the calculated results by the lognormal formula and the symbols are those of the modified Weibull distribution. In Eq. (3), i.e., the cumulative distribution of the Weibull distribution, the x corresponds to duration D , which ranges from zero to infinity. In this case, zero as the minimum of the integration range of D is replaced by 60, which is the minimum time resolution of the duration measurement. This replacement is reflected in a calculation by using $x-60$ instead of x in Eq. (3). After this replacement, the curve fitting was accomplished by searching for a suitable set of α and β . Figure 6 shows that the calculated results and target curves agree well.

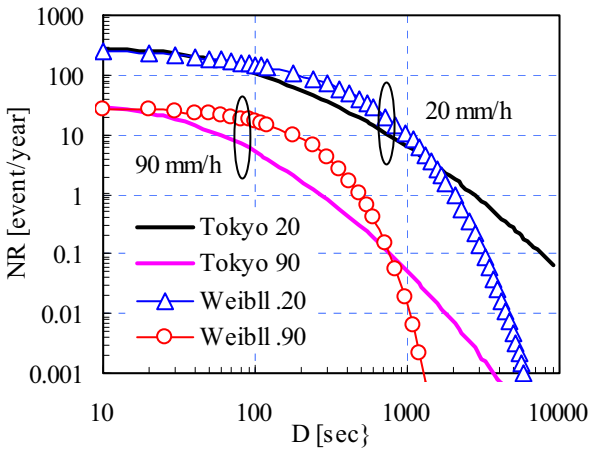


Fig. 5 Comparison of the log-normal model to the Weibull distribution

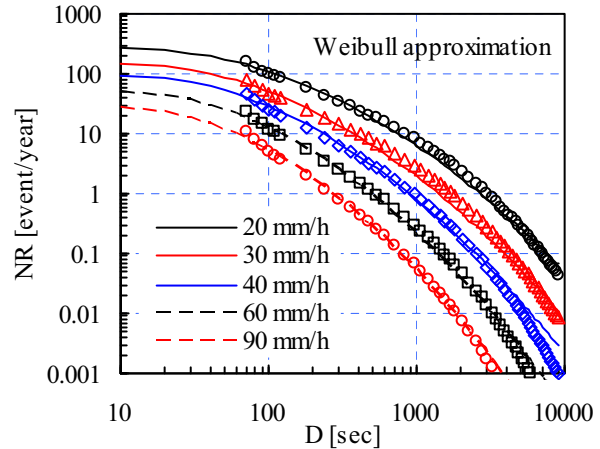


Fig. 6 Comparison of the log-normal model to modified Weibull distribution

From the set of α and β , both the mean values and standard deviations can be calculated. Figure 7 shows the rain rate dependencies of the mean values and standard deviations. Curves “Mean-Weibull” and “Std.-Weibull” are derived from sets of α and β in the modified Weibull distribution. Curves “Mean” and “Std.” are calculated using Eqs. (9) and (10). There are differences between the mean values and standard deviations in the rain rate range around 20 mm/h. According to the increase in the rain rate, the differences become small. In the range of heavy rain, 80 mm/h, all values degenerate to almost the same value. At this point, the mean and the standard deviation are the same. This is a dominant characteristic of the exponential distribution. Therefore, the statistical distribution of the number of events can be estimated using the exponential model in the case of strong rain. However, below the medium rain rate, the differences between the mean and the standard deviation become remarkable. Accordingly, the applicability of the exponential model with a single parameter is reduced below that for the medium rain rate and the effect of the two parameters in the Weibull distribution is notable.

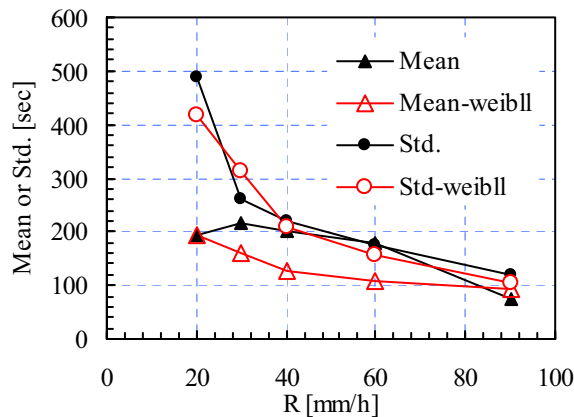


Fig. 7 Rain rate dependencies of mean values and standard deviations

So far, the evaluation criteria for the estimation using the Weibull distribution are calculated results obtained from an existing lognormal formula. However, actual data have differences such as an annual variation. Figure 8 is the cumulative distribution of the number of events for the duration. The plots represent the measured data for three years and the lines represent the estimated results. The dashed lines are estimated using an existing method that employs a lognormal formula and the solid lines are estimated using a cumulative distribution of the Weibull distribution. Although there are some differences between the estimated results of the lognormal formula and those from the Weibull distribution, the Weibull distribution expresses the measured results even in a temperate climate zone by optimizing the parameters.

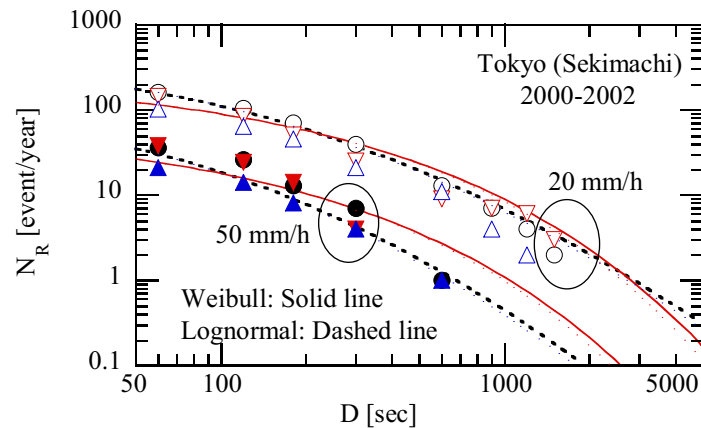


Fig. 8 Comparison of measured and estimated results

4. Conclusion

The annual number of events that exceed a time duration is expressed by a lognormal formula. In this study, the applicability of the Weibull distribution to estimate the annual number of events that exceed a time duration is evaluated. As a generalized exponential distribution, the Weibull distribution has an effectiveness of two degrees of freedom. Based on a report that indicates the applicability of the exponential type of formula in a tropical climatic zone, measured data were used to check the applicability for the temperate climatic zone. We found that the exponential formula can be used in heavy rain situations such as above approximately 60 mm/h in a temperate climatic zone. In cases of medium or light rain, the Weibull distribution can be applied by optimizing the parameters. We also found that by using exponential types of formula the inconvenience of a decrease in the estimated number of events in a narrow range of the duration time can be avoided.

5. References

- [1] WP3J Chairman, "Working document towards a draft new Recommendation on rain dynamics," ITU-R Document 3J/193 Annex 8, WP3J Chairman's Report, 21 June 2007.
- [2] Federative Republic of Brazil, "Dynamic Aspects of Rainfall in Equatorial Brazil", ITU-R Document 3J/137, 19 Sept., 2006.
- [3] Paulson, K., and C. Gibbins, "Rain model for the prediction of fade duration at millimeter wavelengths," IEE Microwaves Antennas and Propagation 147, 6 (2000).
- [4] Aasen, W., "Analysis of three decades of rainfall rate data from dry inland and dry and wet coastal area in Norway," 11th ICAP 480 IEE 2001.
- [5] Ishida, M., O. Sasaki, T. Taga, and S. Ichitubo, "A study on rain fade duration distribution characteristics on millimeter wave radio link," Proc. of Climdiff-2003, Clim52 (2003).

Statistics of Rainfall Rate Dynamics

Rubén Hernández, Ana Benarroch, Pedro García, José M. Riera
Universidad Politécnica de Madrid, Spain
ana@grc.ssr.upm.es

Abstract

A study on rainfall rate dynamics is being carried out using a large data base of rain gauge data recorded in Spanish meteorological stations. The cumulative distributions of rain rate have been used to investigate the seasonal and hourly variability of rainfall rate. The experimental probability of occurrence and the fraction of time of exceedances for given rain rate thresholds have been compared with existing models. Contour line maps have been derived from seasonal and hourly statistics, and also from the distributions of the duration of exceedances.

1. Introduction

Fade compensation may be required by radio communication systems operating in the microwave and millimetre-wave bands. Propagation Impairment Mitigation Techniques are being developed to compensate for link degradations caused by various atmospheric factors at such frequencies, being rain usually the most significant of these factors. Knowledge of the dynamic behaviour of rain attenuation is required to design and operate systems incorporating rain fade mitigation techniques, which must adapt to attenuation changes. Therefore, propagation studies are necessary to gain insight into the behaviour of time variability of rain fades. However, rain attenuation data are available only from a reduced number of sites located in specific regions, whereas rainfall data can be obtained from a large number of meteorological stations worldwide. Thus, rainfall rate dynamics can be analyzed to obtain statistics and other tools useful to assess the expected behaviour of rain fade dynamics.

The Group of Radiocommunications has performed various rainfall rate studies using data from about 50 sites located in Spanish regions of continental, Mediterranean and maritime climates. A large data base is available with over 10 years of rain data per site that were recorded employing an integration time of 5 minutes. Besides, a tipping-bucket rain gauge installed in the University premises has been in operation since 1999. These data are usually processed with an integration time of 1 minute.

All the above data are being used to carry out a study on rainfall rate dynamics, as an extension of an earlier study performed in the framework of COST Action 255 [1]. Statistical distributions of the duration of exceedances above a given rain rate threshold are being compared with existing rain dynamics models. The seasonal and the hourly variability of various rainfall rate statistics are also being investigated. The previous statistics are being incorporated into maps of contour lines that may be used to characterize the time variability of rain fades in the geographical regions of interest. Results of this study are discussed below.

2. Statistical analysis

Two aspects of time variability of rainfall rates have been considered for this analysis. For the first one, the cumulative distributions of rain rate been used to look into the seasonal and diurnal variability. The second one is based both on the probability of occurrence of exceedances of duration d longer than D , given that the rain rate r is greater than R , calculated according to:

$$P(d > D | r > R) = \frac{N(d > D | r > R)}{N(r > R)} \quad (1)$$

and on the total fraction of exceedance time due to exceedances of duration d longer than D , given that the rain rate r is greater than R , calculated as follows:

$$F(d > D | r > R) = \frac{T(d > D | r > R)}{T(r > R)} \quad (2)$$

3. Experimental results

The probability of occurrence and the fraction of time of exceedances are displayed in figure 1 for two years of data (2002 and 2003) measured in Madrid, at the University, using the tipping-bucket rain gauge with an integration time of 1 minute. The number of exceedances allows calculating these probabilities up to a rain rate of 40 mm/h. The differences between the graphs for each year give an indication of the year to year variability.

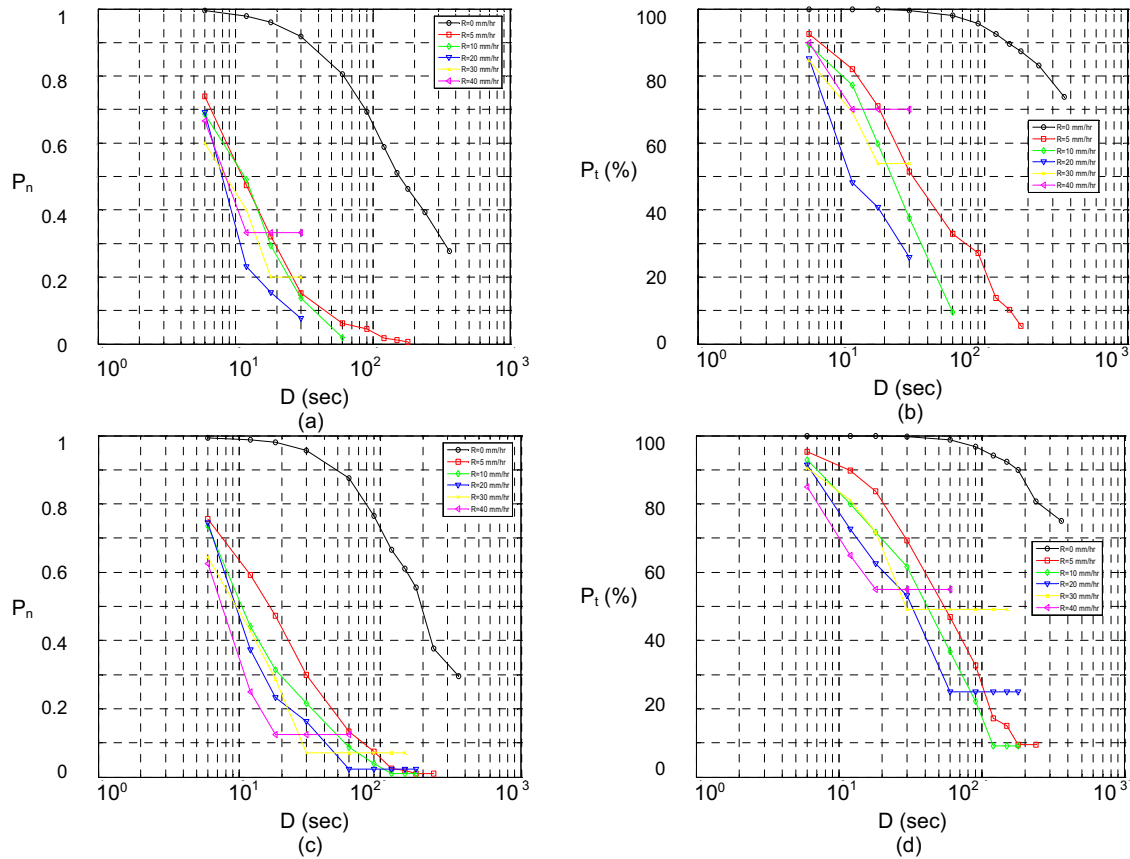


Figure 1. Probability of occurrence (a, c) and fraction of time of exceedances (b, d) for 0, 5, 10, 20, 30 and 40 mm/h. Madrid data, 2002 (a, b) and 2003 (c, d)

The data described in the previous section, recorded with an integration time of 5 minutes has been used for the comparisons with various models shown in figures 2-4. To take into account the existing climatic variations, the sites selected are Santiago de Compostela, with maritime climate, Madrid, with Continental Climate and Valencia, on the Mediterranean seaboard. The probability of occurrence has been compared with the predictions suggested by the following models [2-6]: COST 205 (2), Gibbins, Goldhirsch, Timothy and Vilar. Only two of these models, COST 205 (2) and Vilar, provide predictions for the fraction of time of exceedances. The models by Gibbins and COST 205 (2) appear to give the closest agreement for the probability of occurrence.

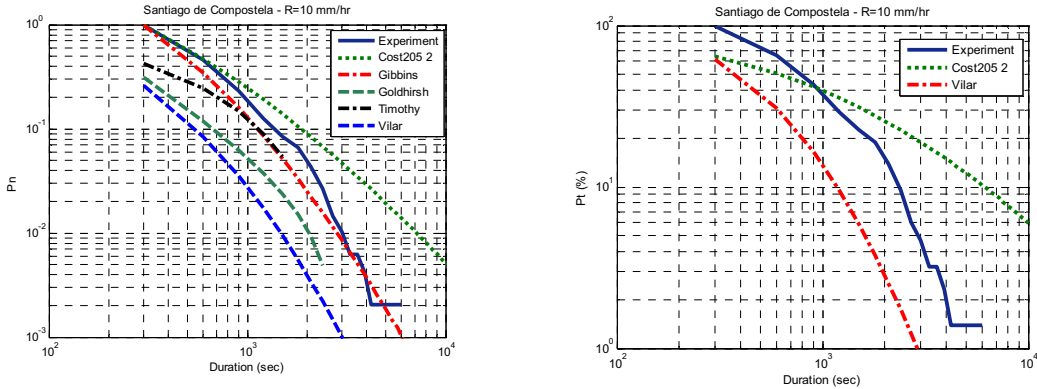


Figure 2. Comparison of the probability of occurrence and fraction of time of exceedances for 10 mm/h with models. Site: Santiago de Compostela.

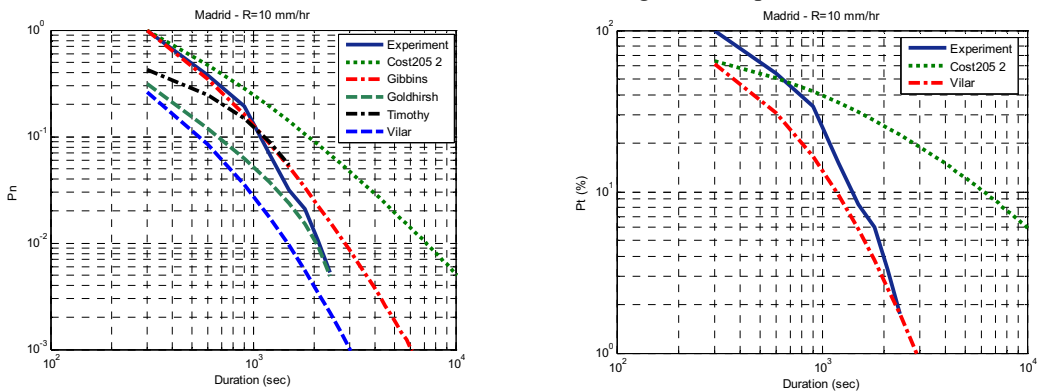


Figure 3. Comparison of the probability of occurrence and fraction of time of exceedances for 10 mm/h with models. Site: Madrid

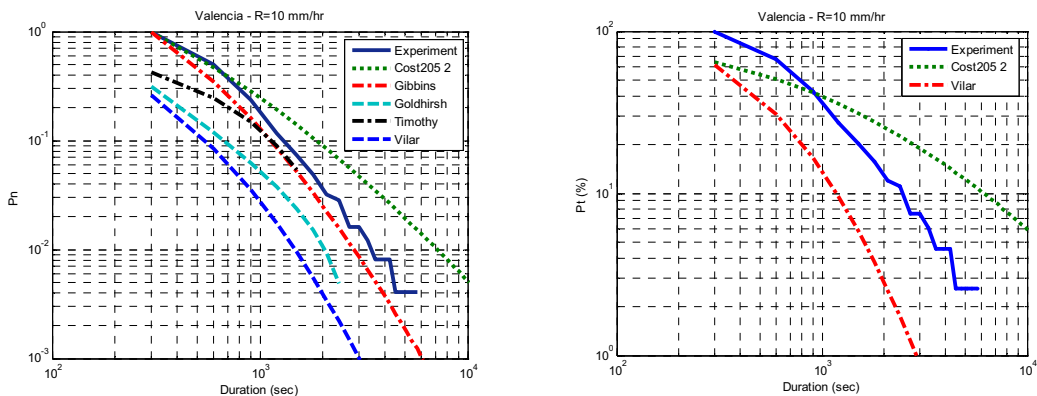


Figure 4. Comparison of the probability of occurrence and fraction of time of exceedances for 10 mm/h with models. Site: Valencia.

The contour maps presented in figures 5-8 have also been derived using the data recorded with an integration time of 5 minutes. The rain rate values in the maps in figure 5(a-c) correspond to the time percentages 1%, 0.1% and 0.01% of the cumulative distribution calculated for the average year for each site. These maps can be compared with the maps in figures 5 (d-f), which show the seasonal variation between winter and summer. A representative month has been chosen for each season: January and July. The maps have been plotted for the 0.1 and 0.01 %. The hourly variations are shown in the maps in figure 6. The seasonal variability is reflected in the different geographical distribution of rain rates, when comparing between winter and summer, and also with respect to the average year. As expected, higher rain rates are observed in July than in January, and lower rain rates in January than in the average year.

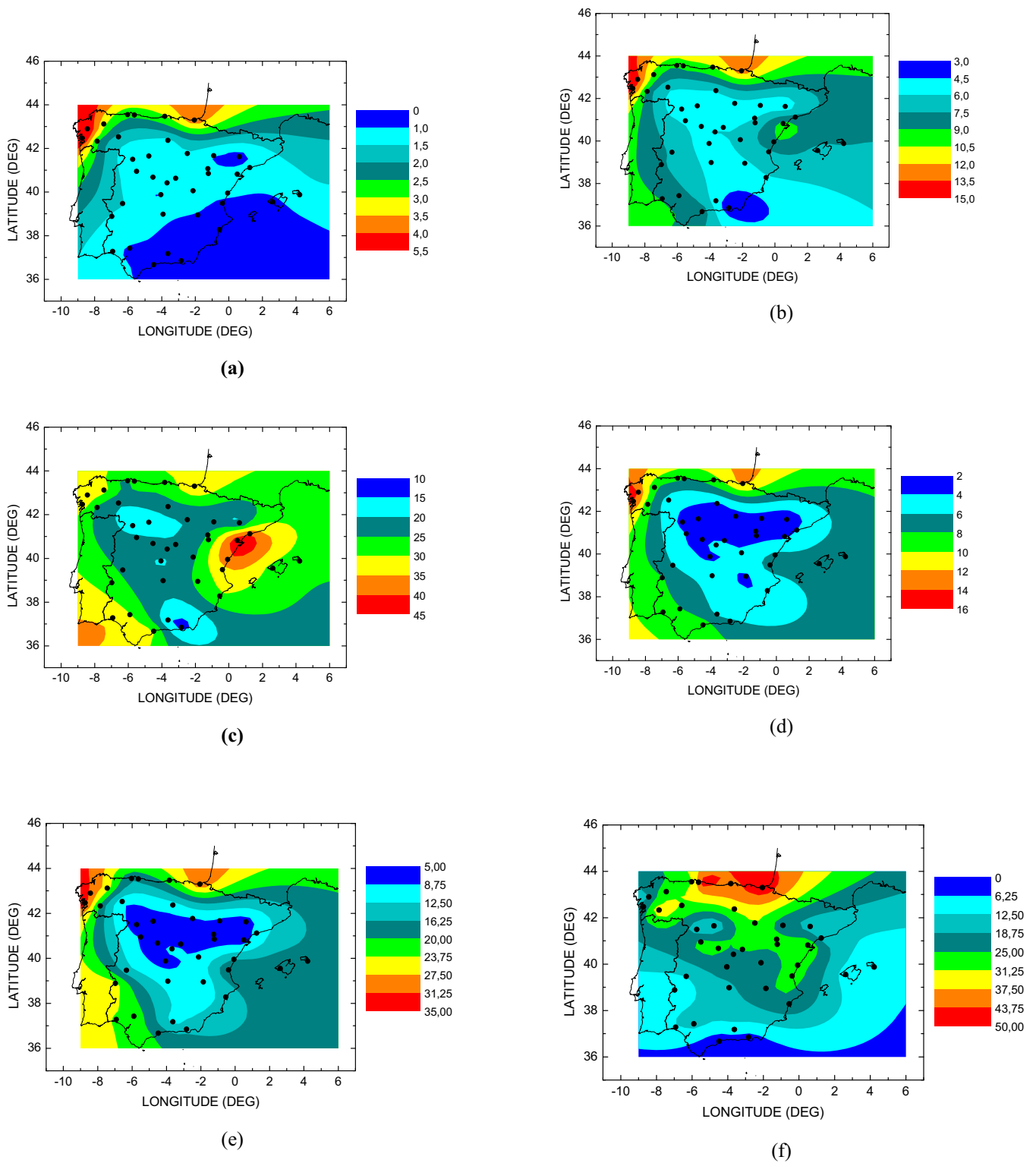


Figure 5. Contour maps of rainfall rate. (a) Exceeded 1 % of the average year, (b) exceeded 0.1 % of the average year, (c) exceeded 0.01 % of the average year, (d) exceeded 0.1 % of the average month of January, (e) exceeded 0.01 % of the average month of January, (f) exceeded 0.01 % of the average month of July.

The rainfall rate also varies significantly depending on the fraction of the day, showing an increase during the afternoon and evening hours, as is noted in figure 6. The geographical distribution is also affected by this variation.

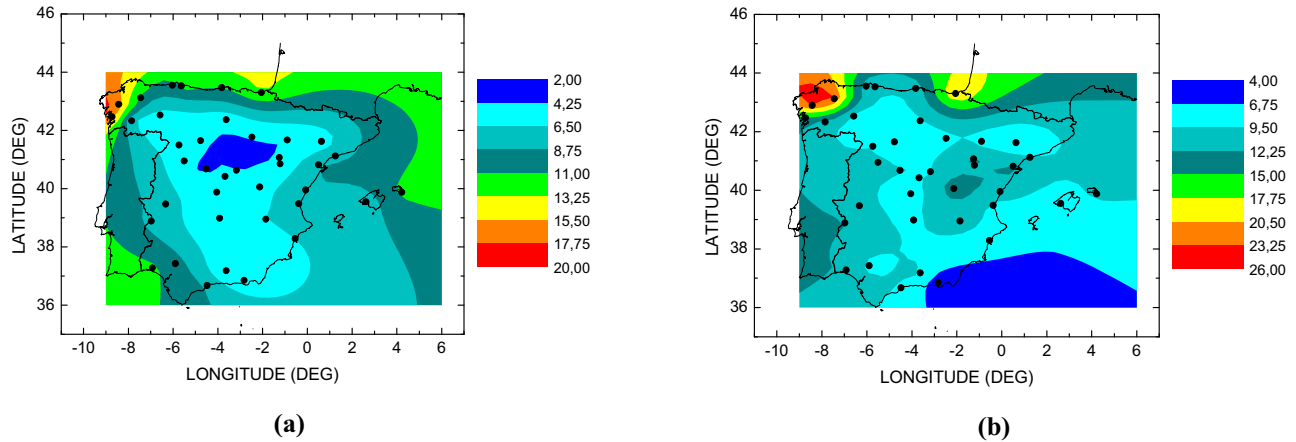


Figure 6. Contour maps of rainfall rate. (a) Exceeded 0.01 % of the average year during the 8-15 h interval, (c) exceeded 0.01 % of the average year during the 16-23 h interval.

The probability of occurrence and the fraction of time of exceedances have also been incorporated into maps of contour lines, such as the ones shown in figure 7, for given rain rates and durations of exceedances.

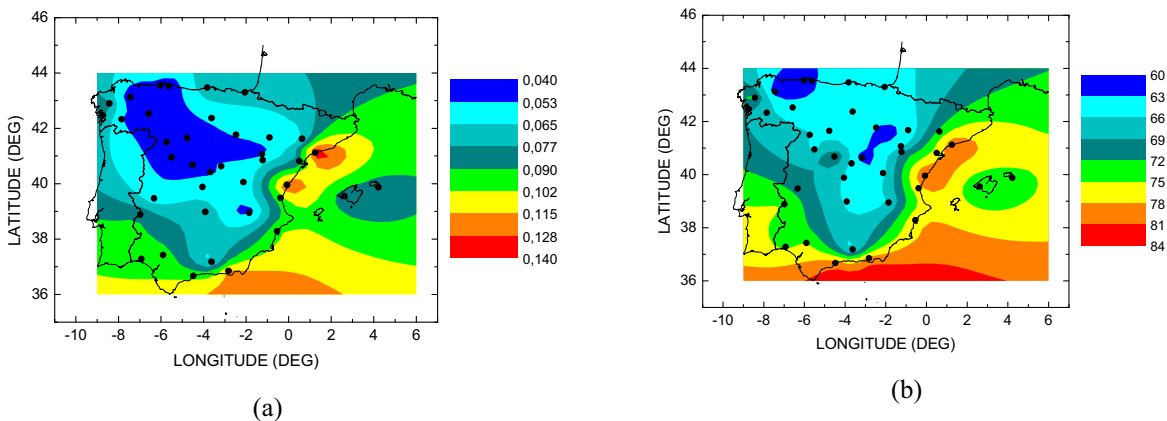


Figure 7. Contour maps of the probability of occurrence and the fraction of time of exceedances. (a) Probability of occurrence for a rain rate threshold of 1 mm/h and duration longer than 60 minutes. (b) Fraction of time of exceedances for a rain rate threshold of 5 mm/h and duration longer than 10 minutes.

4. Conclusions

The behaviour of rainfall rate variability must be further investigated and new and more adequate models need to be developed. The maps of contour lines can be useful tools, providing the means to relate time variability to geographic and climatic effects.

5. References

- [1] Arbesser-Rastburg B., "COST Action 255 Final Report: Radiowave Propagation Modelling for SatCom Services at Ku-Band and Above", ESA Publications Division, 2002
- [2] COST 205, "Influence of the atmosphere on radiopropagation on satellite-earth paths at frequencies above 10 GHz", COST Project 205, Report EUR 9923 EN, ISBN 92-825-5412-0, 1985.
- [3] Gibbins, C.J and K.S. Paulson, "Durations of rain events and rain attenuations at millimetric wavelengths. Millenium Conference on Antennas and Propagation (AP 2000), Davos, Switzerland, SP444, paper 1115, April 2000.
- [4] Goldhirsch, J., "Rain rate duration statistics over a five year-period: a tool for assessing slant path fade durations", *IEEE Trans. Antennas Propagat.*, 43(5), pp. 435-439, 1995.
- [5] Timothy, K I., et al., "Dynamical properties of rainfall for performance assessment of earth/space communication links at Ku and Ka bands", *Int. J. Sat. Com.*, 16, pp. 53-57, 1998.
- [6] Vilar, E., et al., "Analysis of joint rainfall rate and duration statistics: Microwave design systems implications", *IEEE Trans. Commun.* COM-36(6), pp. 650-661, 1988.

Generating Year-Equivalent Databases of Fractally Synthesised Rain Rate Fields

S. A. Callaghan
STFC – Rutherford Appleton Laboratory
Radio Communications Research Unit, Chilton
Didcot, OX11 0QX, United Kingdom
Email: s.a.callaghan@rl.ac.uk
Telephone: +44 1235 445770
Fax: +44 1235 6140

Abstract

The radio spectrum is becoming increasingly congested, due to the demand for high-bandwidth applications such as mobile internet-on-demand. This has increased the pressure to improve the efficiency of existing spectrum allocations and to open up new spectrum to commercial exploitation. Previously, most systems operated at frequencies where the attenuating effects of rain, clouds and atmospheric gases were easily compensated for by use of a fixed fade margin. As the operational frequency of a system increases, it is no longer cost-effective or efficient to do this, so system designers turn to fade mitigation techniques to achieve their required availabilities. Several techniques rely on the spatio-temporal variability of rain fields for their effective operation and require accurate knowledge about the space-time structure of these fields, on scales of hundreds of metres and seconds. Unfortunately, measured data at these scales is limited; hence the need for accurate simulated rain fields.

1. Introduction

1.1. Rain field modelling in radio communications system design

The radio spectrum is a finite resource which is becoming increasingly congested due to the promotion of high bandwidth services such as mobile internet. This has prompted the UK's Ofcom to fund a number of studies investigating methods of improving spectral efficiency and opening up frequencies above 10 GHz to commercial exploitation. Currently, these systems allocate a fixed fade margin to compensate for the attenuating effects of rain, clouds and atmospheric gases. However, as the operational frequency of radio systems increases, the corresponding increase in fade margin is no longer economical, practical, or spectrally efficient.

For frequencies above 10 GHz, rain is the dominant attenuator. The spatio-temporal inhomogeneity of rain fields can be taken advantage of in order to produce methods for mitigating the effects of rain attenuation. Correctly configuring systems that can dynamically compensate for rain fading requires a detailed knowledge of spatial and temporal rain field variation, often on very small temporal and spatial scales. The databases of meteorological radar measurements that are available for such analysis are sometimes not suitable, and for many locations in the world, are not available at all.

The lack of measured data at suitable resolution has led to researchers to investigate methods for simulating rain fields in time and space. Some published methods, including the one discussed in this paper, use fractal techniques, as the fractal nature of rain has been extensively documented in past years. These methods can be used to analyse and synthesise the spatial and temporal variation of rain fields, producing visually and statistically realistic synthetic rain fields. These simulated fields may then be customised for different climactic regions, converted to simulated attenuation time series, and applied to communications engineering scenarios where measured data is not available.

This paper discusses a monofractal, additive (in the logarithmic domain) discrete cascade model for simulating rain fields in two spatial dimensions. Further modification allows extension into a third spatial dimension, or a temporal dimension. The model produces events-on-demand, customised to an input rain rate parameter derived from measured data or ITU-R Recommendations, and desired rain event type (stratiform or convective).

In order to test the long term statistics of a proposed radio system, and accurately compare them with other results and models, simulated rain field datasets are required which will reproduce the annual rain statistics for the average year, preserving the correlation between spatially distributed points in the field. This is of particular interest to those radio systems designers interested in determining the effects of implementing spatial diversity as a rain fade mitigation technique. The model as presented is capable of generating such statistics, provided that enough synthetic rain fields are generated. Unfortunately, generating an annual dataset of synthetic fields at suitable time and space resolutions is computationally intensive and requires significant amounts of memory for storage. Hence there is the requirement for a cut-down set of events which are capable of reproducing annual statistics for a given range of percentage exceedences. This paper outlines the method for producing such a set.

1.2. The fractal nature of rain fields

Previous studies developed by communications engineers have developed rain cell models from radar measurements, but these are statistical in nature and do not enable the construction of typical two dimensional rain-rate fields [1]. Other models proposed for use by system engineers only deal with the spatial variation of the rain-rate within a rain cell [2], or do not take into account the full range of rain rates that are significant for frequencies above 10 GHz [3]. These models assume regular shapes to the rain cells, such as ellipses, or Gaussian functions of position centred on the area of maximum rain rate.

Meteorologists and hydrologists have also studied the space time variability of rain fields, but on coarser scales. It has taken time for ideas from these studies to cross over to radio scientists dealing with rain. Several of these [4,5,6,7,8], suggest that fractal methods may be of use in characterising the shapes of rain cells.

A fractal is an object that is self-similar on many different scales, and can be exactly or statistically self-similar. (Real world examples are trees, broccoli and mountain ranges). In general, the fractal dimension D characterises any self-similar system; if the linear dimension of a fractal observable is changed by a scale factor f , then, for any value of f the values of the fractal observable will be changed by the factor f^D . For surfaces, the value of the surface dimension, D_s , lies in the range $2 \leq D_s \leq 3$. A smooth surface has $D_s=2$. Similarly, for a contour line, the dimension of the line D_L satisfies $1 \leq D_L \leq 2$, and $D_L=1$ for smooth lines. The more twisted and “wiggly” the contour line is, the higher the value of D_L . If pathological cases are disregarded [9] a planar section of a fractal surface has

$$D_L = D_s - 1 \quad (1)$$

The fractal nature of rain has been studied for many years, and its characterisation as a fractal and multifractal field is well documented [10,11,12]. The exact fractal form of the rain field is still under debate, due to differing methods of calculating the fractal dimension and/or characteristic multifractal function. The majority of recent published works use multifractal methods to deal with the intermittency and anisotropy of the rain field (Olsson and Niemczynowicz, 1996, Deidda, 1999, Lovejoy and Schertzer, 1990), but are also predominantly concerned with topics of importance to meteorology and hydrology, such as extreme events.

Rain field modelling for use in radio communication system design has a different emphasis that that used in climate modelling or weather forecasting. The following requirements for a rain model for use by radio system engineers are the ideal [13].

A physically-based rain model should:

- have a time resolution of 1 s
- have a spatial resolution of about 100 m
- be able to take inputs from a weather model
- be suitable for use in spectrum management and simulation software
- be capable of generating databases which replicate average annual statistics

The rain field models developed by meteorologists and hydrologists presented in the literature tend to have spatial resolutions on the order of kilometres, and time resolution of the order of hours/days. Hence there is a need to develop a fine-scale rain field model capable of the resolutions required by system engineers.

The procedure used here to simulate rain fields produces simulated fields which are mono-fractal fields. This is justified by multifractal analysis of meteorological radar data recorded in the south of England [8,14], which

shows that log rain rate fields may be accurately characterised as monofractal fields, as their moment scaling functions are straight lines. The transformation of the variables from rain rate to log rain rate allows us to linearise the problem, showing that rain rate fields can be characterised as “meta-Gaussian”. This is in agreement with other work published recently [15].

This transformation from rain rate to log rain rate simplifies the simulation process, but is valid only for certain spatial resolutions, defined in further detail below. It also necessitates the introduction of a threshold to give areas of rain and non-rain.

2. Example of model to generate synthetic rain intensity fields

The rain field simulator presented here is based on the Voss successive random additions algorithm for generating fractional Brownian motion in multiple dimensions [9]. This method of simulating rain fields uses a monofractal, additive (in the logarithmic domain) discrete cascade model for simulating rain fields in two spatial dimensions. The model produces events-on-demand, customised to an input rain rate parameter and desired rain event type (stratiform or convective). Further details of the model can be found in [8].

Each realization of the simulated rain fields is independent of each other, hence simulating multiple arrays and taking the same point from multiple arrays will not produce realistic simulated time series. However, it is possible to produce a large number of simulated arrays and taking them as a group, scale them to $R_{0.01}$. (This is the rain rate exceeded for 0.01% of an average year, which can be calculated from measurements or from ITU-R Rec. P837-5 [16]). These simulated databases are then capable of reproducing long-term statistics.

As convective and stratiform arrays are produced separately, it is necessary to determine what proportion of rain events in the simulated database should be stratiform and what convective. For a simulated “annual” database, these proportions can be found using the variables M_c and M_s as given in Recommendation ITU-R P.837-5 [16], where:

$$\begin{aligned} M_c &= \text{annual average convective rainfall amount (mm)} \\ M_s &= \text{annual average stratiform rainfall amount (mm)} \end{aligned}$$

2.1. Producing a simulated database which will reproduce annual statistics for the percentage range from 0.05 to 0.001%

If we assume that each simulated field is equivalent to a meteorological radar snapshot at any given minute, then we will require 43 200 arrays to create a simulated month (30 days) and 525 600 arrays for a year. The memory requirements to store the simulated arrays is such that a year’s worth of arrays would take up ~6 150 GB of computer memory and would take ~ 40 days to create (on a standard desktop PC).

It is known that it only rains for a small percentage of a year, however, in the case of the simulated arrays, the rain doesn’t cover the entire array area. (In the final step of the simulation process, a threshold is applied so that all non-zero rain rates which are close to zero mm/hr are set to zero mm/hr to give areas in the arrays with no rain.)

Hence there is a desire to create a subset of events which will accurately reproduce the tail of the annual distribution as given by Recommendation ITU-R P.837-5.

To have a database covering 0.1% of a year requires 526 arrays. We’re therefore looking to fit this smaller simulated dataset to Recommendation ITU-R P.837-5 values in the range 0.1% to 0.001%. As the tail of the distribution is dominated by convective events, only simulated convective rain fields should be used for this scaling.

To do this scaling, we need two new parameters, a and b.

$$R_{sim} = 10^{\frac{V+b}{a}} \quad (2)$$

where:

$$\begin{aligned} R_{sim} &\text{ is the simulated rain array (mm/hr)} \\ V &\text{ is the data array produced by the simulator.} \end{aligned}$$

The parameter a is given by:

$$a = \frac{std(R_{GA} \geq m_{GA})}{std(\log_{10}(I_{R \leq 0.1}))} \quad (3)$$

where:

$$\begin{aligned} R_{GA} &\text{ is the simulated rain gauge data extracted from V (equivalent to log values)} \\ I_{R \leq 0.1} &\text{ is the rainrate exceeded for percentages of time less than 0.1% (from Rec. ITU-R P.837-4)} \end{aligned}$$

m_{GA} is the mean of R_{GA}
 std is the standard deviation.

The parameter b is given by:

$$b = \left| \frac{m_{GA}}{a} \right| + \left| \log_{10}(I_{R=0.1}) \right| \quad (4)$$

R_{GA} is normally distributed and has a mean of 0 hence:

$$b = \left| \log_{10}(I_{R=0.1}) \right| \quad (5)$$

where $I_{R=0.1}$ is the rain rate exceeded for 0.1% of the time (from Rec. ITU-R P.837-4).

Every point in the simulated rain field has the same value of a and b applied to it. Table 1 gives example a and b values for different geographic locations and climate types.

Table 1: Sample a and b values for different geographic locations

Location	Latitude (- for deg. S)	Longitude (- for deg. W)	Mc (from Rec. 837-5)	Ms (from Rec. 837-5)	a	b
Chilbolton (England)	51.1333	-1.4333	158.23	581.29	3.2266	0.9106
Cairo (Egypt)	30.05	31.25	12.7983	45.8753	1.6580	0.1467
Prague (Czech Republic)	50.1	14.4333	149.2240	491.2206	2.3112	0.9372
Buenos Aires (Argentina)	-34.6667	-58.5	164.8082	868.3786	2.5511	1.0789
Jakarta (Indonesia)	-6.1333	106.75	1580.3	820.9559	4.4872	1.6714
Delhi (India)	28.6667	77.2333	322.6315	323.6087	2.5390	1.1243

3. Model validation

3.1. Cumulative distribution statistics derived from the simulated data

In order to validate the simulator, we assume that a spatio-temporal equivalence exists, which allows us to compare cumulative distributions of rain rate exceedence curves as produced by the simulator with the curve from the Recommendation ITU-R P.837-5 (figure 1). The simulated “annual” dataset is made by combinations of stratiform and convective simulated events according to the values M_c and M_s given in Recommendation ITU-R P.837-5, where M_c and M_s are the annual accumulations of rain resulting from stratiform and convective events respectively.

When scaling to the tail of the Rec. P837 distribution, it is assumed that the events that dominate in this tail are convective. This ties in with our understanding of the physical behaviour of rain events, i.e. that convective events are the most intense, with the highest rain rates.

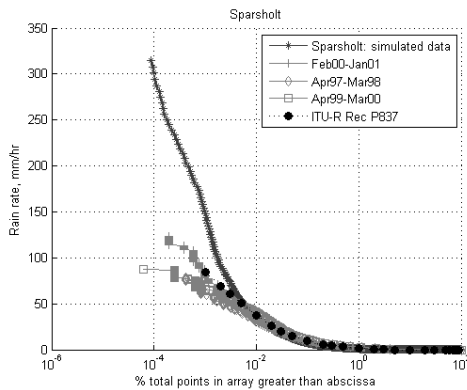


Figure 1(a): Example of a simulated “annual” dataset, in comparison with the Recommendation ITU-R P.837-5 curve for Sparsholt, in the South of England – whole curve

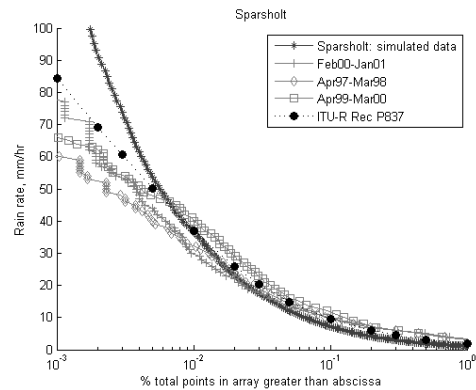


Figure 1(b): Example of a simulated “annual” dataset, in comparison with the Recommendation ITU-R P.837-5 curve for Sparsholt, in the South of England - zoom

Measured rain gauge data from two sites in the south of England, Sparsholt and Chilbolton (~7.5km apart) was used to compare with the simulated data and the ITU-R curves. Figure 2 shows Recommendation ITU-R P.837-5 curve for percentage times less than 0.1%, in comparison with the measured Chilbolton and Sparsholt annual curves (Jan. 05- Dec. 05) and the cdfs for a pair of simulated rain gauges A and B. The simulated gauges are separated in space by a distance equivalent to 7.5 km, approximately equal to the distance between Sparsholt and Chilbolton.

The cumulative distribution function of the simulated gauge A has been scaled using parameters a and b to fit it to the ITU curve (making it equivalent to Chilbolton). The cdf of B uses the same a and b for its scaling, but isn't as closely tied to the ITU curve.

There is good agreement of the simulated curves with the ITU curve for percentage values less than 0.05%. It also should be noted that there is significant annual variability in the measured distribution functions.

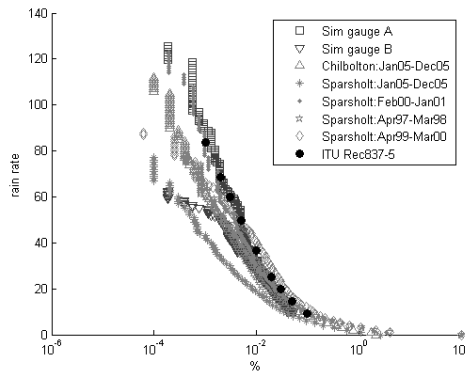


Figure 2: Recommendation ITU-R P.837-5 curve for percentage times less than 0.1%, in comparison with the measured Chilbolton and Sparsholt annual curves and the cumulative distribution functions for simulated rain gauges A and B

Figure 3 shows the Rec. ITU-R P.837-5 curve for percentage times less than 0.1%, in comparison with the cumulative distribution functions for simulated rain gauges A and B for different geographic locations. Again, the simulated gauges are separated by a distance equivalent to 7.5 km. It should be noted that the simulated curves are the same shape for each geographic location, as the same simulated rain fields were chosen, and the simulated gauges were at the same points in the arrays for each location.

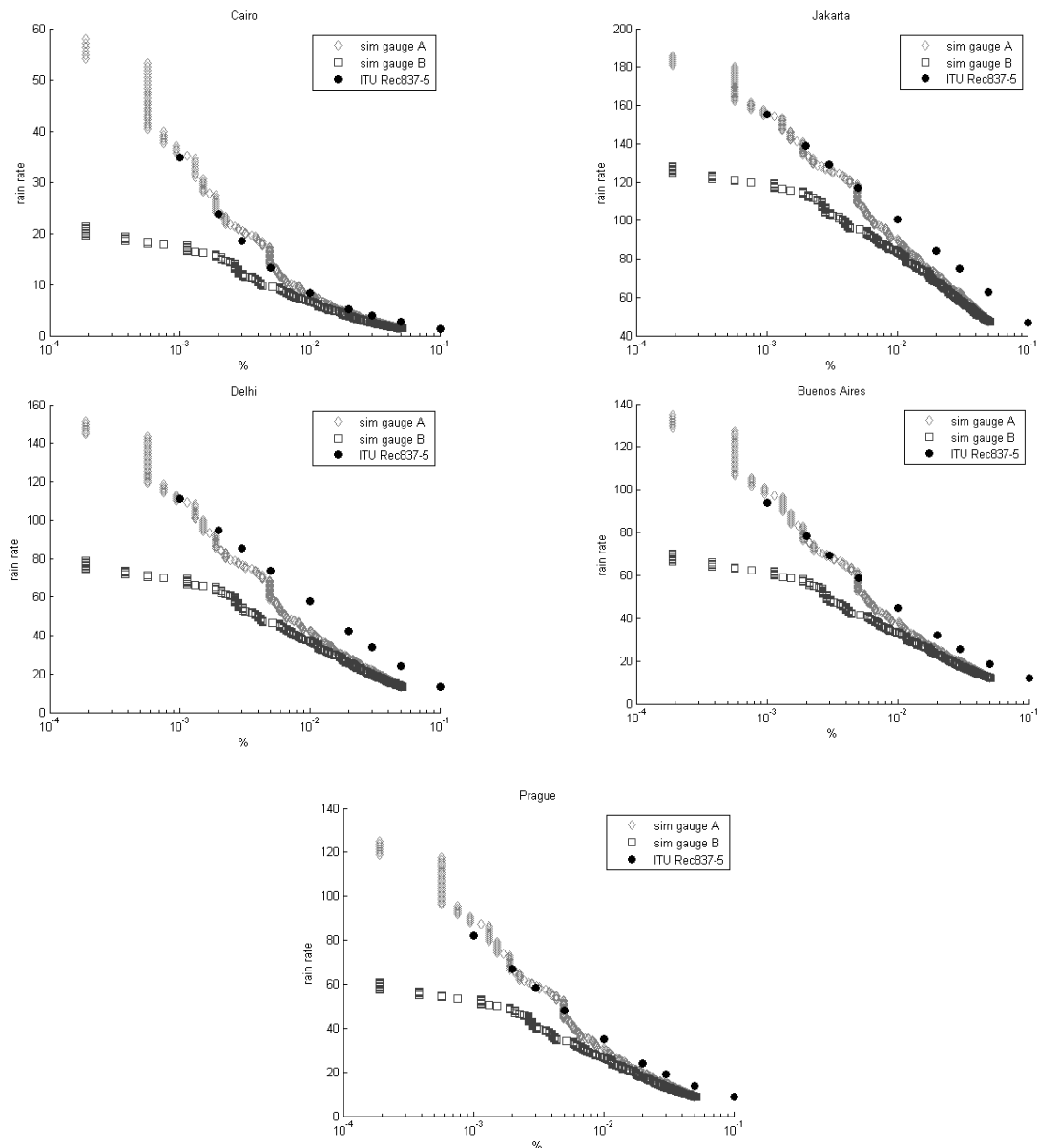


Figure 3: Recommendation ITU-R P.837-5 curve for percentage times less than 0.1%, in comparison with the cumulative distribution functions for simulated rain gauges A and B, 7.5km apart, for different geographic locations

3.2. Spatial autocorrelation of simulated rain fields in comparison with measured data

Gebremicheal et al [17] present results from two TRMM campaigns, looking at the ability of radar-derived rainfall products to characterise the small scale spatial variability of rainfall. Figure 2 in the paper (Figure 4 in this paper) suggests that the correlation measured from these datasets falls off with distance at a comparable rate to the simulated stratiform rain fields shown in Figure 5 (assuming that 1 pixel = 100 m * 100 m). Figure 6 shows the equivalent plot for simulated convective rain fields. All of these simulated fields were scaled using $R_{0,01} = 36.5$ mm/hr (the value of $R_{0,01}$ given for Chilbolton from ITU Rec. P837-5).

The measured distances for a correlation factor of 0.5 (as shown in figure 4) range from 2km to 6km. This relates well to the simulated stratiform fields, where the correlation factor of 0.5 corresponds to distances of 20 to 100 pixels (equivalent to 2 to 10 km). This is confirmed by another paper [18] where the small scale spatial autocorrelation of rain fields was determined for distances from 10 m to several 10s of km using a rain gauge network for distances from 10 m to 5 km and a radar for distances from 2 to 10 km.

The correlation function for the simulated convective fields falls off more quickly (figure 6) with the 0.5 correlation factor corresponding to distances of 10 to 30 pixels (1 to 3km). This is not surprising, as convective rain cells typically have diameters of the order of a few km. Also in figure 6, as the distance increases, a re-coupling effect can be seen which occurs when two distinct rain cells share similar rain rates at a similar time. Again, this fits with our understanding of the physical nature of convective rain fields.

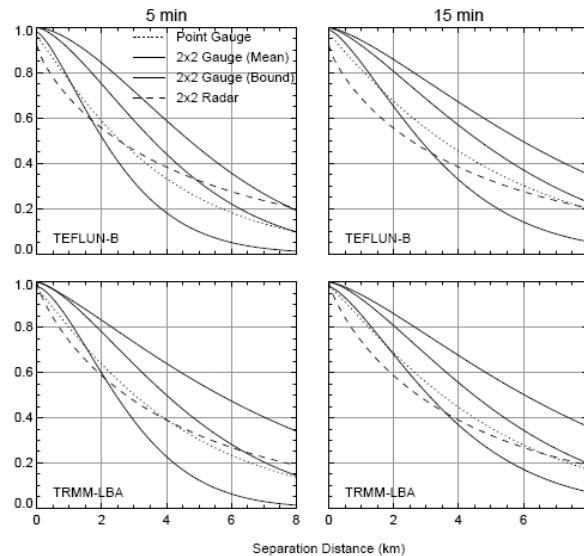


Figure 4: Spatial point- and area-correlation function estimated from gauge-rainfall fields, and the uncertainty bound for the area-correlation function. Also shown is the correlation function estimated from radar-rainfall fields (Gebremichael et al, 2004)

Theoretically, scaling the rain fields to fit the tail of the annual distribution should not impact their fractal dimension or spectral density function exponent, and because of the Wiener–Khinchin theorem should therefore not impact their spatial autocorrelation function. (The Wiener–Khinchin theorem states that the power spectral density of a wide-sense-stationary random process is the Fourier transform of the corresponding autocorrelation function.) However, due to processing constraints and rounding errors, the act of scaling to the tail of the distribution does impact the correlation function of the resulting fields.

Figures 7 and 8 show radial sections through the 2D spatial autocorrelation function of simulated fields when those fields are scaled to $a= 2.3765$ and $b= 0.9711$, to fit the tail of the annual distribution, again as calculated from UTU-R Rec. 837-5 for the location of Chilbolton. As can be seen, this results in the simulated fields becoming more correlated. This is understandable, as the method of scaling to fit the tail alters the standard deviation of the simulated fields and therefore pushing the spread of simulated values closer together.

This can be mitigated by tweaking the equivalent pixel size to make the spatial correlation more consistent with reality, but will reduce the total area covered by the simulated fields. If we assume that 1 simulated pixel is equivalent to 50m*50m, this corresponds consistently with the measured data shown in Figure 4.

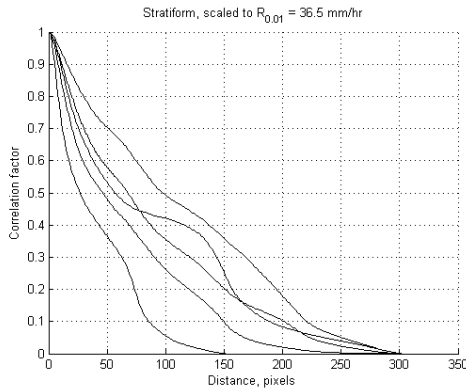


Figure 5: Radial sections through the 2D spatial autocorrelation function of a simulated stratiform rain field – scaled to $R_{0.01}=36.5\text{mm/hr}$

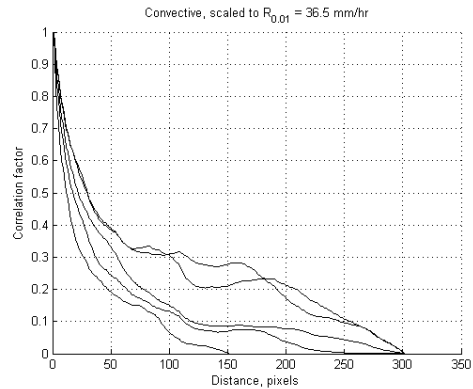


Figure 6: Radial sections through the 2D spatial autocorrelation function of a simulated convective rain field - scaled to $R_{0.01}=36.5\text{mm/hr}$

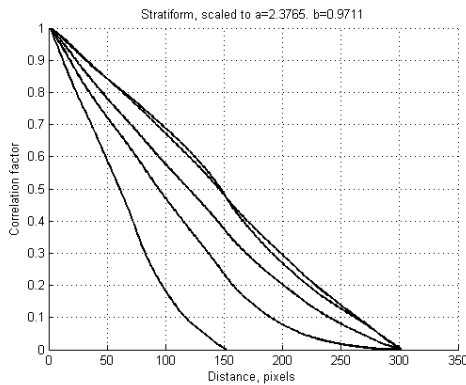


Figure 7: Radial sections through the 2D spatial autocorrelation function of a simulated stratiform rain field – scaled to $a= 2.3765$ and $b= 0.9711$

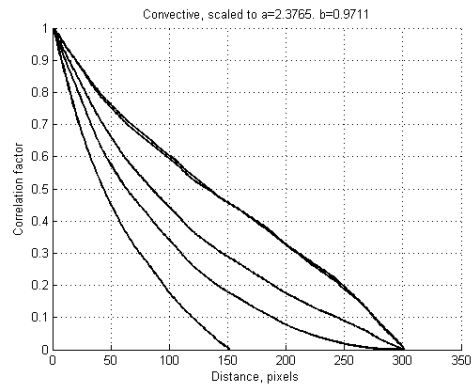


Figure 8: Radial sections through the 2D spatial autocorrelation function of a simulated convective rain field - scaled to $a= 2.3765$ and $b= 0.9711$

4. Conclusions

This paper builds on a method for simulating two-dimensional rain fields through the use of a discrete additive cascade procedure in the logarithmic domain, in order to create a cut-down database capable of reproducing the statistics of the tail of the ITU-R Rec. P837-5 distribution. These simulated rain fields have the same fractal dimension, spectral density exponent and can be customised to different climactic regions through the use of the parameter $R_{0.01}$. They can also produce stratiform-like and convective-like behaviour, according to the type of event desired by the operator. The introduction of rainy/non-rainy regions is accomplished through the use of a threshold.

The results presented in here suggest that simulating an entire year's worth of two-dimensional rain fields in the proportions given by M_c and M_s and scaling them to $R_{0.01}$ results in statistics that are consistent with measurements and the model in ITU Rec. P9837-5. Unfortunately, this is not practical, due to computer memory and processing time constraints.

The method for producing a cut-down "annual" dataset presented here works well in comparison with the ITU Rec. P837-5 model, and with measured data recorded in the south of England. Further testing with data from other geographic locations is required.

It should also be noted that there are a number of caveats associated with the use of this method. Tails of distributions are never that well defined, due to the limited numbers of data points that create them. Hence, fitting simulated data to the tail of the ITU model relies on the assumption that the tail of the model is accurate. The scaling procedure also alters the mean and standard deviation of the distribution of the simulated rain rate values, thereby

requiring that the pixel size be mapped to 50m*50m, instead of the previous 100m*100m (as given when scaling to $R_{0.01}$).

Also, after scaling, the simulated cumulative distribution function percentage values only map to the ITU-R curve for percentage values less than 0.05%. This however may not be that much of an issue to systems designers, as most systems are designed for outage times of 0.01% of an average year (which is covered by the simulated curve).

The rain field simulator has been used as a source of rain field data in order to investigate the spectrum efficiency benefits of introducing adaptive transmit power control into the 38GHz fixed terrestrial link band in the UK [19]. Results from this showed that when a fixed link plan constructed with the objective of achieving a 0.01% unavailability was exposed to annualised simulated rain events, the measured unavailability was 0.008%. This is close enough to demonstrate the general method, and it is probable that further improvements to the simulated rain will improve the ability of that rain to provoke the expected unavailability.

Future work is planned to expand the model to take into account the vertical variation of rain fields, allowing it to be applied more accurately to satellite system planning, as well as to introduce an accurate method of simulating the temporal variation of the field (evolution and advection of the rain cells). Also, it is further investigations with measured rain field data into the spatial autocorrelation of rain fields on different scales, in different locations and using different spatial resolutions be carried out.

5. Acknowledgements

The research presented in this paper was funded by the UK's Ofcom.

6. References

- [1] Crane, R.K., Electromagnetic Wave Propagation through Rain, Wiley Ser. Remote Sens., John Wiley, New York 1996
- [2] Manning, R.M., A rain attenuation model for satellite link attenuation predictions incorporating the spatial inhomogeneity of rainrate. Int. Jnl. of Satellite Communications, Vol. 2, 187-197, 1984
- [3] Capsoni, C., Fedi, F., Magistroni, C., Paraboni, A. and Pawlina, A., Data and theory for a new model of the horizontal structure of rain cells for propagation applications, Radio Science, 22(3), 395-404, 1987b
- [4] Lovejoy, S., Area-Perimeter Relation for Rain and Cloud Areas, Science, Vol 216, 185-187, April 1982
- [5] Rys, F.S., Waldvogel, A. Fractal Shape of Hail Clouds, Physical Review Letters, Vol. 56, Number 7, 784-787, February 1986
- [6] Feral, L. and Sauvageot, H, "Fractal identification of supercell storms", Geophysical Research Letters, Vol. 29, No. 14, 2002
- [7] Callaghan, S.A., Vilar, E. Analysis of the Fractal Dimension of Rain Rate Contours with Reference to Wide Area Coverage of Satellite Communications. "Foreign radioelectronics. Successes of modern radioelectronics" No 6, 2003, RADIOTECHNIKA, Moscow
- [8] Callaghan, S.A, Vilar, E., "Fractal Generation of Rain Fields: Synthetic realisation for radio communication systems", IET Microwaves, Antennas and Propagation, Vol. 1, Number 6, 1204-1211, December 2007
- [9] Voss, R. F., "Random fractal forgeries", in Fundamental Algorithms for Computer Graphics, editor R.A. Earnshaw, NATO ASI Series F, Computer and System Sciences, Vol 17, 1985
- [10] Lovejoy, S. and Schertzer, D., "Multifractals, universality classes and satellite and radar measurements of clouds and rain fields", Journal of Geophysical Research, Vol. 95, 2021-2034, 1990
- [11] Olsson, J., and Niemczynowicz, J., "Multifractal analysis of daily spatial rainfall distributions", Journal of Hydrology, 187, 29-43, 1996
- [12] Deidda, R., "Multifractal analysis and simulation of rainfall fields in space", Physics and Chemistry of the Earth Part B – Hydrology, Oceans and Atmosphere, 24 (1-2), 73-78, 1999
- [13] Bacon, 2005 "Rain Modelling and the Future of Telecommunications" Rainmap Kick-off conference, Jan 2005 (http://www.rainmap.rl.ac.uk/pdfs/jan2005_workshop/Bacon.pdf)

- [14] Callaghan, S.A, "Fractal analysis and synthesis of rain fields for radio communication systems" PhD thesis, University of Portsmouth, June 2004
- [15] Ferraris, L., Gabellani, S., Parodi, U., Rebora, N., von Hardenberg, J., Provnzale, A., "Revisiting multifractality in rainfall fields" J. Hydromet. 4, pp 544-551, 2003
- [16] ITU-R Recommendation P.837-4 "Characteristics of precipitation for propagation modeling"
- [17] Gebremichael, M., Krajewski, W., Ciach, G. "Assessment of the statistical characterization of small scale rainfall variability from radar" Sixth Int. Sympos. on Hydrological Applications of Weather Radar, Melbourne, Australia, 2-4 Feb 2004
- [18] Moszkowicz, S, "Small-scale structure of rain field – preliminary results basing on a digital gauge network and on MRL-5 Legionowo radar" Phys. Chem. Earth (B), Vol 25, No 10-12 pp933-938, 2000
- [19] Callaghan, S.A., Hansell, P., Inglis, I., "Impact of introducing Automatic Transmit Power Control in P-P Fixed Service Systems operating in bands above 13 GHz" Final report for Ofcom, 19th December 2005 (available from <http://www.ofcom.org.uk/research/technology/overview/ese/atpc/atpcfina12.pdf>)

Preliminary Study of Rain Attenuation Time Series Synthesizers for Tropical and Equatorial Areas

Marcio Rodrigues^(1,2), Guillaume Carrie⁽¹⁾, Laurent Castanet⁽¹⁾, Frédéric Lacoste⁽³⁾, Luiz Silva Mello⁽²⁾

⁽¹⁾ ONERA, Toulouse, France

Email : Marcio.Da_Costa_Rodrigues@onera.fr, Guillaume.Carrie@onera.fr, Laurent.Castanet@onera.fr

⁽²⁾ CETUC-PUC, Rio de Janeiro, Brazil

Email : marcio.rodrigues@cetuc.puc-rio.br, smello@cetuc.puc-rio.br

⁽³⁾ CNES, Toulouse, France

Email : Frederic.Lacoste@cnes.fr

ABSTRACT

The aim of the preliminary study presented in this paper is to improve and validate time series synthesizers relying on the Maseng-Bakken principle for tropical and equatorial areas. In the first part of this paper, the basic principles of the Maseng-Bakken model are recalled and the parameterisation of this channel model is discussed for temperate European climates. Then, Ku-band beacon data collected in Brazil are used: on the one hand to retrieve the input parameters of the channel models and on the other hand to test them with respect to long-term statistics. The results of this testing analysis constitute the second part of this paper.

1 Introduction

In tropical and sub-tropical areas, the terrestrial telecommunications infrastructure is less developed than in temperate regions and there is a strong need to develop satellite communication systems in the next few years. Satellite communication systems have the advantage of serving wide regions and the possibility to reach a large market size for economic profitability. For new consumer applications, C-band is unattractive because existing satellite communication systems have been developed for large Earth stations, and the deployment of new satellite communication systems with small terminals is incompatible with the large antennas required to protect the existing systems. Regarding Ku-band in the tropics, no spectrum congestion is expected in the near future, so this frequency band will be generally available for some time, with an anticipated evolution towards Ka-band for high data rate multimedia applications. Propagation impairments are expected to be quite severe in general in tropical climates, both in terms of probability of occurrence and in nominal impairment level. Normal signal outage and performance standards of merit may be difficult to achieve in these regions. So, due to propagation conditions, adaptive techniques (physical layer, resource allocation) aimed at mitigating propagation impairments often must be implemented even at Ku-band in tropical and sub-tropical countries.

To design and optimise these adaptive techniques, the knowledge of the dynamic behaviour of the propagation channel is required. This need can be fulfilled by the introduction of time series of propagation impairments in system simulation [1]. As experimental data are on the one hand difficult to obtain for system designers and on the other hand not available for every type of link configuration (frequency, elevation, climate), channel models have been proposed in the present decade (see for instance the review of time series synthesizers in [2]). Among these channel models, the one developed by [3] is at the moment the most popular one and the most mature for consideration in point-to-point satcom simulations. This model has been investigated and constitutes the basis of model implementations proposed by several authors [4], [5], [6]. In terms of model validation, these channel models have been validated in temperate climates and for elevation angles ranging between 25° and 40° [7].

The aim of the preliminary study presented in this paper is to improve and validate time series synthesizers relying on the Maseng-Bakken principle for tropical and equatorial areas. In the first part of this paper, the basic principles of the Maseng-Bakken model are recalled and the parameterisation of this channel model is discussed for temperate European climates. Then, Ku-band beacon data collected in Brazil are used: on the one hand to retrieve

the input parameters of the channel models and on the other hand to test them with respect to long-term statistics. The results of this testing analysis constitute the second part of this paper.

2 Channel models considered in this study

A stochastic model of rain attenuation relying on the first order Markov theory has been proposed by Maseng and Bakken in the eighties [3]. This concept has been applied to generate time-series of rain attenuation for satellite communications systems operating at Ku-band and above [4], [5]. The Maseng and Bakken model has been improved and widely validated for temperate European climates [6], [7], [8]. In the following, only the last model [8] - so-called Enhanced Maseng-Bakken model -, will be described as it relies on the same basis as the others.

2.1 Enhanced Maseng-Bakken model

Relying on the theory described in [3], this stochastic model partly aims at synthesizing rain attenuation time series. Maseng and Bakken have made two main hypotheses concerning the rain attenuation process A_{rain} :

- The long-term distribution of rain attenuation is log-normal, characterized by two parameters: respectively the mean m and the standard deviation σ of its natural logarithm.
- Rain attenuation can be transformed into a first order stationary Markov process using the non linear transformation:

$$X = \frac{\ln A_{rain} - m}{\sigma} \quad (1)$$

Given these theoretical hypotheses, three parameters are necessary to generate rain attenuation time series with this model:

- The log-normal law parameters m and σ , respectively the mean and the standard deviation of the log-attenuation.
- The β parameter introduced to describe the dynamics of rain attenuation.

As explained in [3], the three parameters m , σ and β have to be determined on a long-term basis. Indeed, they are dependent on the link considered and can be evaluated using time series of rain attenuation collected over long periods (months, years).

Initially, the stochastic model developed by Maseng and Bakken aims at synthesizing rain attenuation events and not periods without rain. Consequently, it was advised to assess input parameters values only considering periods of rain [3]. To be able to synthesize time series on a long-term basis, in the Enhanced Maseng-Bakken model, the log-normal fit is realized for the experimental CCDF that takes into account both periods of rain and of no rain. It has been observed that, in this case, the dynamic of synthetic time series is statistically lower than that of experimental time series, especially for low attenuation values. Then, to improve the dynamic of the model, a fourth parameter A_{offset} has been introduced in the channel model [8]. This offset is subtracted to the generated rain attenuation time series. Figure 1 shows the relationship between the white Gaussian noise generating source $n(t)$ and the instantaneous rain attenuation $A(t)$ in dB synthesized by the Enhanced Maseng-Bakken model.

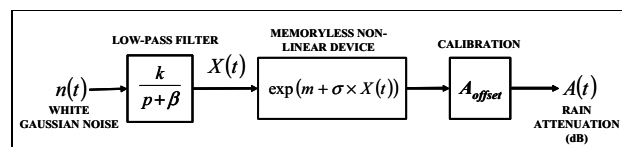


Figure 1. Principle of the Enhanced Maseng-Bakken Model.

If rain attenuation CCDF is calculated from long duration time series generated with this model, nil rain attenuation is exceeded for percentages of time significantly lower than 100 % whereas a classical log-normal CCDF reaches 0 dB for 100 % of the time. Then, to get the right probability to have rain attenuation on the link, it is recommended to set the constant offset value A_{offset} to the attenuation value of the log-normal CCDF that corresponds to P_0 % of the time, where P_0 is the probability to have rain on the link. If no long-term experimental value is available, Rec. ITU-R P. 837 can be used to predict a rough value of P_0 : which is the probability to have rain on a given site. This calibration step is the main difference between the Enhanced Maseng-Bakken model and the classical Maseng-Bakken one.

2.2 Model parameterisation for temperate European climates

2.2.1 Log-normal parameters (m, σ)

The log-normal parameters m and σ can be derived from the long-term Complementary Cumulative Distribution function (CCDF) of the rain attenuation process. The rain attenuation CCDF depends on meteorological parameters and on the link to consider. If the experimental long-term distribution is not available for a given link, the ITU-R recommends a global model that predicts the rain attenuation distribution in all sites for the frequency range of interest (Rec. ITU-R P. 618-7). In the underlying theory, the Enhanced Maseng-Bakken model assumes the rain attenuation to be log-normal on a long-term basis. However, this assumption is not strictly verified by the experimental CCDFs or the ITU-R model. Indeed, the experimental CCDF are not log-normal for the higher and the lower percentages of time. Consequently, it is necessary to identify a time percentage range where the log-normality of the distribution is verified. Then, considering a random variable following a log-normal law of parameters (m, σ), the probability it exceeds a given value x is given by:

$$P(X > x) = \frac{1}{2} \left(1 - \operatorname{erf} \left(\frac{\ln x - m}{\sigma \sqrt{2}} \right) \right) \quad (2)$$

So, $f(P(X > x)) = -\sqrt{2} \operatorname{erf}^{-1}(1 - 2P(X > x))$ is an affine function of $\ln x$. Hence, on the identified percentage range, a linear regression of $f(\text{CCDF})$ enables to infer the log-normal parameters m and σ [8].

2.2.2 β parameter

[6] presents a methodology to infer the β parameter from experimental time series based on the second order conditional moment of attenuation A : $K_{2,A}(A)$, where the analytical expression of $K_{2,A}(A)$ is given by [3]:

$$K_{2,A}(A) = \frac{E\{[A(t + \Delta t) - A(t)]^2 \mid A(t)\}}{\Delta t} = 2\beta A^2 \sigma^2 \quad (3)$$

This methodology is consistent with the Maseng-Bakken model of rain attenuation and it has been proven to be more robust than correlation based or PSD based ones [9]. Time series generated using a β value assessed by this methodology also give the minimum error with respect to the experimental distributions in terms of fade duration and of fade slope distributions [6].

The methodology firstly consists in low pass filtering ($f_c = 0.025$ Hz) the attenuation time series to remove most of the scintillation effects (for example with a 5th order Butterworth filter), then, the second order conditional moment $K_{2,A}(A)$ of rain attenuation events is estimated for a discrete set of attenuation classes (for example at 20 GHz and for 38° of elevation angle, from 0 dB to 10 dB with a step of 0.1 dB) and for time lag values $\Delta t < 100$ s (for example [1;10;20;30;40;50;60;70;80] seconds for 1 Hz sampled data). Afterwards, an attenuation range, on which the relation $\sqrt{\Delta t K_{2,A}(A)} = \gamma(\Delta t) A$ is well verified, is determined and linear regressions ($A, \sqrt{\Delta t K_{2,A}(A)}$) are performed to assess $\gamma(\Delta t)$ for each Δt . Finally, the value of β is given by the slope of the linear regression ($\Delta t, F_{correct} \times \gamma^2 / 2\sigma^2$). Where $F_{correct}$ is introduced to compensate for the effect of the low-pass filter on time series. It is a function of the cut-off frequency f_c of the low-pass filter and on the time lag Δt considered (F_s is the experimental time series sampling rate):

$$F_{correct}(f_c, \Delta t) = \frac{\int_0^{\frac{1}{2}\pi F_s \Delta t} \left(\frac{\sin x}{x} \right)^2 dx}{\int_0^{\pi f_c \Delta t} \left(\frac{\sin x}{x} \right)^2 dx} \quad (4)$$

Figure 2 and Figure 3 show the example of the 18.7 GHz 1 Hz-sampled Italsat rain events recorded at the experimental space station of Politecnico di Milano/CNR in Spino d'Adda (45.4°N, 9.5°E, 84 m above sea level). The database spans a period of 7 years (1994-2000). The attenuation domain on which the linear regression has been realized is chosen equal to 2 dB < A < 10 dB.

This methodology has also been applied to an extensive set of experimental measurements corresponding to typical links in the North-western Europe with elevation angles between 25° and 38° and frequencies between 12

GHz and 50 GHz. For these types of links, this analysis has shown that the following estimate of the β parameter can be used: $\beta = 10^{-4} \text{ s}^{-1}$.

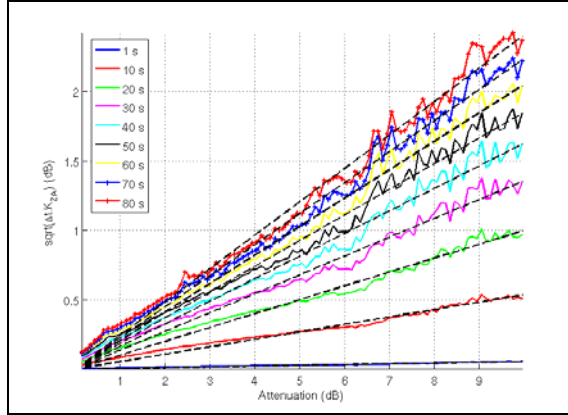


Figure 2. $\sqrt{\Delta t \cdot K_{2A}}(A)$ as a function of attenuation value and linear regressions for each time lag value for the 18.7 GHz 1 Hz-sampled Italsat rain events.

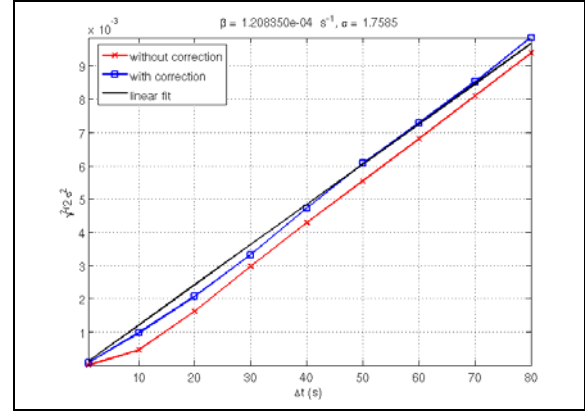


Figure 3. $\frac{\gamma^2}{2\sigma^2}$ as a function of time lag value and corresponding linear regression for the 18.7 GHz 1 Hz-sampled Italsat rain events.

2.2.3 Attenuation offset A_{offset}

Once the log-normal parameters m and σ are assessed, it is possible to infer the attenuation offset to subtract to synthetic time series following the principle shown by Figure 1. Before offset subtraction, synthetic attenuation follows a (m, σ) log-normal law characterized by its CCDF (see equation (2)). Then, P_0 % being the probability to have rain on the link, the attenuation value A_{offset} exceeded during P_0 % of the time is assessed by:

$$A_{\text{offset}} = \exp\left(m + \sigma\sqrt{2} \times \text{erf}^{-1}\left[1 - 2 \times \frac{P_0}{100}\right]\right) \quad (5)$$

The probability to have rain on the receiver location can be used as a rough estimate of P_0 . ITU-R Rec. P.837-5 recommends a model for this parameter wherever in the world.

3 Testing analysis with respect to propagation data collected in Brazil

As the channel model has been tested against experimental data in temperate areas only, it is now interesting to test its behaviour for different climates, and especially in tropical and equatorial regions. Data from Brazil have been used for this analysis.

3.1 Propagation data collected in Brazil

The experimental tropical and equatorial propagation data consists of twelve consecutive months of Italsat beacon (at Ku band, 11.5 GHz), collected in two Brazilian cities: Rio de Janeiro and Mosqueiro. Rio de Janeiro has a typical tropical maritime climate, whereas Mosqueiro (situated just in the Brazilian amazonic region) has an equatorial climate. Summary information is given in Table 1.

Beacon received power was measured and stored in daily binary files, in steps of 0.5 dB, and with a 2 seconds sampling period. Thanks to rain gauge data, the beacon data files were cleaned to remove any gaps or spikes that were clearly not due to rain attenuation events. Corrupted daily files were discarded. The up times for both cities are summarized in Table 1.

For each valid day, a histogram of all received power levels was made and the most probable value was considered to be the nominal received power level for the day. So, the in-excess attenuation levels (due to rain only) were obtained by subtracting the corresponding nominal level to each daily time series.

Table 1. Brazilian experimental data.

Station	Coordinates (degrees)	Altitude above sea level (m)	Link inclination (degrees)	Climate	ITU-R probability of rain (P_0 %)	Type of data	Beacon data sampling period (s)	Consecutive data periods
Mosqueiro (Pará state)	Lat: -1.40 Long: 309.31	16	87.5	Equatorial	13.3	Intelsat* beacon (11.5 GHz)	2	09/1996 to 08/1997 (up time : 90.4 %)
Rio de Janeiro (Rio de Janeiro state)	Lat: -22.92 Long: 316.05	30	62.2	Tropical	9.5			03/1998 to 02/1999 (up time : 87.4 %)

* Geostationary, 50° W.

3.2 Preliminary long-term testing analysis

The data have been calibrated with the same methodology for all locations, with respect to P_0 obtained with Rec. ITU-R P.837-5. To obtain strictly rain attenuation CCDF (zero dB attenuation axis crossed at P_0), for Mosqueiro an amount of 0.5 dB was subtracted from the whole attenuation time series. For Rio de Janeiro data, as the non-calibrated experimental attenuation CCDF was already very close to zero dB at P_0 , no time series calibration was necessary. First order (attenuation CCDF) and second order (fade duration and fade slope) statistics are presented on following Figure 7.

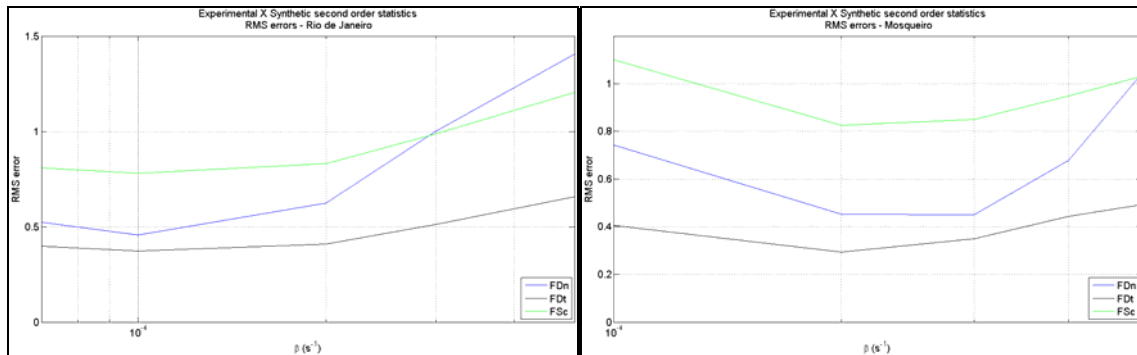
It is well known that the log-normal shape of rain attenuation CCDF is valid just for a specific part of the curve. Figure 7 presents the best log-normal fits found for Brazilian experimental data. As shown in this figure, experimental data adjusts better for high percentages of time, so no good fit was obtained for percentages of time bellow $3e-2$ for Rio de Janeiro and bellow $8e-2$ for Mosqueiro. The obtained log-normal input parameters for the channel model are summarized in Table 2.

Table 2. Channel model input parameters obtained from log-normal fit on brazilian CCDFs.

Station	Mean of log-normal CCDF, m	Standard deviation of log-normal CCDF, σ	Attenuation offset, A_{off}
Mosqueiro	-8.9462	3.4643 dB	0.0062 dB
Rio de Janeiro	-8.2133	3.0829 dB	0.0155 dB

The preliminary long-term testing of the channel model, against long-term experimental data for tropical and equatorial regions in Brazil, was divided in two steps, both concerning the use of the β input parameter. First of all, the Enhanced Maseng-Bakken channel model [8] was used to generate ten years (3650 days, with sampling time of 1 second) of synthetic rain attenuation time series, using the rough estimate of the β parameter for temperate climate ($\beta = 10^{-4} s^{-1}$, see Section 2.2.2). Comparison with experimental statistics is found in Figure 7.

As a second step, the most appropriate β values have been assessed for these Brazilian cities. To do so, fade duration and fade slope statistics have been calculated from 10 years of synthesized data with different β values and from the experimental time series. Then, the most appropriate β value is the one that results in the smallest RMS error of the test variables given in Rec. ITU-R P.311. Results are shown in Figure 4. More details on data processing methodology are given in [7].



Chosen β s for Rio de Janeiro: 7e-5, 1e-4, 2e-4, 3e-4, 5e-4

Chosen β s for Mosqueiro: 1e-4, 2e-4, 3e-4, 4e-4, 5e-4

Figure 4. RMS error for second order statistics, between experimental and synthesized time series for a set of chosen β s (Cut-off frequency for scintillation removal: 0.025 Hz; Time interval for FS: 10 s).

As noted in Figure 4, lower RMS errors for Rio de Janeiro are in the range from $1e-4$ s⁻¹ to $2e-4$ s⁻¹, whereas for Mosqueiro the best β is in the range between $2e-4$ and $3e-4$ s⁻¹. The higher β values for Mosqueiro are in accordance with what is expected from the physics of the rain phenomena. Dynamics of Mosqueiro are more pronounced than that of Rio de Janeiro, partly due to the almost vertical elevation angle of the satellite link for the first locality: the link does not benefit from the dynamics reduction commonly provided by lower elevations.

3.3 Channel model parameter retrieval

Besides the preliminary long-term testing analysis, described in Section 3.2, β was also retrieved by using the β extraction tool (see Section 2.2.2) developed as part of the Enhanced Maseng-Bakken channel model. The objective was to verify if the twelve months of Brazilian rain attenuation data for both regions, as well as the use of log-normal fit (represented in the β extraction tool by the σ parameter) for these tropical and equatorial data, could provide reliable β values.

To find the best attenuation interval to the 1st linear regression, the method has an automated mode, which looks for the smallest error at the 2nd linear regression. Figure 5 and Figure 6 show final results for both regressions. Obtained β values are $1.8e-4$ s⁻¹ for Rio de Janeiro and $3.3e-4$ s⁻¹ for Mosqueiro, in good accordance with the previous results (see Figure 4). The regression lines obtained in Figure 5 exhibit a too high variability that may be due to a too low quantity of rain events to obtain statistical reliability. More analysis is needed at this point, so the estimate of the β parameter obtained from these curves needs to be considered with cautions.

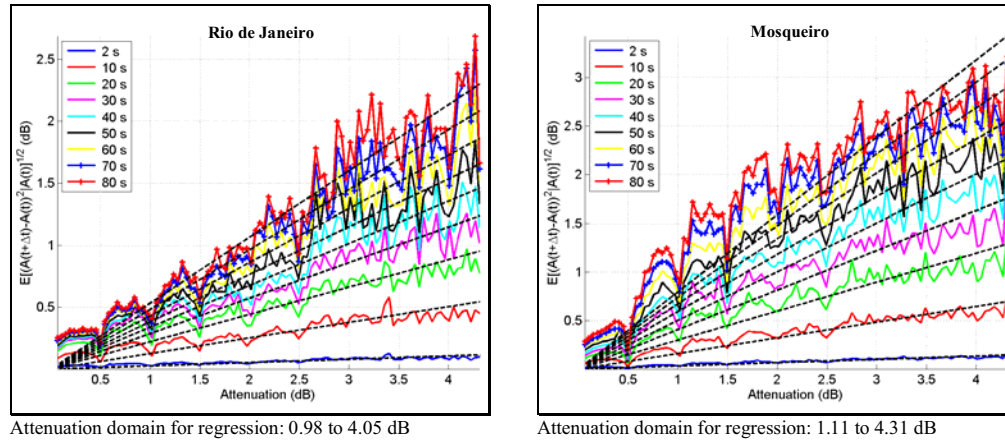


Figure 5. $\sqrt{\Delta t} \cdot K_{2\lambda}(A)$ as a function of attenuation value and linear regressions for each time lag value for the 11.5 GHz 0.5 Hz-sampled Intelsat data.

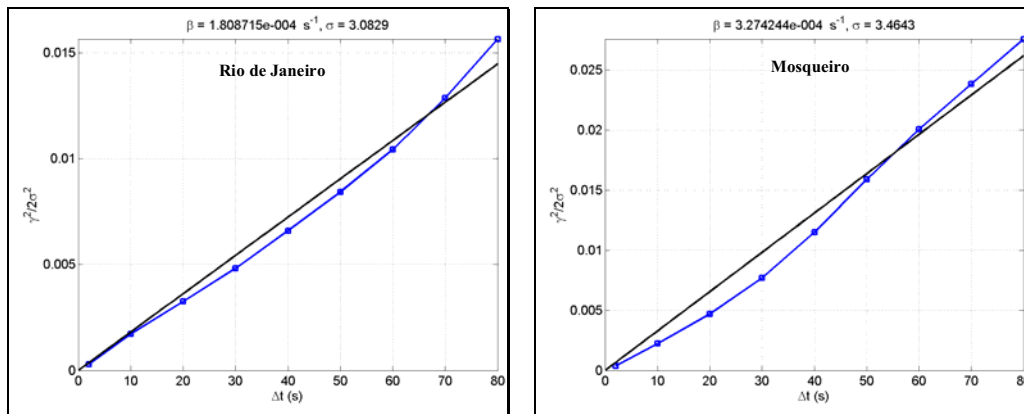
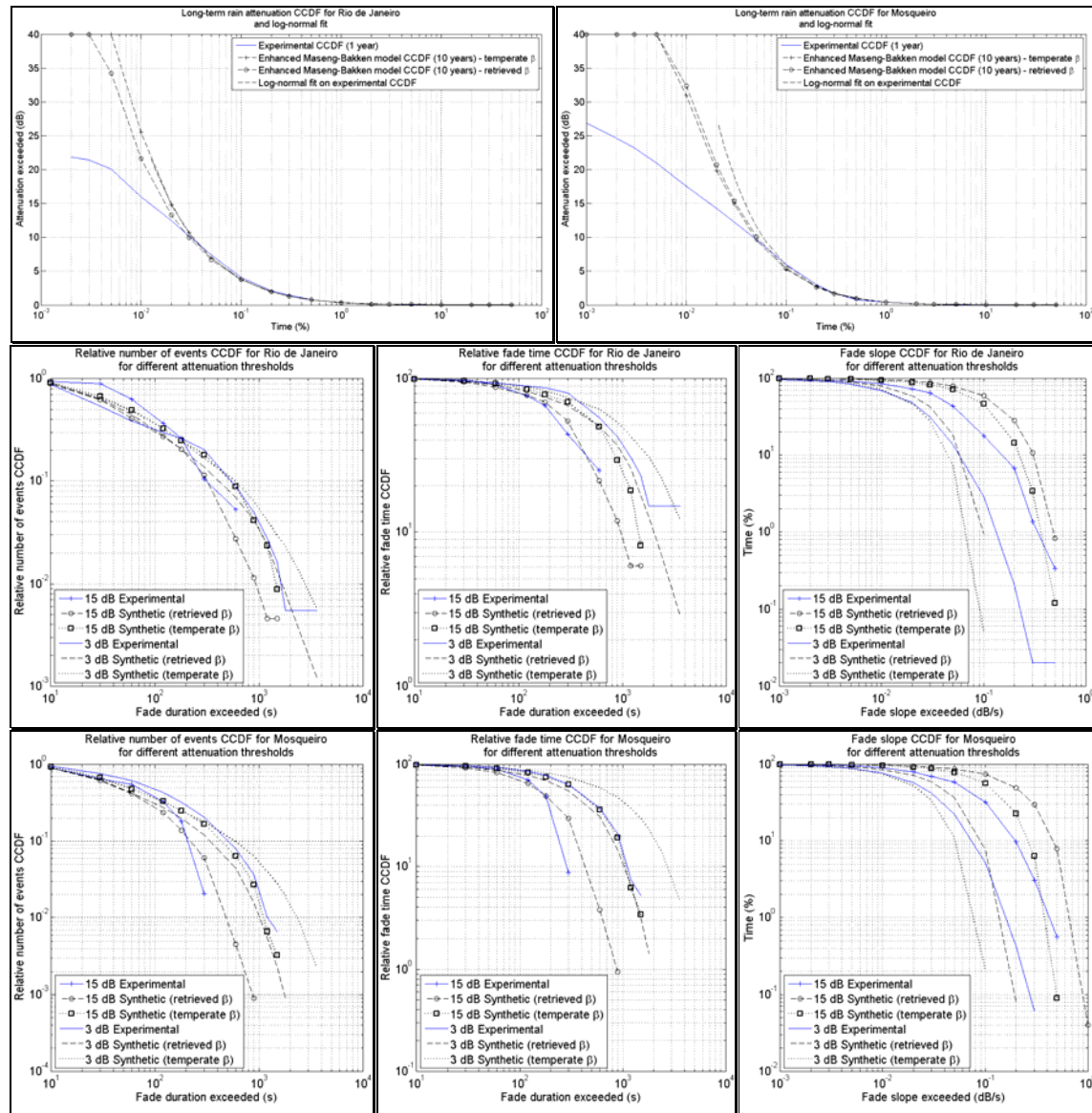


Figure 6. $\frac{\gamma^2}{2\sigma^2}$ as a function of time lags and linear regression for the 11.5 GHz 0.5 Hz-sampled Intelsat data.

Figure 7 illustrates the comparison between the statistics of ten years of synthetic time series (3650 days sampled at 1 Hz, generated with the β s indicated in Figure 6) and the experimental (1 year) statistics for both Brazilian areas. On the one hand, we can note, from the attenuation CCDF in Figure 7, that the synthetic and experimental statistics are in good agreement for percentages of time above 0.05%. While, on the other hand, the channel model overestimates the attenuation values for very low percentages of time compared to the experimental statistics. As a consequence, fade durations and fade slopes are also overestimated by the model for high attenuation thresholds.



Rio de Janeiro: retrieved $\beta = 1.808715e-4 \text{ s}^{-1}$; Mosqueiro: retrieved $\beta = 3.274244e-4 \text{ s}^{-1}$; Temperate $\beta = 1e-4 \text{ s}^{-1}$

Cut-off frequency for scintillation removal in 2nd order statistics: 0.025 Hz; Time interval for FS: 10 s

Figure 7. Log-normal fit and first (attenuation CCDF) and second (FD_n, FD_t and FS) order statistics comparison between experimental and synthesized attenuation time series.

A summary of RMS errors (computed according to the testing variable defined in Rec. ITU-R P.311-11) obtained for the experimental and synthetic attenuation time series comparison is found in Table 3. The table also shows the errors found for temperate experimental data. Regarding temperate climate, the experimental database used for this analysis is a portion of the one described in [6] & [11]. It consists of rain attenuation time series collected at 18.7 GHz, in a 37.8° slant path to Italsat (launched in January 1991, ended its mission in January 2001). No definite improvement is obtained with the retrieved β values on Brazilian data, which confirms the need of further analysis at this point (lack of rain events).

Table 3. RMS errors summary.

β	Att. CCDF			FD _n			FD _t			FS _c		
	RIO	MOS	SPI	RIO	MOS	SPI	RIO	MOS	SPI	RIO	MOS	SPI
1e-4	0.285	0.332	0.170	0.458	0.743	0.379	0.374	0.405	0.340	0.781	1.102	0.748
Retrieved by the method of Section 2.2.2	0.252	0.340		0.535	0.507		0.407	0.370		0.828	0.844	

“RIO” – Rio de Janeiro ; “MOS” – Mosqueiro ; “SPI” – Spino d’Adda

4 Conclusion

The current version of the Enhanced Maseng-Bakken channel model [8], which is based on the principles established by Maseng and Bakken [3], was preliminary tested with tropical and equatorial experimental data at 11.5 GHz. Preliminary retrieved dynamic input parameter β is not too far from the values retrieved up to now in temperate areas.

To arrive at definite conclusions, deeper analysis is needed which must be mainly focused in: a) using a bigger quantity of data to obtain better statistical reliability; b) critical analysis of the method used to retrieve the β parameter; c) test of a better long-term distribution (Gamma [10] or Weibull could be good choices) for the distribution of rain attenuation.

From the results of these deeper analyses, improvements of the Maseng-Bakken models could be proposed.

5 References

- [1] Castanet L., Mertens D., Bousquet M.: “Simulation of the performance of a Ka-band VSAT videoconferencing system with uplink power control and data rate reduction to mitigate atmospheric propagation effects”, *International Journal of Satellite Communications and Networking*, Vol. 20, July-August 2002, pp. 231-249.
- [2] Castanet L. (editor) et al.: “Influence of the variability of the propagation channel on mobile, fixed multimedia and optical satellite communications”, *SatNEx JA-2310 book*, Volume 2, Chapter 2.3, ISBN 978-3-8322-6904-3, Shaker, 2008.
- [3] Maseng, T., Bakken P.M.: “A Stochastic Dynamic Model of Rain Attenuation”, *IEEE Trans. Com.*, Vol. 29, n°5, May 1981, pp. 660-669.
- [4] Gremont B., Filip M.: “Spatio-temporal rain attenuation model for application to fade mitigation techniques”, *IEEE IEEE Trans. on Antennas and Propagation.*, vol. 52, n°5, May 2004, pp. 1245-1256.
- [5] Kanellopoulos S.A., Panagopoulos A.D., Kanellopoulos J.D.: “Calculation of the dynamic input parameter for a stochastic model simulating rain attenuation: a novel mathematical approach”, *IEEE Trans. on Antennas and Propagation*, Vol.5, n°11, November 2007, pp.3257-3264.
- [6] Lacoste F., Bousquet M., Castanet L., Cornet F., Lemorton J.: “Improvement of the ONERA-CNES rain attenuation time series synthesiser and validation of the dynamic characteristics of the generated fade events”, *Space Communication Journal*, Vol. 20, n°1-2, 2005.
- [7] Lemorton J., Castanet L., Lacoste F., Riva C., Matricciani E., Fiebig U-C., Van de Kamp M.M.J.L., Martellucci A.: “Development and validation of time series synthesizers of rain attenuation for Ka-band and Q/V-band satellite communication systems”, *International Journal of Satellite Communications and Networking*, Volume 25, October 2007, pp 575-601.
- [8] F. Lacoste, M. Bousquet, F. Cornet, L. Castanet, J. Lemorton: “Classical and On-Demand Rain Attenuation Time Series Synthesis: Principle and Applications”, *Proceedings of 24th AIAA-ICSSC Conference*, San Diego, California, June 2006.
- [9] G. Carrie, F. Lacoste, L. Castanet: “A Robust Estimator of the Dynamic Characteristics of Rain Attenuation Events”, *Proceedings of 2nd JA2310 SatNEx Workshop*, Oberpfaffenhofen, Germany, April 2008.
- [10] Panagopoulos, A.D.: “Physical Models for the Prediction of Slant Path and Site Diversity Statistics in Tropical Regions at Ku-Band and Above”, *Proceedings of 2nd JA2310 SatNEx Workshop*, Oberpfaffenhofen, Germany, April 2008.
- [11] Riva C.: “Seasonal and diurnal variations of total attenuation measured with the ITALSAT satellite at Spino d’Adda at 18.7, 39.6 and 49.5 GHz”, *Int. J. Sat. Com. Network.*, vol. 22, n°4, July-August 2004, pp.449-476.

An Empirical Study of Location Variability for Mobile Systems

R.F.Rudd
Aegis Systems Ltd, UK
Richard.rudd@aegis-systems.co.uk

Abstract

A robust understanding of the statistics of location variability is a prerequisite for the planning of any radio system with terminals distributed in space. A significant problem in the application of such statistics is that there is a wide spread of reported values, all of which have been gathered using different (and often insufficiently well documented) methods. The present paper initially summarises existing empirical results, paying particular attention to the measurement and data reduction methods used. Details are then given of an empirical study of location variability undertaken in the UK. This study sought to characterise location variability in urban, suburban and rural environments at frequencies between 200 MHz and 3.4 GHz, and made use of both narrow and wide-band measurement systems.

1.Introduction

This paper describes a study undertaken with the primary aim of informing the treatment of location variability in ITU-R Recommendation P.1546 (“Method for point-to-area predictions for terrestrial services in the frequency range 30 MHz to 3000 MHz”).

2.Background

The field strength of a given radio service, incident on a receiving aerial, is, in practice, never constant. Even for the case of fixed terminals separated by a short line of sight path, small variations in received field strength will occur due to variations in the local scattering environment (e.g. people moving). Over longer paths, between fixed terminals, there will be significant temporal variability, due to changes in the ionosphere or troposphere.

In addition to such temporal variations, a system in which one or both of the terminals is mobile or portable will need to account for spatial variations in the field strength (in the mobile case, of course, such spatial variation in field strength will be transformed to temporal variation in received power).

Accounting correctly for such spatial variability is also of critical importance in the planning of point-to-multipoint (area-coverage) services to fixed receivers. In such cases, the location of individual receivers will not be known when planning the network (e.g. broadcast television), but the statistics of variability need to be accounted for to ensure adequate levels of coverage within the nominal service area.

Spatial variability of field strength arises due to a number of separate mechanisms: Firstly the field strength will decrease with range due to spreading (‘ d^2 loss’); secondly there will be variations due to diffraction loss along the path, due to terrain, buildings and other clutter, and finally, fading will occur due to vector addition of multipath components.

2.1. Definitions

The term ‘location variability’ is variously defined, but is always understood to exclude the spreading loss (i.e. relates to the excess loss with respect to the free space value). Some common understandings of the term include:

- (A) The variability of path loss measured at all points at a given radius from the transmitter. [12], [13].
- (B) The variability of excess path loss within a small area (e.g. a 500m x 500m square) [7][8].
- (C) The variability of the excess path loss throughout the service area [2].
- (D) The variability of excess path loss along a route of a given length (e.g. 4 km) [9]

These different understandings of the term are illustrated in the sketches of Figure 1, below:

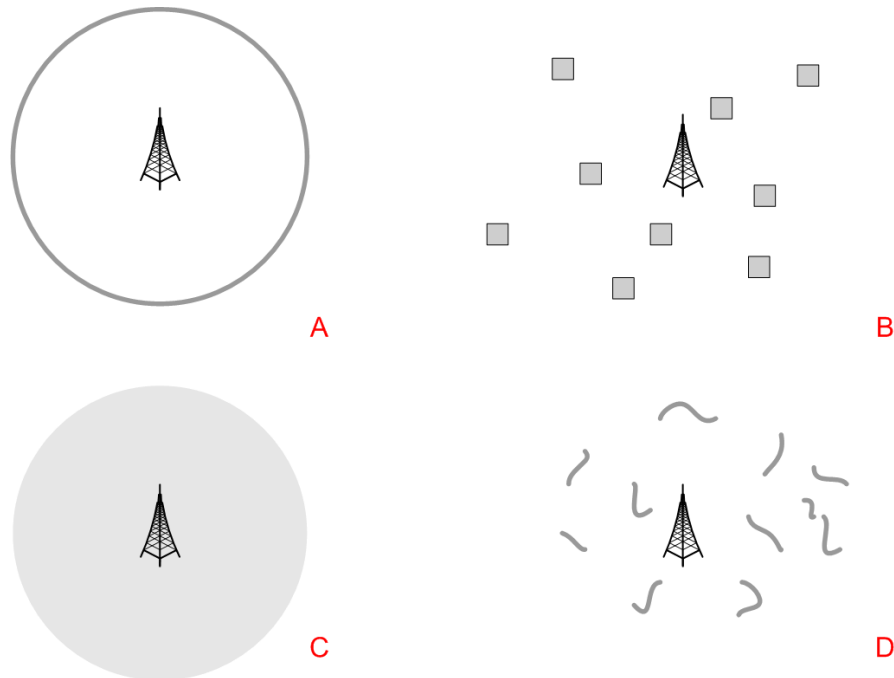


Figure 1: Definitions of location variability

If definitions (A) or (C) are adopted, this will clearly reflect the impact of diffraction due to bulk changes in terrain over paths at different azimuths from the transmitter. If definitions (B) or (D) are used, however, the most significant diffraction effects will be those associated with local clutter.

2.2. Scale of fading regimes

It is generally the case that the term ‘location variability’ is assumed to exclude the consideration of multipath effects. This assumption, however, is not always explicit, and this has led to considerable difficulty in comparing values quoted in the literature.

While there is a clear conceptual distinction between multipath fading and slow fading in terms of the mechanisms responsible, there is no such distinction between the slow fading over a small area and the bulk changes in field strength over an entire service area, both of which are largely due to diffraction effects. The small area fading may be dominated by building shadowing, but will also, generally, include some terrain effects, particularly if the area is relatively large (e.g. 1 km sides). The distinction is partly made to reflect the point at which propagation modelling is forced, by limitations of input data resolution, to cease being deterministic and to adopt a statistical approach. With the availability of, e.g. Lidar data and ray tracing software the boundary can, theoretically be set at very small areas indeed, but this may not accord with economic or practical considerations.

From a theoretical point of view, the optimum distinction between the bulk (terrain dominated) and small area (building, vegetation & clutter dominated) effects might be given by a choice of area with sides of around 100m. Such a choice would, however, have the serious drawback that for most VHF and UHF frequencies, the measurement dataset that could be collected would not be sufficient to give high statistical confidence.

In many cases, particularly where older studies are concerned, it is often unclear to what extent (if at all) multipath effects have been excluded from location variability data.

2.3. Historical survey

A considerable body of data relating to location variability has been collected over the years, and the ‘headline’ figures from these studies have often been compared in review papers and textbooks. This is illustrated in Figure 2, below - similar figures are reproduced in a number of texts [12], [15].

Such direct comparisons are potentially misleading, however, as the measurement and processing techniques for the different data sets are quite disparate. Thus, from Figure 2, at around 200 MHz, the standard

deviation of location variability appears to lie in the range 3.5 to 11.5 dB. If a location coverage of 99% were required, this would imply an uncertainty in the required median field strength of 18.6 dB.

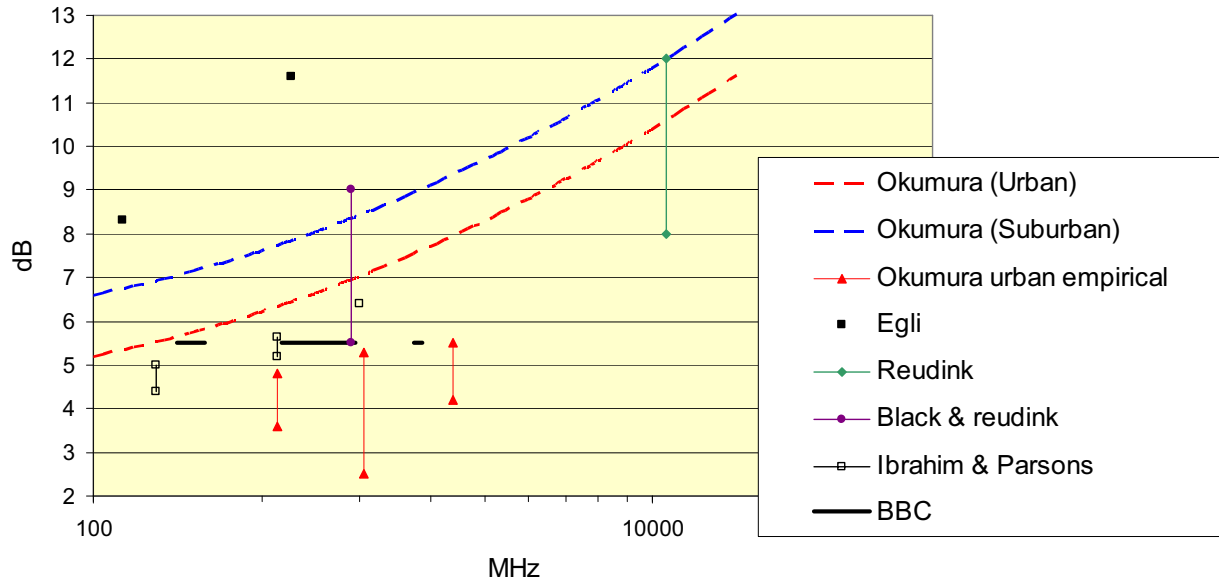


Figure 2: Comparison of empirical values for location variability

To understand the spread in statistics, it is necessary to refer to the detail of the original studies. For example, the Okumura curves (Fig.39 in [9]) are frequently cited and reproduced, and these show a location variability of ~6dB in urban areas at ~450 MHz. The actual measurements (Fig.38 in [9]) on which these curves are based, however, show an SD of ~4dB. The difference is due to a scaling introduced to convert from the measurement distance of ~1km to the distance assumed to be travelled during a typical R/T call at 60 km/hr. The value of 4dB is very close to measurements made by the BBC in 1995 [7], in which multipath was carefully averaged.

Much of the early work, however, omits to average multipath effects. Thus the values reported by Egli in [2] are rather high, at 8.3 and 11.6 dB. These values are, however, comparable with those given for analogue signals in ITU-R Recommendation P.370.

The key point to appreciate is that presentations such as that of Figure 2 above are misleading, as the data is not directly comparable. The table below attempts to summarise the different approaches taken in a number of measurement campaigns.

Table 1: Summary of empirical data

	Measurement routes	Rx height	Data logging	LV statistics	Mean	Notes	Ref
Egli (50-910 MHz)	USA Radial (Review of measurements made by several third parties)	various	(UHF) samples at 0.2 miles (VHF) continuous data averaged over 1-2 mile sectors	Wide area, all ranges 6.5 - 12.5dB	??	Considers deviation from 2-ray FS at all ranges	2
Okumura (453 – 1920 MHz)	Tokyo Radial, 1-100km	Van roof	Chart recorder	1-1.5 km 5-7dB	From chart, over 20m	Suggested that LV be defined over 3-4km route, giving values ~2dB greater	9
Ibrahim/Parsons (168, 445 & 896 MHz)	London 500m squares 2, 5 & 9 km from tx	Car roof	Digital samples at 2.8 cm interval	All 500m squares at a given range. 5-7dB	Averaged over 40 or 20m	CW	10
Reudink (11 GHz)	New York New Providence, NJ	??	??	No variation with range in suburbs. In urban, fell from ~12 to ~8dB at <1 mile.	Wide areas at 11 GHz. Also sorted by range. Stats are distribution of Excess path loss, not LV	CW	11
Black & Reudink (836 MHz)	Philidelphia	Van roof	Continuous, logged on tape	SD increases close to base.	Stats are distribution of Excess path loss, not LV	CW	3
BBC (UHF)	UK urban	10m	Field strength logged to PC at measurement points	5.4 dB	Frequency domain averaging	7 MHz bandwidth (DTT)	14
BBC (211 MHz)	London	Car roof	Digital sampling at fixed distance interval	5.7 dB	No averaging	1.5 MHz bandwidth (DAB)	6
BBC (226 MHz)	London	Car roof	Digital sampling at fixed distance interval	4.1 dB	Moving average	1.5 MHz bandwidth (DAB)	7
Aegis (237, 1477, 3430 Hz)	London	Car roof	Digital sampling at fixed distance interval	2.9 – 4.0 dB	Moving average (40m)	CW and wideband (5/20 MHz)	-

3. Empirical study

Measurements have been carried out, primarily in the London area, at three frequencies: 237.5 MHz, 1477 MHz and 3430 MHz. The measurements were made using both wideband and narrowband signals. A small set of data was also collected around Bognor Regis, on the UK south coast.

3.1.Method

The transmitter was sited on an office block in Croydon, South London, with antennas at a height of 80m above ground level. Measurements were made using vehicle mounted, omnidirectional antennas, in a number of areas at between 5 km and 15 km from the transmitter.

Some of the measurement routes in London are illustrated in the figure below, which shows an area of 15x15 km.

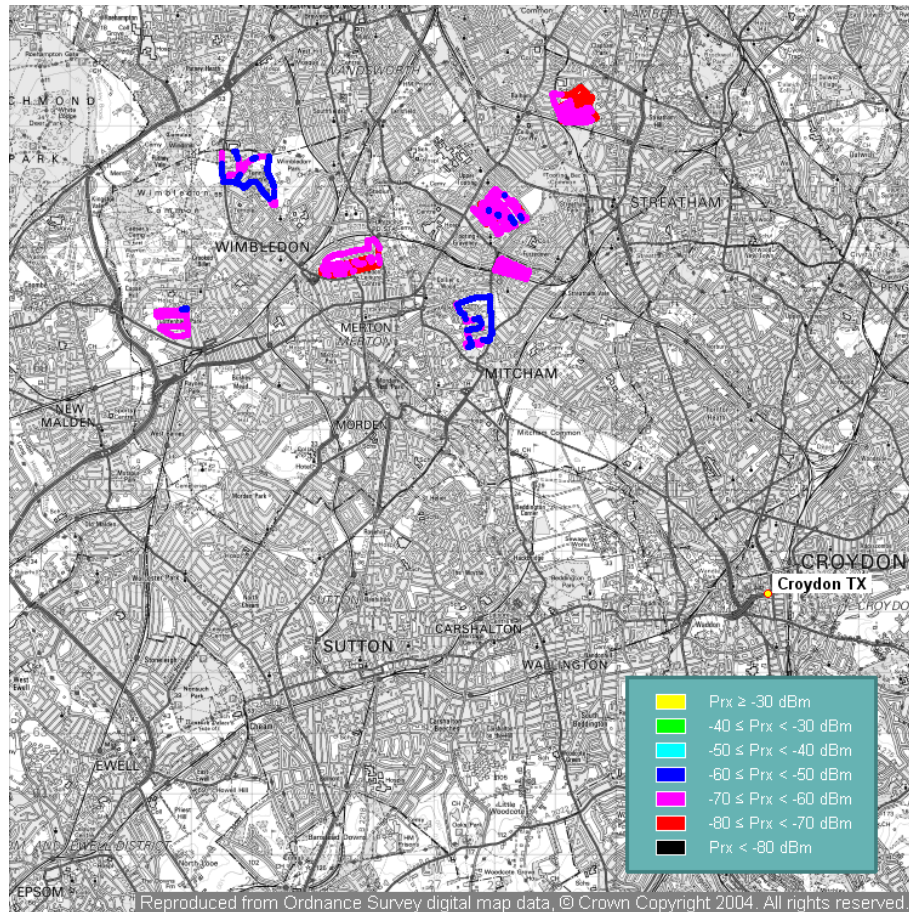


Figure 3 Measurement areas (1477 MHz)

Fast fading was filtered from the results using a running mean, the length of which could be varied in post-processing.

The intention of the measurements was to determine the variability of signals over areas of 500m x 500m (i.e. quarter-square-km). To this end, the vehicle position was logged using a GPS receiver, and post-processed to separate the results into individual quarter-square-kms). Figure 4 shows a number of measurements routes, with the quarter-kilometre grid overlain, and values of location variability for each square indicated.

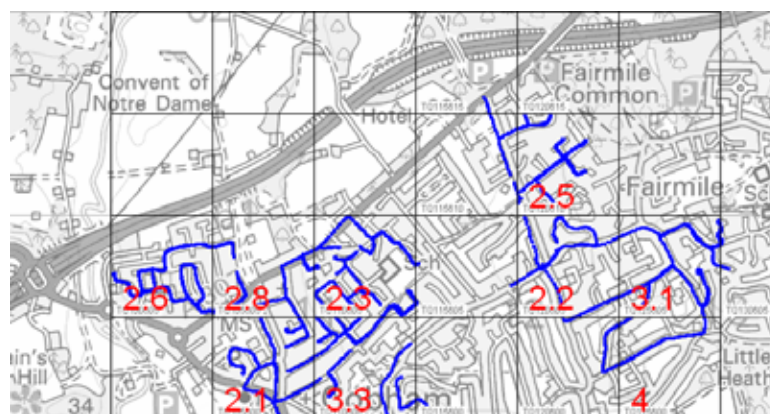


Figure 4: Analysis of measured data within 500m squares

3.2.Results

Initial measurements were made using CW transmissions, and with a spectrum analyser as the receiver. Some results from these measurements are summarised in the plot below, having been averaged over 40m.

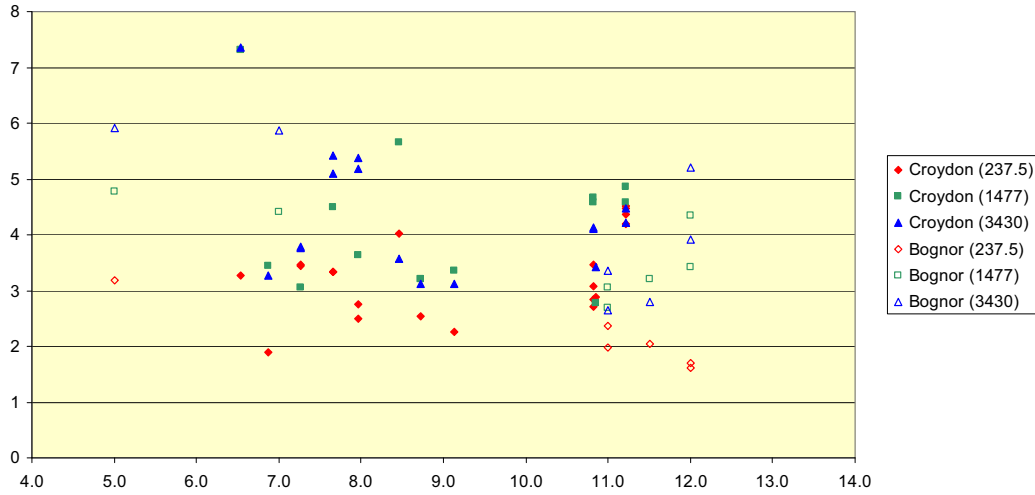


Figure 5: CW location variability (40m smoothing)

It can be seen that there is no clear dependence on path length, but the results do show the expected frequency dependence, albeit with a wide scatter.

The measurements were then repeated in each area, using wideband transmissions. These used a 511-bit PN sequence to phase modulate the transmitter, clocked at 10 MHz, except at VHF where interference considerations limited the clock rate to 2.5 MHz.

The receiver used quadrature sampling to recover the complex channel information, which was logged using a high speed ADC. Post-processing allows the channel frequency response or power delay profile to be recovered. For the exercise reported here, however, only the variability of the overall wideband received power was examined by integrating individual power delay profiles sampled along the measurement route.

It was found that there was a very repeatable correspondence, both between measurements made in the same area on different days, and between measurements (Figure 6) made using the CW and wideband systems.

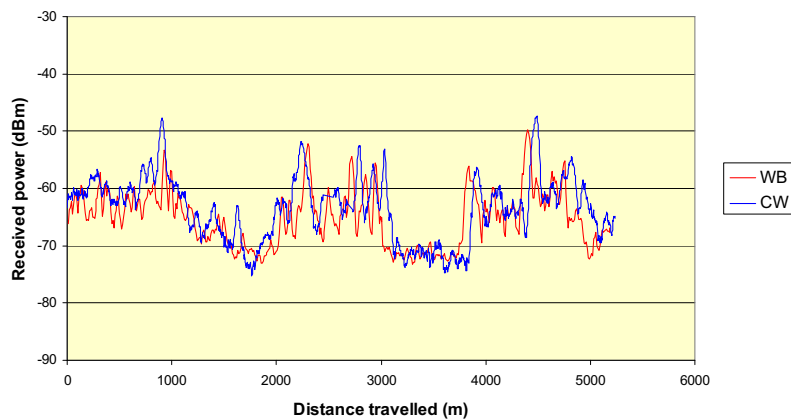


Figure 6: Comparison of wideband and CW measurements

The location variabilities measured using the two methods are compared in the plot below, which relates to one of the London areas studied. This shows the impact of changing the length of the sliding average filter; for small averaging distances, the location variability measured using the wideband systems is much smaller than that for CW, owing to the averaging of multipath fading in the frequency domain. The wideband and narrowband results

converging for a averaging length of 20-40m, at which point only flat (log-normal) fading remains in the measured data. Beyond this point the location variability falls slowly as the detail of local shadowing and terrain effects is averaged.

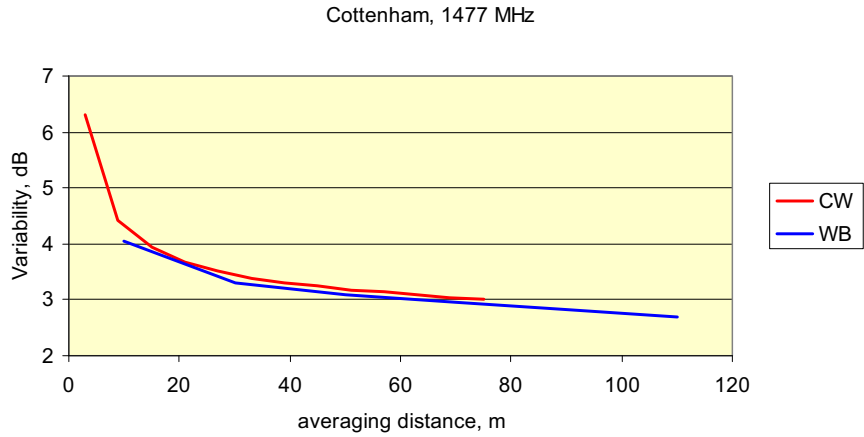


Figure 7: Location variability vs. averaging distance

The choice of an appropriate averaging distance involves the consideration of a number of factors; for CW measurements it must be sufficient to remove multipath fading, and this value will change with frequency [5]. On the other hand, it is appropriate to use a standard averaging distance to allow meaningful comparison between measurements on different frequencies. For the present study, a choice of 40m allowed sufficient spatial filtering at the lowest frequency.

The summary results for the three frequencies studied, applying spatial filtering of 40m, and considering the statistics for elemental areas of 500m x 500m are given in Table 2:

Table 2: Summary results

Frequency	Location variability
237 MHz	3.2 dB
1477 MHz	4.2 dB
3430 MHz	4.5 dB

These values are plotted below for comparison with other reported results. The upper (dashed) curve plots the original expression for location variability given in ITU-R P.1546, while the lower (solid) curve plots the revised version adopted in the revision of the Recommendation in 1996. The revised curve still gives location variability values higher than the empirical results presented here, but in line with the generality of comparable measurements.

It is of interest to note that the variability of raw data covering areas of between half- and one-square-km was typically 0-0.5dB greater than that of the quarter-square-km results.

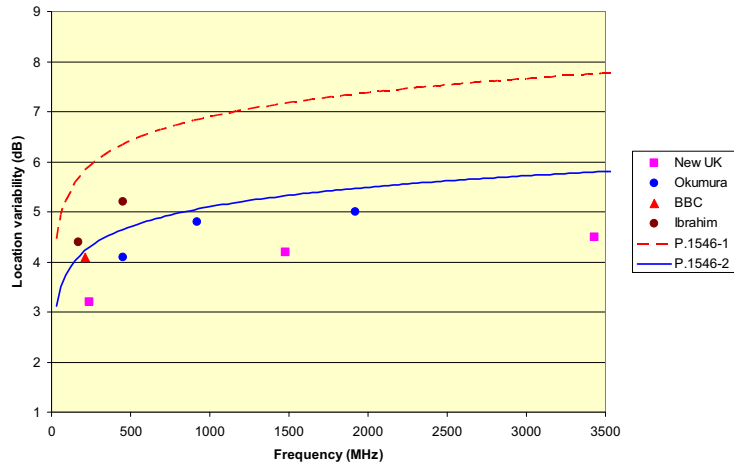


Figure 8: Location variability in P.1546 compared with measurement

4. Conclusions

This paper has sought to emphasise the differences in definitions and measurement methods that have been applied to the apparently simple concept of ‘location variability’. Many of the figures often quoted either include an element of multipath fading, or relate to variability over areas larger than may be appropriate. As a consequence, such values overestimate location variability. An experimental campaign in urban areas of England has provided material which formed the basis of a recent revision of ITU-R Recommendation P.1546.

The author wishes to thank Ofcom (formerly the Radiocommunications Agency), who funded the work described in this paper.

5. References

- [1] Clarke, R.H., “A statistical theory of mobile-radio reception”, *Bell system technical journal*, Vol.47, July-August 1968, pp.957–1000.
- [2] Egli, J.J., “Radio propagation above 40Mc over irregular terrain”, *Proc. IRE*, 1383–91, 1957
- [3] Black, D.M. and Reudink, D.O., “Some characteristics of mobile radio propagation at 836 MHz in the Philadelphia area”, *IEEE Trans on Veh. Tech*, VT-31, No.2, May 1972
- [4] Jakes, W.C., “*Microwave Mobile Communications*”, IEEE press reprint 1994.
- [5] Lee W.C.-Y., “Estimate of local average power of a mobile radio signal”, *IEE Trans on Veh. Tech*, VT-34(1), 22-7.
- [6] “Experimental work to assist in planning a DAB single-frequency network”, Maddocks, M.C.D., Pullen, I.R. and Lee, M.B.R. *IEE Colloquium digest 1993/043*, pp.9/1 to 9/8
- [7] “Digital Audio Broadcasting: Measuring techniques and coverage performance for a medium power VHF single frequency network”, Maddocks, M.C.D., Pullen, I.R. and Green, J.A., *BBC R&D report 1995/2*. 1995.
- [8] Middleton, J. “Prediction of VHF/UHF mobile reception in urban areas”, *BBC Research Department Report, RD1989/11*, 1989.
- [9] Okumura, Y et al., “Field strength and its variability in VHF and UHF land mobile radio service”, *Rev. Electr. Commun. Lab.*, 16, pp.825–73, 1968.
- [10] Parsons, J.D. and Ibrahim, M.F., “Signal strength prediction in Urban areas. Part 2: signal variability”, *Proc. IEE part F*, 130(5), 385–91, 1983.
- [11] Reudink, D.O., “Comparison of radio transmission at X-band frequencies in suburban and urban areas”, *IEEE Trans on AP*, 20, p.470, 1972
- [12] Saunders, S.R., “*Antennas and Propagation for Wireless Communication Systems*”, Wiley, Chichester, 1999.
- [13] Rappaport, T.S., “*Wireless communications: Principles and Practice*”, Prentice-Hall, 1996.
- [14] “Receiving location variation for broadband digital systems in Bands IV and V”, *ITU-R contribution 3k/18 (study period 1996-1997)*, Geneva, June 1997
- [15] Jakes, W.C., “*Microwave Mobile Communications*”, IEEE press reprint 1994.

Wave Propagation over Irregular and Inhomogeneous Terrain

Mauro S. Assis

Fluminense Federal University - Rua Coelho Neto, 17 apt. 301 – Rio de Janeiro – RJ,
22231-110 – Brazil - msassis@openlink.com.br

Jorge L. Cerqueira

Military Institute of Engineering - Rua Pinto Guedes 140 apt. 303 – Rio de Janeiro – RJ,
20511-320 – Brazil - jlcerq@ime.eb.br

Abstract

This paper deals with problem of radio wave over irregular and inhomogeneous earth. Two solutions based on the Green's theorem are described. An integral equation solved by numerical methods and a generalization of the classical residue series approach. Advantages and limitations of each solution are pointed out.

1. Introduction

When terrain irregularities and non-homogeneities are known, the field strength may be put into the form of an integral equation derived either by the compensation theorem or Green's theorem. It should be pointed out that these two approaches are equivalent, leading to the same mathematical formulation of a given problem. This paper describes two solutions based on the Green's theorem, the integral equation [1] and the multiple residue series [2].

In the integral equation derived by Hufford [1], the terrain is represented by a completely arbitrary profile along the great circle path and the electrical properties of the medium can vary continuously. In other words, it can deal with complicated variations of terrain without introducing approximations based on the geometry of problem. However, this solution has some limitations such as the need of a great deal of computer storage, a numerical instability for high frequencies and to the fact that steep slopes and cliffs cannot be included.

Furutsu [2] has developed a theory of wave propagation over a multi-section terrain. Each section can have different electrical properties and different heights and the transmitter and receiver can be elevated. This theory can be used to model mixed paths, ridges, bluffs, coastlines with cliffs, islands, etc. In this context, Furutsu approach complements the integral solution. A practical limitation refers to the number of sections to be modeled before the method becomes too complex.

2. Integral Equation

Refinements to the original Hufford integral were introduced by Ott [3,4]. Following Ott notation, the field $f(x)$ normalized to twice the free-space value is given by,

$$f(x) = W(x,0) - \sqrt{\frac{j}{\lambda_0}} \int_0^x f(\xi) e^{-jkW(x,\xi)} \left\{ y'(\xi) W(x,\xi) - \frac{y(x) - y(\xi)}{x - \xi} + [\Delta(\xi) - \Delta_r] W(x,\xi) \right\} \left[\frac{x}{\xi(x - \xi)} \right]^{1/2} d\xi \quad (1)$$

where x , ξ , $y(x)$ and $y(\xi)$ are defined in Fig. 1. The term $y'(\xi) = d[y(\xi)]/d\xi$ is an indication of the terrain slope. The factor $[\Delta(\xi) - \Delta_r]$ arise in mixed-path problems, being zero for a homogeneous path. The function $\Delta(\xi)$ is the normalized surface impedance along the path, with Δ_r its value at the transmitting antenna. As shown below, the normalized surface impedance depends on the values of ϵ_r (relativity permittivity of the Earth), s (conductivity of the Earth) and frequency [5]. The remaining factors in (1) are defined by,

$$w(x,\xi) = \frac{[y(x) - y(\xi)]^2}{2(x - \xi)} + \frac{y^2(\xi)}{2\xi} - \frac{y^2(x)}{2x}$$

$$W(x, \xi) = 1 - j\sqrt{\pi p} e^{-u} \operatorname{erfc}(ju^{1/2})$$

$$p = -jk_0 \Delta^2 (x - \xi) / 2; \quad u = p \left\{ 1 - \frac{y(x) - y(\xi)}{\Delta(x - \xi)} \right\}^2; \quad \xi < x;$$

$$p = -jk_0 \Delta^2 (x - \xi) / 2; \quad u = p \left\{ 1 - \frac{y(x) - y(\xi)}{\Delta(x - \xi)} \right\}^2; \quad \xi < x;$$

$$\Delta = \begin{cases} \frac{\sqrt{\eta - 1}}{\eta} & \text{- vertical polarization} \\ \sqrt{\eta - 1} & \text{- horizontal polarization} \end{cases}$$

$$\eta = \varepsilon_r - j60\sigma\lambda$$

$$\operatorname{erfc}(x) = \frac{2}{\sqrt{\pi}} \int_x^\infty e^{-u^2} du \text{ - complementary error function.}$$

As shown in Figure 1, the transmitter at zero height serves as a reference height. $W(x, \xi)$ is the flat Earth attenuation function. The integral equation computes the relative field $f(x)$ at a point x along the path in terms of its value $f(\xi)$ at all previous points along the path. The numerical solution of the integral equation is obtained by dividing the path into discrete intervals. The field $f(\xi)$ must be known initially at a series of discrete points. The field at the next very point is determined by fitting a second order polynomial in each of the intervals, and then performing a numerical integration. More details are available in Ott et al. [5] and DeMinco [6]. One example is given in Figure 2 [7], which shows the profile corresponding to path 13.6 km long operating in the frequency of 10.254 MHz. Figure 3 compares the evaluation of field intensity for different horizontal resolutions (Δx). As expected, as Δx decreases the computer time increases. On the other hand, the measured point (x) at a distance of 13.6 km shows a better agreement with $\Delta x = 50$ m. This value is about 1.6λ and proves that the maximum Δx is around one wavelength.

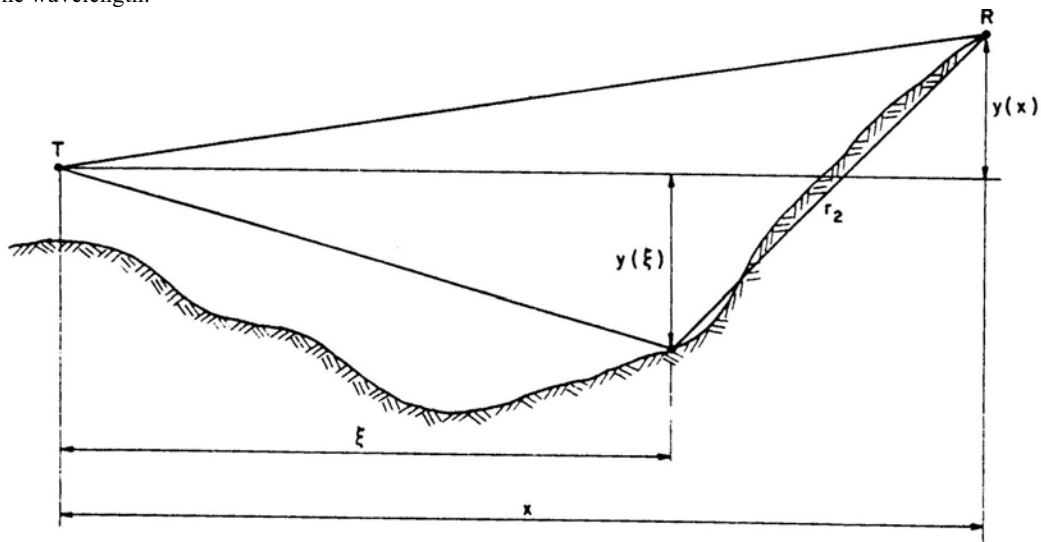


Figure 1. Geometry for the integral equation

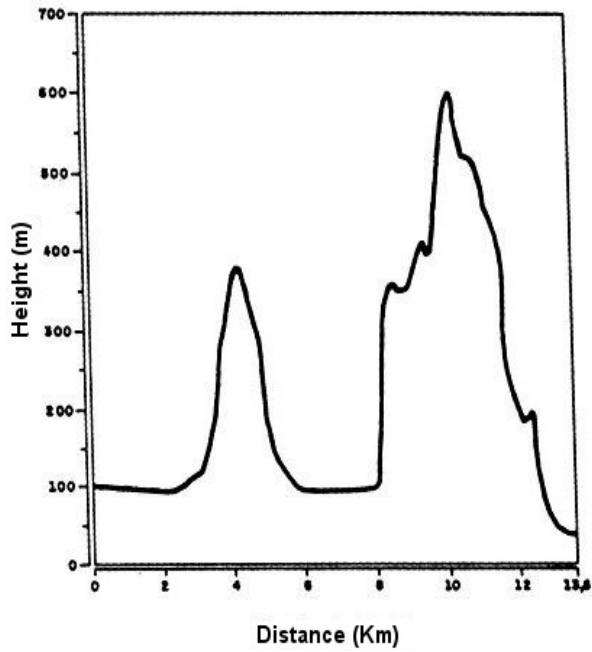


Figure 2. Path profile for integral equation.

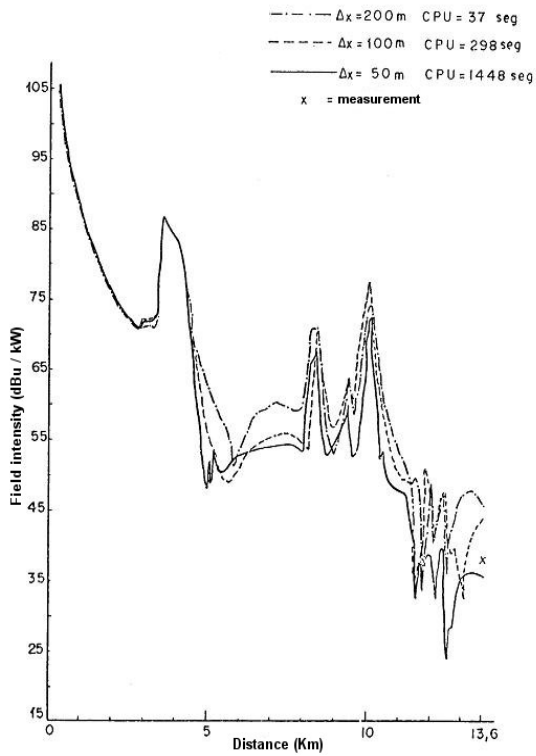


Figure 3: Integral equation – computer time and measured point.

Under the practical point of view, the diffraction by terrain is normally considered for two specific models [8]: diffraction over a smooth spherical earth and diffraction by single or isolated obstacles. In spite of solving important engineering problems, these models do not provide a general solution for the propagation over a rolling terrain or when the terrain discontinuities should be taken into account. This question is being considered in the working program of the ITU-R Rapporteur Group 3J-5/1 [9]. In this context, it should be mentioned that the field intensity in the profile of Figure 3 was also calculated by the Assis method [10] for multiple diffraction. The numerical result was the same as the one corresponding to the integral equation. On the other hand, as it was shown by Ott and Berry [3], for the case of a smooth and homogeneous Earth there is a close agreement between values evaluated by the integral equation (1) and by the residue series [11]. Consequently, the integral equation can be seen as the bridge for connecting the above limiting cases.

3. Furutsu solution

This solution is based on a general model in which the terrain changes discontinuously in both height and electrical properties along the propagation path as shown in Fig. 4. With the transmitter and receiver located, respectively, at points x_1 and x_{n+1} , the attenuation (A) relative to free space is given by

$$A = \sum_{t_n, t_{(n-2)}, \dots, t_4, t_2} \sqrt{(c_n + c_{n-2} + \dots + c_4 + c_2) f_{tn}(y_{n+1, n})} A_{tn}(c_n) T_{tnt(n-2)}^{n-1}(c_{n-2}) \dots T_{t6, t4}^5(c_3) T_{t4, t2}^3(c_2) f_{t2}(y_{12}) \quad (2)$$

where,

$$A_{tn}(c_n) = \sqrt{\pi}(t_n - q_n^2)^{-1} \exp\{-j[c_n(t_n + y_n) + \pi/4]\}$$

$$T_{tnt(n-2)}^{(n-1)}(c_{n-2}) = (y_n - y_{n-2} + t_n - t_{n-2})^{-1} (t_{n-2} - q_{n-2}^2)^{-1} \cdot \exp[-jc_{n-2}(t_{n-2} + y_{n-2})].$$

$$[q_n f'_{tn}(y_{(n-1)n}) f_{n-2}(y_{(n-1)(n-2)}) - q_{n-2} f_{tn}(y_{(n-1)n}) f'_{(n-2)}(y_{(n-1)(n-2)})]$$

$$c_n = \left(\frac{k_o a_e}{2}\right)^{1/3} \frac{r_n}{a_e}; \quad y_1 = \left(\frac{2}{k_o a_e}\right)^{1/3} k_o(z_1 - a); \quad y_{n+1} = \left(\frac{2}{k_o a_e}\right)^{1/3} k_o(z_{n+1} - a)$$

$$y_n = \left(\frac{2}{k_o a}\right)^{1/3} k_o(a_n - a); \quad n = 2, 3, 4, \dots \quad y_{nm} = y_n - y_m$$

$$f_{t_n}(y) = \frac{w(t_n - y)}{w(t_n)}; \quad f'_{t_n}(y) = \frac{w'(t_n - y)}{w'(t_n)}$$

$$w(-t) = \left(\frac{\pi t}{3}\right)^{1/2} e^{-j2\pi/3} H_{1/3}^{(2)}\left(\frac{2t^{3/2}}{3}\right)$$

$w(t)$ – Airy function; $H_{1/3}^{(2)}$ – Hankel function of 2nd kind

$w''(t) - tw(t) = 0$ - Airy equation

$$q_n = \begin{cases} -j \left(\frac{k_o a_e}{2}\right)^{1/3} \frac{k_o^2}{k_n^2} \sqrt{\frac{k_n^2}{k_o^2} - 1} & \text{- vertical polarization} \\ -j \left(\frac{k_o a_e}{2}\right)^{1/3} \sqrt{\frac{k_n^2}{k_o^2} - 1} & \text{- horizontal polarization} \end{cases};$$

$$k_o = 2\pi / \lambda; \quad k_n = k_o \sqrt{\epsilon_{rn} - j60\sigma_n \lambda}$$

λ - wavelength; ϵ_{rn} and σ_{rn} are, respectively, the relative permittivity and conductivity of terrain section n and t_n are roots of the equation

$$w'(t_n) - q_n w(t_n) = 0$$

Equation (2) can be used to derive expressions for several special cases such as, smooth terrain (homogenous or not), ridges, bluffs and so on. Numerical examples for these geometries are given in Furutsu papers [2;12-14].

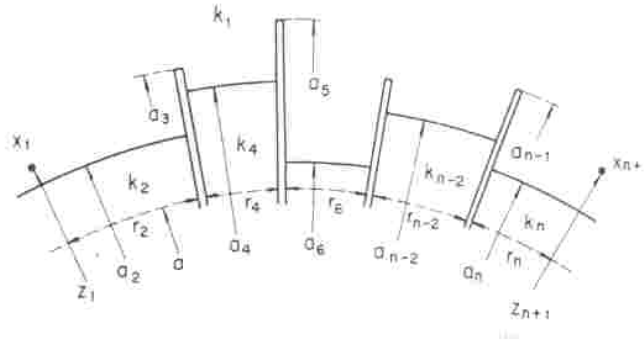


Figure 4. The general case of a terrain consisting of several sections.

4. Concluding remarks

In spite of its complexity, the integral equation described in this paper provides a general solution to the problem of radio wave propagation over an irregular and inhomogeneous terrain. It attends the requirement to be a connection between the limiting cases of propagation over a smooth earth and the diffraction by several isolated obstacles. Additionally, it has an easy physical interpretation where the terms corresponding to terrain slope and terrain non-homogeneities are clearly defined. The main limitations of this solution refer to the computation time, numerical instability at high frequencies and to the fact that steep slopes cannot be included.

The computer algorithm (called Wagner) developed by Ott [3,4] becomes numerically instable for frequencies above 20 MHz. This limit was extended up by Ott [15] to 100 MHz through a modification to Wagner algorithm called Ring. On the hand, in paper by Lipa and Barrick [16] it was proposed a method to circumvent the numerical instability at steep slopes. In this case (ridges, bluffs, cliffs, etc.), Furutsu solution can also be used as a complement to the integral equation. The only restriction is the number of sections to be modeled before the method becomes too complex. For instance, numerical calculations evaluated by Furutsu [2;12-14] are limited to three sections. Anyway, considering that the solutions described here are quite rigorous, they constitute two powerful tools to solve the problem of radio wave propagation. An effort should be done to overcome the above limitations.

5. References

- [1] Hufford, G., "An integral equation approach to the problem of wave propagation over an irregular surface", Quarterly Applied Mathematics, vol. 9, n.4, pp. 391-, 1952;
- [2] Furutsu, K., "A systematic theory of wave propagation over irregular terrain", Radio Science, vol. 17, n.5, pp1037-1059, May, 1982;
- [3] Ott, R.H. and L. A. Berry, "An alternative integral equation for propagation over irregular terrain", Radio Science, vol. 5, n. 5, pp.767-771, May, 1970;
- [4] Ott, R.H., "An alternative integral equation for propagation over irregular terrain, 2", Radio Science, vol. 6, n.4, pp. 429-435, April, 1971;
- [5] Ott, R.H., L.E. Vogler and G.H. Hufford, "Ground-wave propagation over irregular inhomogeneous terrain: Comparisons of calculations and measurements", IEEE Trans. on Antennas and Propagation, volume AP-37, n.2, pp.283-285, March, 1979;
- [6] DeMinco, N. "Propagation prediction techniques and antenna modeling (150 to 1705 kHz) for intelligent transportation systems (ITS) broadcast applications, IEEE Antennas and Propagation Magazine, vol. 42, n.4, pp. 9-34, August 2000;

- [7] Assis, M.S. and J.L. Cerqueira, "Diffraction by terrain irregularities", International Conference on Radio Science - ICRS 2008, Jodhpur, India, February, 2008;
- [8] UIT-R, "Propagation by diffraction", Recommendation ITU-R P.526-9, Geneva, 2005;
- [9] UIT-R, "Vegetation and obstacle diffraction", Annex to Doc.3J/193 – WP 3 Chairman Report, Geneva 2007;
- [10] Assis, M.S., "A simplified solution to the problem of multiple diffraction over rounded obstacles", IEEE Transactions on Antennas and Propagation, volume AP-19, n.2, pp. 291-295, March, 1971;
- [11] Bremmer, H., "Terrestrial Radio Waves", Elsevier Publishing Company, Amsterdam, 1949;
- [12] Furutsu, K., "On the theory of radio wave propagation over inhomogeneous earth", Journal of Research of the NBS, volume 67D, n.1, pp. 39-62, January-February, 1963;
- [13] Furutsu, K., R.E. Wilkerson and R.F. Hartmann, "Some numerical results based on the theory of radio wave propagation over inhomogeneous earth", Journal of Research of the NBS, volume 68D, n.7, pp. 827-846, July, 1964;
- [14] Furutsu, K. and K. Wilkerson, "Obstacle gain in radio-wave propagation over inhomogeneous earth", Proceedings of the IEE, volume 117, n.5, pp. 887-893, May, 1970;
- [15] Ott, R.H., "RING: An integral equation algorithm for HF-VHF radio wave propagation over irregular, inhomogeneous terrain", Radio Science, volume 27, n.6, pp. 867-882, November-December, 1992;
- [16] Lipa, B.L. and D.E. Barrick, "Improved numerical solution of Ott's integral for HF ground wave attenuation", IEEE Transactions on Antennas and Propagation, volume 37, n.2, pp.260-262, February, 1989.

Anomalies in the Application of the Cascaded Knife-Edge Diffraction Model

Carol Wilson
CSIRO ICT Centre
Carol.Wilson@csiro.au

Steve Salamon
Telstra Radio Transport
Steve.Salamon@team.telstra.com

Abstract

Multiple knife-edge diffraction models are commonly used to predict radiowave propagation over irregular terrain. The ITU-R Recommendation P.526 is based on a modification of the Deygout cascaded knife-edge method. Software application of this method over a region in Western Australia has revealed anomalous behaviour where two nearly identical paths give quite different results, or where significant terrain points are ignored. The extent and causes of these anomalies are discussed in comparison to other models from the literature, and a proposed new method, described in a companion paper, is assessed for the problematic paths.

1. Introduction

Many radio applications, such as broadcasting planning or cellular radio system design, require the prediction of propagation loss over long distances or over wide geographic areas. The analysis in this paper arose from the evaluation of potential interference to the Murchison Radio-astronomy Observatory (MRO) site which has been proposed by Australia as the location for the Square Kilometre Array. [1] The sensitivity of radioastronomy observations requires that interference must be assessed from long distances over paths with high propagation loss.

For paths at or beyond the radio horizon, diffraction over terrain is a major propagation mechanism. ITU-R Recommendation P.526 [2] provides several diffraction prediction methods, of which the most general is the cascaded knife-edge method. This method is further used in Recommendations ITU-R P.452 [3], for calculating interference between terrestrial systems, and P.1812 [4], for predicting coverage over an area. It is based on the work of Deygout in 1966 [5], but instead of his 1991 correction for two edges [6], a different empirical correction for at most three edges is used.

The availability of digital databases has made it possible to use the characteristics of a specific site in diffraction calculations with software which selects the edges, calculates the loss at each edge, and combines the results. However, in automating the process, there is scope for anomalies which would not arise if edges were selected manually by viewing the terrain profile. In his 1991 paper [6], Deygout himself noted that “As long as one deals with maps and obtains full control of the profile by a glance, ... one selects only a few hills... It is a fact, however, that more extensive use of terrain databases can lead to unacceptable evaluation errors.”

Recommendations P.526 notes that calculation with different atmospheric parameters can introduce discontinuities in diffraction loss when different terrain points are selected as the principal diffraction edge [2]. The analysis of this paper revealed similar discontinuities with a small change in the location of one end of the path. For atmospheric variability, the median condition acts as a convenient reference, but there is no obvious corresponding reference for terrain variations.

A second anomaly arises because the algorithm selects a main edge and, at most, one other edge on either side of the main obstacle. When there is a major obstacle that has more than one significant terrain feature on one side of it, key terrain points are ignored.

2. Cascaded knife-edge diffraction model

The details of the cascaded knife-edge diffraction method are given in [2]. A terrain profile is extracted from a digital database; a point spacing of 250 metres is typical and is used in the analysis of this paper. At each profile point, a height h is calculated, representing the height of the terrain above a line joining the first and last point of the profile and accounting for earth curvature. Using the same unit for all variables, where h_n is the n^{th} terrain point, d_{ab} is the distance from the first point of the profile to the last point, d_{an} and d_{nb} are the distances from the n^{th} point to the first and last point, respectively, and r_e is the effective earth radius, h is calculated as:

$$h = h_n + [d_{an} d_{nb} / 2 r_e] - [(h_a d_{nb} + h_b d_{an}) / d_{ab}] \quad (1)$$

The dimensionless diffraction parameter v is then calculated for wavelength λ (still in self-consistent units):

$$v_n = h \sqrt{2 d_{ab} / \lambda d_{an} d_{nb}} \quad (2)$$

The point with the highest value of v is termed the principal edge, p , and the v value is v_p . If v_p is greater than -0.78 , the process is repeated twice, once from the beginning of the path to p , and then from p to the end of the path. (If v_p is less than -0.78 , diffraction loss is negligible and the calculation can be abandoned.) The points with the largest value of v on either side of the principal edge are termed “auxiliary edges” with values v_t and v_r . Diffraction is then calculated for the path of length D (km) by:

$$L = J(v_p) + \{1 - \exp(-J(v_p)/6)\} [J(v_t) + J(v_r) + 10 + 0.04D] \quad (3)$$

where $J(v)$ is approximated (for v greater than -0.78) by:

$$J(v) = 6.9 + 20 \log \left(\sqrt{(v - 0.1)^2 + 1} + v - 0.1 \right) \quad \text{dB} \quad (4)$$

3. Anomalous behaviour on nearly identical paths

To evaluate interference at the MRO site, diffraction loss was calculated using Matlab from points 65 km away in all directions, at frequencies from 100 MHz to 25 GHz. The same effects were found at all frequencies, but the values at 2.3 GHz are used in the example below. The median value of the effective earth radius was used. Initial calculations took points 0.5 degrees apart, that is, paths with a common centre and endpoints separated by about 560 metres. Discontinuities where the loss changed by 10, 20 or (in one case) 28 dB between adjacent paths occurred in several directions.

Two paths, one at bearing 17.73° (clockwise from North) and one at 17.74° , were selected for closer analysis. The endpoints are about 11 metres apart, significantly closer than the 250 m resolution of the underlying terrain database. The maximum difference between (interpolated) terrain heights is 186 mm; the average difference is 20 mm. The profiles are shown in Figure 1.

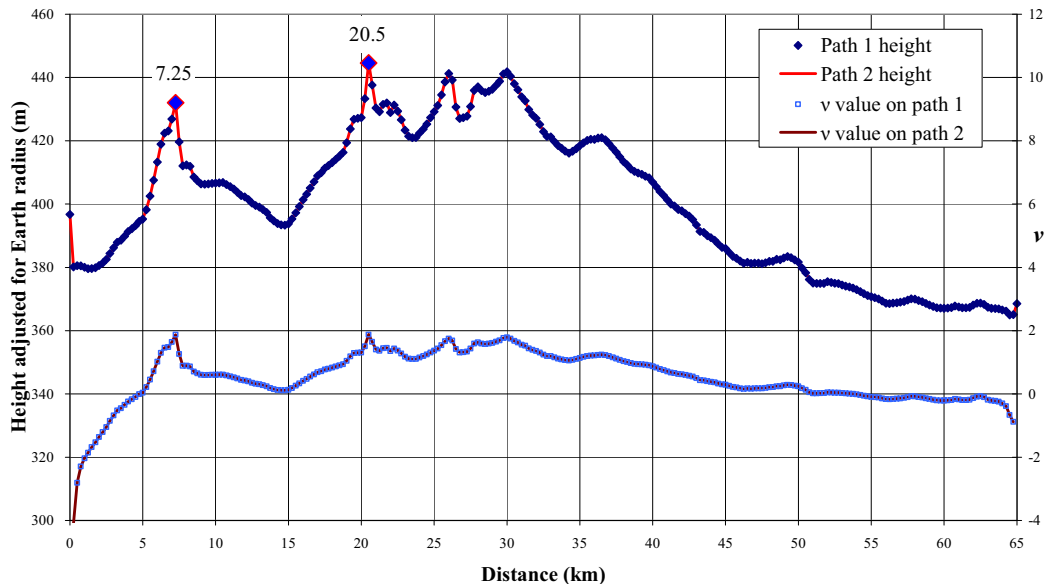


Figure 1. Adjacent path profiles (adjusted for median Earth radius) and v at 2.3 GHz

A visual inspection of the profiles in Figure 1 would suggest that the three main obstacles are the peaks at 7.25 km, 20.5 km and 30 km. In Matlab, those three edges are indeed selected on path 2. On path 1, however, the v value at 7.25 km is very slightly more than that at 20.5 km, shifting the principal edge. The left-hand auxiliary edge is then found at 6.5 km but is too low ($v = -0.9$) to contribute to the diffraction loss. The 30 km point is again chosen as the right-hand side auxiliary, and contributes nearly 4 dB more loss than it did on path 2, due to the distance dependence in (2). The diffraction calculations for the two paths are summarised in Table 1.

Table 1. Diffraction values for the two paths (calculated at 2.3 GHz)

	v at 7.25	v at 20.5	Principal edge	$J(v_p)$	Auxiliary edge t	$J(v_t)$	Auxiliary edge r	$J(v_r)$	total loss
Path 1	1.8739	1.8705	7.25 km	19 dB	6.5 km	0 dB	30 km	15 dB	45 dB
Path 2	1.8761	1.8774	20.5 km	19 dB	7.25 km	14 dB	30 km	11 dB	55 dB

In total, the tiny difference in v at the two distances on the two paths leads to a difference of 10 dB in predicted loss. This is mainly due to using only two edges on path 1 (14 dB), compensated slightly by the 4 dB difference in diffraction loss at the right hand (30 km) edge.

The same edge “jumping” occurs at all frequencies. At 100 MHz the discontinuity is 3 dB, while at 1 GHz the difference is 7 dB.

4. Consideration of other multiple-edge models

Diffraction loss on the same two paths was calculated with a number of other prediction methods and over the full frequency range of interest, 100 MHz to 25 GHz. The results are shown in Figure 2.

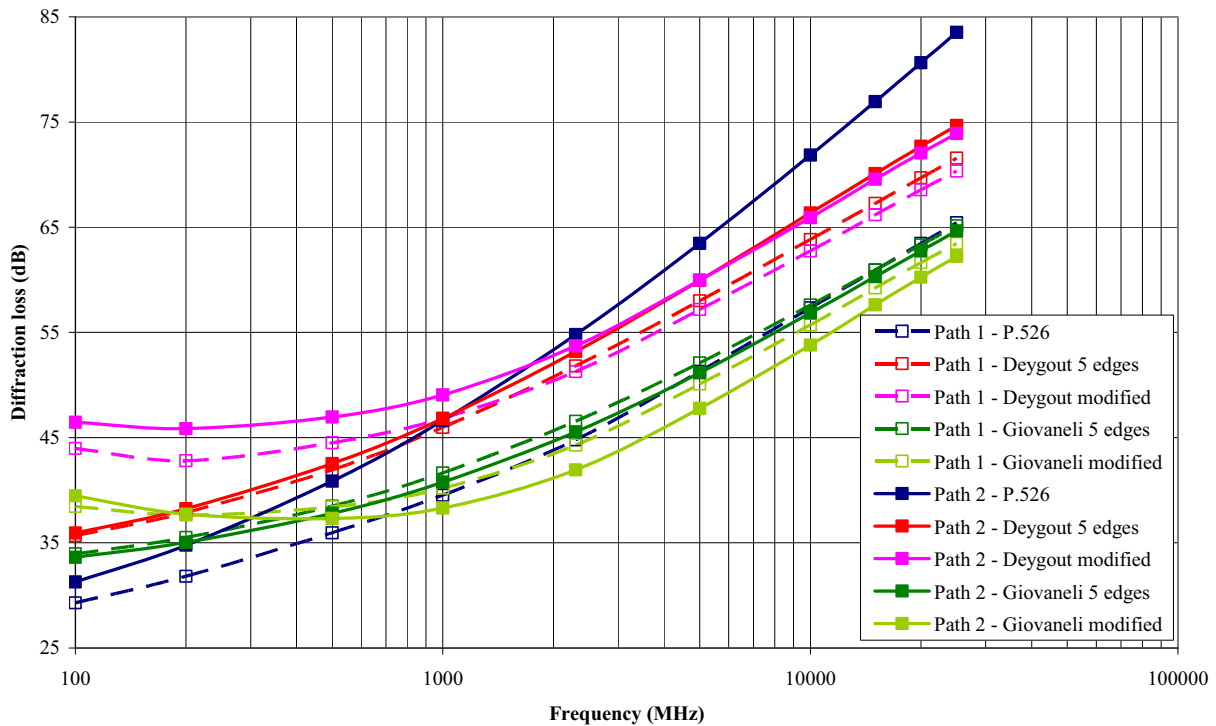


Figure 2. Calculation of diffraction loss on the profiles in Figure 1 with a range of methods

The Deygout calculations (red curves) are performed for the five highest-loss edges. The modified Deygout (pink curves) are calculated by finding the losses from the main and auxiliary obstacles as proposed by Deygout, but combining them as:

$$L = \sum_{i=1}^n J(v_i) \left\{ 1 - \exp(-J(v_{left})/6) \right\} \left\{ 1 - \exp(-J(v_{right})/6) \right\} \quad (5)$$

where $J(v_i)$ is the loss at each edge, and $J(v_{left})$ and $J(v_{right})$ are the losses at the endpoints of each subpath. (If the subpath ends at either the transmitter or receiver, the corresponding $\{1 - \exp(-J(v)/6)\}$ term equals 1.) The modified Deygout method also calculates edges until no further edges are found which contribute loss.

Giovanelli [7] proposed a model where the angle of diffraction at each edge was based on edges on either side, as opposed to Deygout's model which treated the main obstacle as if it were the only obstruction on the path. These are shown, calculated with the 5 highest-diffraction edges as dark green curves in Figure 2. The modified Giovanelli method in Figure 2 (light green curves) uses the same angles as Giovanelli, but with the combination function of equation (5). Again, the modified method uses as many edges as necessary.

Compared to the P.526 method, the modified Deygout and Giovanelli models give a smaller discontinuity between the two paths, although even at higher frequencies, the Giovanelli methods only give a few dB of difference. In general, they give values between the values predicted by Recommendation ITU-R P.526 for the two curves, suggesting that P.526 over-predicts when using three edges and under-predicts with two edges.

5. Missing significant terrain features

A second anomaly in the Recommendation P.526 method occurs when there are two (or more) significant obstructions on one side of the principal edge. Only one of the two obvious obstructions is selected as the auxiliary edge for that side. It is possible that there is nothing of interest on the other side, in which case the P.526 method only uses two edges and, by ignoring the other obstructions on the same side as the first auxiliary edge, is likely to underpredict the diffraction loss of the path.

An example is shown in Figure 3. The point at 33 km is clearly the main obstacle. Following the P.526 algorithm, the left-hand auxiliary edge is found at 32.75 km (adjacent to the main edge) but does not contribute to the overall path loss. The point at 58 km is the other auxiliary edge, and the total path diffraction loss is predicted to be 48 dB. However, the point at 50.75 km is not taken into account, despite being slightly above the line joining the main and auxiliary edges.

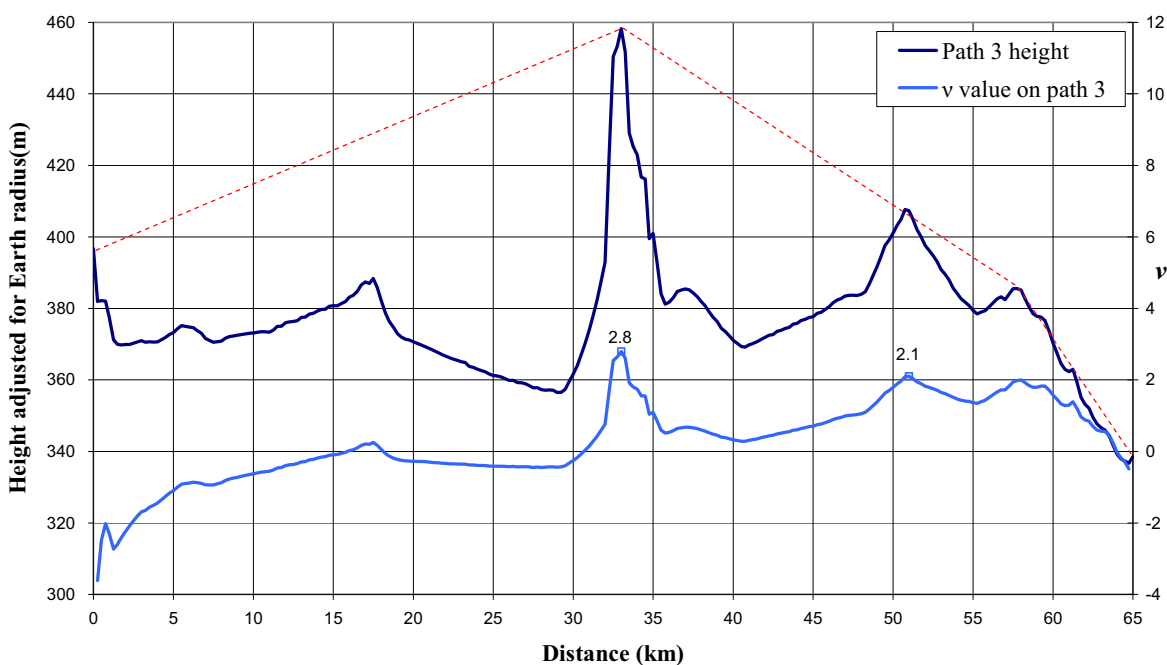


Figure 3. Path profile (adjusted for median Earth radius) and v at 2.3 GHz

Analysis of this path with the models described in Section 4 is shown in Figure 4. By taking more edges into account, the predicted path loss increases significantly compared to the P.526 cascaded knife-edge model.

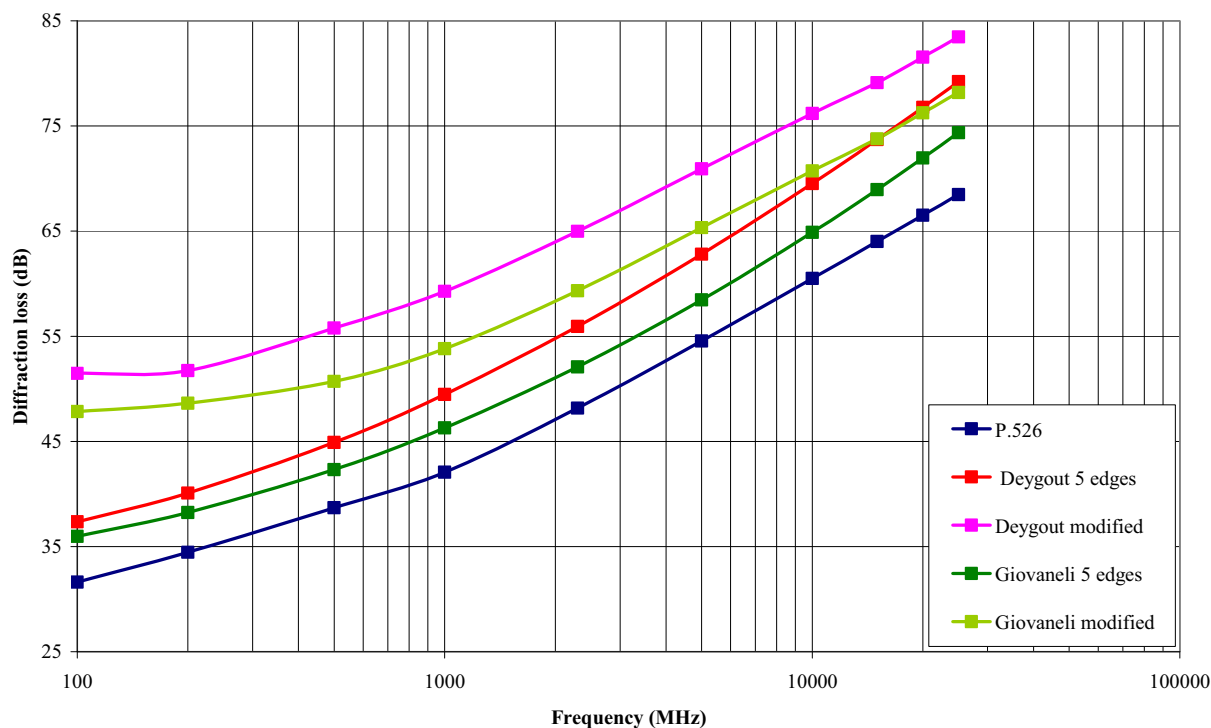


Figure 4. Calculation of diffraction loss on the profile in Figure 3 with a range of methods

6. Solutions

As shown in Figure 2, it appears that increasing the number of edges from 3 to at least 5 reduces the discontinuity between two nearly identical paths. This would also overcome the shortcoming described in Section 5 of only having one auxiliary edge on each side of the main obstacle. Figure 2 also suggests that the modified Deygout and modified Giovaneli predict higher loss at lower frequencies compared to their unmodified versions, but slightly lower loss at higher frequencies. In Figure 4, the modified methods give significantly higher losses than the corresponding original method. It is therefore necessary to compare the predictions against measurements across the frequency range to evaluate the overall accuracy of the method.

Another approach, known as a slack-string method, will be described in a companion paper [8] and effectively eliminates the discontinuity between the two paths shown in Figure 1. As it also calculates all edges contributing to the overall loss, it eliminates the potential for missing edges described in Section 5.

Figure 5 shows the diffraction loss on the paths illustrated in Figure 1, using the P.526 method, the simple slack-string method, and a modified slack-string method (where “modified” again refers to using equation (5)). With both the slack-string and modified slack-string method, the difference between the two paths is insignificant (less than 0.1 dB). It is also noticeable that the modified slack-string method, despite taking many edges into account, predicts a lower overall loss than the P.526 method when only two edges were used.

Figure 6 shows the slack-string methods applied to the profile of Figure 3. Here it is noted that the slack-string methods both predict a higher loss than the P.526 method above 1 GHz, while below 1 GHz the modified slack-string method gives a slightly lower predicted loss.

As the site being studied is a remote protected zone for radioastronomy, measurements to evaluate these predictions are not available. However, the related paper [8] will provide a comparison of measurements against the slack-string methods for other locations.

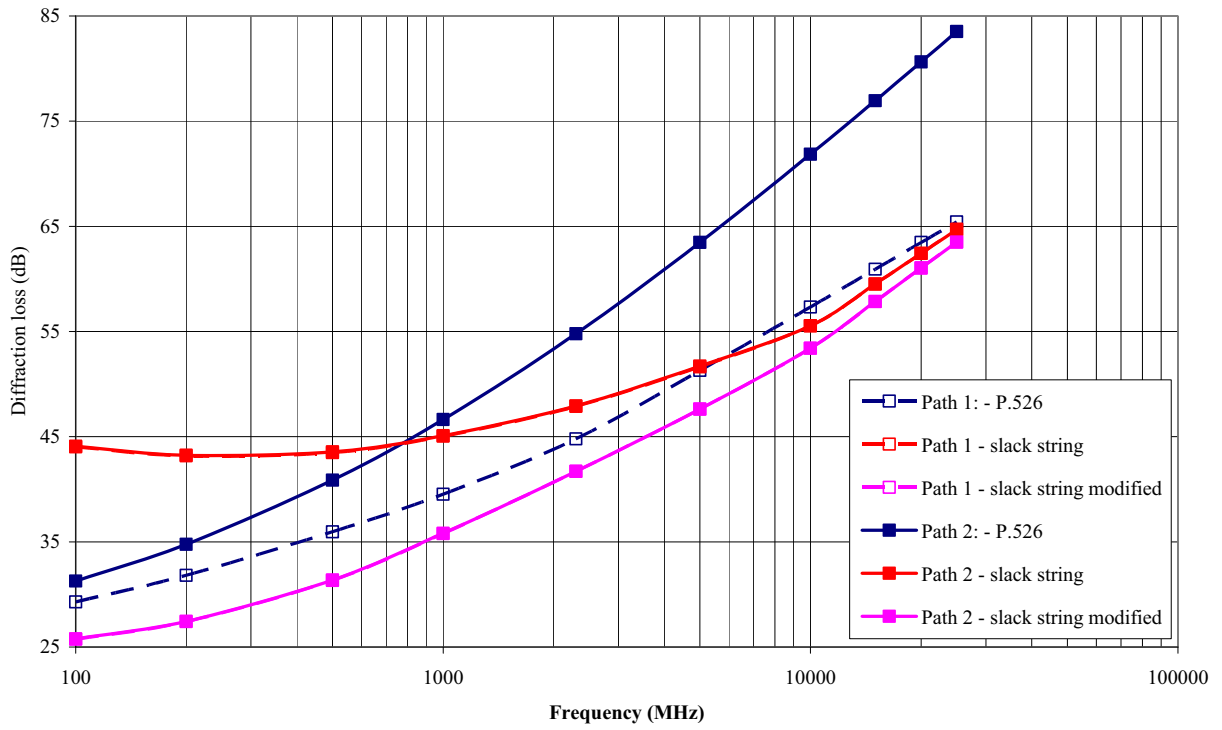


Figure 5. Calculation of diffraction loss on the profiles in Figure 1 with slack-string methods

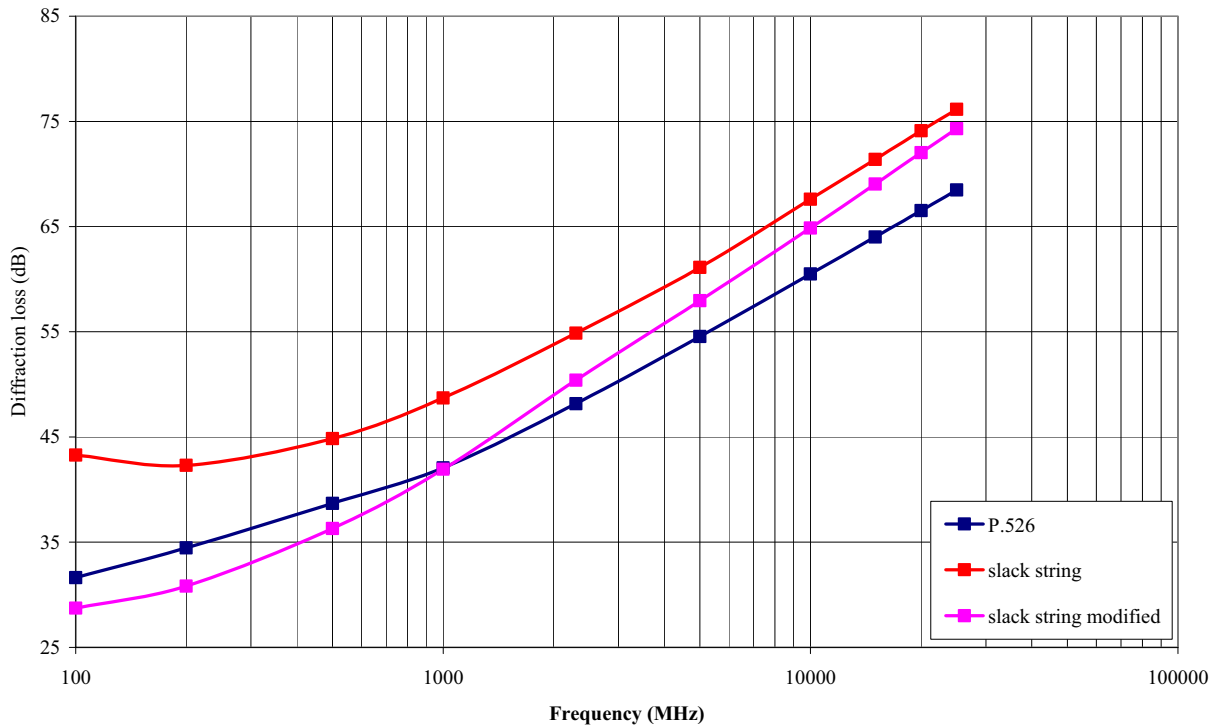


Figure 6. Calculation of diffraction loss on the profile in Figure 3 with slack-string methods

7. Conclusions

For practical prediction of diffraction loss across terrain, both accuracy and consistency are essential. The current Recommendation P.526 cascaded knife-edge model, while simple to implement, exhibits some anomalies when applied to real terrain; these anomalies also call into question the accuracy of this method for certain types of terrain. While it is desirable to maintain the simplicity of the method for the purposes of an ITU-R Recommendation, other possibilities may give equally accurate results while eliminating these anomalies. The additional computational requirements are not excessive in the light of current computing technology.

A promising method using a slack-string approach can overcome the anomalies outlined in this paper and will be presented in a companion paper.

8. Acknowledgement

The authors thank Dr Hajime Suzuki for the development of the P.526 Matlab code, and the Australia Telescope National Facility for encouraging this research.

9. References

- [1] <http://www.skatelescope.org/>
- [2] International Telecommunication Union, "Recommendation ITU-R P.526-10: Propagation by diffraction", Geneva, 2007.
- [3] International Telecommunication Union, "Recommendation ITU-R P.452-12: Prediction procedure for the evaluation of microwave interference between stations on the surface of the Earth at frequencies above about 0.7 GHz", Geneva, 2005.
- [4] International Telecommunication Union, "Recommendation ITU-R P.1812: A path-specific propagation prediction method for point-to-area terrestrial services in the VHF and UHF bands", Geneva, 2007.
- [5] J. Deygout, "Multiple knife-edge diffraction of microwaves," *IEEE Trans Antennas and Propagation*, vol 14, pp 480-489, July 1966.
- [6] J. Deygout, "Correction factor for multiple knife-edge diffraction," *IEEE Trans Antennas and Propagation*, vol 39, pp 1256-1258, August 1991.
- [7] Giovaneli, C. L., "An analysis of simplified solutions for multiple knife-edge diffraction", *IEEE Trans Antennas Propagation*, vol 32, pp. 297-301, March 1984.
- [8] Salamon, S. and Wilson, C, "Reducing Discontinuity in Practical Prediction of Diffraction Loss in Irregular Terrain", *ClimDiff 2008*, paper Diff.15, Boulder Colorado USA, June 2008.

Reducing Discontinuity in Practical Prediction of Diffraction Loss in Irregular Terrain

Steve Salamon
Telstra Radio Transport
Steve.Salamon@team.telstra.com

Carol Wilson
CSIRO ICT Centre
Carol.Wilson@csiro.au

Abstract

Practical radio applications often require prediction of diffraction loss over irregular terrain, using an accurate general algorithm simple enough to be automatically applied. The Recommendation ITU-R P.526 cascaded knife-edge model is found here to perform well compared to 478 measurements on 64 Central Australian paths without tree-cover, but a companion paper studying severely obstructed paths demonstrates this model can suffer severe discontinuities. In the search for a solution to this problem, a multiple knife-edge model has been developed which models the multiple knife-edge problem as an approximately equivalent multiple slit problem. This approach appears to have reduced sensitivity to path profile variation, compared to the P.526 cascaded knife-edge model, Deygout or Giovanelli multiple knife-edge models. It is also tested as an alternative multiple knife-edge basis for the P.526 cascaded cylinder model.

1. Introduction

One of the simplest practical solutions to the multiple knife-edge diffraction problem has been the approximate solution presented by Deygout [1], which first evaluates the diffraction loss of a knife-edge at the point of maximum Fresnel obstruction between transmitter and receiver, ignoring in this loss calculation any effect of lesser obstructions on the diffraction angle. The lesser obstructions are then considered by dividing the path into two sub-paths which are then evaluated in the same way, by assuming an effective point-source at the top of the knife-edge already evaluated.

The ITU-R Recommendation P.526 cascaded knife-edge model [2] limits the Deygout process to evaluating the loss of the main edge $J(v_p)$, and the two most significant edges $J(v_t)$ and $J(v_r)$ on the transmit and receive-side subpaths respectively as described above, and then instead of continuing the evaluation any further by analysing the four sub-paths thus created for more intervening obstructions, it uses the empirical formula (1) to estimate the diffraction loss L_{cke} of the path in terms of these three knife-edge losses and the total path length D (km).

$$L_{cke} = J(v_p) + T[J(v_t) + J(v_r) + C] \quad \text{dB} \quad (1)$$

with $C = 10 + 0.04 \cdot D$ and $T = 1 - \exp[-J(v_p)/6]$

The multiplier T corrects for over-prediction when diffraction angles are small, and constant C empirically accounts for (1) ignoring minor obstructions and assuming the three considered to be ideal knife-edges.

The pessimism of the Deygout model for multiple horizon paths could be described as being due to it ignoring the reduction in diffraction angle of the main obstruction by lesser obstructions that form horizons between it and the antenna at either end of the path. The Deygout model expresses the diffraction parameter v in terms of the height h_k of the obstruction top above the direct ray-line, and the first Fresnel-zone radius R_1 as in (2), but it can also be expressed as in (3) in terms of diffraction angle θ , Fresnel-zone radius R_1 , and wavelength λ .

$$v = \sqrt{2} \cdot h_k / R_1 \quad (2)$$

$$v = \sqrt{2} \cdot \theta R_1 / \lambda \quad (3)$$

The Giovanelli model [3] can be described as using the same methodology as Deygout, evaluating the most

significant obstruction first, then dividing the path into sub-paths, and continuing, but using (3) instead of (2) to determine diffraction parameter v , with diffraction angle θ evaluated to include the effect of any lesser obstructions that reduce the diffraction angle at the main obstruction (figure 1). The obstructions appear here as narrow wedges to clarify the location of their top, but ideal knife-edge obstructions are what is being represented.

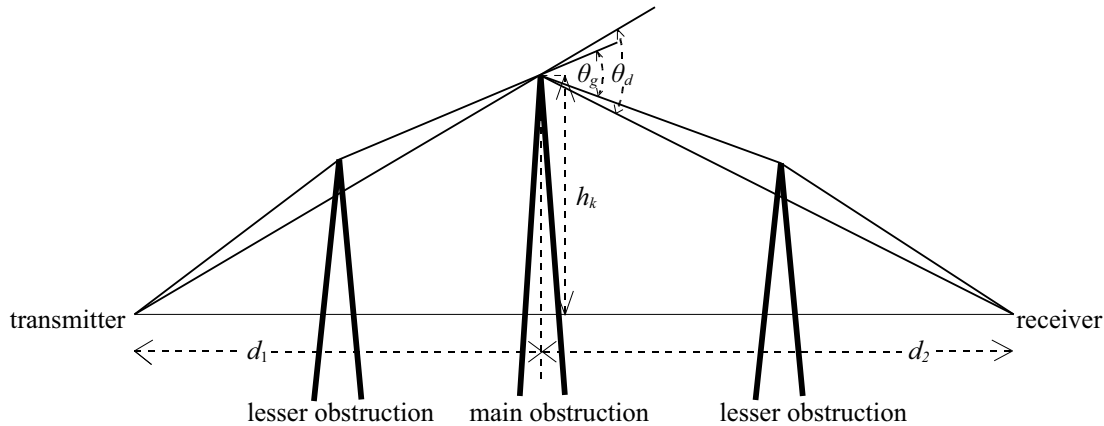


Figure 1. Evaluation of obstruction parameter v , showing difference between Deygout model (θ_d) and Giovaneli model (θ_g), for multiple horizons.

In both models the first Fresnel-zone radius R_1 , given by the usual approximation in (4), is evaluated over the whole path or subpath $d_1 + d_2$.

$$R_1 \approx \sqrt{\frac{\lambda d_1 d_2}{d_1 + d_2}} \quad (4)$$

A companion paper [4] describes how discontinuities in the evaluation of diffraction loss can occur when the order that obstructions are evaluated depends on which obstruction has the greater v , especially if this choice can lead to significant obstructions being ignored. This discontinuity might be avoided by using a model which progressively analyses the path from one end to the other. The best known of these is the Epstein-Peterson model [5] which evaluates the single knife-edge obstruction loss of each obstruction with respect to its immediately adjacent terminal or horizon point, and then adds the individual losses. As all obstructions are analysed with respect to their immediately adjacent horizons or terminals, multiple horizon paths are not analysed from end to end before the path is subdivided, as is done in the Deygout and Giovaneli models. This leads to an under-estimate of loss, which can be accurately compensated for, if all diffraction angles are sufficiently positive, by adding a correction factor [6] calculated from the distances between obstructions.

The P.526 Cascaded Cylinder Model [2] uses this as its multiple knife-edge basis, including all obstructions with positive diffraction angles (non line-of-sight between adjacent horizons or terminals) in the calculation of the correction factor. Obstructions with negative diffraction angles (clear line-of-sight) with respect to adjacent horizons (“string-point obstructions”) do not contribute to the calculation of the correction factor, and only one of them (the most severe one) is evaluated for each sub-path between adjacent “string-point obstructions”.

The Epstein-Peterson model applied in this way eliminates discontinuity that may result from the choice of worst obstruction on the path, as experienced by Deygout or Giovaneli, but introduces a potential discontinuity due to determination of whether an obstruction has a positive diffraction angle or not. Once an obstruction has a positive diffraction angle, it creates two new sub-paths which might each have a lesser obstruction contributing close to 6 dB to the calculated loss.

In this paper, an alternative diffraction model is developed, which replaces the knife-edge diffraction problem by a diffracting slit with approximately equal loss. This is extended to multiple knife-edges, and tested for accuracy of the two knife-edge case, by comparing with the Millington integral solution [7].

All the above models are tested against accurate measurements from a number of Central Australian VHF and UHF paths having path profiles produced from topographic mapping. Sensitivity to profile variation is also

tested, and the new model and the Giovaneli model are both trialled as alternatives to the corrected Epstein-Peterson model, as a multiple knife-edge basis for the P.526 Cascaded Cylinder Model [2].

2. Slack-string knife-edge diffraction model

Diffraction loss $J(v)$ of a knife-edge obstruction with diffraction parameter v can be accurately determined from the Fresnel Integral as

$$J(v) = -20 \log \left| \frac{u_d}{u_0} \right| \quad \text{dB} \quad (5)$$

$$\text{with } \frac{u_d}{u_0} = \sqrt{\left(\frac{j}{2}\right)} \int_v^\infty \exp[-j(\pi/2)t^2] dt \quad (6)$$

but as (6) cannot be expressed in closed form the following asymptotic representation [6] is useful for $v > 1$

$$\left| \frac{u_d}{u_0} \right| \approx \frac{1}{\pi v \sqrt{2}} \quad (7)$$

Alternatively, the diffraction loss of an infinite slit, centred on the line-of-sight, can also be determined from the Fresnel integral. If the slit has height h_s and is at distance d_1 from the transmitter and d_2 from the receiver, and h_s is small compared to the first Fresnel zone radius R_1 defined by (4), then resultant field strength due to diffraction by the slit, can be approximated by

$$\left| \frac{u_d}{u_0} \right| \approx \frac{h_s}{R_1} \quad (8)$$

Equating (7) and (8) gives in (9) the slit height h_s of an infinite slit, at the same direct line-of-sight distances from transmitter and receiver as the knife-edge, whose loss approximates the loss of the knife-edge with parameter v .

$$h_s \approx \frac{R_1}{v \pi \sqrt{2}} = \frac{\lambda}{2 \pi \theta} \quad (9)$$

This approximate effective slit height h_s is only a function of diffraction angle θ and wavelength λ , suggesting the following simple physical model for determining the equivalent loss slit height h_s .

Suppose a string is stretched from transmitter to receiver over the knife-edge, and then relaxed in length by $\lambda/(2\pi)$. If the string immediately above the knife-edge is then pulled upwards until the string is again tight, this point will be $1/\pi$ of a Fresnel zone above the knife-edge top. The n -th Fresnel zone radius, using the usual approximation is

$$R_n \approx \sqrt{\frac{n \lambda d_1 d_2}{d_1 + d_2}} \quad (10)$$

so for large v , using $n = v^2/2$, the increase in string height due to slackening the string by $\lambda/(2\pi)$ is

$$R_n - R_{(n+1/\pi)} \approx \left\{ \sqrt{1 + 1/n\pi} - 1 \right\} \sqrt{\frac{n \lambda d_1 d_2}{d_1 + d_2}} \approx \frac{R_1}{2 \pi \sqrt{n}} = \frac{R_1}{v \pi \sqrt{2}} \quad (11)$$

This is the same as expression (9) for the equivalent slit height h_s .

2.1. Extension to small and negative diffraction angles

Suppose that for small positive, zero, or negative diffraction angles, the upper limit height of the string, increased in length by $\lambda/(2\pi)$ after being stretched tight over the knife-edge, minus the knife-edge height, still defines the approximately equivalent slit height h_s , until the diffraction angle so negative that the slackened string could no longer be pulled down to the top of the knife-edge, and beyond this point h_s is defined as the difference between the upper and lower height limits of the slackened string. This is shown diagrammatically in figure 2.

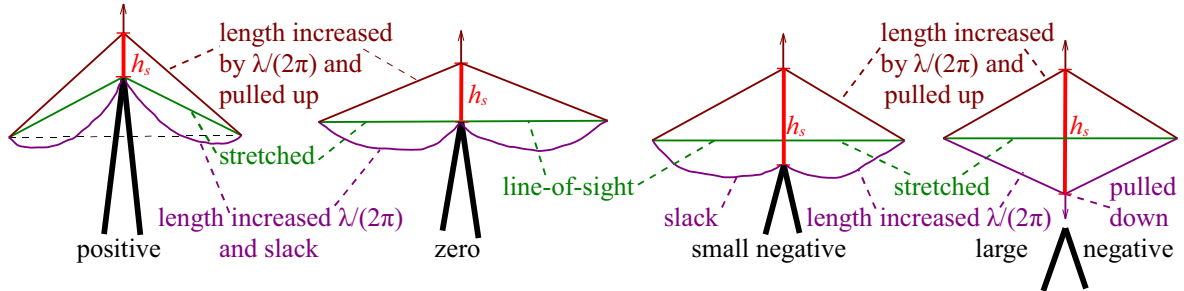


Figure 2. Proposed definition of equivalent slit height for positive, zero and negative diffraction angles.

Fresnel integral analysis of the equivalent slit height h_s as defined above results in predicted loss for the knife-edge as shown in figure 3, as a function of v , compared with the actual Fresnel integral result for knife-edge diffraction. The simple narrow-slit approximation (8) is also shown, as well as the expression at (12), which reproduces the knife-edge loss within 0.3 dB for $v \geq -0.83$, and within 1.2 dB for $v < -0.83$.

$$L = 20\log\left(\frac{R_1}{h_s}\right) + \left[10\log\left(\frac{4}{\pi}\right)\right] \cdot \max\left\{\min\left[\frac{h_s}{0.28 R_1} - 1, 1\right], 0\right\} \quad (12)$$

This is the simple field-strength expression (8), with a correction term for $h_s > 0.28 R_1$ (corresponding to $v < +0.626$ for the knife-edge) which adds a maximum of $10 \cdot \log(4/\pi) = 1.05$ dB to the calculated loss for all $v \leq 0.006$. As expression (12) has good accuracy for the single knife-edge case, it is used for all the following analysis of equivalent slit or multiple slit diffraction loss.

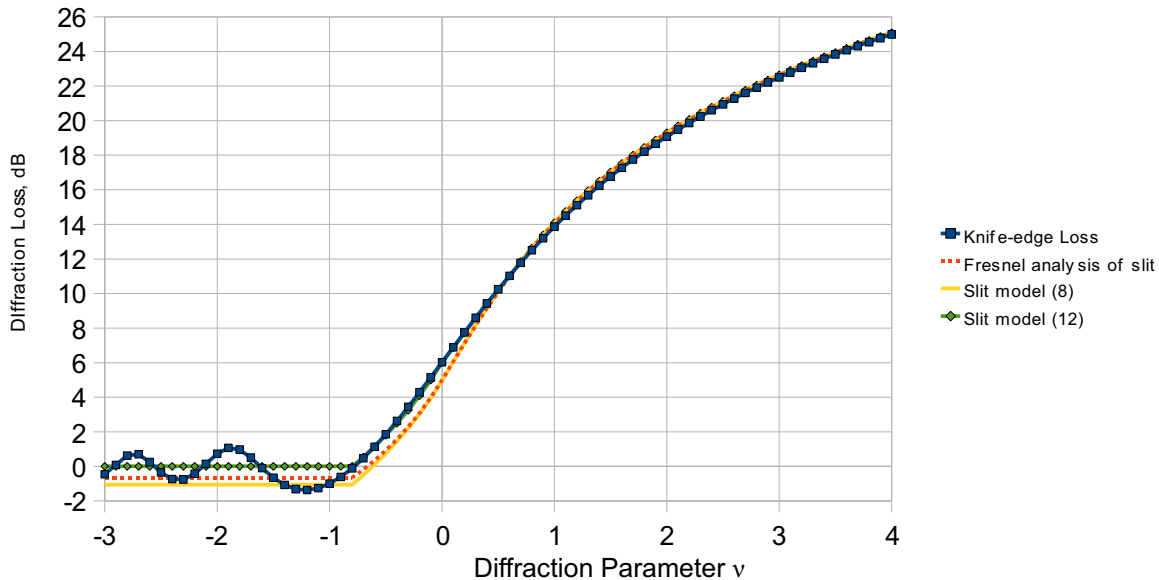


Figure 3. Modelling knife-edge diffraction loss using an equivalent slit.

2.2. Extension to multiple knife-edges

Extension of this model to multiple knife-edges would involve the same process of notionally stretching a string over the whole path between antennas, and then as before increasing the length of the string by $\lambda/(2\pi)$. Above each knife-edge in turn, the string, remaining fixed at the two ends on the antennas, is pulled up as far as it goes, and then down as far as it goes (without going below the obstruction top). This concept is demonstrated in figure 4.

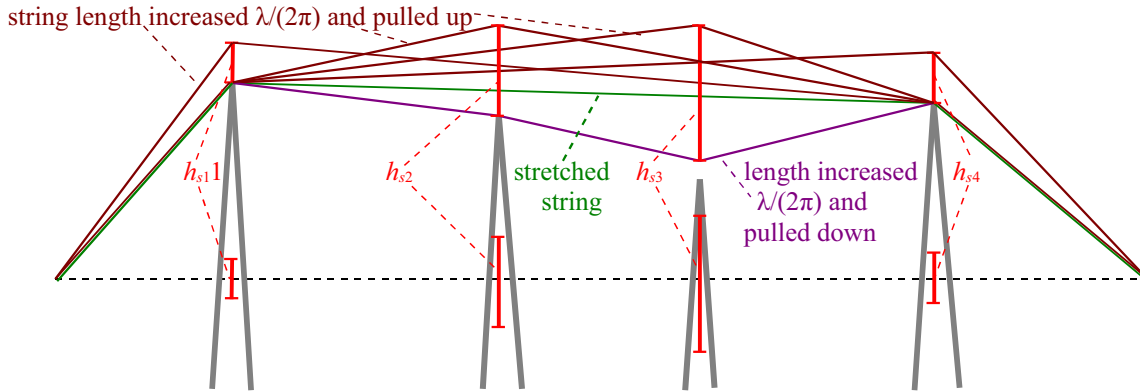


Figure 4. Representing the diffraction loss of multiple knife-edges by multiple slits on line-of-sight (- - -).

The height of an equivalent slit for each knife-edge (at the same distances from each terminal) is then found so that the multiple knife-edge problem can be approximated by a multiple slit problem, with all slits located on the line-of-sight; a relatively simple problem if the heights of the slits are sufficiently small.

Calculation of the height limits of the lengthened string above each knife-edge can be computationally intensive on some paths. Despite this, adherence to the simple physical concept of figure 4 may be important as it would ensure that no discontinuity is introduced into the prediction model by the step of representing the loss of the multiple knife-edge problem by the loss of a multiple slit problem.

Evaluation of the loss of the multiple slit problem is probably most easily performed using a similar approach to the Deygout model [1]. Firstly, identify for the end-to-end path the slit which would on its own cause the greatest diffraction loss, that is, the one with smallest slit height divided by first Fresnel zone radius. Calculate its loss, and then split the path into two sub-paths, assuming a point source at the centre of the slit just calculated. The repeat this process for each sub-path, and continue until all slits causing diffraction loss have been evaluated.

3. Testing double knife-edge predictions

Diffraction by N knife-edges can be accurately determined by the Millington solution [7] by evaluating the Fresnel integral over an N -dimensional volume. For multiple knife-edges on line-of-sight this reduces to the trivial problem of determining the angles between the surfaces forming the bounds of the volume over which the integral is performed, as all the bounds intersect at the origin. An expression for this angle α for the two knife edge case is shown at (13). For three knife-edges, three such angles are calculated using similar expressions.

$$\tan \alpha = \sqrt{\frac{b(a+b+c)}{ac}} \quad (13)$$

with a : distance between terminal 1 and knife-edge 1
 b : distance between the two knife-edges
 c : distance between knife-edge 2 and terminal 2

For multiple knife-edges not on the line-of-sight, the Millington solution becomes much more difficult, but can still be performed for the two knife-edge case without too much trouble. This was done to test the accuracy of the “slack string” diffraction model, and also the Deygout and Giovanelli models.

All three models were tested, both in the original form, and in a modified form to correct over-prediction at small diffraction angles, as described in the companion paper [4].

The Epstein-Peterson model with correction factor [5], as applied as the basis of the P.526 cascaded cylinder model [2] was also tested. When the diffraction angle of the minor obstruction is negative the correction factor is not calculated, and the loss becomes the same as estimated using either Deygout or Giovaneli models.

The above models were tested with one fixed obstruction with diffraction parameter v_1 (as calculated with respect to the two terminals). A second obstruction, with diffraction parameter v_2 (again calculated with respect to the two terminals), is placed at a fixed distance to give α as defined in (14) a value of $\pi/4$ radians (45 degrees). Figures 5 and 6 show the effect of varying v_2 with values of v_1 of 0.5 and 4 respectively.

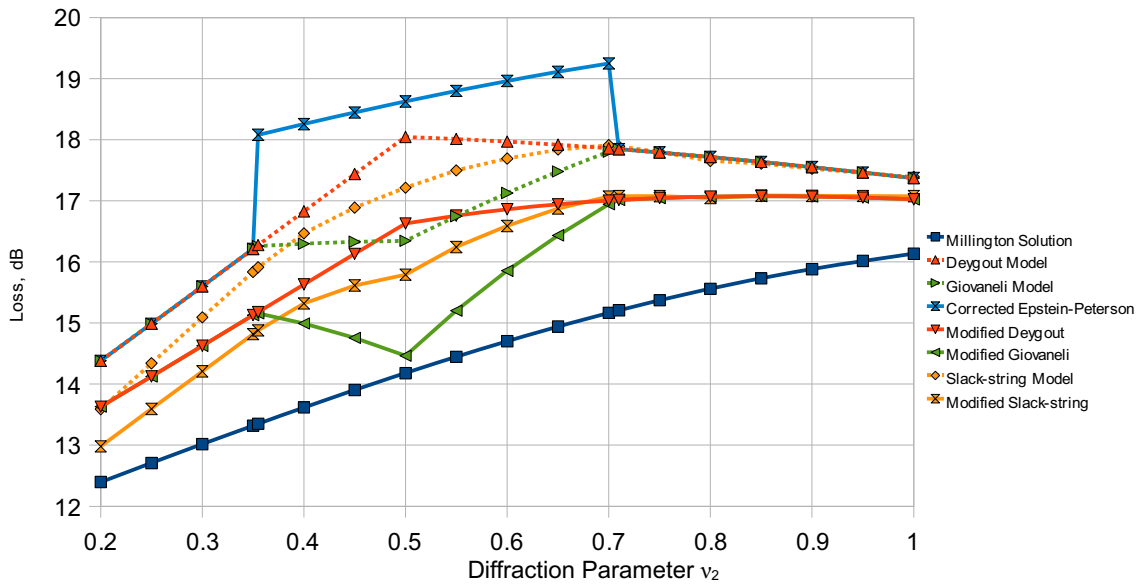


Figure 5. Double knife-edge models with $v_1 = 0.5$ and $\alpha = \pi/4$.

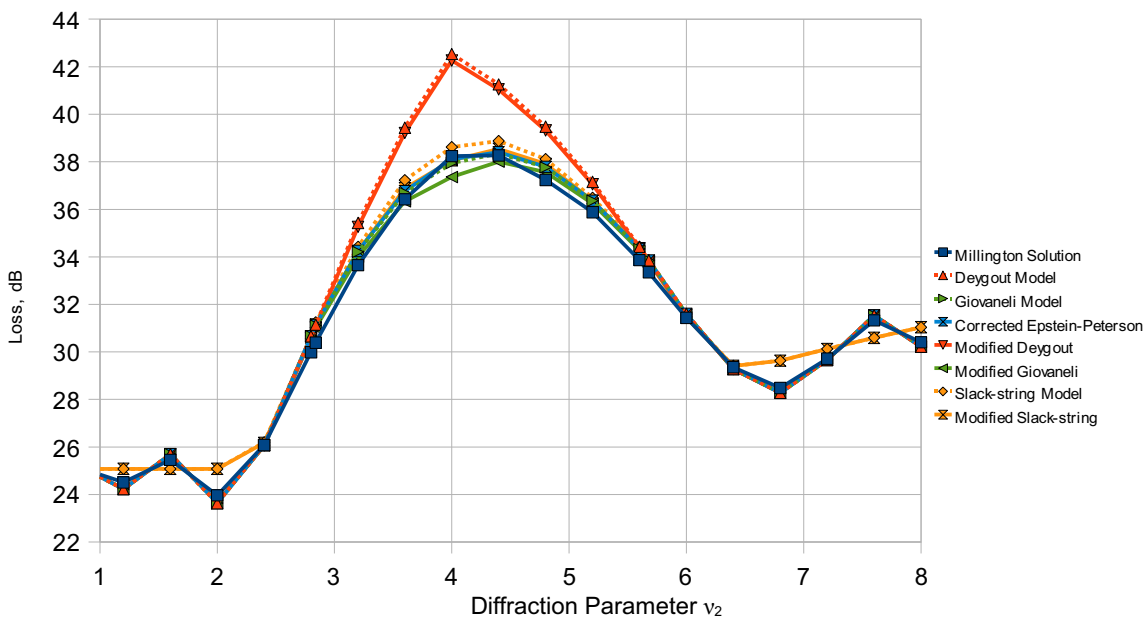


Figure 6. Double knife-edge models with $v_1 = 4$ and $\alpha = \pi/4$.

Figure 5 demonstrates all the models suffering from over-prediction at small diffraction angles, but this is helped by using the “modified” version of the models [4]. The small diffraction angles also result in discontinuity in the corrected Epstein-Peterson model, which disappears at large diffraction angles (figure 6).

Figure 6 also demonstrates that for large diffraction angles all models tested, except Deygout, agree well with the Millington solution. A correction factor for the Deygout model based on the trivial Millington solution for $v_1 = v_2 = 0$ has been suggested [8]. It may be possible to extend this to the general case of 3 or more knife-edges, but use of one of the other models which inherently avoid over-prediction with multiple horizons may be simpler. The “slack string” model cannot replicate the oscillation in the tails of the curves in figure 6, which Deygout, Giovanelli and Epstein-Peterson all show when accurately calculated from the Fresnel integral.

4. Testing model predictions and profile sensitivity against path measurements

A data set of carefully calibrated VHF and UHF measurements, performed between 1982 and 1993 in inland regions Australia, together with path profiles generated from 1:50,000 and 1:100,000 scale topographic maps with 10 and 20 m contours respectively, was used to test the accuracy of these models as general diffraction models. These profiles were linearly interpolated before adding “Earth bulge” for Earth radius factor $k_e = 1.33$. Only the 64 obstructed paths in the data set that did not have trees were used in this study, as tree heights are generally not accurately known. On these 64 paths, a total of 478 measurements were done, at different heights and at frequencies between 150 MHz and 1.5 GHz. All measurements were done between late morning and afternoon with the aim of Earth radius factor $k_e = 1.33$ being reasonably representative of the refractivity gradient at the time of measurement.

The main purpose of this study is to identify serious model discontinuities, which would be expected to produce extreme sensitivity to profile variation. After testing with the original path profile, Gaussian noise with an r.m.s. amplitude of 0.1 metre was added to the heights of the 0.25 km interpolated profile. The results of this testing for multiple knife-edge models are shown in table 1.

Initially, adjacent profile points forming part of the same obstruction were not grouped together and analysed as one broad obstruction. Instead, the profile was treated as consisting of a series of knife-edges 0.25 km apart. The corrected Epstein-Peterson model [6], cannot be used in this way, as the accumulation of over-prediction with small diffraction angles and closely spaced edges (figure 5) leads to massive over-prediction. Instead, the knife-edges identified by the P.526 cascaded cylinder model [2], were used for this model, and also repeated for the Giovanelli and slack-string models, as shown in the last three rows of table 1.

Multiple knife-edge model	Correlation of measured loss with predicted	Prediction Error (dB):		Difference (dB) with 0.1 m rms noise	
		Mean	Std. Dev.	Mean	Std. Dev.
P.526 Cascaded knife-edge	0.785	0.3	7.2	0.03	0.18
Deygout 5 worst edges	0.855	0.4	6.3	0.06	0.22
Giovanelli 5 worst edges	0.846	-0.2	6.2	0.04	0.24
Modified Deygout all points	0.858	0.8	9.1	0.01	1.01
Modified Giovanelli all points	0.861	-0.2	8.0	-0.02	1.22
Slack String all points	0.902	-5.3	5.4	0.03	0.16
Modified Slack String all points	0.832	-8.5	6.2	0.02	0.12
Corrected Epstein-Peterson *	0.829	-6.7	7.1	4.20	16.90
Giovanelli *	0.831	-7.4	6.7	2.99	10.83
Slack String *	0.874	-6.8	5.6	0.81	2.33

* Using knife-edges identified by P.526 cascaded cylinder model

Table 1. Multiple knife-edge model accuracy compared to measurements, and sensitivity to profile noise.

The slack-string model showed the lowest sensitivity to added profile noise, but the P.526 cascaded knife-edge model had the next lowest sensitivity, showing no evidence of the problems identified in the companion paper [4]. This may be due to these paths being generally lower diffraction loss (mean measured loss 24.9 dB).

The corrected Epstein-Peterson model showed extreme sensitivity to noise added to the profile. The

addition of noise caused broad single obstructions identified by the model to break up into a number of narrower obstructions. Using the slack-string model instead greatly reduced this sensitivity; this may be partly because this model allowed line-of-sight subpaths to have more than one intervening obstruction evaluated.

The complete P.526 Cascaded cylinder model was also tested against the same measurements, both as presented in the recommendation [2] using the corrected Epstein-Peterson model, and also using the Giovaneli [3] or the slack-string model instead, with results shown in table 2. In all cases, the sensitivity to added noise was slightly less than it was with the evaluation of the knife-edges alone, but in all three cases the error standard deviation was larger with the complete cascaded cylinder model. This appeared to be due to a tendency of the cascaded cylinder model to under-predict low loss paths and over-predict high loss paths.

Cascaded cylinder model – multiple knife-edge model used	Correlation of measured loss with predicted	Prediction Error (dB):		Difference (dB) with 0.1 m rms noise	
		Mean	Std. Dev.	Mean	Std. Dev.
Corrected Epstein-Peterson	0.838	-2.9	9.8	3.88	15.72
Giovaneli	0.832	-3.6	9.4	2.63	9.56
Slack String	0.857	-3.1	8.6	0.44	2.03

Table 2. Cascaded cylinder model accuracy compared to measurements, and sensitivity to profile noise.

5. Conclusions

The P.526 Cascaded Knife-edge model has been found to be reasonably accurate and immune to profile variation due to added noise, for the paths with measured diffraction losses all less than 49 dB studied in this paper, in contrast to the severe anomalies noted in [4] for a number of predicted high diffraction-loss paths.

A new method of estimating the diffraction loss of multiple knife-edge paths, the “slack-string” method, has been found to have very low sensitivity to noise added to the profiles of the paths studied in this paper, and to the differences between two nearly identical profiles studied in the companion paper [4]. Further work is needed to optimise the algorithm for this method, but it shows promise as a multiple knife-edge model to replace the corrected Epstein-Peterson model [6] in the P.526 cascaded cylinder model [2].

6. Acknowledgement

The authors wish to thank Martin Turner, Chris Bannah and Tomy Ng for their enthusiastic support of this collaboration between CSIRO and Telstra Corporation. We would also acknowledge the contribution of the late Robert Burrow and Malcolm Chamberlain who conducted some of the early path measurements used in this paper.

7. References

- [1] Deygout, J., “Multiple knife-edge diffraction of microwaves”, *IEEE Trans. Antennas Propagation*, vol. 14, pp. 480-489, July 1966.
- [2] International Telecommunication Union, “Recommendation ITU-R P.526-10, Propagation by diffraction”, Geneva 2007.
- [3] Giovaneli, C. L., “An analysis of simplified solutions for multiple knife-edge diffraction”, *IEEE Trans. Antennas Propagation*, vol. 32, pp. 297-301, March 1984.
- [4] Wilson, C. and Salamon, S., “Anomalies in the application of the cascaded knife-edge diffraction model”, *ClimDiff 2008*, paper Diff.14, Boulder Colorado USA, June 2008.
- [5] Epstein, J. and Peterson, D.W., “An experimental study of wave propagation at 850 MC”, *Proc. IEEE*, vol. 41, pp. 595-611, May 1953.
- [6] Beyer, J., “A GTD-based correction of the Epstein-Peterson method”, *IEEE Trans. Antennas Propagation*, vol. 52 No. 3, pp. 888-891, March 2004.
- [7] Millington, G., Hewitt, R. and Immirzi, F.S., “Double knife-edge diffraction in field-strength prediction”, *IEE Monograph 507E*, pp 419-429, March 1962.
- [8] Deygout, J., “Correction factor for multiple knife-edge diffraction”, *IEEE Trans. Antennas Propagation*, vol. 39, pp. 1256-1258, August 1991.